Lecture Notes in Physics 908

Elena Tobisch *Editor*

New Approaches to Nonlinear Waves

Springer

Lecture Notes in Physics

Volume 908

The Lecture Notes in Physics

The series Lecture Notes in Physics (LNP), founded in 1969, reports new developments in physics research and teaching-quickly and informally, but with a high quality and the explicit aim to summarize and communicate current knowledge in an accessible way. Books published in this series are conceived as bridging material between advanced graduate textbooks and the forefront of research and to serve three purposes:

- to be a compact and modern up-to-date source of reference on a well-defined topic
- to serve as an accessible introduction to the field to postgraduate students and nonspecialist researchers from related areas
- to be a source of advanced teaching material for specialized seminars, courses and schools

Both monographs and multi-author volumes will be considered for publication. Edited volumes should, however, consist of a very limited number of contributions only. Proceedings will not be considered for LNP.

Volumes published in LNP are disseminated both in print and in electronic formats, the electronic archive being available at springerlink.com. The series content is indexed, abstracted and referenced by many abstracting and information services, bibliographic networks, subscription agencies, library networks, and consortia.

Proposals should be sent to a member of the Editorial Board, or directly to the managing editor at Springer:

Christian Caron
Springer Heidelberg
Physics Editorial Department I
Tiergartenstrasse 17
69121 Heidelberg/Germany
christian.caron@springer.com

More information about this series at
http://www.springer.com/series/5304

Elena Tobisch
Editor

New Approaches to Nonlinear Waves

Springer

Editor
Elena Tobisch
Institute for Analysis
Johannes Kepler University
Linz, Austria

ISSN 0075-8450 ISSN 1616-6361 (electronic)
Lecture Notes in Physics
ISBN 978-3-319-20689-9 ISBN 978-3-319-20690-5 (eBook)
DOI 10.1007/978-3-319-20690-5

Library of Congress Control Number: 2015947251

Springer Cham Heidelberg New York Dordrecht London

Printed on acid-free paper

Springer International Publishing AG Switzerland is part of Springer Science+Business Media (www.springer.com)

Preface

The theory of nonlinear waves is located right at the intersection of the linear wave theory, the theory of nonlinear oscillations, and the theory of nonlinear partial differential equations (PDEs), radiating into numerous fields of applied science, including studies in oceanography, nonlinear optics, plasma physics, weather and climate prediction.

It is hard to imagine that just a few decades ago the same equations arising in different fields of science were studied independently of each other, and the phenomena which they describe were called by different names. Probably one of the most illustrative examples of this kind is the phenomenon discovered in early 1960s, which is named modulational instability in purely mathematical texts, while known as modulation instability in nonlinear optics, as Benjamin-Feir instability in theory of water waves, as Oraevsky instability in plasma physics, etc. etc.

Only in the late 1980s gradually began to crystallize the idea of creating a new *nonlinear science* that would synthesize all known results into a single overall scheme and would allow to describe them all in one and the same language. I remember the annual meeting of the physical branch of the Russian Academy of Sciences, traditionally held at the Institute of Oceanology in Moscow, where Vladimir Eugenievich Zakharov very emotionally expounded the idea of creating such a language and writing an encyclopedia on nonlinear science, in which all of the most important results would be collected in one place. The late V.I. Arnold, who was in the audience, said that such language has long been there and it's called mathematics. Roars of laughter drowned out the answer of V.E. Zakharov.

Every physicist knows how long the road is from the physical level of accuracy, which is sufficient for solving many theoretical and practical problems in physics, to a rigorous mathematical definition and proof. The simplest example, as very often in physics, gives us the study of the physical pendulum. Galileo studied its movement and discovered the phenomenon of resonance in 1637. The rigorous mathematical definition of resonance was given by Poincaré 250 years later. And without an accurate notion of resonance, most of the chapters in this book principally could not have been written. In fact, much of the modern theory of nonlinear waves could not have been developed.

Since then many years have flown, and the notion of nonlinear science has become an integral part of our scientific language, and the first encyclopedia of nonlinear science saw the light of day in 2002 already, thanks to the invaluable effort of the late Alwyn Scott, who edited this great work of more than 1000 pages, written by scholars from all over the world.

However, the science does not halt, and new questions are coming forth, to which there is no answer in this encyclopedia. How to describe both discrete and kinetic regimes of wave turbulence resting on a unified strict mathematical approach? What new physical phenomena can be described if Phillips' definition of resonance is generalized to the case of moderate nonlinearity? Why does generalized NLS describe weakly nonlinear processes in water waves and strong nonlinear processes in optics? Etc. etc.

Answers to these and some other questions are given in this volume. A brief overview of individual chapters of the book is provided in the introductory Chap. 1. I also tried to position all the subjects in a logical consequence, i.e., scientific results, yielding new questions and then new results and again new questions *ad infinitum*. The choice of topics, of course, is biased and reflects my research interests and expertise. The last and longest Chap. 8 in the book has been written by Lev Shemer, one of the best modern experimentalists with water waves. The main goal of this chapter is to demonstrate why direct comparison of theoretical and numerical results with experimental measurements is often challenging; the author discusses in detail experiments devised to provide a basis for evaluation of the domain of validity of a theoretical model.

Understanding came to me already in 2011 that time is ripe again for gathering stones in the theory of nonlinear waves. At first, it was transformed into the idea of organizing a series of regular bi-annual conferences called *Wave Interaction* (WIN) to discuss new and promising topics in the area. The idea of writing a book was already discussed at *WIN*-2012. The format and content of the present volume was finalized during several meetings being held in 2012–2014:

- (2012) *Wave Interaction (WIN-2012)*, 23–26 April (Johannes Kepler University Linz, Austria)
- (2013) *Thematic Program on the Mathematics of Oceans*, April 29–June 28 (Fields Institute for Research in Mathematical Sciences, Toronto, Canada)
- (2014) *Weak Chaos and Weak Turbulence*, 3–7 February (Max Planck Institute for the Physics of Complex Systems, Dresden, Germany)
- (2014) *Wave Interaction (WIN-2014)*, 23–26 April (Johannes Kepler University Linz, Austria)
- (2014) *Theory of Water Waves*, 14 July–8 August (Isaac Newton Institute, Cambridge, UK)

All chapters are based on talks delivered at these conferences by selected invited speakers. I am very grateful to all attendants of these conferences who actively helped me to make a choice of topics. I would like to mention particularly N. Akhmediev, T. Bridges, W. Craig, A. Degasperis, K. Dysthe, R. Grimshaw,

P. Janssen, C.C. Mei, M. Onorato, D. Pelinovsky, E. Pelinovsky, A. Pikovsky, D. Shepelyansky, V. Shrira, and S.K. Turitsyn.

My aim was to create a book accessible to graduate students, engineers and researchers working in various fields of physics and applied mathematics. Consequently, the authors tried to make their exposition as clear as possible without harming scientific rigor. All theoretical chapters contain not only a conceptual background, but also illustrative examples of how these new techniques and approaches can be applied to specific problems. I am very much obliged to all the authors of this volume for their contributions and their patience when handling my remarks and making revisions.

I am also greatly indebted to all reviewers of the individual chapters which took over the hard and unremunerated work that resulted in tangible improvement of the quality of this book.

I am specially grateful to Shalva Amiranashvili, whose invaluable remarks and suggestions allowed me to improve the text of the introductory chapter.

I also would like to thank Dr. Aldo Rampioni and Kirsten Theunissen, Editors of the Springer Series Lecture Notes in Physics, who constantly assisted me during the preparation of the manuscript.

Linz, Austria Elena Tobisch
April 2015

Contents

1 Introduction 1
Elena Tobisch
1.1 Brief Historical Overview 1
1.2 Main Notions 3
1.2.1 Resonance Clusters 6
1.2.2 Power Law Energy Spectrum 7
1.2.3 Detuned Resonances 8
1.2.4 Summary 10
1.3 Resonant Interactions 11
1.4 Modulation Instability 13
1.5 Frameworks 15
1.6 Reality Check 16
References 17

2 The Effective Equation Method 21
Sergei Kuksin and Alberto Maiocchi
2.1 Introduction 21
2.2 How to Construct the Effective Equation 22
2.3 Structure of Resonances 26
2.3.1 The Equations 27
2.3.2 Structure of Resonances for the NLS Equation 29
2.3.3 Structure of Resonances for CHM 30
2.4 NLS: The Power-Law Energy Spectrum 32
2.4.1 The Limit $L \to \infty$ 32
2.4.2 Power Law Spectra 37
2.5 CHM: Resonance Clustering 38
2.6 Concluding Remarks 40
References 41

3 On the Discovery of the Steady-State Resonant Water Waves 43
Shijun Liao, Dali Xu, and Zeng Liu
3.1 Introduction 44
3.2 Basic Ideas of Homotopy Analysis Method 46
3.3 Steady-State Resonant Waves in Constant-Depth Water 52
3.3.1 Mathematical Formulation 52
3.3.2 Steady-State Resonant Waves in Deep Water 59
3.3.3 Steady-State Resonant Waves in Finite Depth Water 69
3.4 Steady-State Class-I Bragg Resonant Waves 71
3.4.1 Mathematical Formulations 74
3.4.2 Brief Results 75
3.5 Experimental Observation 79
3.6 Concluding Remarks 79
References 81

4 Modulational Instability in Equations of KdV Type 83
Jared C. Bronski, Vera Mikyoung Hur, and Mathew A. Johnson
4.1 Introduction 83
4.2 Periodic Traveling Waves of Generalized KdV Equations 85
4.2.1 Some Explicit Solutions 86
4.2.2 General Existence Theory 89
4.3 Formal Asymptotics and Whitham's Modulation Theory 92
4.3.1 Linear Dispersive Waves 92
4.3.2 Nonlinear Dispersive Waves 94
4.4 Rigorous Theory of Modulational Instability 98
4.4.1 Analytic Setup 98
4.4.2 Modulational Instability in Generalized KdV Equations 101
4.4.3 Connection to Whitham Modulation Theory 108
4.4.4 Evaluation of Δ_{MI} 110
4.5 Applications 111
4.5.1 The KdV Equation 112
4.5.2 The Modified KdV Equation 113
4.5.3 The Schamel Equation 115
4.5.4 Extensions to Equations with Nonlocal Dispersion 116
4.6 Concluding Remarks 130
References 130

5 Modulational Instability and Rogue Waves in Shallow Water Models 135
R. Grimshaw, K.W. Chow, and H.N. Chan
5.1 Introduction 135
5.2 Korteweg-de Vries Equations 137
5.2.1 Modulational Instability 137
5.2.2 Breathers 137

5.3 Boussinesq Model 140
5.3.1 Modulational Instability 141
5.3.2 Breathers 141
5.4 Hirota-Satsuma Model 142
5.4.1 Modulational Instability 143
5.4.2 Breathers 144
5.5 Discussion 146
References 149

6 Hamiltonian Framework for Short Optical Pulses 153
Shalva Amiranashvili
6.1 Introduction 153
6.1.1 Ultrashort Pulses 153
6.1.2 Envelope Definition 155
6.2 Poisson Brackets 161
6.2.1 Discrete Systems 161
6.2.2 Complex Variables 165
6.2.3 One Continuous Field 168
6.2.4 Canonical Bracket for Two Fields 171
6.2.5 GZF Bracket for Two Fields 173
6.3 Pulses in Optical Fibers 176
6.3.1 Problem Setting 177
6.3.2 Forward and Backward Waves 179
6.3.3 Envelope Equations 180
6.4 Hamiltonian Description of Pulses 183
6.4.1 z-Propagation 184
6.4.2 z-Hamiltonian 185
6.4.3 Energy Transport 190
6.4.4 Photon Number 191
6.4.5 Analytic Signal 191
6.5 Concluding Remarks 192
References 193

7 Modeling Water Waves Beyond Perturbations 197
Didier Clamond and Denys Dutykh
7.1 Introduction 197
7.2 Preliminaries 199
7.3 Variational Formulations 200
7.4 Examples 203
7.4.1 Shallow Water: Serre's Equations 203
7.4.2 Deep Water: Generalized Klein–Gordon Equations 205
7.4.3 Arbitrary Depth 207
7.5 Discussion 207
References 208

8 Quantitative Analysis of Nonlinear Water-Waves: A Perspective of an Experimentalist 211
Lev Shemer
8.1 Introduction 211
8.2 The Experimental Facilities 214
8.3 The Nonlinear Schrödinger Equation 215
8.4 The Modified Nonlinear Schrödinger (Dysthe) Equation 226
8.4.1 Formulation of Temporal and Spatial Evolution Problems ... 226
8.4.2 Experiments on Spatial and Temporal Evolution of Wave Groups Based on Digital Video Image Processing 230
8.4.3 Experimental Studies of Evolution of Peregrine Breather 239
8.5 The Spatial Zakharov Equation 245
8.5.1 The Model Equations 245
8.5.2 The Spatial Zakharov Equation vs. the Dysthe Model 248
8.5.3 Nonlinear Focusing Based on the Spatial Zakharov Equation 257
8.6 Statistics of Nonlinear Unidirectional Water Waves 269
8.7 Discussion and Conclusions 286
References 290

Index 295

List of Contributors

Shalva Amiranashvili Weierstrass Institute for Applied Analysis and Stochastics, Berlin, Germany

Jared C. Bronski University of Illinois Urbana-Champaign, Urbana, IL, USA

H.N. Chan Department of Mechanical Engineering, University of Hong Kong, Pokfulam, Hong Kong

K.W. Chow Department of Mechanical Engineering, University of Hong Kong, Pokfulam, Hong Kong

Didier Clamond Université de Nice – Sophia Antipolis, Laboratoire J.A. Dieudonné, Parc Valrose, Nice Cedex 2, France

Denys Dutykh LAMA, UMR 5127 CNRS, Université de Savoie, Le Bourget-du-Lac Cedex, France

Roger Grimshaw Department of Mathematics, University College London, London, UK

Vera Mikyoung Hur University of Illinois Urbana-Champaign, Urbana, IL, USA

Mathew A. Johnson University of Kansas, Lawrence, KS, USA

Sergey Kuksin CNRS and I.M.J, Université Paris-Diderot-Paris 7, Paris, France

Shijun Liao Shanghai Jiao Tong University, Shanghai, China

Zeng Liu Shanghai Jiao Tong University, Shanghai, China

Alberto Maiocchi Dipartimento di Matematica, Università degli Studi di Milano, Milano, Italy

Lev Shemer School of Mechanical Engineering, Tel Aviv University, Ramat Aviv, Israel

Elena Tobisch Institute for Analysis, Johannes Kepler University Linz, Linz, Austria

Dali Xu Shanghai Jiao Tong University, Shanghai, China

Acronyms

Here is the list of acronyms frequently used in this volume:

CHM	Charny-Hasegawa-Mima equation
IST	Inverse Scattering Transform
(g)NLS	(generalized) Nonlinear Schrödinger equation
(m)NLS	(modified) Nonlinear Schrödinger equation
(g)KdV	(generalized) Korteweg–de Vries equation
(m)KdV	(modified) Korteweg–de Vries equation
HAM	Homotopy Analysis Method
MI	Modulational Instability
ODE	Ordinary Differential Equation
PB	Peregrin Breather
PDE	Partial Differential Equation
RVP	Relaxed Variational Principle
SVEA	Slowly Varying Envelope Approximation
WTT	Weak (Wave) Turbulence Theory

Chapter 1
Introduction

Elena Tobisch

Abstract In the first chapter, we throw a brief glance at the topics presented in the following chapters and their place in the context of the general theory of nonlinear wave systems with dispersion. Starting with the concept of the wave resonance, we proceed through the formalism and presently known results in the theory of discrete and kinetic wave turbulence to the list of open questions and possible theoretical generalizations. At the end of the introductory chapter, we outline a few challenging problems in the area of matching theory and experiment, generally overlooked.

1.1 Brief Historical Overview

The study of nonlinear waves started over 150 years ago with seminal works of Stokes [45] and Riemann [42] and continues to evolve rapidly to this day.

One of the most important developments in mathematical physics in the past 40 years is the development of the method of Inverse Scattering Transform (IST), [8]. The method can be regarded as a nonlinear analogue of the Fourier transform and can be applied to a number of exactly solvable model equations such as the Korteweg-de Vries equation (KdV), nonlinear Schrödinger equation (NLS), Kadomtsev-Petviashvili equation and some others. The great success of this method is due to the fact that it allows to find *exact* solutions of some nonlinear PDEs, without explicit restrictions on the magnitude of their nonlinearity. This does not exclude, of course, introduction of one or more small parameters while deriving a specific model PDE.

The most known particular solution of this kind has been called *soliton* in 1965 [48], though first observed as a hydrodynamical phenomenon by John Scott Russell in 1834 while conducting experiments to determine the most efficient design for channel boats. These solutions have the characteristic property to resume their shape after highly nonlinear mutual interactions.

E. Tobisch (✉)
Johannes Kepler University, Linz, Austria
e-mail: Elena.Tobisch@jku.at

E. Tobisch (ed.), *New Approaches to Nonlinear Waves*, Lecture Notes in Physics 908, DOI 10.1007/978-3-319-20690-5_1

This remarkable convergence of theory with practice attracted great attention of the scientific community to this novel method. It turned out that the set of solutions which can be found with the IST is much richer. For example, besides solitons it also contains kinks, breathers, multi-soliton solutions, to name a few. Later these exact solutions were observed in many fields of physics other than fluid mechanics, e.g. nonlinear optics, plasma physics, radioelectronics, etc. The modern state-of-the-art in experimental observation of various exact solutions in a laboratory wave tank will be given in Chap. 8 of this book. During the last 50 years all these outstanding developments were discussed in numerous journals, monographs and volumes of collected papers. We do not provide here a complete literature review. As two reference points in this field one can use the monumental *Encyclopedia of Nonlinear Science* [44] written by Scott and the more recent monograph of Osborne [36].

One of the main drawbacks of the IST is that the class of integrable PDEs is only a tiny part of all equations appearing in mathematical physics, and probably not even the most interesting class. As students of the late Vladimir Arnold remember, he liked to say that if an equation is integrable, then it has necessarily lost some very important information about the world around us, for example, about chaos.

Another general approach to the study of nonlinear problems consists in introducing into equations one or more small parameters which can be chosen in a number of ways, depending on the phenomenon under consideration. For instance, wave steepness $\varepsilon = Ak$ (here k is the wavenumber and A is the wave amplitude) is taken as a small parameter while studying modulation instability in the frames of both KdV-type and NLS-type equations. On the other hand, in soliton studies a small parameter for KdV-type equations is chosen as $\varepsilon = A/h$, where h is the depth of undisturbed fluid.

The presence of a small parameter ε is used in fluid dynamics to reduce the original PDE problem to the study of resonantly interacting waves whose time evolution is governed by one or more systems of nonlinear ordinary differential equations (ODEs). Various technical questions about this reduction and some properties of resulting dynamical systems, resonance curves, invariants, etc. were discussed in [28], which is presumably the first volume devoted to the nonlinear theory of wave propagation and edited by Lighthill in 1967. The first laboratory experiments on wave resonances have been also described in that volume.

On the other hand, practical needs stemming from oceanography led Phillips [38] in 1960 to the idea of considering coupled dynamics of ODEs in statistically averaged sense. Later this approach was successfully finalized by Hasselmann [10] in 1962, who derived the first wave kinetic equation for surface water waves in deep water possessing 4-wave interactions. Soon afterwards similar wave kinetic equations were derived for other 3- and 4-wave systems. Henceforth, the kinetic approach, based on *statistical description* of a weakly nonlinear wave system, became the central topic of the Wave Turbulence Theory (WTT).

The first stationary solution of the wave kinetic equation was found by Zakharov and Filonenko in 1967 [49] for capillary water waves. Their method was later successfully applied to other wave kinetic equations; details can be found in the

original monograph on the WTT published in 1992 by Zakharov et al. [51]. The developments in the WTT during the next 20 years are summarized by Nazarenko in his comprehensive educational volume [34].

The following years highlighted a list of important open problems of the WTT, coming mostly from experiments (e.g. nonexistence of an inertial interval) but also the lack of rigor in the underlying mathematical theory. An excellent review with the list of open problems was written by Newell and Rumpf in 2011 [35]. All open problems can be conventionally divided into internal problems of the theory (e.g. divergence of the cumulants) and external problems coming from the theory's limited applicability.

The most significant external problem of the WTT is the description of large scale systems, also known as resonators, with characteristic wavelengths comparable to the system size. In this practically important case the wave kinetic equation does not apply, having been obtained in the large box limit, i.e. for wave lengths much smaller than the size of the box. Hence, the need for novel approaches was realized. Several attempts were undertaken to extend the WTT to include large scale systems into the overall picture. A non-exhaustive list of recent attempts includes the frozen [39], mesoscopic [52], laminated and discrete [13] and finite-dimensional [29] wave turbulence theories.

The main feature of large scale systems is that the set of resonantly interacting modes can be partitioned in the Fourier space into non-intersecting subsets with independent time evolution, which *does not allow* a statistical description of such a system.

This fundamental fact was established for the first time by Kartashova in 1990 [14] while the general theory of these systems is presented in her monograph [19]. The new approach was called *discrete* WTT in contrast to the original WTT, which is referred to nowadays as the *kinetic* WTT. Until recently, any rigorous transition between discrete and kinetic regimes in the WTT was not known. Very recently a theory developed by Kuksin and his disciples, presented in Chap. 2, finally yielded a concise answer to the question whether discrete or kinetic regime will be observed as a result of time evolution of a given weakly nonlinear system.

Before proceeding with a more detailed analysis of methods and approaches presented in this volume, we shall give a few simple definitions and present some ideas needed for further understanding.

1.2 Main Notions

It is inherent to human nature to describe the external world in terms of different objects and interactions between them. A physicist, more focused on the practical application of his theoretical descriptions, is always trying to find a number of simple basic objects with clear features, and then combine them into more complex objects. An ideal set of simple objects is given by linear Fourier harmonics which

are solutions of linear PDEs with constant coefficients

$$\psi = A \exp\{i\,[\mathbf{kx} - \omega t]\} \tag{1.1}$$

which are called waves in physics for an obvious reason (for real wave vector and frequency). Accordingly, A, $\mathbf{k}$ and ω are called wave amplitude, wave vector and wave frequency, while $\mathbf{k}$ and t are space and time variables. Direct substitution of ψ into a linear PDE yields (for periodic boundary conditions) a polynomial connection between $\mathbf{k}$ and ω which is called dispersion relation (or dispersion function), e.g.

$$L(\psi) = \psi_{tt} - \psi_{xxxx} = 0 \quad \Rightarrow\ \omega^2(k) = k^4, \tag{1.2}$$

where $k = |\mathbf{k}|$. Accordingly, a nonlinear PDE possessing time- and space-like variables and linear part with wave-like solutions is called an evolutionary dispersive PDE. Notice that the standard mathematical classification into elliptic, hyperbolic and parabolic PDEs is based on the form of a PDE while the physical classification—into dispersive and non-dispersive PDEs—is based rather on the form of their solutions, and they are not complementary [47].

Notoriously, there is no general method for solving an arbitrary nonlinear PDE. On the other hand, there exist some general methods for finding *approximate* solutions of a *weakly* nonlinear evolutionary dispersive PDE which can be written as a perturbation of the linear equation $\mathcal{L}(\varphi) = 0$

$$\mathcal{L}(\varphi) = \varepsilon \mathcal{N}(\varphi) \tag{1.3}$$

where $\mathcal{N}$ is an arbitrary nonlinear operator and ε is a small parameter, $0 < \varepsilon \ll 1$.

Indeed, if nonlinearity $\varepsilon\mathcal{N}(\varphi)$ is small enough, as it usually happens in many applied problems, the general form of solutions of Eq. (1.3) remains the same as in Eq. (1.1), only the amplitude A turns into a slowly changing function of time, $A = A(\tau)$, $\tau \sim \varepsilon^{\alpha}$ for some rational α. If waves with slowly changing amplitudes do not form a resonance, the overall picture is virtually identical to the linear case. If resonance conditions are satisfied and $\varepsilon\mathcal{N}(\varphi)$ remains small, an unlimited growth of solutions occurs and this is an interesting case to study. The resonant conditions read

$$\omega_1 \pm \omega_2 \pm \ldots \pm \omega_N = 0, \tag{1.4}$$

$$\mathbf{k}_1 \pm \mathbf{k}_2 \pm \ldots \pm \mathbf{k}_N = 0, \tag{1.5}$$

where $\mathbf{k}_j$, $j = 1, \ldots, N$ are the wavevectors of resonantly interacting waves and wave frequencies $\omega_j = \omega(\mathbf{k}_j)$, $j = 1, \ldots, N$ are related to $\mathbf{k}_j$ through the dispersion relation. This implies in particular that, for example, 3- and 4-wave resonances can be regarded on different time scales and, thus, studied independently. In a 3-wave system the dynamical time scale (discrete WTT) $\tau_{dyn} \sim \varepsilon^{-1}$ while the kinetic time scale is $\tau_{kin} \sim \varepsilon^{-2}$.

In particular, resonance conditions for a 3-wave system read

$$\omega_1 + \omega_2 = \omega_3, \quad \mathbf{k}_1 + \mathbf{k}_2 = \mathbf{k}_3; \quad \omega_j = \omega(\mathbf{k}_j) \tag{1.6}$$

and any multi-scale method produces a dynamical system for complex amplitudes of three resonantly interacting waves (in canonic variables a_j):

$$\dot{a_1} = V_{12}^3 a_2^* a_3, \quad \dot{a_2} = V_{12}^3 a_1^* a_3, \quad \dot{a_3} = -V_{12}^3 a_2 a_3, \quad V_{12}^3 = V_{12}^3(\mathbf{k}_1, \mathbf{k}_2, \mathbf{k}_3) \tag{1.7}$$

which should be supplemented by 3 complex conjugate equations in order to produce a completely integrable system. Such an abbreviated form of dynamical system is commonly used in fluid dynamics as $a(\mathbf{k}) = a^*(-\mathbf{k})$; accordingly the word *mode* is a common word uniting waves with wave vectors $\mathbf{k}$ and $-\mathbf{k}$. The form of the initial PDE is now hidden in the form of the interaction coefficient V_{12}^3 which is a function of the wave vectors satisfying resonance conditions given by Eq. (1.6).

If no 3-wave resonance occurs, one proceeds the same way looking for a 4-wave resonance,[1] with resonance conditions being

$$\omega_1 \pm \omega_2 \pm \omega_3 \pm \omega_4 = 0, \quad \mathbf{k}_1 \pm \mathbf{k}_2 \pm \mathbf{k}_3 \pm \mathbf{k}_4 = 0, \tag{1.8}$$

and so on. Dynamical systems, both for 3- and 4-wave resonances can be solved analytically in terms of Jacobian elliptic functions. More details and examples can be found in [19].

Now that an isolated resonance (say, a triad or a quartet) is fully described, there exist two different frameworks for further study of the initial PDE.

The first framework is called *discrete* WTT; in this case an approximate solution to the original PDE given by Eq. (1.3) is constructed without making use of any additional assumptions.

The second framework is called *kinetic* WTT. It does not provide any direct solution of the initial PDE; instead, the original PDE is replaced with a wave kinetic equation whose stationary solutions describe approximately the energy spectrum of the original PDE. Some additional assumptions are used while applying this approach.

A brief description of these two frameworks is given below. It aims to demonstrate the most important open problem in the WTT, namely, the lack of constructive transition between discrete and kinetic regimes.

[1] There is no general theory answering the question whether indeed exact 4-wave resonances or approximate 3-wave resonances should be studied in this case. Even an unambiguous definition of approximate resonance is not yet available, [46]. This is the reason why we do not consider this topic, which undoubtedly has a great potential in applications, in the present volume. A brief overview of the problem is given in Sect. 1.2.3.

1.2.1 Resonance Clusters

Discrete WTT describes weakly nonlinear wave systems with periodic or zero boundary conditions, i.e. waves with length comparable to the size of the interaction domain. This means that the resonance conditions given by Eqs. (1.6), (1.8) should be fulfilled for wave vectors with integer coordinates. Existence of independent sets of resonantly interacting modes (called *resonance clusters*) among many non-resonant modes and other general properties of wave resonant systems with discrete spectra were demonstrated in early 1990s in [14, 15]. Physical implications of these results were discussed in [16] which is the foundational paper of the discrete WTT.[2]

To understand what a resonance cluster is, let us imagine that in a 3-wave system with resonance conditions (1.6) we have found two resonant triads which have one mode $\mathbf{k}_3$ in common:

$$\omega_1 + \omega_2 = \omega_3, \quad \mathbf{k}_1 + \mathbf{k}_2 = \mathbf{k}_3, \tag{1.9}$$

$$\omega_4 + \omega_5 = \omega_3, \quad \mathbf{k}_4 + \mathbf{k}_5 = \mathbf{k}_3. \tag{1.10}$$

Such a system is called a 2-triad resonance cluster and is described by the dynamical system

$$\dot{a_1} = V^3_{12} a^*_2 a_3, \quad \dot{a_2} = V^3_{12} a^*_1 a_3, \quad \dot{a_3} = -V^3_{12} a_2 a_3 - V^3_{45} a_4 a_5, \tag{1.11}$$

$$\dot{a_4} = V^3_{45} a^*_5 a_3, \quad \dot{a_5} = V^3_{45} a^*_4 a_3. \tag{1.12}$$

A resonance cluster can contain from a few to many hundred waves and energy exchange among the waves of a cluster can be periodic or chaotic, while non-resonant modes do not change their energy at the corresponding time scale and are called *frozen* modes. Their existence has been first demonstrated in numerical simulations with spherical planetary waves in [16] and later on for capillary waves in [39, 40] where the term "frozen" modes has been first introduced.

The dynamical system for an arbitrary resonance cluster is energy conserving. When all the clusters are constructed and their dynamical systems solved (analytically or numerically), an approximate solution $\tilde{\varphi}$ of the original PDE given by Eq. (1.3) can be found:

$$\tilde{\varphi} = \sum_{\mathbf{k}_j \in \{RC\}} a_j(\tau) \exp i\{\mathbf{k}_j \mathbf{x} - \omega_j t\} + \text{c.c.}, \tag{1.13}$$

where the sum is taken over all resonance clusters $\{RC\}$ and c.c. means complex conjugate. The so-called *slow* dynamical time is $\tau_{dyn} \sim \varepsilon^{-1}$ in a 3-wave system and

[2] Modern terminology "discrete WTT" and "resonance clusters" has been first introduced almost 20 years later, in [18].

$\tau_{dyn} \sim \varepsilon^{-2}$ in a 4-wave system. Another (equivalent) way to represent $\tilde{\varphi}$ is to sum all Fourier modes but additionally use the multiplicative Kronecker symbol in the r.h.s. of Eq. (1.13) which is equal to 1 for resonant modes $\mathbf{k}_j$ and 0 for non-resonant ones, as it is done in Chap. 2.

1.2.2 Power Law Energy Spectrum

Kinetic WTT describes long-time evolution of a system of weakly nonlinear dispersive waves possessing resonances. To this aim, a wave kinetic equation is deduced which is in a sense similar to the Bolzmann kinetic equation (indeed, both are different limiting cases of the quantum Bose-Einstein equation) and is used for describing the evolution of wave energy spectra in Fourier space. Kinetic equations have been used since late 1920s in optics and plasma physics.

A qualitative leap that led to the creation of a constructive theory was the development of a new method for finding stationary solutions of kinetic equations in 1967 [49]. These stationary solutions are called Kolmogorov-Zakharov energy spectra and have power-law shape, $\sim |\mathbf{k}|^{-\alpha}$, $\alpha > 0$ if dispersion function $\omega(\mathbf{k})$ is proportional to some rational power of $|\mathbf{k}|$. Here α depends only on the form of the dispersion function and the space dimension.

For this great achievement one had to pay by introducing some additional assumptions which are absent in the discrete WTT. The main idea underlying the deduction of the wave kinetic equation is the transition from the dynamical description given by Eq. (1.13) to the statistical one given in full detail in [51].

First of all, assuming that wave phases are random and independent one can eliminate them by transition from dynamical variables to interaction representation in terms of correlation functions, $\langle a_k a_k^* \rangle$ in a 3-wave system. Further on, two limiting procedures are performed: the size of the spectral domain goes to infinity and the small parameter to zero, $\varepsilon \to 0$, yielding the 3-wave kinetic equation

$$\frac{\mathbf{d}}{\mathbf{d}t}\langle a_3^2 \rangle = \int |V_{12}^3|^2 \delta(\omega_3 - \omega_1 - \omega_2)\delta(\mathbf{k}_3 - \mathbf{k}_1 - \mathbf{k}_2) \cdot (a_1 a_2 - a_1^* a_3 - a_2^* a_3)\mathbf{d}\mathbf{k}_1 \mathbf{d}\mathbf{k}_2. \tag{1.14}$$

Unlike a dynamic system for a resonance cluster, the wave kinetic equation is obtained as a result of averaging and limiting procedures which do not necessarily conserve the energy. To ensure that we are still dealing with an energy conserving system, one has to introduce forcing and dissipation far separated in the Fourier space, and *to assume* the existence of an energy conserving *inertial interval* in between.

Making some more assumptions, stationary solutions of the kinetic equation given by Eq. (1.14) are found which exist within the inertial interval, and they are called Kolmogorov-Zakharov energy spectra. These solutions are valid within the

inertial interval and at *kinetic* time scales: $\sim \varepsilon^{-2}$ in a 3-wave system and $\sim \varepsilon^{-4}$ in a 4-wave system.

1.2.3 Detuned Resonances

An unambiguous definition of a detuned resonance (also called quasi-resonance and approximate resonance) is not yet available [46]. We illustrate this using as an example a 3-wave system. Usually a detuned resonance is described by three vectors which approximately satisfy the resonance conditions given by Eq. (1.6), i.e.

$$|\omega(\mathbf{k}_1) + \omega(\mathbf{k}_2) - \omega(\mathbf{k}_3)| = \Delta\omega, \ \mathbf{k}_1 + \mathbf{k}_2 = \mathbf{k}_3, \tag{1.15}$$

with $\Delta(\omega) > 0$ being called resonance detuning.

However, such a definition does not define a unique object. In fact, this definition is quite open, admitting solutions with *completely different dynamics*. We mention just two of them to emphasize the point: *quasi-resonances*, all three wave vectors having integer coordinates satisfying Eq. (1.15), and *non-resonant interactions*, with real wave numbers. The difference between these two types of detuned resonances is illustrated schematically in the Fig. 1.1.

Three wave vectors $(m_1, n_1), (m_2, n_2), (m_3, n_3)$ satisfying the exact conditions of resonance given by Eq. (1.6) are connected by bold red lines. Quasi-resonant triads $(m_1, n_1), (m_2 - 1, n_2), (m_3, n_3)$ and $(m_1, n_1), (m_2 + 1, n_2), (m_3, n_3)$ are shown by (green) dashed-dotted and (blue) dotted lines correspondingly. Obviously, the set

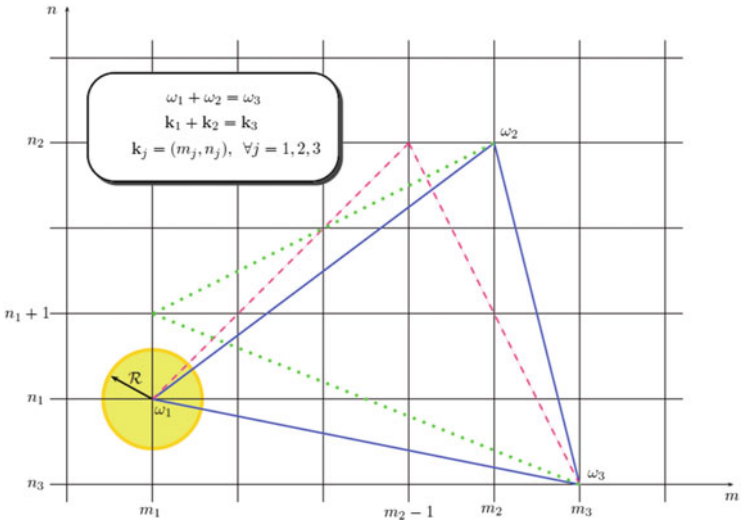

Fig. 1.1 Graphical illustration of the notion of resonance detuning (Color figure online)

of all quasi-resonances for a given resonant triad is countable (finite in a limited spectral domain) and is defined *uniquely*.

On the other hand, detuning for non-resonant interactions can be regarded e.g. as a circle with radius R around one node of the lattice (M, N) shown as a (yellow) circle around the node (m_2, n_2). Obviously, any point on its circumference gives the same resonance detuning $\Delta\omega$. This means that an infinite number of waves with different wavelengths and different phases will produce the same $\Delta\omega$, i.e. in this case *no unique representation* in the k-space exists for the set of non-resonances.

The main difference between these two types of detuned resonances is that in the case of quasi-resonances frequency detuning $\Delta\omega$ is bounded from below [17], while for the case of non-resonant interactions detuning can be arbitrary small.

This leads to the situation that at first sight is paradoxical. On the one hand, the general dynamics of a non-resonant triad with small enough $\Delta\omega$ is well understood: it well known that their contribution to energy exchange is negligible at time scale t/ε, e.g. [6, 37]. On the other hand, recent research of Annenkov and Shrira demonstrate that detuned resonances of wind waves can be used for constructing the so-called generalized kinetic equation (GKE) [1].

The GKE has faster time evolution than the Hasselmann equation given by Eq. (1.14) with $\omega \sim (m^2 + n^2)^{1/4}$ and "includes all interactions, although only those not too far from resonance contribute to spectral evolution" [2]. The study of wave field dynamics under squall action demonstrates that temporal spectral evolution of the GKE and the Hasselmann equation are almost identical—before the appearance of the squall but not after it. During the squall, a dip in the shape of the energy spectrum is observed in the GKE which is followed by "noticeably more narrow spectra characterized by a substantially higher peakedness parameter" [2].

Quite similar effect can be observed in numerical simulations with the simplest possible model of a detuned resonance triad. Indeed, let us regard dynamical system of 3 resonantly interacting spherical Rossby waves

$$\begin{cases} N_1\dot{A}_1 = -2iZ(N_2 - N_3)A_2^*A_3 \exp\{-i\widetilde{\Delta\omega}T\}, \\ N_2\dot{A}_2 = -2iZ(N_3 - N_1)A_1^*A_3 \exp\{-i\widetilde{\Delta\omega}T\}, \\ N_3\dot{A}_3 = 2iZ(N_1 - N_2)A_1A_2 \exp\{i\widetilde{\Delta\omega}T\} \end{cases} \tag{1.16}$$

(and their complex conjugate equations) where $\widetilde{\Delta\omega} := \Delta\omega/\varepsilon$ [23]. Chose the coefficients Z, N_j corresponding to a fixed resonance triad (the data are given in [22]) and plot the energy variation range as a function of the frequency detuning (shown in Fig. 1.2).

The fact that a detuned resonant triad may have a substantially larger energy variation range than the corresponding exact resonant triad contradicts physical intuition. However, there exists a simple qualitative explanation of this phenomenon, in terms of quasi-resonances and approximate interaction defined above.

Indeed, our intuition comes from the *linear* pendulum usually taken as the model of a linear wave, and an exact resonance is due to the action of an external force which is modeled by the nonlinearity $\mathcal{N}$ on the right hand side of Eq. (1.3), with

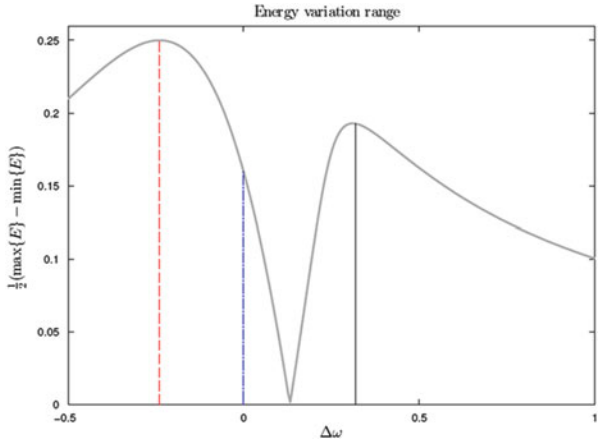

Fig. 1.2 Typical dependency of the energy variation range $\Delta\mathcal{E}$ on the frequency detuning $\Delta\omega$. The *vertical* (*red*) *dashed* and *black solid lines* show local maximums of $\Delta\mathcal{E}$ while the (*blue*) *dash-dotted line* shows the location of the exact resonance (Color figure online)

periodic boundary conditions. Exact and quasi-resonances then can be regarded as a particular case of free motion of an *elastic* pendulum [19].

In the case of approximate interactions detuning is so small that it can not be implemented via the nonlinearity $\mathcal{N}$ and we need to introduce an additional term into our initial PDE,

$$\mathcal{L}(\varphi) = \varepsilon\mathcal{N}(\varphi) + \mathcal{F} \tag{1.17}$$

where $\mathcal{F}$ is a small non-zero forcing/dissipation term and the resonance detuning $\widetilde{\Delta\omega}$ is regarded as frequency of an external force. Accordingly, in this case we have a system similar to elastic pendulum under the action of an external force, and it has exact resonances different from those of a freely moving elastic pendulum. That is, an approximate resonance in a system governed by Eq. (1.3) may become an exact resonance in the frame of systems described by Eq. (1.17).

This is a novel area of research which is not yet ripe for a constructive theory and therefore it is not presented in our further chapters.

1.2.4 Summary

Summing up the aforesaid, two regimes are described in which weakly nonlinear dispersive wave system can exist, for each on its own time scale. However, answers to a multitude of important questions are not known. It transition from discrete to kinetic regime always possible? Can independent resonance clusters survive during long time evolution under the action of forcing and/or dissipation? If yes, is it possible to distinguish between these two situations beforehand taking into account only the form of the original PDE and the boundary conditions? etc.

Answers to these questions are given in the Chap. 2, where a novel theoretical approach is described which uses the same main assumption as the WTT: there exist independent time scales for 3- and 4-wave resonant interactions.

This assumption is violated in fluid dynamic systems if the small parameter $\varepsilon \sim \mathcal{O}(10^{-1})$, as has been shown by direct numerical simulations in [1]. This observation opens up two important research areas.

The first is related to *detuned resonances* of waves with *linear* dispersion which was discussed above. The second important approach in the further study of wave resonances is examination of *exact* resonances of waves with *nonlinear* dispersion function depending on wave amplitudes. This study is performed in the Chap. 3.

1.3 Resonant Interactions (Chaps. 2 and 3)

In Chap. 2 the same weakly nonlinear dispersive wave systems are studied as in discrete and kinetic WTT. This means that: (a) nonlinear resonances are formed by modes with linear dispersion (i.e. with dispersion function not depending on wave amplitudes); and (b) the small parameter in the system is small enough to provide time-scale separation for 3- and 4-wave resonances.

A novel approach of studying these systems is presented in Chap. 2. It allows to answer the questions formulated at the end of the previous section and gives constructive conditions for determining whether or not transition from discrete to kinetic regime exists. This method consists of two main steps. In the first step the so-called *effective equation(s)* is (are) derived from the original PDE with stochastic forcing and dissipation. The resulting effective equations include only resonant interactions and are obtained using special averaging techniques for stochastic PDEs developed in [26].

If one effective equation is sufficient to describe all resonant interactions in Fourier space, then the second step is applied and energy spectrum can be obtained. The shape of this spectrum is power-law similar to the predictions of kinetic WTT, however the dissipation coefficient ν enters explicitly into the exponent, $\sim k^{-\alpha(\nu)}$. In the case when effective equations apply only to disjoint parts of the Fourier spectrum, a power-law spectrum cannot be generally formed. Instead, energy oscillations within individual resonance clusters are observed (as predicted by discrete WTT for the simplest case of an energy conserving wave system).

Thus, this methodology encompasses both types of evolutionary behavior: formation of an energy cascade in the entire Fourier space and quasi-periodic energy oscillations in low-dimensional independent subspaces of the Fourier space. The former is illustrated by the Nonlinear Schrödinger (NLS) equation while the latter—by the Charney-Hasegawa-Mima (CHM) equation.

In order to facilitate reading Chap. 2, we should mention that notations used for describing resonances in discrete and kinetic regimes are slightly different. In discrete WTT resonant wave vectors of an N-wave system are consequently numbered as $\mathbf{k}_1, \mathbf{k}_2, .., \mathbf{k}_N$ while in kinetic WTT they are numbered as $\mathbf{k}, \mathbf{k}_1, \mathbf{k}_2, .., \mathbf{k}_{N-1}$. This

is done in order to emphasize that **k** is a running index, i.e. that the kinetic equation is written for an arbitrary wave vector. In Chap. 2 the latter presentation is used for both discrete and kinetic regimes.

In Chap. 3 a different type of resonances is considered, namely, with dispersion function depending on wave amplitude. They are studied by the Homotopy Analysis Method (HAM) which is the main focus of this chapter. The HAM does not require introduction of a small parameter and guarantees convergence of series solutions in most cases. If you just ask Google about "homotopy analysis method" + name of any applied branch of science, you get hundreds of thousands, sometimes millions of links. For instance, geography yields 1,420,000 (Lorenz equation being the most popular), chemistry 163,000, finance 119,000, etc.

From the mathematical point of view, the HAM was, in recent years, widely generalized beyond its original definition. It is enough to mention its application to solving important integral equations, like Volterra-Fredholm equation [12], and even integro-differential equations [33]. One of the most outstanding generalizations is, of course, the homotopy perturbation method and its synthesis with integral transformations [24].

Every branch of applied science which uses mathematics seriously is—rather sooner than later—challenged by nonlinear problems with both weak and strong nonlinearities. And the HAM comes to rescue in nearly every tricky and cumbersome situation when classical methods fail—as soon as the researcher is aware of its existence. There belong e.g. flow problems in areas as wide apart (on the first glance) as polymer processing, coating, ink-jet printing, microfluids, geological flows in the earth mantle, homodynamics and many others [43]. The HAM has been successfully applied for solving various problems emerging in the theory of electrohydrodynamics [32], heat transfer [11] or diffusion-convection [31].

In Chap. 3 it is demonstrated how to find steady-state resonant quartets and their clusters for surface water waves with dispersion function depending on wave amplitude. It was established by Stokes in 1847 that dispersion function for the surface water waves has the form

$$\omega^2 = g\,k[1 + \frac{1}{2}(Ak)^2 + \ldots], \tag{1.18}$$

i.e. it depends on the wave amplitude A. An assumption $\varepsilon := Ak \sim \mathcal{O}(10^{-2})$ allows to omit the term $(Ak)^2$ and high-order terms in Eq. (1.18) and to obtain standard linear dispersion relation $\omega^2 = g\,k$ widely used in the weakly nonlinear theory of water waves. In laboratory experiments with water waves, the small parameter ε is usually chosen of the order of $\sim \mathcal{O}(10^{-1})$ in order to reduce characteristic times of wave interactions in which one can observe effects predicted by the weakly nonlinear theory. For these magnitudes of small parameter, dependence of dispersion function on wave amplitude can be substantial. Some special type of 4-wave resonances among the surface water waves with dispersion function depending on amplitude is studied in Chap. 3. To distinguish between resonances described

above and this new type of resonances, dispersion function in this chapter is denoted by σ, not by ω.

The 4-wave resonance conditions in this case read

$$\sigma_1 \pm \sigma_2 \pm \sigma_3 \pm \sigma_4 = 0, \tag{1.19}$$

$$\mathbf{k}_1 \pm \mathbf{k}_2 \pm \mathbf{k}_3 \pm \mathbf{k}_4 = 0, \tag{1.20}$$

and have the form similar to Eqs. (1.4) and (1.5). However, dispersion function σ depends not only on the corresponding wavevector but also on the amplitudes of four resonantly interacting waves, $\sigma_j = \sigma(\mathbf{k}_j, A_1, \ldots, A_4)$.

Unlike in the previous Chapter where each resonant quartet is characterized by periodic energy exchange among the modes of the quartet, there exist so-called *steady-state quartets* of resonant modes satisfying Eq. (1.19). In a steady-state quartet all amplitudes A_j, wavevectors $\mathbf{k}_j$ and frequencies σ_j of the resonant wave system are constant, i.e. independent of time, so that the spectrum of wave energy is also independent of time.

This peculiar type of resonances has been first found theoretically by the Homotopy Analysis Method (HAM) and later also observed experimentally.

1.4 Modulation Instability (Chaps. 4 and 5)

Our Chap. 4 is devoted to various aspects of PDEs possessing the Modulation Instability (MI). The MI is a widely known phenomenon appearing in various physical systems met in nonlinear optics, plasmas, electrodynamics, etc. [53]. In the theory of water waves, the MI is also known as the Benjamin-Feir instability or side-band instability. It was discovered in 1967 by Benjamin and Feir while performing experiments with surface water waves [3]. The existence of small water waves of permanent shape (stationary nonlinear Stokes waves) was suggested by Stokes in 1845 [45] and proven by Levi-Chivita in 1925 [27]. However it occurred nobody to explore stability of these waves, and the observation of the wave train's disintegration was a big surprise. A wave with constant frequency and wavelength generated by the wave maker was breaking up into groups of waves with varying frequencies and wavelengths. After a year of attempts and efforts to improve the accuracy of the experiments, Benjamin and Feir concluded that the reason lies not in some imperfectness of the wave maker but rather in the instability of a nonlinear Stokes wave itself [3].

The MI is a process of disintegrating of a monochromatic wave train called carrier wave into two waves with close frequencies and wave vectors called side-band waves. This can only happen under certain conditions that have been derived

by Benjamin and Feir for the Stokes waves on infinitely deep water. This condition reads

$$0 \leq \frac{\Delta\omega}{ak\omega} \leq \sqrt{2}, \tag{1.21}$$

where $\Delta\omega$ is a small frequency mismatch defining the distance between the carrier wave and its side-bands in Fourier space. It is deduced as a result of the linear stability analysis, which means that under this condition amplitudes of the side-bands may exhibit unbounded growth. The simplest mathematical model for studying surface water waves is the so-called *focusing* NLS

$$i\,\varphi_t + \alpha\,\varphi_{xx} = \beta\,|\varphi|^2\varphi, \quad \text{with } \alpha\,\beta < 0. \tag{1.22}$$

If $\alpha\,\beta > 0$, the NLS does not possess the MI and is called non-focusing.

The simplest mathematical description[3] of the MI can be given in terms of four-wave resonances of the special form

$$\omega_1 + \omega_2 = 2\omega_3, \quad \mathbf{k}_1 + \mathbf{k}_2 = 2\mathbf{k}_3, \tag{1.23}$$

with $\omega_{1,2} = \omega_3 \pm \Delta$, $0 < \Delta \ll 1$, and $\mathbf{k}_{1,2} = \mathbf{k}_3 \pm \delta$, $0 < \delta \ll 1$.

From the theoretical point of view, any Stokes wave train with finite value of $k\,a$, however small, is modulationally unstable. However, "since viscous damping rates are approximately independent of wave amplitude, the effect of dissipation can be expected to suppress the instability if $k\,a$ is sufficiently small" [3]. Benjamin and Feir confirmed experimentally that for water waves $k\,a = \mathcal{O}(10^{-1})$. This allows to consider the MI as a main physical mechanism underlying various nonlinear phenomena in systems with moderate nonlinearity in which the WTT does not work, for instance, appearance of freak waves [25] or formation of dynamic energy cascades [20, 21].

The Benjamin-Feir theory can be extended to water waves of finite depth: the MI may occur only if the undisturbed water depth h is large enough compared to the wave amplitudes a. Consequently, the NLS type equations are usually taken as model equations for modulation instability, with a monochromatic wave train being unstable only if

$$k\,h > 1.363. \tag{1.24}$$

For many decades, it was understood that the condition given by Eq. (1.24) excludes the shallow water case which is modeled by the KdV equation and modulation instabilities have only been studied for modified KdV equations. These

[3]This definition has been used successfully in many physical applications for several decades. However, a rigorous mathematical proof of instability of the Stokes periodic wavetrain (within the Hamiltonian framework) was given by Bridges and Mielke almost 30 years later in [5].

studies in physical science are presently rather scarce and restricted to the case when modification of the KdV equation can be transformed (after making a number of assumptions and changes of variables) into a focusing NLS equation, e.g.[9, 41].

Quite recently, a new theory leading to the emergence of the KdV equation has been proposed by Bridges. The theory is based on modulation and implies that the assumption of shallow water is neither necessary nor sufficient for the emergence of KdV as a model for water waves [4]. This achievement opens up a totally new perspective on the relevance of the KdV and KdV-type equations for modeling physical phenomena. Consequently, it becomes very important to understand what mathematical results in this area already exist and whether or not they are constructive.

In Chap. 4 MI in KdV-type equations is investigated from the rigorous mathematical point of view. In 1965 Whitham introduced his now famous modulation theory that provides an asymptotic (WKB) method of analyzing this question. This theory is purely formal, however, and there has been much recent interest in the mathematical community in providing rigorous justifications of predictions from Whitham's theory. In Chap. 4, the authors present a detailed survey of recently developed analytical methods for studying modulational instability of periodic traveling waves for KdV-type equations. This general theory is independent of integrability of the governing equations and may also include systems with dissipation. To illustrate robustness of the theory, the authors also discuss its possible extensions and present detailed results for a number of examples including Shamel equation, Benjamin–Oro equation, Whitham equation for water waves, etc.

In Chap. 5 the authors discuss a problem which has important physical applications: connection between modulational instability and possible existence of breathers in the context of integrable KdV-type equations. This connection is well studied in the frame of the focusing nonlinear Schrödinger equation which possesses both the MI and breather solutions which are often used as models for rogues waves. In Chap. 5 this connection is reviewed for a suite of long wave models, such as the KdV equation, the extended KdV (Gardner) equation and a coupled set of Korteweg-de Vries equations (Hirota-Satsuma model). For each model conditions for the MI are written out explicitly and also a non-singular breather solution is found, if it exists, based on a two-soliton solution. This is a simple and robust method to establish a connection between modulation instability and breathers.

1.5 Frameworks (Chaps. 6 and 7)

Since the end of the eighteenth century two main paradigms, stemming from classical mechanics, are known. The first is the Lagrangian description of physical systems involving the action integral which contains generalized positions and momenta, and the second one is the Hamiltonian approach when canonical variables can be chosen. In most practical situations these two approaches are equivalent since they can be related with the Legendre transformation applied to the Lagrangian

functional. It may appear that both approaches can be applied with equal success to a problem in hand. The major difference consists in the choice of dynamical variables which are the generalized position and momenta in the Hamiltonian formalism, and the generalized coordinates and velocities in the Lagrangian framework. Consequently, the final choice has to be made depending on the problem under consideration. For instance, in the presence of holonomic constraints the Lagrangian formulation is preferred, while in the water wave community it is the Hamiltonian formulation of Zakharov which is widely used [50], in particular as the theoretical base for efficient numerical algorithms of wave propagation [7].

In Chap. 6 it is shown that Hamiltonian formalism allows to explain why extremely short and strongly nonlinear optical pulses can be fairly well described by the standard (envelope) generalized NLS equation (gNLS), usually regarded as the weakly-nonlinear limit of primitive equations. This paradoxical situation is due to the fact that the standard optical gNLS equation is just a reformulation of general Hamiltonian equations and, in a sense, no approximations are required. Thus it is demonstrated that the Hamiltonian formalism can indeed be used as a universal approach also in extremely nonlinear optics.

In Chap. 7 the Relaxed Variational Principle (RVP) is introduced and illustrated by several examples. It generalizes the classical Luke's Lagrangian formulation [30]. The introduction of additional variables into the variational Lagrangian framework allows for easier and more flexible derivation of approximate models for water waves. This method should not be necessary opposed to the Hamiltonian formalism, since in many cases the corresponding Hamiltonian functional can be recovered. However, the Hamiltonian framework is too tight for the approximation process, since the choice of canonical variables is quite rigid. In connection to water waves, it is the velocity potential at the free surface $\varphi(x,t) = \phi(x, y = \eta(x,t), t)$ which necessarily appears in the Hamiltonian. However, for modeling purposes it is sometimes advantageous to choose the velocity potential at an arbitrary level $\alpha > 0$ inside the fluid domain, i.e. $\varphi_\alpha(x,t) = \phi(x, y = -\alpha h, t)$. The Lagrangian framework is flexible enough to allow for this kind of simplifications. A few examples illustrating advantages of this approach are given.

1.6 Reality Check (Chap. 8)

The last and the largest Chap. 8 in the book is entirely devoted to the critical discussion of how theoretical and numerical predictions could be verified in a laboratory experiment. What are the factors to be taken into account? What are the applicability limitations of existing mathematical models in fluid dynamics? One major simplification in water waves' studies is decoupling of randomness and nonlinearity. One can thus concentrate first on deterministic, as opposed to stochastic, wave fields. The problem of evolution of a deterministic nonlinear wave system still remains extremely complex, and additional simplifications are required. In view of numerous simplifying assumptions accepted not just in theoretical

models but also in fully nonlinear solutions, the validity of the results has to be verified by carrying out controlled experiments that allow quantitative comparison of theoretical predictions with measurements. Direct comparison of theoretical and experimental results is often challenging, just because numerical solutions customarily consider evolution of waves in time while in experiments the wave field evolves in space. The numerical and the experimental results may thus differ both quantitatively and qualitatively. This chapter presents the perspective of an experimentalist on these questions. This analysis seems to indicate that we stand rather in the beginning of a long way towards successful confirmation of theory by practice.

References

1. Annenkov, S.Y., Shrira, V.I.: Role of non-resonant interactions in the evolution of nonlinear random water wave fields. Fluid Mech. **561**, 181–207 (2006)
2. Annenkov, S., Shrira, V.: Modelling the impact of squall on wind waves with the generalized kinetic equation. J. Phys. Ocean. **45**(3), 807–812 (2015)
3. Benjamin, T.B., Feir, J.E.: The disintegration of wavetrains in deep water, Part 1. Fluid Mech. **27**, 417–31 (1967)
4. Bridges, T.J.: A universal form for the emergence of the Korteweg – de Vries equation. Proc. R. Soc. Lond. A **469**(2153), 20120707 (2013)
5. Bridges, T.J., Mielke, A.: A proof of the Benjamin-Feir instability. Arch. Ration. Mech Anal. **133**, 145–98 (1995)
6. Craik, A.D.: Wave Interactions and Fluid Flows. Cambridge University Press, Cambridge (1985)
7. Craig, W., Sulem, C.: Numerical simulation of gravity waves. J. Comput. Phys. **108**, 73–83 (1993)
8. Gardner, C., Greene, J., Kruskal, M., Miura, R.: Method for Solving the Korteweg – de Vries Equation. Phys. Rev. Lett **19**(19), 1095–1097 (1967)
9. Grimshaw, R., Pelinovsky D., Pelinovsky E., Talipova T.: Wave group dynamics in weakly nonlinear long-wave models. Phys. D **159**(1–2), 35–57 (2001)
10. Hasselmann, K.: On the non-linear energy transfer in a gravity-wave spectrum, Part 1. General theory. Fluid Mech. **12**(04), 481–500 (1962)
11. Hetmaniok, E., Nowak, I., Slota, D., Witula, R., Zielonka, A.: Solution of the inverse heat conduction problem with Neumann boundary condition by using the homotopy perturbation method. Therm. Sci. **17**(3), 643–650 (2013)
12. Izadian, J., Salahshour, S., Soheil Salahshour, S.: A numerical method for solving Volterra and Fredholm integral equations using homotopy analysis method. AWER Proc. Inf. Technol. Comput. Sci. **1** 406–411 (2012)
13. Kartashova, E.: Model of laminated wave turbulence. JETP Lett. **83**(7), 283–287 (2006)
14. Kartashova, E.A.: Partitioning of ensembles of weakly interacting dispersing waves in resonators into disjoint classes. Phys. D **46**(1), 43–56 (1990)
15. Kartashova, E.A.: On properties of weakly nonlinear wave interactions in resonators. Phys. D **54**, 125–34 (1991)
16. Kartashova, E.A.: Weakly nonlinear theory of finite-size effects in resonators. Phys. Rev. Lett. **72**, 2013–2016 (1994)
17. Kartashova, E.: Exact and quasi-resonances in discrete water-wave turbulence. Phys. Rev. Lett. **98**, 214502-1–214502-4 (2007)
18. Kartashova, E.A.: Discrete wave turbulence. Europhys. Lett. **87**, 44001-1–44001-5 (2009)

19. Kartashova, E.: Nonlinear Resonance Analysis. Cambridge University Press, Cambridge (2010)
20. Kartashova, E.: Energy transport in weakly nonlinear wave systems with narrow frequency band excitation. Phys. Rev. E **86**, 041129 (2012)
21. Kartashova, E.: Time scales and structures of wave interaction exemplified with water waves. Europhys. Lett. **102**(4), 44005 (2013)
22. Kartashova, E., L'vov, V.S.: A model of intra-seasonal oscillations in the Earth atmosphere. Phys. Rev. Lett. **98**, 198501-1–198501-4 (2007)
23. Kartashova, E.A., Piterbarg, L.I., Reznik, G.M.: Weakly nonlinear interactions between Rossby waves on a sphere. Oceanology **29**, 405–411 (1990)
24. Kashuri, A., Fundo, A., Kreku, M.: Mixture of a new integral transform and homotopy perturbation method for solving nonlinear partial differential equations. Adv. Pure Math. **3** 317–323 (2013)
25. Kharif, C., Pelinovsky E., Slunyaev, A.: Rogue Waves in the Ocean. Advances in Geophysical and Environmental Mechanics and Mathematics. Springer, Berlin (2009)
26. Kuksin, S., Shirikyan, A.: Mathematics of Two-Dimensional Turbulence, p. 336. Cambridge University Press, Cambridge (2012)
27. Levi-Civita, T.: Détermination rigoureuse des ondes permanents d'ampleur fini. Math. Ann. **93**, 264 (1925)
28. Lighthill M.J. (ed.): A Discussion on Nonlinear Theory of Wave Propagation in Dispersive Systems. Royal Society, London (1967)
29. Lvov, V.S., Pomyalov, A., Procaccia, I., Rudenko, O.: Finite-dimensional turbulence of planetary waves. Phys. Rev. E **80**(6), 066319 (2009)
30. Luke, J.C.: A variational principle for a fluid with a free surface. J. Fluid Mech. **27**, 375–397 (1967)
31. Mahmood, B., Manaa, S.A., Easif, F.H.: Homotopy analysis method for solving nonlinear diffusion equation with convection term. Int. J. Appl. Math. Res. **3**(3), 244–250 (2014)
32. Mastroberardino, A.: Homotopy analysis method applied to electrohydrodynamic flow. Commun. Nonlinear Sci. Numer. Simul. **16**(7), 2730–2736 (2011)
33. Matinfar, M., Saeidy, M., Gharahsuflu, B.: Homotopy analysis method for systems of integro-differential equations. J. Intel. Fuzzy Syst. Appl. Eng. Technol. **26**(3), 1095–1102 (2014)
34. Nazarenko, S.: Wave Turbulence. Lecture Notes in Phyics, vol. 825. Springer, Berlin (2011)
35. Newell, A.C., Rumpf, B.: Wave Turbulence. Ann. Rev. Fluid Mech. **43**(1), 59–78 (2011)
36. Osborne, A.: Nonlinear Ocean Waves and the Inverse Scattering Transform. International Geophysics Series, vol. 97. Elsevier Academic, Amsterdam (2010)
37. Pedlosky, J.: Geophysical Fluid Dynamics. Springer, New York (1987)
38. Phillips, O.M.: On the dynamics of unsteady gravity waves of finite amplitude, Part 1. The elementary interactions. Fluid Mech. **9**, 193–217 (1960)
39. Pushkarev, A.N.: On the Kolmogorov and frozen turbulence in numerical simulation of capillary waves. Eur. J. Mech. B/Fluids **18**(3), 345–351 (1999)
40. Pushkarev, A.N., Zakharov, V.E.: Turbulence of capillary waves - theory and numerical simulation. Phys. D **135**(1–2), 98–116 (2000)
41. Ruderman M., Talipova T., Pelinovsky E.: Dynamics of modulationally unstable ion-acoustic wavepackets in plasmas with negative ions. Plasma Phys. **74**(5), 639–656 (2008)
42. Riemann, B.: Über die Fortpflanzung ebener Luftwellen von endlicher Schwindungsweite. Göttingen Abhandlungen **VIII**, 43 (1858)
43. Sajid, M.: Some Flow Problems in Differential Type Fluids: Series Solutions Using Homotopy Analysis Method (HAM). VDM (Verlag Dr. Müller, Germany) (2009)
44. Scott, A.: Encyclopedia of Nonlinear Science. Routledge, New-York (2004)
45. Stokes, G.G.: On the theories of internal friction of fluids in motion. Trans. Camb. Philos. Soc. **8**, 287–305 (1845)
46. Tobisch, E.: What can go wrong when applying wave turbulence theory. E-print: arXiv:1406.3780 [physics.flu-dyn] (2014)

47. Whitham, G.B.: Linear and Nonlinear Waves. Pure and Applied Mathematics, Wiley, New York (1999)
48. Zabusky, N.J., Kruskal, M.D.: Interaction of solitons in a collisionless plasma and the recurrence of initial states. Phys. Rev. Lett. **15**, 240–243 (1965)
49. Zakharov, V.E., Filonenko, N.N.: Weak turbulence of capillary waves. J. Appl. Mech. Tech. Phys. **8**(5), 37–40 (1967)
50. Zakharov, V.E.: Stability of periodic waves of finite amplitude on the surface of a deep fluid. J. Appl. Mech. Tech. Phys. **9**, 190–194 (1968)
51. Zakharov, V.E., Lvov, V.S., Falkovich, G.: Kolmogorov Spectra of Turbulence I. Wave Turbulence. Nonlinear Dynamics. Springer, Berlin (1992)
52. Zakharov, V.E., Korotkevich, A.O., Pushkarev, A.N., Dyachenko, A.I.: Mesoscopic wave turbulence. JETP Lett. **82**, 487–491 (2005)
53. Zakharov, V.E., Ostrovsky L.A.: Modulation instability: the beginning. Phys. D **238**, 540–548 (2009)

Chapter 2
The Effective Equation Method

Sergei Kuksin and Alberto Maiocchi

Abstract In this chapter we present a general method of constructing the effective equation which describes the behavior of small-amplitude solutions for a nonlinear PDE in finite volume, provided that the linear part of the equation is a hamiltonian system with a pure imaginary discrete spectrum. The effective equation is obtained by retaining only the resonant terms of the nonlinearity (which may be hamiltonian, or may be not); the assertion that it describes the limiting behavior of small-amplitude solutions is a rigorous mathematical theorem. In particular, the method applies to the three- and four-wave systems. We demonstrate that different possible types of energy transport are covered by this method, depending on whether the set of resonances splits into finite clusters (this happens, e.g. in case of the Charney-Hasegawa-Mima equation), or is connected (this happens, e.g. in the case of the NLS equation if the space-dimension is at least two). For equations of the first type the energy transition to high frequencies does not hold, while for equations of the second type it may take place. Our method applies to various weakly nonlinear wave systems, appearing in plasma, meteorology and oceanography.

2.1 Introduction

It is well known that solutions of linear evolution PDEs in finite volume are superpositions of normal modes of oscillations (in most cases of interest these are the Fourier modes). When a nonlinearity is added as a perturbation, different modes start to interact and the solutions of the equation can be approximated by suitable power series expansions, provided that the nonlinearity is sufficiently small (or, in other words, the PDE is *weakly* nonlinear). In such cases, the equation can be

S. Kuksin (✉)
CNRS and I.M.J, Université Paris-Diderot, Paris 7, France
e-mail: kuksin@math.jussieu.fr

A. Maiocchi
Dipartimento di Matematica, Università degli Studi di Milano, via Saldini 50, 20133, Milano, Italy
e-mail: alberto.maiocchi@unimi.it

E. Tobisch (ed.), *New Approaches to Nonlinear Waves*, Lecture Notes in Physics 908, DOI 10.1007/978-3-319-20690-5_2

written as

$$u_t + L(u) = \varepsilon N(u)\,, \tag{2.1}$$

where L is the linear operator, N denotes the nonlinearity and ε is a small parameter, $0 < \varepsilon \ll 1$. The equation may contain a stochastic force, and in that case it reads

$$u_t + L(u) = \varepsilon N(u) + \sqrt{\varepsilon}\,\langle \text{random force} \rangle \tag{2.2}$$

(the scaling of the random force by the factor $\sqrt{\varepsilon}$ is the most natural, see below). We will show that the limiting, as $\varepsilon \to 0$, exchange of energy between the modes may be described by replacing the original system with a suitable *effective equation*. This result may be regarded as a PDE-version of the Bogolyubov averaging principle (see [1]) which implies a similar property for distribution of energy between the oscillating modes for small-amplitude oscillations in finite-dimensional nonlinear systems.

The mentioned above convergence that holds as $\varepsilon \to 0$ and various properties of the corresponding effective equations have been rigorously established (see [7, 10–14] and the discussion in [7]). The treatments of the deterministic and stochastic equations are similar, but the results, obtained in the stochastic case, are significantly stronger: while the deterministic effective equation controls the dynamics only on time intervals of order ε^{-1}, in the presence of stochastic forcing the corresponding effective equation also approximates the stationary measure for the original equation, thus controlling the asymptotical in time behavior of solutions when $\varepsilon \ll 1$. Moreover, in the absence of forcing we only get information concerning the exchange of energy between the modes, whereas in the stochastically forced case, the stationary measure for the effective equation controls both the energies and the phases of the normal modes of solutions.

Below we explain how to construct the effective equations for Eqs. (2.1) and (2.2) from the resonant terms of the nonlinearities. We will discuss two examples: the nonlinear Schrödinger equation and the Charney-Hasegawa-Mima equation on the β plane. These two equations display completely different types of energy exchange between modes, and we will explain why this happens.

2.2 How to Construct the Effective Equation

We consider hamiltonian PDEs, whose linear parts have imaginary pure point spectra and are diagonal in Fourier modes. Written in terms of the complex Fourier coefficients $v = \{v_{\mathbf{k}}\}$ (also called waves), the equations which we study read

$$\frac{d}{dt} v_{\mathbf{k}} = i\omega_{\mathbf{k}} v_{\mathbf{k}} + P_{\mathbf{k}}(v)\,, \qquad \mathbf{k} \in \mathbb{Z}^d\,. \tag{2.3}$$

Here $\omega_{\mathbf{k}}$ are real numbers and $P(v) = (P_{\mathbf{k}}(v), \mathbf{k} \in \mathbb{Z}^d)$ is a polynomial nonlinearity in v of certain order q, of the form

$$P_{\mathbf{k}}(v) = \sum_{p \le q} \sum_{\mathbf{k}_1 \dots \mathbf{k}_p \mathbf{k}_{p+1} \dots \mathbf{k}_q} c_{\mathbf{k}_1 \dots \mathbf{k}_q \mathbf{k}} v_{\mathbf{k}_1} \cdots v_{\mathbf{k}_p} v^*_{\mathbf{k}_{p+1}} \cdots v^*_{\mathbf{k}_q} \delta^{1\dots p}_{p+1\dots q\,\mathbf{k}} , \tag{2.4}$$

where $c_{\mathbf{k}_1 \dots \mathbf{k}_q \mathbf{k}}$ are some complex coefficients, v^* is the complex conjugate of v and

$$\delta^{1\dots p}_{p+1\dots q\mathbf{k}} = \begin{cases} 1 \text{ if } \mathbf{k}_1 + \ldots + \mathbf{k}_p = \mathbf{k}_{p+1} + \ldots + \mathbf{k}_q + \mathbf{k} \\ 0 \qquad\qquad\qquad\quad \text{else} \end{cases} . \tag{2.5}$$

We always assume that "the nonlinearity does not pump energy in the system":

$$\mathrm{Re} \sum_{\mathbf{k}} P_{\mathbf{k}}(v) \bar{v}_{\mathbf{k}} \le 0 \tag{2.6}$$

(in most case of interest the l.h.s. vanishes).

The quantities $I_{\mathbf{k}} := |v_{\mathbf{k}}|^2/2$, $E_{\mathbf{k}} = \omega_{\mathbf{k}} I_{\mathbf{k}}$ and $\varphi_{\mathbf{k}} = \mathrm{Arg}(v_{\mathbf{k}})$ are called, respectively, the wave action, wave energy and wave phase. The relation between ω and $\mathbf{k}$, i.e. the function $\mathbf{k} \to \omega_{\mathbf{k}}$, is called the *dispersion relation*, or *dispersion function*.

The *weakly nonlinear regime* corresponds to solutions of small amplitude ε. We will study it in the presence of damping and, possibly, a random force, whose magnitude is controlled by another parameter, call it ν. So, instead of Eq. (2.3), we will consider

$$\frac{d}{dt} v_{\mathbf{k}} = i\omega_{\mathbf{k}} v_{\mathbf{k}} + \varepsilon^q P_{\mathbf{k}}(v) - \nu \gamma_{\mathbf{k}} v_{\mathbf{k}} + \mu \sqrt{\nu}\, b_{\mathbf{k}} \dot{\boldsymbol{\beta}}_{\mathbf{k}} , \qquad \mathbf{k} \in \mathbb{Z}^d , \tag{2.7}$$

where $\gamma_{\mathbf{k}} \ge \gamma_* > 0$ controls the damping term, $b_{\mathbf{k}} > 0$ controls the forcing and the parameter $\mu \in \{0, 1\}$ is introduced to consider at the same time the forced and non-forced cases. The $\dot{\boldsymbol{\beta}}_{\mathbf{k}}$s are complex white noises, independent from each other.[1] The factors ν and $\sqrt{\nu}$ in front of the damping and the dissipation are so chosen that, in the limit of $\nu \to 0$, the solutions stay of order one, uniformly in $t > 0$.

Note that, while ε controls the size of the solutions, $1/\nu$ is the time-scale on which the forcing acts significantly, as it is the time needed for the standard deviations of the processes $\sqrt{\nu}\boldsymbol{\beta}_{\mathbf{k}}$ to become of order one. If $\mu = 0$ and the system of Eq. (2.7) is deterministic, still its time-scale is $1/\nu$ since, as we explain below, its solutions with initial data of order one stay of order one for $t \lesssim \nu^{-1}$, while for much bigger values of time they are very small since in view of Eq. (2.6) their ℓ_2-norms

[1] That is, $\dot{\boldsymbol{\beta}}_{\mathbf{k}} = (d/dt)\boldsymbol{\beta}_{\mathbf{k}}$, $\boldsymbol{\beta}_{\mathbf{k}} = \boldsymbol{\beta}^+_{\mathbf{k}} + i\boldsymbol{\beta}\mathbf{k}^-$, where $\boldsymbol{\beta}^{\pm}_{\mathbf{k}}$ are standard independent real Wiener processes.

satisfy

$$|v(t)|^2_{\ell_2} \le |v(0)|^2_{\ell_2} e^{-t\nu\gamma_*} . \tag{2.8}$$

We will consider the regime

$$\nu = \varepsilon^q \tag{2.9}$$

(where q is the degree of P), and study solutions of the equation with given initial conditions on the time-scale $1/\nu$, examining them under the limit $\nu \to 0$. Passing to the slow time $\tau = \nu t$ (so that time $t \sim 1/\nu$ corresponds to τ of order 1), Eq. (2.7) becomes

$$\dot v_{\mathbf{k}} = i\nu^{-1}\omega_{\mathbf{k}} v_{\mathbf{k}} + P_{\mathbf{k}}(v) - \gamma_{\mathbf{k}} v_{\mathbf{k}} + \mu b_{\mathbf{k}} \dot{\boldsymbol\beta}_{\mathbf{k}} , \qquad \mathbf{k} \in \mathbb{Z}^d , \tag{2.10}$$

where the upper dot stands for $\frac{d}{d\tau}$.

We claim that, in the limit when ν (or, equivalently, ε) goes to zero, the distribution of the energies $E_{\mathbf{k}}$ on times τ of order one is described by an *effective equation* whose nonlinearity is constituted by resonant terms of the nonlinearity (see Eq. (2.20) below).

It is easier to understand the role of resonances and the form of the effective equation by passing to the interaction representation (cf. [1, 16, 18]), i.e., by performing the time-dependent change of variables from $v_{\mathbf{k}}$ to

$$a_{\mathbf{k}} = e^{-i\nu^{-1}\omega_{\mathbf{k}}\tau} v_{\mathbf{k}} , \tag{2.11}$$

which transforms Eq. (2.10) to

$$\dot a_{\mathbf{k}} = \mathbf{R}_{\mathbf{k}}(a, \nu^{-1}\tau) - \gamma_{\mathbf{k}} a_{\mathbf{k}} + \mu b_{\mathbf{k}} e^{-i\nu^{-1}\omega_{\mathbf{k}}\tau} \dot{\boldsymbol\beta}_{\mathbf{k}} , \qquad \mathbf{k} \in \mathbb{Z}^d , \tag{2.12}$$

where $\mathbf{R}_{\mathbf{k}}$ denotes the nonlinearity, written in the a-variables. That is

$$\begin{aligned} \mathbf{R}_{\mathbf{k}}(a, \nu^{-1}\tau) = \sum_{p\le q} \sum_{\mathbf{k}_1\dots\mathbf{k}_p\mathbf{k}_{p+1}\dots\mathbf{k}_q} & c_{\mathbf{k}_1\dots\mathbf{k}_q\mathbf{k}} v_{\mathbf{k}_1}\cdots v_{\mathbf{k}_p} v^*_{\mathbf{k}_p+1}\cdots v^*_{\mathbf{k}_q} \delta^{1\dots p}_{p+1\dots q\,\mathbf{k}} \\ & \times \exp\left(i\nu^{-1}\tau\left(\omega_{\mathbf{k}_1} + \dots + \omega_{\mathbf{k}_p} - \omega_{\mathbf{k}_{p+1}} - \dots - \omega_{\mathbf{k}_q} - \omega_{\mathbf{k}}\right)\right) . \end{aligned} \tag{2.13}$$

Noting that the collection of the processes $\{e^{-\nu^{-1}\omega_{\mathbf{k}}\tau}\dot\beta_{\mathbf{k}}\}$ is another set of standard independent complex white noises, we re-write Eq. (2.12) as

$$\dot a_{\mathbf{k}} = \mathbf{R}_{\mathbf{k}}(a, \nu^{-1}\tau) - \gamma_{\mathbf{k}} a_{\mathbf{k}} + \mu b_{\mathbf{k}} \dot{\boldsymbol\beta}_{\mathbf{k}} , \qquad \mathbf{k} \in \mathbb{Z}^d . \tag{2.14}$$

In the sum defining $\mathbf{R}_{\mathbf{k}}$, the terms for which the *resonance conditions*

$$\begin{cases} \omega_{\mathbf{k}_1} + \ldots + \omega_{\mathbf{k}_p} = \omega_{\mathbf{k}_{p+1}} + \ldots + \omega_{\mathbf{k}_q} + \omega_{\mathbf{k}} \\ \mathbf{k}_1 + \cdots + \mathbf{k}_p = \mathbf{k}_{p+1} + \cdots \mathbf{k}_q + \mathbf{k} \end{cases} \tag{2.15}$$

are satisfied (called the *resonant terms*) under the limit $\nu \to 0$ behave completely differently from others terms (called the *nonresonant terms*). Namely, the nonresonant terms oscillate faster and faster, whereas the resonant terms do not. We will say that a set of $\mathbb{Z}^d$-vectors $\{\mathbf{k}_1, \ldots, \mathbf{k}_q, \mathbf{k}\}$ forms a *resonance* if relations given by Eqs. (2.15) are satisfied, if $c_{\mathbf{k}_1 \ldots \mathbf{k}_q \mathbf{k}} \neq 0$, and the set $\{\mathbf{k}_1, \ldots, \mathbf{k}_p\}$ does not equal the set $\{\mathbf{k}_{p+1}, \ldots, \mathbf{k}_q, \mathbf{k}\}$. The collection of all resonances is called the *resonant set*.

In the spirit of the finite-dimensional averaging, following the Bogolyubov averaging principle (see [1]), the behavior of solutions of Eq. (2.14) under the limit $\nu \to 0$ is obtained by replacing the nonlinearity $\mathbf{R}_{\mathbf{k}}$ with its time average, i.e. with

$$\lim_{T \to \infty} \frac{1}{T} \int_0^T \mathbf{R}_{\mathbf{k}}(a, t) dt \, . \tag{2.16}$$

Since for any real number λ we have

$$\lim_{T \to \infty} \frac{1}{T} \int_0^T e^{i\lambda t} dt = \begin{cases} 1 \text{ if } \lambda = 0 \\ 0 \text{ if } \lambda \neq 0 \end{cases} , \tag{2.17}$$

then only the resonant terms survive in the averaged nonlinearity. We write their sum as

$$R_{\mathbf{k}}(a) = \sum_{p \leq q} \sum_{\mathbf{k}_1 \ldots \mathbf{k}_p \mathbf{k}_{p+1} \ldots \mathbf{k}_q} c_{\mathbf{k}_1 \ldots \mathbf{k}_q \mathbf{k}} v_{\mathbf{k}_1} \cdots v_{\mathbf{k}_p} v^*_{\mathbf{k}_p + 1} \cdots v^*_{\mathbf{k}_q} \delta^{1 \ldots p}_{p+1 \ldots q \mathbf{k}} \delta(\omega^{1 \ldots p}_{p+1 \ldots q \mathbf{k}}) \, , \tag{2.18}$$

where

$$\delta(\omega^{1 \ldots p}_{p+1 \ldots q \mathbf{k}}) = \begin{cases} 1 \text{ if } \omega_{\mathbf{k}_1} + \ldots + \omega_{\mathbf{k}_p} = \omega_{\mathbf{k}_{p+1}} + \ldots + \omega_{\mathbf{k}_q} + \omega_{\mathbf{k}} \\ 0 \qquad\qquad\qquad\qquad \text{else} \end{cases} . \tag{2.19}$$

This suggests to take for the effective equation the following system:

$$\dot{\tilde{a}}_{\mathbf{k}} = R_{\mathbf{k}}(\tilde{a}) - \gamma_{\mathbf{k}} \tilde{a}_{\mathbf{k}} + \mu b_{\mathbf{k}} \dot{\boldsymbol{\beta}}_{\mathbf{k}} \, , \qquad \mathbf{k} \in \mathbb{Z}^d \, . \tag{2.20}$$

Indeed, it is proved in [7] (also see [10–12]) that, if the original Eq. (2.7) is well posed on time intervals $t \lesssim 1/\nu$, then Eq. (2.20) describes the limiting behavior of the variables $a_{\mathbf{k}}$ (and, as well, the distribution of energy since $|v_{\mathbf{k}}| = |a_{\mathbf{k}}|$) in the time-scale $t \sim 1/\nu$, for any sufficiently regular initial data. This holds both in the presence and in the absence of the random forcing (i.e., both for $\mu = 0$ and $\mu = 1$).

Moreover, in the forced case we also control the limiting behavior of the stationary solutions for Eq. (2.7). So if Eq. (2.7) and the effective equation both are mixing, then we control the behavior of all solutions for Eq. (2.7) under the iterated limit

$$\lim_{\varepsilon\to 0}\lim_{t\to\infty}\,. \tag{2.21}$$

Remarkably, in this case the effective equation describes not only the limiting behavior of the actions, but also that of the angles. That is, it completely controls the limiting distribution of solutions. So if $f(v)$ is a functional on the space of sequences $v = (v_{\mathbf{k}})$, satisfying some mild restriction on its growth as the norm of v goes to infinity, and $v^\varepsilon(t)$ is any solution for Eq. (2.7), then

$$\lim_{\varepsilon\to 0}\lim_{t\to\infty}\mathbf{E}f(v^\varepsilon(t)) \to \int f(v)\,\mu(dv)\,, \tag{2.22}$$

where μ is the unique stationary measure for the effective Eq. (2.20) and $\mathbf{E}$ signifies the expectation. See in [7, 11, 12].

2.3 Structure of Resonances

We intend to use the effective equations as a tool to investigate the energy transport in different physically relevant PDEs. We will show that the limiting, as $\varepsilon \to 0$, energy transport for any specific equation depends on the structure of the resonances (which, in turn, is determined by the form of the dispersion function $\omega_{\mathbf{k}}$).

Three possibilities can occur:

(1) The resonant set is empty. Then if the degree q of the nonlinearity is even, the effective equation is linear. If q is odd, the equation may contain nonlinear integrable terms of the form $f(I)v_{\mathbf{k}}$. But these terms do not contribute to the dynamics of the wave actions. So in any case different modes do not exchange energy, and no energy transport to high frequencies occurs.

Now assume that the resonant set is not empty. We say that integer vectors $\mathbf{k}_1, \mathbf{k}_2 \in \mathbb{Z}^d$ are *equivalent* if there exist vectors $\mathbf{k}_3, \dots, \mathbf{k}_q, \mathbf{k} \in \mathbb{Z}^d$, such that the relations given by Eqs. (2.15) hold. This equivalence divides $\mathbb{Z}^d$ to clusters, formed by elements which can be joined by chains of equivalences (see [8, 9] for a discussion of the role of resonant clusters in weak turbulence).

The two remaining cases are:

(2) All resonances are connected, so the whole $\mathbb{Z}^d$ is a single cluster. In this case, in the limit when the volume of the space-domain goes to infinity, under some additional assumptions a new type of kinetic equation can be derived, the energy transport takes place and power law stationary spectra, which depend only on the form of the dissipation, can be obtained.

(3) All resonances are divided to non intersecting clusters. Now the energy transfer should be studied separately within each cluster. If sizes of the clusters are bounded, then no energy transport to high frequencies occurs.

See [5, 11] for the case (1), [12, 14] for the stochastic case (2) and [6] for the deterministic case, and see [13] for the stochastic case (3). See [7] for discussion and for theorems, applicable in all three cases, deterministic and stochastic.

Note that many examples of systems which fall to type (2) are given by Eq. (2.7) with completely resonant spectra $\{\omega_{\mathbf{k}}\}$, i.e. with spectra of the form $\omega_{\mathbf{k}} = \omega_* \, \Omega_{\mathbf{k}}$, where $\Omega_{\mathbf{k}}$ are integers. Averaging theorems for completely resonant deterministic Eq. (2.7) with $\nu = 0$ were discussed in [3, 4, 6]; also see [7].

Below we discuss examples for the case (2) when all resonances are connected (Sect. 2.4), and for the case (3) when the resonances make non intersecting finite clusters (Sect. 2.5). For more examples of systems of types (2) and (3) see [9].

2.3.1 The Equations

Our first example is the cubic NLS equation on the d-dimensional torus of size L (see [12, 14]):

$$\partial_t u - i\Delta u = i\varepsilon^2 \delta \, |u|^2 \, u + \nu \langle \text{dissipation} \rangle + \mu \sqrt{\nu} \langle \text{random forcing} \rangle \, , \quad (2.23)$$
$$\text{where} \quad u = u(t, \mathbf{x}) \in \mathbb{C} \, , \quad \mathbf{x} \in \mathbb{T}^d_L = \mathbb{R}^d / (2\pi L \mathbb{Z}^d)$$

and the parameter $\delta = \delta(L)$ is introduced in order to control different scaling for solution as the size L of the torus varies.[2] The dissipation is a linear operator, diagonal in the exponential base of functions on $\mathbb{T}^d_L$

$$\{\phi_{\mathbf{k}}(x) = e^{iL^{-1}\mathbf{k}\cdot x}, \ \mathbf{k} \in \mathbb{Z}^d\} \, . \quad (2.24)$$

As before, by $v = \{v_{\mathbf{k}}, \mathbf{k} \in \mathbb{Z}^d\}$ we denote the Fourier coefficients of $u(x)$:

$$u(x) = \sum_{\mathbf{k} \in \mathbb{Z}^d} v_{\mathbf{k}} \phi_{\mathbf{k}}(x) \, . \quad (2.25)$$

If $d = 1$, the resonance condition given by Eq. (2.15) takes the form

$$k_1^2 + k_2^2 = k_3^2 + k^2, \qquad k_1 + k_2 = k_3 + k \, . \quad (2.26)$$

[2] More exactly, Eq. (2.23) is the damped/driven cubic NLS equation. See [16, 18] for the non-perturbed NLS equations.

All solutions for this system are such that $k_1 = k, k_2 = k_3$, or $k_1 = k_3, k_2 = k$. So in this case the resonant set is empty, and no energy cascade to high frequencies happens when $\varepsilon^2 = \nu \to 0$. This is well known.

Now consider a higher-dimensional NLS equation, write it in the Fourier variables $\{v_{\mathbf{k}}, \mathbf{k} \in \mathbb{Z}^d\}$, and pass to the slow time $\tau = \nu t$. Then, if the forcing and the dissipation are chosen in accordance with the prescription of the previous section (cf. Eq. (2.7)), the equation reads

$$\dot{v}_{\mathbf{k}} = -i\nu^{-1}\omega^N_{\mathbf{k}} v_{\mathbf{k}} + i\delta \sum_{\mathbf{k}_1,\mathbf{k}_2,\mathbf{k}_3 \in \mathbb{Z}^d} v_{\mathbf{k}_1} v_{\mathbf{k}_2} v^*_{\mathbf{k}_3} \delta^{12}_{3\mathbf{k}} - \gamma_{\mathbf{k}} v_{\mathbf{k}} + \mu b_{\mathbf{k}} \dot{\boldsymbol{\beta}}_{\mathbf{k}} \,. \tag{2.27}$$

Here $-\gamma_{\mathbf{k}}$ are the eigenvalues of the dissipation operator. The eigenvalues of the operator $-\Delta$, call them $\omega^N_{\mathbf{k}}$, follow the dispersion relation

$$\omega^N_{\mathbf{k}} = |\mathbf{k}|^2 / L^2 \,, \quad \mathbf{k} \in \mathbb{Z}^d \,. \tag{2.28}$$

Below we will see that if $d \geq 2$, then the whole $\mathbb{Z}^d$ forms a single cluster, so the equation fits the case (2).

An interesting example of the case (3) of isolated clusters is provided by the Charney-Hasegawa-Mima (CHM) equation on the β plane (see [13, 16, 18] for this equation with $\nu = 0$), which we write as

$$\begin{aligned} (-\Delta + F)\partial_t \psi - \varepsilon J(\psi, \Delta\psi) - \partial_x \psi &= \nu \langle \text{ dissipation} \rangle + \mu\sqrt{\nu} \langle \text{random forcing} \rangle \,, \\ \psi &= \psi(t, \mathbf{x}) \in \mathbb{R} \,. \end{aligned} \tag{2.29}$$

Here the constant $F \geq 0$ is called the Froude number and $J(\psi, \Delta\psi)$ denotes the Jacobian determinant of the vector $(\psi, \Delta\psi)$. The space-domain is a strip of horizontal size ρ and vertical size one, under double periodic boundary conditions, i.e.,

$$\mathbf{x} = (x, y) \in \mathbb{T}^2_{\rho,1} = \mathbb{R}/(2\pi\rho\mathbb{Z}) \times S^1 \,, \quad S^1 = \mathbb{R}/(2\pi\mathbb{Z}) \,. \tag{2.30}$$

Again we pass to the Fourier modes[3] $\{v_{\mathbf{k}}, \mathbf{k} = (m, n) \in \mathbb{Z}^2\}$ and to the slow time τ to re-write the equation as

$$\begin{aligned} \dot{v}_{\mathbf{k}} = -i\nu^{-1}\omega^C_{\mathbf{k}} v_{\mathbf{k}} + \frac{1}{\rho(m^2 + n^2\rho^2 + F\rho^2)} \sum_{\mathbf{k}_1,\mathbf{k}_2 \in \mathbb{Z}^2} \left(m_1^2 + n_1^2\rho^2\right) \\ \times (m_1 n_2 - n_1 m_2)\, v_{\mathbf{k}_1} v_{\mathbf{k}_2} \delta^{12}_{\mathbf{k}} - \gamma_{\mathbf{k}} v_{\mathbf{k}} + \mu b_{\mathbf{k}} \dot{\boldsymbol{\beta}}_{\mathbf{k}} \,, \end{aligned} \tag{2.31}$$

[3] Note that, due to the fact that the function ψ is real, $v_{\mathbf{k}} = v^*_{-\mathbf{k}}$.

where $\mathbf{k}_1 = (m_1, n_1)$, $\mathbf{k}_2 = (m_2, n_2)$ and the dispersion function has the form

$$\omega_{\mathbf{k}}^C = -\frac{m\rho}{m^2 + n^2\rho^2 + F\rho^2}\,, \quad \mathbf{k} = (m, n) \in \mathbb{Z}^2\,. \tag{2.32}$$

The effective equations for Eqs. (2.27) and (2.31) can be easily obtained on account of the general formula given by Eq. (2.20). Using it, for the NLS equation we get the effective equation

$$\dot{\tilde{a}}_{\mathbf{k}} = i\delta \sum_{\mathbf{k}_1,\mathbf{k}_2,\mathbf{k}_3 \in \mathbb{Z}^d} \tilde{a}_{\mathbf{k}_1}\tilde{a}_{\mathbf{k}_2}\tilde{a}^*_{\mathbf{k}_3}\delta^{12}_{3\mathbf{k}}\delta(\omega^{N}{}^{12}_{3\mathbf{k}}) - \gamma_{\mathbf{k}}\tilde{a}_{\mathbf{k}} + \mu b_{\mathbf{k}}\dot{\boldsymbol{\beta}}_{\mathbf{k}}\,, \quad \mathbf{k} \in \mathbb{Z}^d\,, \tag{2.33}$$

while for CHM the effective equation is the system

$$\begin{aligned}\dot{\tilde{a}}_{\mathbf{k}} =& \frac{1}{\rho(m^2 + n^2\rho^2 + F\rho^2)} \sum_{\mathbf{k}_1,\mathbf{k}_2 \in \mathbb{Z}^2} \left(m_1^2 + n_1^2\rho^2\right)(m_1 n_2 - n_1 m_2) \\ &\times \tilde{a}_{\mathbf{k}_1}\tilde{a}_{\mathbf{k}_2}\delta^{12}_{\mathbf{k}}\delta(\omega^{C}{}^{12}_{\mathbf{k}}) - \gamma_{\mathbf{k}}\tilde{a}_{\mathbf{k}} + \mu b_{\mathbf{k}}\dot{\boldsymbol{\beta}}_{\mathbf{k}}\,, \quad \mathbf{k} \in \mathbb{Z}^2\,.\end{aligned} \tag{2.34}$$

It is clear that the behavior of solutions for Eqs. (2.33)–(2.34) is dictated by the structure of resonances since they determine the surviving terms of the nonlinearity. The geometric properties of the resonant set for the higher dimensional NLS equations are described in the following section, whereas the resonances for CHM are discussed in Sect. 2.3.3.

2.3.2 *Structure of Resonances for the NLS Equation*

In the case of $2d$ NLS equation each resonance is formed by four points of $\mathbb{Z}^2$ which have a simple geometrical characterization: they form the vertices of a rectangle. Indeed, if a quadruple $\{\mathbf{k}, \mathbf{k}_1, \mathbf{k}_3, \mathbf{k}_2\}$ satisfies Eqs. (2.15) with $q = 3$, then on account of the second relation we have $\mathbf{k}_1 - \mathbf{k} = \mathbf{k}_3 - \mathbf{k}_2$. So the polygonal $\{\mathbf{k}, \mathbf{k}_1, \mathbf{k}_3, \mathbf{k}_2\}$ is a parallelogram. Substituting $\mathbf{k} = \mathbf{k}_1 + \mathbf{k}_2 - \mathbf{k}_3$ in the first relation and using Eq. (2.28) we get

$$2(\mathbf{k}_3\cdot\mathbf{k}_3 + \mathbf{k}_1\cdot\mathbf{k}_2 - \mathbf{k}_2\cdot\mathbf{k}_3 - \mathbf{k}_1\cdot\mathbf{k}_3) = 0 \quad \Rightarrow \quad (\mathbf{k}_3 - \mathbf{k}_2)\cdot(\mathbf{k}_3 - \mathbf{k}_1) = 0\,. \tag{2.35}$$

That is, $\mathbf{k}_3 - \mathbf{k}_2$ is orthogonal to $\mathbf{k}_3 - \mathbf{k}_1$. So $\{\mathbf{k}, \mathbf{k}_1, \mathbf{k}_3, \mathbf{k}_2\}$ is a rectangle in $\mathbb{Z}^2$.

It is easy to see that for any vectors $\mathbf{k}, \mathbf{k}_1 \in \mathbb{Z}^2$ there is an integer rectangle of the form $\{\mathbf{k}, \mathbf{k}_1, \mathbf{k}_2, \mathbf{k}_3\}$. So the equivalence, defined by the clusters of the 2d NLS equation makes $\mathbb{Z}^2$ a single cluster, and the equation falls in the case (2). A graphical illustration of some resonant quadruples and their connections in $\mathbb{Z}^2$ is displayed in Fig. 2.1.

Similar all higher-dimensional NLS equations fall in case (2).

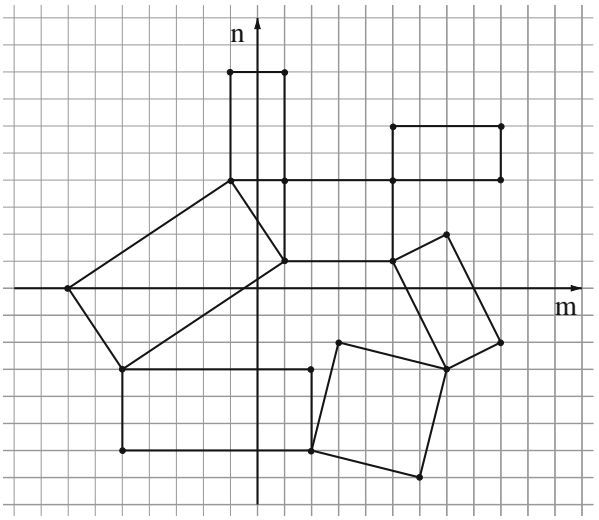

Fig. 2.1 Examples of connected resonant quadruples for the NLS equation in the $\mathbb{Z}^2$ lattice. Each point is the vertex of at least one rectangle

2.3.3 *Structure of Resonances for CHM*

The structure of resonances for the CHM equation depends on the shape-factor ρ. Below we discuss it, supposing for simplicity that the Froude number F is kept fixed (see [13] for the general case). We start with explicitly rewriting for the present case the resonance condition given be Eq. (2.15) (recall that $\mathbf{k}_1 = (m_1, n_1)$, $\mathbf{k}_2 = (m_2, n_2)$ and $\mathbf{k} = (m, n)$):

$$m_1 + m_2 = m\,, \qquad n_1 + n_2 = n\,,$$
$$\frac{m_1}{m_1^2 + n_1^2\rho^2 + F\rho^2} + \frac{m_2}{m_2^2 + n_2^2\rho^2 + F\rho^2} = \frac{m}{m^2 + n^2\rho^2 + F\rho^2}\,. \tag{2.36}$$

Solutions $(\mathbf{k}_1, \mathbf{k}_2, \mathbf{k})$ to these equations can be divided to different classes, according to how many numbers among m_1, m_2 and m are non-zero:

(i) If all three are zero, then any triad $\mathbf{k}_1 = (0, n_1)$, $\mathbf{k}_2 = (0, n_2)$, $\mathbf{k} = (0, n_1 + n_2)$ constitutes a solution. As $c_{\mathbf{k}_1,\mathbf{k}_2,\mathbf{k}}$ vanish in this case (see Eq. (2.34)), such triads do not form a resonance.
(ii) If only one number is different from zero, then Eq. (2.36) admits no solution.
(iii) If only one among m_1, m_2 and m_3 vanishes, two subcases arise (as $\mathbf{k}_1$ and $\mathbf{k}_2$ play an exchangeable role):
   (a) if $m_1 = 0$ (which implies $m_2 = m$), then $n_2^2 = n^2$ and there are two solutions, one for $n_1 = 0$, $n_2 = n$, and another for $n_2 = -n_1/2 = -n$;
   (b) if $m = 0$ (which implies $m_1 = -m_2$), then $n_1^2 = n_2^2$ and again there are two solutions, one for $n = 0$, $n_1 = -n_2$, and another for $n_1 = n_2 = n/2$.

(iv) All three are different from zero. This is the only case when the solutions depend on ρ. Indeed, let us fix a triad $(\mathbf{k}_1, \mathbf{k}_2, \mathbf{k})$ and look for which values of ρ it constitutes a resonance. The second line of Eq. (2.36) may be re-written as

$$a_0(\mathbf{k}_1, \mathbf{k}_2, \mathbf{k}) + a_1(\mathbf{k}_1, \mathbf{k}_2, \mathbf{k}, F)\rho^2 + a_2(\mathbf{k}_1, \mathbf{k}_2, \mathbf{k}, F)\rho^4 = 0\,, \tag{2.37}$$

where a_0, a_1 and a_2 are polynomials. In particular,

$$a_0 = m_1 m_2 m\,(m_2 m + m_1 m - m_1 m_2)\,. \tag{2.38}$$

In view of the inequality $(x^2 + y^2 + xy) > 0$, valid for non-vanishing x and y,

$$a_0 = m_1 m_2 m\left(m_1^2 + m_2^2 + m_1 m_2\right) \neq 0\,, \tag{2.39}$$

where the use is made of the first line of Eq. (2.36). This shows that the second order polynomial in ρ^2 at the l.h.s. of Eq. (2.37) is nontrivial. So for any fixed triad $(\mathbf{k}_1, \mathbf{k}_2, \mathbf{k})$, where m_1, m_2 and m are nonzero, relation given be Eq. (2.37) holds for at most two nonnegative values of ρ.

The different types of resonances are represented in Fig. 2.2, where only the points above the horizontal axis are displayed (cf. footnote 3). There the resonances of type (iii) (which we will call standard resonances) are connected by solid lines: they form triangles symmetric with respect to the vertical axis $m = 0$, in which each point $(2m, 0)$ is connected with (m, n) and $(m, -n)$, for any n. The resonances of type (iv) (which we will call non-standard) are displayed as dashed lines: they constitute triangles in which none of the vertices lies on the vertical axis.

Since each non-standard resonance appears only for at most two values of ρ, then by removing (at most) a countable set of ρs we kill all of them. Let us denote this removed set $\mathcal{Z} \subset \mathbb{R}_+$. The set $\mathbb{R}^+ \backslash \mathcal{Z}$ of remaining values of ρ, for which no non-standard resonance appear, can be regarded as "typical". Accordingly

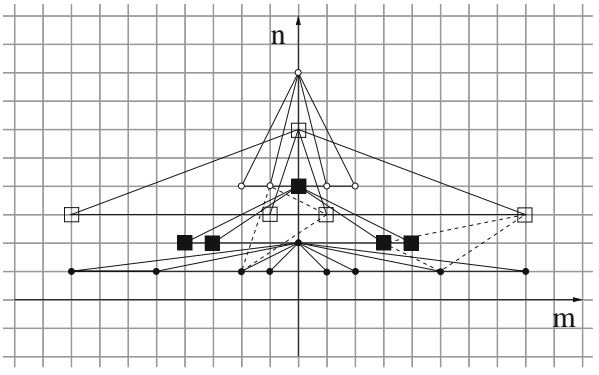

Fig. 2.2 Example of connected resonant triads for the CHM equation in the $\mathbb{Z}^2$ lattice. Points belonging to different clusters of standard resonances are marked with *different symbols*, *solid lines* connect standard resonances, *dashed lines* non-standard ones

we will refer to $\rho \in \mathbb{R}^+ \setminus \mathbb{Z}$ as *typical* values of ρ (or as to the *typical case*). Below in Sect. 2.5 we show that in the typical case all resonances are divided to non-intersecting clusters of size at most 3, thus fitting the third option, considered in Sect. 2.3.

2.4 NLS: The Power-Law Energy Spectrum

Effective equation (2.33) for NLS (which, as we have seen, determines the energy spectrum) is not easy to handle since its completely connected resonance structure (see Sect. 2.3.2) makes impossible to split it to simpler subsystems (on contrary to the CHM equation, see Sect. 2.5). We present here a way to investigate the behavior of solutions of Eq. (2.33) when the size L of the box goes to infinity, based on certain traditional for the wave turbulence heuristic approximation (see [16–18]), following our work [14]. This will lead us to a wave kinetic (WK) equation of the form, usually encountered in the wave turbulence. The treatment follows closely the paper [14], to which the reader can refer for further details.

2.4.1 The Limit $L \to \infty$

From the point of view of mathematics, the limit when the size L of the torus $\mathbb{T}^d_L$ tends to infinity in Eq. (2.33) presents a serious problem. In particular, for what concerns the definition of a possible limiting stochastic equation. Instead of trying to resolve this difficulty, for any finite L we will study the expectations $\mathbf{E}(\tilde{I}_\mathbf{k})$ of the actions $\tilde{I}_\mathbf{k} = \frac{1}{2}|\tilde{a}_\mathbf{k}|^2$ of solutions for the corresponding equation (the function $\mathbf{k} \mapsto \mathbf{E}(\tilde{I}_\mathbf{k})$ is called called *the wave-action spectrum*), and then pass to the limit as $L \to \infty$ only for these quantities. [4]

We fix L and, by making use of Ito's formula for $\tilde{I}_\mathbf{k}$, get from Eq. (2.33) that

$$\begin{aligned} \frac{d}{d\tau}\tilde{I}_\mathbf{k} = &\frac{i\delta}{2} \sum_{\mathbf{k}_1,\mathbf{k}_2,\mathbf{k}_3 \in \mathbb{Z}^d} \left(\tilde{a}_{\mathbf{k}_1}\tilde{a}_{\mathbf{k}_2}\tilde{a}^*_{\mathbf{k}_3}\tilde{a}^*_\mathbf{k} - \tilde{a}^*_{\mathbf{k}_1}\tilde{a}^*_{\mathbf{k}_2}\tilde{a}_{\mathbf{k}_3}\tilde{a}_\mathbf{k}\right) \delta^{12}_{3\mathbf{k}} \delta\left(\omega^{N\,12}_{3\mathbf{k}}\right) \\ &- \gamma_\mathbf{k}\tilde{I}_\mathbf{k} + \frac{\mu}{2} b_\mathbf{k}\left(\tilde{a}^*_\mathbf{k}\dot{\boldsymbol{\beta}}_\mathbf{k} + \tilde{a}_\mathbf{k}\dot{\boldsymbol{\beta}}^*_\mathbf{k}\right) + b^2_\mathbf{k}\,, \quad \mathbf{k} \in \mathbb{Z}^2\,. \end{aligned} \tag{2.40}$$

[4] In the case of the non-forced equation the expectations should be taken with respect to the distribution of the initial data, while for the forced equation—with respect to the distribution of the forcing (and, possibly, of the initial data).

Now we pass to the expected values, and define the moment $M^{\mathbf{k}_1\dots\mathbf{k}_{n_1}}_{\mathbf{k}_{n_1+1}\dots\mathbf{k}_{n_1+n_2}}(\tau)$ of $\tilde{a}(\tau)$ of order n_1+n_2 as

$$M^{\mathbf{k}_1\dots\mathbf{k}_{n_1}}_{\mathbf{k}_{n_1+1}\dots\mathbf{k}_{n_1+n_2}}(\tau) = \left\langle \tilde{a}_{\mathbf{k}_1}\cdots\tilde{a}_{\mathbf{k}_{n_1}}\tilde{a}^*_{\mathbf{k}_{n_1+1}}\cdots\tilde{a}^*_{\mathbf{k}_{n_1+n_2}}\right\rangle_\tau , \tag{2.41}$$

where $\langle\cdot\rangle_\tau$ stands for the expected value at time τ, i.e., $\langle f(\tilde{a})\rangle_\tau = \mathbf{E}\big(f(\tilde{a}(\tau))\big)$ for any measurable function $f(\tilde{a})$. Then from the system of Eqs. (2.40) we get

$$\dot{M}^{\mathbf{k}}_{\mathbf{k}} = -2\gamma_{\mathbf{k}}M^{\mathbf{k}}_{\mathbf{k}} + 2b^2_{\mathbf{k}} + 2\delta\sum_{\mathbf{k}_1,\mathbf{k}_2,\mathbf{k}_3}\mathrm{Im}\,M^{\mathbf{k}_1\mathbf{k}_2}_{\mathbf{k}\mathbf{k}_3}\delta^{\mathbf{k}_1\mathbf{k}_2}_{\mathbf{k}\mathbf{k}_3}\delta(\omega^{N\,\mathbf{k}_1\mathbf{k}_2}_{\mathbf{k}\mathbf{k}_3}) , \quad \mathbf{k}\in\mathbb{Z}^d . \tag{2.42}$$

This system is not closed since it involves the moments of order 4. By applying again Ito's formula, we can express the time derivative of moments of any order n_1+n_2 as a function of the moments of order n_1+n_2-2 and those of order n_1+n_2+2. The coupled system, containing the equations for all moments, is called the *chain of moments equation* (see [15]).[5] Systems of this kind are usually treated by approximating moments of high order by suitable functions of lower order moments in order to get a closed system of equations. We will show that if the quasi-stationary and quasi-Gaussian approximations (see below) are chosen to close the system of moment equations, then under the limit $L\to\infty$ we recover a modified version of the WK equation.

To study the sum in the r.h.s. of Eq. (2.42), we notice that if the Krönecker deltas are different from zero because $\mathbf{k}$ equals to one vector among $\mathbf{k}_1,\mathbf{k}_2$ and $\mathbf{k}_3$ is equal to another, then the moment is real and does not contribute to the sum. So we may assume that $\mathbf{k}\neq\mathbf{k}_1,\mathbf{k}_2$, $\mathbf{k}_3\neq\mathbf{k}_1,\mathbf{k}_2$. In this case we calculate the fourth order moments in the r.h.s. of Eq. (2.42) through Ito's formula (see [14]) and get

$$\begin{aligned}\dot{M}^{\mathbf{k}_1\mathbf{k}_2}_{\mathbf{k}\mathbf{k}_3} =& -(\gamma_{\mathbf{k}}+\gamma_{\mathbf{k}_1}+\gamma_{\mathbf{k}_2}+\gamma_{\mathbf{k}_3})M^{\mathbf{k}_1\mathbf{k}_2}_{\mathbf{k}\mathbf{k}_3}\\ &+i\delta\sum_{\mathbf{k}_4,\mathbf{k}_5,\mathbf{k}_6}\Big(M^{\mathbf{k}_1\mathbf{k}_2\mathbf{k}_4}_{\mathbf{k}_3\mathbf{k}_5\mathbf{k}_6}\delta^{\mathbf{k}\mathbf{k}_4}_{\mathbf{k}_5\mathbf{k}_6}\delta(\omega^{N\,\mathbf{k}\mathbf{k}_4}_{\mathbf{k}_5\mathbf{k}_6}) + M^{\mathbf{k}_1\mathbf{k}_2\mathbf{k}_4}_{\mathbf{k}\mathbf{k}_5\mathbf{k}_6}\delta^{\mathbf{k}_3\mathbf{k}_4}_{\mathbf{k}_5\mathbf{k}_6}\delta(\omega^{N\,\mathbf{k}_3\mathbf{k}_4}_{\mathbf{k}_5\mathbf{k}_6})\\ &-M^{\mathbf{k}_2\mathbf{k}_5\mathbf{k}_6}_{\mathbf{k}\mathbf{k}_3\mathbf{k}_4}\delta^{\mathbf{k}_5\mathbf{k}_6}_{\mathbf{k}_1\mathbf{k}_4}\delta(\omega^{N\,\mathbf{k}_5\mathbf{k}_6}_{\mathbf{k}_1\mathbf{k}_4}) - M^{\mathbf{k}_1\mathbf{k}_5\mathbf{k}_6}_{\mathbf{k}\mathbf{k}_3\mathbf{k}_4}\delta^{\mathbf{k}_5\mathbf{k}_6}_{\mathbf{k}_2\mathbf{k}_4}\delta(\omega^{N\,\mathbf{k}_5\mathbf{k}_6}_{\mathbf{k}_2\mathbf{k}_4})\Big) .\end{aligned} \tag{2.43}$$

We make now the first approximation by neglecting the term containing the time derivative at the l.h.s. of Eq. (2.43). This can be justified, if τ is large enough, by the quasi-stationary approximation (cf. Sect. 2.1.3 in [18]). Namely, let us write

[5] Notice that, since the equation which we consider has a cubic nonlinearity, equations for moments of even order are decoupled from those for moments of odd order.

Eq. (2.43) as

$$\left(\frac{d}{d\tau} + (\gamma_{\mathbf{k}} + \gamma_{\mathbf{k}_1} + \gamma_{\mathbf{k}_2} + \gamma_{\mathbf{k}_3})\right) M^{\mathbf{k}_1\mathbf{k}_2}_{\mathbf{k}\mathbf{k}_3} = f\,. \tag{2.44}$$

Notice that since all $\gamma_{\mathbf{k}}$s are positive, then the linear differential equation in the l.h.s. is exponentially stable. Assume that f as a function of τ is almost constant during time-intervals, sufficient for relaxation of the differential equation. Then

$$M^{\mathbf{k}_1\mathbf{k}_2}_{\mathbf{k}\mathbf{k}_3} \approx \frac{f}{\gamma_{\mathbf{k}} + \gamma_{\mathbf{k}_1} + \gamma_{\mathbf{k}_2} + \gamma_{\mathbf{k}_3}}\,. \tag{2.45}$$

We insert this in Eq. (2.42) and get

$$\begin{aligned}\dot{M}^{\mathbf{k}}_{\mathbf{k}} \approx -2\gamma_{\mathbf{k}} M^{\mathbf{k}}_{\mathbf{k}} + 2b^2_{\mathbf{k}} + 2\delta^2 \sum_{\mathbf{k}_1,\mathbf{k}_2,\mathbf{k}_3} \frac{1}{\gamma_{\mathbf{k}} + \gamma_{\mathbf{k}_1} + \gamma_{\mathbf{k}_2} + \gamma_{\mathbf{k}_3}} \delta^{\mathbf{k}_1\mathbf{k}_2}_{\mathbf{k}\mathbf{k}_3} \delta(\omega^{N\,\mathbf{k}_1\mathbf{k}_2}_{\mathbf{k}\mathbf{k}_3}) \\ \times \Re\left(\sum_{\mathbf{k}_4,\mathbf{k}_5,\mathbf{k}_6} \left(M^{\mathbf{k}_1\mathbf{k}_2\mathbf{k}_4}_{\mathbf{k}_3\mathbf{k}_5\mathbf{k}_6} \delta^{\mathbf{k}\mathbf{k}_4}_{\mathbf{k}_5\mathbf{k}_6} \delta(\omega^{N\,\mathbf{k}\mathbf{k}_4}_{\mathbf{k}_5\mathbf{k}_6}) + M^{\mathbf{k}_1\mathbf{k}_2\mathbf{k}_4}_{\mathbf{k}\mathbf{k}_5\mathbf{k}_6} \delta^{\mathbf{k}_3\mathbf{k}_4}_{\mathbf{k}_5\mathbf{k}_6} \delta(\omega^{N\,\mathbf{k}_3\mathbf{k}_4}_{\mathbf{k}_5\mathbf{k}_6})\right.\right. \\ \left.\left. - M^{\mathbf{k}_2\mathbf{k}_5\mathbf{k}_6}_{\mathbf{k}\mathbf{k}_3\mathbf{k}_4} \delta^{\mathbf{k}_5\mathbf{k}_6}_{\mathbf{k}_1\mathbf{k}_4} \delta(\omega^{N\,\mathbf{k}_5\mathbf{k}_6}_{\mathbf{k}_1\mathbf{k}_4}) - M^{\mathbf{k}_1\mathbf{k}_5\mathbf{k}_6}_{\mathbf{k}\mathbf{k}_3\mathbf{k}_4} \delta^{\mathbf{k}_5\mathbf{k}_6}_{\mathbf{k}_2\mathbf{k}_4} \delta(\omega^{N\,\mathbf{k}_5\mathbf{k}_6}_{\mathbf{k}_2\mathbf{k}_4})\right)\right)\,.\end{aligned} \tag{2.46}$$

We then apply the second approximation, generally accepted in the WT (see [2, 16–18]) which enables us to transform the previous relation to a closed equation for the second order moments. This consists in the quasi-Gaussian approximation, i.e., in the assumption that the higher-order moments given by Eq. (2.41) can be approximated by polynomials of the second-order moments, as if the random variables $v_{\mathbf{k}}$ were independent complex Gaussian variables. In particular,

$$\begin{aligned}M^{\mathbf{l}_1\mathbf{l}_2\mathbf{l}_3}_{\mathbf{l}_4\mathbf{l}_5\mathbf{l}_6} \approx M^{\mathbf{l}_1}_{\mathbf{l}_1} M^{\mathbf{l}_2}_{\mathbf{l}_2} M^{\mathbf{l}_3}_{\mathbf{l}_3} \\ \times \left(\delta^{\mathbf{l}_1}_{\mathbf{l}_4}(\delta^{\mathbf{l}_2}_{\mathbf{l}_5}\delta^{\mathbf{l}_3}_{\mathbf{l}_6} + \delta^{\mathbf{l}_2}_{\mathbf{l}_6}\delta^{\mathbf{l}_3}_{\mathbf{l}_5}) + \delta^{\mathbf{l}_1}_{\mathbf{l}_5}(\delta^{\mathbf{l}_2}_{\mathbf{l}_4}\delta^{\mathbf{l}_3}_{\mathbf{l}_6} + \delta^{\mathbf{l}_2}_{\mathbf{l}_6}\delta^{\mathbf{l}_3}_{\mathbf{l}_4}) + \delta^{\mathbf{l}_1}_{\mathbf{l}_6}(\delta^{\mathbf{l}_2}_{\mathbf{l}_4}\delta^{\mathbf{l}_3}_{\mathbf{l}_5} + \delta^{\mathbf{l}_2}_{\mathbf{l}_5}\delta^{\mathbf{l}_3}_{\mathbf{l}_4})\right)\,.\end{aligned} \tag{2.47}$$

At this point we pass in Eq. (2.46), closed using the relation given by Eq. (2.47), to the limit $L \to \infty$. This can be done by approximating sums with integrals if, instead of parameterizing the modes by integer vectors $\mathbf{k} \in \mathbb{Z}^d$, we parameterize them by vectors $\tilde{\mathbf{k}} = \mathbf{k}/L$ from the shrunk lattice $\mathbb{Z}^d_L = L^{-1}\mathbb{Z}^d$. Accordingly we define

$$\tilde{M}^{\tilde{\mathbf{k}}_1\ldots\tilde{\mathbf{k}}_{n_1}}_{\tilde{\mathbf{k}}_{n_1+1}\ldots\tilde{\mathbf{k}}_{n_1+n_2}} := M^{\mathbf{k}_1\ldots\mathbf{k}_{n_1}}_{\mathbf{k}_{n_1+1}\ldots\mathbf{k}_{n_1+n_2}}\,, \quad \tilde{\gamma}_{\tilde{\mathbf{k}}} := \gamma_{\mathbf{k}}\,, \quad \tilde{b}_{\tilde{\mathbf{k}}} := b_{\mathbf{k}}\,, \tag{2.48}$$

and note that since the restriction, imposed by the Krönecker deltas, is homogeneous, then it does not change under this re-parametrization. Abusing notation, we will drop the tildes in the rest of the Section, but will use the parametrization by points of $\mathbb{Z}_L^d$.

We denote by $S_{\mathbf{k}}$ the sum, given by the second and third lines of Eq. (2.46), written in the new parametrization, and note that it splits into a finite number of sums like

$$S_{\mathbf{k}}^j = \sum_{(\mathbf{k}_1,\mathbf{k}_2,\mathbf{k}_3,\mathbf{k}_4,\mathbf{k}_5,\mathbf{k}_6)\in\mathbb{Z}_L^{6d}\cap\Sigma_{\mathbf{k}}^j} F_{\mathbf{k}}^j(\mathbf{k}_1,\mathbf{k}_2,\mathbf{k}_3,\mathbf{k}_4,\mathbf{k}_5,\mathbf{k}_6)\,. \tag{2.49}$$

Here $\Sigma_{\mathbf{k}}^j$ is a manifold in $\mathbb{R}^{6d}$, defined as

$$\begin{aligned}\Sigma_{\mathbf{k}}^j = \big\{&(\mathbf{x}_1,\mathbf{x}_2,\mathbf{x}_3,\mathbf{x}_4,\mathbf{x}_5,\mathbf{x}_6)\ : \mathbf{x}_1+\mathbf{x}_2=\mathbf{k}+\mathbf{x}_3, |\mathbf{x}_1|^2+|\mathbf{x}_2|^2=|\mathbf{k}|^2+|\mathbf{x}_3|^2\\ &\mathbf{x}^j+\mathbf{x}_4=\mathbf{x}_5+\mathbf{x}_6, |\mathbf{x}^j|^2+|\mathbf{x}_4|^2=|\mathbf{x}_5|^2+|\mathbf{x}_6|^2, \mathbf{x}_1^j=\mathbf{x}_2^j,\\ &\mathbf{x}_3^j=\mathbf{x}_4^j, \mathbf{x}_5^j=\mathbf{x}_6^j\big\}\ ,\end{aligned} \tag{2.50}$$

where $\mathbf{x}^j$ stands for one among the vectors $\mathbf{k}, \mathbf{x}_1, \mathbf{x}_2, \mathbf{x}_3$, and $\{\mathbf{x}_1^j,\dots,\mathbf{x}_6^j\}$—for a permutation of the set $\{\mathbf{k},\mathbf{x}_1,\dots,\mathbf{x}_6\}\backslash\{\mathbf{x}^j\}$.[6] It is easy to see that since every F^j is a regular function, then when passing from the sums to integrals in the limit $L\to\infty$, each term $S_{\mathbf{k}}^j$ as a function of L becomes proportional to L^m, where m is the dimension of the manifold $\Sigma_{\mathbf{k}}^j$. A detailed analysis of all cases shows that the terms of the highest order in L in the integral correspond to terms of the form

$$S_{\mathbf{k}}^j = \sum_{\mathbf{k}_1,\mathbf{k}_2,\mathbf{k}_3} F_{\mathbf{k}}(\mathbf{k}_1,\mathbf{k}_2,\mathbf{k}_3)\delta_{\mathbf{k}\mathbf{k}_3}^{\mathbf{k}_1\mathbf{k}_2}\delta(\omega^{N}{}_{\mathbf{k}\mathbf{k}_3}^{\mathbf{k}_1\mathbf{k}_2})$$

in the sum $S_{\mathbf{k}}$, where $\mathbf{k}:=(\mathbf{k}_1,\mathbf{k}_2,\mathbf{k}_3)\in\mathbb{Z}_L^{3d}$. Denote

$$\Sigma_{\mathbf{k}} = \big\{\mathbf{x}=(\mathbf{x}_1,\mathbf{x}_2,\mathbf{x}_3)\in\mathbb{R}^{3d} : \mathbf{x}_1+\mathbf{x}_2=\mathbf{k}+\mathbf{x}_3, |\mathbf{x}_1|^2+|\mathbf{x}_2|^2=|\mathbf{k}|^2+|\mathbf{x}_3|^2\big\}\ . \tag{2.51}$$

This is a manifold of dimension $3d-d-1=2d-1$, smooth outside the origin. The latter lies outside $\Sigma_{\mathbf{k}}$ if $\mathbf{k}\neq 0$, and is a singular point of $\Sigma_{\mathbf{k}}$ if $\mathbf{k}=0$.

As shown in [14], in the limit $L\to\infty$ the sum $S_{\mathbf{k}}$ can be approximated by the integral

$$S_{\mathbf{k}} \approx L^{2d-1}\int_{\Sigma\backslash\{0\}} \frac{F_{\mathbf{k}}(\mathbf{x})}{\varphi_{\mathbf{k}}(\mathbf{x})}d\mathbf{x}\,, \tag{2.52}$$

[6] Note that the relations, defining $\Sigma_{\mathbf{k}}^j$ are not independent.

where $\varphi_{\mathbf{k}}(\mathbf{x})$ is a certain function on $\Sigma_{\mathbf{k}}$, smooth outside zero, such that

$$\begin{aligned} V_1 \le \varphi_{\mathbf{k}}(\mathbf{x}) \le V_1(3d)^{d-1/2}\,, \quad \varphi_{\mathbf{k}}(\mathbf{x}) := \varphi_{m\mathbf{k}}(m\mathbf{x})\,, \\ \varphi_{\mathbf{k}}(\mathbf{x}_1,\mathbf{x}_2,\mathbf{x}_3) = \varphi_{\mathbf{k}}(\mathbf{x}_2,\mathbf{x}_1,\mathbf{x}_3)\,, \quad \varphi_{\mathbf{k}}(\mathbf{x}_1,\mathbf{x}_2,\mathbf{x}_3) = \varphi_{\mathbf{x}_3}(\mathbf{x}_1,\mathbf{x}_2,\mathbf{k})\,, \end{aligned} \tag{2.53}$$

where V_1 is the volume of the 1-ball in $\mathbb{R}^{2d-1}$.

By substituting Eq. (2.47) in Eq. (2.46) and using Eq. (2.52) we get the limiting (as $L \to \infty$) equation in the form

$$\begin{aligned} \dot M^{\mathbf{k}}_{\mathbf{k}} \approx -2\gamma_{\mathbf{k}} M^{\mathbf{k}}_{\mathbf{k}} + 2b^2_{\mathbf{k}} + 4\delta^2 L^{2d-1} \int_{\mathbb{R}^{3d}\setminus\{0\}} d\mathbf{k}_1 d\mathbf{k}_2 d\mathbf{k}_3 \frac{\varphi^{-1}_{\mathbf{k}}(\mathbf{k}_1,\mathbf{k}_2,\mathbf{k}_3)}{\gamma_{\mathbf{k}}+\gamma_{\mathbf{k}_1}+\gamma_{\mathbf{k}_2}+\gamma_{\mathbf{k}_3}} \delta^{\mathbf{k}_1\mathbf{k}_2}_{\mathbf{k}\mathbf{k}_3} \\ \times \delta(\omega^{N\,\mathbf{k}_1\mathbf{k}_2}_{\mathbf{k}\mathbf{k}_3}) \Big(M^{\mathbf{k}_1}_{\mathbf{k}_1} M^{\mathbf{k}_2}_{\mathbf{k}_2} M^{\mathbf{k}_3}_{\mathbf{k}_3} + M^{\mathbf{k}}_{\mathbf{k}} M^{\mathbf{k}_1}_{\mathbf{k}_1} M^{\mathbf{k}_2}_{\mathbf{k}_2} - M^{\mathbf{k}}_{\mathbf{k}} M^{\mathbf{k}_2}_{\mathbf{k}_2} M^{\mathbf{k}_3}_{\mathbf{k}_3} - M^{\mathbf{k}}_{\mathbf{k}} M^{\mathbf{k}_1}_{\mathbf{k}_1} M^{\mathbf{k}_3}_{\mathbf{k}_3} \Big)\,. \end{aligned} \tag{2.54}$$

Finally, we define

$$n_{\mathbf{k}} = L^d M^{\mathbf{k}}_{\mathbf{k}}/2\,, \quad \mathfrak{b}_{\mathbf{k}} = L^{d/2} b_{\mathbf{k}}\,, \tag{2.55}$$

(so that $\sum_{\mathbf{k}} M^{\mathbf{k}}_{\mathbf{k}}/2 \to \int n_{\mathbf{k}}$ and $\sum_{\mathbf{k}} b^2_{\mathbf{k}} \to \int \mathfrak{b}^2_{\mathbf{k}}$ as L goes to infinity), choose

$$\delta(L) = \tilde\varepsilon^2 L^{1/2} = \frac{\varepsilon^{2q*}}{\nu} \tilde\varepsilon^2 L^{1/2}\,, \tag{2.56}$$

for some $\tilde\varepsilon > 0$, and get the kinetic equation

$$\begin{aligned} \dot n_{\mathbf{k}} = -2\gamma_{\mathbf{k}} n_{\mathbf{k}} + \mathfrak{b}^2_{\mathbf{k}} + 16\tilde\varepsilon^4 \int_{\mathbb{R}^{3d}\setminus\{0\}} d\mathbf{k}_1\, d\mathbf{k}_2\, d\mathbf{k}_3 \delta^{\mathbf{k}_1\mathbf{k}_2}_{\mathbf{k}\mathbf{k}_3} \delta(\omega^{N\,\mathbf{k}_1\mathbf{k}_2}_{\mathbf{k}\mathbf{k}_3}) \\ \times \frac{\varphi^{-1}_{\mathbf{k}}(\mathbf{k}_1,\mathbf{k}_2,\mathbf{k}_3)}{\gamma_{\mathbf{k}}+\gamma_{\mathbf{k}_1}+\gamma_{\mathbf{k}_2}+\gamma_{\mathbf{k}_3}} \Big(n_{\mathbf{k}_1} n_{\mathbf{k}_2} n_{\mathbf{k}_3} + n_{\mathbf{k}} n_{\mathbf{k}_1} n_{\mathbf{k}_2} - n_{\mathbf{k}} n_{\mathbf{k}_2} n_{\mathbf{k}_3} - n_{\mathbf{k}} n_{\mathbf{k}_1} n_{\mathbf{k}_3} \Big)\,. \end{aligned} \tag{2.57}$$

We have thus shown that, with the proper scaling of δ and b given by Eqs. (2.55)–(2.56), the function $n_{\mathbf{k}}$ satisfies a kinetic equation, similar to the WK equation for NLS in the classical wave turbulence theory (see, for instance, formula (6.81) of [16], where $d = 2$). The differences are two: obviously in our case there are forcing and dissipation, absent in the traditional WK equations. More interesting is the nonvanishing denominator $\gamma_{\mathbf{k}} + \gamma_{\mathbf{k}_1} + \gamma_{\mathbf{k}_2} + \gamma_{\mathbf{k}_3}$ which regularizes the integral since it growths to infinity with $\mathbf{k}$, and which modifies the spectra.

2.4.2 Power Law Spectra

Now, under some additional approximation and using the well known Zakharov's argument (see [16–18]) we will get stationary solutions of Eq. (2.57) with power law energy spectra (more properly, wave-action spectra) $\{n_{\mathbf{k}}\}$.

To do this we have to restrain our analysis to the inertial interval, i.e., to the spectral interval, where the damping and forcing are negligible. That is, we should consider Eq. (2.57), supposing that the wave-vector $\mathbf{k}$ belongs to a sufficiently large spectral region, where the first two terms at the r.h.s. of Eq. (2.57) can be neglected, compared with the third. This happens, e.g., if there the solution $\{n_{\mathbf{k}}\}$ is of order one, while $\mathfrak{b}_{\mathbf{k}} \ll 1$ and $\gamma_{\mathbf{k}} \ll 1$ (i.e., the damping and the dissipation are small at that spectral region). In the inertial interval we end up with the equation

$$\begin{aligned} \dot{n}_{\mathbf{k}} \approx 16\,\tilde{\varepsilon}^4 \int_{\mathbb{R}^{3d}\setminus\{0\}} d\mathbf{k}_1\, d\mathbf{k}_2\, d\mathbf{k}_3 \delta^{\mathbf{k}_1\mathbf{k}_2}_{\mathbf{k}\mathbf{k}_3} \delta(\omega^{N\,\mathbf{k}_1\mathbf{k}_2}_{\mathbf{k}\mathbf{k}_3}) \frac{\varphi_{\mathbf{k}}^{-1}(\mathbf{k}_1,\mathbf{k}_2,\mathbf{k}_3)}{\gamma_{\mathbf{k}}+\gamma_{\mathbf{k}_1}+\gamma_{\mathbf{k}_2}+\gamma_{\mathbf{k}_3}} \\ \times \left(n_{\mathbf{k}_1} n_{\mathbf{k}_2} n_{\mathbf{k}_3} + n_{\mathbf{k}} n_{\mathbf{k}_1} n_{\mathbf{k}_2} - n_{\mathbf{k}} n_{\mathbf{k}_2} n_{\mathbf{k}_3} - n_{\mathbf{k}} n_{\mathbf{k}_1} n_{\mathbf{k}_3} \right). \end{aligned} \tag{2.58}$$

Notice that, while in the inertial interval we can simply approximate $\mathfrak{b}_{\mathbf{k}}$ with zero, this cannot be done to $\gamma_{\mathbf{k}}$ since these numbers appear in the denominator of the integral at the r.h.s. of Eq. (2.57) (their sum makes the denominator of the so-called *collision term*), and play an essential role in determining of the spectrum.

The previous equation has the form of the four-wave kinetic equation (see, for instance, formula 2.1.29 of [18]). It is well known (see [16, 18]) how to solve such equations for stationary spectra with the aid of the Zakharov transformations, provided that the terms

$$\mathcal{T}^{\mathbf{k},\mathbf{k}_3}_{\mathbf{k}_1,\mathbf{k}_2} = \frac{\varphi_{\mathbf{k}}^{-1}(\mathbf{k}_1,\mathbf{k}_2,\mathbf{k}_3)}{\gamma_{\mathbf{k}}+\gamma_{\mathbf{k}_1}+\gamma_{\mathbf{k}_2}+\gamma_{\mathbf{k}_3}} \tag{2.59}$$

satisfy, for some $m \in \mathbb{R}$, the following conditions of symmetry and homogeneity:

$$\mathcal{T}^{\mathbf{k},\mathbf{k}_3}_{\mathbf{k}_1,\mathbf{k}_2} = \mathcal{T}^{\mathbf{k}_3,\mathbf{k}}_{\mathbf{k}_1,\mathbf{k}_2} = \mathcal{T}^{\mathbf{k},\mathbf{k}_3}_{\mathbf{k}_2,\mathbf{k}_1} = \mathcal{T}^{\mathbf{k}_1,\mathbf{k}_2}_{\mathbf{k},\mathbf{k}_3}\,, \qquad \mathcal{T}^{\lambda\mathbf{k},\lambda\mathbf{k}_3}_{\lambda\mathbf{k}_1,\lambda\mathbf{k}_2} = \lambda^m \mathcal{T}^{\mathbf{k},\mathbf{k}_3}_{\mathbf{k}_1,\mathbf{k}_2}\,. \tag{2.60}$$

Since φ is a homogeneous function of degree 0 due to (2.53), the requirements above are met if on the inertial range the function $\gamma_{\mathbf{k}}$ can be approximated by a homogeneous function of the form $\gamma_{\mathbf{k}} = \varepsilon' |\mathbf{k}|^m$, where m is a real number and $\varepsilon' \ll 1$ is a small parameter to guaranty that the dissipation term indeed is negligible.

We abbreviate $|\mathbf{k}| = k$ and look for stationary isotropic, spectra behaving as power laws of k, i.e. $n_{\mathbf{k}} = n_k \propto k^\nu$ for some real ν, by searching ν such that the r.h.s. of Eq. (2.58) vanishes. The result (see [14]) is that, in addition to the equilibrium solutions $n_k = C$ and $n_k = C/k^2$, which correspond, respectively, to the equipartition of the wave action and of the quadratic energy (Rayleigh-Jeans distribution), two nontrivial power law stationary distributions appear. These are the

solutions:

$$n_k \propto k^{-(m+3d-2)/3}\,, \qquad n_k \propto k^{-(m+3d)/3}\,. \tag{2.61}$$

If $m = 0$, they coincide with the well known in the wave turbulence power-law spectra for the free NLS equation $(2.23)_{\nu=0}$ (for $d \geq 2$, see [16]), but the dissipation modifies the power law of the decay if $m \neq 0$.

2.5 CHM: Resonance Clustering

Let us consider in more detail the effective equation (2.34) for the CHM equation for typical values of the shape-factor ρ. By the definition of a typical ρ (see Sect. 2.3.3), no resonances corresponding to the case (iv) of Sect. 2.3.3 occur. We can then write the effective equation explicitly, following [13]. It will only involve resonances of type (iii).

Let us consider the equations for the variables $\tilde{a}_{\mathbf{k}}$ with $\mathbf{k} = (m, n)$, separating the cases $m = 0$ and $m \neq 0$. When $m = 0$, the only terms which survive in the nonlinearity $R_{\mathbf{k}}(\tilde{a})$ are those where $\mathbf{k}_1$ and $\mathbf{k}_2$ satisfy the relation (iii-b) of Sect. 2.3.3, while for $m \neq 0$ only the terms falling in the case (iii-a) give contribution. For $m = 0$, the nonlinearity vanishes if n is odd, while if it is even, then

$$\begin{aligned} R_{\mathbf{k}}(\tilde{a}) = &\frac{1}{\rho(m^2 + n^2\rho^2 + F\rho^2)} \\ &\times \sum_{m_1 \in \mathbb{Z}} \left(m_1^2 + \frac{n^2\rho^2}{4}\right) m_1 n\, \tilde{a}_{(m_1, n/2)}\, \tilde{a}_{(-m_1, n/2)}\,, \quad m = 0\,, \end{aligned} \tag{2.62}$$

which in turn vanishes because the odd symmetry in m_1. On the other hand, if $m_1 \neq 0$, then $\mathbf{k}_1$ and $\mathbf{k}_2$ are completely determined by $\mathbf{k}$. So we get that

$$R_{\mathbf{k}}(\tilde{a}) = \left(\frac{2mn}{\rho(m^2 + n^2\rho^2 + F\rho^2)} \left(3n^2\rho^2 - m^2\right) \tilde{a}_{\bar{\mathbf{k}}}\, \tilde{a}_{(0,2n)}\right)\,, \tag{2.63}$$

where we denoted $\bar{\mathbf{k}} := (m, -n)$. Note that this formula applies for the both case $m = 0$ and $m \neq 0$.

Expression given by Eq. (2.63) entails the remarkable consequence that the hamiltonian part of the effective equation, i.e., the system in which forcing and dissipation are removed,

$$\frac{d}{d\tau}\tilde{a}_{\mathbf{k}} = R_{\mathbf{k}}(\tilde{a})\,, \quad \mathbf{k} \in \mathbb{Z}^2\,, \tag{2.64}$$

is integrable and decomposes to invariant subsystems of complex dimension at most three. Indeed, if m or n vanish, then $R_{\mathbf{k}} = 0$ and $\tilde{a}_{\mathbf{k}}(t) = \text{const}$. Now let $m, n \neq 0$. If $3\rho^2 n^2 = m^2$, then again the equation for $\tilde{a}_{\mathbf{k}}$ trivializes. Suppose that $3L^2 n^2 \neq m^2$ and denote

$$A_{\mathbf{k}} = \frac{2mn}{m^2 + n^2\rho^2 + F\rho^2} \left(3n^2\rho^2 - m^2\right) \in \mathbb{R}\,. \tag{2.65}$$

Then $A_{\bar{\mathbf{k}}} \equiv -A_{\mathbf{k}}$. Equation (2.64) (with any fixed $\mathbf{k}$) belongs to the following invariant sub-system of (2.64):

$$\begin{aligned} \frac{d}{d\tau}\tilde{a}_{\mathbf{k}} &= A_{\mathbf{k}}\, \tilde{a}_{(0,2n)}\tilde{a}_{\bar{\mathbf{k}}}, \\ \frac{d}{d\tau}\tilde{a}_{\bar{\mathbf{k}}} &= -A_{\mathbf{k}}\, \tilde{a}^*_{(0,2n)}\tilde{a}_{\mathbf{k}}, \\ \frac{d}{d\tau}\tilde{a}_{(0,2n)} &= 0 \end{aligned} \tag{2.66}$$

(we recall that $\tilde{a}_{(0,2n)} = \tilde{a}^*_{(0,-2n)}$ by the reality condition, see footnote 3). This system is explicitly soluble: if $\tilde{a}_{(0,2n)}(0) \neq 0$, then

$$\begin{aligned} \tilde{a}_{(0,2n)}(t) &= \text{Const}\,, \\ \tilde{a}_{\mathbf{k}}(t) &= \tilde{a}_{\mathbf{k}}(0)\cos(|A_{\mathbf{k}}\tilde{a}_{(0,2n)}|t) + \tilde{a}_{\bar{\mathbf{k}}}(0)\,\mathrm{sgn}(A_{\mathbf{k}}\tilde{a}_{(0,2n)})\sin(|A_{\mathbf{k}}\tilde{a}_{(0,2n)}|t)\,, \end{aligned} \tag{2.67}$$

where for a complex number z we denote

$$\mathrm{sgn}(z) = z/|z| \text{ if } z \neq 0, \text{ and } \mathrm{sgn}(0) = 0\,. \tag{2.68}$$

The formula for $\tilde{a}_{\bar{\mathbf{k}}}(t)$ is obtained from that for $\tilde{a}_{\mathbf{k}}(t)$ by swapping $\mathbf{k}$ with $\bar{\mathbf{k}}$ and replacing $\tilde{a}_{(0,2n)}$ by its complex conjugate. All these solutions are periodic, and it is easy to check that $|\tilde{a}_{\mathbf{k}}|^2 + |\tilde{a}_{\bar{\mathbf{k}}}|^2$ and $|\tilde{a}_{(0,2n)}|^2$ are integrals of motion for Eq. (2.66).

We have established that there is no Hamiltonian exchange of energy between different modes, apart the coupled modes $\tilde{a}_{\mathbf{k}}$ and $\tilde{a}_{\bar{\mathbf{k}}}$. The situation does not change much when we switch in the forcing and the dissipation since the effective equation given by Eq. (2.34), too, splits to invariant subsystems of complex dimension one (if $mn = 0$ or $3n^2\rho^2 = m^2$), or of dimension three (otherwise). These systems either are independent, or have *catalytic interaction* through the variables $\tilde{a}_{(0,2n)}$, which satisfy the Ornstein-Uhlenbeck equation

$$\frac{d}{d\tau}\tilde{a}_{(0,2n)} = -\gamma_{(0,2n)}v_{(0,2n)} + \mu b_{(0,2n)}\dot{\boldsymbol{\beta}}_{(0,2n)}\,, \tag{2.69}$$

and are independent from other variables.

Being particularly interested in the exchange of energy, let us consider the equation for the actions $\tilde{I}$. Due to the conservation of $|\tilde{a}_{\mathbf{k}}|^2 + |\tilde{a}^2_{\bar{\mathbf{k}}}|^2$, Ito's formula gives (cf. Eq. (2.40))

$$\frac{d}{d\tau}\left(\tilde{I}_{\mathbf{k}} + \tilde{I}_{\bar{\mathbf{k}}}\right) = -\gamma_{\mathbf{k}}\tilde{I}_{\mathbf{k}} - \gamma_{\bar{\mathbf{k}}}\tilde{I}_{\bar{\mathbf{k}}} + \frac{\mu}{2}b_{\mathbf{k}}\left(\tilde{a}^*_{\mathbf{k}}\dot{\boldsymbol{\beta}}_{\mathbf{k}} + \tilde{a}_{\mathbf{k}}\dot{\boldsymbol{\beta}}^*_{\mathbf{k}}\right) + \frac{\mu}{2}b_{\bar{\mathbf{k}}}\left(\tilde{a}^*_{\bar{\mathbf{k}}}\dot{\boldsymbol{\beta}}_{\bar{\mathbf{k}}} + \tilde{a}_{\bar{\mathbf{k}}}\dot{\boldsymbol{\beta}}^*_{\bar{\mathbf{k}}}\right) + b^2_{\mathbf{k}} + b^2_{\bar{\mathbf{k}}}\,. \tag{2.70}$$

By taking the expected value, we see that the second order moments satisfy

$$\dot{M}^{\mathbf{k}}_{\mathbf{k}} + \dot{M}^{\bar{\mathbf{k}}}_{\bar{\mathbf{k}}} = -\gamma_{\mathbf{k}}M^{\mathbf{k}}_{\mathbf{k}} - \gamma_{\bar{\mathbf{k}}}M^{\bar{\mathbf{k}}}_{\bar{\mathbf{k}}} + 2(b^2_{\mathbf{k}} + b^2_{\bar{\mathbf{k}}})\,,\ \dot{M}^{(0,n)}_{(0,n)} = -\gamma_{(0,n)}M^{(0,n)}_{(0,n)} + b^2_{(0,n)} \tag{2.71}$$

This equations should be compared with Eq. (2.42): they show that the amount of energy contained in a given cluster is not transferred to other clusters and depends only on the forcing and the dissipation, acting in its interior. Thus the energy cascades cannot occur for *typical* values of ρ.

2.6 Concluding Remarks

In this chapter we presented a method to study a weakly nonlinear PDE by investigating properties of the corresponding *effective equation*, written in terms of the nonlinearity and the resonances in the spectrum of the linear part of the equation.

We have considered two examples of equations, where the structures of resonances are completely different. Namely, for the NLS equation all resonances are connected and we can use (in addition to the rigorous mathematical theory) some heuristic approximation from the arsenal of wave turbulence to show that under the iterated limit "the volume goes to infinity", taken after the limit "the amplitude of oscillations goes to zero", the energy spectrum of solutions for the effective equation is described by a Zakharov-type kinetic equation. Evoking the Zakharov's Ansatz we show that stationary in time and homogeneous in space solutions for the latter equation have a power law form.

On the other hand, for the Charney-Hasegawa-Mima equation the resonances form finite clusters, and for this equation we have shown (completely rigorously) that, in the *typical* case, no exchange of energy between different oscillating modes occurs.

References

1. Bogoljubov, N.N., Mitropol'skij, J.A.: Asymptotic Methods in the Theory of Non-linear Oscillations. Gordon & Breach, New York (1961)
2. Cardy, J., Falkovich, G., Gawedzki, K.: Non-equilibrium Statistical Mechanics and Turbulence. Cambridge University Press, Cambridge (2008)
3. Faou, E., Germain, P., Hani, Z.: The weakly nonlinear large box limit of the 2d cubic nonlinear Schrödinger equation. E-print: arXiv:1308.6267 (2013)
4. Gérard, P., Grellier, S.: Effective integrable dynamics for a certain non-linear wave equation. Anal. PDE **5**, 1139–1155 (2012)
5. Huang, G.: An averaging theorem for nonlinear Schrödinger equations with small nonlinearities. Discrete Continuous Dyn. Syst. Ser. A **34**(9), 3555–3574 (2014)
6. Huang, G.: Long-time dynamics of resonant weakly nonlinear CGL equations. J. Dyn. Diff. Equat. 1–13 (2014). doi:10.1007/s10884-014-9391-0
7. Huang, G., Kuksin, S., Maiocchi, A.: Time-averaging for weakly nonlinear CGL equations with arbitrary potentials. In: Guyenne, P., Nicholls, D., Sulem, C. (eds.) Hamiltonian Partial Differential Equations and Applications, vol. 75, Fields Inst. Commun. (2015)
8. Kartashova, E.: Partitioning of ensembles of weakly interacting dispersing waves in resonators into disjoint classes. Phys. D **46**, 43–56 (1990)
9. Kartashova, E.: Nonlinear Resonance Analysis. Cambridge University Press, Cambridge (2010)
10. Kuksin, S.B.: Damped-driven KdV and effective equations for long-time behaviour of its solutions. GAFA Geom. Funct. Anal. **20**, 1431–1463 (2010)
11. Kuksin, S.B.: Weakly nonlinear stochastic CGL equations. Ann. Inst. Henri Poincaré Probab. Stat. **49**(4), 1033–1056 (2013)
12. Kuksin, S., Maiocchi, A.: Resonant averaging for small solutions of stochastic NLS equations. E-print: arXiv:1311.6793 (2013)
13. Kuksin, S.B., Maiocchi, A.: The limit of small Rossby numbers for the randomly forced quasi-geostrophic equation on the β-plane. Nonlinearity **28**, 2319–2341 (2015)
14. Kuksin, S.B., Maiocchi, A.: Derivation of a wave kinetic equation from the resonant-averaged stochastic NLS equation. Phys. D. (2015, in press)
15. Monin, A.S., Yaglom, A.M.: Statistical Fluid Mechanics: Mechanics of Turbulence, vol. II. Dover, New York (2007)
16. Nazarenko, S.: Wave Turbulence. Lecture Notes in Physics, vol. 825. Springer, Berlin (2011)
17. Newell, A.C., Rumpf, B.: Wave turbulence. Ann. Rev. Fluid Mech. **43**(1), 59–78 (2011)
18. Zakharov, V.E., L'vov, V.S., Falkovich, G.: Kolmogorov spectra of turbulence 1. Wave Turbulence. Springer, Berlin (1992)

Chapter 3
On the Discovery of the Steady-State Resonant Water Waves

Shijun Liao, Dali Xu, and Zeng Liu

Abstract In 1960 Phillips gave the criterion of wave resonance and showed that the amplitude of a resonant wave component, if it is zero initially, grows linearly with time. In 1962 Benney derived evolution equations of wave-mode amplitudes and demonstrated periodic exchange of wave energy for resonant waves. However, in the past half century, the so-called steady-state resonant waves with time-independent spectrum have never been found for order higher than three, because perturbation results contain secular terms when Phillips' criterion is satisfied so that "the perturbation theory breaks down due to singularities in the transfer functions", as pointed out by Madsen and Fuhrman in 2012.

Recently, by means of the homotopy analysis method (HAM), an analytic approximation method for highly nonlinear problems, steady-state resonant waves have been obtained not only in deep water but also for constant water depth and even over a bottom with an infinite number of periodic ripples. In addition, steady-state resonant waves were observed experimentally in a basin at the State Key Laboratory of Ocean Engineering, Shanghai, China, showing excellent agreement with theoretical predictions.

In this chapter we briefly describe the history of research of steady-state resonant water waves, from theoretical predictions to their experimental verification. All of these illustrate that the HAM is a novel method which indeed renders something new and different.

S. Liao (✉)
Ocean and Civil Engineering, State Key Laboratory of Ocean Engineering, School of Naval Architecture, Shanghai Jiao Tong University, Shanghai 200240, China
e-mail: sjliao@sjtu.edu.cn

D. Xu • Z. Liu
Ocean and Civil Engineering, School of Naval Architecture, Shanghai Jiao Tong University, Shanghai 200240, China
e-mail: xudali0903@sjtu.edu.cn; z_liu@sjtu.edu.cn

E. Tobisch (ed.), *New Approaches to Nonlinear Waves*, Lecture Notes in Physics 908, DOI 10.1007/978-3-319-20690-5_3

3.1 Introduction

The study of resonance mechanism among water waves is of fundamental importance, as nonlinear interactions between different wave components may result in energy transfers in the spectrum. In 1960 Phillips [31] found the resonance criterion of a quartet of progressive waves in deep water

$$\boldsymbol{k}_1 \pm \boldsymbol{k}_2 \pm \boldsymbol{k}_3 \pm \boldsymbol{k}_4 = 0, \quad \omega_1 \pm \omega_2 \pm \omega_3 \pm \omega_4 = 0, \tag{3.1}$$

where $\boldsymbol{k}_i$ denotes the wave number, $\omega_i = \sqrt{gk_i}$ with $k_i = |\boldsymbol{k}_i|$ being the angular frequency given by the linear wave theory in deep water and g is the gravity acceleration, respectively. Phillips [31] revealed that the amplitude of the resonant wave component, if it is zero initially, grows linearly with time. Obviously, this result is valid only for a short time. In 1962 Benney [4] derived evolution equations of wave-mode amplitudes, and demonstrated periodic exchange of wave energy when Phillips resonance criterion is fully or nearly satisfied. This is a more general result about resonant waves than Phillips' linearly growing amplitude. Thereafter, the resonant interaction theory became one of the principle catalysts in the understanding of nonlinear wave phenomena [7].

According to Benney [4], when Phillips' resonance criterion is satisfied, the amplitudes of wave components change periodically, if their initial values are given arbitrarily, i.e. randomly. In other words, for a resonant wave system, spectrum of wave energy *changes* periodically in general, and thus is *dependent* upon time in most cases.

Are there the so-called "steady-state" resonant waves whose spectrums are independent of time? Such kind of steady-state resonant waves should be in such an equilibrium that wave amplitudes, wave numbers and phase speeds of all wave components are constant.

Unfortunately, in the context of perturbation techniques, such kind of equilibrium states have never been found at order higher than three, because perturbation results (mostly at the third-order approximation) contain secular terms when Phillips' criterion is satisfied so that "the perturbation theory breaks down due to singularities in the transfer functions", as pointed out by Madsen and Fuhrman [25] in 2012.

Without doubt, perturbation technique [9, 29, 30, 32] is one of most famous analytic tools to gain analytic approximations of nonlinear differential equations. However, perturbation techniques have some restrictions. First of all, it is based on the existence of small physical parameters, called perturbation quantities—but not all problems contain such kind of small physical parameters. Especially, perturbation results often break down when such a perturbation quantity becomes large. In other words, perturbation techniques can not guarantee the convergence of perturbation results. Therefore, perturbation techniques are often valid for weakly nonlinear problems. All of these greatly restrict the applicability of perturbation techniques.

In 1992 Liao [10] proposed a new analytic approximation technique for nonlinear problems in his Ph.D. dissertation, namely the homotopy analysis method (HAM) [11–15, 18]. Based on homotopy, a fundamental concept in topology, the HAM works even if there exist no small/large physical parameters at all: one can always reduce a nonlinear problem into an infinite number of linear sub-problems, *without* small/large physical parameters. Liao [11] introduced, for the first time, the so-called "convergence-control parameter", which has no physical meaning but provides us a simple way to adjust and control the convergence of solution series. Thus, unlike perturbation techniques and other traditional (non-perturbation) methods such as Adomian Decomposition Method [1–3], "Lyapunov artificial small parameter method" [23] and so on, this method can guarantee convergence of solution series. Moreover, we may choose a simple and adequate equation-type of linear sub-problems so that high-order approximations can be obtained easily, especially by means of computer algebra software like Mathematica, Maple and so on. So this method is valid for various types of highly nonlinear problems in science and engineering, as illustrated in Liao's book [12, 18] and hundreds of related publications.

In 2011 Liao [17] successfully applied the HAM to solve the exact wave equation and obtained for the first time (to the best of our knowledge), a quartet of steady-state resonant progressive waves in deep water. He revealed that there exist multiple resonant waves in deep water and that the resonant wave component may contain much less wave energy than the two primary ones [17]. Furthermore, the wave resonance criterion for an arbitrary number of progressive waves is given by Liao [17], which logically contains Phillips' four-wave resonance criterion (3.1). In 2012 Xu et al. [33] further applied the HAM to solve exact wave equations and obtained a quartet of steady-state resonant progressive waves in finite-depth water through qualitatively similar conclusions. Besides, Xu et al. [33] confirmed the existence of these multiple steady-state resonant waves by numerically solving Zakharov equation with the given initial conditions that had been obtained analytically in a similar way. In 2014 Liu and Liao [20] reconsidered the steady-state resonance of multiple surface gravity waves in deep water so as to extend the existing results of Liao [17] and Xu et al. [33] from a special quartet to more general and coupled resonant quartets, and even to a sextet with higher-order resonant interactions. Multiple steady-state resonant waves have been obtained for all the considered cases, and it is found that the number of multiple solutions tends to increase when more wave components participate in resonance sets [20]. Significance of near-resonance and nonlinearity has been also demonstrated [20]. It has been found [20] that all near-resonant components as a whole contain more and more wave energy, as the wave patterns tend from two dimensions to one dimension, or as the nonlinearity of wave system increases. In addition, linear stability of the steady-state resonant waves has been analyzed. It has been demonstrated [20] that steady-state resonant waves are stable if the disturbance does not resonate with any components of the basic wave. All of these theoretical works [17, 20, 33] indicate that steady-state resonant waves exist not only in deep water but also in finite-depth water.

Note that these theoretical results for steady-state resonant waves have never been reported in experimental studies. Can we observe such kind of steady-state resonant waves in laboratory?

In 2014 Liu et al. [22] did some experiments to confirm the existence of the steady-state resonant progressive waves in a basin at the State Key Laboratory of Ocean Engineering, Shanghai, China. These steady-state resonant waves have been first calculated theoretically under the exact resonance criterion with high enough nonlinearity, and then generated in the basin by means of the main wave components containing more than 95 % wave energy. The steady-state wave spectra have been quantitatively observed within the inherent system error of the basin, and identified by means of a contrast experiment. Multiple steady-state resonant waves have been observed, with excellent agreement between the experimental and theoretical results. These results offer the first experimental evidence of the existence of steady-state resonant progressive waves with multiple solutions.

In 2014 Xu et al. [34] investigated the class-I Bragg resonant waves [21] in the case that a primary surface wave propagates obliquely over a bottom with an infinite number of ripples. Two kinds of steady-state resonant wave systems are obtained. For the first kind, the primary and resonant wave components have the same wave amplitude and thus contain the same wave energy. However, for the second kind, they contain different wave energy. Especially, the bifurcations of the steady-state resonant waves with respect to the wave propagation angle, the water depth, the bottom slope and the nonlinearity of free surface were found, for the first time [34]. To the best of our knowledge, the second kind of the steady-state class-I Bragg resonant waves and especially the bifurcations have never been reported.

Therefore, the above-mentioned theoretical and experimental investigations show that the so-called steady-state resonant waves exist not only in deep water but also in a constant-depth water and over a bottom with an infinite number of ripples. All of these theoretical and experimental findings are helpful to deepen our understanding and enrich our knowledge about resonant water waves as a whole.

In this chapter we briefly describe these theoretical and experimental works about the steady-state resonant waves. For simplicity, we mainly focus on the importance and physical meaning of the main results but neglect most of mathematical formulas and detailed experimental data, since they can be found in related journal articles [17, 20, 22, 33, 34].

3.2 Basic Ideas of Homotopy Analysis Method

The homotopy analysis method (HAM) [11–16, 18] is used as an analytic tool in the discovery of steady-state resonant waves [17, 20, 22, 33, 34]. So it is helpful to give a simple description of the basic ideas of the HAM at first.

Homotopy is a basic concept in topology, which can describe a continuous variation between two functions. For example, a continuous variation between $\sin x$ and $\cos x$ can be constructed via the homotopy

$$\mathcal{H}(x;q) = (1-q)\ \sin x + q\ \cos x, \tag{3.2}$$

where $q \in [0,1]$ is called the embedding parameter, which has no physical meaning. Obviously, as q increases from 0 to 1, $\mathcal{H}(x;q)$ varies from $\sin x$ to $\cos x$, *continuously*. Here, $\sin x$ and $\cos x$ are regarded as homotopic, denoted as

$$\mathcal{H}(x;q) : \sin x \sim \cos x. \tag{3.3}$$

This concept is widely used by pure mathematicians to prove solution existence and uniqueness of differential equations, and by applied mathematicians to develop numerical methods, such as the homotopy continuation method and so on. Unlike them, the HAM is an *analytic* approximation technique based on the homotopy for highly nonlinear problems.

For the sake of simplicity, let us consider the following simple equation

$$u' + u^2 = 0, \qquad u(0) = 1, \qquad 0 \le t < +\infty. \tag{3.4}$$

The above equation has the close-form solution $u(t) = 1/(1+t)$. Regarding t as a small physical variable, it is straightforward to obtain its perturbation series

$$u = 1 - t + t^2 - t^3 + t^4 - t^5 + \cdots \tag{3.5}$$

which is however divergent for $t \ge 1$.

To solve Eq. (3.4) in the frame of the HAM, we first of all construct such a family of equations in parameter $q \in [0,1]$, called the "zeroth-order deformation equation",

$$(1-q)\mathcal{L}\left[\phi(t;q) - u_0(t)\right] = c_0\ q\ \left\{\frac{\partial \phi(t;q)}{\partial t} + \phi^2(t;q)\right\}, \qquad \phi(0;q) = 1, \tag{3.6}$$

where $\mathcal{L}$ is an auxiliary linear operator with the property $\mathcal{L}[0] = 0$, $u_0(t)$ is an initial guess satisfying the initial condition $u_0(0) = 1$, $c_0 \neq 0$ is a constant to be chosen, called the "convergence-control parameter", and $q \in [0,1]$ is the homotopy parameter (i.e. embedding parameter), respectively.

The equation above seems more complicated than the original one given by Eq. (3.4). However, it brings us something *new* and *different*: we have now great *freedom* to choose the auxiliary linear operator $\mathcal{L}$, the initial guess $u_0(t)$ and the convergence-control parameter c_0. Especially, the convergence-control parameter c_0 provides us a simple way to *guarantee* the convergence of solution series.

Obviously, when $q = 0$, we have

$$\phi(t;0) = u_0(t), \tag{3.7}$$

since $\mathcal{L}[0] = 0$ and $u_0(t)$ satisfies the initial condition $u_0(0) = 1$. Besides, when $q = 1$, the zeroth-order deformation equation (3.6) is equivalent to the original equation (3.4), since $c_0 \neq 0$, so that it holds

$$\phi(t; 1) = u(t). \tag{3.8}$$

Thus, as $q \in [0, 1]$ increases from 0 to 1, the solution $\phi(t; q)$ varies from the initial guess $u_0(t)$ to the unknown solution $u(t)$ of the original equation (3.4). Thus, $u_0(t)$ and $u(t)$ are homotopic, i.e.

$$\phi(t; q) : u_0(t) \sim u(t). \tag{3.9}$$

Note that we have great freedom to choose the auxiliary linear operator $\mathcal{L}$, the initial guess $u_0(t)$ and the convergence-control parameter c_0. Assume that all of them are so properly chosen that the solution $\phi(t; q)$ of Eq. (3.6) exists for all $q \in [0, 1]$, and that $\phi(t; q)$ is analytic on $q \in [0, 1]$, and besides that its Maclaurin series on the homotopy-parameter q, i.e.

$$\phi(t; q) = u_0(t) + \sum_{m=1}^{+\infty} u_m(t)\, q^m, \tag{3.10}$$

is convergent at $q = 1$. Then, setting $q = 1$ in the above expression and using $\phi(t; 1) = u(t)$, we have the homotopy-series solution

$$u(t) = u_0(t) + \sum_{m=1}^{+\infty} u_m(t), \tag{3.11}$$

where the unknown $u_m(t)$ can be determined, step by step, by the following higher-order deformation equations.

Substituting the series (3.10) into the zeroth-order deformation equation (3.6) and equating equal powers of the homotopy-parameter q, we have the high-order deformation equation

$$\mathcal{L}\left[u_m(t) - \chi_m\, u_{m-1}(t)\right] = c_0\, \delta_{m-1}(t), \quad u_m(0) = 0, \tag{3.12}$$

where $\chi_1 = 0$, $\chi_m = 1$ for $m > 1$, and

$$\delta_n(t) = \mathcal{D}_n\left\{\frac{\partial \phi(t; q)}{\partial t} + \phi^2(t; q)\right\} = u_n'(t) + \sum_{k=0}^{n} u_k(t)\, u_{n-k}(t), \tag{3.13}$$

with the definition of the so-called nth-order homotopy-derivative

$$\mathcal{D}_n F = \frac{1}{n!}\frac{\partial^n F}{\partial q^n}\bigg|_{q=0}. \tag{3.14}$$

The right-hand side term δ_{m-1} is dependent upon the previous approximations $u_0, u_1, \cdots, u_{m-1}$ and thus is known. Besides, according to the properties of $\mathcal{D}_n$ proved by Liao [14], it is straightforward to gain δ_{m-1} for a given equation. For more general types of zeroth-order deformation equations and the properties of the homotopy-derivative $\mathcal{D}_n$, please refer to [14] and Sect. 4 of Liao's book [18].

For simplicity, let us choose the auxiliary linear operator $\mathcal{L}u = u'$ and the initial guess $u_0(t) = 1$. Then it is very easy to solve the higher-order deformation equation (3.12) step by step, starting from $m = 1$, say,

$$u_1(t) = c_0\, t, \tag{3.15}$$

$$u_2(t) = c_0(1 + c_0)t + c_0^2\, t^2, \tag{3.16}$$

$$\vdots$$

It is found that the mth-order approximation of $u(t)$ reads

$$u(t) \approx \sum_{n=0}^{m} u_n(t) = \sum_{n=0}^{m} \mu_0^{m,n}(c_0)(-t)^n, \tag{3.17}$$

where

$$\mu_0^{m,n}(c_0) = (-c_0)^n \sum_{k=0}^{m-n} \binom{n-1+k}{k} (1 + c_0)^k. \tag{3.18}$$

It should be emphasized that, unlike the perturbation series given by Eq. (3.5), the convergence of the homotopy-series

$$u(t) = \lim_{m \to +\infty} \sum_{n=0}^{m} \mu_0^{m,n}(c_0)(-t)^n \tag{3.19}$$

is dependent upon the so-called "convergence-control parameter c_0". It is exactly the same as the perturbation series (3.5) when $c_0 = -1$, but its convergence domain increases as c_0 varies from -1 to 0, as shown in Fig. 3.1. In fact, it can be strictly proved (see Sect. 2.3.4 and Theorem 2.3 on page 82 of Liao's book [18]) that the homotopy-series (3.19) converges in the interval

$$-1 < t < \frac{2}{|c_0|} - 1, \qquad \text{when } c_0 < 0, \tag{3.20}$$

$$-\frac{2}{|c_0|} - 1 < t < -1, \qquad \text{when } c_0 > 0. \tag{3.21}$$

Therefore, unlike the perturbation series (3.5) that diverges for $t > 1$, the homotopy-series (3.19) can converge (as $c_0 \to 0$) to the exact solution $(1 + t)^{-1}$ on the *whole* axis $-\infty < t < +\infty$, only except the singular point $t = -1$ that has no physical meaning for the considered equation (3.4).

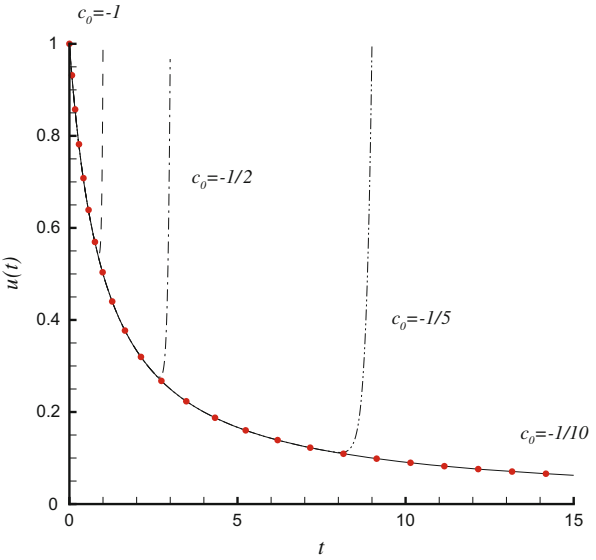

Fig. 3.1 Comparison of exact solution $u = 1/(1 + t)$ with the 30th-order HAM approximation. *Symbol*: exact solution; *dashed line*: perturbation series; *dash-dotted line*: $c_0 = -1/2$; *dash-dot-dotted line*: $c_0 = -1/5$; *solid line*: $c_0 = -1/10$

The HAM has some advantages, compared to other analytic approximations. First of all, note that *all* of the higher-order deformation equations (3.12) for an unknown $u_m(t)$ are governed by the *same* auxiliary *linear* operator $\mathcal{L}$ with known right-hand side term δ_{m-1} that depends on the initial guess $u_0(t)$ and the known previous solutions $u_1(t), u_2(t), \cdots, u_{m-1}(t)$. Thus, according to Eq. (3.11), we transform the original nonlinear problem (3.4) into an infinite number of linear sub-problems governed by Eq. (3.12). However, it should be emphasized that, in the frame of the HAM, such kind of transform does *not* need any small physical parameters at all. This is quite different from perturbation techniques that use small/large physical parameters to realize such a kind of transformation.

Secondly, unlike perturbation methods, the HAM provides us great freedom and flexibility to choose the auxiliary linear operator $\mathcal{L}$. In other words, we can choose the equation-type of the high-order deformation equations, and the base-functions of their solutions. Note that, for the illustrative Eq. (3.4), we choose the auxiliary linear operator $\mathcal{L}u = u'$ that is the same as the linear term of Eq. (3.4). However, this is *not* generally necessary. For example, using the auxiliary linear operator

$$\mathcal{L}u = e^{\alpha t}\left[u' + \alpha u\right] \tag{3.22}$$

and the initial guess

$$u_0(t) = e^{-\alpha t} \tag{3.23}$$

in the high-order deformation equation (3.12), we can get convergent series solution in the interval $t \in [0, 20]$ of Eq. (3.4) by means of $c_0 = -1/3$ and $\alpha = 1/10$. Such kind of freedom and flexibility is so large that for a 2nd-order nonlinear differential equation, one can even choose $\mathcal{L}$ as a 4th-order or 6th-order differential operator in some cases, as illustrated by Liao and Tan [19]. As a result, one can easily obtain high-order approximations in the frame of the HAM by choosing a simple but good enough auxiliary linear operator $\mathcal{L}$.

Especially, the high-order deformation equation contains the convergence-control parameter c_0, which has no physical meaning but can provide us a simple way to guarantee the convergence of homotopy-series solution. As illustrated above, the convergence-control parameter can fantastically improve the convergence of series solution. This is completely different from *all* other analytic approximation methods. In general, the residual error square at the mth-order approximation reads

$$\mathcal{E}_m(c_0) = \int_a^b \left\{ \mathcal{N}\left[\sum_{k=0}^{m} u_k(t) \right] \right\}^2 dt \tag{3.24}$$

for a nonlinear differential equation $\mathcal{N}[u] = 0$, where $\mathcal{N}$ is a nonlinear operator. In most cases, if the initial guess u_0 and the auxiliary linear operator $\mathcal{L}$ are properly chosen, there often exists such a domain Ω_c that for all $c_0 \in \Omega_c$ it holds

$$\lim_{m \to +\infty} \mathcal{E}_m(c_0) \to 0. \tag{3.25}$$

Mathematically speaking,

$$\Omega_c = \left\{ c_0 : \lim_{m \to +\infty} \mathcal{E}_m(c_0) \to 0 \right\}. \tag{3.26}$$

In general, the optimal value of the convergence-control parameter c_0 is determined by the minimum of the residual error square $\mathcal{E}_m(c_0)$, as suggested by Liao [15]. In this way, unlike all other analytic approximations, the HAM provides us a simple way to guarantee the convergence of series solution. In fact, it is the so-called "convergence-control parameter" that differs the HAM from all other analytic approximation methods.

In addition, traditional non-perturbation methods, such as the Adomian Decomposition Method, Lyapunov's artificial small parameter method and so on, are only special cases of the HAM for some specially chosen auxiliary linear operator $\mathcal{L}$ and convergence-control parameter c_0, as pointed out by Liao [12]. Besides, in the frame of the HAM, one can derive the generalized Newton's iteration formulas (on pages 24–25 in [18]) and the so-called homotopy-transform (Sect. 5.3 in [18]): the former contains the famous Newton's iteration formula as a special case, and the latter contains the famous Euler transformation as a special case. These proofs make a mathematical cornerstone of the HAM, and well explain why the HAM is generally valid for so many nonlinear problems in science and engineering.

For details about the HAM, please refer to the articles [11, 13–16, 19] and Liao's books [12, 18].

3.3 Steady-State Resonant Waves in Constant-Depth Water

3.3.1 Mathematical Formulation

Let us consider nonlinear interactions of two trains of progressive gravity waves with small amplitudes, propagating in deep water.[1] We assume that the fluid is inviscid and incompressible, the flow is irrotational and the surface tension is neglected. The coordinate system (x, y, z) is set on the free surface, with z-axis positive vertically upwards. The velocity potential $\varphi(x, y, z, t)$ is governed by Laplace equation

$$\nabla^2\varphi = 0, \quad -\infty < z < \eta(x, y, t), \tag{3.27}$$

and obeys kinematic and dynamic conditions on the *unknown* free surface $z = \eta(x, y, t)$:

$$\frac{\partial^2\varphi}{\partial t^2} + g\frac{\partial\varphi}{\partial z} + \frac{\partial|\nabla\varphi|^2}{\partial t} + \nabla\varphi\cdot\nabla\left(\frac{1}{2}|\nabla\varphi|^2\right) = 0, \tag{3.28}$$

$$g\eta + \frac{\partial\varphi}{\partial t} + \frac{1}{2}|\nabla\varphi|^2 = 0, \tag{3.29}$$

respectively, and the impermeability condition at the bottom:

$$\lim_{z\to-\infty}\frac{\partial\varphi}{\partial z} = 0, \tag{3.30}$$

where $\eta(x, y, t)$ denotes wave elevation, g is the gravity acceleration, t denotes the time, and

$$\nabla = \mathbf{i}\frac{\partial}{\partial x} + \mathbf{j}\frac{\partial}{\partial y} + \mathbf{k}\frac{\partial}{\partial z} \tag{3.31}$$

is a differential operator with $\mathbf{i}, \mathbf{j}, \mathbf{k}$ denoting the unit vector in the x, y, z direction, respectively.

Consider nonlinear interaction of a wave system of κ primary progressive waves with $\boldsymbol{k}_n$ denoting the wavenumber and σ_n the actual frequency, respectively. For

[1] The same problem in finite-depth water can be solved in a rather similar way. For simplicity, let us first consider the problem in deep water.

steady-state wave systems, all wave amplitudes a_i, wave numbers $\boldsymbol{k}_i$ and actual wave frequencies σ_i are constant, i.e. *independent* of time. Therefore, the original initial/boundary-value problem given by Eqs. (3.27)–(3.30) can be transformed into a boundary-value one by defining the new variables

$$\xi_i = \boldsymbol{k}_i \cdot \boldsymbol{r} - \sigma_i\, t, \quad i = 1, 2, \cdots, \kappa, \tag{3.32}$$

where $\boldsymbol{r} = x\ \mathbf{i} + y\ \mathbf{j}$. In the new coordinate system $(\xi_1, \xi_2, \cdots, \xi_\kappa, z)$, the Laplace equation (3.27) becomes

$$\sum_{i=1}^{\kappa}\sum_{j=1}^{\kappa} \boldsymbol{k}_i \cdot \boldsymbol{k}_j \frac{\partial^2 \varphi}{\partial \xi_i \partial \xi_j} + \frac{\partial^2 \varphi}{\partial z^2} = 0, \tag{3.33}$$

obeying two boundary conditions on the free surface $z = \eta(\xi_1, \xi_2, \cdots, \xi_\kappa)$:

$$\begin{aligned} \mathcal{N}_1[\varphi] = &\sum_{i=1}^{\kappa}\sum_{j=1}^{\kappa} \sigma_i \sigma_j \frac{\partial^2 \varphi}{\partial \xi_i \partial \xi_j} + g\frac{\partial \varphi}{\partial z} - 2\sum_{i=1}^{\kappa} \sigma_i \frac{\partial f}{\partial \xi_i} \\ &+ \sum_{i=1}^{\kappa}\sum_{j=1}^{\kappa} \boldsymbol{k}_i \cdot \boldsymbol{k}_j \frac{\partial \varphi}{\partial \xi_i}\frac{\partial f}{\partial \xi_j} + \frac{\partial \varphi}{\partial z}\frac{\partial f}{\partial z} = 0, \end{aligned} \tag{3.34}$$

$$\mathcal{N}_2[\varphi, \eta] = \eta - \frac{1}{g}\left(\sum_{i=1}^{\kappa} \sigma_i \frac{\partial \varphi}{\partial \xi_i} - f\right) = 0, \tag{3.35}$$

and also the impermeability condition at the bottom

$$\lim_{z \to -\infty} \frac{\partial \varphi}{\partial z} = 0, \tag{3.36}$$

where $\mathcal{N}_1$ and $\mathcal{N}_2$ are two nonlinear operators defined above, and

$$f = \frac{1}{2}\left[\sum_{i=1}^{\kappa}\sum_{j=1}^{\kappa} \boldsymbol{k}_i \cdot \boldsymbol{k}_j \frac{\partial \varphi}{\partial \xi_i}\frac{\partial \varphi}{\partial \xi_j} + \left(\frac{\partial \varphi}{\partial z}\right)^2\right]. \tag{3.37}$$

Since a steady-state solution means that no exchange of wave energy among wave components (in other words, all the physical quantities related to the wave system are constant), the steady-state wave elevation η can be expressed by

$$\begin{aligned} \eta(\boldsymbol{\xi}) = &\sum_{m_1=0}^{+\infty}\ \sum_{m_2=-\infty}^{+\infty} \cdots \sum_{m_\kappa=-\infty}^{+\infty} C^{\eta}_{m_1, m_2, \cdots, m_\kappa} \\ &\times \cos(m_1\xi_1 + m_2\xi_2 + \cdots + m_\kappa \xi_\kappa), \end{aligned} \tag{3.38}$$

where $C^{\eta}_{m_1,m_2,\cdots,m_\kappa}$ is a constant to be determined later, and

$$\boldsymbol{\xi} = \{\xi_1, \xi_2, \cdots, \xi_\kappa\}. \tag{3.39}$$

To satisfy the linear governing Eq. (3.33) and the bottom boundary condition (3.36), the velocity potential $\varphi(\boldsymbol{\xi}, z)$ should have the form

$$\varphi(\boldsymbol{\xi}, z) = \sum_{m_1=0}^{+\infty} \sum_{m_2=-\infty}^{+\infty} \cdots \sum_{m_\kappa=-\infty}^{+\infty} C^{\varphi}_{m_1,m_2,\cdots,m_\kappa} \Psi_{m_1,m_2,\cdots,m_\kappa}(\boldsymbol{\xi}, z), \tag{3.40}$$

where

$$\Psi_{m_1,m_2,\cdots,m_\kappa}(\boldsymbol{\xi}, z) = \sin\left(\sum_{i=1}^{\kappa} m_i\, \xi_i\right) \exp\left(\left|\sum_{i=1}^{\kappa} m_i\, \boldsymbol{k}_i\right| z\right), \tag{3.41}$$

and $C^{\varphi}_{m_1,m_2,\cdots,m_\kappa}$ is a constant to be determined later. Since the linear governing Eq. (3.33) and the bottom condition (3.36) are *automatically* satisfied by (3.40), the unknown coefficients $C^{\eta}_{m_1,m_2,\cdots,m_\kappa}$ and $C^{\varphi}_{m_1,m_2,\cdots,m_\kappa}$ are determined only by the two nonlinear boundary conditions (3.34) and (3.35) on the *unknown* free surface $z = \eta(\boldsymbol{\xi})$.

The above nonlinear partial differential equations are solved in the following way [17]. Let $\varphi_0(\boldsymbol{\xi}, z)$ and $\eta_0(\boldsymbol{\xi})$ denote the initial guesses of $\varphi(\boldsymbol{\xi}, z)$ and $\eta(\boldsymbol{\xi}, z)$. First of all, we construct such two continuous transformations with respect to the embedding parameter $q \in [0, 1]$:

$$\Phi(\boldsymbol{\xi}, z; q) : \varphi_0(\boldsymbol{\xi}, z) \sim \varphi(\boldsymbol{\xi}, z), \qquad Z(\boldsymbol{\xi}; q) : \eta_0(\boldsymbol{\xi}) \sim \eta(\boldsymbol{\xi}) \tag{3.42}$$

via the zeroth-order deformation equation

$$\sum_{i=1}^{\kappa} \sum_{j=1}^{\kappa} \boldsymbol{k}_i \cdot \boldsymbol{k}_j \frac{\partial^2 \Phi(\boldsymbol{\xi}, z; q)}{\partial \xi_i \partial \xi_j} + \frac{\partial^2 \Phi(\boldsymbol{\xi}, z; q)}{\partial z^2} = 0, \tag{3.43}$$

satisfying two boundary conditions on the *unknown* free surface $z = Z(\boldsymbol{\xi}; q)$:

$$(1-q)\mathcal{L}\left[\Phi(\boldsymbol{\xi}, z; q) - \varphi_0(\boldsymbol{\xi}, z)\right] = c_0\, q\, \mathcal{N}_1\left[\Phi(\boldsymbol{\xi}, z; q)\right], \tag{3.44}$$

$$(1-q)\left[Z(\boldsymbol{\xi}; q) - \eta_0(\boldsymbol{\xi})\right] = c_0\, q\, \mathcal{N}_2\left[\Phi(\boldsymbol{\xi}, z; q), Z(\boldsymbol{\xi}; q)\right], \tag{3.45}$$

and the bottom condition

$$\lim_{z \to -\infty} \frac{\partial \Phi(\boldsymbol{\xi}, z; q)}{\partial z} = 0, \tag{3.46}$$

where c_0 is a convergence-control parameter and $\mathcal{L}$ is an auxiliary linear operator with the property $\mathcal{L}[0] = 0$ (which will be chosen later), respectively. Note that the free surface $z = Z(\boldsymbol{\xi}; q)$ changes as q increases from 0 to 1.

Obviously, the initial guess $\varphi_0(\boldsymbol{\xi}, z)$ must be chosen according to Eq. (3.40) so that the governing Eq. (3.33) and the bottom condition (3.36) are automatically satisfied. Thus, when $q = 0$, the zeroth-order deformation equations (3.43)–(3.46) have the solution

$$\Phi(\boldsymbol{\xi}, z; 0) = \varphi_0(\boldsymbol{\xi}, z), \qquad Z(\boldsymbol{\xi}; 0) = \eta_0(\boldsymbol{\xi}), \tag{3.47}$$

since $\mathcal{L}[0] = 0$. When $q = 1$, since $c_0 \neq 0$, the zeroth-order deformation equations (3.43)–(3.46) are equivalent to the original ones given by Eqs. (3.33)–(3.36), so that we have the solution

$$\Phi(\boldsymbol{\xi}, z; 1) = \varphi(\boldsymbol{\xi}, z), \qquad Z(\boldsymbol{\xi}; 1) = \eta(\boldsymbol{\xi}). \tag{3.48}$$

Therefore, as q increases from 0 to 1, $\Phi(\boldsymbol{\xi}, z; q)$ and $Z(\boldsymbol{\xi}; q)$ indeed vary continuously from the initial guess $\varphi_0(\boldsymbol{\xi}, z)$, $\eta_0(\boldsymbol{\xi})$ to the solution $\varphi(\boldsymbol{\xi}, z)$, $\eta(\boldsymbol{\xi})$ of the considered problem.

Assuming that the auxiliary linear operator $\mathcal{L}$, the initial guesses φ_0 and η_0, and especially the convergence-control parameter c_0 are chosen so well that the Maclaurin series

$$\Phi(\boldsymbol{\xi}, z; q) = \varphi_0(\boldsymbol{\xi}, z) + \sum_{n=1}^{+\infty} \varphi_n(\boldsymbol{\xi}, z)\, q^n, \tag{3.49}$$

$$Z(\boldsymbol{\xi}; q) = \eta_0(\boldsymbol{\xi}) + \sum_{n=1}^{+\infty} \eta_n(\boldsymbol{\xi})\, q^n, \tag{3.50}$$

converge at $q = 1$, we have the homotopy-series solution

$$\varphi(\boldsymbol{\xi}, z) = \varphi_0(\boldsymbol{\xi}, z) + \sum_{n=1}^{+\infty} \varphi_n(\boldsymbol{\xi}, z), \tag{3.51}$$

$$\eta(\boldsymbol{\xi}) = \eta_0(\boldsymbol{\xi}) + \sum_{n=1}^{+\infty} \eta_n(\boldsymbol{\xi}). \tag{3.52}$$

Substituting the series given by Eqs. (3.49) and (3.50) into the zeroth-order deformation equations (3.43)–(3.46), and equating the coefficients of the same powers of q, we obtain the high-order deformation equation

$$\sum_{i=1}^{\kappa} \sum_{j=1}^{\kappa} \boldsymbol{k}_i \cdot \boldsymbol{k}_j \frac{\partial^2 \varphi_m(\boldsymbol{\xi}, z)}{\partial \xi_i \partial \xi_j} + \frac{\partial^2 \varphi_m(\boldsymbol{\xi}, z)}{\partial z^2} = 0, \tag{3.53}$$

obeying linear boundary conditions

$$\mathcal{L}[\varphi_m(\boldsymbol{\xi}, z)] = R_m^{\varphi}(\boldsymbol{\xi}, \eta_0, c_0), \qquad \text{on } z = \eta_0(\boldsymbol{\xi}), \tag{3.54}$$

$$\eta_m(\boldsymbol{\xi}) = \chi_m\ \eta_{m-1}(\boldsymbol{\xi}) + R_m^{\eta}(\boldsymbol{\xi}, \eta_0, c_0), \qquad \text{on } z = \eta_0(\boldsymbol{\xi}), \tag{3.55}$$

and boundary condition at bottom

$$\lim_{z \to -\infty} \frac{\partial \varphi_m(\boldsymbol{\xi}, z)}{\partial z} = 0, \tag{3.56}$$

where the right-hand side terms $R_m^{\varphi}(\boldsymbol{\xi}, \eta_0, c_0)$ and $R_m^{\eta}(\boldsymbol{\xi}, \eta_0, c_0)$ depends on the previous results φ_n and η_n $(0 \le n \le m-1)$, and the convergence-control parameter c_0. (For detailed expressions of $R_m^{\varphi}(\boldsymbol{\xi}, \eta_0, c_0)$ and $R_m^{\eta}(\boldsymbol{\xi}, \eta_0, c_0)$ in case of $\eta_0 = 0$ please refer to Liao [17] and Liu & Liao [20] for resonant waves in deep water and Xu et al. [33] in finite-depth water.)

For simplicity, below we choose $\eta_0 = 0$, although this is not absolutely necessary. Considering the linear part of the boundary condition (3.34), we directly choose the auxiliary linear operator

$$\mathcal{L}[\varphi] = \sum_{i=1}^{\kappa} \sum_{j=1}^{\kappa} \omega_i \omega_j \frac{\partial^2 \varphi}{\partial \xi_i \partial \xi_j} + g \frac{\partial \varphi}{\partial z}, \tag{3.57}$$

where

$$\omega_n = \sqrt{g|\boldsymbol{k}_n|}, \quad n = 1, 2, \cdots, \kappa \tag{3.58}$$

is the linear frequency of nth primary wave, which is slightly different from the actual frequency σ_n in (3.34). On $z = 0$, its inverse operator has the property

$$\mathcal{L}^{-1}[\sin(m_1\xi_1 + m_2\xi_2 + \cdots + m_\kappa \xi_\kappa)] = \frac{\Psi_{m_1, m_2, \cdots, m_\kappa}}{\lambda_{m_1, m_2, \cdots, m_\kappa}}, \quad \lambda_{m_1, m_2, \cdots, m_\kappa} \neq 0, \tag{3.59}$$

when the eigenvalue

$$\lambda_{m_1, m_2, \cdots, m_\kappa} = g \left| \sum_{i=1}^{\kappa} m_i\, \boldsymbol{k}_i \right| - \left(\sum_{i=1}^{\kappa} m_i\, \omega_i \right)^2 \tag{3.60}$$

of the eigenfunction $\Psi_{m_1, m_2, \cdots, m_\kappa}$ is non-zero. Since $\omega_n^2 = g|\boldsymbol{k}_n|$, we have at least κ zero eigenvalues

$$\lambda_{1,0,0,\cdots,0} = \lambda_{0,1,0,\cdots,0} = \cdots = \lambda_{0,0,0,\cdots,1} = 0. \tag{3.61}$$

Except these, $\lambda_{m_1,m_2,\cdots,m_\kappa} = 0$ in case of $\sum_{i=1}^{\kappa} m_i^2 > 1$ for integers m_i leads to a singularity, corresponding to the so-called generalized resonance criterion [17]:

$$g\left|\sum_{i=1}^{\kappa} m_i\,\boldsymbol{k}_i\right| = \left(\sum_{i=1}^{\kappa} m_i\,\omega_i\right)^2, \quad \text{when} \quad \sum_{i=1}^{\kappa} m_i^2 > 1, \tag{3.62}$$

for integers m_i. Note that Phillips' resonance criterion given by Eq. (3.1) is a special case of it.

Therefore, when there exist l resonant waves and κ primary waves, we have $(\kappa + l)$ eigenvalues $\lambda_{m_1,m_2,\cdots,m_\kappa}$ whose values are zero. In this case the common solution of the high-order deformation equations for φ_m reads

$$\begin{aligned}\varphi_m = \varphi_m^* + A_{m,1}\,\Psi_{1,0,\cdots,0} + A_{m,2}\,\Psi_{0,1,\cdots,0} + \cdots \\ + A_{m,\kappa}\,\Psi_{0,0,\cdots,1} + \sum_{i=1}^{l} A_{m,\kappa+i}\,\Psi_i^*,\end{aligned} \tag{3.63}$$

where φ_m^* is the special solution of φ_m,

$$\begin{aligned}\Psi_{1,0,\cdots,0} &= \sin(\xi_1)\exp(|\boldsymbol{k}_1|z),\\ \Psi_{0,1,\cdots,0} &= \sin(\xi_2)\exp(|\boldsymbol{k}_2|z),\\ &\vdots\\ \Psi_{0,0,\cdots,1} &= \sin(\xi_\kappa)\exp(|\boldsymbol{k}_\kappa|z),\end{aligned}$$

corresponding to the primary wave components, Ψ_i^* is the eigenfunction corresponding to resonant wave components, and $A_{m,i}$ is a constant to be determined. The expression above also indicates that we should choose such initial guess

$$\varphi_0 = A_{0,1}\,\Psi_{1,0,\cdots,0} + A_{0,2}\,\Psi_{0,1,\cdots,0} + \cdots + A_{0,\kappa}\,\Psi_{0,0,\cdots,1} + \sum_{i=1}^{l} A_{0,\kappa+i}\,\Psi_i^*, \tag{3.64}$$

that contains $(\kappa + l)$ unknown coefficients $A_{0,n}$, where $n = 1, 2, 3, \cdots, \kappa + l$. Thereupon, the right-hand side term $R_m^{\varphi}(\boldsymbol{\xi}, \eta_0, c_0)$ in Eq. (3.54) always contains $(\kappa + l)$ unknown coefficients $A_{m-1,n}$, where $1 \le n \le \kappa + l$.

According to the definition (3.59), all the terms of $\sin(m_1\xi_1 + m_2\xi_2 + \cdots + m_\kappa\xi_\kappa)$ corresponding to $\lambda_{m_1,m_2,\cdots,m_\kappa} = 0$ may not appear on the right-hand side of Eq. (3.54), otherwise secular terms are generated. This gives us a set of algebraic equations for the $(\kappa + l)$ unknown coefficients $A_{m-1,n}$, where $n = 1, 2, 3, \cdots, \kappa + l$. It is a set of algebraic equations which are nonlinear for the 1st-order deformation equation, but linear for others. Since nonlinear algebraic equations often have

multiple solutions, we can find multiple steady-state resonant waves in many cases, as illustrated in [17, 20, 33].

Thereafter, we straightforwardly obtain the special solution

$$\varphi_m^* = \mathcal{L}^{-1} R_m^{\varphi}(\boldsymbol{\xi}, \eta_0, c_0) \tag{3.65}$$

by means of the inverse linear operator $\mathcal{L}^{-1}$ defined by Eq. (3.59). And η_m is directly given by Eq. (3.55). In this way, we calculate φ_0, η_1, then φ_1, η_2, and so on. Using a computer algebra software like Mathematica, one can easily gain high-order approximations of φ and η.

It should be emphasized that the right-hand terms $R_m^{\varphi}(\boldsymbol{\xi}, \eta_0, c_0)$ in Eq. (3.54) and $R_m^{\eta}(\boldsymbol{\xi}, \eta_0, c_0)$ in Eq. (3.55) contain the convergence-control parameter c_0 that has no physical meaning. Thus, both of $\varphi_m(\boldsymbol{\xi}, z)$ and $\eta_m(\boldsymbol{\xi})$ contain c_0, which provides us a simple way to guarantee the convergence of the series solution given by Eqs. (3.51) and (3.52). Let

$$\mathcal{E}_m^{\varphi}(c_0) = \frac{1}{\pi^2} \int_0^{\pi} \int_0^{\pi} \left\{ \mathcal{N}_1 \left[\sum_{n=0}^{m} \varphi_n \right] \right\}^2 d\xi_1 \, d\xi_2, \quad \text{on} \quad z = \sum_{n=0}^{m} \eta_n, \tag{3.66}$$

$$\mathcal{E}_m^{\eta}(c_0) = \frac{1}{\pi^2} \int_0^{\pi} \int_0^{\pi} \left\{ \mathcal{N}_2 \left[\sum_{n=0}^{m} \varphi_n, \sum_{n=0}^{m} \eta_n \right] \right\}^2 d\xi_1 \, d\xi_2, \quad \text{on} \quad z = \sum_{n=0}^{m} \eta_n, \tag{3.67}$$

denote the residual error squares of the two boundary conditions on the free surface (at the mth order of approximation) respectively. There exists such an interval Ω_c that for an arbitrary $c_0 \in \Omega_c$ the solution series given by Eqs. (3.51) and (3.52) converge, say,

$$\Omega_c = \left\{ c_0 : \mathcal{E}_m^{\varphi}(c_0) \to 0, \mathcal{E}_m^{\eta}(c_0) \to 0, \text{as } m \to +\infty \right\}. \tag{3.68}$$

As suggested by Liao [15], the optimal value of the convergence-control parameter c_0 is determined by the minimum of the sum of residual error squares $\mathcal{E}_m^{\varphi}(c_0)$ and $\mathcal{E}_m^{\eta}(c_0)$ of the two boundary conditions on the free surface. In this way, it is guaranteed that one can always obtain a convergent analytic approximation if it exists. Such kind of guarantee is very important for us, especially when very little is known about a new problem.

For more detailed mathematical formulae, please refer to Liao [17] and Liu and Liao [20] for steady-state resonant waves in deep water, or to Xu et al. [33] in finite water depth, respectively.

3.3.2 *Steady-State Resonant Waves in Deep Water*

Due to nonlinear effects, the actual wave frequencies, σ_i, are often slightly different from the linear one $\omega_i = \sqrt{g|\boldsymbol{k}_i|}$. The amplitude dispersion, as emphasized by Madsen and Fuhrman [24], is generally necessary to include to fully satisfy the nonlinear resonance condition

$$\boldsymbol{k_1} \pm \boldsymbol{k_2} \pm \boldsymbol{k_3} \pm \boldsymbol{k_4} = 0, \quad \sigma_1 \pm \sigma_2 \pm \sigma_3 \pm \sigma_4 = 0. \tag{3.69}$$

Note that each actual frequency σ_i in Eq. (3.69) depends on all of the amplitudes in the wave system, therefore a combination of constant amplitudes a_i is required so as to keep the actual frequencies σ_i not only constant but also satisfying the nonlinear resonance condition given by Eq. (3.69) all the time. To consider the nonlinear effects on the steady-state resonance waves, we assume[2]

$$\frac{\sigma_n}{\omega_n} = \varepsilon, \tag{3.70}$$

where ε is a constant larger than 1 and $\omega_n = \sqrt{g\ |\boldsymbol{k}_n|}$ is the linear frequency, so that both the linear resonance criterion given by Eq. (3.1) and the nonlinear ones given by Eq. (3.69) are satisfied at the same time.

3.3.2.1 A Special Resonant Quartet

Using our method [11–15, 18], Liao [17] has investigated steady-state resonances in deep water and found that multiple steady-state resonant waves exist for such a special quartet:

$$2\boldsymbol{k_1} - \boldsymbol{k_2} = \boldsymbol{k_3}, \quad 2\omega_1 - \omega_2 = \omega_3, \quad 2\sigma_1 - \sigma_2 = \sigma_3, \tag{3.71}$$

which is a special case of the resonance criterion given by Eq. (3.1) when $\boldsymbol{k}_1 = \boldsymbol{k}_4$.

For example, in case of

$$\boldsymbol{k}_n = k_n\ (\cos\alpha_n\ \mathbf{i} + \sin\alpha_n\ \mathbf{j})\,, \quad n = 1, 2, \tag{3.72}$$

[2] As pointed out by Liu and Liao [20], such an assumption is not absolutely necessary: only the nonlinear resonance criterion given by Eq. (3.69) must be satisfied, but the linear ones given by Eq. (3.1) are unnecessary. In other words, most of the conclusions reported in this chapter about the steady-state resonant waves qualitatively stand up as long as the nonlinear resonance criterion given by Eq. (3.69) is satisfied, even if the linear resonance criterion given by Eq. (3.1) is violated.

with

$$\alpha_1 = 0, \quad \alpha_2 = \frac{\pi}{36}, \quad k_1 = 0.703998, \quad k_2 = \frac{\pi}{5}, \tag{3.73}$$

both linear resonance criteria given by Eq. (3.1) and the nonlinear resonance criteria given by Eq. (3.69) are exactly satisfied with the corresponding resonant wave component

$$\boldsymbol{k}_3 = 2\boldsymbol{k}_1 - \boldsymbol{k}_2 = (0.782068, -0.0547616). \tag{3.74}$$

The corresponding actual frequencies σ_1 and σ_2 are obtained by (3.70) for a given value of ϵ. In this case, we have the initial guess $\eta_0 = 0$ and

$$\varphi_0 = A_{0,1} \ \sin(\xi_1)\ e^{k_1 z} + A_{0,2} \ \sin(\xi_2)\ e^{k_2 z} + A_{0,3} \ \sin(2\xi_1 - \xi_2)\ e^{|2\boldsymbol{k}_1 - \boldsymbol{k}_2| z}, \tag{3.75}$$

where $A_{0,1}, A_{0,2}$ and $A_{0,3}$ are constants to be determined. So, we have three eigenfunctions

$$\Psi_{1,0} = \sin(\xi_1)\ e^{k_1 z}, \quad \Psi_{0,1} = \sin(\xi_2)\ e^{k_2 z}, \quad \Psi_{2,-1} = \sin(2\xi_1 - \xi_2)\ e^{|2\boldsymbol{k}_1 - \boldsymbol{k}_2| z}, \tag{3.76}$$

whose eigenvalues are zero, i.e. $\lambda_{1,0} = 0$, $\lambda_{0,1} = 0$ and $\lambda_{2,-1} = 0$. According to (3.59), in order to avoid the secular terms, $\sin\xi_1, \sin\xi_2$ and $\sin(2\xi_1 - \xi_2)$ must disappear in the right-hand side term R_m^{φ} of the boundary condition (3.54). This provides a set of three nonlinear algebraic equations on $A_{0,1}, A_{0,2}$ and $A_{0,3}$, having three types of real-valued solutions corresponding to the three different groups of steady-state resonant waves (Liao [17]).

These three groups of steady-state resonant waves have different wave spectra. The corresponding wave energy distribution of primary and resonant wave components are listed in Table 3.1. It is interesting that the steady-state resonant wave component of Group-I contains rather small portion of the total wave energy, as illustrated in Table 3.1. In fact, the resonant wave component may contain the largest (Group-III), the middle (Group-II) and the smallest (Group-I) portion of wave energy among them. It should be emphasized that Liao's work [17] revealed for the first time (to the best of our knowledge) the existence of steady-state resonant waves in deep water with multiple solutions.

Table 3.1 Wave energy distribution of primary and resonant wave components of a special quartet of a steady-state resonant wave system (3.71) in case given by Eq. (3.73) when $\epsilon = 1.0003$

	1st primary wave (%)	2nd primary wave (%)	Resonant wave (%)
Group-I	39.97	51.19	7.65
Group-II	40.17	18.54	39.56
Group-III	10.88	12.29	76.58

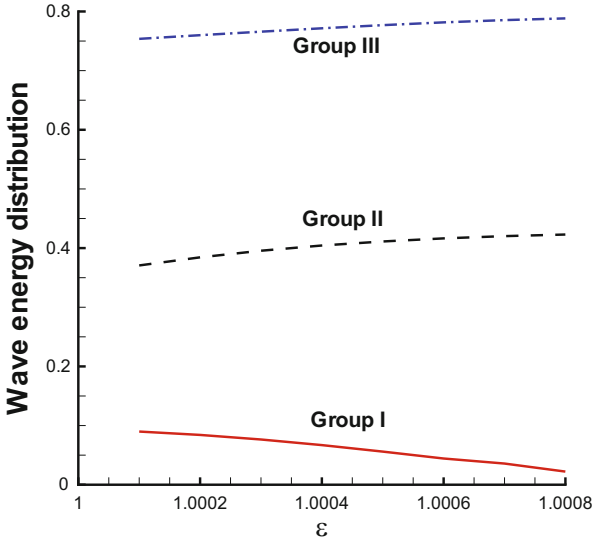

Fig. 3.2 Wave energy distribution of steady-state resonant wave component in case given by Eq. (3.73) for different values of $\epsilon = \sigma_1/\sqrt{g|\boldsymbol{k}_1|} = \sigma_2/\sqrt{g|\boldsymbol{k}_2|}$. *Solid line*: Group-I; *dashed line*: Group-II; *dash-dotted line*: Group-III

Similarly, in case given by Eq. (3.73) for different values of ϵ, three groups of steady-state resonant waves were obtained by Liao [17] using the above-mentioned approach. It has been found that the Group-I steady-state resonant wave component always contains the smallest portion of wave energy, and the Group-III component—the largest portion of wave energy, respectively, as shown in Fig. 3.2. This work illustrates that steady-state resonant waves are abundant in deep water, and besides there often exist multiple solutions for a given ϵ.

3.3.2.2 General Resonant Quartets

Note that the resonance criterion given by Eq. (3.71) considered by Liao [17] is just a special case of Eq. (3.69) when $\boldsymbol{k}_1 = \boldsymbol{k}_4$. Do the so-called steady-state resonant waves exist in the general case? The answer is positive, as shown below.

Without loss of generality, let us consider such a resonant quartet in a more general case:

$$\begin{cases} \boldsymbol{k}_1 + \boldsymbol{k}_2 = \boldsymbol{k}_3 + \boldsymbol{k}_0 = (2, 0) \\ \omega_1 + \omega_2 = \omega_3 + \omega_0 = C\sqrt{g}, \end{cases} \tag{3.77}$$

where $\boldsymbol{k_i}$ $(i = 1, 2, 3)$ denotes the primary wave component, $\boldsymbol{k_0}$ the resonant one, $\omega_i = \sqrt{g|\boldsymbol{k}_i|}$ is the linear frequency, g denotes the gravity acceleration and C is a

constant to be chosen later, respectively. According to Eq. (3.77), we obtain wave vectors

$$\boldsymbol{k_1} = (k_{1x}, k_{1y}), \quad \boldsymbol{k_2} = (2 - k_{1x}, -k_{1y}), \tag{3.78}$$

$$\boldsymbol{k_3} = (k_{3x}, k_{3y}), \quad \boldsymbol{k_0} = (2 - k_{3x}, -k_{3y}). \tag{3.79}$$

Given C, curves for $\boldsymbol{k}_1$ and $\boldsymbol{k}_3$ can be found in the (k_x, k_y) wavenumber plane by the resonance criterion given by Eq. (3.77).

Let's first consider the case $C = 2$, corresponding to the famous "figure of eight" given by Phillips [31]. Note that the special quartet case of $\boldsymbol{k}_1 = \boldsymbol{k}_2$ in Eq. (3.77) was investigated by Liao [17]. So, unlike Liao [17], let us consider here $k_{1x} = 1.10$ and $k_{3x} = 1.05$, as an extension of the general case $\boldsymbol{k}_1 \neq \boldsymbol{k}_2$ when $C = 2$. The corresponding values of $k_{1,y}$ and $k_{3,y}$ are determined by the resonant criterion given by Eq. (3.77). The corresponding resonance curve and wavevector configuration are shown in Fig. 3.3.

Compared to the case described by Eq. (3.71) of the special resonant quartet, we have now one more primary wave. Thus, there are one more term in the initial guess of potential function

$$\varphi_0 = A_{0,1}\Psi_{1,0,0} + A_{0,2}\Psi_{0,1,0} + A_{0,3}\Psi_{0,0,1} + A_{0,4}\Psi_{1,1,-1}, \tag{3.80}$$

where $A_{0,i}$ $(1 \leq i \leq 4)$ is an unknown constant to be determined, $\Psi_{1,0,0}$, $\Psi_{0,1,0}$ and $\Psi_{0,0,1}$ correspond to the primary waves, and $\Psi_{1,1,-1}$ the resonant one, respectively.

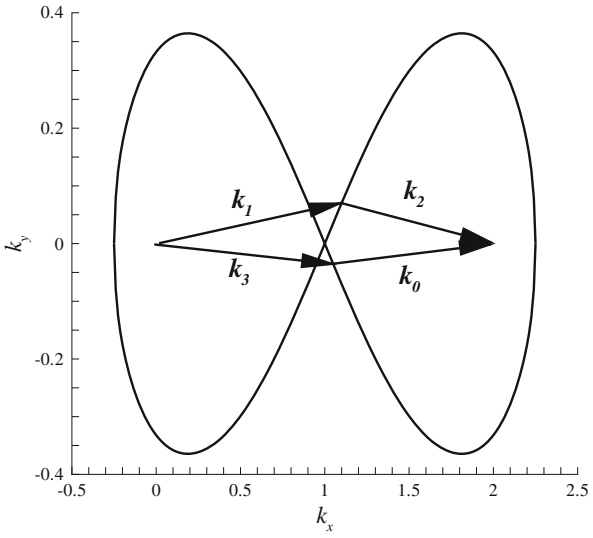

Fig. 3.3 Wavevector configuration of a resonant quartet in case given by Eq. (3.77) when $C = 2$, $\boldsymbol{k}_1 = (1.10, 0.070227)$ and $\boldsymbol{k}_3 = (1.05, -0.0352947)$

Table 3.2 Wave energy distribution for different groups of steady-state resonant wave systems in the case given by Eq. (3.77) when $C = 2$, $\boldsymbol{k}_1 = (1.10, 0.070227)$, $\boldsymbol{k}_3 = (1.05, -0.0352947)$ and $\varepsilon = 1.00003$

	1st primary wave (%)	2nd primary wave (%)	3rd primary wave (%)	Resonant wave (%)
Group-I	30.38	19.08	28.47	22.07
Group-II	71.30	13.90	5.59	9.21
Group-III	6.33	17.67	65.96	10.04
Group-IV	10.98	25.54	11.91	51.56

Similarly, these four unknown constants are determined by avoiding the four secular terms

$$\sin\xi_1, \quad \sin\xi_2, \quad \sin\xi_3, \quad \sin(\xi_1 + \xi_2 - \xi_3). \tag{3.81}$$

When $\varepsilon = 1.0003$ in the case given by Eq. (3.77) with $C = 2$, four groups of steady-state resonant waves have been obtained [20]. The corresponding wave energy distributions are listed in Table 3.2. Note that the resonant wave components may contain the most part (51.56 %) of the total wave energy, the same amount (22.07 %) as that of the primary wave component, or only a small amount (9.21 %, 10.04 %), as shown in Table 3.2 for Group-IV, Group-I, and Groups-II and III, respectively.

When $C < 2$, the resonance curve splits from the "figure of eight" into two symmetrical curves, as shown in Fig. 3.4 (the top panel) for the case $C = 1.997$, $k_{1x} = 1.20$ and $k_{3x} = 0.88$. Similarly, when $\varepsilon = 1.00003$, it is found that there exist three steady-state resonant waves, and besides the resonant wave component may contain the most part (78.15 %) of the total wave energy, the same amount (34.84 %) as that of the primary wave component, or only quite a small amount (0.03 %), as shown in Table 3.3 for Group-III, Group-II and Group-I, respectively.

When $C > 2$, the resonance curves merge into a single one, as shown in Fig. 3.4 (the bottom panel) for the case $C = 2.003$, $k_{1x} = 1.15$ and $k_{3x} = 0.95$. It has been found [20] that there exist four steady-state resonant waves, and besides the resonant wave component may contain the greater part (67.39 %) of the total wave energy, the same amount (28.69 %) as that of the primary wave component, or only a small amount (2.31 %, 8.60 %), as shown in Table 3.4 for Group-IV, Group-I, and Group-II and III, respectively.

Note that Liao [17] only considered the case described by Eq. (3.71) of a special resonant quartet, corresponding to $\boldsymbol{k}_1 = \boldsymbol{k}_4$ and $C = 2$ of the resonance criterion given by Eq. (3.77). So, Liu and Liao's work [20] extended Liao's conclusions to more general cases represented by Eq. (3.77) for a general resonant quartet when $C < 2$, $C = 2$ and $C > 2$. The similar conclusions can be further extended to multiple and coupled resonant quartets, as mentioned in Sect. 3.3.2.3, and even to a resonant sextet, as mentioned in Sect. 3.3.2.4.

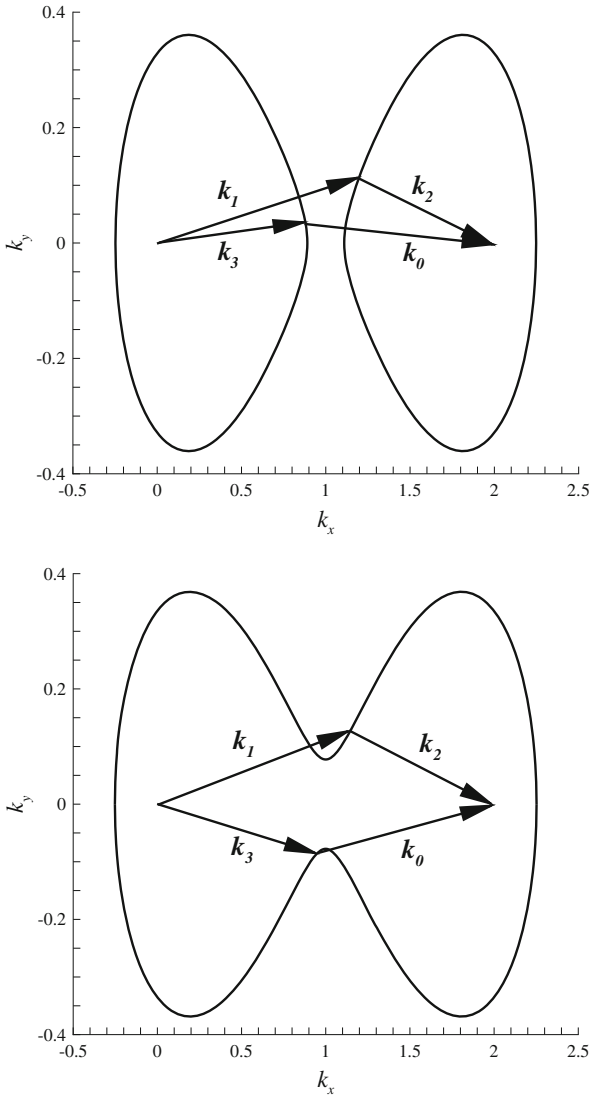

Fig. 3.4 Wavevector configuration of a general resonant quartet for the case of (3.77) when $C \neq 2$. *Top panel*: when $C = 1.997$, $\boldsymbol{k}_1 = (1.20, 0.115293)$ and $\boldsymbol{k}_3 = (0.88, 0.0346442)$. *Bottom panel*: when $C = 2.003$, $\boldsymbol{k}_1 = (1.15, 0.12933)$ and $\boldsymbol{k}_3 = (0.95, -0.0850699)$

Table 3.3 Wave energy distribution for different groups of steady-state resonant waves for the case given by Eq. (3.77) when $C = 1.997$, $\boldsymbol{k}_1 = (1.20, 0.115293)$, $\boldsymbol{k}_3 = (0.88, 0.0346442)$ and $\varepsilon = 1.00003$

	1st primary wave (%)	2nd primary wave (%)	3rd primary wave (%)	Resonant wave (%)
Group-I	86.93	12.98	0.06	0.03
Group-II	39.65	11.08	14.43	34.84
Group-III	0.94	17.88	3.03	78.15

Table 3.4 Wave energy distribution for different groups of steady-state resonant waves in the case given by Eq. (3.77) when $C = 2.003$, $\boldsymbol{k}_1 = (1.15, 0.12933)$, $\boldsymbol{k}_3 = (0.95, -0.0850699)$ and $\varepsilon = 1.00003$

	1st primary wave (%)	2nd primary wave (%)	3rd primary wave (%)	Resonant wave (%)
Group-I	33.33	15.97	22.00	28.69
Group-II	78.04	15.91	3.74	2.31
Group-III	7.41	27.39	56.59	8.60
Group-IV	4.04	21.56	7.01	67.39

3.3.2.3 Multiple and Coupled Resonant Quartets

To further investigate whether or not steady-state resonant waves exist for more general and complicated cases, let us consider a wave system combined of three coupled resonant quartets:

$$\begin{cases} \boldsymbol{k}_1 + \boldsymbol{k}_2 = \boldsymbol{k}_3 + \boldsymbol{k}_{0,1} = \boldsymbol{k}_4 + \boldsymbol{k}_{0,2} = (2, 0), \\ \omega_1 + \omega_2 = \omega_3 + \omega_{0,1} = \omega_4 + \omega_{0,2} = 2\sqrt{g}, \end{cases} \tag{3.82}$$

where $\boldsymbol{k}_i$ denote primary wave components, $\boldsymbol{k}_{0,i}$ represents resonant ones and $\omega_i = \sqrt{g|\boldsymbol{k}_i|}$ is the linear frequency, respectively. Without loss of generality, let us consider the case

$$\boldsymbol{k}_1 = (1.10, 0.070227), \boldsymbol{k}_3 = (1.05, -0.0352947), \boldsymbol{k}_4 = (1.03, 0.0212001).$$

The corresponding resonant wavenumbers $\boldsymbol{k}_{0,1}$, $\boldsymbol{k}_{0,2}$ and $\boldsymbol{k}_2$ are determined by the resonance criterion given by Eq. (3.82). The resonant wavevector configuration is shown in Fig. 3.5. The geometrical structure is more complicated than in the case of a single resonant quartet, although their external configurations are the same.

Compared to the case of a single resonant quartet, we have now one more primary wave and one more resonant one. Thus, there are two more terms in the initial guess of potential function

$$\begin{aligned} \varphi_0 = {} & A_{0,1}\Psi_{1,0,0,0} + A_{0,2}\Psi_{0,1,0,0} + A_{0,3}\Psi_{0,0,1,0} + A_{0,4}\Psi_{0,0,0,1} \\ & + A_{0,5}\Psi_{1,1,-1,0} + A_{0,6}\Psi_{1,1,0,-1}, \end{aligned} \tag{3.83}$$

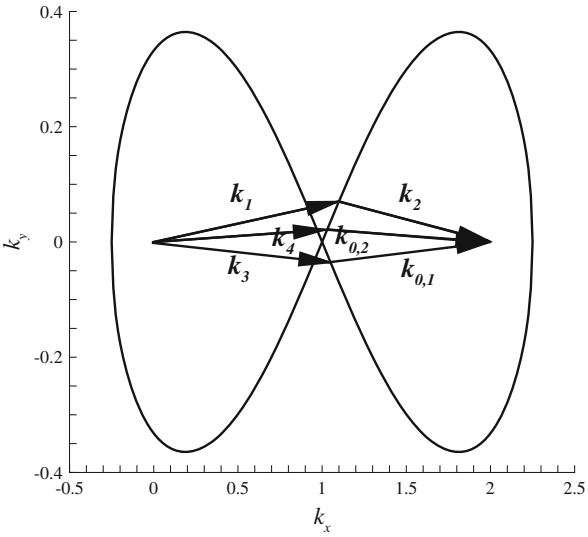

Fig. 3.5 Wavevector configuration of three coupled resonant quartets given by Eq. (3.82) when $\boldsymbol{k}_1 = (1.10, 0.070227)$, $\boldsymbol{k}_3 = (1.05, -0.0352947)$ and $\boldsymbol{k}_4 = (1.03, 0.0212001)$. The corresponding resonant wavenumbers $\boldsymbol{k}_{0,1}$, $\boldsymbol{k}_{0,2}$ and $\boldsymbol{k}_2$ are determined by Eq. (3.82)

Table 3.5 Wave energy distribution for different groups of steady-state resonant wave systems of three coupled resonant quartets in the case represented by Eq. (3.82) when $\boldsymbol{k}_1 = (1.10, 0.070227)$, $\boldsymbol{k}_3 = (1.05, -0.0352947)$, $\boldsymbol{k}_4 = (1.03, 0.0212001)$ and $\varepsilon = 1.00003$. The corresponding resonant wave numbers $\boldsymbol{k}_{0,1}$, $\boldsymbol{k}_{0,2}$ and $\boldsymbol{k}_2$ are determined by Eq. (3.82)

	1st primary wave (%)	2nd primary wave (%)	3rd primary wave (%)	4th primary wave (%)	1st resonant wave (%)	2nd resonant wave (%)
Group-I	45.28	0.51	39.91	3.37	0.87	10.02
Group-II	3.96	7.37	5.52	57.78	8.48	16.89
Group-III	19.57	12.50	18.80	18.80	14.82	15.34
Group-IV	47.49	0.21	3.84	2.06	16.83	29.57
Group-V	46.06	0.08	0.49	40.78	12.48	0.11
Group-VI	0.001	34.48	9.51	9.07	21.59	25.12

where $A_{0,i}$ $(1 \leq i \leq 6)$ are unknown constants to be determined. Similarly to the previous case, these six unknown constants are determined by means of avoiding the secular terms. In the considered case, six groups of steady-state resonant waves were found [20]. Note that the corresponding wave energy distribution changes dramatically from group to group, as shown in Table 3.5. Especially, the two resonant components of Group-I may contain quite a small amount (both together 10.89 %) of the total wave energy.

3.3.2.4 Resonant Sextet

To show existence of steady-state resonant waves in even more complicated wave systems, let us consider resonant sextet

$$\begin{cases} 3\boldsymbol{k}_1 = 2\boldsymbol{k}_2 + \boldsymbol{k}_0 = (2,0), \\ 3\omega_1 = 2\omega_2 + \omega_0 = \sqrt{6\,g}, \end{cases} \tag{3.84}$$

where $\boldsymbol{k}_1$ and $\boldsymbol{k}_2$ denote primary wave components, $\boldsymbol{k}_0$ the resonant ones, and $\omega_i = \sqrt{g|\boldsymbol{k}_i|}$ is the linear frequency, respectively. The corresponding resonance curve is still a kind of "figure of eight", but symmetry along the vertical line is broken, as shown in Fig. 3.6. Note that $\boldsymbol{k}_1 = (2/3, 0)$ is determined automatically by the resonance criterion given by Eq. (3.84). For the second primary wavevector, let us consider $\boldsymbol{k}_2 = (0.625, 0.030217)$, then the corresponding resonant wavenumber $\boldsymbol{k}_0$ is determined by Eq. (3.84).

Multiple steady-state resonant waves exist due to cubic nonlinear terms of potential functions. However, it was found that higher-order harmonic term $\cos(m\xi_1 + n\xi_2)$ $(|m| + |n| > 3)$ can not be directly affected by the first-order harmonics terms $\cos(\xi_1)$ and $\cos(\xi_2)$ within the triad interactions, thus no multiple solutions can be gained if the same kind of initial guess is used as for a resonant quartet. Formally, one can add such a tertiary component in the initial guess that the primary and resonant components can be affected through the triad interaction. In the case described by Eq. (3.84), the possible candidates for the tertiary component are

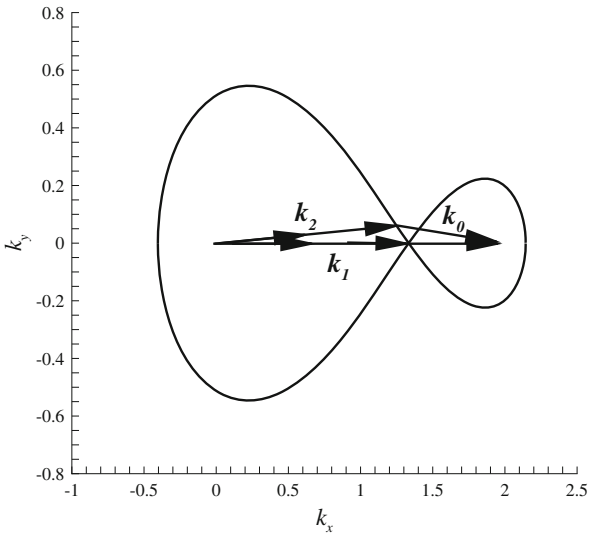

Fig. 3.6 Wavevector configuration of a resonant sextet in the case of (3.84) when $\boldsymbol{k_1} = (0.667, 0)$ and $\boldsymbol{k_2} = (0.625, 0.0302171)$. The corresponding resonant wavenumber $\boldsymbol{k}_0$ is determined by (3.84)

$\sin(\xi_1 - 2\xi_2)$, $\sin(2\xi_1 - \xi_2)$ and $\sin(3\xi_1)$. Taking $\sin(\xi_1 - 2\xi_2)$ as an example, the initial guess of the potential function now reads

$$\varphi_0 = A_{0,1}\Psi_{1,0} + A_{0,2}\Psi_{0,1} + A_{0,3}\Psi_{3,-2} + A_{0,4}\Psi_{1,-2}, \tag{3.85}$$

where $A_{0,1}, A_{0,2}, A_{0,3}$ and $A_{0,4}$ are unknown constants to be determined, $\Psi_{1,0}$ and $\Psi_{0,1}$ are eigenfunctions for the primary waves, $\Psi_{3,-2}$ is the eigenfunction for the resonant wave component, and $\Psi_{1,-2}$ is the tertiary component, respectively. Similarly, avoiding secular terms gives us three nonlinear algebraic equations, which however are *not* enough, since we have now four unknown constants at the first-order of approximation. Because the additional tertiary component is a trivial one, we can enforce the coefficient of $\sin(\xi_1 - 2\xi_2)$ on the right-hand side of Eq. (3.54) to be zero only at the first-order of approximation. In this way, we have a set of four coupled nonlinear algebraic equations, which leads to three groups of real solutions, as reported by Liu and Liao [20]. Note that, without the tertiary component added in the initial guess, only one solution can be found.

It was found [20] that there exist three groups of the steady-state resonant waves in the considered case given by Eq. (3.84), and the resonant wave component may contain the greater part (52.25 %) of the total wave energy, or only a rather small amount (0.44 %), as shown in Table 3.6 for Group-III and Group-I, respectively.

Similarly, when the tertiary component $\sin(2\xi_1 - \xi_2)$ is considered in the initial guess, the same three groups of the steady-state resonant waves were found [20] for the resonant sextet given by Eq. (3.84). In addition, when both $\sin(\xi_1 - 2\xi_2)$ and $\sin(2\xi_1 - \xi_2)$ are considered in the initial guess, the same three groups of the steady-state resonant waves were found, too [20].

It should be emphasized that, not only the primary and resonant wave components but also the trivial ones are considered here in the initial guess, so that the primary and resonant wave components can affect each other through triad interactions. In the considered case described by Eq. (3.84) for a resonant sextet, it was found that the amplitudes of primary and resonant components are much greater than that of the trivial tertiary ones [20]. However, the order of the resonant component is not always the same as that of the primary ones. Even so, our HAM-based approach works quite well, no matter whether the amplitudes of wave components are of the same order or not. This is mainly because the HAM is *independent* of small physical parameters at all. This relies strongly on the

Table 3.6 Wave energy distribution of a resonant sextet in the case given by Eq. (3.84) when $\boldsymbol{k_1} = (0.667, 0)$, $\boldsymbol{k_2} = (0.625, 0.0302171)$ and $\varepsilon = 1.00001$. The corresponding resonant wavenumber $\boldsymbol{k}_0$ is determined by Eq. (3.84)

	1st primary wave (%)	2nd primary wave (%)	Resonant wave (%)
Group-I	51.61	47.7	0.44
Group-II	34.27	19.36	46.31
Group-III	34.4	13.18	52.25

advantage of HAM: unlike perturbation methods, it does *not* need any assumptions about the small amplitudes of wave components.

In all of the above-mentioned cases, both the linear resonance criterion given by Eq. (3.1) and the nonlinear resonance criterion given by Eq. (3.69) are satisfied. However, as pointed out by Liu and Liao [20], this is *not* absolutely necessary: only the nonlinear resonance criterion (3.69) must be satisfied.

In summary, multiple steady-state resonant wave sets exist in deep water, not only for a special quartet [17] but also for a general quartet and some complicated wave systems such as three coupled quartets and even a high-order sextet [20]. Besides, the resonant wave components may contain the greater part of the total wave energy, or approximately the same amount as that of the primary wave components, or only a rather small portion. In addition, the number of multiple solutions may increase as more wave components are involved in resonant sets [20].

3.3.3 Steady-State Resonant Waves in Finite Depth Water

Steady-state resonant waves exist not only in deep water but also in finite water depth, as reported by Xu et al. [33], who considered a special quartet of resonant waves in a constant water depth d:

$$\boldsymbol{k}_3 = 2\boldsymbol{k}_1 - \boldsymbol{k}_2, \quad \omega_3 = 2\omega_1 - \omega_2, \tag{3.86}$$

where $\boldsymbol{k}_1$ and $\boldsymbol{k}_2$ denote the wavenumbers of the primary waves, $\boldsymbol{k}_3$ is the wavenumber of the resonant one, and

$$\omega_i = \sqrt{g|\boldsymbol{k}_i| \tanh(|\boldsymbol{k}_i|d)} \tag{3.87}$$

is the linear frequency, σ_i is the actual frequency, respectively.

Nearly all mathematical formulations are the same as those in deep water [17], except that the base function of the velocity potential now reads

$$\Psi_{m,n} = \sin(m\xi_1 + n\xi_2)\, \frac{\cosh\left[|m\,\boldsymbol{k}_1 + n\,\boldsymbol{k}_2|(z+d)\right]}{\cosh\left[|m\,\boldsymbol{k}_1 + n\,\boldsymbol{k}_2|d\right]} \tag{3.88}$$

and that the bottom boundary $\partial\varphi/\partial z = 0$ must be satisfied on $z = -d$. For detailed mathematical formulations, please refer to Xu et al. [33] and Liao [17].

Write

$$\boldsymbol{k}_1 = k_1\,\mathbf{i}, \quad \boldsymbol{k}_2 = k_2\,\left(\cos\alpha\,\mathbf{i} + \sin\alpha\,\mathbf{j}\right), \tag{3.89}$$

where $k_i = |\boldsymbol{k}_i|$, $\mathbf{i}$ and $\mathbf{j}$ are unit vectors for the x and y axis, α is a constant, respectively. Without loss of generality, Xu et al. [33] considered the case

$$\alpha = \frac{\pi}{36}, \quad k_2\,d = \frac{3\pi}{5}, \quad \epsilon = \frac{\sigma_i}{\omega_i} = 1.0003. \tag{3.90}$$

Table 3.7 Wave energy distribution of a quartet of steady-state resonant waves in finite water depth in case represented by Eq. (3.86) when $\alpha = \pi/36$, $k_2 d = 3\pi/5$, $\epsilon = 1.0003$ and $k_2/k_1 = 0.913835$

	1st primary wave (%)	2nd primary wave (%)	Resonant wave (%)
Group-I	13.72	10.48	75.64
Group-II	40.43	20.38	37.93
Group-III	37.80	53.54	8.03

Table 3.8 Wave energy distribution of a quartet of steady-state resonant waves in finite water depth in case represented by Eq. (3.86) when $\alpha = \pi/36$, $k_2 d = 3\pi/5$, $\epsilon = 1.0003$ and $k_2/k_1 = 1.11165$

	1st primary wave (%)	2nd primary wave (%)	Resonant wave (%)
Group-I	37.37	9.07	53.45
Group-II	41.67	36.53	21.51
Group-III	13.51	76.05	10.40

In this case, the resonance criterion given by Eq. (3.86) gives three solutions $k_1 d = 2.06269$, 1.69564 and 0.867072, respectively, corresponding to the three resonance-states with $k_2/k_1 = 0.913835$, 1.11165 and 2.173797.

It was found [33] that, when $k_2/k_1 = 0.913835$, there exist three groups of steady-state resonant waves, whose wave energy distribution is listed in Table 3.7. Besides, the resonant wave component may contain the greater, or almost the same, or rather a small portion of the total wave energy. These conclusions are exactly the same as those [17, 20] in deep water.

Similarly, when $k_2/k_1 = 1.11165$, there also exist three groups of steady-state resonant waves, as pointed out by Xu et al. [33]. Again, exactly the same conclusions were obtained: the resonant wave component may contain the greater, or almost the same, or rather a small portion of the total wave energy, as shown in Table 3.8.

Xu et al. [33] investigated influence of water depth d and found that, in the cases of $k_2/k_1 = 0.913835$ and $k_2/k_1 = 1.11165$, there always exist three groups of the steady-state resonant waves as d varies from a finite water depth ($k_2 d = 3\pi/5$) to deep water ($k_2 d \to \infty$).

However, when $k_2/k_1 = 2.173797$, the steady-state resonant waves were not found, as mentioned by Xu et al. [33]. This illustrates that the steady-state resonant waves do not exist unconditionally.

In addition, Xu et al. [33] investigated some different cases and always came to the same conclusions. For example, in the case

$$\alpha = \frac{\pi}{60}, \quad k_2 d = \frac{3\pi}{5}, \quad \epsilon = 1.0003, \tag{3.91}$$

the criterion described by Eq. (3.86) gives three steady-state resonance solutions $k_2/k_1 = 0.946172$, 1.06268 and 2.205672, respectively. Similarly, it was found [33] that, in the cases of $k_2/k_1 = 0.946172$ and $k_2/k_1 = 1.06268$, there exist three groups of steady-state resonant waves, and besides the resonant wave component can contain only a small portion of wave energy. However, no steady-state fully-resonant waves

were found when $k_2/k_1 = 2.205672$. Furthermore, in the case

$$\alpha = \frac{2\pi}{45}, \quad k_2 d = \frac{3\pi}{5}, \quad \epsilon = 1.0003, \tag{3.92}$$

the criterion represented by Eq. (3.86) gives three steady-state resonance solutions $k_2/k_1 = 0.869372$, 1.20261 and 2.090427, respectively. Similarly, in case of $k_2/k_1 = 0.869372$ and $k_2/k_1 = 1.20261$, it was found that there also exist three groups of steady-state resonant waves and that the resonant wave component may contain only a small portion of wave energy. Especially, in the case of $k_2/k_1 = 1.20261$, the resonant wave component never contains the greater portion of wave energy, namely, the amplitude of the resonant wave component is always less than that of primary ones: this is an extreme example to verify our conclusion that the resonant wave component may contain only a small portion of wave energy. However, no steady-state resonant waves were found in the case of $k_2/k_1 = 2.090427$.

Note that Xu et al. [33] obtained the above-mentioned conclusions by means of fully nonlinear wave equations. To further confirm these results, they also solved the famous Zakharov equation, a simplified wave model, and came to qualitatively the same conclusions in a similar way [33].

3.4 Steady-State Class-I Bragg Resonant Waves

Do multiple steady-states resonant waves exist in more complicated cases? The answer is positive, as revealed by Xu et al. [34] and described below briefly.

Resonance occurs for nonlinear wave-bottom interaction, too. The simplest case is the class-I Bragg resonance, which occurs when a primary surface wave propagates over an undulated bed that contains ripples with a wavenumber $\boldsymbol{k}_b$, as shown in Fig. 3.7. Without loss of generality, let $\boldsymbol{k}_a$ denote the wavenumber of the primary surface wave and $\boldsymbol{k}_c$ that of the resonant one at free surface, respectively. Note that the names of the so-called primary and resonant waves can be interchanged, since there exists a kind of symmetry on the perpendicular bisector of the bottom wavenumber $\boldsymbol{k}_b$, as shown in Fig. 3.7. So, without loss of generality, we can simply call them wave A and wave C, respectively.

The corresponding class-I Bragg resonance criterion is

$$\boldsymbol{k}_a - \boldsymbol{k}_b = \boldsymbol{k}_c, \quad \omega_a = \omega_c, \tag{3.93}$$

where

$$\omega_a = \sqrt{g|\boldsymbol{k}_a| \tanh(|\boldsymbol{k}_a| d)}, \quad \omega_c = \sqrt{g|\boldsymbol{k}_c| \tanh(|\boldsymbol{k}_c| d)}$$

denote the linear wave frequency in the mean water depth d. This criterion comes from Phillips' resonance criterion given by Eq. (3.1) at a low order for a fixed

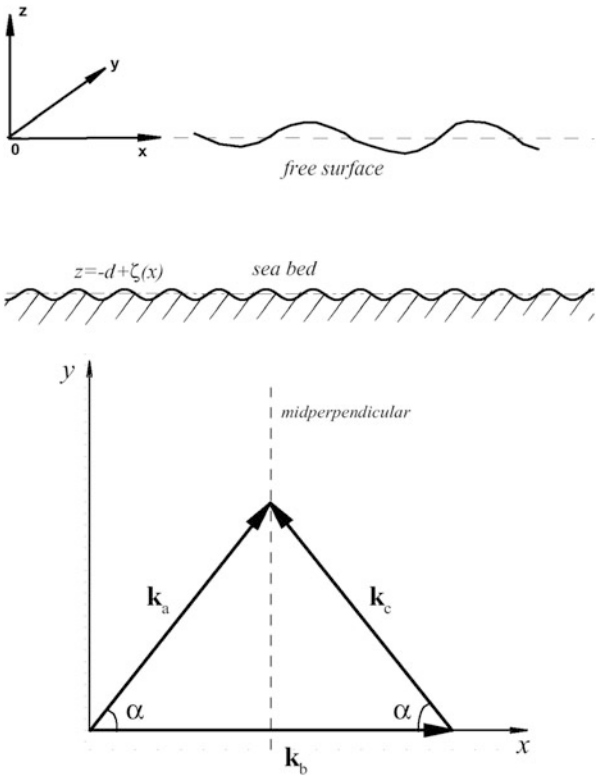

Fig. 3.7 *Top panel*: physical model. *Bottom panel*: sketch map of class-I Bragg resonant waves

bottom, i.e. $\omega_b = 0$. The resonance criterion given by Eq. (3.93) leads to

$$|\boldsymbol{k}_a| = |\boldsymbol{k}_c| = k.$$

In addition, the relationship holds

$$|\boldsymbol{k}_b| = 2|\boldsymbol{k}_a| \cos\alpha = 2\, k \cos\alpha, \tag{3.94}$$

as shown by Fig. 3.7, where α is the angle between the wavenumber $\boldsymbol{k}_a$ and the x-axis.

The class-I Bragg resonance was studied a lot in the past decades. Heathershaw [8] did an experiment when an incidental wave normally propagates over a *patch* of fixed sinusoidal ripples and the class-I Bragg resonance occurs. In this experiment, the amplitude of the resonant wave component was zero initially beyond the rippled patch, and grew linearly with the propagation distance over the ripples.

Using the multiple-scale perturbation method, Mei [26] solved the *linearized* governing equations when an incident wave over a bottom with *finite* ripples

was slightly detuned from the Bragg resonance. In the so-called "perfect tuning" case, the two theoretical results of Mei [26] agree well with the experiment of Heathershaw [8]. According to Mei [26], the transmission coefficient $T(x)$ and the reflection coefficient $R(x)$ are given by

$$T(x) = \frac{A}{A_0} = \frac{\cosh \frac{\Omega_0}{C_g}(L-x)}{\cosh \frac{\Omega_0 L}{C_g}}, \quad R(x) = \frac{B}{A_0} = \frac{-i \sinh \frac{\Omega_0}{C_g}(L-x)}{\cosh \frac{\Omega_0 L}{C_g}}, \quad 0 < x < L, \tag{3.95}$$

respectively, where A_0 is the wave amplitude of the incidental wave beyond the rippled patch ($x < 0$), A and B are the wave amplitudes of the transmission and reflection wave modes over the ripples in a finite interval $0 < x < L$. Thus, as the interval of ripples tends to infinity, i.e. $L \to +\infty$, the ratio of amplitudes of these two components reads

$$\lim_{L\to\infty} \left|\frac{B}{A}\right| = \lim_{L\to\infty} \left|-i \tanh \frac{\Omega_0}{C_g}(L-x)\right| = 1, \tag{3.96}$$

which reveals that the reflection and transmission wave components have the same amplitude. In addition, Mei [26] considered the oblique incidence of slightly detuned wave propagating over the infinite ripples as well, and obtained the ratio of amplitudes of these two components

$$R = \frac{B}{A} = \frac{\cos^2 \alpha}{\cos 2\alpha} \left\{ \frac{\Omega}{\Omega_0} - \left[\left(\frac{\Omega}{\Omega_0}\right)^2 - \left(\frac{\cos 2\alpha}{\cos^2 \alpha}\right)^2 \right]^{\frac{1}{2}} \right\}, \tag{3.97}$$

which leads to

$$|R| = 1 \quad \text{when} \quad \Omega = 0, \tag{3.98}$$

i.e. the reflection and transmission wave components have the same wave amplitude and thus share the same wave energy, where α is the angle between the x-axis and the reflection/transmission wave component. Note that multiple resonant waves were *not* reported in this case [26], mainly because the *linearized* governing equations were solved. Note that the so-called reflection and transmission wave components in the paper of Mei [26] correspond to the resonant and primary components of the steady-state class-I Bragg resonant waves, respectively.

Let us consider here the class-I Bragg resonance, i.e. nonlinear interaction between an oblique surface wave and a bottom with an infinite number of ripples. Mitra and Greenberg [28] solved the same problem by regarding it as an initial value problem, and found slowly periodic energy exchanges between the primary and resonant waves. However, they did not report any multiple resonant waves, since an initial value problem has only one solution. Davies [5, 6] applied perturbation

method to search for steady-states of the class-I Bragg resonant waves, but failed, mainly because "the perturbation theory breaks down due to singularities in the transfer functions", as currently pointed out by Madsen and Fuhrman[25]. Especially, bifurcations have never been reported in this case, to the best of our knowledge.

In 2014, two steady-state class-I Bragg resonant waves were obtained by Xu et al. [34]. One of them is similar to that reported by Mei [26], whose primary wave has the same wave energy as the resonant wave. However, the other does not possess such kind of equality and had never been reported, say, the primary and resonant waves have different wave amplitudes. In addition, the effects of propagation angle, water depth, bottom slope and nonlinearity on the steady-states of the class-I Bragg resonant waves were investigated in detail, and bifurcations of steady-states resonant waves with respect to these physical parameters were found [34] for the first time, to the best of our knowledge.

3.4.1 Mathematical Formulations

Consider the propagation of progressive waves in water of a constant mean depth d over a fixed bed with an infinite number of ripples in a sinusoidal form, as depicted by Fig. 3.7. Assume that the fluid is inviscid and incompressible, the flow is irrotational, and the surface tension is negligible. Let (x, y) and z denote the horizontal and vertical coordinates, with the x-axis in the direction of the wavenumber $\boldsymbol{k}_b$ of the bottom ripples and the z-axis upward, t denote the time, $\eta(x, y, t)$ the unknown wave elevation moving around the mean free surface $z = 0$, and $z = -d + \zeta(x)$ denote the bottom elevation with a constant mean depth d, respectively. The velocity potential $\varphi(x, y, z, t)$ is governed by the Laplace equation

$$\nabla^2\varphi = 0, \qquad -d + \zeta(x) < z < \eta(x, y, t), \tag{3.99}$$

subject to the boundary conditions at the unknown free surface $z = \eta(x, y, t)$:

$$\frac{\partial^2\varphi}{\partial t^2} + g\frac{\partial\varphi}{\partial z} + \frac{\partial|\nabla\varphi|^2}{\partial t} + \nabla\varphi\cdot\nabla\left(\frac{1}{2}|\nabla\varphi|^2\right) = 0, \tag{3.100}$$

and the dynamical condition

$$g\eta + \frac{\partial\varphi}{\partial t} + \frac{1}{2}|\nabla\varphi|^2 = 0, \qquad \text{on } z = \eta(x, y, t). \tag{3.101}$$

The bottom kinematical condition reads

$$\varphi_z - \zeta_x\varphi_x = 0, \qquad \text{on } z = -d + \zeta(x), \tag{3.102}$$

where the bottom profile

$$\zeta(x) = b\cos(k_b x), \quad k_b = |\boldsymbol{k}_b|, \tag{3.103}$$

is given, $\boldsymbol{k}_b$ denotes the wavenumber of the periodic ripples in sinusoidal form on the bottom, b is the amplitude of bottom undulation, respectively.

Note that, for resonant wave systems, the resonance criterion given by Eq. (3.93) must be satisfied, too. The above fully nonlinear wave equations can be found in textbooks. For details, please refer to Mei et al. [27].

Define

$$\xi_1 = \boldsymbol{k}_a \cdot \boldsymbol{r} - \sigma_a\, t, \quad \xi_2 = \boldsymbol{k}_b \cdot \boldsymbol{r}, \tag{3.104}$$

where $\boldsymbol{r} = x\ \mathbf{i} + y\ \mathbf{j}$. According to the resonance criterion given by Eq. (3.93), it holds

$$\boldsymbol{k}_c \cdot \boldsymbol{r} - \sigma_c\, t = \xi_1 - \xi_2. \tag{3.105}$$

Then, the original initial/boundary-value problem becomes a nonlinear boundary value problem with unknown velocity potential $\varphi(\xi_1, \xi_2)$ and wave elevation $\eta(\xi_1, \xi_2)$. It can be solved similarly [17, 20, 33], since only the linear bottom condition given by Eq. (3.102) is different, which is much easier to handle than the two nonlinear boundary conditions at free surface. For the sake of simplicity, all related mathematical formulations are neglected here. For details, please refer to Xu et al. [34].

3.4.2 *Brief Results*

Without loss of generality, let us consider such a case

$$\alpha = 70^\circ,\ k_b/k = 0.68404,\ \ k\,d = 2.5,\ \ b\,k_b = 0.005,\ \ \epsilon = \frac{\sigma_a}{\omega_a} = 1.0003. \tag{3.106}$$

Four groups of steady-state class-I Bragg resonant waves were found [34]. Note that Group-I and Group-IV have anti-symmetric wave energy distribution, as shown in Table 3.9. So do Group-II and Group III. This is reasonable, since the wavenumbers $\boldsymbol{k}_a$ and $\boldsymbol{k}_c$ are symmetric, as shown in Fig. 3.7. Thus, due to the antisymmetry, there exist essentially only two kinds of steady-state class-I Bragg resonant waves. For the first kind (corresponding to Group-II and III in Table 3.9), the primary and resonant wave components contain the same wave energy. This is the same as the multiple-scale perturbation approximation given by Mei [26] in the case of an infinite number of ripples. However, for the second kind (corresponding to Group-I and IV in Table 3.9), the primary and resonant wave components contain different

Table 3.9 Wave energy distribution for different steady-states of the class-I Bragg resonant waves in the case of $\alpha = 70°$, $k_b/k = 0.68404$, $k\,d = 2.5$, $bk_b = 0.005$ and $\epsilon = 1.0003$

	Wave A (%)	Wave C (%)
Group-I	86.20	13.78
Group-II	49.99	49.99
Group-III	49.99	49.99
Group-IV	13.78	86.20

Table 3.10 Wave energy distribution of the second kind of steady-state class-I Bragg resonant waves with different propagation angle α in the case of $kd = 2.5$, $bk_b = 0.005$ and $\epsilon = 1.0003$

α (degree)	Wave A (C) (%)	Wave C (A) (%)
66.9	49.00	50.99
67	53.84	46.15
67.2	63.17	36.82
67.5	70.29	29.70
68	76.67	23.32
68.5	80.47	19.52
69	83.03	16.96
69.5	84.85	15.13
70	86.20	13.78
72	89.03	10.96
73.5	89.72	10.26
75	89.70	10.28

wave energy. To the best of our knowledge, this kind of steady-state class-I Bragg resonant waves have never been reported before.

Xu et al. [34] investigated in details the effect of the physical parameters such as wave propagation angle α, water depth (kd), bottom slope (bk_b) and nonlinearity (ϵ) on the steady-states of the class-I Bragg resonant waves, and found that steady-state class-I Bragg resonant waves exist in general. For example, in the case

$$k\,d = 2.5, \quad b\,k_b = 0.005, \quad \epsilon = \frac{\sigma_a}{\omega_a} = 1.0003, \tag{3.107}$$

they gained two kinds of steady-state class-I Bragg resonant waves for different values of wave propagation angle α. For the first kind ($0 \le \alpha \le 90°$), the primary and resonant waves contain the same wave energy. This agrees well with Mei's result [26]. For the second kind ($66.9° \le \alpha \le 90°$), they have different wave energy, and such kind of difference of wave energy decreases as α decreases from 90° to 66.9°, as shown in Table 3.10. Thus, there exists a bifurcation of the steady-state class-I Bragg resonant waves with respect to the wave propagation angle α, as shown in Fig. 3.8 (top-left). To the best of our knowledge, such kind of bifurcation has never been reported.

From physical viewpoint, when $\alpha = 90°$, there exist no resonant wave and reflection wave, so that the primary wave has the total wave energy. Then, as

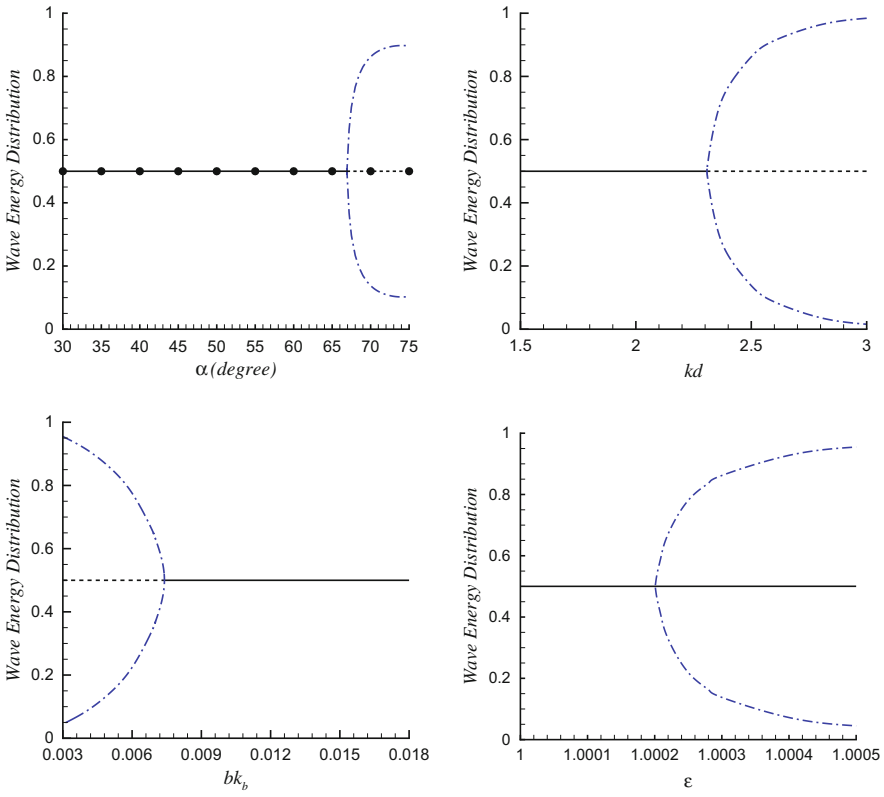

Fig. 3.8 Wave energy distributions of the two kinds of steady-state class-I Bragg resonant wave with respect to the wave propagation angle α (*top-left*), the water depth $k\ d$ (*top-right*), the bottom slope bk_b (*bottom-left*) and the nonlinearity ϵ (*bottom-right*). *Solid* or *dashed line*: the first kind; *dash-dotted line*: the second kind; *dashed line*: mathematically unstable or without physical meaning; *symbols*: first-order multiple-scale perturbation results given by Mei [26]

α decreases from 90°, the resonant wave component has larger and larger wave amplitude and thus contains more and more wave energy, until $\alpha \approx 66.9°$ when the resonant and primary waves have the same wave energy and the bifurcation occurs. Thus, when $\alpha = 90°$, the first kind solution, whose resonant wave component has the same wave energy as the primary one, is physically incorrect. This conclusion should stand for large α, since it is quite possible that the first kind of solution might be mathematically unstable for large wave propagation angle α.

The influence of the mean water depth kd on the existence of the steady-state class-I Bragg resonant waves was also investigated in details by Xu et al. [34] in the case

$$\alpha = 70°, \quad bk_b = 0.005, \quad \frac{k_b}{k} = 0.68404, \quad \epsilon = 1.0003. \tag{3.108}$$

Two kinds of steady-state class-I Bragg resonant waves were found, with a bifurcation with respect to the dimensionless mean water depth kd, as shown in Fig. 3.8 (top-right). The primary and resonant waves have the same wave energy for the first kind ($1 < kd < +\infty$), but different for the second ($2.3 < kd < +\infty$), respectively. From physical point of view, there exist no resonant waves (caused by ripples at bottom) in deep water, i.e. $kd \to \infty$, since the bottom can not influence the free surface in this case, so that the primary wave contains the total wave energy. Thus, the first kind of resonant wave is physically incorrect in deep water. Possibly, it is mathematically unstable for large enough kd. Then, as the mean water depth kd decreases, the bottom influence becomes larger and larger so that the resonant wave component has more and more wave energy, until $kd \approx 2.3$ when the resonant and primary waves have the same wave energy and the bifurcation occurs. So, such kind of bifurcation with respect to the mean water depth kd has a physical meaning.

The influence of the bottom slope bk_b on the existence of a steady-state class-I Bragg resonant waves was studied in detail by Xu et al. [34] in the case

$$\alpha = 70^\circ, \quad kd = 2.5, \quad \frac{k_b}{k} = 0.68404, \quad \epsilon = 1.0003. \tag{3.109}$$

Two kinds of steady-state class-I Bragg resonant waves were found, with a bifurcation with respect to the bottom slope bk_b, as shown in Fig. 3.8 (bottom-left). For the first kind, the primary and resonant waves have the same wave energy. For the second kind, they have different wave energy. However, from physical viewpoint, as the bottom slope $bk_b \to 0$, i.e. the bottom is flat, there should be no resonance caused by the bottom ripples, say, the class-I Brag resonance should not exist at all. Thus, the first kind of steady-state class-I Bragg resonant waves should have no physical meanings for the flat bottom, say, as $bk_b \to 0$. Possibly, it is mathematically unstable for small bk_b. Then, as bk_b becomes larger and larger, the resonant wave contains more and more wave energy, until $bk_b \approx 0.0074$ when both the primary and resonant waves have the same wave amplitude and a bifurcation occurs. Thus, such kind of bifurcation with respect to the bottom slope is reasonable from the physical viewpoint.

The influence of the nonlinearity ($\epsilon = \sigma_i/\omega_i$) of the surface waves on existence of steady-state class-I Bragg resonant waves was investigated [34] in detail in the case

$$\alpha = 70^\circ, \quad kd = 2.5, \quad k_b/k = 0.68404, \quad bk_b = 0.005. \tag{3.110}$$

Two kinds of steady-state resonant waves were found with a bifurcation at $\epsilon \approx 1.0002$, as shown in Fig. 3.8 (bottom-right). The primary and resonant waves contain the same wave energy for the first kind, but different for the second. As the nonlinearity increases to $\epsilon \approx 1.0002$, the bifurcation occurs. This is reasonable, since bifurcation is often due to nonlinearity.

Therefore, there exist two kinds of steady-state class-I Bragg resonant waves. It should be emphasized that the second kind of steady-state class-I Bragg resonant

waves, and especially the above-mentioned bifurcations with respect to wave propagation angle, mean water depth, bottom slope and nonlinearity of free surface, have never been reported before, to the best of our knowledge.

3.5 Experimental Observation

Steady-state resonant waves were found *theoretically* not only in deep water [17, 20] but also either in constant water depth [33] or over a bottom with periodic ripples (Bragg resonance) [34]. To the best of our knowledge, these steady-state resonant waves have never been found before either in theory or in experiments.

Do these steady-state resonant waves indeed exist in practice? Can we observe them in experiments?

In 2014 such kind of experiment was done by Liu et al. [22] in a basin of State Key Laboratory of Ocean Engineering (SKLOE) at Shanghai, China. Several co-propagated short-crested wave trains were generated in the basin, and wave fields were measured and analyzed both along and normal to the wave propagation. The steady-state resonant waves were first calculated theoretically under the exact resonance criterion with high enough nonlinearity and then were generated experimentally in the basin by means of the main wave components that contain at least more than 95 % wave energy. The steady-state wave spectra were quantitatively observed within the inherent system error of the basin, and identified by means of a contrast experiment. Both symmetrical and anti-symmetrical steady-state resonant waves were observed, with excellent agreement with theoretical results, as shown in Fig. 3.9. These results offer the first experimental evidence of existence of steady-state resonant waves with multiple solutions. For details, please refer to Liu et al. [22].

3.6 Concluding Remarks

In his pioneering work, Phillips [31] revealed the resonance criterion for water waves and reported that the amplitude of a resonant wave component, if it is zero initially, grows linearly with time. Benney [4] established the evolution equations of wave-mode amplitudes and demonstrated the well-known time-dependent periodic exchange of wave energy for resonant waves. However, the steady-state resonant waves, whose wave spectrum is independent of time, had never been found at a order higher than three, because perturbation results contain secular terms when Phillips' criterion is satisfied so that "the perturbation theory breaks down due to singularities in the transfer functions", as pointed out by Madsen and Fuhrman [25] in 2012.

By means of the HAM [11–15, 18], a new analytic approximation technique for highly nonlinear problems, the steady-state resonant waves were successfully

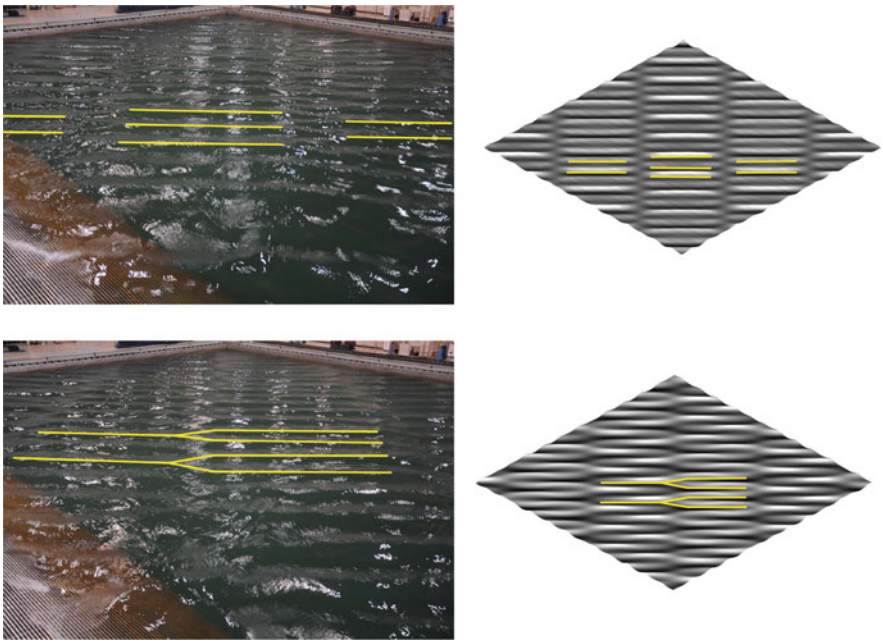

Fig. 3.9 Comparison of steady-state resonant waves in deep water between theoretical and experimental results. *Top-left*: experimental result of the symmetrical wave system. *Top-right*: theoretical result of a kind of symmetrical wave system. *Bottom-left*: experimental result of the antisymmetrical wave system. *Bottom-right*: theoretical result of a kind of antisymmetrical wave system

obtained in theory, for the first time, not only in deep water for a general resonant quartet, three coupled resonant quartets and even a resonant sextet [17, 20], but also in a constant water depth [33] and over a bottom with an infinite number of periodic ripples (Bragg resonance) [34]. In addition, the steady-state resonant waves were further verified experimentally [22] in a basin of State Key Laboratory of Ocean Engineering (SKLOE) at Shanghai, China.

Therefore, the "discovery" of such kind of steady-state resonant waves is a good example illustrating the great potential and general validity of the HAM as a useful tool to investigate some complicated nonlinear problems. Compared to perturbation methods and most of other analytic approximation methods, the HAM has some obvious advantages, as mentioned in Sect. 3.2, and thus could be applied to attack some challenging problems in science and engineering. More importantly, as described in this chapter, the HAM as a powerful novel method could provide us something new and different, since any a truly new method must provide us something new.

Acknowledgements This work is partly supported by the National Natural Science Foundation of China (Approval No. 11272209 and 11432009) and State Key Laboratory of Ocean Engineering (Approval No. GKZD010063).

References

1. Adomian, G.: Nonlinear stochastic differential equations. J. Math. Anal. Appl. **55**, 441–452 (1976)
2. Adomian, G.: A review of the decomposition method and some recent results for nonlinear equations. Comput. Math. Appl. **21**, 101–127 (1991)
3. Adomian, G.: Solving Frontier Problems of Physics: The Decomposition Method. Kluwer Academic, Boston (1994)
4. Benney, D.J.: Non-linear gravity wave interactions. J. Fluid Mech. **14**, 577–584 (1962)
5. Davies, A.G.: Some interactions between surface water waves and ripples and dunes on the seabed. http://eprints.soton.ac.uk/14524/1/14524-01.pdf (1980)
6. Davies, A.G., Heathershaw, A.D.: Surface-wave propagation over sinusoidally varying topography. J. Fluid Mech. **144**, 419–443 (1984)
7. Hammack, J.L., Henderson, D.M.: Resonant interactions among surface water waves. Annu. Rev. Fluid Mech. **25**, 55–97 (1993)
8. Heathershaw, A.D.: Seabed-wave resonance and sand bar growth. Nature. **296**, 343–345 (1982)
9. Hinch, E.J.: Perturbation Methods. Cambridge University Press, Cambridge (1991)
10. Liao, S.J.: On the proposed homotopy analysis techniques for nonlinear problems and its application. Ph.D. dissertation, Shanghai Jiao Tong University (1992)
11. Liao, S.J.: An explicit, totally analytic approximation of Blasius' viscous flow problems. Int. J. Nonlinear Mech. **34**, 759–778 (1999)
12. Liao, S.J.: Beyond Perturbation: Introduction to the Homotopy Analysis Method. Chapman & Hall/CRC, Boca Raton (2003)
13. Liao, S.J.: On the homotopy analysis method for nonlinear problems. Appl. Math. Comput. **147**, 499–513 (2004)
14. Liao, S.J.: Notes on the homotopy analysis method: some definitions and theorems. Commun. Nonlinear Sci. Numer. Simul. **14**, 983–997 (2009)
15. Liao, S.J.: An optimal homotopy-analysis approach for strongly nonlinear differential equations. Commun. Nonlinear Sci. Numer. Simul. **15**, 2315–2332 (2010)
16. Liao, S.J.: On the relationship between the homotopy analysis method and Euler transform. Commun. Nonlinear Sci. Numer. Simul. **15**, 1421–1431 (2010)
17. Liao, S.J.: On the homotopy multiple-variable method and its applications in the interactions of nonlinear gravity waves. Commun. Nonlinear Sci. Numer. Simul. **16**, 1274–1303 (2011)
18. Liao, S.J.: Homotopy Analysis Method in Nonlinear Differential Equations. Springer, Heidelberg (2012)
19. Liao, S.J., Tan, Y.: A general approach to obtain series solutions of nonlinear differential equations. Stud. Appl. Math. **119**, 297–354 (2007)
20. Liu, Z., Liao, S.J.: Steady-state resonance of multiple wave interactions in deep water. J. Fluid Mech. **742**, 664–700 (2014)
21. Liu, Y.M., Yue, D.K.P.: On generalized Bragg scattering of surface waves by bottom ripples. J. Fluid Mech. **356**, 297–326 (1998)
22. Liu, Z., Xu, D.L., Li, J., Peng, T., Alsaedi, A., Liao, S.J.: On the existence of steady-state resonant waves in experiment. J. Fluid Mech. **763**, 1–23 (2015) doi:10.1017/jfm.2014.658
23. Lyapunov, A.M.: General Problem on Stability of Motion (English translation). Taylor & Francis, London (1992) [the original one was published in 1892 in Russian]
24. Madsen, P.A., Fuhrman, D.R.: Third-order theory for bichromatic bi-directional water waves. J. Fluid Mech. **557**, 369–397 (2006)

25. Madsen, P.A., Fuhrman, D.R.: Third-order theory for multi-directional irregular waves. J. Fluid Mech. **698**, 304–334 (2012)
26. Mei, C.C.: Resonant reflection of surface water waves by periodic sandbars. J. Fluid Mech. **152**, 315–335 (1985)
27. Mei, C.C., Stiassnie, M., Yue, D.: Theory and Applications of Ocean Surface Waves: Nonlinear Aspects, vol. 2. World Scientific, Singapore (2005)
28. Mitra, A., Greenberg, M.D.: Slow interactions of gravity waves and a corrugated sea bed. J. Appl. Mech. **51**, 251–255 (1984)
29. Murdock, J.A.: Perturbations: Theory and Methods. Wiley, New York (1991)
30. Nayfeh, A.H.: Perturbation Methods. Wiley, New York (1973)
31. Phillips, O.M.: On the dynamics of unsteady gravity waves of finite amplitude. J. Fluid Mech. **9**, 193–217 (1960)
32. Van Dyke, M.: Perturbation Methods in Fluid Mechanics. Parabolic, Stanford (1975)
33. Xu, D.L., Lin, Z.L., Liao, S.J., Stiassnie, M.: On the steady-state fully resonant progressive waves in water of finite depth. J. Fluid Mech. **710**, 379–418 (2012)
34. Xu, D.L., Lin, Z.L., Liao, S.J.: Equilibrium states of class-I Bragg resonant wave system. Eur. J. Mech. B. Fluids. **50**, 38–51 (2015) doi:10.1016/j.euromechflu.2014.10.006

Chapter 4
Modulational Instability in Equations of KdV Type

Jared C. Bronski, Vera Mikyoung Hur, and Mathew A. Johnson

Abstract It is a matter of experience that nonlinear waves in a dispersive medium, propagating primarily in one direction, may appear periodic in small space and time scales, but their characteristics—the amplitude, the phase, the wave number, etc.—slowly vary in large space and time scales. In the 1960s, Whitham developed an asymptotic (WKB) method to study the effects of small "modulations" on nonlinear dispersive waves. Since then, there has been a great deal of work aiming at rigorously justifying the predictions from Whitham's formal theory. We discuss some recent advances in the mathematical understanding of the dynamics, in particular, the instability, of slowly modulated waves for equations of KdV type.

4.1 Introduction

The modulational instability, at the core, is the observation that nonlinear wave trains in a dispersive medium may be unstable to self modulation, developing nontrivial large-scale structures, which continue to evolve as they propagate. The phenomenon is familiar to researchers in many branches of science. Moreover, it is a fundamental issue in the theory of wave motion. The history of the modulational instability of nonlinear dispersive waves is long and fascinating. We do not have space here for a complete account of it, and we will discuss only selected high points. For more details, the interested reader is encouraged to read the excellent review article by Zakharov and Ostrovsky [77].

J.C. Bronski • V.M. Hur
Department of Mathematics, University of Illinois at Urbana-Champaign, Urbana, IL 61801, USA
e-mail: jared@math.uiuc.edu; verahur@math.uiuc.edu

M.A. Johnson (✉)
Department of Mathematics, University of Kansas, Lawrence, KS 66045, USA
e-mail: matjohn@ku.edu

E. Tobisch (ed.), *New Approaches to Nonlinear Waves*, Lecture Notes in Physics 908, DOI 10.1007/978-3-319-20690-5_4

The first understanding of the importance of the modulational instability arose in hydrodynamics in the 1960s. Benjamin and Feir [7], motivated by laboratory experiments [28], showed that Stokes' periodic waves in deep water are unstable. About the same time, Whitham [73] applied his newly developed theory of nonlinear dispersion to Stokes waves, associating the hyperbolic (or elliptic) nature of the resulting modulation equations with the stability (or instability, respectively) of the underlying wave; he showed that a Stokes wave is unstable if $kh_0 > 1.363\ldots$, where k is the wave number of the underlying wave and h_0 is the undisturbed fluid depth. Benjamin and Feir, additionally, discovered the sideband nature of the instability—the marginal stability of the wave number, with a band of unstable wave numbers to either side. Corroborating results arrived nearly simultaneously, but independently, by Lighthill [59], Ostrovsky [62], Benney and Newell [8], and Zakharov [75, 76].

The modulational instability has been experimentally observed, either directly or indirectly, in many physical systems. For example, pulses in nonlinear optical fibers with so-called anomalous dispersion are (approximately) governed by the focusing, cubic nonlinear Schrödinger equation, which exhibits the modulational instability. The importance of the effect was noted in early papers by Anderson and Lisak [2] and Hasegawa [39], where it was proposed as a method for generating short optical pulses; it was later observed experimentally by Tai et al. [69]. Since then, there have been a great deal of work observing the phenomenon in a number of optical settings; see [14, 32, 57, 67, 70], for instance.

The modulational instability and associated Whitham equations for integrable systems, such as the KdV and nonlinear Schrödinger equations, were studied by Flashka et al. [30] and by Lax and Levermore [58], and it has grown into a large and active field of research; see [23, 27, 35, 56, 71], for instance. Moreover, there has been a great deal of recent work aiming at making connections between the elliptic nature of the modulation equations and the instability of the underlying wave. To single out a few in the vein, we mention [10, 11, 20, 21, 24, 54]. Here we will mainly be concerned with the latter program, how Whitham's formal theory translates into rigorous stability results. This has led to many applications in nonlinear dispersive equations; see [5, 6, 13, 33, 34, 37, 38, 43, 44, 46–50], for instance.

We begin Sect. 4.2 by constructing periodic traveling waves to the generalized KdV equations. In Sect. 4.3 we will review Whitham's modulation theory and discuss implications for the modulational instability. Section 4.4 contains the main analytical contributions, providing a rigorous mathematical program to determine the modulational instability of periodic traveling waves of KdV type equations. For illustrative purposes, in Sect. 4.5, we will discuss applications to the KdV, modified KdV and Schamel equations. We will then extend the theory to equations admitting *nonlocal* dispersion and discuss applications to the Benjamin-Ono equation, as well as small amplitude waves of the fractional KdV, intermediate long-wave equations and Whitham's equation for water waves.

4.2 Periodic Traveling Waves of Generalized KdV Equations

Much of the chapter is devoted to the modulational instability of periodic traveling waves of the generalized KdV equation

$$u_t = u_{xxx} + f(u)_x. \tag{4.1}$$

Here, $t \in \mathbb{R}$ is typically proportional to elapsed time and $x \in \mathbb{R}$ is related to the spatial variable in the predominant direction of wave propagation; $u = u(x,t)$ is real valued, representing the wave profile or a velocity, and f is a suitable nonlinearity. In many examples of interest, f obeys a power law. Throughout we express partial differentiation either by a subscript or using the symbol ∂.

Perhaps the best known among equations of the form given by Eq. (4.1) is the KdV equation

$$u_t = u_{xxx} + (u^2)_x, \tag{4.2}$$

which was put forward in [17, 55] to model the unidirectional propagation of surface water waves with small amplitudes and long wavelengths in a channel. It has since found relevances in other situations such as Fermi-Pasta-Ulam lattices; see [29], for instance. In the case of $f(u) = au^3 + bu^2$, a, b constants, Eq. (4.1) is called the modified KdV or Gardner equation, which models internal waves propagating in a density stratified fluid; see [36], for instance. In the case of $f(u) = |u|^{3/2}$, moreover, Eq. (4.1) is called the Schamel equation; see [66], for instance.

By a traveling wave, we mean a solution which propagates at a constant speed without changing the shape. It takes the form $u(x,t) = u(z)$, $z = x - ct$, where $c \in \mathbb{R}$ is the wave speed and u is a stationary solution of

$$u_t = u_{zzz} + cu_z + f(u)_z. \tag{4.3}$$

It then reduces by quadrature to

$$u_{zz} + cu + f(u) = a \tag{4.4}$$

for some constant $a \in \mathbb{R}$. It further reduces by quadrature to

$$\frac{1}{2}u_z^2 = E + au - \frac{1}{2}cu^2 - F(u) \tag{4.5}$$

for some constant $E \in \mathbb{R}$, where $F' = f$, $F(0) = 0$. We refer to Eq. (4.5) as the profile ODE associated with Eq. (4.1). One may employ elementary phase plane analysis to infer the existence of periodic, homoclinic (pulses) and heteroclinic

(fronts) orbits of Eq. (4.5). Note that their existence and non-existence depend on properties of the effective potential

$$V(u;a,c) := F(u) + \frac{1}{2}cu^2 - au. \tag{4.6}$$

4.2.1 Some Explicit Solutions

In some special cases, Eq. (4.5) may be integrated to yield classes of explicit solutions. In the case of $f \equiv 0$ in Eq. (4.1), namely the (linear) Airy equation, for instance, Eq. (4.1) admits plane wave solutions $u(x,t) = e^{ik(x-ct)}$, where k represents the wave number and c is the wave speed, provided that the temporal frequency $\omega = kc$ is related to k through the dispersion relation $\omega = k^3$. We will return to these linear waves in Sect. 4.3.1 when we discuss Whitham's modulation theory. Their modulational stability, it turns out, is trivial and follows directly from the dispersion relation. As a matter of fact, all these waves are modulationally stable. Therefore we will be concerned with a genuine nonlinearity, typically of the form $f(u) = \sigma u^{p+1}$ for some $p > 0$ and $\sigma \neq 0$ real. Thanks to the scaling invariance of Eq. (4.1), by the way, $|\sigma|$ may be taken to be arbitrary. As a matter of fact, the stability of periodic traveling waves of Eq. (4.1) is independent of the choice of $|\sigma|$. Further, the sign of σ is inconsequential if p is odd.

In the case of $f(u) = \frac{1}{2}u^2$ in Eq. (4.1), namely the KdV equation, to proceed, simple phase plane analysis implies that periodic solutions of Eq. (4.5) exist, depending on a, E and c, provided that the cubic polynomial $E - V(\cdot\,;a,c)$ possesses three distinct real roots, which we label as $\gamma < \beta < \alpha$. Periodic solutions then correspond to oscillation between in the interval $[\alpha,\beta]$, and a, E and c are related to α, β and γ as

$$E = \frac{\alpha\beta\gamma}{6}, \qquad a = -\frac{\alpha\beta + \beta\gamma + \alpha\gamma}{6}, \qquad c = \frac{\alpha+\beta+\gamma}{3}. \tag{4.7}$$

In particular, Eq. (4.5) may be written as $u_z^2 = (\alpha - u)(u-\beta)(u-\gamma)/3$ and hence u may be defined implicitly as

$$\frac{z+z_0}{\sqrt{3}} = \int_u^\alpha \frac{dw}{\sqrt{(\alpha-w)(w-\beta)(w-\gamma)}}, \tag{4.8}$$

where z_0 is a constant of integration associated with translational invariance and can be chosen to satisfy $u(0) = \alpha$. We then make the change of variables

$$w = \alpha - (\alpha-\beta)\sin^2\phi, \qquad \sin\phi = \sqrt{\frac{\alpha-w}{w-\beta}}, \tag{4.9}$$

and we solve Eq. (4.8) for u explicitly as

$$u(z;\alpha,\beta,\gamma,z_0) = \beta + (\alpha-\beta)\mathrm{cn}^2\Big(\sqrt{\frac{\alpha-\gamma}{12}}\,(z+z_0);m\Big), \quad m = \frac{\alpha-\beta}{\alpha-\gamma}, \tag{4.10}$$

where $\mathrm{cn}(\cdot\,;m)$ denotes the Jacobi cnoidal function with elliptic modulus $m \in [0,1)$. These cnoidal waves form a four-parameter family of periodic traveling waves of the KdV equation. Note that the period is $T = 4\sqrt{3}K(m)/\sqrt{\alpha-\beta}$, where K is the complete elliptic integral of the first kind. Incidentally $\mathrm{cn}(z;m) \to \mathrm{sech}(z)$ and $K(m) \to \infty$ as $m \to 1^-$, and therefore Eq. (4.10) reduces to the well-known formula for the KdV soliton in the long wave limit.

Another example of explicit solutions is when $f(u) = \pm\frac{1}{3}u^3$ in (4.1), which we call the focusing $(+)$ and defocusing $(-)$ modified KdV equations. In the focusing case, $V(\cdot\,;a,c)$ represents a bistable double-well potential and simple phase plane analysis implies that non-constant periodic solutions of Eq. (4.5) exist, depending on a, E and c, provided that the quartic polynomial $E - V(\cdot\,;a,c)$ has four distinct roots (i.e. its discriminant is not zero), α, β, γ and δ, say, with at least two of them being real; see Fig. 4.1. The general solution is rather tedious with a number of cases to consider, but it amounts to reducing the elliptic integral to the standard form. Indeed, if we write the solution in the form

$$\int \frac{du}{\sqrt{(u-\alpha)(u-\beta)(u-\gamma)(u-\delta)}} = \omega t \tag{4.11}$$

for some appropriate constant $\omega \in \mathbb{R}$ and if we make the Möbius transformation

$$v = \frac{au+b}{u-\alpha} \tag{4.12}$$

for some constants a, b, which maps one of the roots of the quartic to ∞, then Eq. (4.11) becomes

$$\int \frac{dv}{\sqrt{P_3(v)}} = \omega t \tag{4.13}$$

for some cubic polynomial P_3, which may be studied similarly to the KdV equation. Of course, α must not be an end point of the interval over which solutions oscillate.

In the case of $a = 0$, furthermore, the effective potential $V(\cdot\,;0,c)$ is symmetric (even) and the expressions for explicit solutions simplify greatly. Specifically, there are two families of solutions, one in terms of the Jacobi elliptic cnoidal function and the other in terms of the Jacobi dnoidal function. The cnoidal waves correspond to solutions for $E > 0$ and their orbits in the phase plane lie outside the separatrix; see Fig. 4.1a. The dnoidal waves correspond to solutions for $E < 0$ and their orbits in the phase plane are bounded by a homoclinic orbit (corresponding to a solitary wave). In the case of $c < 0$ and $E < 0$, for instance, the quartic on the right side of

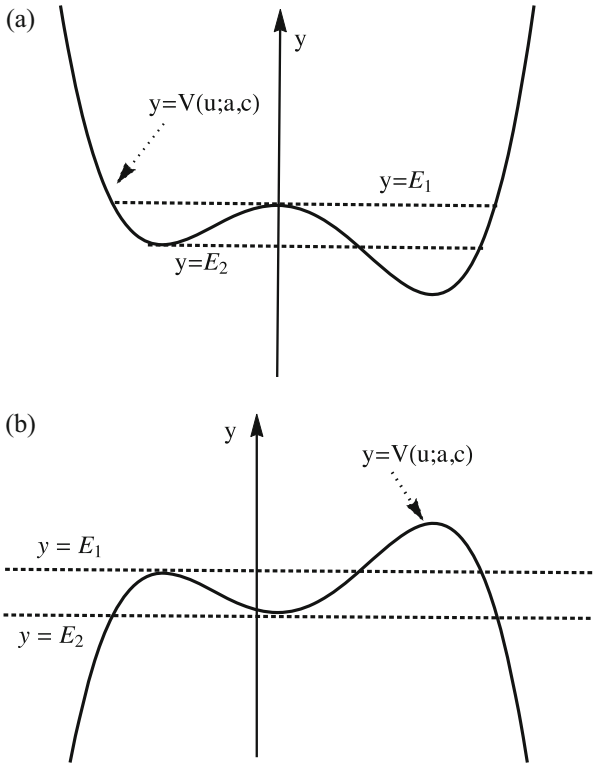

Fig. 4.1 Representative graphics of the effective potential $V(\cdot\,; a, c)$ in the case of the (**a**) focusing and (**b**) defocusing modified KdV equations. In the focusing case, periodic traveling waves exist only for $E > E_2(a, c)$. There are two families of solutions when $E \in (E_2, E_1)$ while there is only one family when $E > E_1$. In the defocusing case, periodic traveling waves exist only for $E \in (E_2, E_1)$ and there is only one family of solutions

the profile ODE

$$u_z^2 = 2E - cu^2 - \frac{u^4}{6} \tag{4.14}$$

has four real roots, $u = \pm k_1, \pm k_2$, where $k_1 = -3\Big(c + \sqrt{c^2 + \frac{4E}{3}}\Big)$ and $k_2 = -3\Big(c - \sqrt{c^2 + \frac{4E}{3}}\Big)$. We then make the change of variables $u = k_2 v$ and Eq. (4.14) becomes

$$v_z^2 = \frac{k_2^2}{6}(v^2 - 1)\Big(\frac{k_2^2}{k_1^2} - v^2\Big). \tag{4.15}$$

Note that the Jacobi dnoidal function $y(z) = \mathrm{dn}(z;k)$ solves

$$y_z^2 = (y^2 - 1)(1 - k^2 - y^2). \tag{4.16}$$

Therefore $v = \mathrm{dn}(k_2 z/\sqrt{6}; k)$, $k^2 = 1 - k_1^2/k_2^2$. The other case when $c < 0$ and $E > 0$, which is solvable in terms of the Jacobi cnoidal function, may be treated similarly.

In the defocusing case, non-constant periodic solutions of Eq. (4.5) exist, depending on a, E and c, only when the quartic polynomial $E - V(\cdot\,; a, c)$ has four distinct real roots; see Fig. 4.1b. In the case of $a = 0$, the effective potential is symmetric likewise and one may find explicit solutions in terms of the Jacobi snoidal function.

4.2.2 General Existence Theory

While an extensive amount of literature is devoted to studying properties of explicit periodic traveling waves of Eq. (4.1), e.g. the elliptic function solutions of the KdV and modified KdV equations discussed in the previous subsection, our modulational instability theory does not make use of such formulae. (Nevertheless, we will strive to state our results in the context of explicit solutions when possible.) Rather, of importance to us are properties of the *parametrization* of periodic traveling waves with respect to various coordinate systems and the Jacobians between them. As a first step in the direction, we remark that the Jacobian of the map given by Eq. (4.7) from $\mathbb{R}^3$ to itself is not singular, provided that the cubic polynomial $E - V(\cdot\,; a, c)$ has three distinct roots, a property fundamentally related to the sign of its *discriminant*. As a matter of fact, in the set where the discriminant of the polynomial is positive and it has three distinct real roots, the transformation Eq. (4.7) is smoothly invertible. Consequently, the cnoidal wave solutions in Eq. (4.10) of the KdV equation may be considered as a four-parameter family of periodic traveling waves, parameterized by a, E, c and z_0, whose profile and fundamental period depend smoothly on the parameters. Analogous results hold for elliptic function solutions of the focusing and defocusing modified KdV equations: within the domain of existence they may be smoothly parameterized in terms of E, c and z_0 (recalling that $a = 0$ in these explicit solutions).

With the above in mind, we note that if f in Eq. (4.1) is a polynomial nonlinearity then the zero set of the discriminant of $E - V(\cdot\,; a, c)$, given by

$$\Gamma = \Big\{(a, E, c) \in \mathbb{R}^3 : \mathrm{disc}\Big(E + au - \frac{1}{2}cu^2 - F(u)\Big) = 0\Big\}, \tag{4.17}$$

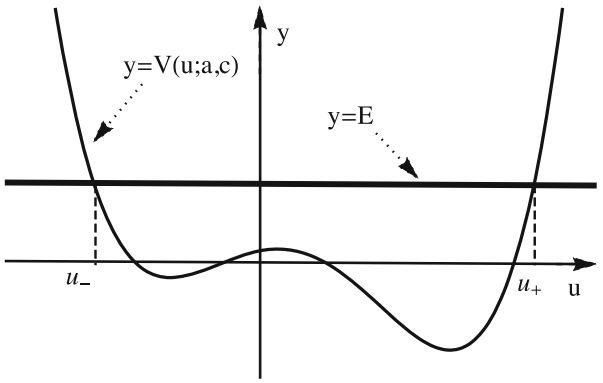

Fig. 4.2 Schematic drawing showing the locations of the roots u_+ and u_- of $E - V(\cdot\,; a, c)$

defines a *variety* dividing the parameter space into open sets with a constant number of periodic traveling waves. Moreover solutions of Eq. (4.5) with $(a, E, c) \in \Gamma$ make either equilibria or homoclinic orbits, which correspond to constant solutions or solitary waves of Eq. (4.1), respectively. In particular, $(0, 0, c) \in \Gamma$ represents solitary waves homoclinic to zero.

In order to ensure the existence of periodic orbits of Eq. (4.5), we therefore take $(a, E, c) \in \mathbb{R}^3 \setminus \Gamma$ so that there exist simple and distinct roots of $E - V(\cdot\,; a, c)$ and that there are real roots $u_\pm$ satisfying $u_- < u_+$ such that $V(u; a, c) < E$ for $u \in (u_-, u_+)$; see Fig. 4.2. It follows that $u_\pm$ are smooth functions of the traveling wave parameters a, E, c and, without loss of generality, we may assume $u(0) = u_-$. The corresponding periodic solution of Eq. (4.5) is an even function of $z = x - ct$ and its period can be expressed by quadrature as

$$\begin{aligned} T = T(a, E, c) &= \sqrt{2} \int_{u_-}^{u_+} \frac{du}{\sqrt{E - V(u; a, c)}} \\ &= \frac{\sqrt{2}}{2} \oint_\gamma \frac{du}{\sqrt{E - V(u; a, c)}}, \end{aligned} \tag{4.18}$$

where integration over γ represents a complete integration from u_- to u_+ and then back to u_- again. Note however that the branch of the square root must be chosen appropriately in each direction. Alternatively, the contour γ can be interpreted as a closed loop (Jordan curve) in the complex plane that encloses a bounded set containing $u_\pm$. By a standard procedure, the above integral can be regularized at the square root branch points, and hence it represents a C^1 function of a, E and c.

In general, Eq. (4.1) admits three conserved quantities, physically corresponding to the Hamiltonian, the mass and the momentum. For a T-periodic traveling wave $u = u(\cdot\,; a, E, c)$, they are defined by

$$\begin{aligned} H(a,E,c) &= \int_0^T \left(\frac{u_x^2}{2} - F(u)\right) dx = \frac{\sqrt{2}}{2} \oint_\gamma \frac{E - V(u;a,c) - F(u)}{\sqrt{E - V(u;a,c)}}\, du, \\ M(a,E,c) &= \int_0^T u\, dx = \frac{\sqrt{2}}{2} \oint_\gamma \frac{u}{\sqrt{E - V(u;a,c)}}\, du, \\ P(a,E,c) &= \int_0^T u^2\, dx = \frac{\sqrt{2}}{2} \oint_\gamma \frac{u^2}{\sqrt{E - V(u;a,c)}}\, du, \end{aligned} \tag{4.19}$$

respectively, where the integral over γ is defined as before. These integrals can be regularized at their square root branch points and hence they represent C^1 functions of the traveling wave parameters. As we will see, the gradients of the period and these conserved quantities play a crucial role in the stability of periodic traveling waves in Eq. (4.1). To help with calculations involving gradients of these conserved quantities, we point out a useful identity. The classical action (in the sense of action-angle variables) for Eq. (4.5) is given by

$$K(a,E,c) = \sqrt{2} \oint_\gamma \sqrt{E - V(u;a,c)}\, du \tag{4.20}$$

and it serves as a generating function for the conserved quantities of Eq. (4.1) evaluated at the traveling wave. Specifically,

$$T = \frac{\partial K}{\partial E}, \qquad M = \frac{\partial K}{\partial a}, \qquad P = 2\frac{\partial K}{\partial c}, \tag{4.21}$$

so that, in particular, the Jacobian $\frac{\partial(T,M,P)}{\partial(a,E,c)}$ agrees (up to a constant factor) with the Hessian of the map

$$\mathbb{R}^3 \ni (a,E,c) \mapsto K(a,E,c) \in \mathbb{R}. \tag{4.22}$$

In summary, Eq. (4.1) in the case of polynomial nonlinearity admits a four-parameter family of periodic traveling waves, smoothly parameterized by a, E and c in Eq. (4.5) and an auxiliary parameter z_0 associated with the translational invariance of the equation. Solitary waves, whose profile asymptotically vanishes, correspond to $a = E = 0$, and hence they form a co-dimension two subset of the full set of traveling waves.

4.3 Formal Asymptotics and Whitham's Modulation Theory

We are interested in the stability to slow modulations of periodic traveling waves of nonlinear dispersive equations. That means, we wish to understand the long time dynamics of "slightly" modulated, periodic traveling waves. In particular, we wish to determine whether the long time dynamics will be appropriately described by small modulations of the carrier wave. In this section, we illustrate some asymptotic calculations that shed light on this and hence on the modulational stability. Mainly, we will utilize a formal multiple scale expansion to derive a first order system of equations governing the slow dynamics of averaged quantities of the modulated wave over the fast scale. Such an approach was pioneered by Whitham in the 1960s and early 1970s (see [72–74], for instance), and it has since been widely applied in both the physics and mathematics communities. As such, it has been termed Whitham's modulation theory.

To illustrate the key ideas, we begin by considering slow modulations of linear wave packets, for which the modulational dynamics is simplified thanks to the direct coupling of spatial and temporal frequencies through the dispersion relation. We will then extend the calculation to nonlinear wave packets, for which one must make use of a nonlinear dispersion relation to close the modulation system. In Sect. 4.4.3, we will discuss rigorously validating the predictions from these calculations.

4.3.1 Linear Dispersive Waves

Notice that any constant function $u(x,t) = u_0$ is a solution of Eq. (4.1). Seeking nearby solutions of the form

$$u(x,t) = u_0 + \varepsilon v(x,t), \qquad |\varepsilon| \ll 1, \quad v = \mathcal{O}(1), \tag{4.23}$$

we arrive at that

$$v_t = v_{xxx} + f'(u_0)v_x + \mathcal{O}(\varepsilon). \tag{4.24}$$

Ignoring all $\mathcal{O}(\varepsilon)$ terms, we find that as long as v remains $\mathcal{O}(1)$ we may approximate it by a solution of

$$v_t = v_{xxx} + f'(u_0)v_x. \tag{4.25}$$

Notice that it admits plane wave solutions of the form

$$v(x,t) = Ae^{i(kx-\omega t)} + c.c., \tag{4.26}$$

where A is the (real) amplitude, k is the wave number and the temporal frequency ω is related to u_0 and k through the dispersion relation

$$\omega = k^3 - f'(u_0)k. \tag{4.27}$$

Here and elsewhere $c.c.$ means the complex conjugate.

We wish to describe the modulation of the linear wave packet. That is, we consider solutions of Eq. (4.25) of the form given by Eq. (4.26), where A, k and ω are allowed to depend on space and time. Note that if A, k and ω are allowed to vary significantly over one wavelength of the carrier wave, taken with A, k and ω constant, then there is no reason to expect that the evolving wave packet must be described as a modulated periodic wave. Hence, we only consider modulations where A, k and ω vary slowly over space and time. This naturally leads one to consider two separate space and time scales—the "fast" oscillations of the carrier wave and the slow evolution of A, k and ω.

Utilizing a multiple scale approach, we therefore seek a solution of Eq. (4.25) of the form

$$v(x,t,X,S) = A(X,S)e^{i(k(X,S)x-\omega(X,S)t)} + c.c., \tag{4.28}$$

where x, t denote the "fast" variables and $X = \varepsilon x$, $S = \varepsilon t$ denote the "slow" variables. Here and elsewhere, ε indicates a small, but non-zero, quantity. Substituting Eq. (4.28) into Eq. (4.25) and collecting terms of order up to $\mathcal{O}(\varepsilon)$, we arrive at that

$$\begin{aligned}(-i\omega + ik^3 - ikf'(u_0)) + i\varepsilon A\Big(\Big(\frac{\partial k}{\partial S} + (f'(u_0) - 3k^2)\frac{\partial k}{\partial X}\Big)(x - (u_0 - 3k^2 t))\Big)\\ +\varepsilon\Big(\frac{\partial A}{\partial S} + (f'(u_0) - 3k^2)\frac{\partial A}{\partial X} + 6kA\frac{\partial k}{\partial X}\Big) = 0.\end{aligned} \tag{4.29}$$

At the order of $\mathcal{O}(1)$, this merely requires that the slowly evolving temporal and spatial frequencies satisfy the dispersion relation, i.e. [see Eq. (4.27)]

$$\omega(k) = k^3 - f'(u_0)k, \qquad k = k(X,S), \tag{4.30}$$

for all $X, S \in \mathbb{R}$. Since it forces ω to be real valued regardless of the slow evolution of the wave number k, the modulated solutions given by Eq. (4.28) are bounded for all times, implying that the constant solution is modulationally stable.

At the order of $\mathcal{O}(\varepsilon)$, to describe the slow evolution more precisely, (4.29) yields two equations for k and A:

$$\frac{\partial k}{\partial S} + \omega'(k)\frac{\partial k}{\partial X} = 0 \quad \text{and} \quad \frac{\partial A}{\partial S} + (\omega'(k)A)_X = 0, \tag{4.31}$$

where $\omega'(k) = 3k^2 - f'(u_0)$ depends on X and S through the evolution of k. The system (4.31), together with the dispersion relation, describes to leading order the

evolution of slowly modulated wave packets in Eq. (4.25). Since $\omega(k)$ is real valued for all $k \in \mathbb{R}$, the linearization of the system about $(k, A) = (k_0, A_0)$, corresponding to a linear wave train of the form given by Eq. (4.26) with $k = k_0$ and $A = A_0$ constant, is hyperbolic, and hence both k and A will remain bounded for all times. This again implies the modulational stability of the constant solution.

Note that the Whitham modulation equations given by Eq. (4.31) for slow modulations of a constant state prescribe the evolution of only *two* quantities, namely the wave number and the amplitude. Moreover, the evolution equation for k is *independent of the evolution of the amplitude*. These observations are due to the fact that the dispersion relation [see Eq. (4.27)] directly relates the temporal and spatial frequencies.

4.3.2 Nonlinear Dispersive Waves

We now wish to understand the long time dynamics of arbitrary amplitude and slowly modulated, periodic traveling waves of Eq. (4.1). The main technical difference is that the spatial and temporal frequencies are no longer coupled through the dispersion relation, and hence we need to find modulation equations describing the slow evolution of *three* wave characteristics parameters.

Recall from Sect. 4.2 that periodic traveling waves of Eq. (4.1) are parameterized (up to translations) by a, E and c and that the period depends on the parameters. While this parametrization is natural from the existence standpoint, we will see below that it is not well-suited to the formal asymptotic description of Whitham's modulation theory. (We utilize this in the rigorous theory in the following sections, however.) Rather, the modulation equations are most naturally described in terms of the slow evolutions of the period and conserved quantities associated with the modulated solution. The Jacobian between these parameterizations will play a vital role in our theory.

We seek an asymptotic description of modulated, periodic traveling waves of Eq. (4.1). To account for the separate fast and slow scales of space and time involved, we utilize a multiple scale expansion. Specifically we introduce "slow" variables $(X, S) = (\varepsilon x, \varepsilon t)$ and note that in the slow coordinates given by Eq. (4.1) becomes

$$u_S = \varepsilon^2 u_{XXX} + f(u)_X. \tag{4.32}$$

Following [72, 74], we seek a solution of Eq. (4.32) of the form

$$u(X, S) = u^{(0)}\Big(\frac{\phi(X, S)}{\varepsilon}, X, S\Big) + \varepsilon u^{(1)}\Big(\frac{\phi(X, S)}{\varepsilon}, X, S\Big) + \mathcal{O}(\varepsilon^2), \tag{4.33}$$

where the phase ϕ is chosen to ensure that $u^{(j)}$, $j = 0, 1$, are 1-periodic functions in the variable $y = \phi(X, S)/\varepsilon$. Note that the local period of oscillation of the modulated wave train is $\varepsilon/\partial_X \phi$, where we assume that the unknown phase a priori

satisfies $\partial_X \phi \neq 0$. Note that periodic traveling waves of Eq. (4.1) fit this asymptotic description if one takes $u = u^{(0)}$ constant in the slow variables and chooses $\phi(X, S) = k(X - cS)$. That is, periodic traveling waves of Eq. (4.1) correspond to *constant solutions* in the slow coordinates.

We then substitute Eq. (4.33) into Eq. (4.32) and collect like powers of ε, resulting in a hierarchy of equations that must be satisfied at each order. At the order of $\mathcal{O}(\varepsilon^{-1})$, we find that

$$\phi_S \partial_y u^{(0)} = (\phi_X \partial_y)^3 u^{(0)} + (\phi_X \partial_y) f(u^{(0)}), \tag{4.34}$$

which is merely Eq. (4.4) for $u^{(0)}$ differentiated in the variable y, under the identification $k = \phi_X$ as the spatial frequency and $c = \omega/k$ as the wave speed, where $\omega = \phi_S$ is the temporal frequency of the modulation, and all of which are considered as functions of the slow variables X and S. For X and S fixed, we may thus choose $u^{(0)}$ to be a periodic traveling wave of Eq. (4.1), and hence of the form

$$u^{(0)}(y, X, S) = u(y; a(X, S), E(X, S), c(X, S)) \tag{4.35}$$

for some solution u of Eq. (4.5), where a, E and c are independent of y. In particular, the compatibility condition $\phi_{SX} = \phi_{XS}$ implies that

$$k_S + \omega_X = 0, \tag{4.36}$$

which serves as a nonlinear dispersion relation. It effectively replaces the dispersion relation in the case of linear waves. Linear waves satisfy Eq. (4.36) thanks to the dispersion relation and the first equation in Eq. (4.31). In the literature, Eq. (4.36) is sometimes referred to as the equation of conservation of waves.

At the order of $\mathcal{O}(1)$, continuing,

$$\partial_z \mathcal{L}[u^{(0)}] u^{(1)} = \partial_S u^{(0)} - \partial_X f(u^{(0)}) - \partial_X (\phi_X^2 \partial_y^2) u^{(0)} \tag{4.37}$$

supplemented with the 2π-periodic boundary conditions, where

$$\mathcal{L}[u^{(0)}] = \partial_z^2 - s u^{(0)} + f'(u^{(0)}), \qquad z = ky, \tag{4.38}$$

is recognized as the linear operator obtained from linearizing Eq. (4.1) about the carrier wave $u^{(0)}$. The Fredholm alternative implies that Eq. (4.37) has a solution, provided that the right hand side is orthogonal to the kernel of the adjoint operator $(\partial_y \mathcal{L}[u^{(0)}])^\dagger = -\mathcal{L}[u^{(0)}]\partial_y$ in $L^2(0, 2\pi)$. Here and elsewhere, the dagger means the adjoint. Since $u^{(0)}$ is not constant, upon differentiation of Eq. (4.5), it is readily seen that

$$\ker(\mathcal{L}[u^{(0)}]\partial_y) = \operatorname{span}\{1, u^{(0)}\}. \tag{4.39}$$

Hence Eq. (4.37) has a solution, provided that the orthogonality conditions

$$\begin{cases} M_S + \partial_X G(u^{(0)}) = 0, \\ P_S + \partial_X Q(u^{(0)}) = 0 \end{cases} \tag{4.40}$$

hold, where

$$M(X,S) = \int_0^1 u^{(0)}(y,X,S)\,dy \quad \text{and} \quad P(X,S) = \int_0^1 (u^{(0)})^2(y,X,S)\,dy \tag{4.41}$$

are functions of the slow variables X and S, and the fluxes G and Q are the inner products of the right hand side of Eq. (4.37) with 1 and $u^{(0)}$, respectively; in particular, they are y-independent functions of X and S that may be written out explicitly, if desired; see [46], for instance.

Together, three equations in Eqs. (4.36) and (4.40) form the Whitham averaged system for Eq. (4.1), describing the mean behavior of the slowly varying functions a, E and c in Eq. (4.35) *implicitly* in terms of the slow evolutions of the functions k, M and P. In particular, formally, Eq. (4.1) admits a modulated wave train solution that, to leading order, can be described as

$$u(x,t) = u\Big(\frac{\phi(X,S)}{\varepsilon}; a(X,S), E(X,S), c(X,S)\Big) + \mathcal{O}(\varepsilon), \tag{4.42}$$

where a, E and c evolve in the slow variables in such a way that k, M and P evolve according to the (nonlinear) first order system, Eqs. (4.36) and (4.40).

To ascertain the modulational stability of the periodic traveling wave $u(a_0, E_0, c_0)$ of Eq. (4.1), say, we seek to understand whether the functions a, E and c in Eq. (4.35) evolve away from a_0, E_0 and c_0 in the slow scale or not. The modulation equations, Eqs. (4.36) and (4.40), however, describe the evolution of a, E and c *implicitly* through the evolution of k, M and P. As such, if we want to measure deviation of a, E, c from a_0, E_0, c_0 in terms of the evolution of k, M, P, we must require that, at least in the vicinity of the carrier wave u, nearby periodic traveling waves of Eq. (4.1) can be *re-parameterized* by k, M and P. By the implicit function theorem, such a (local) re-parametrization is possible, provided that the Jacobian matrix

$$\frac{\partial(k,M,P)}{\partial(a,E,c)} \tag{4.43}$$

is not singular at (a_0, E_0, c_0).

Under the assumption that Eq. (4.43) is not singular, the modulational stability can be analyzed by linearizing the modulation equations, Eqs. (4.36) and (4.40), about the constant solution (a_0, E_0, c_0). We seek solutions of Eqs. (4.36) and (4.40) of the form

$$(a(X,S), E(X,S), c(X,S)) = (a_0, E_0, c_0) + \varepsilon(\tilde{a}(X,S), \tilde{E}(X,S), \tilde{c}(X,S)), \tag{4.44}$$

which, upon substitution into Eqs. (4.36) and (4.40) and dropping of all $\mathcal{O}(\varepsilon^2)$ terms,[1] satisfy that

$$\left(\frac{\partial(k_0, M_0, P_0)}{\partial(a, E, c)}\partial_S(\tilde{a}, \tilde{E}, \tilde{c}) + \frac{\partial(\omega_0, G_0, Q_0)}{\partial(a, E, c)}\partial_X(\tilde{a}, \tilde{E}, \tilde{c})\right) = 0, \tag{4.45}$$

where the 0 subscript denotes evaluation at (a_0, E_0, c_0). This is a constant-coefficient, linear system of PDEs, and we may seek solutions of the form

$$(\tilde{a}, \tilde{E}, \tilde{c})(X, S) = e^{\lambda S - ikX}(\tilde{a}_0, \tilde{E}_0, \tilde{c}_0), \qquad \lambda \in \mathbb{C} \quad \text{and} \quad k \in \mathbb{R} \tag{4.46}$$

for some $(\tilde{a}_0, \tilde{E}_0, \tilde{c}_0) \in \mathbb{R}^3$, where the temporal and spatial frequencies of the perturbation can be determined from the dispersion relation

$$\mathcal{D}_W(\lambda, k) := \det\left(\lambda\frac{\partial(k_0, M_0, P_0)}{\partial(a, E, c)} - ik\frac{\partial(\omega_0, G_0, Q_0)}{\partial(a, E, c)}\right) = 0, \tag{4.47}$$

a homogeneous cubic polynomial in the variables λ and k. In particular, $\mathcal{D}_W(\lambda, k) = \lambda^3\mathcal{D}_W(1, k/\lambda)$ and hence if z_j's, $j = 1, 2, 3$ are roots of

$$\widehat{\mathcal{D}}_W(z) := \mathcal{D}_W(1, z) \tag{4.48}$$

then the dispersion relation defines three spectral curves

$$\lambda_j(k) = iz_jk, \qquad j = 1, 2, 3. \tag{4.49}$$

Therefore, $u(a_0, E_0, c_0)$ must be modulationally stable, provided that the reduced dispersion relation $\hat{\mathcal{D}}_W$ has three real roots, while it must be modulationally unstable if the dispersion relation admits at least one complex root with non-zero imaginary part.

The above suggests that a necessary condition for the modulational stability of a periodic traveling wave of Eq. (4.1) is that the linearized Whitham system given by Eq. (4.45) be hyperbolic, i.e. eigenvalues of

$$\frac{\partial(k_0, M_0, P_0)}{\partial(\omega_0, G_0, Q_0)} = \left(\frac{\partial(k_0, M_0, P_0)}{\partial(a, E, c)}\right)\left(\frac{\partial(\omega_0, G_0, Q_0)}{\partial(a, E, c)}\right)^{-1} \tag{4.50}$$

be all real. Note that while Eq. (4.21) implies that $\frac{\partial(k_0, M_0, P_0)}{\partial(a, E, c)}$ is symmetric, and hence its eigenvalues are all real, the hyperbolicity of $\frac{\partial(k_0, M_0, P_0)}{\partial(\omega_0, G_0, Q_0)}$ naturally depends on the fluxes, and hence on the specific nonlinearity and waves involved. In the following

[1] Note that $\mathcal{O}(1)$ terms cancel out thanks to the definition of (a_0, E_0, c_0), and hence the leading order term is $\mathcal{O}(\varepsilon)$.

section, we will derive a rigorous, modulational stability theory whose main result, Theorem 4.1, relates the stability of a periodic traveling wave of Eq. (4.1) to slow modulations of eigenvalues of some 3×3 matrix. The eigenvalues end up agreeing precisely with the roots of $\hat{\mathcal{D}}_W$, providing a rigorous justification of the above formal calculations; see Theorem 4.2 below.

4.4 Rigorous Theory of Modulational Instability

We discuss how to make rigorous the formal argument sketched in the previous section in various settings. In the process we provide a general methodology of determining the modulational instability for a large class of nonlinear dispersive equations.

4.4.1 Analytic Setup

Let $u_0 = u_0(\cdot\,; a, E, c)$ denote a $T = T(a, E, c)$-periodic traveling wave of Eq. (4.1). The idea of "stability" can formally be stated as requiring that if a solution to Eq. (4.1) starts close to the solution u_0 then it stays close to u_0 for all times. To understand the evolution of solutions that start near u_0, one typically linearizes the governing equation about the solution u_0, a process we now describe.

Notice that u_0 is a stationary T-periodic solution of

$$u_t = cu_z + u_{zzz} + f(u)_z, \tag{4.51}$$

which is merely Eq. (4.1) written in the spatially traveling frame $z = x - ct$. We seek a solution of Eq. (4.51) with the initial datum $u(0) = u_0 + v_0$ for some $v_0 \in H^3(\mathbb{R})$ with $\|v_0\|_{H^3(\mathbb{R})}$ sufficiently small.[2] Writing $u(t) = u_0 + v(t)$ for $t > 0$ for which $u(t)$ is defined,[3] we see that v satisfies

$$v_t = Lv + \mathcal{N}[u_0, v], \tag{4.52}$$

[2]The requirement that the perturbation be integrable is not the only choice possible. Other natural candidates of classes of perturbations include periodic perturbations with fundamental period nT for some $n = 1, 2, 3, \ldots$. While such periodic classes of perturbations are natural from a variational viewpoint, they may impose artificial constraints on the physical problem. As we will see below, the class of localized, i.e. integrable on the line, perturbations includes information about all quasi-periodic perturbations.

[3]Here we ignore issues of well-posedness of Eq. (4.1) to such initial data.

where $L = \partial_u F(u_0) : H^3(\mathbb{R}) \subset L^2(\mathbb{R}) \to L^2(\mathbb{R})$ is the linear operator, given as

$$L = \partial_z(\partial_z^2 + c + f'(u_0)), \tag{4.53}$$

and $\mathcal{N}[u_0, v] = \partial_z(f(u_0 + v) - f(u_0) - f'(u_0)v)$ is a nonlinear operator satisfying the quadratic estimate

$$\|\mathcal{N}[u_0, v]\|_{L^2(\mathbb{R})} \leq C\|v\|^2_{H^1(\mathbb{R})} \tag{4.54}$$

for some constant $C = C(\|u_0\|_{H^1(\mathbb{R})}) > 0$ independent of v. We expect that as long as v_0 is sufficiently small in $L^2(\mathbb{R})$, say, the solution $v(t)$ must be small in $L^2(\mathbb{R})$ at least for short times. Moreover, so long as $v(t)$ remains sufficiently small, it is reasonable to expect that the nonlinear evolution Eq. (4.52) may well be approximated by the linear evolution equation

$$v_t = Lv, \tag{4.55}$$

posed on $H^3(\mathbb{R}) \subset L^2(\mathbb{R})$. Thanks to linearity, we may relax the smallness assumption.

The underlying wave u_0 is said to be *linearly stable* (to $L^2(\mathbb{R})$-perturbations), provided that all solutions of Eq. (4.55) remain bounded in time, whereas it is *linearly unstable* (to $L^2(\mathbb{R})$-perturbations) if there exists some initial datum $v_0 \in H^3(\mathbb{R})$ such that the associated solution of Eq. (4.55) grows in time.

The linear stability may further be reduced to a problem in spectral analysis as follows. Since the linear evolution given by Eq. (4.55) is autonomous in time, we may take the Laplace transform in time, arriving at

$$\lambda v = Lv, \tag{4.56}$$

where $v(z) = v(z; \lambda)$ denotes the Laplace transform of the function $v(z, t)$ in Eq. (4.55) and $\lambda \in \mathbb{C}$ is the Laplace (temporal) frequency. The spectral problem given by Eq. (4.56) is posed on $L^2(\mathbb{R})$, and as such the stability of u_0 may be studied by analyzing the spectrum of L considered as a densely defined operator on $L^2(\mathbb{R})$. Indeed, if the $L^2(\mathbb{R})$-spectrum of L intersects the open right half plane in $\mathbb{C}$, then one expects the solution of Eq. (4.56) to grow in time and hence the underlying wave be unstable. With this in mind, we say that u_0 is *spectrally unstable* (to $L^2(\mathbb{R})$-perturbations) if there exists λ in the $L^2(\mathbb{R})$-spectrum of L with $\mathrm{Re}(\lambda) > 0$. Otherwise, we say it is *spectrally stable* (to $L^2(\mathbb{R})$-perturbations).[4] Since Eq. (4.56) is left invariant under the transformations

$$v \mapsto \bar{v} \quad \text{and} \quad \lambda \mapsto \bar{\lambda}, \tag{4.57}$$

[4] In general, spectral stability does *not* imply linear stability, as is familiar from the ODE theory. Nevertheless, spectral *instability* often does imply linear (and nonlinear) instability.

where the bar denotes complex conjugation, and

$$z \mapsto -z \quad \text{and} \quad \lambda \mapsto -\lambda, \tag{4.58}$$

the spectrum of L is symmetric with respect to reflections about both the real and imaginary axes. Consequently, u_0 is spectrally stable if and only if the $L^2(\mathbb{R})$-spectrum of L is contained in the imaginary axis.

Since Eq. (4.56) is a spectral problem for a linear operator with periodic coefficients, its spectrum is most conveniently characterized by Floquet-Bloch theory. A standard theory (see [19, 64], for instance) dictates that non-trivial solutions of Eq. (4.56) cannot be integrable over $\mathbb{R}$, i.e. they cannot have a finite $L^p(\mathbb{R})$-norm for any $1 \leq p < \infty$, and that they can at best be bounded functions over $\mathbb{R}$. Moreover, any bounded solution of Eq. (4.56) must be of the form

$$v(x) = e^{i\xi x} w(x) \tag{4.59}$$

for some $w \in L^2_{\text{per}}([0, T])$ and $\xi \in [-\pi/T, \pi/T)$. In particular, $\lambda \in \mathbb{C}$ belongs to the $L^2(\mathbb{R})$-spectrum of L if and only if there is a non-trivial solution of the quasi-periodic spectral problem

$$\begin{cases} \lambda v = Lv, \\ v(x+T) = e^{i\xi T} v(x) \end{cases} \tag{4.60}$$

for some $\xi \in [-\pi/T, \pi/T)$. Alternatively, $\lambda \in \text{spec}_{L^2(\mathbb{R})}(L)$ if and only if for some $\xi \in [-\pi/T, \pi/T)$ there exists a non-trivial T-periodic solution of

$$\lambda w = L_\xi w, \qquad \text{where} \quad L_\xi = e^{-i\xi x} L e^{i\xi x}. \tag{4.61}$$

We remark that for each $\xi \in [-\pi/T, \pi/T)$, the spectrum of the operator L_ξ, considered as a densely defined operator on $L^2_{\text{per}}([0, T])$, is comprised merely of discrete eigenvalues with finite multiplicities and, furthermore,

$$\text{spec}_{L^2(\mathbb{R})}(L) = \bigcup_{\xi \in [-\pi/T, \pi/T)} \text{spec}_{L^2_{\text{per}}([0,T])}(L_\xi). \tag{4.62}$$

The parameter ξ is referred to as the Bloch frequency and the operators L_ξ are called the Bloch operators associated with L.

Rather than analyzing the essential spectrum of the operator L directly, the above discussion indicates that we may choose to study the T-periodic discrete spectra of the Bloch operators L_ξ for $\xi \in [-\pi/T, \pi/T)$. In practice, one does not expect to be able to explicitly compute the eigenvalues of L_ξ for an arbitrary Bloch frequency ξ, except for few very special cases, e.g. completely integrable systems (see [16],

for instance). Thankfully, however, for the purposes of the modulational stability analysis, we only need to consider the spectra of the operators L_ξ in a neighborhood of the origin in the spectral plane and only for ξ sufficiently small. Indeed, notice that if the eigenvalues of L_0 are confined to the imaginary axis, then the underlying wave is spectrally stable to perturbations which themselves are T-periodic. When $0 < |\xi| \ll 1$ small, the period of the perturbation is nearly that of the underlying wave, and hence the effect of the perturbation is seen only on very large space and time scales. That means, the spectrum of the operators L_ξ with $0 < |\xi| \ll 1$ describes the stability to *long wavelength perturbations*.

Modulational perturbations fall into the class of long wavelength perturbations, but they form a special subclass where the effect of the perturbation is simply to modulate the wave characteristics, which presently are given by the parameters a, E, c, and the translational mode z_0. The point is that variations in these parameters provide spectral information of L_0 at the origin in the spectral plane. Formally, this can be seen upon differentiating Eq. (4.4) with respect to a, E, c and z and noting that

$$L_0 \text{span}\{\partial_z u_0, \partial_a u_0, \partial_E u_0\} = 0, \qquad L_0 \partial_c u_0 = -\partial_z u_0, \tag{4.63}$$

where the T-periodic boundary conditions have not yet been enforced; see Lemma 4.1 below for a precise description of the generalized kernel of L_0.

It is natural from the above remarks that the spectral stability of the underlying wave to slow modulations corresponds to ensuring the spectra of the Bloch operators L_ξ near the origin is confined in the imaginary axis for all $0 \leq |\xi| \ll 1$ sufficiently small. Our program is in two steps. First we study the structure of the generalized kernel of the unmodulated operator L_0. We then use perturbation theory to examine how the spectrum near the origin of the modulated operator L_ξ bifurcates from the origin for $0 < |\xi| \ll 1$. This program is carried out in the next section.

4.4.2 Modulational Instability in Generalized KdV Equations

We begin our program by demonstrating that, under a generic nondegeneracy condition, the unmodulated operator L_0 has a two dimensional, generalized T-periodic kernel with a Jordan chain of length one. Henceforth we employ the notation

$$\{f, g\}_{x,y} := \det\left(\frac{\partial(f, g)}{\partial(x, y)}\right) \quad \text{and} \quad \{f, g, h\}_{x,y,z} := \det\left(\frac{\partial(f, g, h)}{\partial(x, y, z)}\right) \tag{4.64}$$

for determinants of 2×2 and 3×3 Jacobians, respectively.

Lemma 4.1 ([13, 15]) *Suppose that $u = u(\cdot\,; a_0, E_0, c_0)$ is a T-periodic solution of Eq. (4.5) and that the Jacobian determinants T_E, $\{T, M\}_{a,E}$ and $\{T, M, P\}_{a,E,c}$ are not zero at (a_0, E, c_0). Then*

$$\begin{aligned} \phi_0 &:= \{T, u\}_{a,E}, & \psi_0 &:= 1, \\ \phi_1 &:= \{T, M\}_{a,E} u_x, & \psi_1 &:= \textstyle\int_0^x \phi_2(s)\, ds, \\ \phi_2 &:= \{u, T, M\}_{a,E,c}, & \psi_2 &:= \{T, M\}_{a,E} + \{T, M\}_{a,E} u \end{aligned} \tag{4.65}$$

are all T-periodic and satisfy

$$\begin{aligned} L_0\phi_0 = L_0\phi_1 = 0, \qquad & L_0^\dagger \psi_0 = L_0^\dagger \psi_2 = 0, \\ L_0\phi_2 = -\phi_1, \qquad & L_0^\dagger \psi_1 = \psi_2. \end{aligned} \tag{4.66}$$

In particular, ϕ_j's, $j = 0, 1, 2$, form a basis for the generalized null space of L_0 and ψ_j's, $j = 0, 1, 2$, form a basis for the generalized null space of the adjoint $L_0^\dagger$. Moreover $\langle \psi_j, \phi_i \rangle_{L^2_{\text{per}}([0,T])} = 0$ if $i \neq j$.

The proof follows from a straightforward application of the Fredholm alternative; see [13, 15], for details. The main observation is that while u_x is T-periodic, the derivatives u_a, u_E and u_c are generally *not* T-periodic because of the dependence of the period on the parameters a, E, c. Instead, the change in these functions across a period is proportional to derivatives of the period; for instance,

$$\begin{pmatrix} u_E(T) \\ u_{Ex}(T) \\ u_{Exx}(T) \\ \cdots \end{pmatrix} - \begin{pmatrix} u_E(0) \\ u_{Ex}(0) \\ u_{Exx}(0) \\ \cdots \end{pmatrix} = T_E \begin{pmatrix} u_E(0) \\ u_{Ex}(0) \\ u_{Exx}(0) \\ \cdots \end{pmatrix} \tag{4.67}$$

and similarly for the change in u_a and u_c across a period. It is then easy to check that the functions ϕ_j's, $j = 0, 1, 2$, are T-periodic and, thanks to Eq. (4.63), satisfy the desired relations under the action of L_0. Since ϕ_2 clearly has mean zero, moreover, the functions ψ_j's, $j = 0, 1, 2$ are T-periodic and, again seen upon differentiating the profile equation, satisfy the desired relations under the action of $L_0^\dagger$. Note that u can be chosen, through appropriate translation, to be an even function, and that L_0 sends odd functions to even functions and even functions to odd functions, all while preserving periodicity, namely L_0 is parity reversing. We may then verify that $\langle \psi_j, L_0\phi_k \rangle_{L^2_{\text{per}}([0,T])} = 0$ for all $j, k = 0, 1, 2$ which, by the Fredholm alternative, implies the desired structure of the generalized kernels of L_0 and $L_0^\dagger$.

Henceforth, we assume that the quantities T_E, $\{T, M\}_{a,E}$ and $\{T, M, P\}_{a,E,c}$ are not zero at the underlying T-periodic traveling wave. Recalling Eq. (4.21), we point out

that the key Jacobian determinants in our theory correspond to the three principle minor determinants of the Hessian of K, namely

$$K_{EE} = T_E, \quad \{K_E, K_a\}_{E,a} = \{T, M\}_{E,a}, \tag{4.68}$$

$$\{K_E, K_a, K_c\}_{E,a,c} = \{T, M, P\}_{E,a,c}. \tag{4.69}$$

Each of the above are determinants of symmetric matrices given by Eq. (4.21), and hence their eigenvalues are real and assumed to be non zero. Lemma 4.1 then implies that the elements of the T-periodic kernel of the unmodulated operator L_0 are given by the elements of the tangent space to the (two dimensional) manifold of solutions *of fixed period and fixed wave speed* at the underlying wave, while the generalized T-periodic kernel of L_0 consists also of a vector in the tangent space to the (three dimensional) manifold of solutions *of fixed period* at the underlying wave with no restrictions on the wave speed. It immediately follows that the origin is a T-periodic eigenvalue of L_0 with algebraic multiplicity three and geometric multiplicity two.

To proceed, we turn to how these triple eigenvalues bifurcate from the state of $\lambda = 0$ and $\xi = 0$. A Baker-Campbell-Hausdorff expansion reveals that

$$L_\xi = L_0 + i\xi L_1 + \frac{1}{2}(i\xi)^2 L_2 + \mathcal{O}(\xi^3), \tag{4.70}$$

where

$$L_0 = \partial_x \mathcal{L} \quad \text{and} \quad L_1 := [L_0, x] = \mathcal{L} - 2\partial_x^2, \quad L_2 := [L_1, x] = -3\partial_x. \tag{4.71}$$

Here and throughout, $[A, B] = AB - BA$ denotes the commutator. Note that these operators are well-defined on $L^2_{\text{per}}([0, T])$ even though the function x is not. A useful observation is that

$$\langle \psi_j, L_k \phi_\ell \rangle_{L^2_{\text{per}}([0,T])} = 0 \tag{4.72}$$

whenever $j + k + \ell = 0 \bmod(2)$, which can readily be verified by using Lemma 4.1 and noting that L_0 and L_2 reverse parity while L_1 preserves parity. That is, L_0 and L_2 send even (or odd) functions to odd (or even, respectively) functions, while L_1 sends even (or odd) functions to even (or odd, respectively) functions.

Since L_ξ is a relatively compact perturbation of L_0 depending analytically on the Bloch frequency ξ, it follows that the operator L_ξ will have three eigenvalues $\lambda_j(\xi)$'s, $j = 1, 2, 3$, defined for $|\xi| \ll 1$, bifurcating from $\lambda = 0$ for $0 < |\xi| \ll 1$. To determine whether the underlying wave is modulationally stable or not, it remains to track these eigenvalues as functions of ξ and, in particular, determine whether these eigenvalues are confined to the imaginary axis for all $0 < |\xi| \ll 1$ or not.

Notice from Lemma 4.1 that we may use the functions ϕ_j's and ψ_j's, $j = 0, 1, 2$, to construct explicit rank 3 eigenprojections

$$\Pi_0 : L^2_{\text{per}}([0,T]) \to \text{gker}(L_0) \quad \text{and} \quad \tilde{\Pi}_0 : L^2_{\text{per}}([0,T]) \to \text{gker}(L_0^\dagger) \tag{4.73}$$

onto the total eigenspace of the operators L_0 and $L_0^\dagger$. Note in passing that $\text{gker}(L_0) = \ker(L_0^2)$ and $\text{gker}(L_0^\dagger) = \text{range}(L_0^2)$. We can thus represent the action of the operator L_0 on its generalized kernel as the 3×3 matrix operator

$$M_0 = \tilde{\Pi}_0 L_0 \Pi_0 = \begin{pmatrix} 0 & 0 & 0 \\ 0 & 0 & \langle \psi_1, L_0 \phi_2 \rangle \\ 0 & 0 & 0 \end{pmatrix}. \tag{4.74}$$

Specifically, $M_0 = (\langle \psi_j, L_0 \phi_k \rangle_{L^2_{\text{per}}([0,T])})_{j,k=1,2,3}$ and similarly for the projection of the identity; see below. In Sect. 4.5.4 when we discuss small amplitude waves of nonlocal equations, we will utilize a slightly different re-scaling of these matrix operators.

Note that $\langle \psi_1, L_0 \phi_2 \rangle = \frac{1}{2}\{T, M\}_{a,E}\{T, M, P\}_{a,E,c} \neq 0$ by assumption, reflecting the Jordan structure of the unmodulated operator L_0. Note moreover that the above projections are nondegenerate in the sense that the action of the identity operator

$$\tilde{\Pi}_0 \Pi_0 = \begin{pmatrix} \langle \psi_0, \phi_0 \rangle & 0 & 0 \\ 0 & \langle \psi_1, \phi_1 \rangle & 0 \\ 0 & 0 & \langle \psi_2, \phi_2 \rangle \end{pmatrix} \tag{4.75}$$

is not singular with its determinant $-\{T, M\}^3_{a,E}\{T, M, P\}_{a,E,c}$.

Since $\lambda = 0$ is an *isolated* eigenvalue of L_0, it follows from the standard theory of spectral perturbation that the above eigenprojections can be continued for $|\xi| \ll 1$ into analytically varying, rank 3 projections

$$\Pi_\xi : L^2_{\text{per}}([0,T]) \to \bigoplus_{j=1}^{3} \ker(L_\xi - \lambda_j(\xi)\mathbf{I}), \tag{4.76}$$

$$\tilde{\Pi}_\xi : L^2_{\text{per}}([0,T]) \to \bigoplus_{j=1}^{3} \ker(L_\xi^\dagger - \overline{\lambda_j(\xi)}\mathbf{I}) \tag{4.77}$$

whose ranges coincide with the total left and right eigenspaces associated with the eigenvalues $\lambda_j(\xi)$'s, $j = 1, 2, 3$, of L_ξ; see [53], for instance. In particular, we may find analytically varying bases $v_j(\xi)$'s and $\tilde{v}_j(\xi)$'s, $j = 0, 1, 2$, of the total right and left eigenspaces for the eigenvalues $\lambda_j(\xi)$'s, $j = 1, 2, 3$, in such a way that $v_j(0) = \phi_j$ and $\tilde{v}_j(0) = \psi_j$. Note in particular that we need not require that v_j's and $\tilde{v}_j$'s, $j = 0, 1, 2$, be *eigen-bases* for the total eigenspace, a degree of flexibility that is helpful in the course of explicit calculations. Using these ξ-dependent projections, for each

$|\xi| \ll 1$ fixed, we can project the infinite dimensional spectral problem (4.56) onto the three dimensional total eigenspace associated with $\lambda_j(\xi)$'s, $j = 1, 2, 3$, and, in particular, the action of the operators L_ξ on this subspace can be represented by the 3×3 matrix operator

$$M_\xi = \tilde{\Pi}_\xi L_\xi \Pi_\xi. \tag{4.78}$$

Specifically, $M_\xi = (\langle \tilde{v}_j(\xi), L_\xi v_k(\xi) \rangle_{L^2_{\text{per}}([0,T])})_{j,k=1,2,3}$ and similarly with the projection of the identity. The key observations are that M_ξ is a constant matrix for each ξ fixed and, moreover, that eigenvalues of the matrix M_ξ coincide *precisely* with eigenvalues $\lambda_j(\xi)$'s, $j = 1, 2, 3$, for the modulated operators L_ξ. In particular, for each $|\xi| \ll 1$ eigenvalues $\lambda_j(\xi)$'s, $j = 1, 2, 3$, are roots of the cubic characteristic equation

$$\det(M_\xi - \lambda \tilde{\Pi}_\xi \Pi_\xi) = 0. \tag{4.79}$$

Note that since $\tilde{\Pi}_0 \Pi_0$ is invertible, it follows by continuity that $\tilde{\Pi}_\xi \Pi_\xi$ is not singular for all $|\xi| \ll 1$. Therefore three eigenvalues bifurcating from the triple eigenvalue at the origin of L_0 for $|\xi| \ll 1$ can be studied by analyzing the eigenvalues of the 3×3 matrix M_ξ, which is seemingly a much easier task.

The eigenvalues of the matrix M_ξ may now be studied using standard techniques in matrix perturbation theory. Note that M_ξ depends analytically on ξ for $|\xi| \ll 1$, thanks to the analyticity of the associated eigenprojections Π_ξ and $\tilde{\Pi}_\xi$ and the analytic dependence of the operators L_ξ on ξ. Hence it can be expanded for $|\xi| \ll 1$ as

$$M_\xi = M_0 + (i\xi)M^{(1)} + \frac{1}{2}(i\xi)^2 M^{(2)} + \mathcal{O}(|\xi|^3) \tag{4.80}$$

for some 3×3 matrices $M^{(1)}$ and $M^{(2)}$ whose coefficients are independent of ξ. It is well known that the eigenvalues of M_ξ in general bifurcate merely continuously in the perturbation parameter ξ, but *not* in a C^1 manner. Rather, due to the Jordan block at $\xi = 0$, these eigenvalues are generically expected to admit a Puiseaux series expansion in fractional powers of ξ. In order to guarantee that the eigenvalues are at least C^1 in ξ near $\xi = 0$, it is sufficient to verify that the $(1, 2)$ and $(3, 2)$ entries on the matrix $M^{(1)}$ both vanish. A straightforward calculation, in the present setting, reveals that

$$(M^{(1)})_{1,2} = \langle \psi_0, L_1 \phi_1 \rangle_{L^2_{\text{per}}([0,T])} \quad \text{and} \quad (M^{(1)})_{3,2} = \langle \psi_2, L_1 \phi_1 \rangle_{L^2_{\text{per}}([0,T])}, \tag{4.81}$$

both of which vanish by virtue of Eq. (4.72). Consequently, the eigenvalues $\lambda_j(\xi)$'s, $j = 1, 2, 3$, are C^1 functions of ξ and they each admits an expansion of the form

$$\lambda_j(\xi) = i\xi\mu_j(\xi) = i\xi\mu_j(0) + o(\xi), \qquad |\xi| \ll 1 \tag{4.82}$$

for some C^1 function $\mu_j(\xi)$ determined by the roots of the characteristic equation

$$\det\left(\frac{1}{i\xi}M_\xi - \mu\tilde{\Pi}_\xi\Pi_\xi\right) = 0. \tag{4.83}$$

The modulational stability of the underlying wave may therefore be inferred from determining to leading order the values of $\mu_j(0) \in \mathbb{C}$ in Eq. (4.82). Note that if we further assume that $\mu_j(0)$'s are distinct (which generically holds in the present setting) then the eigenvalues $\lambda_j(\xi)$'s, $j = 1, 2, 3$, depend analytically on ξ for $|\xi| \ll 1$.

To determine the values $\mu_j(0)$ in Eq. (4.82), we appeal to Dunford integral calculus to find that the bases elements $v_j(\xi)$'s and $\tilde{v}_j(\xi)$'s, $j = 0, 1, 2$, have the same regularity in ξ as the eigenvalues μ_j's, $j = 1, 2, 3$. Hence they may be expanded near $\xi = 0$ as

$$v_j(\xi) = \phi_j + (i\xi)v_j^{(1)} + o(\xi), \quad \tilde{v}_j(\xi) = \psi_j + (i\xi)\tilde{v}_j^{(1)} + o(\xi) \tag{4.84}$$

for some functions $v_j^{(1)}$ and $\tilde{v}_j^{(1)}$ independent of ξ. We wish to use these expansions to compute asymptotic expansions of the projections Π_ξ and $\tilde{\Pi}_\xi$ valid near $\xi = 0$. Note however that the non-trivial Jordan structure of M_0 indicates an inherent degeneracy in the limit $\xi \to 0$. Indeed, while the kernel of M_0 is two dimensional, there are three eigenvalues of M_ξ defined near the origin for $\xi = 0$. Moreover, the three eigenvectors of M_ξ tend to *the same limit* as $\xi \to 0$. (This is a consequence of the fact that all three of the eigenfunctions for L_ξ associated with the eigenvalues $\lambda_j(\xi)$, $j = 1, 2, 3$ tend to ϕ_1 as $\xi \to 0$, a fact seen both analytically and numerically.) An efficient way of unfolding this degeneracy is to re-scale the matrices $(i\xi)^{-1}M_\xi$ and $\tilde{\Pi}_\xi\Pi_\xi$ as

$$\hat{M}_\xi := \frac{1}{i\xi}\Sigma(\xi)^{-1}M_\xi\Sigma(\xi) \quad \text{and} \quad \hat{I}_\xi := \Sigma(\xi)^{-1}\tilde{\Pi}_\xi\Pi_\xi\Sigma(\xi), \tag{4.85}$$

where

$$\Sigma(\xi) = \begin{pmatrix} i\xi & 0 & 0 \\ 0 & 1 & 0 \\ 0 & 0 & i\xi \end{pmatrix}. \tag{4.86}$$

It then follows from a straightforward calculation that for $|\xi| \ll 1$

$$\hat{M}_\xi = \begin{pmatrix} \langle\psi_0, L_1\phi_0\rangle & m_{1,2} & \langle\psi_0, L_1\phi_2\rangle + \langle\tilde{v}_0^{(1)}, L_0\phi_2\rangle \\ 0 & \langle\psi_1, L_1\phi_1 + L_0v_1^{(1)}\rangle & \langle\psi_1, L_0\phi_2\rangle \\ \langle\psi_2, L_1\phi_0\rangle & m_{3,2} & \langle\psi_2, L_1\phi_2\rangle + \langle\tilde{v}_2^{(1)}, L_0\phi_2\rangle \end{pmatrix} + o(1), \tag{4.87}$$

where

$$m_{j,2} = \langle \psi_j, L_2\phi_1 + L_1 v_1^{(1)} \rangle + \langle \tilde{v}_j^{(1)}, L_1\phi_1 + L_0 v_1^{(1)} \rangle, \quad j = 1, 3, \tag{4.88}$$

and, similarly,

$$\hat{I}_\xi = \begin{pmatrix} \langle \psi_0, \phi_0 \rangle & \langle \psi_0, v_1^{(1)} \rangle + \langle \tilde{v}_0^{(1)}, \phi_1 \rangle & 0 \\ 0 & \langle \psi_1, \phi_1 \rangle & 0 \\ 0 & \langle \psi_2, v_1^{(1)} \rangle + \langle \tilde{v}_2^{(1)}, \phi_1 \rangle & \langle \psi_2, \phi_2 \rangle \end{pmatrix} + o(1). \tag{4.89}$$

Therefore, it follows that $\mu_j(0)$ are determined as the roots of the (cubic) *effective dispersion relation*

$$\mathcal{D}(\mu) := \det(\hat{M}_0 - \mu \hat{I}_0) = 0 \tag{4.90}$$

Theorem 4.1 ([47]) *Let $u = u(\cdot; a_0, E_0, c_0)$ be a $T = T(a_0, E_0, c_0)$-periodic traveling wave of Eq. (4.1). Suppose that T_E, $\{T, M\}_{a,E}$ and $\{T, M, P\}_{a,E,c}$ are not zero at a_0, E_0 and c_0. Then for $|\xi| \ll 1$ the triple eigenvalue at the origin of L_0 bifurcates into three eigenvalues $\lambda_j(\xi)$, $j = 1, 2, 3$, that are C^1 in ξ near $\xi = 0$ and satisfy*

$$\lambda_j(\xi) = i\mu_j \xi + o(\xi), \quad j = 1, 2, 3, \tag{4.91}$$

where $\mu_j \in \mathbb{C}$ are eigenvalues of the effective dispersion matrix

$$\mathbf{D}(a, E, c) := (\hat{I}_0)^{-1} \hat{M}_0)(a, E, c) \tag{4.92}$$

at $(a, E, c) = (a_0, E_0, c_0)$. In particular, a necessary condition for u to be modulationally stable is that the dispersion matrix be weakly hyperbolic, i.e. its eigenvalues are all real.

To utilize Theorem 4.1 in practice, one must determine the first-order correctors $\tilde{v}_0^{(1)}$, $\tilde{v}_2^{(1)}$ and $v_1^{(1)}$ in Eq. (4.84). Note however that in the *small amplitude limit*, these correctors do not contribute to leading order and hence are not necessary in computing the roots of $\mathcal{D}$; see Sect. 4.5.4 below. Outside of this asymptotic regime, of course, these correctors play an important role. First, notice that the functions $v_j(\xi)$'s and $\tilde{v}_j(\xi)$'s, $j = 0, 1, 2$, satisfy the relations

$$\Pi_\xi(L_\xi v_j(\xi)) = L_\xi v_j(\xi) \quad \text{and} \quad \tilde{\Pi}_\xi(L_\xi^\dagger \tilde{v}_j(\xi)) = L_\xi^\dagger \tilde{v}_j(\xi), \tag{4.93}$$

respectively, for all $|\xi| \ll 1$. Moreover, we expand in ξ to find that

$$L_0 v_j^{(1)} + (L_1 + \Pi_1 L_0)\phi_j \in \text{range}(\Pi(0)) \tag{4.94}$$

and

$$L_0^\dagger \tilde{v}_j^{(1)} + (L_1^\dagger + \tilde{\Pi}_1 L_0^\dagger)\psi_j \in \text{range}(\tilde{\Pi}(0)). \tag{4.95}$$

In particular, since $L_0\phi_j = 0$ we may choose $v_1^{(1)}$ so that $L_0 v_1^{(1)} = -L_1\phi_1$. An explicit formula for $v_1^{(1)}$ can then be found by noting that

$$L_1 u_x = [L_0, x]u_x = L_0(xu_x), \tag{4.96}$$

by definition, and that $T_E x u_x + T u_E$ is T-periodic. Since $\ker(L_0^\dagger) = \text{span}\{\psi_0, \psi_2\}$, similarly, we may choose $\tilde{v}_0^{(1)}$ and $\tilde{v}_2^{(1)}$ such that $L_0^\dagger \tilde{v}_j^{(1)} = -L_1^\dagger \psi_j$ for $j = 0, 2$. Unlike $v_1^{(1)}$, explicit forms of $\tilde{v}_j^{(1)}$, $j = 0, 2$, are not needed; their defining relations are sufficient for calculation purposes. With these choices one can, through tedious but straightforward calculations, compute the effective dispersion relation *explicitly* as

$$\mathcal{D}(\mu) = C\Big(-\mu^3 + \frac{\mu}{2}\left(\{T, P\}_{E,c} + 2\{M, P\}_{a,E}\right) - \frac{1}{2}\{T, M, P\}_{a,E,c}\Big) \tag{4.97}$$

for some non-zero constant $C = C(a, E, c)$. The nature of the roots of $\mathcal{D}$ follows from the sign of its discriminant, given as

$$\Delta_{MI} = \frac{1}{2}\left(\{T, P\}_{E,c} + 2\{M, P\}_{a,E}\right)^3 - \frac{27}{4}\{T, M, P\}_{a,E,c}^2. \tag{4.98}$$

In particular, the polynomial $\mathcal{D}$ has three distinct real roots provided that $\Delta_{MI} > 0$, while it has one real and two (non-real) complex conjugate roots if $\Delta_{MI} < 0$. Moreover it follows that if $\Delta_{MI} < 0$ then u is modulationally unstable with one branch of spectrum bifurcating from the origin along the imaginary axis and two branches bifurcating in complex directions. It follows that a necessary condition for modulational stability is $\Delta_{MI} \geq 0$. Furthermore, when $\Delta_{MI} > 0$ a simple symmetry argument implies that the three spectral branches bifurcating from the origin are confined (locally) to the imaginary axis, corresponding to a triple covering, implying modulational stability.

Corollary 4.1 ([13]) *Under the hypotheses of Theorem 4.1, a necessary condition for the modulational stability of the underlying wave u is $\Delta_{MI} \geq 0$. Furthermore, a sufficient condition for u to be modulationally stable is that $\Delta_{MI} > 0$.*

4.4.3 Connection to Whitham Modulation Theory

In Sect. 4.3 we employed a formal asymptotics method to determine a dispersion relation $\hat{\mathcal{D}}_W$ in Eq. (4.48) with the property that the linearized Whitham system given by Eq. (4.45) has eigenvalues of the form $\lambda = ik\mu$ whenever $\mu \in \mathbb{C}$ satisfies

$\hat{\mathcal{D}}_W(z) = 0$. In the previous subsection, on the other hand, we demonstrated that the eigenvalues for the Bloch operators L_ξ expand as $\lambda = i\mu\xi + o(\xi)$, where $\mu \in \mathbb{C}$ is one of the three (distinct by assumption) eigenvalues of the effective dispersion matrix $\mathbf{D}(a, E, c)$ in (4.92). These two approaches are in fact equivalent for generalized KdV equations.

Theorem 4.2 ([46, 47]) *Under the hypotheses of Theorem 4.1, the eigenvalues of the effective dispersion matrix in Eq.* (4.92) *agree with the roots of the reduced Whitham dispersion relation* $\hat{D}_W(z) = 0$ *in Eq.* (4.48)*. In particular, a necessary condition for the modulational stability of the underlying periodic wave is that the linearized Whitham system given by Eq.* (4.45) *be weakly hyperbolic, or equivalently, that* $\hat{\mathcal{D}}_W(z) = 0$ *has three real roots. Furthermore, a sufficient condition for modulational stability is for Eq.* (4.45) *to be strictly hyperbolic, or equivalently, for* $\hat{\mathcal{D}}_W(z) = 0$ *to have three distinct real roots.*

Theorem 4.2 rigorously justifies predictions from Whitham's formal modulation theory in the context of generalized KdV equations. It implies that a sufficient condition for the modulational instability of the underlying wave is the *ellipticity* of the associated linearized Whitham system. The proof follows by a long and tedious calculation demonstrating that there exists a constant $C \neq 0$ such that

$$\det(\mathbf{D}(a, E, c) - \mu\mathbf{I}) = C\hat{\mathcal{D}}_W(\mu) \tag{4.99}$$

for all $\mu \in \mathbb{C}$: see [46, 47] for details. We merely pause to note that, in a sense, Theorem 4.2 implies that the processes of averaging and linearizing commute: the linearized Whitham system in Sect. 4.3 is obtained from an averaging process (the Fredholm alternative) and then linearization, while the rigorous theory in the previous subsection is obtained from linearizing the governing equation and then applying the Fredholm alternative (averaging). This observation suggests that the above program may readily be extended to equations outside of KdV type.

A class of equations for which the above program has been particularly successful is in the dissipative PDEs of the form

$$u_t + f(u)_x + g(u) = (B(u)u_x)_x, \quad x \in \mathbb{R}, \quad u \in \mathbb{R}^n. \tag{4.100}$$

In the case of $f = 0$, it corresponds to systems of reaction diffusion equations, and in the case of $g = 0$, systems of conservation laws. Not only Whitham's modulation theory has been rigorously validated in Eq. (4.100) at the level of spectral stability, but it has also provided key insights into the *nonlinear dynamics* of modulated waves, as well as the stability and dynamics to *nonlocalized perturbations*, consisting of a localized part plus an asymptotic phase shift at the spatial infinities; see [3, 48–51], for instance. These additional insights come from continuing the asymptotic expansion in Sect. 4.3 to the next order in ε, obtaining a diffusive correction to the Whitham modulation system. The details of this program are

beyond the scope of the current manuscript, and the reader is referred to the above references for details.

4.4.4 Evaluation of Δ_{MI}

In Sect. 4.4.2, we derived a modulational instability index Δ_{MI}, the sign of which determines the modulational stability and instability of a periodic traveling wave of Eq. (4.1). To compute Δ_{MI}, in practice, we must compute derivatives of T, M and P with respect to the traveling wave parameters a, E and c, a task that in general is formidable. When f is a polynomial nonlinearity, nevertheless, these derivatives may be computed *explicitly* in terms of the underlying wave. Indeed, note that if f is a polynomial then T, M and P may be expressed in terms of the moments

$$\zeta_k := \int_0^T u^k(x)\,dx = \oint_\gamma \frac{u^k}{\sqrt{E - V(u;a,c)}}\,du, \tag{4.101}$$

where $E - V(u;a,c)$ is a polynomial of one degree higher than f. Indeed, $T = \zeta_0$, $M = \zeta_1$ and $P = \zeta_2$. Moreover, derivatives of T, M and P may be expressed in terms of the moments

$$I_k := \oint_\gamma \frac{u^k}{\sqrt{E - V(u;a,c)^3}}\,du. \tag{4.102}$$

For example, $T_E = I_0$ and $P_c = \frac{1}{2}I_2$. The amazing fact is that if f is a polynomial of degree n then I_k, $k = 0, 1, \ldots, 2n-2$, can be expressed as linear combinations of the $n-1$ moments ζ_k's, $k = 0, 1, \ldots, n-2$, a fact known as the Picard-Fuchs relation. Therefore the modulational instability index Δ_{MI} can be *explicitly computed* in terms of moments of the underlying wave u; see [15] for more details.

To illustrate how this process works, suppose that f is a polynomial of degree $n-1$ and set $P(u) = E - V(u;a,c)$. We may then write $P(u) = a_0 + a_1 u + a_2 u^2 + \cdots + a_n u^n$ for some constants a_j's, $j = 0, 1, \ldots, n$. Defining the moments ζ_k and I_k by Eqs. (4.101) and (4.102), it follows that

$$\frac{d\zeta_k}{da_j} = \frac{d\zeta_j}{da_k} = -\frac{1}{2}I_{k+j}, \quad j,k = 0, 1, \ldots, n. \tag{4.103}$$

Observing that

$$\zeta_k = \oint_\gamma \frac{u^k P(u)}{P(u)^{3/2}}\,du = \sum_{j=0}^{n} a_j I_{j+k}, \quad k = 0, 1, 2, \ldots, n-1 \tag{4.104}$$

and that[5]

$$2k\zeta_{k-1} = 2k \oint_\gamma \frac{u^{k-1}}{\sqrt{P(u)}}\, du = \oint_\gamma \frac{u^k P'(u)}{P(u)^{3/2}}\, du$$
$$= \sum_{j=0}^{n} j a_j I_{j+k-1}, \quad k = 0, \ldots, n-1, \tag{4.105}$$

we arrive at the linear system of $2n-1$ equations in the unknowns I_k's, $k = 0, 1, \ldots, 2n-2$:

$$\begin{pmatrix} a_0 & a_1 & \cdots & a_n & 0 & 0 & \cdots \\ 0 & a_0 & a_1 & \cdots & a_n & 0 & \cdots \\ \vdots & \ddots & \ddots & \ddots & \ddots & \ddots & \ddots \\ 0 & \cdots & 0 & a_0 & a_1 & \cdots & a_n \\ a_1 & 2a_2 & \cdots & n a_n & 0 & 0 & \cdots \\ 0 & a_1 & 2a_2 & \cdots & n a_n & 0 & \cdots \\ \vdots & \ddots & \ddots & \ddots & \ddots & \ddots & \ddots \\ 0 & \cdots & 0 & a_1 & 2a_2 & \cdots & n a_n \end{pmatrix} \begin{pmatrix} I_0 \\ I_1 \\ I_2 \\ I_3 \\ \vdots \\ \vdots \\ I_{2n-3} \\ I_{2n-2} \end{pmatrix} = \begin{pmatrix} \zeta_0 \\ \zeta_1 \\ \vdots \\ \zeta_{n-2} \\ 0 \\ 2\zeta_0 \\ \vdots \\ 2(n-1)\zeta_{n-2} \end{pmatrix}, \tag{4.106}$$

which we refer to as the Picard-Fuchs system. The matrix that arises in Eq. (4.106) may be recognized as the Sylvester matrix of the polynomials $P(u)$ and $P'(u)$. A standard result in commutative algebra states that the Sylvester matrix of two polynomials is not singular if and only if they have no common roots. The matrix in Eq. (4.106) is therefore invertible, provided that the polynomial P has only simple roots, in which case the moments I_k's, $k = 0, 1, \ldots, 2n-2$, can explicitly be expressed as a linear combination of ζ_k's, $k = 0, 1, \ldots, n-2$, with coefficients explicitly determined by the coefficients of P.

For a given polynomial P with simple roots, Eq. (4.106) can be easily solved with the aid of a computer algebra system. In the following section, we discuss applications of the above procedure in the case when $P(u) = E - V(u; a, c)$ and V is the effective potential associated with Eq. (4.1) for various nonlinearities f.

4.5 Applications

In the previous section, we derived a modulational instability index Δ_{MI}, the sign of which determines the modulational stability and instability of a periodic traveling wave of Eq. (4.1). Here we discuss a few examples, where one can use

[5] Here, we take the convention that the left hand side is zero when $k = 0$.

the Picard-Fuchs system [see Eq. (4.106)] to explicitly evaluate Δ_{MI} in terms of the underlying wave. We note that these examples are *not exhaustive* but are chosen for illustrative purposes.

4.5.1 The KdV Equation

Consider the KdV equation

$$u_t = u_{xxx} + (u^2)_x, \tag{4.107}$$

for which the effective potential [see Eq. (4.6)] is

$$V(u; a, c) = \frac{1}{3}u^3 + \frac{1}{2}cu^2 - au. \tag{4.108}$$

Recall from Sect. 4.2 that a periodic traveling wave $u(\cdot\,; a, E, c)$ of Eq. (4.107) exists, provided that the discriminant

$$\operatorname{disc}(E - V(\cdot\,; a, c)) = \frac{1}{12}(16a^3 + 3a^2c^2 - 36Eac - 6Ec^3 - 36E^2) \tag{4.109}$$

is positive so that $E - V(u; a, c)$ has three real roots in u. Recall moreover that the only periodic traveling waves along the surface where $\operatorname{disc}(E - V(\cdot\,; a, c)) = 0$ are constants. It is well known that Eq. (5.2) is completely integrable, although we do not make use of the fact. Let

$$\zeta_k := \oint_\gamma \frac{u^k\, du}{\sqrt{2(E - V(u; a, c)}} \quad \text{and} \quad I_k = \oint_\gamma \frac{u^k\, du}{\sqrt{2(E - V(u; a, c))}^3}, \tag{4.110}$$

$k = 0, 1, 2$, and note that $(T, M, P) = (\zeta_0, \zeta_1, \zeta_2)$ and

$$\nabla_{E,a,c}\zeta_k = \Big\langle -I_k, -I_{k+1}, -\frac{1}{2}I_{k+2}\Big\rangle. \tag{4.111}$$

The Picard-Fuchs system given by Eq. (4.106) then becomes

$$\begin{pmatrix} E & a & c/2 & 1/3 & 0 \\ 0 & E & a & c/2 & 1/3 \\ a & c & -1 & 0 & 0 \\ 0 & a & c & -1 & 0 \\ 0 & 0 & a & c & -1 \end{pmatrix} \begin{pmatrix} I_0 \\ I_1 \\ I_2 \\ I_3 \\ I_4 \end{pmatrix} = \begin{pmatrix} T \\ M \\ 0 \\ 2T \\ 4M \end{pmatrix} \tag{4.112}$$

which, after some elementary matrix algebra, implies that

$$\begin{aligned} T_E &= \frac{1}{12}\frac{(4a+c^2)M+(6E+ac)T}{\operatorname{disc}(E-V(\cdot;a,c))},\\ \{T,M\}_{a,E} &= -\frac{1}{12}\frac{T^2V'(M/T;a,c)}{\operatorname{disc}(E-V(\cdot;a,c))},\\ \{T,M,P\}_{a,E,c} &= \frac{1}{12}\frac{T^3(E-V(M/T;a,c))}{\operatorname{disc}(E-V(\cdot;a,c))} \end{aligned} \tag{4.113}$$

and

$$\Delta_{MI} = \frac{(\alpha_{3,0}T^3+\alpha_{2,1}T^2M+\alpha_{1,2}TM^2+\alpha_{0,3}M^3)^2}{2^{11}3^7\operatorname{disc}(E-V(\cdot;a,c))^3}; \tag{4.114}$$

see [15] for details. Here the coefficients α_{ij} are given by

$$\begin{aligned} \alpha_{3,0} &= 36E+18aEc-8a^3, \quad & \alpha_{2,1} &= 18Ec^2-6a^2c+36aE,\\ \alpha_{2,1} &= -18cE+24a^2+3ac^2, \quad & \alpha_{0,3} &= c^3+6ac+12E. \end{aligned} \tag{4.115}$$

The monotonicity of the period, i.e. $T_E > 0$, holds by a result of Schaaf (see [65], for instance) and $\{T,M,P\}_{a,E,c} > 0$ clearly holds. Moreover, $\{T,M\}_{a,E}$ is positive thanks to Jensen's inequality and the fact that

$$\oint \frac{V'(u;a,c)}{\sqrt{E-V(u;a,c)}}\,du = 0. \tag{4.116}$$

The hypotheses of Theorem 4.1 are thus satisfied, and Corollary 4.1 implies that the sign of Δ_{MI} in Eq. (4.114) determines the modulational stability of a periodic traveling wave of Eq. (5.2). Since the numerator of Δ_{MI} is seen numerically not to vanish, it follows that $\Delta_{MI} > 0$. Therefore *all periodic traveling waves of the KdV equation are modulationally stable*; see [15] for details.

4.5.2 The Modified KdV Equation

To proceed, consider the focusing and defocusing modified KdV equations

$$u_t = u_{xxx} \pm (u^3)_x. \tag{4.117}$$

Like the KdV equation, Eq. (4.117) is completely integrable and hence its spectrum can, in principle, be explicitly computed with the aid of algebro-geometric techniques. Of course, our methods are independent of integrability.

As discussed in Sect. 4.2, the existence of periodic traveling waves of Eq. (4.117) differs between the focusing and defocusing cases. In each case, however, existence may be inferred from properties of the associated effective potential

$$V_{\pm}(u;a,c) = \mp\frac{1}{4}u^4 + \frac{1}{2}cu^2 - au. \tag{4.118}$$

Indeed, in the focusing case, periodic traveling waves exist provided that the quartic polynomial $E - V_+(\cdot\,;a,c)$ has at least two real roots and that its discriminant is not zero. In the defocusing case, periodic traveling waves only exist when the discriminant of $E - V_-(\cdot\,;a,c)$ is positive, indicating that the polynomial has four distinct real roots. See Fig. 4.1 in Sect. 4.2.

The Picard-Fuchs system for Eq. (4.117) reads

$$\begin{pmatrix} E & a & c/2 & 0 & \mp 1/4 & 0 & 0 \\ 0 & E & a & c/2 & 0 & \mp 1/4 & 0 \\ 0 & 0 & E & a & c/2 & 0 & \mp 1/4 \\ a & c & 0 & \mp 1 & 0 & 0 & 0 \\ 0 & a & c & 0 & \mp 1 & 0 & 0 \\ 0 & 0 & a & c & 0 & \mp 1 & 0 \\ 0 & 0 & 0 & a & c & 0 & \mp 1 \end{pmatrix} \begin{pmatrix} I_0 \\ I_1 \\ I_2 \\ I_3 \\ I_4 \\ I_5 \\ I_6 \end{pmatrix} = \begin{pmatrix} T \\ M \\ P \\ 0 \\ 2T \\ 4M \\ 6P \end{pmatrix}, \tag{4.119}$$

which can be readily solved to provide explicit formulae for T_E, $\{T,M\}_{a,E}$ and $\{T,M,P\}_{a,E,c}$ in terms of T, P and the parameters a, E, c. Incidentally one can easily explain by complex analysis why M does *not* enter the formulae for the gradients of T, M, P with respect to a, E, c; see [15] for details. Furthermore, we find

$$\Delta_{MI} = \frac{\Gamma_{mKdV}(T,P,a,E,c)^2}{\mathrm{disc}(E - V_{\pm}(\cdot\,;a,c))^3}, \tag{4.120}$$

where Γ_{mKdV} is a homogeneous polynomial of degree 6 in T and P with coefficients depending on a, E and c. The sign of this clearly agrees with that of the discriminant of the quartic polynomial $E - V_{\pm}(\cdot\,;a,c)$, which in turn is positive if it has four distinct real roots and negative if it has only two distinct real roots and two distinct complex conjugate roots. This leads us to the surprisingly simple characterization of the modulational instability for the modified KdV equation.

Theorem 4.3 ([15]) *Periodic traveling waves of the modified KdV equation given by Eq.* (4.117) *are modulationally unstable for a given set of parameters a, E, c if the polynomial*

$$\mathcal{P}(u;a,E,c) = E + au - \frac{1}{2}cu^2 \pm \frac{1}{4}u^4 \tag{4.121}$$

has only two distinct real roots and two distinct complex conjugate roots, and it is modulationally stable if it has four distinct real roots.

The structure of the roots of $\mathcal{P}(\cdot\,; a, E, c)$, of course, depends greatly on whether the nonlinearity is focusing or defocusing. In the focusing case, Theorem 4.3 implies that if the parameter values give rise to only one periodic solution then this solution is modulationally unstable. Conversely, if the parameters give rise to two periodic solutions, then both are modulationally stable. While Theorem 4.3 applies to *all* periodic traveling wave solutions of the mKdV (focusing or defocusing), it is worth while to state the result for the explicit solutions described in Sect. 4.2.1.

Corollary 4.2 *For the focusing modified KdV equation, all dnoidal wave solutions constructed in Sect. 4.2.1 are modulationally stable and all cnoidal waves are modulationally unstable.*

In the defocusing case, in contrast, $\mathcal{P}$ *must have four distinct zeros* for periodic traveling waves to exist. This simple observation leads to the following result.

Corollary 4.3 *All periodic traveling waves of the defocusing modified KdV equation are modulationally stable.*

Corollary 4.3 implies the snoidal wave solutions described in Sect. 4.2.1 are modulationally stable.

4.5.3 The Schamel Equation

Lastly, we consider the Schamel equation [after taking $u \mapsto -u$ in Eq. (4.107)]

$$u_t + u_{xxx} + \frac{5}{2}(|u|^{3/2})_x = 0, \tag{4.122}$$

where u must be taken to be positive. Periodic traveling waves of Eq. (4.122) are given implicitly as

$$\oint \frac{du}{\sqrt{2\left(E + au + \frac{1}{2}cu^2 - u^{5/2}\right)}} = x - ct. \tag{4.123}$$

After the change of variables $u = v^2$, alternatively, the traveling wave solution of Eq. (4.122) may be found from

$$\frac{v_x^2}{2} = E + av^2 + \frac{1}{2}cv^4 - v^5. \tag{4.124}$$

Therefore the parameter regime physically admissible corresponds to the set of all $(a, E, c) \in \mathbb{R}^3$ for which there exists a bounded interval in $(0, \infty)$ such that the

quintic polynomial $E + av^2 + \frac{c}{2}v^4 - v^5$ is non-negative, corresponding to a non-negative periodic solution.

The Picard-Fuchs system for Eq. (4.122) is the set of nine equations

$$\begin{pmatrix} E & 0 & a & 0 & c/2 & -1/5 & 0 & 0 & 0 \\ 0 & E & 0 & a & 0 & c/2 & -1/5 & 0 & 0 \\ 0 & 0 & E & 0 & a & 0 & c/2 & -1/5 & 0 \\ 0 & 0 & 0 & E & 0 & a & 0 & c/2 & -1/5 \\ 0 & 2a & 0 & 2c & -1 & 0 & 0 & 0 & 0 \\ 0 & 0 & 2a & 0 & 2c & -1 & 0 & 0 & 0 \\ 0 & 0 & 0 & 2a & 0 & 2c & -1 & 0 & 0 \\ 0 & 0 & 0 & 0 & 2a & 0 & 2c & -1 & 0 \\ 0 & 0 & 0 & 0 & 0 & 2a & 0 & 2c & -1 \end{pmatrix} \begin{pmatrix} I_0 \\ I_2 \\ I_3 \\ I_4 \\ I_5 \\ I_6 \\ I_7 \\ I_8 \\ I_9 \end{pmatrix} = \begin{pmatrix} \zeta_0 \\ \mu_1 \\ \zeta_2 \\ \zeta_3 \\ 0 \\ 2\zeta_0 \\ 4\zeta_1 \\ 6\zeta_2 \\ 8\zeta_3 \end{pmatrix}, \tag{4.125}$$

where

$$\zeta_k := \oint \frac{2v^k\, dv}{\sqrt{2\left(E + av^2 + \frac{1}{2}cv^4 - v^5\right)}}, \quad k = 0, 1, 2, 3, \tag{4.126}$$

and I_k are defined similarly; see [15], for instance. In particular, notice that $T = \zeta_1$, $M = \zeta_3$ and $P = \zeta_5$. While the expressions are too long to list here, they are easily handled with the aid of a computer algebra system, in which case one finds that $\Delta_{MI} > 0$ in the entire domain of existence. In conclusion, *all periodic traveling waves of Eq.* (4.122) *are modulationally stable*; see [15] for details.

4.5.4 Extensions to Equations with Nonlocal Dispersion

The analysis in the previous sections readily extends to equations allowing for *nonlocal* dispersion. We will illustrate this by discussing equations of KdV type

$$u_t = \mathcal{M}u_x + f(u)_x, \tag{4.127}$$

where $\mathcal{M}$ is defined via the Fourier series as

$$u(x) = \sum_{k\in\mathbb{Z}} \hat{u}(k)e^{ikx} \quad \Rightarrow \quad (\mathcal{M}u)(x) = \sum_{k\in\mathbb{Z}} m(k)\hat{u}(k)e^{ikx}, \tag{4.128}$$

characterizing dispersion in the linear limit. Throughout we assume that the symbol m is even and real valued.

In the case of $m(k) = -k^2$, notably, Eq. (4.127) recovers the generalized KdV equation given by Eq. (4.1). Notice however that Eq. (4.127) is nonlocal unless the

dispersion symbol m is a polynomial of ik. Examples include the KdV equation with fractional dispersion

$$u_t = \Lambda^\alpha u_x + f(u)_x, \quad -1 \le \alpha \le 2, \tag{4.129}$$

where $\Lambda = \sqrt{-\partial_x^2}$ is defined via its Fourier multiplier $m(k) = |k|$. In the case of $\alpha = 2$, it recovers the generalized KdV equation, and in the case of $\alpha = 1$ and $f(u) = \frac{1}{2}u^2$, it corresponds to the Benjamin-Ono equation, which was proposed in [4, 61] as a model of the unidirectional propagation of internal waves of small amplitudes in deep water. Recall that the Fourier multiplier of the Hilbert transform $\mathcal{H}$ is $-i\mathrm{sgn}(k)$, and one may write the Benjamin-Ono equation alternatively as

$$u_t = \mathcal{H}\partial_x^2 u + uu_x. \tag{4.130}$$

Like the KdV and modified KdV equations, the Benjamin-Ono equation is completely integrable, although our methods do not rely on this. In the case of $\alpha = -1/2$ and $f(u) = \frac{1}{2}u^2$, moreover, Eq. (4.127) was argued in [40] to have relevances to water waves in two dimensions and in the infinite depths. Incidentally fractional powers of the Laplacian occur in many applications, such as dislocation dynamics in crystals (see [18], for instance) and financial mathematics (see [22], for instance). Notice that the dispersion symbol of Eq. (4.129) is *homogeneous* in the sense that $m(\lambda k) = \lambda^\alpha m(k)$ for all $k \in \mathbb{R}$ and $\lambda > 0$, which makes the analysis for waves of all amplitudes tractable by the methods described in the previous sections.

But many applications require non-homogeneous dispersion symbols. Examples include the intermediate long-wave (ILW) equation

$$u_t + u_x + (1/H)u_x - \mathcal{N}_H u_x + \left(u^2\right)_x = 0, \tag{4.131}$$

which describes the interface between density stratified fluids, both with finite depth; see [52], for instance. Here $H > 0$ is a parameter and $\mathcal{N}_H$ is defined via its symbol $m(k; H) = k\coth(kH)$. The ILW equation is of the form given by Eq. (4.127), where $\mathcal{M} = \mathcal{N}_H - 1 - 1/H$.

Another example with a non-homogeneous dispersion symbol corresponds to $m(k) = \sqrt{\frac{\tanh(k)}{k}}$ and $f(u) = \frac{1}{2}u^2$, which was put forward in [74, p. 477] to model the unidirectional propagation of surface water waves with small amplitudes, but not necessarily long wavelengths, in a channel. Note that $m(k)$ is the phase speed of plane waves with the wave number k near the quintessential state of water. In fact, the Whitham equation combines the dispersion relation of surface water waves and the nonlinearity of shallow water equations. In the long wavelength regime, where $|k| \ll 1$,

$$\sqrt{\frac{\tanh(k)}{k}} = 1 - \frac{1}{6}k^2 + \mathcal{O}(|k|^4). \tag{4.132}$$

Therefore we may regard the KdV equation given by Eq. (4.107) (after normalization of the parameters) as to approximate up to "second" order the dispersion relation of the Whitham equation, and hence the water wave problem, in the long wavelength regime. Unlike the KdV equation, which well explains long wave phenomena such as solitary waves but loses relevances to short and intermediately long waves in water, the Whitham equation may capture short wave phenomena. As a matter of fact, Whitham advocated that it could be used to explain breaking and peaking, both of which are unobserved in the KdV approximation. In light of the famous Benjamin-Feir instability of Stokes waves [7], in particular, it is natural to expect that small-amplitude periodic traveling waves of the Whitham equation be modulationally unstable if their wavelength is sufficiently short.

A traveling wave solution of Eq. (4.127) takes the form $u(x,t) = u(x-ct)$, where $c \in \mathbb{R}$ and u satisfies by quadrature that

$$-\mathcal{M}u + cu + f(u) = a \tag{4.133}$$

for some constant $a \in \mathbb{R}$. Unlike the generalized KdV equation given by Eq. (4.1), the existence of periodic solutions of Eq. (4.133) is not trivial. For a broad range of dispersion symbols and nonlinearities, nevertheless, a plethora of periodic traveling waves of Eq. (4.127) may be attained from variational arguments, e.g. the mountain pass theorem applied to a suitable functional whose critical points satisfy Eq. (4.133). In examples considered below, a smooth four-parameter (including translations) family of periodic traveling waves will exist, in agreement with existence theories for (local) equations of KdV type in the previous sections.

Once existence and an appropriate parametrization of a periodic solution u, say, of Eq. (4.133) are established, its modulational stability may be studied by considering the $L^2(\mathbb{R})$-spectrum of the linearized operator

$$L := \partial_x(-\mathcal{M} + c - f'(u)) \tag{4.134}$$

near the origin. Since u is T-periodic, as in the case of (local) generalized KdV equations, the $L^2(\mathbb{R})$-spectrum of L is readily described by Floquet-Bloch theory:

$$\operatorname{spec}_{L^2(\mathbb{R})}(L) = \bigcup_{\xi \in [-\pi/T, \pi/T)} \operatorname{spec}_{L^2_{\mathrm{per}}([0,T])}(L_\xi), \tag{4.135}$$

where the Bloch operators $L_\xi := e^{-i\xi x} L e^{i\xi x}$ act as usual on $L^2_{\mathrm{per}}([0,T])$. The modulational stability theory developed in Sect. 4.4 can thus be applied directly to this case, *provided* that the Jordan structure of the generalized kernel of L is analogous to that described in Lemma 4.1.

The Benjamin-Ono Equation

Consider the Benjamin-Ono equation [after the change of variables $u \mapsto -u$ in Eq. (4.130)]

$$u_t - \Lambda u_x + (u^2)_x = 0. \tag{4.136}$$

Benjamin in [4] exploited the Poisson summation formula and found that for each $k > 0$ there exists a two-parameter (up to translations) family of $2\pi/k$-periodic traveling waves of (4.136) of the form

$$u(x; a, k, c) = \frac{\dfrac{k^2}{\sqrt{c^2 - 4a - k^2}}}{\sqrt{\dfrac{c^2 - 4a}{c^2 - 4a - k^2} - \cos(kx)}} - \frac{1}{2}(\sqrt{c^2 - 4a} + c), \tag{4.137}$$

where a and c are arbitrary constants constrained by the conditions

$$c < 0 \quad \text{and} \quad k^2 < c^2 - 4a. \tag{4.138}$$

Therefore Eq. (4.136) admits a three-parameter family (up to translations) of periodic traveling waves and they can be parameterized by the period and the parameters a and c. Here the period, or equivalently k, is a parameter that is *independent of a and c* so that, in particular, derivatives of the solution with respect to a and c are *automatically T-periodic in x*. Since (4.136) obeys Galilean invariance under

$$u(x; a - c\lambda + s^2, k, c - 2s) = u(x; a, k, c) + \lambda \tag{4.139}$$

for all $\lambda \in \mathbb{R}$, upon an appropriate choice of λ, one may assume that $a = 0$.

To determine the modulational instability of a solution in Eq. (4.137), we turn our attention to the $L^2_{\text{per}}([0, T])$-spectrum near the origin of the Bloch operators

$$L_\xi := e^{-i\xi x} \partial_x \, (\Lambda + c - 2u) \, e^{i\xi x} \tag{4.140}$$

for $|\xi| \ll 1$. Although the symbol of Λ is not smooth near the origin, the symbol of $\partial_x \Lambda$ is C^1 at the origin and we can expand the Bloch operators as

$$L_\xi = L_0 + (i\xi)L_1 + \frac{1}{2}(i\xi)^2 L_2 + o(|\xi|^2), \tag{4.141}$$

where

$$L_0 := \partial_x(\Lambda - 2u - c) \tag{4.142}$$

and

$$L_1 = [L_0, x] = 2\Lambda - 2u - c, \quad L_2 = [L_1, x] = \Lambda^{-1}\partial_x. \tag{4.143}$$

Following Sect. 4.4, the first step in the modulational stability analysis is to understand the Jordan structure of the kernel of the unmodulated operator L_0. Note that Eq. (4.136) possesses two conserved quantities, the mass and the momentum, denoted M and P, respectively, which are defined similarly to those in Sect. 4.2.

Lemma 4.2 ([12]) *Suppose that $u = u(\cdot\,; a_0, k_0, c_0)$ is a $2\pi/k$-periodic traveling wave of Eq. (4.136) and that $\{M, P\}_{a,c} := \det\left(\frac{\partial(M,P)}{\partial(a,c)}\right)$ is not zero at (a_0, k_0, c_0). Then the generalized $L^2_{\text{per}}([0,T])$-kernel of the linear operator L_0 defined in Eq. (4.142) possesses the following Jordan block structure:*

(i) $\dim(\ker(L_0)) = 2$
(ii) $\dim(\ker(L_0^2)/(\ker(L_0)) = 1$
(iii) $\dim(\ker(L_0^{n+1})/(\ker(L_0^n)) = 0$ *for all integers* $n \geq 2$.

In particular,

$$\begin{aligned} v_0 &:= u_a, \quad w_0 := M_c u - P_c \\ v_1 &:= u_x, \quad w_1 := \textstyle\int_0^x (M_a u_c - M_c u_a)\, dx \\ v_2 &:= u_c, \quad w_2 := P_a - M_a u \end{aligned} \tag{4.144}$$

form a basis and dual basis for the generalized kernel of L_0, respectively:

$$\begin{aligned} L_0 v_0 &= L v_1 = 0, \quad L_0 v_2 = v_2, \\ L_0^\dagger w_0 &= L^\dagger w_2 = 0, \quad L_0^\dagger w_1 = w_2. \end{aligned} \tag{4.145}$$

Moreover, $\langle w_j, v_k\rangle = -\{M, P\}_{a,c}\delta_{jk}$ and $\langle w_j, L_k v_\ell\rangle = 0$ whenever $j + k + \ell$ is even.

The proof follows the same lines as in the proof of Lemma 4.1; see [12]. The key step to extend the proof to the nonlocal case is to verify that the kernel of L_0 is only two dimensional. This would follow essentially immediately provided that one could verify that the linearized operator associated with the traveling wave equation $\mathcal{L} = \Lambda - 2u - c$ is non-degenerate, i.e.

$$\ker(\mathcal{L}) = \text{span}\{u_x\}. \tag{4.146}$$

While this is obvious in the (local) generalized KdV equations, by virtue of Sturm-Liouville theory, it is far from being obvious in general in nonlocal equations. But, Amick and Toland [1] demonstrated the property by relating via complex analysis techniques the nonlocal profile equation to a fully nonlinear ODE. Equipped with this non-degeneracy result, the proof of Lemma 4.2 follows from the same arguments as Lemma 4.1.

To verify the hypothesis of Lemma 4.2, owing to the explicit solution formulae given by Eq. (4.137), a straightforward calculation (see [12] for details) reveals that

$$M(a,k,c) := \int_0^{2\pi/k} u(x;a,k,c)\,dx = 2\pi - \frac{\pi}{k}(\sqrt{c^2-4a}+c) \tag{4.147}$$

and

$$P(a,k,c) := \frac{1}{2}\int_0^{2\pi/k} u^2(x;a,k,c)\,dx = -c\pi + \frac{\pi}{4k}(\sqrt{c^2-4a}+c)^2 \tag{4.148}$$

so that, in particular,

$$\{M,P\}_{a,c} = \frac{2\pi^2}{k\sqrt{c^2-4a}} > 0 \tag{4.149}$$

for all (a,k,c) satisfying Eq. (4.138). Lemma 4.2 thus provides an explicit basis for the generalized kernels of the unmodulated operator L_0 and its adjoint, about a periodic traveling wave of Eq. (4.136).

With Lemma 4.2 in hand, the methodology of Sect. 4.4.2 may be applied *without modification*. In particular, the triple eigenvalue at the origin of L_0 bifurcates into three eigenvalues $\lambda_j(\xi)$'s, $j = 1,2,3$, that are C^1 in ξ near $\xi = 0$ and satisfy

$$\lambda_j(\xi) = i\mu_j\xi + o(\xi), \quad j = 1,2,3, \tag{4.150}$$

where $\mu_j \in \mathbb{C}$ are the eigenvalues of, taking into account the parametrization of solutions in Eq. (4.137), the effective dispersion matrix $\mathbf{D}(a,k,c)$ in Eq. (4.92). Using Eq. (4.137) this matrix can be calculated *explicitly* in terms of the traveling wave parameters a, k, c, *provided* that an explicit formula for the corrector $v_1^{(1)}$ in Eq. (4.84) can be found: due to the parametrization of solutions of Eq. (4.136) by their period, the formula from our generalized KdV analysis must be modified. Since Eq. (4.96) still holds in the present case, $v_1^{(1)}$ may be identified as an appropriate multiple of the $2\pi/k$ periodic function $xu_x + Tu_T$, where $T = 2\pi/k$; see [12, Lemma 9]. With this choice, the matrix $\mathbf{D}(a,k,c)$ can be shown, up to a similarity transformation,[6] to be given (for $a = 0$) by

$$\mathbf{D}(a=0,k,c) = \begin{pmatrix} -\pi T & (\pi T)^2 - (\pi/c)^2 & 0 \\ 1 & \pi T & 0 \\ 2\pi^2 & 0 & \pi T \end{pmatrix}, \tag{4.151}$$

[6]Indeed, this formula for $\mathbf{D}$ was derived in [12] using a direct spectral perturbation expansion, a method equivalent to that described in Sect. 4.4.2.

where $T = 2\pi/k$. A quick calculation shows that the eigenvalues of $\mathbf{D}(0, k, c)$ are πT and $\pm\pi T\sqrt{2-(cT)^{-2}}$. Since periodic traveling waves of (4.136) exist only when $c^2 > k = 1/T$, it follows that the eigenvalues of $\mathbf{D}(0, k, c)$ are real and distinct. By the Galilean invariance given by Eq. (4.139) and Theorem 4.1, this yields the following result.

Theorem 4.4 ([12]) *All periodic traveling waves of the Benjamin-Ono equation* (4.136) *are modulationally stable.*

In fact, the above calculations on the Benjamin-Ono equation (4.136) is merely a special case of the recent analysis of Bronski and Hur [12], where they considered the modulational instability of arbitrary amplitude periodic traveling waves to the fractional KdV equation (4.129) for $1/3 < \alpha < 2$. For such α, one can show through calculus of variations that for each $T > 0$ there exists a two-parameter (up to translations) family of periodic traveling waves parameterized by the constant of integration a and the wave speed c and that, furthermore, these waves depend on a, T and c in a C^1 manner. A key difficulty in this more general setting is to verify the non-degeneracy property given by Eq. (4.146). Although the methods of Amick and Toland [1], described above, do not apply outside the Benjamin-Ono equation, i.e. $\alpha = 1$, it is possible to verify through a periodic adaptation of the recent, nonlocal Sturm-Liouville theory of Frank and Lenzmann [31] for fractional Schrödinger operators to verify that the kernel of L_0 is indeed two dimensional for all $1/3 < \alpha \leq 2$; see [12, 42] for details. Equipped with this non-degeneracy result, the effective dispersion matrix can be numerically computed for all such α; see [12] for details.

The Whitham Equation for Water Waves

In the absence of explicit solution formulae, it is in general difficult to calculate the effective dispersion matrix given by Eq. (4.92) and one must typically rely on well-conditioned numerical techniques. One may however avoid this difficulty in the small amplitude limit. As we will see below, as a matter of fact, small amplitude wave trains can be expanded (in amplitude) explicitly to arbitrarily high orders, for a wide class of nonlocal equations of the form given by Eq. (4.127). Equipped with such an explicit expansion of solutions, one can compute an asymptotic expansion of the amplitude dependent effective dispersion matrix given by Eq. (4.92) and hence ascertain the modulational stability of small amplitude waves.

To illustrate this procedure, we consider the Whitham equation for surface water waves

$$u_t + \mathcal{M}u_x + (u^2)_x = 0, \tag{4.152}$$

where the symbol of the operator $\mathcal{M}$ is given by $m(k) = \sqrt{\frac{\tanh(k)}{k}}$. As described above, Eq. (4.152) combines the dispersion relation of surface water waves with the

nonlinearity of shallow water equations. Details of the forthcoming analysis can be found in [41].

Periodic traveling waves of Eq. (4.152) take the form $u(x,t) = u(x-ct)$, where $c > 0$ and u satisfies

$$\mathcal{M}u - cu + u^2 = (1-c)^2 b \tag{4.153}$$

for some constant $b \in \mathbb{R}$; the normalizing factor of $(1-c)^2$ is added for convenience. To describe small amplitude periodic wave trains of Eq. (4.152), we seek solutions of Eq. (4.153) of the form $u(x) = w(z)$, $z = kx$, where w is required to be 2π-periodic and $k > 0$ is interpreted as a wave number. The 2π-periodic function w is then required to satisfy

$$\mathcal{M}_k w - cw + w^2 = (1-c)^2 b, \tag{4.154}$$

where $\mathcal{M}_k$ is defined via

$$\mathcal{M}_k e^{inz} = m(kn)e^{inz}, \quad n \in \mathbb{Z}. \tag{4.155}$$

Observe that the symbol here is *not homogeneous* and hence the wave number may not be factored out of the symbol.

Since $\mathcal{M}_k : H^s_{2\pi} \to H^{s+1/2}_{2\pi}$ is bounded for all $k > 0$ and $s \geq 0$, a standard argument verifies that solutions of Eq. (4.154) with $\|w\|_{L^\infty} < c/2$ belong to the Sobolev space $H^\infty_{2\pi}$ and hence are smooth. As a result, smooth 2π-periodic solutions of Eq. (4.154) with small amplitudes may be sought as zeros of

$$F(w,k,c,b) = \mathcal{M}_k w - cw + w^2 - (1-c)^2 b. \tag{4.156}$$

Note that $F : H^1_{2\pi} \times \mathbb{R}_+ \times \mathbb{R}_+ \times \mathbb{R} \to H^1_{2\pi}$ by a Sobolev inequality. Clearly $F(0;k,c,0) = 0$ for every $k, c \in \mathbb{R}_+$ and, furthermore,

$$\partial_w F(0,k,c,0) = \mathcal{M}_k - c \tag{4.157}$$

has a trivial kernel in $H^1_{2\pi}$, provided that $c \neq m(kn)$ for any $n \in \mathbb{Z}$. By the implicit function theorem, near any such trivial solution for which $\partial_w F$ has a trivial kernel, there exist only other trivial solutions. Thus, to construct nontrivial solutions of Eq. (4.154) we start at a zero solution for which the kernel of $\partial_w F$ is nontrivial.

To this end, notice that if $c = m(k)$ then

$$\ker\left(\partial_w F(0,k,c,0)\right) = \operatorname{span}\{e^{\pm iz}\}. \tag{4.158}$$

Using a straightforward Lyapunov-Schmidt reduction, it follows that for each $k > 0$ there exists a two-parameter (up to translations) family of nontrivial zeros of F, corresponding to smooth (even) 2π-periodic solutions of Eq. (4.154). Furthermore,

their small amplitude asymptotics may be found by seeking solutions of Eq. (4.154) of the form

$$\begin{aligned} w(k,A,b)(z) &= w_0(k,b) + A\cos(z) + A^2 w_2(z,b) \\ &\quad + A^3 w_3(z,b) + \mathcal{O}(|A|^4), \end{aligned} \tag{4.159}$$

$$c(k,A,b) = m(k) + A^2 c_2(k,b) + \mathcal{O}(|A|^4), \tag{4.160}$$

where A is a real parameter (a sort of generalized amplitude), w_j's are taken to be even, and $w_0(k,b)$ is defined for $|b| \ll 1$ via $F(w_0(k,b),k,m(k),b) = 0$. Plugging the above expansions into Eq. (4.154), we find that

$$\begin{aligned} w(k,A,b)(z) &= w_0(k,b) + A\cos(z) \\ &\quad + \frac{1}{2}A^2\Big(\frac{1}{m(k)-1)} + \frac{\cos(2z)}{m(k)-m(2k)}\Big) + \mathcal{O}(A(A^2+b^2)), \\ c(k,A,b) &= c_0(k,b) \\ &\quad + A^2\Big(\frac{1}{m(k)-1} + \frac{1}{2(m(k)-m(2k))}\Big) + \mathcal{O}(A(A^2+b^2)) \end{aligned} \tag{4.161}$$

as $|A|, |b| \to 0$, where

$$\begin{aligned} c_0(k,b) &= m(k) + 2b(1-m(k)) - 6b^2(1-m(k)) + \mathcal{O}(b^3), \\ w_0(k,b) &= b(1-m(k)) - b^2(1-m(k)) + \mathcal{O}(b^3). \end{aligned} \tag{4.162}$$

Although higher order expressions are obtainable, they are not necessary in our analysis. Together with translation invariance, this yields a four-parameter family of small amplitude periodic traveling waves of the Whitham equation given by Eq. (4.152): see [25, 26, 41] for more details. Throughout the remainder, we take $b = 0$ for simplicity.

We now turn to study the spectrum in $L^2_{2\pi} := L^2_{\text{per}}([0,2\pi])$ near the origin of the Bloch operators

$$L_\xi(k,A) = e^{-i\xi z} L(k,A) e^{i\xi z}, \tag{4.163}$$

where

$$L(k,A) := \partial_z(-\mathcal{M}_k + c(k,A,0) - 2w(k,A,0)) \tag{4.164}$$

for $|(\xi,A)| \ll 1$. Unlike the case of the Benjamin-Ono equation, the symbol m is smooth near the origin and hence we may easily expand the Bloch operators as

$$L_\xi(k,A) = L_0(k,A) + (i\xi)L_1(k,A) + \frac{1}{2}(i\xi)^2 L_2(k,A) + \mathcal{O}(|\xi|^3), \tag{4.165}$$

where

$$\begin{aligned} L_0(k,A) &= \partial_z(-\mathcal{M}_k + m(k)) - 2a\partial_z(\cos(z)\cdot) + \mathcal{O}(A^2+b^2), \\ L_1(k,A) &= [-\partial_z\mathcal{M}_k, z] + m(k) - 2a\cos(z) + \mathcal{O}(A^2+b^2), \\ L_2(k,A) &= [[-\partial_z\mathcal{M}_k, z], z] + \mathcal{O}(A^2+b^2) \end{aligned} \tag{4.166}$$

for $|A| \ll 1$. As in our previous analysis, the key step in the modulational stability analysis is to understand the Jordan structure of the kernel of the unmodulated operator $L_0(k,A)$. To study the spectrum of L_ξ near the origin, we note that

$$\|L_\xi(k,A) - L_\xi(k,0)\|_{L^2_{2\pi}\to L^2_{2\pi}} = \mathcal{O}(A) \tag{4.167}$$

as $A \to 0$ uniformly in $\xi \in [-1/2, 1/2)$, which may be verified by brutal force, implying that the spectrum of $L_\xi(k,A)$ is close to that of $L_\xi(k,0)$ with constant coefficients uniformly in the Bloch frequency ξ. In other words, we may consider the spectrum of $L_\xi(k,A)$ as a small perturbation of that of $L_\xi(k,0)$. In particular, the spectral projections Π_ξ and $\tilde{\Pi}_\xi$ in Sect. 4.4 are *amplitude dependent*, described to leading order by the projections associated to the trivial solution $A = 0$.

We first concentrate on the right eigenprojection. Since $L_\xi(k,0)$ is of constant coefficients, its spectrum for each $k > 0$ and $\xi \in [-1/2, 1/2)$ can be computed via Fourier analysis as

$$\operatorname{spec}(L_\xi(k,0)) = \{i\omega_{n,\xi}(k) : n \in \mathbb{Z}\} \subset i\mathbb{R}, \tag{4.168}$$

where $\omega_{n,\xi}(k) := (n+\xi)\,(m(k) - m(kn+k\xi))$ with associated eigenfunctions e^{inz}. In particular, $\omega_{-1,0} = \omega_{0,0} = \omega_{1,0} = 0$ and hence zero is an eigenvalue of $L_0(k,0)$ of algebraic multiplicity three with (real) associated eigenfunctions $\cos(z)$, $\sin(z)$ and 1. Moreover the eigenspaces associated with the three non-zero eigenvalues $\omega_{\pm1,\xi}$ and $\omega_{0,\xi}$ are independent of ξ, and the associated right spectral projection $\Pi_\xi(k,0)$ is independent of ξ. Furthermore we note that the adjoint operators $L_\xi(k,0)$ with constant coefficients share the same eigenvalues and eigenfunctions, and hence the left spectral projection $\tilde{\Pi}_\xi(k,0)$ is independent of ξ as well. In particular, we find[7] that

$$\begin{aligned} M_0(k,0) &:= (\Pi_\xi L_\xi \Pi_\xi)(k,0) \\ &= \begin{pmatrix} \frac{i}{2}(\omega_{1,\xi} + \omega_{-1,\xi}) & \frac{1}{2}(\omega_{1,\xi} - \omega_{-1,\xi}) & 0 \\ -\frac{1}{2}(\omega_{1,\xi} - \omega_{-1,\xi}) & \frac{i}{2}(\omega_{1,\xi} + \omega_{-1,\xi}) & 0 \\ 0 & 0 & i\omega_{0,\xi} \end{pmatrix}. \end{aligned} \tag{4.169}$$

[7] Following [41], the projections here are slightly re-scaled from those of Sect. 4.4. Here we use $M_\xi := \left[\langle \psi_i, L_\xi \phi_j\rangle / \langle \psi_i, \phi_j\rangle_{L^2_{\mathrm{per}}([0,T])}\right]_{i,j=1,2,3}$ and similarly for the projection of the identity.

For $|A| \ll 1$, it follows that the spectral projections can be expanded as

$$\Pi_\xi(k,A) = \Pi_0(k,A) + \mathcal{O}(A^2+\xi^2), \tag{4.170}$$

$$\tilde{\Pi}_\xi(k,A) = \tilde{\Pi}_0(k,A) + \mathcal{O}(A^2+\xi^2) \tag{4.171}$$

so that, to first order, the spectral projections for the left and right eigenspaces of $L_\xi(k,A)$ agree with those of the unmodulated operator $L_0(k,A)$. In particular, the variations in these projections in ξ do not affect the leading order asymptotics and, furthermore, the bases used to construct these projections agree to first order. As such, to construct the projections $\Pi_\xi(k,A)$ and $\tilde{\Pi}_\xi(k,A)$ to leading order, we only need to find a basis for the generalized kernel of $L_0(k,A)$. The origin is an eigenvalue of $L_0(k,A,b)$ of algebraic multiplicity three and geometric multiplicity two for all $|A|, |b| \ll 1$ and, furthermore,

$$\begin{aligned}\phi_1(z) &:= \frac{1}{2(1-m(k))}\left[(\partial_b c)\partial_a w - (\partial_a c)\partial_b w\right](k,A,b)(z)\\ &= \cos(z) + \frac{-1/2+\cos(2z)}{m(k)-m(2k)}A - 6\cos(z)b + \mathcal{O}(A^2+b^2),\end{aligned} \tag{4.172}$$

$$\begin{aligned}\phi_2(z) &:= -\frac{1}{a}\partial_z w(k,A,b)(z)\\ &= \sin(z) + \frac{\sin(2z)}{m(k)-m(2k)}A + \mathcal{O}(A^2+b^2),\end{aligned} \tag{4.173}$$

$$\phi_3(z) := 1 \tag{4.174}$$

form a basis of the generalized eigenspace for $L_0(k,A,b)$ for all $|A|, |b| \ll 1$. Indeed,

$$L_0\phi_1 = L_0\phi_2 = 0, \quad \text{and} \quad L_0\phi_3 = -2a\phi_2. \tag{4.175}$$

Using this basis, therefore, we compute that

$$\begin{aligned}M_\xi(k,A) &:= (\tilde{\Pi}_\xi L_\xi \Pi_\xi)(k,A)\\ &= \begin{pmatrix}0&0&0\\0&0&2\\0&0&0\end{pmatrix} + i\xi\begin{pmatrix}-km'(k)&0&0\\0&-km'(k)&0\\0&0&m(k)-1\end{pmatrix}\\ &\quad - i\xi A\Big(1+\frac{m(k)-1}{2(m(k)-m(2k))}\Big)\begin{pmatrix}0&0&2\\0&0&0\\1&0&0\end{pmatrix}\\ &\quad + \xi^2\Big(km'(k)+\frac{1}{2}k^2m''(k)\Big)\begin{pmatrix}0&-1&0\\1&0&0\\0&0&0\end{pmatrix} + \mathcal{O}(|\xi|^3+|A|^3)\end{aligned} \tag{4.176}$$

and, similarly, that

$$(\tilde{\Pi}_\xi \Pi_\xi)(k,A) = \mathbf{I} - \frac{A}{m(k)-m(2k)} \begin{pmatrix} 0 & 0 & 1 \\ 0 & 0 & 0 \\ 1/2 & 0 & 0 \end{pmatrix} + \mathcal{O}(A^2). \tag{4.177}$$

We then turn to study the roots of the characteristic polynomial

$$\begin{aligned} P(\lambda,\xi;k,A) &= \det(M_\xi(k,A) - \lambda(\tilde{\Pi}_\xi \Pi_\xi)(k,A)) \\ &= c_3(\xi;k,A)\lambda^3 + ic_2(\xi;k,A)\lambda^2 \\ &\quad + c_1(\xi;k,A)\lambda + ic_0(\xi;k,A) \end{aligned} \tag{4.178}$$

for each fixed $k > 0$ and $|(\lambda,\xi,A)| \ll 1$. The roots of $P(\cdot,\xi;k,A)$ correspond to the eigenvalues of the Bloch operators $L_\xi(k,A)$ bifurcating from the origin for $|(\xi,A)| \ll 1$. We first note that the coefficient functions c_j's depend smoothly on ξ and A for $|(\xi,A)| \ll 1$ and, moreover, the c_j's are real-valued since the spectrum of $L_\xi(k,A)$ is symmetric about the imaginary axis. Furthermore, the spectral symmetry

$$\operatorname{spec}_{L^2_{2\pi}}(L_\xi(k,A)) = \overline{\operatorname{spec}_{L^2_{2\pi}}(L_{-\xi}(k,A))} \tag{4.179}$$

implies that the functions c_3 and c_1 are even functions of ξ while c_2 and c_0 are odd, and that the c_j's are all even in A. Since $\lambda = 0$ is clearly a root of $P(\lambda,0;k,A)$ with multiplicity three and $\xi = 0$ is a root of $P(0,\xi;k,A)$ with multiplicity three for all $|A| \ll 1$, it follows that

$$c_j(\xi;k,A) = d_j(\xi;k,A)\xi^{3-j}, \quad j = 0,1,2,3, \tag{4.180}$$

for some real functions d_j's that depend smoothly on A and ξ and are even in A. Therefore, the roots of $P(\cdot\,,\xi)$ may be written as $\lambda = -i\xi X$, where X is a root of

$$\begin{aligned} (i\xi)^{-3}P(-i\xi X,\xi;k,A) &= \det\Big(\frac{1}{i\xi}M_\xi(k,A) + X(\tilde{\Pi}_\xi \Pi_\xi)(k,A)\Big) \\ &= -d_3(\xi;k,A)X^3 + d_2(\xi;k,A)X^2 \\ &\quad + d_1(\xi;k,A)X - d_0(\xi;k,A); \end{aligned} \tag{4.181}$$

compare to Eq. (4.83). It follows that the underlying periodic traveling wave is modulationally unstable if the characteristic polynomial $P(-i\xi\cdot,\xi;k,A)$ admits a pair of complex roots, i.e. if its discriminant

$$\Delta_{\xi,k,A} := (18d_3d_2d_1d_0 + d_2^2d_1^2 + 4d_2^3d_0 + 4d_3d_1^3 - 27d_3^2d_0^2)(\xi,k,A) < 0 \tag{4.182}$$

for $|(\xi, A)| \ll 1$, and it is modulationally stable if the polynomial admits three real roots, i.e. if $\Delta_{\xi,k,A} > 0$.

Since the d_j's are even in A, we may expand

$$\Delta_{\xi,k,A} = \Delta_{\xi,k,0} + \Delta(k)A^2 + \mathcal{O}(A^2(A^2 + \xi^2)) \tag{4.183}$$

for $|(\xi, A)| \ll 1$, expressing that, to leading order, the modulational stability is governed by that of the limiting constant state at $A = 0$. Using the above explicit formulae, we find that $\Delta_{0,k,0} = 0$ and

$$\Delta_{\xi,k,0} = \frac{(\omega_{0,\xi} - \omega_{1,\xi})^2(\omega_{0,\xi} - \omega_{-1,\xi})^2(\omega_{1,\xi} - \omega_{-1,\xi})^2}{\xi^6} > 0 \tag{4.184}$$

for all $|\xi| \ll 1$. Therefore, the sign of the discriminant $\Delta_{\xi,k,A}$ for $|(\xi, A)| \ll 1$ is determined by the sign of the function $\Delta(k)$. Indeed, from above we see that if $\Delta(k) > 0$ then $\Delta_{\xi,k,A} > 0$ for all $|(\xi, A)| \ll 1$, implying modulational stability, while if $\Delta(k) < 0$ then $\Delta_{\xi,k,A} < 0$ for $|A| \ll 1$ fixed and $|\xi|$ sufficiently small. The modulational stability of the underlying small amplitude waves is therefore determined completely by the wavenumber k.

With the aid of computer algebra software, we find that

$$\Delta(k) = \frac{(k(m(k) - 1))'(k(m(k) - 1))''}{m(k) - m(2k)} \Gamma(k), \tag{4.185}$$

where

$$\Gamma(k) := 2(m(k) - m(2k)) + (k(m(k) - 1))'. \tag{4.186}$$

Recalling that $m(k) := \sqrt{\frac{\tanh(k)}{k}}$, we see that the function $k \mapsto k(m(k) - 1)$ is strictly decreasing and concave down on the interval $(0, \infty)$, so that the sign of $\Delta(k)$ is determined by the sign of $\Gamma(k)$. Furthermore, a numerical evaluation of Γ shows that there exists a unique $k^* \approx 1.146$ such that $\Gamma(k) > 0$ for $k \in (0, k^*)$ and $\Gamma(k) < 0$ for $k > k^*$; see Fig. 4.3.

Theorem 4.5 ([41]) *A $2\pi/k$-periodic traveling wave of Eq. (4.152) of sufficiently small amplitude is modulationally unstable if $k > k^* \approx 1.146$ and modulationally stable if $0 < k < k^*$.*

Theorem 4.5 qualitatively captures the famous Benjamin-Feir instability in [7, 73]: see [41, 68] for more discussion.

Fractional KdV and ILW Equations

The above small amplitude analysis is largely independent of the specific dispersion symbol. Indeed, the only features of the symbol m that was used in the derivation

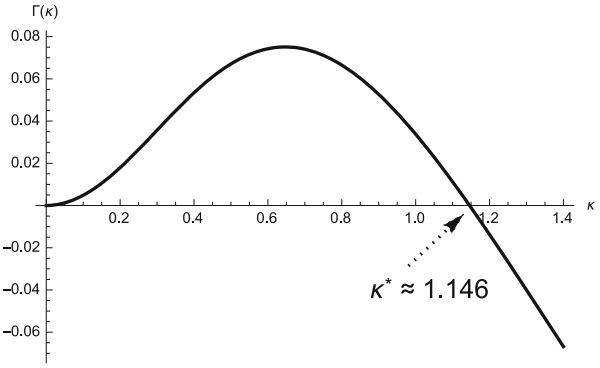

Fig. 4.3 Plot of $\Gamma(k)$ for Whitham equation

of the modulational instability index were: (i) $m(0) = 1$ and (ii) $m(k) \neq m(nk)$ for each $k > 0$ for all $n = 2, 3, 4, \ldots$. While (ii) provides a restriction on k, (i) can be relaxed via a simple scaling argument. The index formula must be modified accordingly, however.

Examples for which the analysis can be applied *without modifications* include the fractional KdV equation, Eq. (4.129) with $f(u) = u^2$, and the intermediate long-wave equation given by Eq. (4.131). For the fractional KdV equation, we find that for each[8] $\alpha > 1/2$

$$\Delta_{\mathrm{fKdV}}(k;\alpha) = \frac{2k^{4\alpha}\alpha(1+\alpha)^4(2^{\alpha+1}-3-\alpha)}{2^\alpha - 1}, \tag{4.187}$$

which is negative (or positive) for all $k > 0$, provided that $\alpha < 1$ (or $\alpha > 1$, respectively), indicating modulational instability (or stability, respectively) of the small amplitude periodic wave trains. Recall that $\alpha = 1$ corresponds to the Benjamin-Ono equation, which was discussed before. The result for more general power-law nonlinearities may be found in [45].

Similarly, for the ILW equation given by Eq. (4.131), we find for each $H>0$ that

$$\Delta_{\mathrm{ILW}}(k;H) = \frac{(4H^2k^2-1)\cosh(Hk) + \cosh(3Hk) - 8Hk\sinh(Hk))^2}{32H^4\sinh(Hk)^{12}}\Gamma_{ILW}(Hk), \tag{4.188}$$

where $\Gamma_{ILW}(z) = 1 - 2z^2 - \cosh(2z) + 2z\sinh(2z)$; see [41]. A numerical evaluation indicates that $\Gamma_{ILW}(z) > 0$ for all $z > 0$, and hence for each $H > 0$, small-amplitude periodic traveling waves of Eq. (4.131) are modulationally stable. This rigorously justifies a formal "amplitude equation" calculation in [63].

[8] The condition $\alpha > 1/2$ is an artifact of the corresponding existence theory. See [45] for details.

4.6 Concluding Remarks

We have made a detailed survey of some recent techniques analytically studying the modulational instability of periodic traveling waves for KdV type equations. They are very general and apply to many other equations, including systems involving dissipation. They are independent of the integrability of the governing equations. The theoretical approach in Sect. 4.4 may be used to rigorously validate formal predictions from Whitham's modulation theory in a variety of settings; see [9, 60], for instance, for more examples, other than those listed in Sect. 4.4.3. We applied our theory to a number of concrete examples in Sect. 4.5. To illustrate the robustness of our theory, we discussed extensions to nonlocal equations of KdV type and obtained detailed results for a number of examples.

We have been concerned with the linear (spectral) stability to slow modulations of periodic traveling waves of KdV type equations. A fundamental open problem is to understand the *nonlinear* dynamics associated with modulationally stable waves and, even more interestingly, induced by a modulational instability. They have been studied in the context of dissipative systems (see [50], for instance, and references therein), but it is not clear how such techniques apply to dispersive equations such as the generalized KdV equations. This is an exciting direction for future work.

Acknowledgements JCB is supported by the National Science Foundation grant DMS-1211364. VMH is supported by the National Science Foundation grant CAREER DMS-1352597 and an Alfred P. Sloan Foundation Fellowship. MAJ is supported by the National Science Foundation grant DMS-1211183.

References

1. Amik, C.J., Toland, J.F.: Uniqueness and related analytic properties for the Benjamin-Ono equation: a nonlinear Neumann problem in the plane. Acta Math. **167**, 107–126 (1991)
2. Anderson, D., Lisak, M.: Modulational instability of coherent optical-fiber transmission signals. Opt. Lett. **9**, 468–470 (1984)
3. Barker, B., Johnson, M.A., Noble, P., Rodrigues, L.M., Zumbrun, K.: Nonlinear modulational stability of periodic traveling-wave solutions of the generalized Kuramoto-Sivashinsky equation. Phys. D. **258**, 11–46 (2013)
4. Benjamin, T.B.: Internal waves of permanent form in fluids of great depth. J. Fluid Mech. **29**, 559–592 (1970)
5. Benjamin, T.B., Bridges, T.J.: Reappraisal of the Kelvin-Helmholtz problem, I. Hamiltonian structure. J. Fluid Mech. **333**, 301–325 (1997)
6. Benjamin, T.B., Bridges, T.J.: Reappraisal of the Kelvin-Helmholtz problem, II. Interaction of the Kelvin-Helmholtz, superharmonic and Benjamin-Feir instabilities. J. Fluid Mech. **333**, 327–373 (1997)
7. Benjamin, T.B., Feir, J.E.: The disintegration of wave trains on deep water I. Theory. J. Fluid Mech. **27**, 417–430 (1967)
8. Benney, D.J., Newell, A.C.: The propagation of nonlinear wave envelopes. J. Math. Phys. **46**, 133–139 (1967)

9. Benzoni-Gavage, S., Noble, P., Rodrigues, L.M.: Slow modulations of periodic waves in Hamiltonian PDEs, with application to capillary fluids. J. Nonlinear Sci. **24**, 711–768 (2014)
10. Bridges, T.J., Mielke, A.: A proof of the Benjamin-Feir instability. Arch. Ration. Mech. Anal. **133**, 145–198 (1995)
11. Bridges, T.J., Rowlands, G.: Instability of spatially quasi-periodic states of the Ginzburg-Landau equation. Proc. R. Soc. Lond. Ser. A. **444**, 347–362 (1994)
12. Bronski, J.C., Hur, V.M.: Modulational instability and variational structure. Stud. Appl. Math. **132**, 285–331 (2014)
13. Bronski, J.C., Johnson, M.A.: The modulational instability for a generalized Korteweg-de Vries equation. Arch. Ration. Mech. Anal. **197**, 357–400 (2010)
14. Bronski, J.C., Segev, M., Weinstein, M.: Mathematical Frontiers in optical solitons. Proc. Natl. Acad. Sci. **98**, 12872–12873 (2001)
15. Bronski, J.C., Johnson, M.A., Kapitula, T.: An index theorem for the stability of periodic travelling waves of Korteweg-de Vries type. Proc. R. Soc. Edinb. Sect. A **141**, 1141–1173 (2011)
16. Bottman, N., Deconinck, B.: KdV cnoidal waves are spectrally stable. Discrete Contin. Dyn. Syst. **25**, 1163–1180 (2009)
17. Boussinesq, M.J.: Essai sur la théorie des eaux courants. Mémoirs présentés par divers savants á l'Acad. des Sciences Inst. France (série 2) **23**, 1–680 (1877)
18. Cardaliaguet, P., Da Lio, F., Forcadel, N., Monneau, R.: Dislocation dynamics: a non-local moving boundary. In: Figueiredo, I.N., Rodrigues, J.F., Santos, L. (eds.) Free Boundary Problems. International Series of Numerical Mathematics, vol. 154, pp. 125–135. Birkhäuser, Basel (2007)
19. Chicone, C.: Ordinary Differential Equations with Applications, 2nd edn. Texts in Applied Mathematics, vol. 34. Springer, New York (2006)
20. Chirilus-Bruckner, M., Düll, W.-P., Schneider, G.: Validity of the KdV equation for the modulation of periodic traveling waves in the NLS equation. J. Math. Anal. Appl. **414**(1), 166–175 (2014)
21. Collet, P., Eckmann, J.-P.: The time dependent amplitude equation for the Swift-Hohenberg problem. Commun. Math. Phys. **132**, 139–152 (1990)
22. Cont, R., Tankov, P.: Financial Modeling with Jump Processes. Chapman & Hall/CRC Financial Mathematics Series. Chapman & Hall/CRC, Boca Raton (2004)
23. Dubrovin, B.A., Novikov, S.P.: Hydrodynamics of weakly deformed soliton lattices. Differential geometry and Hamiltonian theory. Usp. Mat. Nauk. **44**, 29–98 (1989)
24. Düll, W.-P., Schneider, G.: Validity of Whitham's equations for the modulation of periodic traveling waves in the NLS equation. J. Nonlinear Sci. **19**(5), 453–466 (2009)
25. Ehrnström, M., Kalisch, H.: Traveling waves for the Whitham equation. Diff. Integr. Equat. **22**, 1193–1210 (2009)
26. Ehrnström, M., Kalisch, H.: Gobal bifurcation in the Whitham equation. Math. Model. Nat. Phenom. **8**, 13–30 (2013)
27. Ercolani, N., Forest, M.G., McLaughlin, D.W., Montgomery, R.: Hamiltonian structure for the modulation equations of a sine-Gordon wavetrain. Duke Math. J. **55**, 949–983 (1987)
28. Feir, J.E.: Discussion: some results from wave pulse experiments. Proc. R. Soc. Lond. Ser. A **299**, 54–58 (1967)
29. Fermi, E., Pasta, J.R., Ulam, S.: Studies of Nonlinear Problems, I. Report LA-1940. Los Alamos Scientific Laboratory, Los Alamos (1955)
30. Flaschka, H., Forest, M.G., McLaughlin, D.W.: Multiphase averaging and the inverse spectral solution of the Korteweg-de Vries equation. Commun. Pure Appl. Math. **33**, 739–784 (1980)
31. Frank, R., Lenzmann, E.: Uniqueness and nondegeneracy of ground states for $(-\Delta)^s Q + Q - Q^{\alpha+1} = 0$ in $\mathbb{R}$. Acta Math. **210**, 261–318 (2013)
32. Fuerst, R.A., Baboiu, D.-M., Lawrence, B., Torruellas, W.E., Stegeman, G.I., Trillo, S., Wabnitz, S.: Spatial modulational instability and multisolitonlike generation in a quadratically nonlinear medium. Phys. Rev. Lett. **78**, 2756–2759 (1997)

33. Gallay, T., Hărăgus, M.: Orbital stability of periodic waves for the nonlinear Schrödinger equation. J. Dyn. Diff. Equat. **19**, 825–865 (2007)
34. Gallay, T., Hărăguş, M.: Stability of small periodic waves for the nonlinear Schrödinger equation. J. Diff. Equat. **234**, 544–581 (2007)
35. Grava, T.: From the solution of the Tsarev system to the solution of the Whitham equations. Math. Phys. Anal. Geom. **4**, 65–96 (2001)
36. Grimshaw, R.: Internal solitary waves. In: Grimshaw, R. (ed.) Environmental Stratified Flows, pp. 1–29. Kluwer, Boston (2002)
37. Hărăguş, M., Kapitula, T.: On the spectra of periodic waves for infinite-dimensionalHamiltonian systems. Phys. D **237**, 2649–2671 (2008)
38. Haragus, M., Scheel, A.: Finite-wavelength stability of capillary-gravity solitary waves. Commun. Math. Phys. **225**, 487–521 (2002)
39. Hasegawa, A.: Generation of a train of soliton pulses by induced modulational instability in optical fibers. Opt. Lett. **9** (1984)
40. Hur, V.M.: On the formation of singularities for surface water waves. Commun. Pure Appl. Anal. **11**, 1465–1474 (2012)
41. Hur, V.M., Johnson, M.A.: Modulational instability in the Whitham equation for water waves. Stud. Appl. Math. **134**, 120–143 (2015)
42. Hur, V.M., Johnson, M.A.: Stability of periodic traveling waves for nonlinear dispersive equations. Preprint
43. Hur, V.M., Lin, Z.: Unstable surface waves in running water. Commun. Math. Phys. **282**, 733–796 (2008)
44. Johnson, M.A.: On the stability of periodic solutions of the generalized Benjamin-Bona-Mahony equation. Phys. D **239**, 1892–1908 (2010)
45. Johnson, M.A.: Stability of small periodic waves in fractional KdV type equations. SIAM J. Math. Anal. **45**, 2597–3228 (2013)
46. Johnson, M.A., Zumbrun, K.: Rigorous justification for the generalized Korteweg-de Vries equation. Stud. Appl. Math. **125**, 69–89 (2010)
47. Johnson, M.A., Zumbrun, K., Bronski, J.C.: On the modulation equations and stability of periodic gKdV waves via Bloch decompositions. Phys. D **239**, 2037–2065 (2010)
48. Johnson, M.A., Noble, P., Rodrigues, L.M., Zumbrun, K.: Nonlocalized modulation of periodic reaction diffusion waves: nonlinear stability. Arch. Ration. Mech. Anal. **207**, 693–715 (2013)
49. Johnson, M.A., Noble, P., Rodrigues, L.M., Zumbrun, K.: Nonlocalized modulation of periodic reaction diffusion waves: the Whitham equation. Arch. Ration. Mech. Anal. **207**, 669–692 (2013)
50. Johnson, M.A., Noble, P., Rodrigues, L.M., Zumbrun, K.: Behavior of periodic solutions of viscous conservation laws under localized and nonlocalized perturbations. Invent. Math. **197**, 115–213 (2014)
51. Johnson, M.A., Noble, P., Rodrigues, L.M., Zumbrun, K.: Spectral stability of periodic wave trains of the Korteweg-de Vries/Kuramoto-Sivashinsky equation in the Korteweg-de Vries limit. Trans. Am. Math. Soc. **367**, 2159–2212 (2015)
52. Joseph, R.I.: Solitary waves in a finite depth fluid. J. Phys. A **10**, 225–227 (1977)
53. Kato, T.: Perturbation Theory for Linear Pperators. Springer, Berlin (1985)
54. Kirrmann, P., Schneider, G., Mielke, A.: The validity of modulation equations for extended systems with cubic nonlinearities. Proc. R. Soc. Edinb. Sect. A **122**, 85–91 (1992)
55. Korteweg, D., de Vries, G.: On the change of form of long waves advancing in a rectangular canal, and on a new type of long stationary waves. Philos. Mag. **39**, 422–435 (1895)
56. Krichever, I.M.: Whitham theory for integrable systems and topological quantum field theories. In: Fröhlich, J., 't Hooft, G., Jaffe, A., Mack, G., Mitter, P.K., Stora, R. (eds.) New Symmetry Principles in Quantum Field Theory (Cargèse 1991). Plenum, New York (1992)
57. Krylov, D., Leng, L., Bergman, K., Bronski, J.C., Kutz, J.N.: Observation of the breakup of a prechirped *N*-soliton in an optical fiber. Opt. Lett. **24**, 1191–1193 (1999)
58. Lax, P.D., Levermore, C.D.: The small dispersion limit of the Korteweg-de Vries equation. I, II, III. Commun. Pure Appl. Math. **36**, 253–290, 571–593, 809–829 (1983)

59. Lighthill, M.J.: Contributions to the theory of waves in non-linear dispersive systems. IMA J. Appl. Math. **1**, 269–306 (1965)
60. Noble, P., Rodrigues, L.M.: Whitham's modulation equations and stability of periodic wave solutions of the Korteweg-de Vries-Kuramoto-Sivashinsky equation. Indiana Univ. Math. J. **62**, 753–783 (2013)
61. Ono, H.: Algebraic solitary waves in stratified fluids. J. Phys. Soc. Jpn. **39**, 1082–1091 (1975)
62. Ostrovsky, L.A.: Propagation of wave packets in nonlinear dispersive medium. Sov. J. Exp. Theor. Phys. **24**, 797–800 (1967)
63. Pelinovsky, D.E.: Intermediate nonlinear Schrödinger equation for internal waves in a fluid of finite depth. Phys. Lett. A **197**, 401–406 (1995)
64. Reed, M., Simon, B.: Methods of Modern Mathematical Physics, IV. Analysis of Operators. Academic [Harcourt Brace Jovanovich Publishers], New York (1978)
65. Schaaf, R.: A class of hamiltonian systems with increasing periods. J. Reine Angew. Math. **363**, 96–109 (1985)
66. Schamel, H.: A modified Korteweg-de Vries equation for ion acoustic waves due to resonant electrons. J. Plasma Phys. **9**, 377–387 (1973)
67. Soljacic, M., Segev, M., Coskun, T., Christodoulides, D., Vishwanath, A.: Modulational instability of incoherent beams in noninstantaneous nonlinear media. Phys. Rev. Lett. **84**, 467 (2000)
68. Stanford, N., Kodama, K., Carter, J.D., Kalisch, H.: Stability of traveling wave solutions to the Whitham equation. Phys. Lett. A **378**, 2100–2107 (2014)
69. Tai, K., Hasegawa, A., Tomita, A.: Observation of the modulational instability in optical fibers. Phys. Rev. Lett. **56**, 135–138 (1986)
70. Tai, K., Tomita, A., Jewell, J.L., Hasegawa, A.: Generation of subpicosecond solitonlike optical pulses at 0.3THz repetition rate by induced modulational instability. Appl. Phys. Lett. **49**, 236–238 (1986)
71. Tian, F.-R., Ye, J.: On the Whitham equations for the semiclassical limit of the defocusing nonlinear Schrödinger equation. Commun. Pure Appl. Math. **52**, 655–692 (1999)
72. Whitham, G.B.: Non-linear dispersive waves. Proc. R. Soc. Ser. A **283**, 238–261 (1965)
73. Whitham, G.B.: Non-linear dispersion of water waves. J. Fluid Mech. **27**, 399–412 (1967)
74. Whitham, G.B.: Linear and Nonlinear Waves. Wiley-Interscience [John Wiley & Sons], New York (1974)
75. Zakharov, V.E.: Instability of self-focusing of light. Sov. J. Exp. Theor. Phys. **26**, 994 (1968)
76. Zakharov, V.E.: Stability of periodic waves of finite amplitude on the surface of a deep fluid. J. Appl. Mech. Tech. Phys. **9**, 190–194 (1968)
77. Zakharov, V.E., Ostrovsky, L.A.: Modulation instability: the beginning. Phys. D **238**, 540–548 (2009)

Chapter 5
Modulational Instability and Rogue Waves in Shallow Water Models

R. Grimshaw, K.W. Chow, and H.N. Chan

Abstract It is now well known that the focussing nonlinear Schrödinger equation allows plane waves to be modulationally unstable, and at the same time supports breather solutions which are often invoked as models for rogue waves. This suggests a direct connection between modulation instability and the existence of rogue waves. In this chapter we review this connection for a suite of long wave models, such as the Korteweg-de Vries equation, the extended Korteweg-de Vries (Gardner) equation, often used to describe surface and internal waves in shallow water, a Boussinesq equation and, also a coupled set of Korteweg-de Vries equations.

5.1 Introduction

The term rogue wave is commonly identified with an unexpectedly large water wave in the ocean, which is both temporally and spatially localized, see the monographs by Kharif et al. [33] and Osborne [38], the review by Dysthe et al. [22] and the article by Onorato et al. [37] for the occurrence of rogue waves in other physical disciplines. While several physical mechanisms have been invoked, a currently popular concept is the nonlinear focusing of energy associated with modulation instability, based on appropriate solutions of the focussing nonlinear Schrödinger equation (NLS), see [24] for instance amongst many other articles. In dimensional coordinates, the NLS equation is given by

$$i(A_t + c_g A_x) + \delta A_{xx} + \mu |A|^2 A = 0\,, \tag{5.1}$$

R. Grimshaw (✉)
Department of Mathematics, University College London, London, UK
e-mail: r.grimshaw@ucl.ac.uk

K.W. Chow • H.N. Chan
Department of Mechanical Engineering, University of Hong Kong, Pokfulam, Hong Kong
e-mail: kwchow@hku.hk; hnchan@connect.hku.hk

E. Tobisch (ed.), *New Approaches to Nonlinear Waves*, Lecture Notes in Physics 908, DOI 10.1007/978-3-319-20690-5_5

where $A(x,t)$ is the envelope amplitude of a sinusoidal wave with wavenumber k, frequency $\omega = \omega(k)$ and group velocity $c_g = \omega_k$. The coefficient $\delta = \omega_{kk}/2$ but the coefficient μ is system-dependent. The plane wave solution $A = A_0 \exp(i\mu|A_0|^2 t)$ is modulationally unstable when $\delta\mu > 0$, that is when Eq. (5.1) is focussing. Because the NLS equation arises in many other physical systems, notably nonlinear optics and Bose-Einstein condensates, it has been realized that rogue waves can also occur there, see [3] and the articles which follow. In particular, the various breather solutions of the focussing NLS equation have been invoked as models for rogue waves, with a special interest in the Peregrine breather [41], since this is spatially and temporally localized, see [8, 45] for instance. Indeed recently [24] demonstrated in the framework of the focussing NLS equation that a generic outcome of modulation instability was the generation of a family of Peregrine breathers.

While the focussing NLS equation is usually associated with short waves in deep water, rogue waves can also potentially arise in shallow water, see [27] for a possible tsunami context, or [26] for internal waves. Long waves are often modelled by the Korteweg-de Vries (KdV) equation or the extended KdV (eKdV) equation which contains both quadratic and cubic nonlinear terms, see [23] for instance. Here it is especially interesting that the asymptotic reduction of the KdV, or eKdV, equation to an NLS equation leads to the defocussing case for the KdV equation, or the eKdV when the cubic nonlinear term and the linear dispersive term have opposite signs, and hence modulational stability. But for the eKdV equation when the cubic nonlinear term and the linear dispersive term have the same sign, the asymptotic reduction leads to the focussing NLS equation and hence modulational instability, see [25].

In this Chapter we explore the connection between modulational instability and the possible existence of breathers in the context of this suite of KdV equations (Sect. 5.2), in a Boussinesq equation (Sect. 5.3) and in the Hirota-Satsuma version of a coupled KdV system (Sect. 5.4). As all these equations are integrable, the strategy we employ to find breathers is to first find a 2-soliton solution and then impose a complex-conjugate wavenumber on this solution. If the resulting outcome is a non-singular solution, then we have found a breather, but if it is singular then we infer that a useful breather solution does not exist. This is not a complete existence proof *per se*, and so does not rule out the possibility that there may be non-singular breather solutions which can be found by other methods, such as using the inverse scattering transform with a complex-conjugate pair of eigenvalues. Nevertheless it will be seen to be a simple and robust method to establish a connection between modulation instability and breathers.

5.2 Korteweg-de Vries Equations

In canonical form the extended KdV equation is

$$u_t + 6uu_x + 6\beta u^2 u_x + u_{xxx} = 0\,. \tag{5.2}$$

This is a KdV equation when $\beta = 0$, and an extended KdV equation when $\beta = \pm 1$, and is integrable in all cases.

5.2.1 Modulational Instability

In order to determine the criterion for modulation instability, we first exhibit the asymptotic reduction to an NLS equation, as obtained by Grimshaw [25]. Thus, we get that

$$u = \epsilon A(X,T)\exp(i\theta) + \text{c.c.} + \cdots\,, \tag{5.3}$$

$$\theta = kx - \omega t\,, \quad X = \epsilon(x - c_g t)\,, \quad T = \epsilon^2 t\,. \tag{5.4}$$

Here $\omega = \omega(k) = -k^3$ so that the group velocity $c_g = \omega_k = -3k^2$, and then the NLS equation (5.1) is given by

$$iA_T + \delta A_{XX} + \mu|A|^2 A = 0\,, \tag{5.5}$$

$$\delta = \frac{\omega_{kk}}{2} = -3k\,, \quad \mu = 6k(\frac{1}{k^2} - \beta)\,. \tag{5.6}$$

Thus the NLS is focussing ($\mu\delta > 0$) when $k^2\beta > 1$ and defocussing ($\mu\delta < 0$) otherwise. Thus it is defocussing and modulationally stable for $\beta = 0, -1$, but focussing and so modulationally unstable for $\beta = 1$ and also $k^2 > 1$.

5.2.2 Breathers

5.2.2.1 Korteweg-deVries Equation: $\beta = 0$

The 2-soliton solution is well-known. Here we present it using the Hirota bilinear form, see for instance [31], in terms of the far-field parameters γ_1, γ_2,

$$u = 2\{\log(f)\}_{xx}\,, \tag{5.7}$$

$$f = 1 + \exp(\phi) + \exp(\psi) + a_{12}\exp(\phi + \psi)\,, \tag{5.8}$$

$$\phi = \gamma_1(x - \gamma_1^2 t)\,, \quad \psi = \gamma_2(x - \gamma_2^2 t)\,, \quad a_{12} = \frac{(\gamma_1 - \gamma_2)^2}{(\gamma_1 + \gamma_2)^2}\,. \tag{5.9}$$

Without loss of generality, take $\gamma_2 > \gamma_1$. In the far field as $t \to \pm\infty$ the soliton limits are found by either fixing the phase ϕ and letting $\psi \to \mp\infty$ for the index 1, or fixing the phase ψ and letting $\phi \to \pm\infty$ for the index 2. The outcome is

$$f \sim 1 + \exp(\phi)\,, \quad t \to \infty\,, \quad f \sim 1 + a_{12}\exp(\phi) \quad t \to -\infty\,, \tag{5.10}$$

$$f \sim 1 + a_{12}\exp(\psi)\,, \quad t \to \infty\,, \quad f \sim 1 + \exp(\psi) \quad t \to -\infty\,. \tag{5.11}$$

Each of these are easily recognised as the corresponding 1-soliton solutions, but with a phase shift from $t \to -\infty$ to $t \to \infty$, given by

$$\exp(\Delta\phi), \exp(-\Delta\psi) = \frac{(\gamma_2 - \gamma_1)^2}{(\gamma_2 + \gamma_1)^2}\,. \tag{5.12}$$

The strategy for finding a breather solution is to put $\gamma_{1,2} = m \pm in$ where m, n are real-valued. Then (5.8) becomes

$$f = 1 + 2\exp(\theta)\cos(\Theta) + \tilde{a}_{12}\exp(2\theta)\,, \tag{5.13}$$

$$\theta = m(x - (m^2 - 3n^2)t)\,, \quad \Theta = n(x - (3m^2 - n^2)t)\,, \quad \tilde{a}_{12} = -\frac{n^2}{m^2}\,. \tag{5.14}$$

Although this does generate a solution, it is singular as now f can pass through zero and takes negative values as $\exp(\theta)$ increases. Thus, as expected, this procedure fails to find a non-singular breather solution.

5.2.2.2 Extended Korteweg-de Vries Equation: $\beta = -1$

Curiously, although the Hirota bilinear form for the modified KdV equation, that is Eq. (5.2) without a quadratic nonlinear term is quite well-known, there seem to be very few papers for this case, exceptions being [14, 31, 42, 47]. From [14] we extract the following expression

$$u = 2\{\log(\frac{G}{F})\}_x = 2\frac{FG_x - GF_x}{FG} \tag{5.15}$$

$$G = 1 + a_1\exp(\phi) + a_2\exp(\psi) + a_{12}\exp(\phi + \psi)\,, \tag{5.16}$$

$$F = 1 + b_1\exp(\phi) + b_2\exp(\psi) + b_{12}\exp(\phi + \psi)\,, \tag{5.17}$$

$$\phi = \gamma_1(x - \gamma_1^2 t)\,, \quad \psi = \gamma_2(x - \gamma_2^2 t)\,, \tag{5.18}$$

$$a_1 = 1 - \gamma_1\,, \quad a_2 = 1 - \gamma_2\,, \quad a_{12} = a_1 a_2\frac{(\gamma_1 - \gamma_2)^2}{(\gamma_1 + \gamma_2)^2}\,, \tag{5.19}$$

$$b_1 = 1 + \gamma_1\,, \quad b_2 = 1 + \gamma_2\,, \quad b_{12} = b_1 b_2\frac{(\gamma_1 - \gamma_2)^2}{(\gamma_1 + \gamma_2)^2}\,, \tag{5.20}$$

The far field behaviour can now be found as for the KdV case in the Sect. 5.2.2.1 and describes the interaction of two solitons in a similar way. Detailed descriptions can be found in [14, 47].

As in the Sect. 5.2.2.1 the strategy for finding a breather solution is to put $\gamma_{1,2} = m \pm in$ where m, n are real-valued. Then Eqs. (5.16) and (5.17) become

$$G = 1 + 2|a_1| \exp(\theta) \cos(\Theta + \arg[a_1]) + a_{12} \exp(2\theta), \tag{5.21}$$

$$F = 1 + 2|b_1| \exp(\theta) \cos(\Theta + \arg[b_1]) + b_{12} \exp(2\theta), \tag{5.22}$$

$$\theta = m(x - (m^2 - 3n^2)t), \quad \Theta = n(x - (3m^2 - n^2)t), \tag{5.23}$$

$$\tilde{a}_{12} = -|a_1|^2 \frac{n^2}{m^2}, \quad \tilde{b}_{12} = -|b_1|^2 \frac{n^2}{m^2}. \tag{5.24}$$

Thus, as for the KdV case in the Sect. 5.2.2.1 a solution has been found but it is singular as both F, G take zero values. This is expected as both the KdV and this extended KdV equation are modulationally stable.

5.2.2.3 Extended Korteweg-de Vries Equation: $\beta = 1$

Here the soliton and breather solutions can be found using a variety of methods, including the Darboux transformation, see [46], and the Hirota bilinear method, see [18]. The latter yields

$$u = 2\{\tan^{-1}(\frac{g}{f})\}_x = \frac{2}{f^2 + g^2}(fg_x - gf_x), \tag{5.25}$$

The 2-soliton solution with far-field parameters γ_1, γ_2 is given by, adapted by Grimshaw et al. [27] from Chow et al. [18],

$$g = 1 + s_1 a_1 \exp(\phi) + s_2 a_2 \exp(\psi) + s_1 s_2 a_{12} \exp(\phi + \psi), \tag{5.26}$$

$$f = 1 + s_1 b_1 \exp(\phi) + s_2 b_2 \exp(\psi) + s_1 s_2 b_{12} \exp(\phi + \psi), \tag{5.27}$$

$$\phi = \gamma_1(x - \gamma_1^2 t), \quad \psi = \gamma_2(x - \gamma_2^2 t), \tag{5.28}$$

$$a_n, b_n = \frac{1 \pm \gamma_n}{\sqrt{1 + \gamma_n^2}}, \quad n = 1, 2, \tag{5.29}$$

$$a_{12}, b_{12} = \frac{(\gamma_1 - \gamma_2)^2}{(\gamma_1 + \gamma_2)^2} \frac{[1 \pm (\gamma_1 + \gamma_2) - \gamma_1 \gamma_2]}{\sqrt{1 + \gamma_1^2}\sqrt{1 + \gamma_2^2}}. \tag{5.30}$$

Here $s_{1,2} = \pm 1$ corresponding to waves of elevation or depression, since for this case there are two families of 1-soliton solutions, one of elevation waves and one of depression waves. Again, the far field behavior can now be found as for the KdV

case in the Sect. 2.1 and describes the interaction of two solitons in a similar way. A detailed description can be found in [18, 27, 46].

Next breather solutions can be found by formally putting $\gamma_{1,2} = m \pm in$, $m, n > 0$ in Eqs. (5.26) and (5.27), see Eq. (14) in [46] or Eq. (13) in [18]. The outcome is, after adjusting the phases appropriately,

$$g = 1 - \frac{n^2}{m^2} \frac{1 + 2m - (m^2 + n^2)}{1 - 2m + (m^2 + n^2)} \exp(2\theta) + 2(\xi \cos(\Theta) - \eta \sin(\Theta)) \exp(\theta) , \tag{5.31}$$

$$f = 1 - \frac{n^2}{m^2} \frac{1 - 2m - (m^2 + n^2)}{1 - 2m + (m^2 + n^2)} \exp(2\theta) + 2 \cos(\Theta) \exp(\theta) , \tag{5.32}$$

$$\theta = m(x - (m^2 - 3n^2)t) , \quad \Theta = n(x - (3m^2 - n^2)t) , \tag{5.33}$$

$$\xi = \frac{1 - (m^2 + n^2)}{1 - 2m + m^2 + n^2} , \quad \eta = \frac{2n}{1 - 2m + m^2 + n^2} . \tag{5.34}$$

This solution was first found by Pelinovsky and Grimshaw [40] using the inverse scattering transform, see also [25], and exists for all m, n. The breather has two phases, θ and Θ. It is localized in the phase θ and propagates with a speed $c = m^2 - 3\,n^2$, and oscillates in the phase Θ with a frequency Ω, $\Omega = n(3\,m^2 - n^2)$. In the reference frame moving with speed c, set $y = x - ct$ and then $\Theta = n(y - 2(m^2 + n^2)t)$ and hence oscillates with a frequency $2\,n(m^2 + n^2)$. In the limit $n \gg m$ there are many crests inside the envelope and it resembles an envelope wave packet. In the opposite limit when $n \ll m$, it resembles a 2-soliton interaction, see Fig. 5 of [46] or Fig. 4 of [18].

5.3 Boussinesq Model

There are several Boussinesq equations used to describe waves in shallow water, but most are not integrable, and hence explicit 2-soliton solutions are not available. An exception is, see [30],

$$u_{tt} - u_{xx} + 3(u^2)_{xx} - u_{xxxx} = 0 . \tag{5.35}$$

Although formally it can describe two-way wave propagation, in fact its asymptotic derivation from the full water wave equations invokes a one-way hypothesis in the reduction of the nonlinear term. It also has the disadvantage that its linear dispersion relation is temporally unstable for high wave numbers. Nevertheless we shall use it here as an example of the connection between modulational instability and breathers for a higher-order in time case.

5.3.1 Modulational Instability

The derivation of the reduction to an NLS equation follows the same lines as that for the KdV models described in [25]. That is, insert the asymptotic expansion (5.3) into (5.35). First note that the linear dispersion relation is $\omega^2 = k^2 - k^4$ and so we must choose $k^2 < 1$ to ensure linear stability. Then at the second order we find that the second harmonic and mean terms are

$$u_2 = \epsilon^2\{\mu_2 A^2 \exp(2i\theta) + \bar{\mu}_2 \bar{A}^2 \exp(-2i\theta) + \mu_0 |A|^2\} + \cdots , \tag{5.36}$$

$$\mu_2 = -\frac{1}{k^2} , \quad \mu_0 = \frac{6(1-k^2)}{k^2(3-4k^2)} . \tag{5.37}$$

Note that there is a long-short wave resonance at $k^2 = 3/4$. At the third order we obtain the required NLS equation (5.1) for A where

$$\mu = \frac{3k^2}{2\omega}(\mu_2 + \mu_0) = \frac{3(3-2k^2)}{2\omega(3-4k^2)} . \tag{5.38}$$

$$\omega\delta = \frac{\omega\omega_{kk}}{2} = \frac{-3k^2 + 2k^4}{2(1-k^2)} . \tag{5.39}$$

Over the range of interest when $k^2 < 1$, there is modulation stability when $k^2 < 3/4$ but modulation instability when $3/4 < k^2 < 1$.

5.3.2 Breathers

Here the Hirota method to exhibit the 2-soliton solution is, see [30],

$$u = 2\{\log(f)\}_{xx} , \tag{5.40}$$

$$f = 1 + \exp(\phi) + \exp(\psi) + a_{12}\exp(\phi + \psi) , \tag{5.41}$$

$$\phi = \gamma_1(x - s_1 v_1 t) , \quad \psi = \gamma_2(x - s_2 v_2 t) , \tag{5.42}$$

$$v_{1,2} = (1 + \gamma_{1,2}^2)^{1/2} , \quad s_{1,2} = \pm 1 , \tag{5.43}$$

$$\begin{aligned} a_{12} &= \frac{(s_1 v_1 - s_2 v_2)^2 + 3(\gamma_1 - \gamma_2)^2}{(s_1 v_1 - s_2 v_2)^2 + 3(\gamma_1 + \gamma_2)^2} \\ &= \frac{(\gamma_1 - \gamma_2)^2}{(\gamma_1 + \gamma_2)^2} \frac{(\gamma_1 + \gamma_2)^2 + 3(s_1 v_1 + s_2 v_2)^2}{(\gamma_1 - \gamma_2)^2 + 3(s_1 v_1 + s_2 v_2)^2} . \end{aligned} \tag{5.44}$$

Making use of the similarity in structure with the KdV case and the expressions given by Eqs. (5.7) and (5.8), the far field behavior can now be found as for the KdV case in the Sect. 5.2.2.1. The choice of signs $s_{1,2}$ determines whether the collision is overtaking or head-on.

Next seek a breather solution by putting $\gamma_{1,2} = m \pm in$ as before, using first the case when both $s_1 = s_2 = 1$ corresponding to a bifurcation from a collision of two solitons moving in the same direction. Then we get that

$$f = 1 + 2\exp(\theta)\cos(\Theta) + \tilde{a}_{12}\exp(2\theta)\,, \tag{5.45}$$

$$\phi, \psi = \theta \pm i\Phi\,, \tag{5.46}$$

$$\tilde{a}_{12} = \frac{-3n^2 - I^2}{3m^2 - I^2} = -\frac{n^2}{m^2}\{\frac{m^2 + 3R^2}{-n^2 + 3R^2}\}\,, \tag{5.47}$$

$$R = \mathrm{Re}[v_1]\,, \quad I = \mathrm{Im}[v_1]\,, \quad v_1 = (1 + m^2 - n^2 + 2imn)^{1/2}\,. \tag{5.48}$$

It is useful to note here that $RI = mn$ and that $R^2 - I^2 = 1 + m^2 - n^2$, and it then follows that $I^2 = -K + (K^2 + m^2n^2)^{1/2}$, $2K = 1 + m^2 - n^2$. For this expression to be non-singular for all θ, Θ it is required that $\tilde{a}_{12} > 1$, and it is readily shown that this is only possible if $I^2 > 3\,m^2$. This condition can be realized when $n^2 > 3/4 + m^2$. Significantly note that if we identify n with the wavenumber k in the modulational stability calculation, then this can be regarded as a bifurcation as m^2 increases from zero above $k^2 = 3/4$ for modulation instability.

If instead $s_1 = -s_2 = 1$ corresponding to a bifurcation from a collision of two solitons moving in the opposite direction then a similar expression is obtained but instead

$$\tilde{a}_{12} = \frac{R^2 - 3n^2}{R^2 + 3m^2} = \frac{n^2}{m^2}\{\frac{m^2 - 3I^2}{n^2 + 3I^2}\}\,. \tag{5.49}$$

It can be shown that $\tilde{a}_{12} < 1$ for all m, n and hence this is a singular breather.

5.4 Hirota-Satsuma Model

A coupled Korteweg-de Vries model

$$u_t - a(u_{xxx} + 6uu_x) = 2bvv_x\,, \quad v_t + v_{xxx} + 3uv_x = 0\,. \tag{5.50}$$

was proposed in [32] to describe the interaction of two long waves with different dispersion relations. It is important to note that these equations are coupled only through the nonlinear terms, and that there is a family of solutions with $v \equiv 0$ and u satisfying a KdV equation. They are integrable when $a = 1/2$, see [20, 35]. Essentially u scales with v^2 (formally exact for the 1-soliton solution, see below) so

that the equation for v is analogous to a modified KdV equation, while the equation for u is analogous to a KdV equation. Also for every solution (u, v) there is another solution $(u, -v)$. Thus in the linearized theory there are two modes. One has $v = 0$ and a dispersion relation $\omega = ak^3$ and the other has $u = 0$ and a dispersion relation $\omega = -k^3$.

5.4.1 Modulational Instability

As for the KdV models presented in the Sect. 5.2.1 we seek asymptotic solutions of the form

$$(u, v) = \epsilon(A(X, T), B(X, T)) \exp(i\theta) + \text{c.c.} + \cdots, \tag{5.51}$$

$$\theta = kx - \omega t, \quad X = \epsilon(x - c_g t), \quad T = \epsilon^2 t. \tag{5.52}$$

First we consider the case when the linear dispersion relation is $\omega = ak^3$ and then $c_g = 3ak^2$. Then $B = 0$ to all orders in ϵ and indeed this case reduces to $v \equiv 0$. Hence the outcome is the same well-known NLS equation for a KdV alone, that is (5.5) with $\delta = 3ak$ and $\mu = -3a/2k$. Thus the NLS equation is defocussing and there is modulational stability.

In the second case the linear dispersion relation is $\omega = -k^3$ and then $c_g = -3k^2$. In this case u is order ϵ^2 and to leading order consists only of second harmonic and mean terms,

$$u = \epsilon^2\{\mu_2 B^2 \exp(2i\theta) + \bar{\mu}_2 \bar{B}^2 \exp(-2i\theta) + \mu_0 |B|^2\} + \cdots, \tag{5.53}$$

$$\mu_2 = \frac{b}{(1 + 4a)k^2}, \quad \mu_0 = \frac{2b}{3k^2}. \tag{5.54}$$

Note that μ_2 is singular when $4a = -1$ indicating a second harmonic resonance. Then the equation for B, the first harmonic component of v, is

$$iB_T - 3kB_{XX} + 3k\mu_2 B^2 \bar{B} - 3k\mu_0 |B|^2 B = 0. \tag{5.55}$$

Substituting for the coefficients μ_2, μ_0 leads to the NLS equation

$$iB_T - 3kB_{XX} + \mu |B|^2 B = 0, \quad \mu = \frac{b(1 - 8a)}{k(1 + 4a)}. \tag{5.56}$$

This is modulationally unstable when $b(1 - 8a)(1 + 4a) < 0$. The case of main interest here is when $a = 1/2$ and then $\mu = -b/k$ and there is modulation instability when $b > 0$. In general, there is modulation instability when $b > 0$ for $a > 1/8$ and $a < -1/4$, and when $b < 0$ for $-1/4 < a < 1/8$.

5.4.2 Breathers

The Hirota method applied to the system of Eq. (5.50) can be found in several places, see [1, 32] for instance,

$$u = 2\{\log f\}_{xx}\,, \quad v = \frac{g}{f}\,. \tag{5.57}$$

The 1-soliton solution is

$$f = 1 + \exp(2P)\,, \quad g = 2\alpha \exp(P)\,, \tag{5.58}$$

$$P = \gamma(x - \gamma^2 t)\,, \quad \alpha^2 = -\frac{2\gamma^4(1+4a)}{b}\,, \tag{5.59}$$

$$u = 2\gamma^2 \mathrm{sech}^2(P)\,, \quad v = \alpha\,\mathrm{sech}(P)\,, \tag{5.60}$$

Note that there are two solutions here as α can be either positive or negative, and that these exist only when $b(1+4a) < 0$ ($b < 0$ when $a = 1/2$).

Next, the 2-soliton solution when $a = 1/2$ can be written in the form

$$f = 1 + \exp(2P_1) + \exp(2P_2) + \alpha_{11}\exp(P_1 + P_2) + \alpha_{22}\exp(2P_1 + 2P_2)\,, \tag{5.61}$$

$$g = 2\alpha_1 \exp(P_1)\{1 + \alpha_{12}\exp(2P_2)\} + 2\alpha_2 \exp(P_2)\{1 + \alpha_{21}\exp(2P_1)\}\,, \tag{5.62}$$

$$\alpha_{11} = \frac{16\gamma_1^2\gamma_2^2}{(\gamma_1+\gamma_2)^2(\gamma_1^2+\gamma_2^2)}\,, \alpha_{22} = \frac{(\gamma_1-\gamma_2)^4}{(\gamma_1+\gamma_2)^4}\,, \tag{5.63}$$

$$\alpha_1^2 = -\frac{6\gamma_1^4}{b}\,, \quad \alpha_2^2 = -\frac{6\gamma_2^4}{b}\,, \quad \alpha_{12} = \alpha_{21} = \frac{(\gamma_1-\gamma_2)^2}{(\gamma_1+\gamma_2)^2}\,, \tag{5.64}$$

Like the 1-soliton solution, this exists only when $b < 0$.

A breather solution can be found by putting $\gamma_{1,2} = m \pm in$ and so

$$P_{1,2} = \theta \pm i\Theta\,, \quad \theta = m(x - (m^2 - 3n^2)t)\,, \quad \Theta = n(x - (3m^2 - n^2)t)\,. \tag{5.65}$$

$$f = 1 + 2\exp(2\theta)\cos(2\Theta) + \alpha_{11}\exp 2\theta + \alpha_{22}\exp 4\theta\,, \tag{5.66}$$

$$g = 2\alpha_1 \exp(\theta + i\Theta)\{1 + \alpha_{12}\exp(2(\theta - i\Theta))\} + \mathrm{c.c}\,, \tag{5.67}$$

$$\alpha_{11} = \frac{2(m^2+n^2)^2}{m^2(m^2-n^2)}\,, \quad \alpha_{22} = \frac{n^4}{m^4}\,, \quad \alpha_1^2 = -\frac{6(m+in)^4}{b}\,, \quad \alpha_{12} = -\frac{n^2}{m^2}\,. \tag{5.68}$$

Note that unlike the 2-soliton solution, there is now no restriction on the sign of b. However, in order for $f > 0$ for all θ, Θ, we require that either $m^2 > n^2$ when $\alpha_{11} > 1$, or that $n^2 > 3m^2$ when $\alpha_{11} < 0,\ 2\alpha_{22} > 2 - \alpha_{11}$. Like the breathers of the extended KdV equation described in the Sect. 5.2.2.3, this breather moves steadily at a speed $m^2 - 3n^2$ and in that reference frame oscillates with a frequency $2n(m^2 + n^2)$. Figure 5.1 shows a typical plot of this breather over a half period.

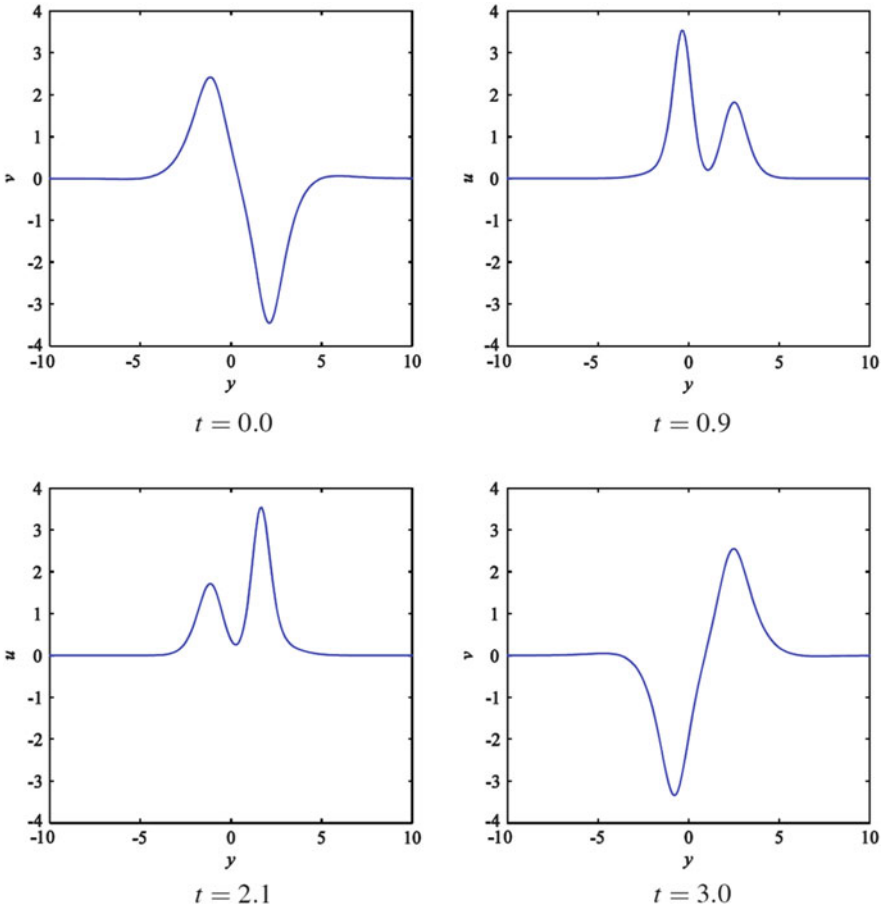

Fig. 5.1 A plot of the breather (5.66) and (5.67) with $m = 1.0, n = 0.5, b = -1$ as a function of $y = x - ct, c = m^2 - 3n^2$ over a half period. (**a**) $t = 0.0$; (**b**) $t = 0.9$; (**c**) $t = 2.1$; (**d**) $t = 3.0$

5.5 Discussion

In this Chapter we have examined the connection between modulational instability and non-singular breathers in the context of several long-wave models. For the KdV equations discussed in the Sect. 5.2 we confirm the well-known result that such breathers only exist when the NLS asymptotic reduction leads to modulational instability, that is when $\beta = 1$ in Eq. (5.2) so that the cubic nonlinear term is non-zero and has the same sign as the linear dispersive term. In the Sect. 5.3 we discuss the Boussinesq equation (5.40) which is modulationally unstable and confirm that then there is indeed a non-singular breather solution. Then in the Sect. 5.4 we discuss the Hirota-Satsuma version of a coupled KdV system given by Eq. (5.50), and find the rather surprising outcome that although this system is modulationally unstable when $b > 0$, non-singular breathers can exist for both signs of b. This unexpected result may be related to the rather unusual structure of this coupled system where a scaling $u \sim v^2$ (formally exact for the 1-soliton solution) suggests that the u-equation behaves as a KdV equation which is modulationally stable, but the v-equation behaves as a modified KdV equation which can support a breather.

Although the focus here has been on a suite of long-wave models it is useful to review the analogous properties for various NLS equations and some other short wave models. The literature is voluminous but a few representative examples will prove to be illuminating in this line of currently very active research. We focus on those studies where analytical closed form solutions are obtained, rather than those using perturbation methods, or numerical simulations. For the simplest NLS model given by Eq. (5.1), the Peregrine breather and the second order rogue wave solutions were derived using the Darboux transformation by Akhmediev et al. [4]. Similar analysis was performed for the integrable extension of the NLS with third order dispersion, that is the Hirota equation, by Ankiewicz et al. [5]. The close connection between the criteria for the occurrence of rogue waves and modulation instability, when the dispersion and nonlinearity have the same sign in Eq. (5.1) has been recognized by Zakharov and Gelash [51]. A close relative of the Hirota equation is the Sasa-Satsuma equation, another integrable wave packet evolution model with third order dispersion. This apparent similarity is at times deceptive, as the Sasa-Satsuma equation typically has a much more complicated analytical structure, and rogue waves can be obtained only in special parameter regimes [6].

For coupled NLS systems obeying the same criteria, attention is usually focused on the Manakov model where analytical solutions are feasible. Rational solutions like the Peregrine breather which are localized in both space and time have been derived using the Darboux transformation by Degasperis and Lombardo [19]and He et al. [29] and using the Hirota bilinear method by Vishnu et al. [49]. A broader theoretical perspective is obtained by regarding breathers as almost a superposition of a periodic array of rogue waves, see [49]. Interestingly, such localized entities have been generated in a water wave tank for deep water conditions, see [29].

However, modulational instability can still occur for Manakov systems when the nonlinearity and dispersion in each component are of opposite signs. One possible condition is that the coefficient of cross-phase modulation (XPM) must exceed the coefficient of self-phase modulation (SPM), see [2]. Another alternative is to implement a group velocity difference between the two wave packets, see [7]. This feature is equivalent to a scenario where the wavenumbers of the carrier packet differ from each other. It is relevant to note that these discoveries were made about twenty years before the current intensive interest in rogue waves. The intimate connection between modulation instability and rogue waves can indeed be well illustrated for this parameter regime. For Manakov models (identical SPM and XPM) with dispersion and nonlinearity of opposite signs, rogue waves do arise whenever modulation instability occurs [7]. In terms of field measurements, these modes have been proposed to model "three-sister" rogue wave formation observed in the Great Lakes region of North America, see [16].

Rogue wave modes for coupled Hirota and Sasa-Satsuma equations have also been investigated, although the picture there is less complete. Localized modes for equal and unequal background amplitudes of the two participating waveguides have been computed for a coupled Hirota system, see [15]. The Sasa-Satsuma equation is even more intriguing, as exotic wave profiles involving "twisted" and "W-shaped" structures have been found even for the single component case, see [13, 52]. These novel structures continue to exist in the coupled case, see [53].

Further, in recent ongoing work, we have found that a difference in the group velocity components can by itself generate modulational instability. Thus, the coupled Hirota equations are given by [17, 39]

$$iA_t - i\delta A_x + \frac{A_{xx}}{2} - \sigma(|A|^2 + |B|^2)A + i\lambda\{A_{xxx} - 3\sigma(|A|^2 + |B|^2)A_x - 3\sigma(A^*A_x + B^*B_x)A\} = 0\,, \tag{5.69}$$

$$iB_t + i\delta B_x + \frac{B_{xx}}{2} - \sigma(|A|^2 + |B|^2)B + i\lambda\{B_{xxx} - 3\sigma(|A|^2 + |B|^2)B_x - 3\sigma(A^*A_x + B^*B_x)B\} = 0\,. \tag{5.70}$$

If $B = 0$, (5.69) reduces to the ordinary Hirota equation [5], whereas $\lambda = 0$ yields the Manakov equations. From earlier studies [49], we expect $\sigma > 0 (\sigma < 0)$ will give a regime of modulational stability (instability) respectively. The parameter δ measures a difference in the group velocities of the wave packets, a "detuning" parameter. Similar to the situation in the Manakov equations, we expect that the presence of δ will induce modulation instabilities in parameter ranges which would otherwise indicate stability. Thus consider the plane wave solutions $A = B = \rho \exp\{-2i\sigma\rho^2 t\}$. Then imposing small perturbations of the form $\exp\{i(rx - st)\}$, a

fourth order dispersion relation is obtained. With $c = s/r$ and small r, the dispersion relation is reduced to

$$\begin{aligned} & c^4 + 36\lambda\sigma\rho^2 c^3 - 2(\delta^2 - 234\lambda^2\sigma^2\rho^4 + \sigma\rho^2)c^2 \\ & -12\lambda\sigma\rho^2(3\delta^2 - 216\lambda^2\sigma^2\rho^4 + 2\sigma\rho^2)c \\ & +(\delta^2 - \sigma\rho^2 - 72\lambda^2\sigma^2\rho^4)^2 - \sigma^2\rho^4 - 216\lambda^2\sigma^3\rho^6 = 0. \end{aligned} \tag{5.71}$$

The connection to the existence of breathers is an ongoing study. Here we display a few examples highlighting the possibility of modulational instability in the regime with dispersion and nonlinearity of opposite signs ($\sigma > 0$) in Eqs. (5.69) and (5.70).

For NLS models incorporating the next order nonlinear terms, the most commonly studied ones are the derivative NLS equations. Rogue waves of the Kaup-Newell equation (KN) were obtained using the Darboux transformation [28], while those of the Chen-Lee-Liu equation (CLL) were obtained using the Hirota bilinear transform [12]. Note that the KN and CLL models are related by a gauge transformation. For the CLL model, the criterion for the onset of rogue waves matches exactly with that for modulation instability, see [12]. For many other members of this NLS family of evolution equations, the connections among modulational instability, homoclinic solutions and localized modes have not yet been fully examined, although rogue waves have been obtained explicitly through the Darboux and other transformations, see for instance the Kundu-derivative-NLS equation considered by Shan et al. [43] (Table 5.1).

Several further classes of NLS type-models are also relevant in this context. One group of such equations involves cubic-quintic nonlinearity, see [37, 54], and even fourth order linear dispersion, see [50]. Another example is the Maxwell-Bloch system, where a complex valued envelope is coupled to another complex valued field (polarization) and a real valued scalar field (population inversion). This system arises in the femtosecond pulse propagation through an erbium doped fiber, see [34].

A close relative of the Manakov system is a set of coherently coupled NLS equations, where the phase of each individual component is crucial, in sharp contrast to those incoherently coupled systems such as the Manakov equations. Here the analysis is more complicated, see [48]. Finally, most studies in the literature are for evolution equations in $1 + 1$ spatial and temporal dimensions. An important exception is the Davey-Stewartson system, where the interaction of a wave packet

Table 5.1 Numerical examples of stable and unstable regimes

σ	ρ	λ	δ	
1	1	0.1	0	Stable
1	1	0.1	0.1	Unstable
1	1	0.1	1	Unstable
1	1	0.1	1.5	Stable
1	1	0.5	0.1	Stable

and the mean flow governs the dynamics of slowly modulated surface water waves in two mutually perpendicular horizontal dimensions, see [36].

A most remarkable feature about the recent intensive interest in rogue waves is that these theoretical predications can be verified in both fluid dynamic and optical experiments. As well as the traditional context, where the classical Benjamin-Feir instability predicts the growth of sidebands, higher-order N-soliton solutions can also be observed in carefully controlled hydrodynamic wave groups. Irreversible spectral broadening has been observed, and was termed a "hydrodynamic supercontinuum", by analogy with a similar generation of broad range of frequencies in optics, see [11]. The lowest order rogue wave, the Peregrine breather, has been measured in an experimental setting by Chabchoub et al. [9] and Shemer and Alperovich [44], and compared with higher order versions of NLS, such as the Dysthe equation. Super rogue waves with amplitude up to five times the background have been observed in a wave tank by Chabchoub et al. [10]. An overview on the theory of breathers and modulation instability in the optics context has recently been given [21]. Finally we note that in this article and in most of the works cited here the connection between modulational instability and breathers is circumstantial, that is co-existence of each phenomenon. An exception is [24] where it is shown that at least for the NLS model given by Eq. (5.1) a wide class of initial conditions of a modulated plane wave generically leads to the formation of a wave train of Peregrine breathers.

Acknowledgements Partial financial support has been provided by the Research Grants Council through contract HKU 711713E.

References

1. Ablowitz, M., Segur, H.: Solitons and the Inverse Scattering Transform. SIAM, Philadelphia (1981)
2. Agrawal, G.P.: Modulation instability induced by cross-phase modulation. Phys. Rev. Lett. **59**, 880–883 (1987)
3. Akhmediev, N., Pelinovsky, E.: Editorial, introductory remarks on discussion & debate: rogue waves—towards a unifying concept? Eur. Phys. J. **185**, 1–4 (2010) [Special Topics]
4. Akhmediev, N., Ankiewicz, A., Soto-Crespo, J.M.: Rogue waves and rational solutions of the nonlinear Schrodinger equation. Phys. Rev. E **80**, 026601 (2009)
5. Ankiewicz, A., Soto-Crespo, J.M., Akhmediev, N.: Rogue waves and rational solutions of the Hirota equation. Phys. Rev. E **81**, 046602 (2010)
6. Bandelow, U., Akhmediev, N.: Persistence of rogue waves in extended nonlinear Schrodinger equations: integrable Sasa-Satsuma case. Phys. Lett. A **376**, 1558–1561 (2012)
7. Baronio, F., Conforti, M., Degaperis, A., Lombardo, S., Onorato, M., Wabnitz, S.: Vector rogue waves and baseband modulation instability in the defocusing regime. Phys. Rev. Lett. **113**, 034101 (2014)
8. Chabchoub, A., Vitanov, N., Hoffmann, N.: Experimental evidence for breather type dynamics in freak waves. Proc. Appl. Math. Mech. **10**, 495–496 (2010)
9. Chabchoub, A., Hoffmann, N., Akhmediev, N.: Rogue wave observation in a water wave tank. Phys. Rev. Lett. **106**, 204502 (2011)

10. Chabchoub, A., Hoffmann, N., Onorato, M., Akhmediev, N.: Super rogue raves: observation of a higher-order breather in water waves. Phys. Rev. X **2**, 011015 (2012)
11. Chabchoub, A., Hoffmann, N., Onorato, M., Genty, G., Dudley, J.M., Akhmediev, N.: Hydrodynamic supercontinuum. Phys. Rev. Lett. **111**, 054104 (2013)
12. Chan, H.N., Chow, K.W., Kedziora, D.J., Grimshaw, R.H.J., Ding, E.: Rogue wave modes for a derivative nonlinear Schrodinger model. Phys. Rev. E **89**, 032914 (2014)
13. Chen, S.: Twisted rogue-wave pairs in the Sasa-Satsuma equation. Phys. Rev. E **88**, 023202 (2013)
14. Chen, Y., Liu, P.L.-F.: On interfacial waves over random topography. Wave Motion **24**, 169–184 (1996)
15. Chen, S., Song, L.Y.: Rogue waves in coupled Hirota systems. Phys. Rev. E **87**, 0321910 (2013)
16. Chen, S., Soto-Crespo, J.M., Grelu, P.: Dark three-sister rogue waves in normally dispersive optical fibers with random birefringence. Opt. Express **22**, 27632–27642 (2014)
17. Chow, K.W.: Periodic waves for a system of coupled, higher order nonlinear Schrödinger equations with third order dispersion. Phys. Lett. A **308**, 426–431 (2003)
18. Chow, K.W., Grimshaw, R., Ding, E.: Interactions of breathers and solitons in the extended Korteweg de Vries equation. Wave Motion **43**, 158–166 (2005)
19. Degasperis, A., Lombardo S.: Rational solitons of wave resonant-interaction models. Phys. Rev. E **88**, 052914 (2013)
20. Dodd, R., Fordy, A.: On the integrability of a system of coupled KdV equations. Phys. Lett. A **89**, 168–170 (1982)
21. Dudley, J.M., Dias, F., Erkintalo, M., Genty, G.: Instabilities, breathers and rogue waves in optics. Nat. Photonics **8**, 755–764 (2014)
22. Dysthe, K., Krogstad, H.E., Muller, P.: Oceanic rogue waves. Annu. Rev. Fluid Mech. **40**, 287–310 (2008)
23. Grimshaw, R.: Internal solitary waves. In: Grimshaw, R. (ed.) Environmental Stratified Flows, pp. 1–27. Kluwer, Boston (2001)
24. Grimshaw, R., Tovbis, A.: Rogue waves: analytical predictions. Proc. R. Soc. **469**, 20130094 (2013)
25. Grimshaw, R., Pelinovsky, D., Pelinovsky E.: Wave group dynamics in weakly nonlinear long-wave models. Phys. D **159**, 35–52 (2001)
26. Grimshaw, R., Pelinovsky E., Talipova, T., Sergeeva, A.: Rogue internal waves in the ocean: long wave model. Eur. Phys. J. **185**, 195–208 (2010) [Special Topics]
27. Grimshaw, R.H.J., Hunt, J.C.R., Chow, K.W.: Changing forms and sudden smooth transitions of tsunami waves. J. Ocean Eng. Mar. Energy **1** (2), 145 – 156 (2015)
28. Guo, G., Ling, L., Liu, Q.P.: Higher-order solutions and generalized Darboux transformations of derivative nonlinear Schrodinger equations. Stud. Appl. Math. **130**, 317–344 (2012)
29. He, J., Guo, L., Zhang, Y., Chabchoub, A.: Theoretical and experimental evidence of non-symmetric doubly localized rogue waves. Proc. R. Soc. A **470**, 20140318 (2014)
30. Hirota, R.: Exact *N*-soliton solutions of the wave equation of long waves in shallow-water and in nonlinear lattices. J. Math. Phys. **14**, 810–814 (1973)
31. Hirota, R.: Reduction of soliton equations in bilinear form. Phys. D **18**, 161–170 (1986)
32. Hirota, R., Satsuma, J.: Soliton solutions of a coupled Korteweg-de Vries equation. Phys. Lett. A **85**, 8–9 (1981)
33. Kharif, C., Pelinovsky, E., Slunyaev, A.: Rogue waves in the ocean. In: Advances in Geophysical and Environmental Mechanics and Mathematics, vol. 14. Springer, Berlin (2009)
34. Li, C., He, J., Porsezian, K.: Rogue waves of the Hirota and the Maxwell-Bloch equations. Phys. Rev. E. **87**, 012913 (2013)
35. Oevel, W.: On the integrability of the Hirota-Satsuma system. Phys. Lett. A **94**, 404–407 (1983)
36. Ohta, Y., Yang, J.: Dynamics of rogue waves in the Davey-Stewartson II equation. J. Phys. A Math. Theor. **46**, 105202 (2013)
37. Onorato, M., Residori, S., Bortolozzo, U., Montina, A., Arecchi, F.T.: Rogue waves and their generating mechanisms in different physical contexts. Phys. Rep. **528**, 47–89 (2013)

38. Osborne, A.R.: Nonlinear Ocean Waves and the Inverse Scattering Transform. Elseveier, San Diego (2010)
39. Park, Q.H., Shin, H.J.: Higher order nonlinear optical effects on polarized dark solitons. Opt. Commun. **178**, 233–244 (2000)
40. Pelinovsky, D.E., Grimshaw, R.H.J.: Structural transformation of eigenvalues for a perturbed algebraic soliton potential. Phys. Lett. A **229**, 165–172 (1997)
41. Peregrine, D.H.: Water waves, nonlinear Schrodinger equations and their solutions. J. Aust. Math. Soc. B **25**, 16–43 (1983)
42. Perelman, T.L., Fridman, A.X., Elyashevich, M.M.: A modified Korteweg-de Vries equation in electrohydrodynamics. J. Exp. Theor. Phys. **39**, 643–646 (1974)
43. Shan, S., Li, C., He, J.: On rogue wave in the Kundu-DNLS equation. Commun. Nonlinear Sci. Numer. Simul. **18**, 3337–3349 (2013)
44. Shemer, L., Alperovich, L.: Peregrine breather revisited. Phys. Fluids **25**, 051701 (2013)
45. Shrira, V.I., Georgiaev, V.V.: What makes the Peregrine soliton so special as a prototype of freak waves. J. Eng. Math. **67**, 478–509 (2010)
46. Slunyaev, A.V.: Dynamics of localized waves with large amplitude in a weakly dispersive medium with a quadratic and positive cubic nonlinearity. J. Exp. Theor. Phys. **92**, 529–534 (2001)
47. Slunyaev, A.V., Pelinovsky, E.N.: Dynamics of large-amplitude solitons. J. Exp. Theor. Phys. **89** 173–181 (1999)
48. Vishnu, P.N., Senthilvelan, M.: Generalized Darboux transformation and n-th order rogue wave solution of a general coupled nonlinear Schrodinger equations. Commun. Nonlinear Sci. Numer. Simul. **20**, 401–420 (2015)
49. Vishnu, P.N., Senthilvelan, M., Lakshmanan, M.: Akhmediev breathers, Ma solitons and general breathers from rogue waves: a case study in the Manakov system. Phys. Rev. E **88**, 022918 (2013)
50. Wang, L.H., Porsezian, K., He, J.S.: Breather and rogue wave solutions of a generalized nonlinear Schrodinger equation. Phys. Rev. E **87**, 053202 (2013)
51. Zakharov, V., Gelash, A.: Freak waves as a result of modulation instability. Proc. IUTAM **9**, 165–175 (2013)
52. Zhao, L., Li, S.C., Ling, L.: Rational W-shaped solitons on a continuous wave background in the Sasa-Satsuma equation. Phys. Rev. E **89**, 023210 (2014)
53. Zhao, L., Yang, Y.Z., Ling, L.: Localized waves on continuous wave background in a two-mode nonlinear fiber with high-order effects. J. Phys. Soc. Jpn. **83**, 104401 (2014)
54. Zhaqilao, Z.: On N-th order rogue wave solution to the generalized nonlinear Schrodinger equation. Phys. Lett. A **377**, 855–859 (2013)

Chapter 6
Hamiltonian Framework for Short Optical Pulses

Shalva Amiranashvili

Abstract Physics of short optical pulses is an important and active research area in nonlinear optics. In this Chapter we theoretically consider the most extreme representatives of short pulses that contain only several oscillations of electromagnetic field. Description of such pulses is traditionally based on envelope equations and slowly varying envelope approximation, despite the fact that the envelope is not "slow" and, moreover, there is no clear definition of such a "fast" envelope. This happens due to another paradoxical feature: the standard (envelope) generalized nonlinear Schrödinger equation yields very good correspondence to numerical solutions of full Maxwell equations even for few-cycle pulses, the thing that should not be.

In what follows we address ultrashort optical pulses using Hamiltonian framework for nonlinear waves. As it appears, the standard optical envelope equation is just a reformulation of general Hamiltonian equations. In a sense, no approximations are required, this is why the generalized nonlinear Schrödinger equation is so effective. Moreover, the Hamiltonian framework contributes greatly to our understanding of "fast" envelopes, ultrashort solitons, stability and radiation of optical pulses. Even the inclusion of dissipative terms is possible making the Hamiltonian approach an universal theoretical tool also in extreme nonlinear optics.

6.1 Introduction

6.1.1 Ultrashort Pulses

Remarkable recent progress in pulse generation with femtosecond [4, 17] and even sub-femtosecond [20, 33, 57, 65] durations has resulted in rapidly growing interest to ultrashort or so-called few-cycle optical pulses. These pulses are yielded by modern mode-locking techniques, e.g., a readily accessible pulse duration of 6 fs at a near-infrared wavelength of 900 nm corresponds to two optical cycles. On the

S. Amiranashvili (✉)
Weierstrass Institute for Applied Analysis and Stochastics, 10117 Berlin, Germany
e-mail: shalva@wias-berlin.de

E. Tobisch (ed.), *New Approaches to Nonlinear Waves*, Lecture Notes in Physics 908, DOI 10.1007/978-3-319-20690-5_6

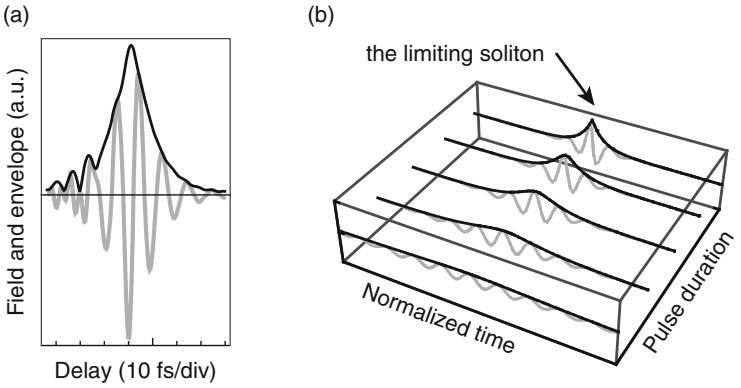

Fig. 6.1 Examples of ultrashort pulses. (**a**) An exemplary single-cycle pulse resulting from pulse compression in a ZBLAN fiber (numerical solution of the general pulse propagation equation, [18]). (**b**) A family of solitons in a cubic media with the Drude dispersion law (exact solutions of the simplified propagation equation, [6, 62]). The shortest limiting soliton contains approximately one and half oscillations at half maximum

other hand, spatially localized field "bursts" with extreme amplitudes and short durations can self-organize in a variety of nonlinear systems at unexpectedly high rate [56]. They are referred to as rogue waves. Similar bursts have been observed in nonlinear fibers and interpreted as optical rogue waves [37, 63]. Here optical setting provides researches with a non-destructive tool to measure statistics of such ultrashort extreme events. Two examples of numerically calculated ultrashort pulses yielded by different pulse propagation models are shown in Fig. 6.1.

Turning to the applications one should stress that few-cycle pulses yield possibility to excite and follow fast relaxation processes with the spatial resolution of order of one micron (a single wavelength) and to study light-matter interactions at extreme intensity levels. For instance, currently available temporal and spatial confinement results in peak intensities higher than $10^{15}\,\mathrm{W/cm^2}$ for pulse energies of the order of one microjoule [17]. The corresponding field strength is comparable to that inside atoms. In particular, intense few-cycle optical pulses are used to trigger and trace chemical reactions, to test high-speed semiconductor devices, and for precision processing of materials. More sophisticated applications include modeling of event horizons of white and black holes [58], recent measurements of Hawking radiation [9, 24], and recent experimental observations of the negative-frequency radiation [11, 59].

Theory of the ultrashort optical pulses has been developed in several directions. For small space scales, e.g., propagation lengths of several tenths of a wavelength, one can address numerical solution of the fundamental Maxwell equations equipped by a suitable medium response model, e.g., Bloch equations [32, 36, 53, 55, 61]. On the other hand, if some approximate but simple medium dispersion law applies, it becomes possible to derive a simplified propagation equation. A typical example is the so-called short pulse equation [10, 38, 43, 60]. Other settings yield the

modified Korteweg-de Vries and sine-Gordon equations [8, 46, 48, 49], and more sophisticated models [47, 51, 52]. However, simple models are not available for the real-world dispersion laws and especially in the presence of dissipative effects. An envelope equation is the method of choice for realistic situations, either the fundamental nonlinear Schrödinger equation or its generalizations [2, 3, 15]. These envelope equations have an unexpected behavior: (1) they seem to describe few- and even sub-cycle pulses that should have no envelope [16, 30, 31, 40] and (2) they show good correspondence to the solutions of more general unidirectional field equations, which are independent of the envelope concept [34, 39, 41, 42].

In what follows we consider pulse propagation using the Hamiltonian point of view for systems with infinitely many degrees of freedom [70, 73]. The promoted approach applies when pulses, otherwise arbitrary, propagate in the transparency window of optical materials, such that dissipation provides small contribution to pulse dynamics. As it appears, the generalized envelope equation is just equivalent to the underlying Maxwell equation [5], and the complex envelope is just a combination of the corresponding canonical coordinate and momentum. Apart from explanation of the paradoxical durability of the envelope equations, the Hamiltonian approach provides a convenient framework for investigation of integrals of motion, solitons, and numerical solutions.

6.1.2 Envelope Definition

From the mathematical side a correct description of the ultrafast phenomena is a challenge because the involved time-scales may differ in many orders of magnitude making direct numerical solution of the fundamental Maxwell and material equations impractical. A common approach to such multi-scale optical systems is based on the slowly varying envelope approximation (SVEA). For instance, let us consider a scalar electric field $E(t)$ at some given point in space. The SVEA postulates possibility of representation

$$E(t) = \frac{1}{2}\Psi(t)e^{-i\omega_0 t} + \text{c.c.} = |\Psi|\cos(\omega_0 t - \arg\Psi) \tag{6.1}$$

where ω_0 is referred to as the carrier frequency and the complex-valued function $\Psi(t)$ is the envelope. The SVEA assumes that both $|\Psi|$ and $\arg\Psi$ are slow, i.e., $\Psi(t)$ does not change on the time scale $1/\omega_0$.

It is usually sufficient to think about optical pulses in terms of observed quantities such as instant power. The latter is proportional to $|\Psi|^2$ and independent on $\arg\Psi$ for a "normal" multi-cycle pulse like one in Fig. 6.2a. Also the local frequency

$$\omega = \omega_0 - \frac{d}{dt}\arg\Psi \tag{6.2}$$

takes no notice of a global shift in phase.

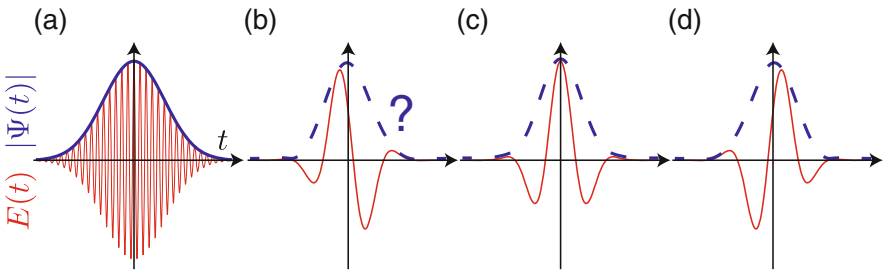

Fig. 6.2 Pulse field (*red*) and its envelope (*blue*) are shown for a gaussian pulse shape. (**a**) For a multi-cycle pulse both $|\Psi|$ is well-defined and the actual value of $\arg\Psi$ in Eq. (6.1) is unimportant. (**b–d**) On the contrary, to derive the envelope from the field of a single-cycle pulse, one should revisit the general envelope definition and specify how the (*dashed*) blue line is calculated from the red one. Moreover, $\arg\Psi$, the quantity that determines an exact "position" of the pulse field inside the envelope, noticeably affects the peak electric field calculated from Eq. (6.1)

The situation is different for a few-cycle pulse: $\arg\Psi$ significantly affects the peak electric field that is actually experienced by an atom (Fig. 6.2b–d). It is clear that an adequate propagation model for such an ultrashort pulse should treat field phase with a great care.

Another difficulty appears if we consider a standard derivation [1, 12, 54] of the SVEA propagation equation that includes the following typical step:

$$\frac{d^2E}{dt^2}+\omega_0^2E=\frac{1}{2}\left(\frac{d^2\Psi}{dt^2}-2i\omega_0\frac{d\Psi}{dt}\right)e^{-i\omega_0 t}+\text{c.c.}\approx-i\omega_0\frac{d\Psi}{dt}e^{-i\omega_0 t}+\text{c.c.}, \qquad (6.3)$$

in which one ignores the second derivative of $\Psi(t)$ because the latter is "slow". This is why all envelope equations are first-order equations, which are simple and suitable for numerical treatment. For an ultrashort pulse, however, both the field and the envelope coexist and evolve on the same scale (Fig. 6.2b–d). Strictly speaking, the envelope may remain stationary for a single stable soliton, but it is subject to quick changes for, e.g., colliding pulses or higher-order solitons. Therefore approximation (6.3) becomes invalid and the derivation of the first-order propagation equation should be reconsidered.

Finally, the very definition (6.1) is ambivalent for short pulses. Namely, if the SVEA applies one can invert (6.1) and express the complex envelope in terms of the field

$$2E(t)e^{i\omega_0 t}=\Psi(t)+\Psi^*(t)e^{2i\omega_0 t}\quad\Rightarrow\quad\Psi(t)=2\left\langle E(t)e^{i\omega_0 t}\right\rangle, \qquad (6.4)$$

where $\langle\rangle$ denotes a sliding average over several oscillations of the carrier field. Here, the SVEA indicates that $\langle\Psi(t)\rangle$ remains unaffected and that $\langle\Psi^*(t)e^{2i\omega_0 t}\rangle$ vanishes. Clearly Eq. (6.4) cannot be applied to a short pulse with the fast envelope and definition of the complex envelope should be reconsidered.

One possible redefinition of the complex envelope explores the fact that the operator in Eq. (6.3) can be factorized

$$\frac{d^2E}{dt^2} + \omega_0^2 E = \left(\omega_0 - i\frac{d}{dt}\right)\left(\omega_0 + i\frac{d}{dt}\right)E. \tag{6.5}$$

Using this factorization we define a generalized complex envelope $\overleftrightarrow{\Psi}(t)$ directly from the equation

$$E + i\omega_0^{-1}\frac{dE}{dt} = \overleftrightarrow{\Psi}\, e^{-i\omega_0 t}, \tag{6.6}$$

such that the standard relations of the theory of linear oscillations

$$E = |\overleftrightarrow{\Psi}|\cos(\omega_0 t - \arg\overleftrightarrow{\Psi}), \qquad \frac{dE}{dt} = -\omega_0|\overleftrightarrow{\Psi}|\sin(\omega_0 t - \arg\overleftrightarrow{\Psi}), \tag{6.7}$$

are just forced by the above definition of $\overleftrightarrow{\Psi}$ (see [13]).

Equation (6.1) still holds and Eq. (6.3) is replaced with

$$\frac{d^2E}{dt^2} + \omega_0^2 E = \omega_0\left(\omega_0 - i\frac{d}{dt}\right)\overleftrightarrow{\Psi}\, e^{-i\omega_0 t} = -i\omega_0\frac{d\overleftrightarrow{\Psi}}{dt}e^{-i\omega_0 t} \tag{6.8}$$

The latter relation is exact, one doesn't have to neglect the second derivative contrary to Eq. (6.3). Moreover, the definition (6.6) is very convenient if combined with the standard sliding average over the fast time. For instance, considering an oscillator with a small "driving force" $f(E, dE/dt)$

$$\frac{d^2E}{dt^2} + \omega_0^2 E = f\left(E, \frac{dE}{dt}\right) \tag{6.9}$$

one immediately obtains an exact equation

$$i\omega_0\frac{d\overleftrightarrow{\Psi}}{dt} + e^{i\omega_0 t} f\left(\frac{\overleftrightarrow{\Psi}\, e^{-i\omega_0 t} + \text{c.c.}}{2}, \frac{-i\omega_0\overleftrightarrow{\Psi}\, e^{-i\omega_0 t} + \text{c.c.}}{2}\right) = 0, \tag{6.10}$$

where the further averaging of the driving force is trivial for any polynomial or Taylor expanded $f(E, dE/dt)$.

On the other hand, if the succeeded averaging of Eq. (6.10) is inappropriate, the new-defined envelope always contains unphysical quickly oscillating terms. Indeed, combining (6.1) and (6.6) we obtain

$$\overleftrightarrow{\Psi} = \Psi + \frac{i}{2\omega_0}\frac{d\Psi}{dt} + \frac{i}{2\omega_0}\frac{d\Psi^*}{dt}e^{2i\omega_0 t} \tag{6.11}$$

where the second-harmonic term on the right-hand-side appears not because of physical reasons, like quadratic nonlinearities, but simply because of the unlucky definition (6.6).

Another alternative for envelope definition was suggested by Gabor. The real-valued $E(t)$ is replaced by a complex-valued $\mathcal{E}(t)$ following the instruction [28]:

> – ... Suppress the amplitudes belonging to negative frequencies, and multiply the amplitudes of positive frequencies by two.

The complex field $\mathcal{E}(t)$ will be referred to as the complex or analytic signal. In what follows, we consider $e^{-i\omega t}$ as harmonic oscillation with (angular) frequency ω. A monochromatic wave with wave vector $\mathbf{k}$ and frequency ω is defined by $e^{i(\mathbf{kr}-\omega t)}$. Consequently, we write the continuous Fourier transform of $E(t)$ as

$$E(\omega) = \int_{-\infty}^{\infty} E(t) e^{i\omega t} dt \qquad \text{and} \qquad E(t) = \int_{-\infty}^{\infty} E(\omega) e^{-i\omega t} \frac{d\omega}{2\pi}, \tag{6.12}$$

and the two latter equations become completely symmetric if one switches to the physical frequency $f = \omega/(2\pi)$. According to Gabor's rule, the analytic signal is given by the relation

$$\mathcal{E}(t) = \int_{0}^{\infty} E(\omega) e^{-i\omega t} \frac{d\omega}{\pi}, \tag{6.13}$$

where

$$E(t) = \frac{\mathcal{E}(t) + \mathcal{E}^*(t)}{2}, \tag{6.14}$$

and $\mathcal{E}^*(t)$ accumulates contributions of all negative frequencies in $E(t)$.

Of course, the analytic signal can be defined without any reference to frequencies

$$\mathcal{E}(t) = E(t) + \frac{i}{\pi} \fint_{-\infty}^{\infty} \frac{E(\tau) d\tau}{\tau - t}, \tag{6.15}$$

where integration in the last term is referred to as the Hilbert transform and is performed using the principal value. We would like to stress the following key points.

1. The analytic signal behaves as expected for the envelope in all simple cases. Taking for instance a carrier cosine oscillation modulated with frequency ν

$$E(t) = \cos(\nu t) \cos(\omega_0 t) = \frac{1}{4} (e^{i\nu t} + e^{-i\nu t})(e^{i\omega_0 t} + e^{-i\omega_0 t}), \tag{6.16}$$

with $\omega_0 > \nu > 0$ we derive

$$\mathcal{E}(t) = \frac{1}{2}\left[e^{-i(\omega_0+\nu)t} + e^{-i(\omega_0-\nu)t}\right] = \cos \nu t e^{-i\omega_0 t}. \tag{6.17}$$

In particular, $|\mathcal{E}(t)|$ is a natural envelope for $E(t)$.

2. Moreover, there is an intrinsic relation between the definitions (6.1) and (6.13). To show this let us assume that the spectrum of the envelope $\Psi(t)$ in Eq. (6.1) completely belongs to the interval $[-\omega_0, \omega_0]$. The assumption is much less restrictive than the standard SVEA with its narrow spectral lines. This relaxed assumption still guaranties that $\Psi(t)e^{-i\omega_0 t}$ contains only positive (and $\Psi(t)e^{i\omega_0 t}$ only negative) frequency components. We immediately derive that

$$\mathcal{E}(t) = \Psi(t)e^{-i\omega_0 t} \tag{6.18}$$

such that the complex envelope $\Psi(t)$ is uniquely defined by the analytic signal $\mathcal{E}(t)$ provided that one has a reasonable definition of the carrier frequency ω_0.

3. The precise definition of ω_0 in Eq. (6.18) may differ and is not critical. A reasonable choice is to avoid fast oscillations of $\Psi(t)$ as good as possible; $\arg \mathcal{E}$ is then approximated by a straight line, $\arg \mathcal{E} \approx -\omega_0 t$. The approximation is perfect for a many-cycle pulse like one in Fig. 6.3a, but not for the few-cycle pulses in Fig. 6.3b–d. However, deviations of $\arg \mathcal{E}$ from $-\omega_0 t$ are localized "outside" the pulses. The splitting of $\mathcal{E}(t)$ into $\Psi(t)$ and $e^{-i\omega_0 t}$ is then still reasonable [16].

4. The values of $|\mathcal{E}|^2$ can be used as weights when approximating $\arg \mathcal{E}$ by $-\omega_0 t$. The resulting expression [19]

$$\omega_0 = \frac{\int_0^\infty \omega |\mathcal{E}(\omega)|^2 d\omega}{\int_0^\infty |\mathcal{E}(\omega)|^2 d\omega} \tag{6.19}$$

will be assumed in what follows.

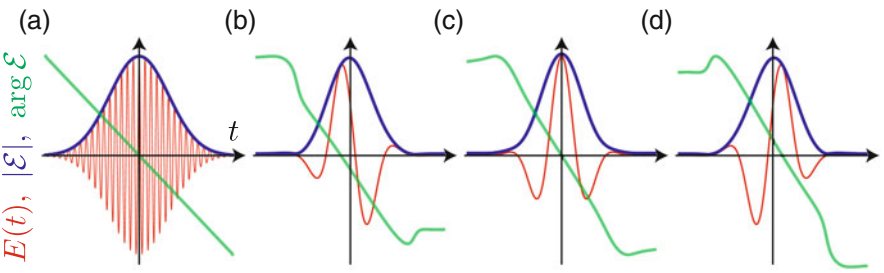

Fig. 6.3 Use of the analytic signal: $|\mathcal{E}|$ (*blue lines*) and $\arg \mathcal{E}$ (*green lines*) are shown for pulses from Fig. 6.2. For a multi-cycle pulse (**a**) $\arg \mathcal{E}$ is perfectly approximated by $-\omega_0 t$ in favor of Eq. (6.18). Even for the few-cycle pulses (**b–d**) the regions with "fast" $\Psi(t)$ are localized outside the pulses

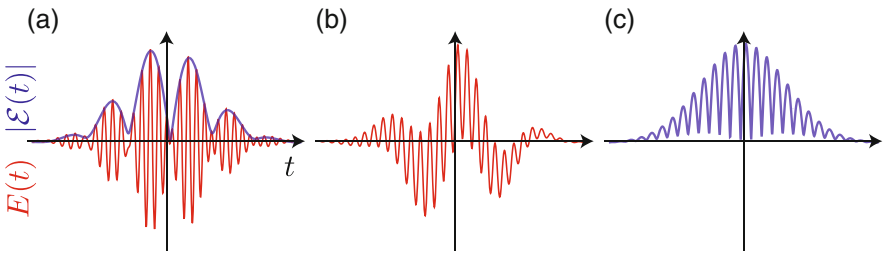

Fig. 6.4 The field $E(t)$ (*red*) and its analytic signal $|\mathcal{E}(t)|$ (*blue*) for superposition of two gaussian pulses. (**a**) The pulses have similar frequencies, the analytic signal is perfectly shaped to the corresponding beat oscillations. (**b**–**c**) The pulses have considerably different frequencies. The field (**b**) and the envelope (**c**) look very different, the latter is neither smooth nor slow

5. The analytic signal can be formally considered for a complex argument $t + it'$

$$\mathcal{E}(t + it') = \int_0^\infty E(\omega) e^{-i\omega t} e^{\omega t'} \frac{d\omega}{\pi}, \tag{6.20}$$

where the resulting function is holomorphic for $t' < 0$ and quickly vanishes for $t' \to -\infty$. In other words, a real $E(t)$ is equipped by an imaginary part such that the resulting complex $\mathcal{E}(t)$ is holomorphic in a half-plane of "complex times". The analytic signal can be investigated using all powerful tools provided by complex analysis. For instance, it is subject to Kramers–Kronig relations having full similarity to the standard response functions [35, 45].

The above properties of the analytic signal are so attractive that $\mathcal{E}(t)$ is usually considered as the "correct" envelope [14, 67]. Unfortunately, Gabor's definition has its own difficulties. First, the analytic signal is neither smooth nor slow when the field in question contains considerably different frequency components, like in Fig. 6.4b–c. This always happens in, e.g., the so-called optical supercontinuum [22]. Of course, correct description of an optical field with wide spectrum is of crucial importance for ultrashort pulses as well. Another difficulty appears due to nonlinearities. Even if $\mathcal{E}(t)$ does contain exclusively positive frequencies, any simple nonlinear expression (e.g., the standard cubic term $|\mathcal{E}|^2\mathcal{E}$) always contains a small negative frequency tail. One has either to get by with such an addition to the complex signal or cut it off. Both possibilities are not quite appropriate. (a) The negative-frequency tail may quickly grow due to nonlinear resonant interactions making definition (6.13) questionable. What is more astonishing, it can lead to observable physical effects like the negative-frequency radiation [11, 59]. (b) Cutting off the negative frequencies (i.e., taking only the positive-frequency-part of $|\mathcal{E}|^2\mathcal{E}$), makes propagation equations unnecessarily complicated for analytical treatment and explanation of the effects just mentioned.

Our approach to description of ultrashort pulses explores the fact that pulse field in optics is not an abstract observable, the field results from well-known

fundamental equations. Moreover, in the region of frequencies that is of interest for, e.g., pulse transmission in optical fibers, these equations are, with good precision, dissipation-free. Ignoring dissipation in the first step, one can (1) find the Poisson bracket for the fundamental equations and (2) introduce the canonical coordinate $Q(\mathbf{r}, t)$ and momentum $P(\mathbf{r}, t)$. Both quantities are continuous fields with possibly more than one component. They are governed by canonical equations in which the standard derivatives are replaced with functional derivatives

$$\partial_t Q = \frac{\delta \mathscr{H}}{\delta P} \qquad \text{and} \qquad \partial_t P = -\frac{\delta \mathscr{H}}{\delta Q}, \tag{6.21}$$

the Poisson bracket $\{P, Q\}$ is proportional to a generalized function. Using Eq. (6.21) one can treat pulse propagation applying the technique that has been developed for Hamiltonian systems with infinitely many degrees of freedom [70, 73–75]. Dissipative terms are included in the final equations as small perturbations.

In particular, a natural complex-valued field variable for the envelope-type description is given by a suitable combination of $Q(\mathbf{r}, t)$ and $P(\mathbf{r}, t)$. The combination is taken in such a way that the Hamiltonian $\mathscr{H}[Q, P]$ takes some simple form, the latter is guaranteed by the fact that in the frequency domain the optical field is described by a set of coupled weakly nonlinear oscillators. The above definition (6.6) is an example of such a combination of position and momentum, more generally the variables in question are classical analogies of the creation and annihilation operators in the second quantization formalism.

Actually there are many competing complex variables that transform the quadratic part of the Hamiltonian to a standard form, a fundamental feature that dictates the next step: to make a sequence of canonical transforms to remove quick oscillations from the complex field. This occurs in quite similar to the classical Hamiltonian perturbation theory that step by step kills non-resonant nonlinearities [44, 50].

6.2 Poisson Brackets

In the this section we briefly outline some key facts from the Hamiltonian mechanics of discrete [7, 44] and continuous [25, 26, 70] systems. The Poisson bracket is regarded as the cornerstone of the theory.

6.2.1 Discrete Systems

We consider a phase-space manifold with a finite number of local coordinates $\xi = (\xi^1, \xi^2, \ldots \xi^N)$. The key mathematical structure on the manifold is given by the

so-called Poisson bracket between observables, scalar functions on the phase-space. Namely, having two observables $f(\xi)$ and $g(\xi)$ one can calculate the third one, $\{f, g\}$, which is bilinear with respect to its arguments. Moreover, the following three rules should be respected

$$\{f, g\} + \{g, f\} = 0, \tag{6.22}$$

$$\{f, gh\} = \{f, g\}h + g\{f, h\}, \tag{6.23}$$

$$\{f, \{g, h\}\} + \{h, \{f, g\}\} + \{g, \{h, f\}\} = 0, \tag{6.24}$$

where, the latter two equations are referred to as the Leibniz and Jacobi identities respectively. In addition, the Poisson bracket should vanish if one of its arguments is a constant observable.

To specify such a Poison structure one may first set the brackets between the coordinates

$$\Lambda^{\alpha\beta}(\xi) = \{\xi^\alpha, \xi^\beta\}, \qquad 1 \le \alpha, \beta \le N, \tag{6.25}$$

and then define the bracket between two arbitrary observables by setting

$$\{f, g\} = \sum_{\alpha,\beta} \Lambda^{\alpha\beta} \partial_\alpha f \partial_\beta g, \tag{6.26}$$

where ∂_α stays for $\partial/\partial\xi^\alpha$. Equation (6.22) simply indicates that $\Lambda^{\alpha\beta}$ is antisymmetric. The Leibniz rule (6.23) is satisfied automatically because $\{f, \ \}$ is a first-order differential operator, its special case

$$\{\xi^\alpha, \ \} = \sum_\beta \Lambda^{\alpha\beta} \partial_\beta \tag{6.27}$$

will play an important role in what follows. The Jacobi identity is first tested for the coordinates

$$\{\xi^\alpha, \{\xi^\beta, \xi^\gamma\}\} + \{\xi^\beta, \{\xi^\gamma, \xi^\alpha\}\} + \{\xi^\gamma, \{\xi^\alpha, \xi^\beta\}\} = 0, \tag{6.28}$$

where all Greek indices change from 1 to N.

Equation (6.28) in accord with (6.25) and (6.27) is equivalent to the following nonlinear matrix relation

$$\Lambda^{\alpha\mu} \partial_\mu \Lambda^{\beta\gamma} + \Lambda^{\beta\mu} \partial_\mu \Lambda^{\gamma\alpha} + \Lambda^{\gamma\mu} \partial_\mu \Lambda^{\alpha\beta} = 0, \tag{6.29}$$

the latter identity should be checked directly. The task is simplified for a non-degenerate Λ. One can change to the inverse Λ^{-1} and obtain for its components,

$\Lambda^{-1}_{\alpha\beta}(\xi)$, that Eq. (6.29) is equivalent to a linear relation

$$\partial_\alpha \Lambda^{-1}_{\beta\gamma} + \partial_\beta \Lambda^{-1}_{\gamma\alpha} + \partial_\gamma \Lambda^{-1}_{\alpha\beta} = 0 \quad \Leftrightarrow \quad d\left(\sum_{\alpha,\beta} \Lambda^{-1}_{\alpha\beta} d\xi^\alpha \wedge d\xi^\beta\right) = 0, \tag{6.30}$$

such that a non-singular Poisson structure yields a symplectic structure and vice versa [7]. We prefer the formulation in which the symplectic structure is the derived one. The Poisson language is promoted because $\Lambda^{\alpha\beta}(\xi)$ may be degenerate, destroying the symplectic form (6.30) and making a direct test of Eq. (6.29) more complicated. In any case, after Eq. (6.29) is satisfied, the general Eq. (6.24) is satisfied as well because all newly appearing terms that do not participate in (6.29) contain second derivatives and cancel each other due to the antisymmetry condition (6.22).

In order to define dynamical equations we specify a special observable, the Hamiltonian $\mathscr{H}(\xi)$, and consider the following system of equations

$$\frac{d\xi^\alpha}{dt} = \{\mathscr{H}, \xi^\alpha\} \qquad \text{or} \qquad \frac{d\xi^\alpha}{dt} = -\sum_\beta \Lambda^{\alpha\beta}\partial_\beta \mathscr{H}. \tag{6.31}$$

In particular, one can check that time evolution of any observable $f(\xi)$ along the solutions of the system (6.31) is yielded by the equation

$$\frac{df}{dt} = \{\mathscr{H}, f\}, \tag{6.32}$$

where for the sake of brevity our observables have no explicit time dependence. The special relation $\{\mathscr{H}, f\} = 0$ implies that f is an integral of motion for the Hamiltonian system (6.31).

Now we consider a situation where $\Lambda^{\alpha\beta}$ is degenerate. This, e.g., happens for any odd N. For instance, if all components $\Lambda^{\alpha\beta}$ are constants and we have found a kernel vector n_β such that

$$\sum_\beta \Lambda^{\alpha\beta} n_\beta \equiv 0, \tag{6.33}$$

then we have found an integral of motion $\mathscr{C} = \sum_\alpha n_\alpha \xi^\alpha$ simply because

$$\frac{d\mathscr{C}}{dt} = \frac{d}{dt}\left(\sum_\alpha n_\alpha \xi^\alpha\right) = -\sum_{\alpha,\beta} n_\alpha \Lambda^{\alpha\beta}\partial_\beta \mathscr{H} = \sum_{\alpha,\beta} \Lambda^{\alpha\beta} n_\beta \partial_\alpha \mathscr{H} = 0. \tag{6.34}$$

The latter integral conserves for any Hamiltonian $\mathscr{H}$ due to the degeneracy of Λ. The conservation law is of geometric nature and independent of the choice of

specific system: phase trajectories just cannot leave the hyperplane $\sum_\alpha n_\alpha \xi_\alpha = \text{const}$ on which they started.

This so-called Casimir integral $\mathscr{C}$ is defined by the relation $\{\mathscr{H}, \mathscr{C}\} = 0$ that should apply to any $\mathscr{H}$. In particular, we will see that pulse area is a geometric integral of motion. Notice that the degeneracy of the Poisson bracket may be eliminated. For instance, one can introduce a reduced Hamiltonian system directly on a fixed hyperplane $\sum_\alpha n_\alpha \xi^\alpha = \text{const}$ to get rid of the degenerate degree of freedom. The trick will be used below.

Dealing with Eq. (6.31), it might be useful to take N independent observables

$$\Xi^\alpha = \Xi^\alpha(\xi^1, \xi^2, \dots \xi^N), \qquad 1 \le \alpha \le N \tag{6.35}$$

and consider them as the new coordinates. Now one has to calculate the Poisson bracket between the new coordinates

$$\{\Xi^\alpha, \Xi^\beta\} = \sum_{\mu\nu} \Lambda^{\mu\nu} \frac{\partial \Xi^\alpha}{\partial \xi^\mu} \frac{\partial \Xi^\beta}{\partial \xi^\nu}, \qquad 1 \le \mu, \nu \le N, \tag{6.36}$$

and set

$$\{f, g\} = \sum_{\alpha,\beta} \{\Xi^\alpha, \Xi^\beta\} \frac{\partial f}{\partial \Xi^\beta} \frac{\partial g}{\partial \Xi^\beta}. \tag{6.37}$$

Indeed, the latter equation is compatible with the definition (6.26) because

$$\begin{aligned} \sum_{\alpha,\beta} \{\Xi^\alpha, \Xi^\beta\} \frac{\partial f}{\partial \Xi^\alpha} \frac{\partial g}{\partial \Xi^\beta} &= \sum_{\alpha,\beta,\mu,\nu} \Lambda^{\mu\nu} \frac{\partial \Xi^\alpha}{\partial \xi^\mu} \frac{\partial \Xi^\beta}{\partial \xi^\nu} \frac{\partial f}{\partial \Xi^\alpha} \frac{\partial g}{\partial \Xi^\beta} \\ &= \sum_{\mu,\nu} \{\xi^\mu, \xi^\nu\} \frac{\partial f}{\partial \xi^\mu} \frac{\partial g}{\partial \xi^\nu}, \end{aligned} \tag{6.38}$$

or, in other words, $\{\xi^\mu, \xi^\nu\}$ is a second-order tensor and the Poisson bracket (6.26) is an invariant convolution [21]. Therefore after switching to the new variables we still deal with the same set of Hamiltonian equations

$$\frac{d\Xi^\alpha}{dt} = \{\mathscr{H}, \Xi^\alpha\} \qquad \text{or} \qquad \frac{d\Xi^\alpha}{dt} = -\sum_\beta \{\Xi^\alpha, \Xi^\beta\} \frac{\partial \mathscr{H}}{\partial \Xi^\beta}, \tag{6.39}$$

where both $\mathscr{H}$ and $\{\Xi^\alpha, \Xi^\beta\}$ are now expressed using the new coordinates.

One natural application of the latter equations is to simplify the Poisson bracket by choosing the most suitable coordinates. Another possibility is to preserve the bracket by setting $\{\Xi^\alpha, \Xi^\beta\} = \{\xi^\alpha, \xi^\beta\}$ and to simplify $\mathscr{H}$ instead. One can even

first simplify the bracket and then preserve the (simplified) bracket and simplify the Hamiltonian, as in the canonical perturbation theory [50].

6.2.2 Complex Variables

The most simple nontrivial example of a Hamiltonian system occurs at $N = 2$ with $\xi^1 = q$ and $\xi^2 = p$, where by construction

$$\Lambda = \begin{pmatrix} \{q,q\} & \{q,p\} \\ \{p,q\} & \{p,p\} \end{pmatrix} = \begin{pmatrix} 0 & -1 \\ 1 & 0 \end{pmatrix} \quad \Rightarrow \quad \{f,g\} = \frac{\partial f}{\partial p}\frac{\partial g}{\partial q} - \frac{\partial f}{\partial q}\frac{\partial g}{\partial p}. \tag{6.40}$$

Equation (6.31) indicates that each Hamiltonian $\mathscr{H}(q,p)$ generates a system

$$\frac{dq}{dt} = \frac{\partial \mathscr{H}}{\partial p} \qquad \text{and} \qquad \frac{dp}{dt} = -\frac{\partial \mathscr{H}}{\partial q}, \tag{6.41}$$

which is a standard set of two Hamiltonian equations. They can be transformed into a single complex equation using the following variable [64], c.f. Eq. (6.6)

$$\mathfrak{z} = \frac{q + ip}{\sqrt{2}}, \tag{6.42}$$

where

$$\{\mathfrak{z},\mathfrak{z}\} = \{\mathfrak{z}^*,\mathfrak{z}^*\} = 0 \quad \text{and} \quad \{\mathfrak{z},\mathfrak{z}^*\} = i. \tag{6.43}$$

The derivatives with respect to $\mathfrak{z}$ (Wirtinger derivatives [68]) are defined by the natural requirement

$$\frac{\partial \mathscr{H}}{\partial q}dq + \frac{\partial \mathscr{H}}{\partial p}dp \equiv \frac{\partial \mathscr{H}}{\partial \mathfrak{z}}d\mathfrak{z} + \frac{\partial \mathscr{H}}{\partial \mathfrak{z}^*}d\mathfrak{z}^*, \tag{6.44}$$

such that

$$\frac{\partial \mathscr{H}}{\partial \mathfrak{z}} = \frac{1}{\sqrt{2}}\left(\frac{\partial \mathscr{H}}{\partial q} - i\frac{\partial \mathscr{H}}{\partial p}\right) \quad \text{and} \quad \frac{\partial \mathscr{H}}{\partial \mathfrak{z}^*} = \frac{1}{\sqrt{2}}\left(\frac{\partial \mathscr{H}}{\partial q} + i\frac{\partial \mathscr{H}}{\partial p}\right). \tag{6.45}$$

One can derive a new expression for the Poisson bracket

$$\{f,g\} = \{\mathfrak{z},\mathfrak{z}^*\}\frac{\partial f}{\partial \mathfrak{z}}\frac{\partial g}{\partial \mathfrak{z}^*} + \{\mathfrak{z}^*,\mathfrak{z}\}\frac{\partial f}{\partial \mathfrak{z}^*}\frac{\partial g}{\partial \mathfrak{z}} = i\left(\frac{\partial f}{\partial \mathfrak{z}}\frac{\partial g}{\partial \mathfrak{z}^*} - \frac{\partial f}{\partial \mathfrak{z}^*}\frac{\partial g}{\partial \mathfrak{z}}\right), \tag{6.46}$$

and the following complex equivalent of the Hamiltonian equations (6.41):

$$i\frac{d\mathfrak{z}}{dt} = \frac{\partial \mathscr{H}}{\partial \mathfrak{z}^*}. \tag{6.47}$$

A continuous analogue of (6.46) and (6.47) will play an important role for optical systems in what follows.

Here we should stress that the same Eqs. (6.46) and (6.47) can be derived for many different definitions of the complex variable. The only thing that matters is the bracket. For instance, one can rescale Eq. (6.42) and set

$$a = \frac{1}{\sqrt{2}}\left(Cq + \frac{ip}{C^*}\right) \quad \text{with} \quad C \in \mathbb{C}, \tag{6.48}$$

check that

$$\{a, a\} = \{a^*, a^*\} = 0, \qquad \{a, a^*\} = i, \tag{6.49}$$

and immediately conclude that

$$\{f, g\} = i\left(\frac{\partial f}{\partial a}\frac{\partial g}{\partial a^*} - \frac{\partial f}{\partial a^*}\frac{\partial g}{\partial a}\right), \qquad i\frac{da}{dt} = \frac{\partial \mathscr{H}}{\partial a^*}, \tag{6.50}$$

where

$$q = \frac{1}{\sqrt{2}}\left(\frac{a}{C} + \frac{a^*}{C^*}\right), \qquad \frac{\partial \mathscr{H}}{\partial a^*} = \frac{1}{\sqrt{2}}\left(\frac{1}{C^*}\frac{\partial \mathscr{H}}{\partial q} + iC\frac{\partial \mathscr{H}}{\partial p}\right).$$
$$p = \frac{i}{\sqrt{2}}(Ca^* - C^*a), \tag{6.51}$$

The freedom in the definition of the complex variable can be used to simplify $\mathscr{H}(a, a^*)$. In our case, the most important Hamiltonian corresponds to nonlinear oscillator

$$\mathscr{H} = \frac{p^2}{2m} + \frac{kq^2}{2} + \mathscr{H}_{\text{nonl}}(q, p), \tag{6.52}$$

where one can set $C = \sqrt[4]{km}$ with

$$a = \frac{1}{\sqrt{2}}\left(q\sqrt[4]{km} + \frac{ip}{\sqrt[4]{km}}\right), \tag{6.53}$$

and obtain that

$$\mathscr{H} = \omega a a^* + \mathscr{H}_{\text{nonl}}(a, a^*), \qquad i\frac{da}{dt} = \omega a + \frac{\partial}{\partial a^*}\mathscr{H}_{\text{nonl}}(a, a^*), \tag{6.54}$$

where $\omega = \sqrt{k/m}$ is the linear frequency.

These results are readily extended to any even N. The canonical Poisson bracket requires special coordinates consisting of $N/2$ generalized positions q_i and $N/2$ generalized momentums p_i, where by construction

$$\begin{aligned} &\{q_i, q_j\} = 0, \\ &\{p_i, p_j\} = 0, \end{aligned} \qquad \{p_i, q_j\} = \begin{cases} 1 & \text{for } i = j, \\ 0 & \text{for } i \neq j, \end{cases} \qquad 1 \leq i, j \leq N/2. \tag{6.55}$$

In other words,

$$\Lambda = \begin{pmatrix} 0 & -I \\ I & 0 \end{pmatrix}, \qquad \{f, g\} = \sum_{i=1}^{N/2} \left(\frac{\partial f}{\partial p_i}\frac{\partial g}{\partial q_i} - \frac{\partial f}{\partial q_i}\frac{\partial g}{\partial p_j} \right), \tag{6.56}$$

where I is the unit matrix $N/2 \times N/2$. Any non-degenerate $\Lambda^{\alpha\beta}$ can be locally reduced to the canonical form (6.56) such that one obtains the textbook pair of Hamiltonian equations [7]

$$\frac{dq_i}{dt} = \frac{\partial \mathscr{H}}{\partial p_i}, \qquad \frac{dp_i}{dt} = -\frac{\partial \mathscr{H}}{\partial q_i}, \qquad 1 \leq i \leq N/2. \tag{6.57}$$

For a set of $N/2$ coupled nonlinear oscillators

$$\mathscr{H} = \sum_{s=1}^{N/2} \left(\frac{p_s^2}{2m_s} + \frac{k_s q_s^2}{2} \right) + \mathscr{H}_{\text{nonl}}, \tag{6.58}$$

one can introduce

$$a_s = \frac{1}{\sqrt{2}} \left(q_s \sqrt[4]{k_s m_s} + \frac{i p_s}{\sqrt[4]{k_s m_s}} \right), \qquad \omega_s = \sqrt{\frac{k_s}{m_s}}, \tag{6.59}$$

where the new representation of the canonical Poisson structure is defined by the only non-trivial bracket between the complex coordinates

$$\{a_s, a_{s'}^*\} = \begin{cases} i & \text{for } s = s', \\ 0 & \text{for } s \neq s', \end{cases} \quad \Rightarrow \quad \{f, g\} = i \sum_{s=1}^{N/2} \left(\frac{\partial f}{\partial a_s}\frac{\partial g}{\partial a_s^*} - \frac{\partial f}{\partial a_s^*}\frac{\partial g}{\partial a_s} \right). \tag{6.60}$$

The complex analogue of Eq. (6.57) reads

$$\mathscr{H} = \sum_{s=1}^{N/2} \omega_s a_s a_s^* + \mathscr{H}_{\text{nonl}}, \qquad i\frac{da_s}{dt} = \omega_s a_s + \frac{\partial \mathscr{H}_{\text{nonl}}}{\partial a_s^*}. \tag{6.61}$$

The latter equations render the starting point of the perturbation theory that step by step removes non-resonant terms from $\mathscr{H}_{\text{nonl}}$ by consequent changes to new canonical variables.

6.2.3 One Continuous Field

Now we turn to systems with infinitely many degrees of freedom [25, 26, 70]. First, we consider one scalar filed u with an infinite number of "coordinates" $u(x)$ for all $x \in \mathbb{R}$. We assume that $u(x) \to 0$ for $x \to \pm\infty$. The observables are now given by functionals, such as pulse area

$$A[u] = \int_{-\infty}^{\infty} u(x)dx. \tag{6.62}$$

Derivatives are replaced by functional derivatives. Similar to Eq. (6.26), which we write in the form

$$\{f, g\} = \sum_{\alpha,\beta} \{\xi^\alpha, \xi^\beta\} \partial_\alpha f \partial_\beta g, \tag{6.63}$$

the Poisson bracket of two observables $F[u]$ and $G[u]$ is defined as

$$\{F, G\} = \iint_{-\infty}^{\infty} \frac{\delta F}{\delta u(x)} \frac{\delta G}{\delta u(y)} \{u(x), u(y)\} dxdy, \tag{6.64}$$

where integration replaces summation over all α and β. Moreover, in the next sections we will deal with multi-component fields, then

$$\{F, G\} = \iint_{-\infty}^{\infty} \sum_{i,j} \frac{\delta F}{\delta u_i(x)} \frac{\delta G}{\delta u_j(y)} \{u_i(x), u_j(y)\} dxdy, \tag{6.65}$$

where summation over all components is assumed.

Here and below we deliberately avoid using $\delta F/\delta u$ or $\delta F/\delta u(x,t)$ and prefer to use $\delta F/\delta u(x)$ even if the field in question evolves with time. This happens because $u(x)$ is considered as a direct generalization of $\xi = (\xi^1, \xi^1, \cdots \xi^N)$. The components of such a "super-point" in the phase space with infinite number of dimensions are indexed by x. Therefore the notation $\delta/\delta u(x)$ is a direct analog of $\partial/\partial\xi^i$.

As a specific example of $\{u(x), u(y)\}$ we take the so-called Gardner-Zakharov-Faddeev bracket (GZF bracket, see [25, 70] and references cited therein)

$$\{u(x), u(y)\} = \delta'(x-y). \tag{6.66}$$

Replacing $\delta'(x-y)$ with $-\frac{\partial}{\partial y}\delta(x-y)$, integrating (6.64) by parts, and finally integrating over dx, one calculates that

$$\{F, G\} = \int_{-\infty}^{\infty} \frac{\delta F}{\delta u(y)} \frac{\partial}{\partial y} \frac{\delta G}{\delta u(y)} dy. \tag{6.67}$$

For instance, considering the pulse area (6.62) we obtain

$$\frac{\delta A}{\delta u(x)} = 1 \quad \Rightarrow \quad \{F, A\} = 0, \tag{6.68}$$

for any observable $F[u]$. The pulse area is then a geometric integral of motion for any Hamiltonian system generated by the bracket (6.66).

To write down an equation of motion analogous to Eq. (6.31), one should be able to calculate the bracket $\{F, u(x)\}$. To this end we consider $u(x)$ as a functional that takes any observable $u(y)$ and returns its value at some fixed point x

$$u(x) = \int_{-\infty}^{\infty} u(y)\delta(x-y)dy \quad \Rightarrow \quad \frac{\delta u(x)}{\delta u(y)} = \delta(x-y). \tag{6.69}$$

Therefore Eq. (6.67) indicates that

$$\{F, u(x)\} = \int_{-\infty}^{\infty} \left[\frac{\delta F}{\delta u(y)} \frac{\partial}{\partial y} \delta(x-y) \right] dy = -\frac{\partial}{\partial x} \frac{\delta F}{\delta u(x)}. \tag{6.70}$$

System evolution in continuous setting means that all "coordinates" $u(x)$ become time-dependent. Therefore one looks for $u = u(x,t)$. The Hamiltonian equation of motion for given $\mathscr{H}[u]$ reads

$$\partial_t u = \{\mathscr{H}, u(x)\} \quad \Rightarrow \quad \partial_t u = -\frac{\partial}{\partial x} \frac{\delta \mathscr{H}}{\delta u(x)}. \tag{6.71}$$

Equation (6.71) looks provoking, because we have a Hamiltonian system with one variable. The corresponding canonic pair [69] is determined on an invariant subspace of pulses $u(x)$ with the area $A[u] = 0$. For each $k > 0$ we define

$$q(k) = \frac{1}{\sqrt{\pi}k} \int_{-\infty}^{\infty} u(x)\cos(kx)dx, \quad p(k) = -\frac{1}{\sqrt{\pi}} \int_{-\infty}^{\infty} u(x)\sin(kx)dx, \tag{6.72}$$

and calculate that

$$\{p(k), q(k')\} = \int_{-\infty}^{\infty} \frac{\delta p(k)}{\delta u(y)} \frac{\partial}{\partial y} \frac{\delta q(k')}{\delta u(y)} dy = \frac{1}{\pi} \int_{-\infty}^{\infty} \sin(ky) \sin(k'y) dy. \tag{6.73}$$

Now we take advantage of the identity

$$\int_{-\infty}^{\infty} \cos(\kappa y) dy = 2\pi \delta(\kappa), \tag{6.74}$$

and derive that

$$\{p(k), q(k')\} = \delta(k - k') - \delta(k + k') = \delta(k - k'), \tag{6.75}$$

because $k + k' \neq 0$ by construction. In the same way one can obtain the remaining brackets

$$\{q(k), q(k')\} = \{p(k), p(k')\} = 0, \qquad \{q(k), p(k')\} = -\delta(k - k'), \tag{6.76}$$

cf. the discrete Eq. (6.55).

Following Eq. (6.48) the complex field can be introduced as

$$a(k) = \frac{1}{\sqrt{2}} \left[q(k)\sqrt{k} + \frac{ip(k)}{\sqrt{k}} \right] = \frac{1}{\sqrt{2\pi k}} \int_{-\infty}^{\infty} u(x) e^{-ikx} dx = \frac{u(k)}{\sqrt{2\pi k}}, \tag{6.77}$$

where we recall that k is positive. The already known brackets between the canonical variables $q(k)$ and $p(k)$ indicate that

$$\{a(k), a(k')\} = 0 \quad \text{and} \quad \{a(k), a^*(k')\} = i\delta(k - k'), \tag{6.78}$$

cf. Eq. (6.43). The general Poisson bracket between two real-valued observables in the complex formulation

$$\{F, G\} = \iint_{-\infty}^{\infty} \left[\frac{\delta F}{\delta a(k)} \frac{\delta G}{\delta a^*(k')} \{a(k), a^*(k')\} + \text{c.c.} \right] dk dk', \tag{6.79}$$

takes the form

$$\{F, G\} = i \int_{-\infty}^{\infty} \left[\frac{\delta F}{\delta a(k)} \frac{\delta G}{\delta a^*(k)} - \frac{\delta F}{\delta a^*(k)} \frac{\delta G}{\delta a(k)} \right] dk, \tag{6.80}$$

which is a continuous analogue of Eq. (6.46).

Below, complex representations will be introduced for several continuous systems. It is important that the fundamental equations (6.78) and (6.80) apply to all of them. In all such systems the Hamiltonian equations

$$\partial_t a = \{\mathscr{H}, a(k)\} = -i\frac{\delta \mathscr{H}}{\delta a^*(k)}, \qquad \partial_t a^* = \{\mathscr{H}, a^*(k)\} = i\frac{\delta \mathscr{H}}{\delta a(k)}, \tag{6.81}$$

are conjugate to each other so that one can deal with a single complex equation for $a(k,t)$

$$i\partial_t a = \frac{\delta \mathscr{H}}{\delta a^*(k)}, \tag{6.82}$$

cf. Eq. (6.47).

For example, consider the following Hamiltonian

$$\mathscr{H}[u] = \int_{-\infty}^{\infty} \left[\frac{(\partial_x u)^2}{2} + u^3\right] dx = \mathscr{H}_2[u] + \mathscr{H}_3[u]. \tag{6.83}$$

For the corresponding dynamic system we apply Eq. (6.71) and obtain a nonlinear wave equation

$$\partial_t u = \partial_x^3 u - 6u\partial_x u, \tag{6.84}$$

which is equivalent to the famous Korteweg-de Vries equation [29]. On the other hand, according to the Parseval theorem and definition (6.77)

$$\mathscr{H}_2 = \int_{-\infty}^{\infty} \frac{k^2|u(k)|^2}{2}\frac{dk}{2\pi} = \int_0^{\infty} k^3|a(k)|^2 dk, \tag{6.85}$$

such that for $a(k,t)$ we have

$$i\partial_t a = \omega(k)a + \frac{\delta \mathscr{H}_3}{\delta a^*(k)}, \qquad \omega(k) = k^3, \qquad k > 0, \tag{6.86}$$

cf. Eq. (6.61). Here all wave-vectors are positive because of unidirectionality.

6.2.4 *Canonical Bracket for Two Fields*

In this section we deal with a more traditional Hamiltonian that depends on two scalar fields, $\mathscr{H}[u,v]$. The multi-component Eq. (6.65) should be used instead of the single-component Eq. (6.64), and one should specify all possible brackets between

the fields. A direct generalization of the canonical discrete Poisson bracket (6.55) with $i \to x$, $q_i \to u(x)$, and $p_i \to v(x)$ is given by

$$\{u(x), u(y)\} = \{v(x), v(y)\} = 0, \qquad \{u(x), v(y)\} = -\delta(x-y). \tag{6.87}$$

The derived Poisson bracket between two observables $F[u, v]$ and $G[u, v]$ is

$$\{F, G\} = \iint_{-\infty}^{\infty} \left[\frac{\delta F}{\delta u(x)} \frac{\delta G}{\delta v(y)} \{u(x), v(y)\} + \frac{\delta F}{\delta v(x)} \frac{\delta G}{\delta u(y)} \{v(x), u(y)\} \right] dxdy, \tag{6.88}$$

and reduces to

$$\{F, G\} = \int_{-\infty}^{\infty} \left[\frac{\delta F}{\delta v(y)} \frac{\delta G}{\delta u(y)} - \frac{\delta F}{\delta u(y)} \frac{\delta G}{\delta v(y)} \right] dy, \tag{6.89}$$

which is a continuous analogue of Eq. (6.56). The corresponding dynamic equations read

$$\partial_t u = \{\mathscr{H}, u(x)\} = \int_{-\infty}^{\infty} \frac{\delta \mathscr{H}}{\delta v(y)} \frac{\delta u(x)}{\delta u(y)} dy = \frac{\delta \mathscr{H}}{\delta v(x)}, \tag{6.90}$$

and

$$\partial_t v = \{\mathscr{H}, v(x)\} = -\int_{-\infty}^{\infty} \frac{\delta \mathscr{H}}{\delta u(y)} \frac{\delta v(x)}{\delta v(y)} dy = -\frac{\delta \mathscr{H}}{\delta u(x)}, \tag{6.91}$$

cf. Eq. (6.21).

Exactly like in the discrete case (6.42), one can replace u and v with a single complex field $\psi = (u + iv)/\sqrt{2}$. The coefficients in the definition of ψ can be chosen differently, the only important thing is the bracket that should obey Eq. (6.78)

$$\{\psi(x), \psi(y)\} = 0, \qquad \{\psi(x), \psi^*(y)\} = i\delta(x-y). \tag{6.92}$$

The Poisson bracket between two real-valued observables that depend on $\psi(x)$ and $\psi^*(x)$ is derived like Eq. (6.80)

$$\{F, G\} = i \int_{-\infty}^{\infty} \left[\frac{\delta F}{\delta \psi(y)} \frac{\delta G}{\delta \psi^*(y)} - \frac{\delta F}{\delta \psi^*(y)} \frac{\delta G}{\delta \psi(y)} \right] dy, \tag{6.93}$$

and yields the Hamiltonian equation

$$i\partial_t \psi = i\{\mathscr{H}, \psi(x)\} = \frac{\delta \mathscr{H}}{\delta \psi^*(x)}, \tag{6.94}$$

cf. Eq. (6.82).

Both the Poisson bracket in the complex representation and the resulting complex Hamiltonian equation are structurally identical to those from the previous section. The only difference is that they now apply to the observables in the physical (x, t) space, as opposed to the observables in Fourier $(k > 0, t)$ space from the previous section. The key example in the physical space is given by

$$\mathscr{H} = \frac{1}{2}\int_{-\infty}^{\infty} \left(|\partial_x \psi|^2 - |\psi|^4\right) dx \tag{6.95}$$

which leads to the (focusing) nonlinear Schrödinger equation

$$i\partial_t \psi + \frac{1}{2}\partial_x^2 \psi + |\psi|^2 \psi = 0. \tag{6.96}$$

Equation (6.96) is commonly abbreviated as the NLS equation and is of fundamental importance for nonlinear optics as well as the generalized equation (gNLS) which in the simplest case is generated by the Hamiltonian

$$\mathscr{H} = -\frac{1}{2}\int_{-\infty}^{\infty} \left[\psi^*(\hat{L}\psi) + \psi(\hat{L}\psi)^* + \gamma|\psi|^4\right] dx. \tag{6.97}$$

Here $\gamma = \text{const}$ and operator $\hat{L}$ is polynomial with real coefficients and with respect to $i\partial_x$. The resulting gNLS equation reads

$$i\partial_t \psi + \hat{L}\psi + \gamma|\psi|^2\psi = 0. \tag{6.98}$$

In more complicated situations γ is an operator as well, and, moreover, Eq. (6.98) contains non-Hamiltonian terms describing linear and nonlinear damping. Note that both Eqs. (6.96) and (6.98) are complex envelope equations. Poisson brackets that are relevant for non-envelope equations will be discussed in the next section.

6.2.5 GZF Bracket for Two Fields

A more sophisticated example of Poisson bracket with two fields, the one that is relevant for the field-level description of optical pulses, is given by the Gardner-Zakharov-Faddeev construction. Non-vanishing brackets are set to

$$\{u(x), v(y)\} = \{v(x), u(y)\} = \delta'(x - y), \tag{6.99}$$

where the bracket (6.99) is antisymmetric because $\delta'(x)$ is an odd function. The resulting bracket between two observables $F[u, v]$ and $G[u, v]$ is calculated from

Eq. (6.65) by partial integration exactly as in Eq. (6.67)

$$\{F,G\} = \int_{-\infty}^{\infty} \left[\frac{\delta F}{\delta u(y)} \frac{\partial}{\partial y} \frac{\delta G}{\delta v(y)} + \frac{\delta F}{\delta v(y)} \frac{\partial}{\partial y} \frac{\delta G}{\delta u(y)} \right] dy. \tag{6.100}$$

To derive the corresponding equations of motion we calculate

$$\{F,u(x)\} = \int_{-\infty}^{\infty} \left[\frac{\delta F}{\delta v(y)} \frac{\partial}{\partial y} \delta(x-y) \right] dy = -\frac{\partial}{\partial x} \frac{\delta F}{\delta v(x)}, \tag{6.101}$$

and

$$\{F,v(x)\} = \int_{-\infty}^{\infty} \left[\frac{\delta F}{\delta u(y)} \frac{\partial}{\partial y} \delta(x-y) \right] dy = -\frac{\partial}{\partial x} \frac{\delta F}{\delta u(x)}. \tag{6.102}$$

Therefore each Hamiltonian $\mathscr{H}[u,v]$ generates the following two equations

$$\partial_t u = -\frac{\partial}{\partial x} \frac{\delta \mathscr{H}}{\delta v(x)} \qquad \text{and} \qquad \partial_t v = -\frac{\partial}{\partial x} \frac{\delta \mathscr{H}}{\delta u(x)}. \tag{6.103}$$

For instance, choosing

$$\mathscr{H} = \int_{-\infty}^{\infty} \left(\frac{u^2}{2} + \frac{v^2}{2} \right) dx, \tag{6.104}$$

we derive the common linear wave equation

$$\begin{aligned} \partial_t u &= -\partial_x v, \\ \partial_t v &= -\partial_x u, \end{aligned} \quad \Rightarrow \quad \partial_t^2 u - \partial_x^2 u = 0, \tag{6.105}$$

with the dispersion law

$$\omega(k) = |k|. \tag{6.106}$$

More complicated Hamiltonians of the type (6.104) can account for dispersion and nonlinearity in the wave equation. This situation is important for pulse propagation in fibers, so it's worth taking time for complex formulation of the system (6.103). A possible choice of the canonical variables reads

$$\begin{aligned} q(k) &= \frac{1}{\sqrt{2\pi|k|}} \int_{-\infty}^{\infty} \left[\Lambda(k) u(x) + \frac{\sigma(k)}{\Lambda(k)} v(x) \right] \cos(kx) dx, \\ p(k) &= -\frac{1}{\sqrt{2\pi|k|}} \int_{-\infty}^{\infty} \left[\Lambda(k) u(x) + \frac{\sigma(k)}{\Lambda(k)} v(x) \right] \sin(kx) dx, \end{aligned} \tag{6.107}$$

where we use the sign function

$$\sigma(k) = \frac{k}{|k|}, \tag{6.108}$$

and the scaling factor $\Lambda(k)$. The latter is a real-valued and even but otherwise arbitrary function

$$\Lambda(k) = \Lambda(-k) \in \mathbb{R}. \tag{6.109}$$

Note that the wave vector k in Eq. (6.107) takes all real values as opposed by only positive ones in Eq. (6.72).

Let us check the Poisson bracket between the new-defined $q(k)$ and $p(k)$. Using Eq. (6.100) we calculate that

$$\begin{aligned}\{p(k), q(k')\} &= \int_{-\infty}^{\infty} \left[\frac{\delta p(k)}{\delta u(y)} \frac{\partial}{\partial y} \frac{\delta q(k')}{\delta v(y)} + \frac{\delta p(k)}{\delta v(y)} \frac{\partial}{\partial y} \frac{\delta q(k')}{\delta u(y)} \right] dy \\ &= \frac{\sqrt{|k'/k|}}{2\pi} \left[\frac{\Lambda(k)}{\Lambda(k')} + \sigma(k)\sigma(k') \frac{\Lambda(k')}{\Lambda(k)} \right] \int_{-\infty}^{\infty} \sin(ky) \sin(k'y) dy \\ &= \frac{1 + \sigma(k)\sigma(k')}{2} [\delta(k - k') - \delta(k + k')] = \delta(k - k').\end{aligned}$$

Furthermore, it is easy to obtain that both $\{q(k), q(k')\}$ and $\{p(k), p(k')\}$ vanish, so that $q(k)$ and $p(k)$ are proper canonical variables.

Following Eq. (6.48) complex field can be introduced as

$$a(k) = \frac{q(k) + ip(k)}{\sqrt{2}} = \frac{1}{2\sqrt{\pi |k|}} \int_{-\infty}^{\infty} \left[\Lambda(k) u(x) + \frac{\sigma(k)}{\Lambda(k)} v(x) \right] e^{-ikx} dx, \tag{6.110}$$

where the fundamental relations (6.78) and (6.80) are satisfied automatically. The original real-valued fields can be reconstructed from the complex-valued one using the relations

$$\Lambda(k) \frac{u(k)}{\sqrt{\pi |k|}} = a(k) + a^*(-k), \qquad \frac{\sigma(k)}{\Lambda(k)} \frac{v(k)}{\sqrt{\pi |k|}} = a(k) - a^*(-k), \tag{6.111}$$

where $u(k)$ and $v(k)$ are the spectral components

$$u(k) = \int_{-\infty}^{\infty} u(x) e^{-ikx} dx, \qquad v(k) = \int_{-\infty}^{\infty} v(x) e^{-ikx} dx. \tag{6.112}$$

For instance, using Parseval's theorem for the Hamiltonian (6.104) and setting $\Lambda = 1$, one directly obtains that

$$\mathscr{H} = \int_{-\infty}^{\infty} \left[\frac{|u(k)|^2}{2} + \frac{|v(k)|^2}{2} \right] \frac{dk}{2\pi} = \int_{-\infty}^{\infty} \omega(k) |a(k)|^2 dk, \tag{6.113}$$

in accordance with the dispersion law (6.106). In more complex situations both $|u(k)|^2$ and $|v(k)|^2$ may come with some weights, the latter can be made equal to each other via a proper choice of $\Lambda(k)$.

6.3 Pulses in Optical Fibers

The electric field $\mathbf{E}(\mathbf{r}, t)$ and the magnetic induction $\mathbf{B}(\mathbf{r}, t)$ created by any optical pulse are, of course, governed by the fundamental microscopic Maxwell equations [14]

$$\begin{aligned} \epsilon_0 \nabla \mathbf{E} = \rho, \qquad & \nabla \times \mathbf{E} = -\partial_t \mathbf{B}, \\ \nabla \mathbf{B} = 0, \quad & \frac{1}{\mu_0} \nabla \times \mathbf{B} = \mathbf{j} + \epsilon_0 \partial_t \mathbf{E}. \end{aligned} \tag{6.114}$$

Here the so-called vacuum permittivity ϵ_0 and the vacuum permeability μ_0 are physical constants, whereas $\rho(\mathbf{r}, t)$ and $\mathbf{j}(\mathbf{r}, t)$ are exact microscopic charge and current densities. On a macroscopic level, however, one can avoid the tremendous task of solving additional equations for each elementary charge composing $\rho(\mathbf{r}, t)$ and $\mathbf{j}(\mathbf{r}, t)$. Instead, one deals with an appropriate simplified material model. For a set of non-destructive electromagnetic waves propagating in a dielectric it is sufficient to introduce a single macroscopic polarization vector $\mathbf{P}(\mathbf{r}, t)$, such that the inhomogeneous pair of Maxwell equations (6.114) changes to the form

$$\nabla(\epsilon_0 \mathbf{E} + \mathbf{P}) = 0, \qquad \frac{1}{\mu_0} \nabla \times \mathbf{B} = \partial_t (\epsilon_0 \mathbf{E} + \mathbf{P}), \tag{6.115}$$

where a macroscopic-level relation between $\mathbf{P}(\mathbf{r}, t)$ and $\mathbf{E}(\mathbf{r}, t)$ is assumed. This so-called material relation $\mathbf{P}(\mathbf{E})$ may be complicated, even given in terms of additional equations; one that is suitable for optical fibers will be specified in the next section. Here, we note that the use of polarization is, of course, automatically compatible with the charge conservation equation

$$\partial_t \rho + \nabla \mathbf{j} = 0, \tag{6.116}$$

that is why the four quantities $\rho(\mathbf{r}, t)$ and $\mathbf{j}(\mathbf{r}, t)$ are safely replaced by the three components of $\mathbf{P}(\mathbf{r}, t)$.

6.3.1 Problem Setting

Below we shall consider a linearly polarized wave in which all the fields involved have only one nontrivial component

$$\mathbf{E} = (E, 0, 0), \qquad \mathbf{B} = (0, B, 0), \qquad \mathbf{P} = (P, 0, 0). \tag{6.117}$$

Moreover, all fields depend on time and a single spatial variable, the propagation coordinate z. In the first place such approximation applies to bulk propagation of plane electromagnetic pulses in dispersive media. On the other hand, the approximation applies to a so-called single-mode polarization-preserving fiber [1, 66]. Namely, a single-mode fiber means that the radial structure of the pulse is approximately the same for all frequencies in question so that the radial degrees of freedom can be integrated out leaving us with quantities depending on (z, t). In addition, the fiber can be intentionally made slightly asymmetric introducing a small difference between two possible polarizations of a plane electromagnetic wave. Such a fiber preserves polarization of the input pulse, that is presumed by Eq. (6.117).

For a plane wave described by Eq. (6.117), the full system (6.114) is reduced to two scalar equations only:

$$\partial_z E = -\partial_t B \qquad \text{and} \qquad -\frac{1}{\mu_0}\partial_z B = \partial_t(\epsilon_0 E + P). \tag{6.118}$$

To proceed we need a specific expression for $P(E)$. The common general expression is given by the sequence [15, 45]

$$P = \epsilon_0 \left(\hat{\chi}^{(1)}E + \hat{\chi}^{(2)}[E, E] + \hat{\chi}^{(3)}[E, E, E] + \cdots\right), \tag{6.119}$$

where $\hat{\chi}^{(1)}$ is a linear operator, $\hat{\chi}^{(2)}$ is a bilinear one, $\hat{\chi}^{(3)}$ is trilinear and so on. This sequence of linear and nonlinear susceptibilities encodes solution of an additional equation for $P(z, t)$ induced by $E(z, t)$.

Below we consider the following reduction of (6.119):

$$\frac{1}{\epsilon_0}P = \hat{\chi}^{(1)}E + \chi^{(3)}E^3. \tag{6.120}$$

Equation (6.120) assumes that $P(-E) = -P(E)$ so that the second-order susceptibility vanishes due to symmetric arguments, which is a typical situation in optical fibers. Nonlinear susceptibility of the third order $\hat{\chi}^{(3)}$ is approximated by a constant, $\chi^{(3)}$. The linear part of the medium response is determined by the standard delay integral [45]

$$\hat{\chi}^{(1)}E(t) = \int_0^\infty \chi^{(1)}(\tau)E(t-\tau)d\tau, \tag{6.121}$$

with memory function $\chi^{(1)}(\tau)$. It is convenient to introduce the linear dispersion operator $\hat{\epsilon} = 1 + \hat{\chi}^{(1)}$ and combine the system (6.118) into a single propagation equation

$$\partial_z^2 E - \frac{1}{c^2}\partial_t^2 \left(\hat{\epsilon} E + \chi^{(3)} E^3\right) = 0 \tag{6.122}$$

which is a self-consistent nonlinear wave equation with $c = 1/\sqrt{\mu_0 \epsilon_0}$.

Considering the operator $\hat{\epsilon}$ in the frequency domain one derives from Eq. (6.121)

$$\hat{\epsilon} e^{-i\omega t} = \epsilon(\omega) e^{-i\omega t} \quad \text{with} \quad \epsilon(\omega) = 1 + \int_0^\infty \chi^{(1)}(\tau) e^{i\omega\tau} d\tau. \tag{6.123}$$

The just defined relative permeability $\epsilon(\omega)$ is a complex-valued function with property

$$\epsilon(\omega) = [\epsilon(-\omega)]^*, \tag{6.124}$$

and it is subject to the Kramers–Kronig relations [45]. Equation (6.124) together with the relation

$$\hat{\epsilon} E(t) = \hat{\epsilon} \int_{-\infty}^{\infty} E(\omega) e^{-i\omega t} \frac{d\omega}{2\pi} = \int_{-\infty}^{\infty} \epsilon(\omega) E(\omega) e^{-i\omega t} \frac{d\omega}{2\pi}, \tag{6.125}$$

guarantees that the operator $\hat{\epsilon}$ transforms a real-valued field into a real-valued one. Moreover, Eq. (6.125) indicates that

$$\hat{\epsilon} = \epsilon(i\partial_t), \tag{6.126}$$

if $\epsilon(\omega)$ is approximated by a polynomial in the frequency range where $E(\omega) \neq 0$.

In more complex situations $\epsilon(\omega)$ is approximated by a polynomial in some interval of positive frequencies only, e.g., by a Taylor expansion of the "true" $\epsilon(\omega)$ near the pulse carrier frequency. Such an expansion typically violates the fundamental Eq. (6.124), and in any case it has a finite convergence radius. To avoid the difficulty one can split positive and negative frequencies in the electric field according to Gabor's rule (6.13) and then apply $\epsilon(i\partial_t)$ only to the positive-frequency part

$$E(z,t) = \frac{1}{2}\mathcal{E}(z,t) + \text{c.c.} \quad \Rightarrow \quad \hat{\epsilon} E(z,t) = \frac{1}{2}\epsilon(i\partial_t)\mathcal{E}(z,t) + \text{c.c.}, \tag{6.127}$$

such a trick is an important step in the derivation of the complex envelope equation.

To conclude this section we stress that Eq. (6.122) is on one hand a nonlinear wave equation and on the other hand a delay differential equation. Not only the initial conditions, $E(t = 0, z)$ and $\partial_t E(t = 0, z)$, are required to find $E(t > 0, z)$ but also the prehistory $E(t < 0, z)$. Moreover, despite the simple $1 + 1$ geometry,

the full numerical solution of Eq. (6.122) may require a great amount of numerical calculations, e.g., for wavelength of 1 μm and fiber length of 1 km. A much more simple formulation can be obtained for a single wave packet or a dense sequence of wave packets that propagate in one direction. One can then neglect backward waves and follow the pulses in the moving frame. This approach leads to the envelope NLS equation and to the "less-envelope" gNLS equation, as described below.

6.3.2 *Forward and Backward Waves*

Neglecting for a while the nonlinear term in Eq. (6.122), one can apply the standard substitution $E \sim e^{i(kz-\omega t)}$ and derive the following dispersion relation:

$$k^2c^2 = \omega^2\epsilon(\omega) \tag{6.128}$$

for linear waves. A given (positive) frequency yields two wave vectors, $k = \pm\beta(\omega)$, for the forward and the backward wave respectively. In fiber optics $\beta(\omega)$ is referred to as the propagation constant. The real-valued field of a monochromatic forward wave is written as

$$E(z,t) = \frac{1}{2}Ae^{i\beta(\omega)z-i\omega t} + \text{c.c.}, \tag{6.129}$$

where A is the complex amplitude. It is convenient to define the propagation constant for negative frequencies in such a way that

$$\beta(-\omega) = -\beta^*(\omega), \tag{6.130}$$

while the latter definition is compatible with the dispersion relation (6.128) and with the fundamental Eq. (6.124). The complex conjugate of $e^{i\beta(\omega)z-i\omega t}$ is then equivalent to replacement $\omega \to -\omega$, which is a convenient property of the Fourier coefficients.

In what follows we will use the index of refraction $n(\omega) = \sqrt{\epsilon(\omega)}$, the corresponding operator $\hat{n}$ is defined as in Eq. (6.125). It is also convenient to relate a suitable operator $\hat{\beta}$ with the propagation constant. The problem is that for a real-valued $E(t)$, the expression $\int_{-\infty}^{\infty}\beta(\omega)E(\omega)e^{-i\omega t}d\omega$ is complex-valued. So instead, we define

$$\hat{\beta} = \frac{1}{c}\hat{n}\partial_t \quad \Rightarrow \quad \hat{\beta}e^{-i\omega t} = -i\beta(\omega)e^{-i\omega t}. \tag{6.131}$$

The key observation is that with the help of $\hat{\beta}$ and $\hat{n}$ one can split Eq. (6.122) into two first-order equations

$$(\hat{\beta} + \partial_z)\underset{\rightarrow}{E} + \frac{\chi^{(3)}}{2c}\hat{n}^{-1}\partial_t\left(\underset{\rightarrow}{E} + \underset{\leftarrow}{E}\right)^3 = 0, \tag{6.132}$$

$$(\hat{\beta} - \partial_z)\underset{\leftarrow}{E} + \frac{\chi^{(3)}}{2c}\hat{n}^{-1}\partial_t\left(\underset{\rightarrow}{E} + \underset{\leftarrow}{E}\right)^3 = 0, \tag{6.133}$$

where by construction

$$E(z,t) = \underset{\rightarrow}{E}(z,t) + \underset{\leftarrow}{E}(z,t). \tag{6.134}$$

Indeed, after we apply $\hat{\beta} - \partial_z$ to (6.132) and $\hat{\beta} + \partial_z$ to (6.133), we add them together and return to Eq. (6.122). Moreover, it is easy to see that the linearized equations (6.132) and (6.133) describe the pure forward and the pure backward wave respectively. These waves are coupled by nonlinearity.

Now let us consider a sequence of the forward pulses. Assuming that the nonlinear excitation of the backward wave is non-resonant, one can neglect the backward field and replace Eq. (6.122) by the so-called forward Maxwell equation

$$\partial_z E + \hat{\beta}E + \frac{\chi^{(3)}}{2c}\hat{n}^{-1}\partial_t(E)^3 = 0, \tag{6.135}$$

where from now on we do not distinguish between the forward field and E. In optical context Eq. (6.135) was first applied in [34], the splitting technique was discussed in [27, 39, 41, 42]. Equation (6.135), being of interest on its own, is a good starting point for derivation of the gNLS equation, because (6.135) already has the first order with respect to the propagation coordinate.

6.3.3 *Envelope Equations*

To derive an envelope equation from Eq. (6.135) we consider a typical situation in which the forward pulse in question has a narrow spectrum localized around the carrier frequency ω_0. For $\omega \approx \omega_0$ we approximate the wave vector $k = \beta(\omega)$ by its Taylor expansion

$$\beta(\omega) = \sum_{m=0}^{M} \frac{\beta_m}{m!}(\omega - \omega_0)^m, \qquad \beta_m = \beta^{(m)}(\omega_0), \tag{6.136}$$

of order $M \geq 2$ at least. The carrier wave reads $e^{i(\beta_0 z-\omega_0 t)}$, the carrier phase velocity is ω_0/β_0. The group velocity $V_{\rm gr} = d\omega/dk$, therefore

$$\frac{1}{V_{\rm gr}(\omega)} = \beta_1 + \beta_2(\omega - \omega_0) + \cdots, \tag{6.137}$$

where β_2 is referred to as the group velocity dispersion (GVD) [1]. The GVD parameter describes frequency dependent correction to the group velocity $1/\beta_1$ of the carrier wave.

We now apply the substitution

$$E(z,t) = \frac{1}{2}\Psi(z,t)e^{i(\beta_0 z-\omega_0 t)} + \text{c.c.}, \tag{6.138}$$

to remove fast oscillations of the pulse electric field in (6.135). First, we ignore the third harmonic in the nonlinear term

$$E^3 \approx \frac{3}{8}|\Psi|^2\Psi e^{i(\beta_0 z-\omega_0 t)} + \text{c.c.}, \tag{6.139}$$

that is, we assume that medium excitation induced by $\Psi^3 e^{3i(\beta_0 z-\omega_0 t)}$ is non-resonant, $\beta(3\omega_0) \neq 3\beta(\omega_0)$.

Second, we note that Eq. (6.126) applies also to the expansion of $\beta(\omega)$

$$\hat{\beta} = -i\sum_{m=0}^{M}\frac{\beta_m}{m!}(i\partial_t - \omega_0)^m, \tag{6.140}$$

and using (6.138) one can derive that

$$\hat{\beta}E = -\frac{i}{2}\left[\sum_{m=0}^{M}\frac{\beta_m}{m!}(i\partial_t)^m\Psi\right]e^{i(\beta_0 z-\omega_0 t)} + \text{c.c.}, \tag{6.141}$$

according to the general principle (6.127).

Third, the operator $\hat{n}^{-1}\partial_t$ in the nonlinear term in (6.135) corresponds to $-i\omega/n(\omega)$ and can be treated exactly like $\hat{\beta}$, namely if

$$\frac{\omega}{n(\omega)} = \sum_{m=0}^{M}\frac{\gamma_m}{m!}(\omega-\omega_0)^m \qquad \text{then} \qquad \hat{n}^{-1}\partial_t = -i\sum_{m=0}^{M}\frac{\gamma_m}{m!}(i\partial_t-\omega_0)^m, \tag{6.142}$$

and in accord with (6.139)

$$\hat{n}^{-1}\partial_t(E^3) = -\frac{3i}{8}\left[\sum_{m=0}^{M}\frac{\gamma_m}{m!}(i\partial_t)^m(|\Psi|^2\Psi)\right]e^{i(\beta_0 z-\omega_0 t)} + \text{c.c.} \tag{6.143}$$

Combining all three steps we see that Eq. (6.135) reduces to the following propagation equation for $\Psi(z,t)$

$$i\partial_z\Psi + \left[\sum_{m=1}^{M}\frac{\beta_m}{m!}(i\partial_t)^m\right]\Psi + \frac{3\chi^{(3)}}{8c}\left[\sum_{m=0}^{M}\frac{\gamma_m}{m!}(i\partial_t)^m\right]|\Psi|^2\Psi = 0, \tag{6.144}$$

in which the β_0-term is canceled out. The latter equation is simplified in two further steps. First, we recall that β_1 is the inverse carrier group velocity. It is then convenient to define the so-called retarded time

$$\tau = t - \beta_1 z, \tag{6.145}$$

and introduce $\psi(z,\tau) = \Psi(z,t)$, i.e., it is convenient to change to a moving frame that follows the pulse. So the β_1-term is canceled out from Eq. (6.144).

Second, coefficients γ_m are usually calculated by replacing $n(\omega)$ with $n(\omega_0)$, then

$$\gamma_0 = \frac{\omega_0}{n(\omega_0)}, \qquad \gamma_1 = \frac{1}{n(\omega_0)}, \qquad \gamma_{m\geq 2} = 0. \tag{6.146}$$

Altogether, Eq. (6.144) reduces to the gNLS equation

$$i\partial_z\psi + \hat{\mathcal{D}}\psi + \frac{\omega_0}{c}n_2(1 + i\omega_0^{-1}\partial_\tau)|\psi|^2\psi = 0, \tag{6.147}$$

where following [1] we use notation $n_2 = (3/8)\chi^{(3)}/n(\omega_0)$ and introduce the so-called dispersion operator

$$\hat{\mathcal{D}} = \sum_{m=2}^{M}\frac{\beta_m}{m!}(i\partial_\tau)^m. \tag{6.148}$$

After $\psi(z,\tau)$ has been calculated, the field is described as

$$E(z,t) = \frac{1}{2}\psi(z, t-\beta_1 z)e^{i(\beta_0 z - \omega_0 t)} + \text{c.c.} \tag{6.149}$$

The standard classical NLS equation, the one that is completely integrable [72], appears if one approximates both operators in (6.147) by the leading terms

$$i\partial_z\psi - \frac{\beta_2}{2}\partial_\tau^2\psi + \frac{\omega_0}{c}n_2|\psi|^2\psi = 0, \tag{6.150}$$

where in a focusing medium ($n_2 > 0$) and anomalous ($\beta_2 < 0$) dispersion domain one can rescale the variables and obtain the normalized Eq. (6.96).

An important observation is that the derived propagation equations should be solved with respect to z. In fiber optics both the gNLS (6.147) and the NLS (6.150)

equations require $E(z = 0, t)$ and yield $E(z > 0, t)$. Physical consequences of this feature will be discussed later on. Another important observation is that in typical settings Eq. (6.147) has an exceptionally good agreement with the solutions of the full nonlinear wave Eq. (6.122) as reported in [16, 31]. To explain this behavior we now consider the Hamiltonian framework for optical pulses.

6.4 Hamiltonian Description of Pulses

We now turn to the Hamiltonian structure of Eq. (6.118). It is of interest that to some extent such a structure can be recognized even without exact knowledge of $P(E)$. To this end we introduce standard displacement field $D(z, t)$ the magnetic intensity $H(z, t)$

$$D = \epsilon_0 E + P, \qquad H = \frac{B}{\mu_0}, \tag{6.151}$$

such that equations (6.118) take the form

$$\partial_z E = -\partial_t B \qquad \text{and} \qquad -\partial_z H = \partial_t D. \tag{6.152}$$

The relation between H and B is trivial because most optical materials are not magnetic [14]. The Hamiltonian is given by a yet unknown functional $\mathscr{H}[E, H]$ for which the following variation is required

$$\delta\mathscr{H}[E, H] = \int_{-\infty}^{\infty} (D\delta E + B\delta H)dt. \tag{6.153}$$

Indeed, such a $\mathscr{H}[E, H]$ implies that the system (6.152) reads

$$\partial_z E = -\partial_t \frac{\delta\mathscr{H}}{\delta H}, \qquad \partial_z H = -\partial_t \frac{\delta\mathscr{H}}{\delta E}, \tag{6.154}$$

and has the same mathematical structure as the Hamiltonian equations (6.103), but one should exchange the time and space variables. For instance, the Poisson bracket (6.99) now reads

$$\{E(t_1), H(t_2)\} = \{H(t_1), E(t_2)\} = \delta'(t_1 - t_2). \tag{6.155}$$

This simple change of variables results in important physical differences and changes the physical meaning of $\mathscr{H}[E, H]$. We will first discuss these differences and then return to Eq. (6.154) and apply results that have already been derived for the GZF bracket (6.155).

6.4.1 z-Propagation

The system (6.154) is solved with respect to z in the context of the so-called z-propagation picture similar to the gNLS equation (6.147). This problem formulation naturally applies to many optical settings, where some source-device creates the input field $E(z = 0, t)$ which is "known" for all times at the beginning of the fiber and some detector-device measures the output field $E(z = L, t)$, or some derived quantity like power, at the end. Here L is the propagation distance. The reflected backward wave is neglected, exactly like in the already derived envelope equation. The pulses are either periodic or localized in time, such that we have a kind of boundary condition for the time axis.

One consequence of z-propagation is that $\mathscr{H}$ is related not to the energy and system invariance with respect to the time shifts [44]. Instead, $\mathscr{H}$ refers to momentum conservation and to invariance of basic equations with respect to space shifts. Another consequence is that now all conserved quantities are obtained by integration of the corresponding flux densities over time. For instance, consider the conservation law (6.116) for one spatial dimension

$$\partial_t \rho(z, t) + \partial_z j_z(z, t) = 0. \tag{6.156}$$

The latter equation is usually integrated over dz assuming that $\rho(z, t)$ and $j(z, t)$ are localized in space. The result

$$\frac{d}{dt} \int_{-\infty}^{\infty} \rho(z, t) dz = 0, \tag{6.157}$$

is interpreted as charge conservation. In the z-propagation picture, however, we integrate Eq. (6.156) over dt assuming that for a given z both the charge density $\rho(z, t)$ and the current density $j(z, t)$ are induced by an isolated pulse and disappear for $t \to \pm\infty$. The resulting conservation law

$$\frac{d}{dz} \int_{-\infty}^{\infty} j(z, t) dt = 0, \tag{6.158}$$

means that the time-averaged current density is the same for all observation points inside the fiber. Consequently $\mathscr{H}[E, H]$ must be a time-averaged momentum flux.

Before proceeding with the explicit expression for $\mathscr{H}[E, H]$ let us revisit the definition of the complex Hamiltonian variable. In the case of t-propagation the canonical variables are parameterized by the wave vector. The standard complex variable was introduced by

$$a(k) = \frac{q(k) + ip(k)}{\sqrt{2}} \quad \Rightarrow \quad i\partial_t a = \frac{\delta \mathscr{H}}{\delta a^*(k)}, \tag{6.159}$$

so that

$$\mathscr{H} = \int_{-\infty}^{\infty} \omega(k)|a(k)|^2 dk \quad \text{yields} \quad a(k,t) \sim e^{-i\omega(k)t}. \tag{6.160}$$

The latter expression agrees with the familiar $e^{i(kz-\omega t)}$ representation of monochromatic waves.

In the case of z-propagation the canonical variables are parameterized by frequency and it is convenient to take

$$\mathcal{A}(\omega) = \frac{q(\omega) - ip(\omega)}{\sqrt{2}} \quad \Rightarrow \quad i\partial_t \mathcal{A} = -\frac{\delta \mathscr{H}}{\delta \mathcal{A}^*(k)}, \tag{6.161}$$

so that, e.g.,

$$\mathscr{H} = \int_{-\infty}^{\infty} \beta(\omega)|\mathcal{A}(\omega)|^2 d\omega \quad \text{yields} \quad \mathcal{A}(\omega, z) \sim e^{i\beta(\omega)t}. \tag{6.162}$$

The actual z-Hamiltonian will be a bit more complicated, as it should describe both forward and backward waves.

6.4.2 *z-Hamiltonian*

Momentum conservation for electromagnetic field in vacuum in the one-dimensional setting (6.118) is given by a well-known relation

$$\partial_t \left(\frac{j_P}{c^2} \right) + \partial_z \left(\frac{\epsilon_0 E^2}{2} + \frac{B^2}{2\mu_0} \right) = 0, \tag{6.163}$$

where $j_P = EB/\mu_0$ is the Poynting vector and the second bracket contains the vacuum momentum flux density. Motivated by this example, we consider the following functional [71]

$$\mathscr{H}[E,H] = \int_{-\infty}^{\infty} \left[\epsilon_0 \left(\frac{E\hat{\epsilon}E}{2} + \frac{\chi^{(3)}E^4}{4} \right) + \frac{\mu_0 H^2}{2} \right] dt. \tag{6.164}$$

Below we will also use the frequency components of the involved fields

$$E(\omega) = \int_{-\infty}^{\infty} E(t) e^{i\omega t} dt, \qquad H(\omega) = \int_{-\infty}^{\infty} H(t) e^{i\omega t} dt, \tag{6.165}$$

and representation of definition (6.164) in the frequency domain.

Notice that the operator $\hat{\epsilon}$ in Eq. (6.164) is not self-adjoint. Indeed, defining the scalar product of two real fields at some fixed point in space by

$$\int_{-\infty}^{\infty} E_1(t)E_2(t)dt = \int_{-\infty}^{\infty} E_1^*(\omega)E_2(\omega)\frac{d\omega}{2\pi}, \tag{6.166}$$

we obtain

$$\int_{-\infty}^{\infty} [E_1(t)\hat{\epsilon}E_2(t) - E_2(t)\hat{\epsilon}E_1(t)]dt = \int_{-\infty}^{\infty} [\epsilon(\omega) - \epsilon^*(\omega)]E_1^*(\omega)E_2(\omega)\frac{d\omega}{2\pi}, \tag{6.167}$$

in agreement with (6.124) and (6.125). The imaginary part of $\epsilon(\omega)$, though always present, can be extremely small for frequencies of interest, as it happens in the transparency region of all fiber-relevant materials. If $\epsilon(\omega)$ can be considered real, the system (6.118) becomes dissipation-free and $\hat{\epsilon}$ becomes self-adjoint. The variation of $\mathscr{H}[E, H]$ from (6.164) is then given by (6.153), and we have found the required Hamiltonian. On the physical side, $\mathscr{H}$ gives the total amount of momentum that is transferred per unit area of the fiber cross-section. $\mathscr{H}$ is an integral of motion in the sense that $\partial_z \mathscr{H}[E(z,t), H(z,t)] = 0$ if $E(z,t)$ and $H(z,t)$ solve (6.118). Equation (6.166) indicates that in the frequency domain the quadratic part of the Hamiltonian (6.164) is given by the relation

$$\mathscr{H}_2[E, H] = \int_{-\infty}^{\infty} \left[\frac{\epsilon_0\epsilon(\omega)}{2}E(\omega)E^*(\omega) + \frac{\mu_0}{2}H(\omega)H^*(\omega)\right]\frac{d\omega}{2\pi}. \tag{6.168}$$

Now we introduce the canonical variables according to (6.107)

$$\begin{aligned} q(\omega) &= \frac{1}{\sqrt{2\pi|\omega|}}\int_{-\infty}^{\infty}\left[\Lambda(\omega)E(t) + \frac{\sigma(\omega)}{\Lambda(\omega)}H(t)\right]\cos(\omega t)dx, \\ p(\omega) &= -\frac{1}{\sqrt{2\pi|\omega|}}\int_{-\infty}^{\infty}\left[\Lambda(\omega)E(t) + \frac{\sigma(\omega)}{\Lambda(\omega)}H(t)\right]\sin(\omega t)dx, \end{aligned} \tag{6.169}$$

where $\sigma(\omega) = \omega/|\omega|$ and $\Lambda(\omega) = \Lambda(-\omega) \in \mathbb{R}$ similar to Eq. (6.109). The complex variable is introduced according to Eq. (6.161)

$$\mathcal{A}(\omega) = \frac{q(\omega) - ip(\omega)}{\sqrt{2}} = \frac{1}{2\sqrt{\pi|\omega|}}\int_{-\infty}^{\infty}\left[\Lambda(\omega)E(t) + \frac{\sigma(\omega)}{\Lambda(\omega)}H(t)\right]e^{i\omega t}dt, \tag{6.170}$$

by construction it obeys the z-propagation equation

$$i\partial_z\mathcal{A}(\omega, z) + \frac{\delta\mathscr{H}}{\delta\mathcal{A}^*(\omega)} = 0, \tag{6.171}$$

which is similar to the t-equation (6.82). The above definition of $\mathcal{A}(\omega)$ suggests to switch to the frequency domain where we have

$$\mathcal{A}(\omega) = \frac{1}{2\sqrt{\pi|\omega|}}\left[\Lambda(\omega)E(\omega) + \frac{\sigma(\omega)}{\Lambda(\omega)}H(\omega)\right], \tag{6.172}$$

and

$$\Lambda(\omega)\frac{E(\omega)}{\sqrt{\pi|\omega|}} = \mathcal{A}(\omega) + \mathcal{A}^*(-\omega), \qquad \frac{\sigma(\omega)}{\Lambda(\omega)}\frac{H(\omega)}{\sqrt{\pi|\omega|}} = \mathcal{A}(\omega) - \mathcal{A}^*(-\omega). \tag{6.173}$$

The scaling factor $\Lambda(\omega)$ is chosen in such a way that

$$\frac{\epsilon_0\epsilon(\omega)}{\Lambda^2(\omega)} = \mu_0\Lambda^2(\omega) \quad \Rightarrow \quad \Lambda(\omega) = \sqrt[4]{\frac{\epsilon_0\epsilon(\omega)}{\mu_0}}, \tag{6.174}$$

then the quadratic part of the Hamiltonian (6.164) is given by

$$\mathscr{H}_2 = \int_{-\infty}^{\infty} |\beta(\omega)|\mathcal{A}(\omega)\mathcal{A}^*(\omega)d\omega, \tag{6.175}$$

this is a z-replacement of the standard t-expression $\int_{-\infty}^{\infty}\omega(k)|a(k)|^2d\omega$. Equation (6.171) takes the form

$$i\partial_z\mathcal{A}(z,\omega) + |\beta(\omega)|\mathcal{A}(z,\omega) + \frac{\delta\mathscr{H}_{\text{int}}}{\delta\mathcal{A}^*(\omega)} = 0, \tag{6.176}$$

which is the pulse propagation equation in the Hamiltonian framework. The linear part of Eq. (6.176) looks unusual just because (6.176) combines both forward and backward waves. Indeed, ignoring for a moment $\mathscr{H}_{\text{int}}$ we obtain

$$\mathcal{A}(z,\omega) = \mathcal{A}(0,\omega)e^{i|\beta(\omega)|z}, \tag{6.177}$$

so that

$$E(z,\omega)e^{-i\omega t} = \sqrt{\frac{\pi|\omega|}{\epsilon_0 cn(\omega)}}\left[\mathcal{A}(0,\omega)e^{i|\beta(\omega)|z-i\omega t} + \mathcal{A}^*(0,-\omega)e^{-i|\beta(\omega)|z-i\omega t}\right]. \tag{6.178}$$

Taking some $\omega > 0$ we immediately see that $\mathcal{A}(0,\omega)$ and $\mathcal{A}^*(0,-\omega)$ describe forward and backward waves with physical frequency ω.

Now we return to the full Eq. (6.176). Before applying it one has to calculate $\delta\mathscr{H}_{\rm int}/\delta\mathcal{A}^*(\omega)$ with $\mathscr{H}_{\rm int} = \frac{1}{4}\epsilon_0\chi^{(3)}\int_{-\infty}^{\infty} E^4 dt$ or

$$\mathscr{H}_{\rm int} = \frac{\epsilon_0\chi^{(3)}}{32\pi^3}\int_{-\infty}^{\infty} E_1E_2E_3E_4\delta_{1234}d\mho, \tag{6.179}$$

where

$$d\mho = d\omega_1 d\omega_2 d\omega_3 d\omega_4, \tag{6.180}$$

E_i abbreviates $E(\omega_i, z)$, and the delta function $\delta(\omega_1 + \omega_2 + \omega_3 + \omega_4)$ is abbreviated by δ_{1234}. Other combinations of frequencies will be denoted by over-bars, e.g.,

$$\delta_{12\bar{3}\bar{4}} = \delta(\omega_1 + \omega_2 - \omega_3 - \omega_4). \tag{6.181}$$

Equation (6.179) can be expressed as

$$\mathscr{H}_{\rm int} = \frac{1}{32\pi}\int_{-\infty}^{\infty} T_{1234}(\mathcal{A}_1 + \mathcal{A}^*_{-1})(\mathcal{A}_2 + \mathcal{A}^*_{-2})(\mathcal{A}_3 + \mathcal{A}^*_{-3})(\mathcal{A}_4 + \mathcal{A}^*_{-4})\delta_{1234}d\mho, \tag{6.182}$$

where T_{1234} denotes

$$T(\omega_1, \omega_2, \omega_3, \omega_4) = \frac{\mu_0\chi^{(3)}\sqrt{|\omega_1\omega_2\omega_3\omega_4|}}{\sqrt{n(\omega_1)n(\omega_2)n(\omega_3)n(\omega_4)}}, \tag{6.183}$$

and is completely symmetric with respect to both permutation of indices and replacement of the sign of any frequency, $\omega \to -\omega$. In many cases $n(\omega)$ is close to a constant for all relevant frequencies and one can use a very simple expression

$$T(\omega_1, \omega_2, \omega_3, \omega_4) = \frac{\mu_0\chi^{(3)}}{n^2(\omega_0)}\sqrt{|\omega_1\omega_2\omega_3\omega_4|}, \tag{6.184}$$

where ω_0 is the carrier frequency. On the other hand, if description of the nonlinearity in terms of a single $\chi^{(3)} = \text{const}$ is inappropriate, $\chi^{(3)}$ is replaced with a full third-order susceptibility $\chi^{(3)}(\omega_1, \omega_2, \omega_3, \omega_4)$ that enters into Eq. (6.183) for T_{1234}. In this case we also assume symmetry with respect to permutation of frequencies, the so-called overall permutation symmetry. The latter applies to the fiber transparency window, where all involved frequencies considerably differ from the transition frequencies of the medium [15].

The above derived representation of $\mathscr{H}_{\rm int}(\mathcal{A}_1, \mathcal{A}_2, \mathcal{A}_3, \mathcal{A}_4)$ is immediately split into three terms

$$\mathscr{H}_{\rm int} = \mathscr{H}_{40} + \mathscr{H}_{31} + \mathscr{H}_{22}, \tag{6.185}$$

with simple physical interpretations: each term is responsible for a separate 4-wave process, namely

$$\mathscr{H}_{40} = \frac{1}{32\pi}\int_{-\infty}^{\infty} T_{1234}\mathcal{A}_1\mathcal{A}_2\mathcal{A}_3\mathcal{A}_4\delta_{1234}d\mho + \text{c.c.},$$
$$\mathscr{H}_{31} = \frac{1}{8\pi}\int_{-\infty}^{\infty} T_{1234}\mathcal{A}_1\mathcal{A}_2\mathcal{A}_3\mathcal{A}_4^*\delta_{123\bar{4}}d\mho + \text{c.c.},$$
$$\mathscr{H}_{22} = \frac{3}{16\pi}\int_{-\infty}^{\infty} T_{1234}\mathcal{A}_1\mathcal{A}_2\mathcal{A}_3^*\mathcal{A}_4^*\delta_{12\bar{3}\bar{4}}d\mho,$$

where, e.g., the last expression is a classical analogue of the quantum-mechanical process in which two photons disappear and two new photons are born.

Although all three constituents of $\mathscr{H}_{\text{int}}$ have amplitudes of the same order, they are of different importance for Eq. (6.176). For instance, using Eq. (6.177) one can estimate that $\mathscr{H}_{40}$ is a weighted average of the quickly oscillating factor

$$e^{i(|\beta(\omega_1)|+|\beta(\omega_2)|+|\beta(\omega_3)|+|\beta(\omega_4)|)z} \tag{6.186}$$

over the hyperplane $\omega_1 + \omega_2 + \omega_3 + \omega_4 = 0$ in the frequency space. Therefore $\mathscr{H}_{40}$ can be just neglected, or more precisely eliminated using the corresponding canonical transform as described in [73, 75]. In a similar way, $\mathscr{H}_{31}$ can essentially contribute to the dynamic if the following conditions are satisfied:

$$|\beta(\omega_1)| + |\beta(\omega_2)| + |\beta(\omega_3)| = |\beta(\omega_4)|, \qquad \omega_1 + \omega_2 + \omega_3 = \omega_4. \tag{6.187}$$

Recall that $\mathcal{A}(z,\omega)$ is related to the forward wave for $\omega > 0$ and to the backward wave for $\omega < 0$. Considering, e.g., only forward waves one can replace $|\beta(\omega)|$ with $\beta(\omega)$ and Eq. (6.187) reduces to the standard resonance conditions [73, 75]. Below we neglect both $\mathscr{H}_{40}$ and $\mathscr{H}_{31}$ so that the propagation Eq. (6.176) finally reads

$$\Big[i\partial_z + |\beta(\omega)|\Big]\mathcal{A}(z,\omega) + \frac{3}{8\pi}\int_{-\infty}^{\infty} T_{123\omega}\mathcal{A}_1\mathcal{A}_2\mathcal{A}_3^*\delta_{12\bar{3}\bar{\omega}}d\omega_1 d\omega_2 d\omega_3 = 0. \tag{6.188}$$

Equation (6.188) has the same mathematical structure as the gNLS equation (6.147) and can be solved using the same numerical methods. Several examples are given in [5]. On the other hand, Eq. (6.188) is just a reformulation of the original Maxwell equations (recall that one doesn't have to neglect non-resonant terms in the Hamiltonian, they can be removed by a suitable canonical transformation) without loss of generality. Beside numerics, the presented Hamiltonian framework has important applications with respect to integrals of motion and an intrinsic relation to the gNLS equation. These topics are described in the rest of the chapter.

6.4.3 Energy Transport

In this section we address the problem of energy transport. The value of the instant power is an important characteristic of optical pulses, in practical applications of the gNLS equation (6.147) it is convenient to renormalize the envelope $\psi(z,\tau)$ so that $|\psi(z,\tau)|^2$ gives the instant power [23]. The renormalization, however, depends on the chosen carrier frequency and may be inappropriate for optical supercontinuum in which very different frequencies can provide comparable contributions to the total power.

Hamiltonian language gives a simple representation for the instant power, a representation that correctly accounts for all frequencies. Energy conservation for the electromagnetic field in vacuum in the one-dimensional setting (6.118) is given by the well-known relation

$$\partial_t \left(\frac{\epsilon_0 E^2}{2} + \frac{B^2}{2\mu_0} \right) + \partial_z j_P = 0, \tag{6.189}$$

where, like in the previous section, $j_P = EB/\mu_0$ is the Poynting vector. For the z-propagation picture the quantity $\int_{-\infty}^{\infty} j_P(z,t)dt$ should be constant, the latter yields the total amount of energy transferred by a pulse per unit area that is transversal to the direction of propagation. If we now account for both fiber dispersion and nonlinearity, the expression for the energy density becomes complicated, however the expression for j_P should be identical to those in the free space [45]. Therefore we consider the following quantity:

$$\mathscr{E}[E,H] = \int_{-\infty}^{\infty} E(z,t)H(z,t)dt = \int_{-\infty}^{\infty} E(z,\omega)H^*(z,\omega)\frac{d\omega}{2\pi}. \tag{6.190}$$

z-conservation of $\mathscr{E}$ can be established directly from Eq. (6.118) because

$$\frac{d}{dz}\int_{-\infty}^{\infty} EHdt = \int_{-\infty}^{\infty} (-H\partial_t B - E\partial_t D)dt = \int_{-\infty}^{\infty} D(E)\partial_t E dt \tag{6.191}$$

and therefore any possible z-dependence of $\mathcal{E}$ is related only with the non-instantaneous part of $D(E)$

$$\frac{d\mathscr{E}}{dz} = \epsilon_0 \int_{-\infty}^{\infty} (\hat{\epsilon}E)(\partial_t E)dt = i\epsilon_0 \int_{-\infty}^{\infty} \omega\epsilon(\omega)E(\omega)E^*(\omega)\frac{d\omega}{2\pi}. \tag{6.192}$$

Equation (6.124) indicates that real and imaginary parts of $\epsilon(\omega)$ are even and odd functions of frequency correspondingly. Therefore the last integral is determined only by the imaginary part of $\epsilon(\omega)$. If the imaginary part can be neglected, the last integral vanishes and $\mathscr{E}[E,H]$ becomes an integral of motion.

Now we express the energy flux in terms of the normal variables $\mathcal{A}(z,t)$ and $\mathcal{A}^*(z,t)$ using (6.173). After simple transformations we obtain

$$\mathscr{E}[E,H] = \int_{-\infty}^{\infty} \omega \mathcal{A}(z,\omega)\mathcal{A}^*(z,\omega)d\omega. \tag{6.193}$$

The latter expression is, of course, of universal nature and gives the desired expression of total energy transferred by the pulse per unit area of the fiber cross-section.

6.4.4 Photon Number

In this section we consider the following functional

$$\mathcal{N}[\mathcal{A},\mathcal{A}^*] = 2\pi k_0 \int_{-\infty}^{\infty} \mathcal{A}(z,t)\mathcal{A}^*(z,t)dt = k_0 \int_{-\infty}^{\infty} \mathcal{A}(z,\omega)\mathcal{A}^*(z,\omega)d\omega, \tag{6.194}$$

where k_0 is an arbitrary constant wave vector. $\mathcal{N}[\mathcal{A},\mathcal{A}^*]$ is a valid Hamiltonian and the corresponding equation of motion yields

$$i\partial_z \mathcal{A}(z,\omega) + \frac{\delta \mathscr{N}}{\delta \mathcal{A}^*(\omega)} = 0 \quad \Rightarrow \quad \mathcal{A}(z,\omega) = \mathcal{A}(0,\omega)e^{ik_0 z}. \tag{6.195}$$

Now, we apply the well known theorem from the classical Hamiltonian mechanics [7]. Namely, if some Hamiltonian $\mathscr{H}[\mathcal{A},\mathcal{A}^*]$ is invariant with respect to one-parametric family of phase shifts (6.195), the quantity $\mathcal{N}[\mathcal{A},\mathcal{A}^*]$ is an integral of motion for the dynamic system generated by $\mathscr{H}[\mathcal{A},\mathcal{A}^*]$. This, e.g., applies to the Hamiltonians $\mathscr{H}_2$ and $\mathscr{H}_{22}$, and therefore to the propagation equation generated by

$$\mathscr{H} = \int_{-\infty}^{\infty} |\beta(\omega)|\mathcal{A}(\omega)\mathcal{A}^*(\omega)d\omega + \frac{3}{16\pi}\int_{-\infty}^{\infty} T_{1234}\mathcal{A}_1\mathcal{A}_2\mathcal{A}_3^*\mathcal{A}_4^*\delta_{12\bar{3}\bar{4}}d\mho. \tag{6.196}$$

The quantity $\mathcal{N}$ can be interpreted as the classical expression for the photon number. The arbitrary factor k_0 remains undetermined because the photon number cannot be defined completely self-consistently in the framework of classical fields.

6.4.5 Analytic Signal

In this section we establish a relation between the Hamiltonian (6.176) and the gNLS (6.147) equations. In particular, we shall demonstrate that the analytic signal

naturally appears in the Hamiltonian framework also. To this end we split the definition (6.172). First a complex field $\mathcal{E}(z,t)$ is derived from $E(z,t)$ and $H(z,t)$ so that

$$\mathcal{E}(z,\omega) = E(z,\omega) + \frac{\sigma(\omega)}{\epsilon_0 cn(\omega)} H(z,\omega) = E(z,\omega) - \frac{i\partial_z E(z,\omega)}{|\beta(\omega)|}, \tag{6.197}$$

then the normal variable $\mathcal{A}(z,t)$ is obtained by a simple rescaling in the frequency domain

$$\mathcal{A}(z,\omega) = \frac{1}{2}\sqrt{\frac{\epsilon_0 cn(\omega)}{\pi|\omega|}}\mathcal{E}(z,\omega). \tag{6.198}$$

These new definitions (6.197) and (6.198) are compatible with the older one (6.172). Let us show that the gNLS equation just stops at the $\mathcal{E}(z,t)$ level, without explicit use of the canonical variable $\mathcal{A}(z,t)$. Indeed Eq. (6.197) indicates that

$$E(\omega) = \frac{\mathcal{E}(\omega) + \mathcal{E}^*(-\omega)}{2} \tag{6.199}$$

so that in the physical space $E(z,t) = \frac{1}{2}\mathcal{E}(z,t) + \text{c.c.}$, as is should be for the complex amplitude. Moreover, applying Eq. (6.197) to a forward wave with $E(z,\omega) \sim e^{i\beta(\omega)z}$ we see that $\mathcal{E}(z,\omega)$ vanishes for $\omega < 0$. In a similar way, for a backward wave with $E(z,\omega) \sim e^{-i\beta(\omega)z}$ we see that $\mathcal{E}(z,\omega)$ vanishes for $\omega > 0$. In other words, if only forward waves are present, $\mathcal{E}(z,t)$ is just an analytic signal and an envelope for the electric field. Moreover, the propagation equation for $\mathcal{E}(z,t)$ appears to be identical to the gNLS equation [5].

6.5 Concluding Remarks

Let us summarize the most important results discussed above. We deal with pulses propagating in optical fibers and use approach originally developed by Zakharov and his coworkers for continuous Hamiltonian systems. The most important peculiarity is that optical equations are solved with respect to the propagation coordinate, not time. Notice that waves in a fiber can propagate in both directions, unlike the standard dynamical systems, which evolve forward in time. This difference leads to some changes in the general formalism, e.g., the quadratic part of the Hamiltonian looses its standard form $\int_{-\infty}^{\infty} \omega(k) a(k) a^*(k) dk$ and appears as $\int_{-\infty}^{\infty} |\beta(\omega)| \mathcal{A}(\omega) \mathcal{A}^*(\omega) d\omega$. One has an unusual representation of the resonant conditions and, moreover, all integrals of motion get an unusual meaning. The new integrals are determined by the time-averaged fluxes of the relevant physical quantities. However, all core features of the Hamiltonian approach are identical for both systems. This makes possible to develop a new framework for pulse

propagation. In particular, one can recognize that the generalized envelope equation, a model of choice in optics, is just a reformulation of the general Hamiltonian equation. In other words, envelope equations can be derived without use of the slowly varying envelope equation and the envelope as such. This explains why the gNLS equation works better than expected.

References

1. Agrawal, G.P.: Nonlinear Fiber Optics, 4th edn. Academic, New York (2007)
2. Agrawal, G.P., Baldeck, P.L., Alfano, R.R.: Optical wave breaking and pulse compression due to cross-phase modulation in optical fibers. Opt. Lett. **14**(2), 137–139 (1989)
3. Akhmediev, N., Ankiewicz, A.: Solitons: Nonlinear Pulses and Beams. Chapman and Hall, London (1997)
4. Akimoto, K.: Properties and applications of ultra-short electromagnetic mono- and sub-cycle waves. J. Phys. Soc. Jpn. **65**(7), 2020–2032 (1996)
5. Amiranashvili, S., Demircan, A.: Hamiltonian structure of propagation equations for ultrashort optical pulses. Phys. Rev. A **82**(1), 013812 (2010)
6. Amiranashvili, S., Vladimirov, A.G., Bandelow, U.: Solitary-wave solutions for few-cycle optical pulses. Phys. Rev. A **77**(6), 063821 (2008)
7. Arnold, V.I.: Mathematical Methods of Classical Mechanics, 2nd edn. Springer, Berlin (1989)
8. Belenov, E.M., Nazarkin, A.V.: Solutions of nonlinear-optics equations found outside the approximation of slowly varying amplitudes and phases. J. Exp. Theor. Phys. Lett. **51**(5), 288–292 (1990)
9. Belgiorno, F., Cacciatori, S.L., Clerici, M., Gorini, V., Ortenzi, G., Rizzi, L., Rubino, E., Sala, V.G., Faccio, D.: Hawking radiation from ultrashort laser pulse filaments. Phys. Rev. Lett. **105**(20), 203901 (2010)
10. Bespalov, V.G., Kozlov, S.A., Shpolyanskiy, Y.A., Walmsley, I.A.: Simplified field wave equations for the nonlinear propagation of extremely short light pulses. Phys. Rev. A **66**(1), 013811 (2002)
11. Biancalana, F.: Viewpoint: Negative frequencies get real. Physics **5**(68) (2012). http://physics.aps.org/articles/v5/68
12. Blow, K.J., Wood, D.: Theoretical description of transient stimulated Raman scattering in optical fibers. IEEE J. Quantum Electron. **25**(15), 2665–2673 (1989)
13. Bogoliubov, N., Mitropolsky, Y.A.: Asymptotic Methods in the Theory of Non-linear Oscillations, 1st edn. Gordon and Breach, New York (1961)
14. Born, M., Wolf, E.: Principles of Optics, 7th edn. Cambridge University Press, Cambridge (1999)
15. Boyd, R.W.: Nonlinear Optics, 3rd edn. Academic, New York (2008)
16. Brabec, T., Krausz, F.: Nonlinear optical pulse propagation in the single-cycle regime. Phys. Rev. Lett. **78**(17), 3282–3285 (1997)
17. Brabec, T., Krausz, F.: Intense few-cycle laser fields: frontiers of nonlinear optics. Rev. Mod. Phys. **72**(2), 545–591 (2000)
18. Demircan, A., Amiranashvili, S., Brée, C., Morgner, U., Steinmeyer, G.: Adjustable pulse compression scheme for generation of few-cycle pulses in the midinfrared. Opt. Lett. **39**(9), 2735–2738 (2014)
19. Diels, J.C., Rudolph, W.: Ultrashort Laser Pulse Phenomena, 2nd edn. Elsevier, Amsterdam (2006)
20. Drescher, M., Hentschel, M., Kienberger, R., Tempea, G., Spielmann, C., Reider, G.A., Corkum, P.B., Krausz, F.: X-ray pulses approaching the attosecond frontier. Science **291**(5510), 1923–1927 (2001)

21. Dubrovin, B.A., Fomenko, A.T., Novikov, S.P.: Modern Geometry - Methods and Applications. Part I: The Geometry of Surfaces, Transformation Groups, and Fields, 2nd edn. Springer, Berlin (1992)
22. Dudley, J.M., Gu, X., Xu, L., Kimmel, M., Zeek, E., O'Shea, P., Trebino, R., Coen, S., Windeler, R.S.: Cross-correlation frequency resolved optical gating analysis of broadband continuum generation in photonic crystal fiber: simulations and experiments. Opt. Express **10**(21), 1215–1221 (2002)
23. Dudley, J.M., Genty, G., Coen, S.: Supercontinuum generation in photonic crystal fiber. Rev. Mod. Phys. **78**(4), 1135–1184 (2006)
24. Faccio, D.: Laser pulse analogues for gravity and analogue hawking radiation. Contemp. Phys. **53**(2), 97–112 (2012)
25. Faddeev, L.D.: New life of complete integrability. Usp. Fiz. Nauk **56**(5), 465–472 (2013)
26. Faddeev, L.D., Takhtajan, L.A.: Hamiltonian Methods in the Theory of Solitons. Springer, Berlin (2007)
27. Ferrando, A., Zacarés, M., Fernández de Córdoba, P., Binosi, D., Montero, Á.: Forward-backward equations for nonlinear propagation in axially invariant optical systems. Phys. Rev. E **71**(1), 016601 (2005)
28. Gabor, D.: Theory of communication. J. Inst. Electr. Eng. **93**(3), 429–457 (1946)
29. Gardner, C.S., Greene, J.M., Kruskal, M.D., Miura, R.M.: Method for solving the Korteweg-deVries equation. Phys. Rev. Lett. **19**(19), 1095–1097 (1967)
30. Geissler, M., Tempea, G., Scrinzi, A., Schnürer, M., Krausz, F., Brabec, T.: Light propagation in field-ionizing media: extreme nonlinear optics. Phys. Rev. Lett. **83**(15), 2930–2933 (1999)
31. Genty, G., Kinsler, P., Kibler, B., Dudley, J.M.: Nonlinear envelope equation modeling of sub-cycle dynamics and harmonic generation in nonlinear waveguides. Opt. Express **15**(9), 5382–5387 (2007)
32. Goorjian, P.M., Taflove, A.: Direct time integration of Maxwell's equations in nonlinear dispersive media for propagation and scattering of femtosecond electromagnetic solitons. Opt. Lett. **17**(3), 180–182 (1992)
33. Hentschel, M., Kienberger, R., Spielmann, C., Reider, G.A., Milosevic, N., Brabec, T., Corkum, P., Heinzmann, U., Drescher, M., Krausz, F.: Attosecond metrology. Nature **414**(6863), 509–513 (2001)
34. Husakou, A.V., Herrmann, J.: Supercontinuum generation of higher-order solitons by fission in photonic crystal fibers. Phys. Rev. Lett. **87**(20), 203901 (2001)
35. Hutchings, D.C., Sheik-Bahae, M., Hagan, D.J., Van Stryland, E.W.: Kramers-krönig relations in nonlinear optics. Opt. Quantum Electron. **24**(1), 1–30 (1992)
36. Kaplan, A.E., Shkolnikov, P.L.: Electromagnetic "Bubbles" and shock waves: unipolar, nonoscillating EM solitons. Phys. Rev. Lett. **75**(12), 2316–2319 (1995)
37. Kibler, B., Fatome, J., Finot, C., Millot, G., Dias, F., Genty, G., Akhmediev, N., Dudley, J.M.: The peregrine soliton in nonlinear fibre optics. Nat. Phys. **6**(10), 790–795 (2010)
38. Kim, A.V., Skobelev, S.A., Anderson, D., Hansson, T., Lisak, M.: Extreme nonlinear optics in a Kerr medium: exact soliton solutions for a few cycles. Phys. Rev. A **77**(4), 043823 (2008)
39. Kinsler, P.: Optical pulse propagation with minimal approximations. Phys. Rev. A **81**(1), 013819 (2010)
40. Kinsler, P., New, G.H.C.: Few-cycle pulse propagation. Phys. Rev. A **67**(2), 023813 (2003)
41. Kolesik, M., Moloney, J.V.: Nonlinear optical pulse propagation simulation: from Maxwell's to unidirectional equations. Phys. Rev. E **70**(3), 036604 (2004)
42. Kolesik, M., Moloney, J.V., Mlejnek, M.: Unidirectional optical pulse propagation equation. Phys. Rev. Lett. **89**(28), 283902 (2002)
43. Kozlov, S.A., Sazonov, S.V.: Nonlinear propagation of optical pulses of a few oscillations duration in dielectric media. J. Exp. Theor. Phys. **84**(2), 221–228 (1997)
44. Landau, L.D., Lifshitz, E.M.: Mechanics. Pergamon, New York (1969)
45. Landau, L.D., Lifshitz, E.M., Pitaevskii, L.P.: Electrodynamics of Continuous Media, 2nd edn. Elsevier, New York (1984)

46. Leblond, H.: Half-cycle optical soliton in quadratic nonlinear media. Phys. Rev. A **78**(1), 013807 (2008)
47. Leblond, H., Michaelis, D.: Models of few optical cycle solitons beyond the slowly varying envelope approximation. Phys. Rep. **523**(2), 61–126 (2013)
48. Leblond, H., Sanchez, F.: Models for optical solitons in the two-cycle regime. Phys. Rev. A **67**(1), 013804 (2003)
49. Leblond, H., Sazonov, S.V., Mel'nikov, I.V., Mihalache, D., Sanchez, F.: Few-cycle nonlinear optics of multicomponent media. Phys. Rev. A **74**(6), 063815 (2006)
50. Lichtenberg, A.J., Lieberman, M.A.: Regular and Chaotic Dynamics, 2nd edn. Applied Mathematical Sciences, vol. 38. Springer, Berlin (1982)
51. Maimistov, A.I.: Some models of propagation of extremely short electromagnetic pulses in a nonlinear medium. Quantum Electron. **30**(4), 287–304 (2000)
52. Malomed, B.A., Mihalache, D., Wise, F., Torner, L.: Spatiotemporal optical solitons. J. Opt. B Quantum Semiclassical Opt. **7**(5), R53–R72 (2005)
53. Mizuta, Y., Nagasawa, M., Ohtani, M., Yamashita, M.: Nonlinear propagation analysis of few-optical-cycle pulses for subfemtosecond compression and carrier envelope phase effect. Phys. Rev. A **72**(6), 063802 (2005)
54. Nayfeh, A.H.: Perturbation Methods. Wiley, New York (1973)
55. Nazarkin, A., Korn, G.: Pulse self-compression in the subcarrier cycle regime. Phys. Rev. Lett. **83**(23), 4748–4751 (1999)
56. Onorato, M., Residori, S., Bortolozzo, U., Montina, A., Arecchi, F.T.: Rogue waves and their generating mechanisms in different physical contexts. Phys. Rep. **528**(2), 47–89 (2013)
57. Paul, P.M., Toma, E.S., Breger, P., Mullot, G., Augé, F., Balcou, P., Muller, H.G., Agostini, P.: Observation of a train of attosecond pulses from high harmonic generation. Science **292**(5522), 1689–1692 (2001)
58. Philbin, T.G., Kuklewicz, C., Robertson, S., Hill, S., Konig, F., Leonhardt, U.: Fiber-optical analog of the event horizon. Science **319**(5868), 1367–1370 (2008)
59. Rubino, E., McLenaghan, J., Kehr, S.C., Belgiorno, F., Townsend, D., Rohr, S., Kuklewicz, C.E., Leonhardt, U., König, F., Faccio, D.: Negative-frequency resonant radiation. Phys. Rev. Lett. **108**(25), 253901 (2012)
60. Schäfer, T., Wayne, C.E.: Propagation of ultra-short optical pulses in cubic nonlinear media. Phys. D **196**(1–2), 90–105 (2004)
61. Semenov, V.E.: Formation of a reflected wave under propagation of a pulse with high peak intensity through a Kerr medium. J. Exp. Theor. Phys. **102**(1), 34–39 (2006)
62. Skobelev, S.A., Kartashov, D.V., Kim, A.V.: Few-optical-cycle solitons and pulse self-compression in a Kerr medium. Phys. Rev. Lett. **99**(20), 203902 (2007)
63. Solli, D.R., Ropers, C., Koonath, P., Jalali, B.: Optical rogue waves. Nature **450**(13), 1054–1057 (2007)
64. Strocchi, F.: Complex coordinates and quantum mechanics. Rev. Mod. Phys. **38**(1), 36–40 (1966)
65. Taylor, Francis.: Fundamentals of Attosecond Optics. CRC Press, Boca Raton (2011)
66. Thyagarajan, K., Ghatak, A.: Fiber Optic Essentials. Wiley, New York (2007)
67. Vakman, D.E., Vainshtein, L.A.: Amplitude, phase, frequency—fundamental concepts of oscillation theory. Usp. Fiz. Nauk **20**(12), 1002–1016 (1977)
68. Wirtinger, W.: Zur formalen Theorie der Funktionen von mehr komplexen Veränderlichen. Math. Ann. **97**(1), 357–376 (1927)
69. Zakharov, V.E., Faddeev, L.D.: Korteweg-de Vries equation: a completely integrable Hamiltonian system. Funct. Anal. Appl. **5**(4), 280–287 (1971)
70. Zakharov, V.E., Kuznetsov, E.A.: Hamiltonian formalism for nonlinear waves. Usp. Fiz. Nauk **40**(11), 1087–1116 (1997)
71. Zakharov, V.E., Kuznetsov, E.A.: Optical solitons and quasisolitons. J. Exp. Theor. Phys. **86**(5), 1035–1046 (1998)

72. Zakharov, V.E., Shabat, A.B.: Exact theory of two-dimensional self-focusing and one-dimensional self-modulation of waves in nonlinear media. Sov. Phys. JETP **34**(1), 62–69 (1972)
73. Zakharov, V.E., Musher, S.L., Rubenchik, A.M.: Hamiltonian approach to the description of non-linear plasma phenomena. Phys. Rep. **129**(5), 287–366 (1985)
74. Zakharov, V.E., L'vov, V.S., Falkovich, G.: Kolmogorov Spectra of Turbulence 1. Wave Turbulence. Springer, Berlin (1992)
75. Zakharov, V., Frédéric, D., Pushkarev, A.: One-dimensional wave turbulence. Phys. Rep. **398**(1), 1–65 (2004)

Chapter 7
Modeling Water Waves Beyond Perturbations

Didier Clamond and Denys Dutykh

Abstract In this chapter, we illustrate the advantage of variational principles for modeling water waves from an elementary practical viewpoint. The method is based on a 'relaxed' variational principle, i.e., on a Lagrangian involving as many variables as possible, and imposing some suitable subordinate constraints. This approach allows the construction of approximations without necessarily relying on a small parameter. This is illustrated via simple examples, namely the Serre equations in shallow water, a generalization of the Klein–Gordon equation in deep water and how to unify these equations in arbitrary depth. The chapter ends with a discussion and caution on how this approach should be used in practice.

7.1 Introduction

Surface water waves are a very rich physical phenomenon with a long research history [5, 35]. In addition to their fundamental physical importance, understanding water waves is also important for many applications related to human safety and economy such as tsunamis, freak waves, harbor protections, beach nourishment/erosion, just to mention a few examples. Water waves are a paradigm for many nonlinear wave phenomena in various physical media. The prominent physicist Richard P. Feynman wrote in his cerebrated lectures [10]: *"Water waves that are easily seen by everyone, and which are usually used as an example of waves in elementary courses, are the worst possible example; they have all the complications that waves can have."* This is precisely these complications that make the richness and interest of water waves. Indeed, despite numerous studies, new waves and new

D. Clamond (✉)
Université de Nice – Sophia Antipolis, Laboratoire J. A. Dieudonné, Parc Valrose, 06108 Nice Cedex 2, France
e-mail: diderc@unice.fr

D. Dutykh
Université Savoie Mont Blanc, LAMA, UMR 5127 CNRS, Campus Scientifique, 73376 Le Bourget-du-Lac Cedex, France
e-mail: Denys.Dutykh@univ-savoie.fr

E. Tobisch (ed.), *New Approaches to Nonlinear Waves*, Lecture Notes in Physics 908, DOI 10.1007/978-3-319-20690-5_7

wave behaviors are still discovered (e.g., [26, 27]) and wave dynamics is still far from being fully understood.

Mathematical and numerical models are unavoidable for understanding water waves. Although the primitive equations governing these waves are rather simple to write, their mathematical analysis is highly non trivial and even their numerical resolution is very demanding. Therefore, simplified models are crucial to gain insight and to derive operational numerical models. Most of the time, simplified models are derived via some asymptotic expansions, exploiting a small parameter in the problem at hands. This approach is very effective leading to well-known equations, such as the Saint-Venant [31, 35], Boussinesq [1], Serre–Green–Naghdi [12, 29], Korteweg-deVries [17] equations in shallow water and the nonlinear Schrödinger [22], Dysthe [9] equations in deep water. These equations being most often derived via some perturbation techniques, they are valid for waves of small amplitude or/and small *wavelength/water depth* ratio. However, for many applications it is necessary to use models uniformly valid for all depths and that are accurate for large amplitudes. Moreover, some phenomena [26, 27] do not involve any small parameter and do not bifurcate from rest. The problem is then to derive models without relying on a small parameter.

It is well-known in theoretical physics that variational formulations are tools of choice to derive approximations when small parameter expansions are inefficient. Fortunately, a variational principle is available for water waves that can be exploited to derive approximations. There are mainly two variational formulations for irrotational surface waves that are commonly used, namely the Lagrangian of Luke [21] and the Hamiltonian of Broer, Petrov and Zakharov [2, 24, 38]. Details on the variational formulations for surface waves can be found in review papers, e.g., [25, 28, 39].

In water wave theory, variational formulations are generally used together with a small parameter expansion. This is not necessary, however, because variational methods can also be fruitfully used without small parameter, as it is well-known in Quantum Mechanics, for example. This was demonstrated in [4], the present chapter being a simpler illustration of this idea, with some complementary remarks. A companion presentation with further comments can be found in [3]. Here, only elementary knowledge in vector calculus is assumed, as well as some familiarity with the Euler–Lagrange equations and variational principles in Mechanics [11, 18].

The chapter is organized as follows. In Sect. 7.2, the physical hypothesis, notations and equations are given for the classical problem of irrotational surface gravity waves. In Sect. 7.3, Luke's Lagrangian is *relaxed* to incorporate explicitly more degrees of freedom. This modification yields the Hamilton principle in its most general form. The advantage of this formulation is subsequently illustrated Sect. 7.4 with examples over a fixed horizontal bottom, for the sake of simplicity. We begin with a shallow water model, followed by a deep water one and ending with an arbitrary depth generalization. Further generalizations, shortcomings and perspectives are discussed in Sect. 7.5.

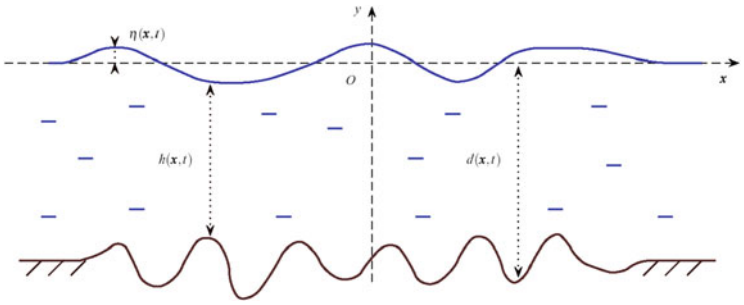

Fig. 7.1 Definition sketch

7.2 Preliminaries

Consider an ideal incompressible fluid of constant density ρ. The horizontal independent variables are denoted by $\boldsymbol{x} = (x_1, x_2)$ and the upward vertical one by y. The origin of the Cartesian coordinate system is chosen such that the surface $y = 0$ corresponds to the still water level. The fluid is bounded below by the bottom at $y = -d(\boldsymbol{x}, t)$ and above by the free surface at $y = \eta(\boldsymbol{x}, t)$. Usually, we assume that the total depth $h(\boldsymbol{x}, t) \equiv d(\boldsymbol{x}, t) + \eta(\boldsymbol{x}, t)$ remains positive $h(\boldsymbol{x}, t) \geqslant h_0 > 0$ at all times t for some constant h_0. A sketch of the physical domain is shown on Fig. 7.1.

We denote $\boldsymbol{u} = (u_1, u_2)$ the horizontal velocity and v vertical one. The fluid density being constant, the mass conservation implies an isochoric motion yielding the continuity equation valid everywhere in the fluid domain

$$\boldsymbol{\nabla} \cdot \boldsymbol{u} + \partial_y v = 0, \tag{7.1}$$

where $\boldsymbol{\nabla}$ denotes the horizontal gradient and $\cdot$ denotes the scalar (inner) product of vectors.

Denoting with over 'tildes' and 'breves' the quantities computed, respectively, at the free surface $y = \eta(\boldsymbol{x}, t)$ and at the bottom $y = -d(\boldsymbol{x}, t)$,[1] the impermeabilities of these boundaries give the relations

$$\partial_t \eta + \tilde{\boldsymbol{u}} \cdot \boldsymbol{\nabla} \eta = \tilde{v}, \qquad \partial_t d + \breve{\boldsymbol{u}} \cdot \boldsymbol{\nabla} d = -\breve{v}. \tag{7.2}$$

Traditionally in water wave modeling, the assumption of flow irrotationality is also adopted because it is relevant in many situations and it brings considerable simplifications. The zero-curl velocity field condition can be written

$$\boldsymbol{\nabla} v = \partial_y \boldsymbol{u}, \qquad \boldsymbol{\nabla} \times \boldsymbol{u} = 0, \tag{7.3}$$

[1] For example $\tilde{\boldsymbol{u}} = \boldsymbol{u}(y = \eta)$, $\breve{v} = v(y = -d)$.

where $\times$ is a two dimensional analog of the cross product.[2] The irrotationality conditions (7.3) are satisfied identically introducing a (scalar) velocity potential ϕ such that

$$\boldsymbol{u} = \nabla\phi, \qquad v = \partial_y\phi. \tag{7.4}$$

For irrotational motions of incompressible fluids, the Euler momentum equations can be integrated into the scalar Lagrange–Cauchy equation

$$p + \partial_t\phi + gy + \tfrac{1}{2}|\nabla\phi|^2 + \tfrac{1}{2}(\partial_y\phi)^2 = 0, \tag{7.5}$$

where p is the pressure divided by the density ρ and $g > 0$ is the acceleration due to gravity. At the free surface the pressure is zero—i.e., $\tilde{p} = 0$—but surface tensions or other effects could be taken into account. Note that for steady flows, i.e. when the velocity field is independent of time, $\partial_t\phi = \text{constant} = -B$ and the Lagrange–Cauchy equation becomes the Bernoulli equation, B being a Bernoulli constant.

In summary, with the hypotheses above, the governing equations of the classical (non overturning) surface water waves are [16, 32, 36]:

$$\nabla^2\phi + \partial_y^2\phi = 0, \qquad -d(\boldsymbol{x},t) \leqslant y \leqslant \eta(\boldsymbol{x},t), \tag{7.6}$$

$$\partial_t\eta + (\nabla\phi)\cdot(\nabla\eta) - \partial_y\phi = 0, \qquad y = \eta(\boldsymbol{x},t), \tag{7.7}$$

$$\partial_t\phi + \tfrac{1}{2}|\nabla\phi|^2 + \tfrac{1}{2}(\partial_y\phi)^2 + g\eta = 0, \qquad y = \eta(\boldsymbol{x},t), \tag{7.8}$$

$$\partial_t d + (\nabla d)\cdot(\nabla\phi) + \partial_y\phi = 0, \qquad y = -d(\boldsymbol{x},t). \tag{7.9}$$

The assumptions of fluid incompressibility and flow irrotationality lead to the Laplace equation (7.6) for the velocity potential $\phi(\boldsymbol{x},y,t)$. The main difficulty of the water wave problem lies on the boundary conditions. Equations (7.7) and (7.9) express the free-surface kinematic condition and bottom impermeability, respectively, while the dynamic condition (7.8) expresses the free surface isobarity.

7.3 Variational Formulations

Equations (7.6)–(7.9) can be derived from the "stationary point" (point where the variation is zero) of the following functional

$$\mathcal{L} = \int_{t_1}^{t_2}\int_{\Omega} \mathscr{L}\,\rho\,\mathrm{d}^2\boldsymbol{x}\,\mathrm{d}t$$

[2] For two-dimensional vectors $\boldsymbol{a} = (a_1, a_2)$ and $\boldsymbol{b} = (b_1, b_2)$, $\boldsymbol{a} \times \boldsymbol{b} = a_1b_2 - a_2b_1$ is a scalar.

(Ω the horizontal domain) where the Lagrangian density $\mathscr{L}$ is [21]

$$\mathscr{L} = -\int_{-d}^{\eta} \left[gy + \partial_t \phi + \tfrac{1}{2}|\nabla\phi|^2 + \tfrac{1}{2}(\partial_y \phi)^2 \right] \mathrm{d}y. \tag{7.10}$$

One can check that the Euler–Lagrange equations for this functional yield directly the water wave equations. (Detailed algebra can be found in [21], but also on Wikipedia.[3]) If the fluid incompressibility and the bottom impermeability are satisfied identically, Luke's Lagrangian is reduced to a form leading directly to the Hamiltonian of Zakharov [38]. However, for many practical applications, it is advantageous *not* to fulfil a maximum of relations, as advocated in [4], further explained in [3] and here.

Integrating by parts and neglecting the terms at the horizontal and temporal boundaries because they do not contribute to the functional variations (this will be done repeatedly below without explicit mention), Luke's variational formulation (7.10) can be rewritten with the following Lagrangian density:

$$\mathscr{L} = \tilde{\phi}\,\eta_t + \breve{\phi}\,d_t - \frac{g\,\eta^2}{2} + \frac{g\,d^2}{2} - \int_{-d}^{\eta} \left[\frac{|\nabla\phi|^2}{2} + \frac{\phi_y^2}{2} \right] \mathrm{d}y. \tag{7.11}$$

The alternative form (7.11) is somehow more convenient. Note that:

(a) the term $\tilde{\phi}\eta_t$, for example, can be replaced by $-\eta\tilde{\phi}_t$ after integration by parts;
(b) the term $gd^2/2$ can be omitted because, d being prescribed, it does not contribute to the variational principle;
(c) the term $g\eta^2/2$ can be replaced by $gh^2/2$ via a change of definition of ϕ.

Luke's Lagrangian involves a velocity potential but not explicitly the velocity field. Thus, any approximation derived from (7.10) has an irrotational velocity field because the latter is calculated from the relations (7.4). The water wave problem involving several equations, there are a priori no reasons to enforce the irrotationality and not, for example, the incompressibility or the surface isobarity or even any combination of these relations. As it is well known in numerical methods, enforcing an exact resolution of as many equations as possible is not always a good idea. Indeed, numerical analysis and scientific computing know many examples when efficient and most used algorithms do exactly the opposite. These so-called *relaxation methods* have proven to be very efficient for stiff problems. When solving numerically a system of equations, the exact resolution of a few equations does not necessarily ensure that the overall error is reduced: What really matters is that the global error is minimized. A similar idea of relaxation may also apply to analytical approximations, as advocated in [4].

In order to give us more freedom for building approximations, while keeping an exact formulation, the variational principle is modified (relaxed) by introducing

[3] http://en.wikipedia.org/wiki/Luke's_variational_principle.

explicitly the horizontal velocity $\boldsymbol{u} = \nabla\phi$ and the vertical one $v = \phi_y$. The variational formulation can thus be reformulated with the Lagrangian density

$$\mathscr{L} = \tilde{\phi}\,\eta_t + \breve{\phi}\,d_t - \frac{g\,\eta^2}{2} - \int_{-d}^{\eta}\left[\frac{\boldsymbol{u}^2+v^2}{2} + \boldsymbol{\mu}\cdot(\nabla\phi-\boldsymbol{u}) + \nu(\phi_y - v)\right]\mathrm{d}y, \tag{7.12}$$

where the Lagrange multipliers $\boldsymbol{\mu}$ and ν have to be determined. By variations with respect of $\boldsymbol{u}$ and v, one finds at once the definition of the Lagrange multipliers:

$$\boldsymbol{\mu} = \boldsymbol{u}, \qquad \nu = v, \tag{7.13}$$

so $(\boldsymbol{\mu}, \nu)$ is another representation of the velocity field, in addition to $(\boldsymbol{u}, v)$ and $(\nabla\phi, \phi_y)$. These relations can be substituted into (7.12), but it is advantageous to keep the most general form of the Lagrangian. Indeed, it allows to choose ansatz for the Lagrange multipliers $\boldsymbol{\mu}$ and ν that can be different from the velocity field $\boldsymbol{u}$ and v. The Lagrangian density (7.12) involving six dependent variables $\{\eta, \phi, \boldsymbol{u}, v, \boldsymbol{\mu}, \nu\}$—while the original Lagrangian (7.11) only two (η and ϕ)—it allows more and different subordinate relations to be fulfilled.

The connection of (7.12) with the variational formulation of the classical mechanics can be seen applying Green's theorem to (7.12) that yields another equivalent variational formulation involving the Lagrangian density

$$\begin{aligned}\mathscr{L} = {} & (\partial_t\eta + \tilde{\boldsymbol{\mu}}\cdot\nabla\eta - \tilde{\nu})\,\tilde{\phi} + (\partial_t d + \breve{\boldsymbol{\mu}}\cdot\nabla d + \breve{\nu})\,\breve{\phi} - \tfrac{1}{2}g\,\eta^2 \\ & + \int_{-d}^{\eta}\left[\boldsymbol{\mu}\cdot\boldsymbol{u} - \tfrac{1}{2}\boldsymbol{u}^2 + \nu v - \tfrac{1}{2}v^2 + (\nabla\cdot\boldsymbol{\mu} + \partial_y\nu)\,\phi\right]\mathrm{d}y,\end{aligned} \tag{7.14}$$

and if the relations (7.13) are used, this Lagrangian density is reduced to

$$\begin{aligned}\mathscr{L} = {} & (\partial_t\eta + \tilde{\boldsymbol{u}}\cdot\nabla\eta - \tilde{v})\,\tilde{\phi} + (\partial_t d + \breve{\boldsymbol{u}}\cdot\nabla d + \breve{v})\,\breve{\phi} - \tfrac{1}{2}g\,\eta^2 \\ & + \int_{-d}^{\eta}\left[\tfrac{1}{2}\boldsymbol{u}^2 + \tfrac{1}{2}v^2 + (\nabla\cdot\boldsymbol{u} + \partial_y v)\,\phi\right]\mathrm{d}y.\end{aligned} \tag{7.15}$$

Thus, the classical Hamilton principle is recovered, i.e., the Lagrangian is the kinetic energy minus the potential energy plus constraints for the incompressibility and the boundary impermeabilities.

The Lagrangians (7.10), (7.11), (7.12), (7.14) and (7.15) yield the same exact relations. However, (7.12), (7.14) and (7.15) allow the constructions of approximations that are not exactly irrotational, that is not the case (7.10) and (7.11). This advantage is illustrated below via some simple examples. Further examples can be found in [4, 6].

7.4 Examples

Here, we illustrate the use of the variational principle via some simple examples. For the sake of simplicity, we always consider the pseudo velocities equal to the velocity, i.e., we take $\boldsymbol{\mu} = \boldsymbol{u}$ and $v = v$. We also focus on two-dimensional problems in constant depth, i.e., one horizontal dimension (denoted x) with $d > 0$ independent of t and x. For brevity, the horizontal velocity is denoted u.

7.4.1 Shallow Water: Serre's Equations

For surface waves propagating in shallow water, it is well known that the velocity fields varies little along the vertical. A reasonable ansatz for the horizontal velocity is thus one such that u is independent of y, i.e., one can consider the approximation

$$u(x, y, t) \approx \bar{u}(x, t), \tag{7.16}$$

meaning that u is assumed close to its depth-averaged value.[4] In order to introduce a suitable ansatz for the vertical velocity, one can assume, for example, that the fluid incompressibility (7.1) and the bottom impermeability (7.2) are fulfilled. These choices lead thus to the ansatz

$$v(x, y, t) \approx -(y + d)\,\bar{u}_x. \tag{7.17}$$

Notice that, with this ansatz, the velocity field is not exactly irrotational, i.e.

$$v_x - u_y \approx -(y + d)\,\bar{u}_{xx}. \tag{7.18}$$

This does *not* mean that we are modeling a vortical motion but, instead, that we are modeling a potential flow via a velocity field that is not exactly irrotational. This should not be more surprising than, e.g., using an approximation such that the pressure at the free surface is not exactly zero.

With the ansatz (7.16)–(7.17), the vertical acceleration (with $\mathrm{D}/\mathrm{D}t$ being the temporal derivative following the motion) is

$$\frac{\mathrm{D}\,v}{\mathrm{D}t} = \frac{\partial\, v}{\partial t} + u\,\frac{\partial\, v}{\partial x} + v\,\frac{\partial\, v}{\partial y} \approx -v\,\bar{u}_x - (y + d)\,\frac{\mathrm{D}\,\bar{u}_x}{\mathrm{D}t} = \gamma\,\frac{y + d}{h}, \tag{7.19}$$

[4] $\bar{u} = \frac{1}{h}\int_{-d}^{\eta} u\,\mathrm{d}y$.

where γ is the vertical acceleration at the free surface:

$$\gamma \equiv \left.\frac{\mathrm{D}\, v}{\mathrm{D}t}\right|_{y=\eta} \approx h\left[\bar{u}_x^2 - \bar{u}_{xt} - \bar{u}\,\bar{u}_{xx}\right]. \tag{7.20}$$

The kinetic energy per water column $\mathscr{K}$ is similarly easily derived

$$\frac{\mathscr{K}}{\rho} = \int_{-d}^{\eta} \frac{u^2+v^2}{2}\,\mathrm{d}y \approx \frac{h\,\bar{u}^2}{2} + \frac{h^3\,\bar{u}_x^2}{6}. \tag{7.21}$$

The Hamilton principle (7.15)—i.e., kinetic minus potential energies plus constraints for incompressibility and boundary impermeabilities—yields, for this ansatz and after some elementary algebra, the Lagrangian density

$$\mathscr{L} = \tfrac{1}{2}\,h\,\bar{u}^2 + \tfrac{1}{6}\,h^3\,\bar{u}_x^2 - \tfrac{1}{2}\,g\,h^2 + \{h_t + [h\,\bar{u}]_x\}\,\tilde{\phi}. \tag{7.22}$$

The Euler–Lagrange equations for this functional are

$$\delta\tilde{\phi}: \quad 0 = h_t + [h\,\bar{u}]_x, \tag{7.23}$$

$$\delta\bar{u}: \quad 0 = \tilde{\phi}\,h_x - [h\,\tilde{\phi}]_x - \tfrac{1}{3}\,[h^3\,\bar{u}_x]_x + h\,\bar{u}, \tag{7.24}$$

$$\delta h: \quad 0 = \tfrac{1}{2}\,\bar{u}^2 - g\,h + \tfrac{1}{2}\,h^2\,\bar{u}_x^2 - \tilde{\phi}_t + \tilde{\phi}\,\bar{u}_x - [\bar{u}\,\tilde{\phi}]_x, \tag{7.25}$$

thence

$$\tilde{\phi}_x = \bar{u} - \tfrac{1}{3}\,h^{-1}\,[h^3\,\bar{u}_x]_x, \tag{7.26}$$

$$\tilde{\phi}_t = \tfrac{1}{2}\,h^2\,\bar{u}_x^2 - \tfrac{1}{2}\,\bar{u}^2 - g\,h + \tfrac{1}{3}\,\bar{u}\,h^{-1}\,[h^3\,\bar{u}_x]_x. \tag{7.27}$$

Differentiation of (7.27) with respect of x yields, after some algebra, the equation

$$\left[\bar{u} - \tfrac{1}{3}\,h^{-1}(h^3\bar{u}_x)_x\right]_t + \left[\tfrac{1}{2}\,\bar{u}^2 + g\,h - \tfrac{1}{2}\,h^2\,\bar{u}_x^2 - \tfrac{1}{3}\,\bar{u}\,h^{-1}(h^3\bar{u}_x)_x\right]_x = 0, \tag{7.28}$$

that can rewritten in the non-conservative form

$$\bar{u}_t + \bar{u}\,\bar{u}_x + g\,h_x + \tfrac{1}{3}\,h^{-1}\,\partial_x\left[h^2\,\gamma\right] = 0. \tag{7.29}$$

After multiplication by h and exploiting (7.23), we also derive the conservative equations

$$[h\,\bar{u}]_t + \left[h\,\bar{u}^2 + \tfrac{1}{2}\,g\,h^2 + \tfrac{1}{3}\,h^2\,\gamma\right]_x = 0. \tag{7.30}$$

In summary, we have derived the system of equations

$$h_t + \partial_x[h\,\bar{u}] = 0, \tag{7.31}$$

$$\partial_t[h\,\bar{u}] + \partial_x\big[h\,\bar{u}^2 + \tfrac{1}{2}g\,h^2 + \tfrac{1}{3}h^2\,\gamma\big] = 0, \tag{7.32}$$

$$h\,\bar{u}_x^2 - h\,\bar{u}_{xt} - h\,\bar{u}\,\bar{u}_{xx} = \gamma, \tag{7.33}$$

that are the Serre equations. With the Serre equations, the irrotationality is not exactly satisfied, and thus these equations cannot be derived from Luke's variational principle.

Assuming small derivatives (i.e., long waves) but not small amplitudes, these equations were first derived by Serre [30] via a different route. They were independently rediscovered by Su and Gardner [33], and again by Green et al. [13]. These approximations being valid in shallow water without assuming small amplitude waves, they are therefore sometimes called *weakly-dispersive fully-nonlinear approximation* [37] and are a generalization of the Saint-Venant [31, 35] and of the Boussinesq equations. The variational derivation above is obvious and straightforward. Further details on the Serre equations concerning their properties and numerical resolutions can be easily found in the literature, e.g., [8, 20, 34].

7.4.2 Deep Water: Generalized Klein–Gordon Equations

For waves in deep water, measurements show that the velocity field varies nearly exponentially along the vertical [14, 15], even for very large unsteady waves (including breaking waves). Thus, this property is exploited here to derive simple approximations for gravity waves in deep water.

Let $\kappa > 0$ be a characteristic wavenumber corresponding, e.g., to the carrier wave of a modulated wave group or to the peak frequency of a JONSWAP spectrum. Following the discussion above, it is natural to seek approximations in the form

$$\{\,\phi\,;\,u\,;\,v\,\} \approx \{\,\tilde{\phi}\,;\,\tilde{u}\,;\,\tilde{v}\,\}\,\mathrm{e}^{\kappa(y-\eta)}, \tag{7.34}$$

where $\tilde{\phi}$, $\tilde{u}$ and $\tilde{v}$ are functions of x and t that can be determined using the variational principle (with or without additional constraints). The ansatz (7.34) is certainly the simplest possible that is consistent with experimental evidences.

The ansatz (7.34) substituted into the Lagrangian density (7.15) yields

$$2\,\kappa\,\mathscr{L} = 2\kappa\,\tilde{\phi}\,\eta_t - g\,\kappa\,\eta^2 + \tfrac{1}{2}\,\tilde{u}^2 + \tfrac{1}{2}\,\tilde{v}^2 - (\tilde{\phi}_x - \kappa\,\tilde{\phi}\,\eta)\,\tilde{u} - \kappa\,\tilde{v}\,\tilde{\phi}. \tag{7.35}$$

With (or without) subordinate relations, this Lagrangian gives various equations. We present here only the case without further constraints, thus the Euler–Lagrange equations yield

$$\begin{aligned}
\delta\tilde{u}: \quad & 0 = \tilde{u} - \tilde{\phi}_x + \kappa\,\tilde{\phi}\,\eta_x,\\
\delta\tilde{v}: \quad & 0 = \tilde{v} - \kappa\,\tilde{\phi},\\
\delta\tilde{\phi}: \quad & 0 = 2\kappa\,\eta_t + \tilde{u}_x - \kappa\,\tilde{v} + \kappa\,\tilde{u}\,\eta_x,\\
\delta\eta: \quad & 0 = 2\,g\,\kappa\,\eta + 2\,\kappa\,\tilde{\phi}_t + \kappa\,[\tilde{\phi}\,\tilde{u}]_x.
\end{aligned}$$

The two first relations imply that this approximation is exactly irrotational and their use in the last two equations gives

$$\eta_t + \tfrac{1}{2}\,\kappa^{-1}\,\tilde{\phi}_{xx} - \tfrac{1}{2}\,\kappa\,\tilde{\phi} = \tfrac{1}{2}\,\tilde{\phi}\left[\,\eta_{xx} + \kappa\,\eta_x^2\,\right], \tag{7.36}$$

$$\tilde{\phi}_t + g\,\eta = -\tfrac{1}{2}\left[\,\tilde{\phi}\,\tilde{\phi}_x - \kappa\,\tilde{\phi}^2\,\eta_x\,\right]_x. \tag{7.37}$$

Since Eqs. (7.36)–(7.37) derive from an irrotational motion, they can also be obtained from Luke's Lagrangian (7.10) under the ansatz (7.34). That would not be the case if, for example, we had enforced the incompressibility in the ansatz because, here, that leads to a rotational ansatz (see [4], § 2784.3).

To the linear approximation, after elimination of $\tilde{\phi}$, Eqs. (7.36)–(7.37) yield

$$\eta_{tt} - (g/2\kappa)\,\eta_{xx} + (g\kappa/2)\,\eta = 0, \tag{7.38}$$

that is a Klein–Gordon equation. For this reason, Eqs. (7.36) and (7.37) are named here *generalized Klein–Gordon* (gKG). The Klein–Gordon equation is prominent in mathematical physics and appears, e.g., as a relativistic generalization of the Schrödinger equation. The Klein–Gordon equation (7.38) admits a special $(2\pi/k)$-periodic traveling wave solution

$$\eta = a\cos k(x-ct), \qquad c^2 = g\left(k^2+\kappa^2\right)\big/\left(2\,\kappa\,k^2\right).$$

Therefore, if $k=\kappa$ the exact dispersion relation of linear waves (i.e., $c^2 = g/k$) is recovered, as it should be. This means, in particular, that the gKG model is valid for spectra narrow-banded around the wavenumber κ. Further details and properties of the gKG are given in [4] (Sect. 4.2) and in [7].

7.4.3 Arbitrary Depth

A general ansatz, for waves in finite constant depth and satisfying identically the bottom impermeability, is suggested by the linear theory of water waves:

$$\phi \approx \frac{\cosh \kappa Y}{\cosh \kappa h}\,\tilde{\phi}(x,t), \qquad u \approx \frac{\cosh \kappa Y}{\cosh \kappa h}\,\tilde{u}(x,t), \qquad v \approx \frac{\sinh \kappa Y}{\sinh \kappa h}\,\tilde{v}(x,t), \tag{7.39}$$

where $Y = y + d$. The parameter $\kappa > 0$ is a characteristic wave number to be made precise a posteriori. This ansatz is uniformly valid for all depths because it yields the shallow water one (7.16) as $\kappa \to 0$, and the deep water one (7.34) as $d \to \infty$. Obviously, the ansatz (7.39) should be valid for wave fields with wavenumber spectra that are narrow-banded around κ.

Substituting the ansatz (7.39) into (7.15), one obtains

$$\begin{aligned}\mathscr{L} = [\,\eta_t + \tilde{u}\,\eta_x\,]\,\tilde{\phi} - \frac{g\,\eta^2}{2} + \frac{\tilde{v}^2}{2}\,\frac{\sinh(2\kappa h) - 2\kappa h}{2\kappa\cosh(2\kappa h) - 2\kappa} + \frac{\tilde{\phi}\,\tilde{v}}{2}\left[\frac{2\kappa h}{\sinh(2\kappa h)} - 1\right] \\ + \left[\frac{\tilde{u}^2}{2} + \tilde{\phi}\,\tilde{u}_x - \kappa\tanh(\kappa h)\,\tilde{\phi}\,\tilde{u}\,\eta_x\right]\frac{\sinh(2\kappa h) + 2\kappa h}{2\kappa\cosh(2\kappa h) + 2\kappa}.\end{aligned} \tag{7.40}$$

Applying various constraints, one obtains generalized equations including the ones derived in Sects. 7.4.1 and 7.4.2 as limiting cases. In particular, one can derive arbitrary depth generalizations of the Serre and Klein–Gordon equations; these derivations are left to the reader. The main purpose of this section is to illustrate the easiness of deriving approximations uniformly valid for all depths, contrary to perturbation methods with which the two main theories (i.e., Stokes-like and shallow water expansions) have separated validity domains.

Indeed, the Serre equations of Sect. 7.4.1 can also be derived from an asymptotic expansion (with the depth over wavelength ratio as small parameter). This is not the case for all approximations obtainable from the variational principle (see examples in [4, 6]). However, this does not mean that approximations obtained this way do not have restricted validity domains, as further discussed below.

7.5 Discussion

Via simple examples, we have illustrated above the advantage of using a relaxed variational principle. Further examples can be found in [4]. The advantages of this approach is greater on variable depth where it is easy to derive simple approximations not derivable from asymptotic expansions [6].

Here, we have used the isochoric velocity field $(\boldsymbol{u}, v)$ as subordinate condition, but other conditions can be imposed, as well as imposing different conditions on

$(\boldsymbol{u}, v)$ and $(\boldsymbol{\mu}, \nu)$. Indeed, the velocity field $(\boldsymbol{u}, v)$ being not more (nor less) physical than the pseudo-velocity field $(\boldsymbol{\mu}, \nu)$ and the potential velocity field $(\boldsymbol{\nabla}\phi, \phi_y)$, the constraints can be imposed by combinations of these three fields.

The relaxed variational principle provides a common platform for deriving several approximate equations from the same ansatz in changing only the constraints. Beside the ansatz and the subordinate conditions, no further approximations are needed to derive the equations. Using more general ansatze (i.e., involving more free functions and parameters) and well chosen constraints, one can hopefully derive more accurate approximations.

Although the possibility of using the variational methods without a small-parameter expansion has been overlooked in the context of water waves, it has long been recognized as a powerful tool in Theoretical Physics, in particular in Quantum Mechanics. This approach is even thought in some undergraduate lectures. For instance, from Berkeley's course on Quantum Mechanics [23]:

- The perturbation theory is useful when there is a small dimensionless parameter in the problem, and the system is exactly solvable when the small parameter is sent to zero.
- ... it is not required that the system has a small parameter, nor that the system is exactly solvable in a certain limit. Therefore it has been useful in studying strongly correlated systems, such as the fractional Quantum Hall effect.

However, in order to be successful, the great power of the variational method needs to be harnessed with skill and care, as it is well-known in Theoretical Physics. Indeed, as quoted in the same lecture on Quantum Mechanics:

- ... there is no way to judge how close your result is to the true result. The only thing you can do is to try out many Ansätze and compare them.
- ... the success of the variational method depends on the initial "guess" ... and an excellent physical intuition is required for a successful application.

But it is also well-known that this approach can be very rewarding:

- For example, R. B. Laughlin [19] proposed a trial wave function that beat other wave functions that had been proposed earlier, such as "Wigner crystal".
- Once your wave function gives a lower energy than your rival's, you won the race.[5]

Thus, despite its "dangers", the variational approach is a tool of choice for modeling water waves, specially for problems when there are no obvious small parameters or if approximations valid for a broad range are needed. We have illustrated these claims in this chapter.

References

1. Boussinesq, J.V.: Théorie de l'intumescence liquide appelée onde solitaire ou de translation se propageant dans un canal rectangulaire. C. R. Acad. Sci. Paris Sér. A-B **72**, 755–759 (1871)

[5] R. B. Laughlin et al. earned the 1998 Physics Nobel price.

2. Broer, L.J.F.: On the Hamiltonian theory of surface waves. Appl. Sci. Res. **29**(6), 430–446 (1974)
3. Clamond, D.: Variational principles for water waves beyond perturbations. http://www-old.newton.ac.uk/programmes/TWW/seminars/2014071814002.html (2014)
4. Clamond, D., Dutykh, D.: Practical use of variational principles for modeling water waves. Phys. D **241**(1), 25–36 (2012)
5. Craik, A.D.D.: The origins of water wave theory. Ann. Rev. Fluid Mech. **36**, 1–28 (2004)
6. Dutykh, D., Clamond, D.: Shallow water equations for large bathymetry variations. J. Phys. A Math. Theor. **44**(33), 332001 (2011)
7. Dutykh, D., Clamond, D., Chhay, M.: Numerical study of the generalised Klein-Gordon equations. Phys. D, 304–305, 23–33 (2015)
8. Dutykh, D., Clamond, D., Milewski, P., Mitsotakis, D.: Finite volume and pseudo-spectral schemes for the fully nonlinear 1D Serre equations. Eur. J. Appl. Math. **24**(05), 761–787 (2013). http://hal.archives-ouvertes.fr/hal-00587994/
9. Dysthe, K.B.: Note on a modification to the nonlinear Schrödinger equation for application to deep water. Proc. R. Soc. Lond. A **369**, 105–114 (1979)
10. Feynman, R.P., Leighton, R.B., Sands, M.: The Feynman Lectures on Physics. Addison-Wesley, San Francisco (1964)
11. Goldstein, H., Poole, C.P., Safko, J.L.: Classical Mechanics, 3rd edn. Addison–Wesley, San Francisco (2001)
12. Green, A.E., Naghdi, P.M.: A derivation of equations for wave propagation in water of variable depth. J. Fluid Mech. **78**, 237–246 (1976)
13. Green, A.E., Laws, N., Naghdi, P.M.: On the theory of water waves. Proc. R. Soc. Lond. A **338**, 43–55 (1974)
14. Grue, J., Clamond, D., Huseby, M., Jensen, A.: Kinematics of extreme waves in deep water. Appl. Ocean Res.**25**, 355–366 (2003)
15. Jensen, A., Clamond, D., Huseby, M., Grue, J.: On local and convective accelerations in steep wave events. Ocean Eng. **34**, 426–435 (2007)
16. Johnson, R.S.: A Modern Introduction to the Mathematical Theory of Water Waves. Cambridge University Press, Cambridge (2004)
17. Korteweg, D.J., de Vries, G.: On the change of form of long waves advancing in a rectangular canal, and on a new type of long stationary waves. Phil. Mag. **39**(5), 422–443 (1895)
18. Lanczos, C.: The Variational Principles of Mechanics. Dover Publications, New York (1970)
19. Laughlin, R.B.: Anomalous Quantum Hall Effect: An Incompressible Quantum Fluid with Fractionally Charged Excitations. Phys. Rev. Lett. **50**(18), 1395–1398 (1983)
20. Li, Y.A.: Hamiltonian structure and linear stability of solitary waves of the Green-Naghdi equations. J. Nonlinear Math. Phys. **9**(1), 99–105 (2002)
21. Luke, J.C.: A variational principle for a fluid with a free surface. J. Fluid Mech. **27**, 375–397 (1967)
22. Mei, C.C.: The Applied Dynamics of Water Waves. World Scientific, Singapore (1989)
23. Murayama, H.: Berkley's 221A Lecture Notes: Variational Method. http://hitoshi.berkeley.edu/221a/index.html (2006)
24. Petrov, A.A.: Variational statement of the problem of liquid motion in a container of finite dimensions. Prikl. Math. Mekh. **28(4)**, 917–922 (1964)
25. Radder, A.C.: Hamiltonian dynamics of water waves. Adv. Coast. Ocean Eng. **4**, 21–59 (1999)
26. Rajchenbach, J., Leroux, A., Clamond, D.: New standing solitary waves in water. Phys. Rev. Lett. **107**(2), 024502 (2011)
27. Rajchenbach, J., Clamond, D., Leroux, A.: Observation of Star-Shaped Surface Gravity Waves. Phys. Rev. Lett. **110**(9), 094502 (2013)
28. Salmon, R.: Hamiltonian fluid mechanics. Ann. Rev. Fluid Mech. **20**, 225–256 (1988)
29. Serre, F.: Contribution à l'étude des écoulements permanents et variables dans les canaux. La Houille blanche **8**, 374–388 (1953)
30. Serre, F.: Contribution à l'étude des écoulements permanents et variables dans les canaux. La Houille blanche **8**, 830–872 (1953)

31. Stoker, J.J.: Water Waves: The Mathematical Theory with Applications. Interscience, New York (1957)
32. Stoker, J.J.: Water waves, the Mathematical Theory with Applications. Wiley, New York (1958)
33. Su, C.H., Gardner, C.S.: KdV equation and generalizations. Part III. Derivation of Korteweg-de Vries equation and Burgers equation. J. Math. Phys. **10**, 536–539 (1969)
34. Su, C.H., Mirie, R.M.: On head-on collisions between two solitary waves. J. Fluid Mech. **98**, 509–525 (1980)
35. Wehausen, J.V., Laitone, E.V.: Surface waves. Handbuch der Physik **9**, 446–778 (1960)
36. Whitham, G.B.: Linear and Nonlinear Waves. Wiley, New York (1999)
37. Wu, T.Y.: A unified theory for modeling water waves. Adv. Appl. Mech. **37**, 1–88 (2001)
38. Zakharov, V.E.: Stability of periodic waves of finite amplitude on the surface of a deep fluid. J. Appl. Mech. Tech. Phys. **9**, 190–194 (1968)
39. Zakharov, V.E., Kuznetsov, E.A.: Hamiltonian formalism for nonlinear waves. Usp. Fiz. Nauk **167**, 1137–1168 (1997)

Chapter 8
Quantitative Analysis of Nonlinear Water-Waves: A Perspective of an Experimentalist

Lev Shemer

Abstract In the present review the emphasis is put on laboratory studies of propagating water waves where experiments were designed with the purpose to enable juxtaposing the measurement results with the theoretical predictions, thus providing a basis for evaluation of the domain of validity of various nonlinear theoretical model of different complexity. In particular, evolution of deterministic wave groups of different shapes and several values of characteristic nonlinearity is studied in deep and intermediate-depth water. Experiments attempting to generate extremely steep (rogue) waves are reviewed in greater detail. Relation between the kinematics of steep nonlinear waves and incipient breaking is considered. Discussion of deterministic wave systems is followed by review of laboratory experiments on propagation of numerous realizations of random wave groups with different initial spectra. The experimental results are compared with the corresponding Monte-Carlo numerical simulations based on different models.

8.1 Introduction

Ocean wave forecasting is indispensable for navigation and coastal activities, however accurate predictions critically depend on detailed understanding of the processes that govern dynamics of water waves. Gaining such an understanding represents a non-trivial intellectual challenge since waves are both nonlinear and stochastic in nature. In recent years the extremely steep (rogue, or freak) waves attract particular attention [23] due to their potential to cause significant damage to marine traffic as well as to off-shore and coastal structures. The complexity of ocean water-waves in general, and of rogue waves in particular, makes it imperative to investigate much simpler nonlinear gravity wave fields in order to identify the dominant mechanisms that govern their behavior. For example, wave energy dissipation by various mechanisms, or energy input due to wind, may

L. Shemer (✉)
School of Mechanical Engineering, Tel-Aviv University, Tel-Aviv 69978, Israel
e-mail: shemer@eng.tau.ac.il

E. Tobisch (ed.), *New Approaches to Nonlinear Waves*, Lecture Notes in Physics 908, DOI 10.1007/978-3-319-20690-5_8

play an important role in wave evolution. These effects are sometimes accounted for in the numerical solutions by invoking phenomenological models [24]. Of particular interest, however, is wave train transformation as a result of the action of energy-conserving factors, like nonlinear interactions and dispersion. In laboratory experiments there is no energy input by wind; moreover, for sufficiently long waves in absence of breaking dissipation may play only a minor role and can thus can often be neglected. This leaves the nonlinearity and dispersion as factors that dominate the evolution process in wave tank experiments.

The theoretical analysis of the effect of nonlinearity on water-waves utilizes the fact that the most important non-trivial interactions in deep-water waves occur among four waves (wave quartets) [51, 52], and consequently are limited to the third order in the wave steepness [86]. In nature, these nonlinear interactions are usually stochastic in nature. Hasselmann [17] was the first to apply statistical approach and the kinetic theory to describe random ocean waves. As a result of nonlinearity, a large number of harmonics with various frequencies exchange energy and transfer it to shorter scales where the wave energy is dissipated by breaking or otherwise. The so-called resonance interactions among four waves are considered. The resonance wave quartets satisfy the following conditions on their wave vectors $\mathbf{k}_i$ and frequencies ω_i, i being the number of the wave:

$$\mathbf{k}_0 + \mathbf{k}_1 = \mathbf{k}_2 + \mathbf{k}_3; \;\; \omega_0 + \omega_1 = \omega_2 + \omega_3 \tag{8.1}$$

This phenomenon is sometimes called wave, or weak, turbulence, to acknowledge similarity to Kolmogorov energy cascade in fluid turbulence. Recently water wave turbulence theory was advanced considerably by Zakharov and his colleagues (see, e.g. Zakharov [87], Nazarenko [42] and references therein). The kinetic wave theory that serves as a basis for modern wave climate prediction is based on two fundamental assumptions: that the wave nonlinearity is weak, and that and the phases of different harmonics are random. The random phase approximation is an essential assumption used for turbulent closures for all stochastic wave systems and even for a much broader range of turbulent systems.

One major simplification in water waves studies is decoupling of randomness and nonlinearity. One can thus concentrate first on deterministic, as opposed to stochastic, wave fields. The problem of evolution of a deterministic nonlinear wave system still remains extremely complex, and additional simplifications are required. Ocean waves exhibit considerable directional spreading; yet accounting for the angular distribution of the wave propagation directions complicates significantly the theoretical analysis. While measurements of evolution of short-crested 2D wave fields are possible in laboratory wave basins, see i.e. [22, 48], most experiments on nonlinear wave propagation were performed in long wave flumes where only unidirectional (1D) waves can be generated.

Numerous attempts have been made to explore the possibility to use deterministic nonlinear wave theories to forecast the evolution of a random wave field, as an alternative to application of the kinetic equation [2, 3, 47, 75]. These studies reveal the crucial role of non-resonant interactions (among wave quartets for which the

second condition in Eq. (8.1) is not satisfied exactly) in evolution of nonlinear random water waves. Shemer [55] demonstrated that nonlinear interactions can be quite significant for non-resonating deterministic wave quartets as well. For unidirectional waves, no exact resonances exist among wave quartets that contain three or four different waves and only near-resonant interactions between such wave quartets are possible. The crucial role of near resonant interactions for wave field evolution make experiments in a wave tank a very convenient vehicle to study nonlinear random waves in laboratory conditions. Some experiments in a long wave tank have been performed on deep narrow-banded waves with random phases (see [41] and references therein). Results of these experiments indicate that in spite of lack of exact resonances in a unidirectional wave field, nonlinear effects are essential and they strongly affect the statistical properties of the wave field.

A number of fully nonlinear solvers for studying the evolution of unidirectional nonlinear waves were developed in recent decades. Nevertheless, simplified theoretical models often offer significant advantages and are widely used. The simplifications in the models may also include assumptions of either vanishing or very narrow spectral width. The effects of wave energy dissipation by various mechanisms, or energy input due to wind, are sometimes accounted for in the numerical solutions by invoking phenomenological models.

It should be stressed that linear water-wave theory is well developed; it accounts for dispersion and in many occasions provides satisfactory solutions, in particular for deep and intermediate-depth water. Involving nonlinearity may be justified in occasions when it modifies the linear solutions considerably. Different nonlinear theoretical models, as well as fully nonlinear computations contain numerous simplifying assumptions. To justify application of these advanced methods of solution of water-waves problems, the validity of the results has to be verified by carrying out controlled experiments that allow estimate of the importance of essentially nonlinear mechanisms and enable quantitative comparison of the theoretical predictions with the measurements.

The structure of this chapter is as following. The description of experimental facilities used is presented first in Sect. 8.2. Comparison between theoretical results and measurements is then carried out for nonlinear wave models with increasing complexity. Deterministic water wave groups are considered first. The limited validity of the results based on the nonlinear Schrödinger (NLS) equation is demonstrated in Sect. 8.3. In order to improve the accuracy of the theoretical results, the modified nonlinear Schrödinger (mNLS, or Dysthe) equation, is employed in Sect. 8.4. Part of this section is devoted to presentation of the essential differences between the analysis of the wave field evolution in time that is customarily carried out in theoretical studies, and the spatial variation observed in wave tanks. Different aspects of application of the spatial version of the Zakharov equation that is the most general third order theoretical model, to the analysis of evolution of unidirectional wave trains are examined in Sect. 8.5. Experiments on random unidirectional waves with different spectra and comparison with Monte-Carlo simulations based on different models are described in Sect. 8.6. In analysis of both deterministic and random waves an emphasis is put on possible mechanisms leading to generation

of extremely large (the so-called freak, or rogue) waves. Such waves, often dubbed killer-waves, appear and disappear fast and unexpectedly, and have the potential of causing substantial damage to marine traffic. Finally, the presented results will be discussed and the conclusions presented in Sect. 8.7.

8.2 The Experimental Facilities

The majority of the experiments discussed here in detail were carried out in the Tel-Aviv University (TAU) wave tank which is 18 m long, 1.2 m wide and has a constant depth of 0.6 m. A paddle-type wavemaker hinged near the floor is located at one end of the tank. The wavemaker consists of four modules, which in all experiments discussed here were adjusted to move in phase with identical amplitudes and frequencies. The wavemaker is driven by a computer-generated signal. At the far end of the tank a wave energy-absorbing sloping beach is installed. The beach starts at the distance of about 14 m from the wavemaker; no measurements were performed in the beach region. The instantaneous surface elevation is measured simultaneously by resistance-type wave gauges. The probes are mounted on a bar parallel to the side walls of the tank and fixed to a carriage which can be moved along the tank. In most experiments the carriage was placed manually at the desired measuring location. More recently, the capability to control the location of the carriage by computer was added. Measurements of the surface elevation are performed at numerous carriage locations along the center line of the tank. The distance between the adjacent gauges on the bar is adjustable, in most cases four wave gauges with a constant spacing not exceeding 0.4 m between the adjacent probes was used. Probes are calibrated using a stepping motor and a computerized static calibration procedure described in detail in Shemer et al. [63]. The calibration is performed at the beginning of each experimental run. The probe response is essentially linear for the range of surface elevations under consideration. The voltages of the four wave gauges, the wavemaker-driving signal and the outputs of position potentiometers of the four wavemaker paddles are sampled using an A/D converter and stored at the computer hard disk for further processing. The sampling frequency is adjusted in each experiment to be by two orders of magnitude higher that the carrier wave frequency. To enable measurements for various water depths, a false bottom made of a number of 1.18 m by 1.25 m marine plywood plates 1.8 cm thick can be installed in the tank. Each plywood plate is independently suspended on stainless steel rods from the steel frame of the tank, so that any desirable effective water depth can be attained.

Some experiments reported here were carried out in the Large Wave Channel (GWK) in Hanover, Germany. The tank has a length of 300 m, width of 5 m and depth of 7 m. Water depth in all experiments was set to be 5 m. At the end of the wave tank, there is a sand beach starting at the distance of 270 m with slope of 30°. The computer-controlled piston-type wavemaker is equipped with the reflected wave energy absorption system. The instantaneous water height is measured using 25 wave gauges of resistance type placed along the tank wall; the distribution of

the wave gauges along the tank was adjusted to the goal of each experiment. The static probe calibration was performed by filling the tank first to the maximum possible depth and then reducing the depth in steps adjusted to the range of surface elevations relative to the undisturbed value. The calibration curve for each wave gauge was obtained by best fit to linear dependence. Due to the size of the facility, the calibration procedure usually takes a whole working day. The wave gauges were therefore calibrated only once in a week. It is estimated that the absolute error in the measured instantaneous surface elevation in most cases did not exceed about 1 cm.

In all experiments the wave train of finite duration was generated by a wavemaker. In the GWK experiments, a single wave group was excited in each experimental run, while in a smaller TAU facility the number of groups in each wave train did not exceed four. In both wave tanks each experimental run started only after a sufficient interval from the previous experiment when the water surface was quiescent and all remaining disturbances decayed totally. In the GWK measurements the reflected wave energy absorption system effectively eliminated the existence of very long waves in the tank and enabled relatively short (about 15 min) intervals between consecutive experimental runs. The output voltages of all wave gauges, as well as of the wavemaker driving signal and of the output of the wavemaker position potentiometer that provides information on the instantaneous wavemaker displacement, were sampled at sufficiently high rate adjusted to the dominant frequency with the total sampling duration of 350 s.

8.3 The Nonlinear Schrödinger Equation

Sea waves can be described quite faithfully by JONSWAP spectrum [18]. One of the important features of this spectrum is its relatively narrow frequency band, which results in a notable wave groupiness. The simplest nonlinear theoretical model which is capable of describing the evolution of propagating wave packet with a sufficiently narrow spectrum in the range of water depths from deep to intermediate is the nonlinear Schrödinger (NLS) equation (see, e.g. Mei [39]). This equation was derived by Zakharov [86] and Hasimoto and Ono [16] and has been extensively applied for description of wave group evolution in deep water. An agreement between the experimentally found growth rates of the unstable sidebands with the theoretical predictions based on the NLS equations was obtained [31]. Zakharov and Shabat [88] demonstrated analytically using the NLS equation that an arbitrarily shaped envelope disintegrates eventually into a finite number of envelope solitons. Wave train disintegration was indeed observed in deep water by Yuen and Lake [84, 85], and by Su [76].

In an attempt to determine the domain of applicability of the NLS equation, Shemer et al. [64] investigated transformation of deterministic wave groups in intermediate water depth in a laboratory wave tank. The measurements were compared with the results of numerical solution based on the NLS equation. Wave group propagation was studied for a number of values of constant water depth

h with $q = k_0 h = O(1)$, $k_0 = 2\pi/\lambda_0$ being the carrier wave number and λ_0 the carrier wave length, covering the range from a nearly shallow water to the values of q approaching deep water conditions. Simplest possible initial shapes of the wavemaker driving signal which satisfy the narrow spectrum condition were selected:

$$s(t) = s_0 cos(\Omega t) cos(\omega_0 t); \quad \Omega = \omega_0/20; \tag{8.2}$$

$$s(t) = s_0 |cos(\Omega t)| cos(\omega_0 t); \quad \Omega = \omega_0/20; \tag{8.3}$$

$$s(t) = s_0 exp(-(t/mT_0)^2) cos(\omega_0 t); \quad 16T_0 < t < 16T_0. \tag{8.4}$$

Here s_0 is the forcing wavemaker amplitude, $\omega_0 = 2\pi/T_0$ is the radian carrier wave frequency and Ω is the modulation frequency. The spectrum given by Eq. (8.2) is bimodal, with two distinct peaks of identical height at $\omega_0 \pm \Omega$. The envelope given by Eq. (8.3) is identical to that given by Eq. (8.2), but the symmetric spectrum of this signal with the period of $2\pi/\Omega$ is considerably more complicated; it has a maximum at the carrier frequency ω_0 and consists of a set of discrete frequencies spaced by $\omega_0/10$. The Gaussian driving signal given by Eq. (8.4) generates widely separated wave groups. The parameter m determines the width of the envelope; the larger is the value of m, the wider is the group. The discrete frequency spectrum of the surface elevation in the wave group defined by Eq. (8.4) also has a Gaussian shape with the maximum at ω_0 and resolution of $\omega_0/32$; the value of $m = 5$ was selected in those experiments, so that the initial spectrum was quite narrow.

Three values of the maximum driving amplitude s_0 were used for each shape of the forcing signal. The maximum driving amplitudes were selected so that close to the wavemaker, the resulting carrier wave had the maximum wave amplitudes a_0 corresponding to the steepness $\epsilon = k_0 a_0$ of about $\epsilon = 0.07$ (low amplitude), $\epsilon = 0.14$ (intermediate amplitude), and $\epsilon = 0.21$ (high amplitude). Two values of the carrier wave periods, $T_0 = 0.7$ s and $T_0 = 0.9$ s, were employed. Experiments were carried out for two positions of the false bottom in the tank, corresponding to the water depths of $h = 11.8$ cm and $h = 17.0$ cm, as well as with the false bottom removed, thus yielding the maximum possible in the facility water depth $h = 60$ cm. The surface elevation for a modulated unidirectional narrow-banded wave can be presented at the leading order as

$$\zeta = Re\left[a(x,t)e^{i(k_0 x - \omega_0 t)}\right], \tag{8.5}$$

where $a(x,t)$ is the slowly varying in time and space complex amplitude of the carrier wave with the frequency ω_0 and the wave number k_0. The dispersion relation for intermediate water depth is

$$\omega_0^2 = kg \cdot tanh(q), \tag{8.6}$$

where g is the acceleration due to gravity.

In order to perform the comparison of the model results with the experiment, the NLS equation has to be written in a form describing the evolution of the wave group along the tank (i.e. in space); thus the enabling determination of the surface elevation variation in time, as measured by wave gauges at fixed measuring stations, $\zeta(t)$. Following Mei [39], the dimensionless scaled variables were introduced as

$$a = a_0 A, \quad \tau = \epsilon\omega_0(x/c_g - t), \quad X = \epsilon^2 k_0 x \tag{8.7}$$

where A is the complex dimensionless wave group envelope, a_0 is the characteristic wave amplitude, x is the coordinate along the tank and t is the time. The group velocity $c_g = \partial\omega/\partial k$. The NLS equation can be written as

$$-i\frac{\partial A}{\partial X} + \alpha\frac{\partial^2 A}{\partial \tau^2} + \beta|A|^2 A = 0. \tag{8.8}$$

The coefficients in the NLS are defined in the dimensionless form by

$$\alpha = -\frac{{\omega_0}^2}{2k_0{c_g}^3}\frac{\partial c_g}{\partial k} \tag{8.9}$$

$$\beta = \frac{1}{n}\left[\frac{cosh(4q) + 8 - 2tanh^2(q)}{16sinh^4(q)} - \frac{1}{2sinh^2(2q)}\frac{(2cosh^2(q) + n^2)}{\frac{q}{tanh(q)} - n^2}\right], \tag{8.10}$$

where the parameter $n = c_g/c_p$ represents the ratio of group and phase velocities and is given by

$$n = \frac{1}{2}\left\{1 + \frac{2q}{sinh(2q)}\right\}. \tag{8.11}$$

Equation (8.8) was solved numerically using an implicit finite difference scheme with periodic in τ boundary conditions. Initial conditions at $X = 0$ are in accordance with the shapes defined by Eqs. (8.2)–(8.4). The variation of the surface elevation ζ is obtained from the solution of Eq. (8.8) using the computed complex amplitudes $A(X, \tau)$ and the relations between the scaled dimensionless (X, τ) and the physical (x, t) variables, given by Eq. (8.7).

As long as characteristic wave lengths are relatively short compared to the water depth, the deep water dispersion relation holds and waves are strongly dispersive. For shallower water, wave dispersion becomes weaker and depth-dependent. Wave propagation in coastal region and in shallow water thus constitutes a separate problem and is not considered in detail here.

Measurements of instantaneous surface elevation at multiple locations along the tank were performed by Shemer et al. [64] for three shapes of wave groups, three values of the dimensional water depth h and for three maximum wave amplitudes a_0. For each condition, wave groups with two carrier wave periods T_0 were investigated. The total number of experimental conditions in this study is thus

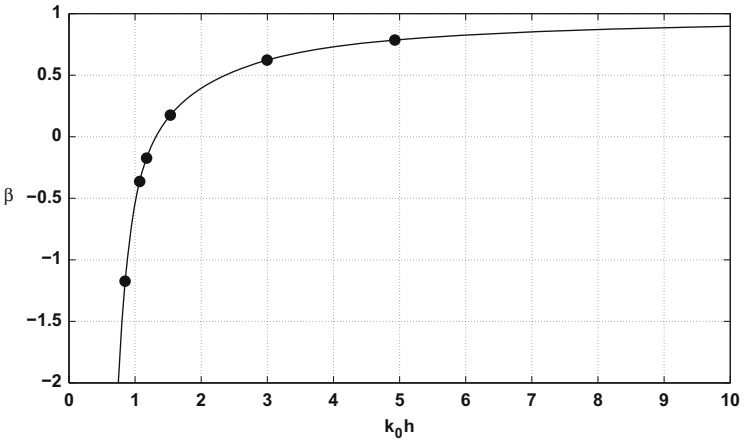

Fig. 8.1 Variation of the nonlinear term coefficient in the NLS equation β with the dimensionless depth k_0h. *Symbols* denote the experimental conditions

was 54. For the sake of brevity, the following discussion is limited to three values of β corresponding to the defocusing regime at $h = 0.118$ m; $T_0 = 0.9$ s ($\beta = -1.17$), approximately linear regime ($h = 0.17$ m, $T_0 = 0.7$ s, $\beta = 0.19 \ll 1$), and nearly deep-water case with $h = 0.60$ m, $T_0 = 0.7$ s, $\beta = 0.79$. The coefficients α and β in the NLS equation (8.8), as well as the parameter n are functions of the dimensionless water depth q. Note that for $q \to \infty$, $\alpha \to 1$, $\beta \to 1$, and $n \to 0.5$. The variation of the coefficient of the nonlinear term β with the dimensionless depth k_0h is plotted in Fig. 8.1. The conditions at which the experiments are performed are marked in the figure. In view of the dispersion relation (9), the range of intermediate water depth is usually defined as $\pi/10 < q < \pi$. The ratio of group to phase velocity n at $q > \pi$ indeed is very close to 0.5. The coefficient of the nonlinear term in the NLS equation, β, though, still differs notably from their asymptotic values for deep water even for $q = 10$. The NLS thus allows to redefine the effective limits of the intermediate water depth range for studying evolution of nonlinear wave groups.

It follows from Fig. 8.1 that as far as the nonlinear effects are concerned, the wave groups with the selected carrier wave periods and water depths in the experiments propagate in water of intermediate depth. For the sake of brevity, only characteristic selected results are presented in the following figures. Additional results can be found in [64] and in [21]. Each one of the following figures in this section consists of six panels, marked (a)–(f). The measured variations of the surface elevation with time in the vicinity of the wavemaker (at $x = 0.24$ m) are presented in the panel (a), while the corresponding amplitude spectra are given in panel (b). Similarly, the results of the measurements performed away from the wavemaker, typically around $x = 9$ m, are presented in panels (c) and (d). Note that only a fraction of the duration of actual records is shown in these frames. The directly measured surface elevation is given in the bottom curves in panels (a) and (c). These records, however, can not

be immediately compared with the computations based on the NLS equation. The model equation describes the variation of the envelope of the carrier wave at the leading order. The second order (ϵ^2) bound second and low frequency harmonics may be deduced from carrier wave amplitude using expressions given for finite water depth in [6]. The experimentally obtained spectra presented in some of the panels (b) and (d) clearly demonstrate the presence of higher order harmonics. The presence of these harmonics in the spectrum is a manifestation of non-negligible contribution of bound waves to the surface elevation. The bound waves are most prominent at the second order, but can be identified at higher orders as well. The second order bound waves cause significant asymmetry of surface elevation ζ relative to the mean water level, with crests heights exceeding the troughs.

In order to provide a basis for comparison of the experimental results with the model predictions, the raw signals were band-pass filtered in the range $0.4f_0 < f < 1.6f_0$, where $f_0 = 1/T_0 = \omega_0/2\pi$ is the carrier frequency, thus leaving free waves only. The envelope of the filtered signal is then computed using the Hilbert transform, as applied for water wave analysis by Melville [40] (for extensive introduction to the Hilbert transform see, e.g. Hahn [15]). Both the band-pass filtered surface elevation and the absolute value of the envelope are also presented (a vertical shift is introduced for convenience) in panels (a) and (c). The computed using Eq. (8.8) shapes of the envelope at the identical locations along the tank are depicted in panel (e) for qualitative comparison with the experiments.

To eliminate the contribution of the second order bound waves, the maximum amplitudes of the waves in the group for each set of experimental conditions and for all distances from the wavemaker can be calculated either as a half of the maximum wave height obtained in the raw signal $A_{max} = \frac{1}{2}H_{max} = \frac{1}{2}(\zeta_{max} - \zeta_{min})$, where ζ_{max} and ζ_{min} are the maximum and the minimum surface elevations measured in each group and averaged over all groups in the record. Alternatively, the amplitude A_{max} may be calculated as the maximum value of the filtered group envelope, averaged overall groups in the record. As demonstrated in [64], both methods lead to similar results. The variation of the maximum wave group amplitudes along the tank calculated as half difference between crests and troughs is presented in panel (f). The maximum wave amplitudes in these figures are normalized by their corresponding values in the vicinity of the wavemaker. The experimentally determined values of A_{max} are compared in panel (f) with computations based on the NLS equation.

The nearly shallow water case ($h = 11.8\,\text{cm}$; $T_0 = 0.9\,\text{s}$, $k_0h = 0.847, \beta = -1.17$) is described first. The results for the bichromatic forcing by the wavemaker given by Eq. (8.2) are presented in Fig. 8.2 for the low forcing amplitude, $\epsilon = 0.07$, and in Fig. 8.3 for the high forcing amplitude, $\epsilon = 0.21$. Close to the wavemaker ($x = 0.24\,\text{m}$, $x/\lambda_0 = 0.28$), the measured wave group envelopes in Figs. 8.2a and 8.3a are quite similar to the shape of the driving signal. At high amplitude, however, some distortion of the shape of the carrier wave in Fig. 8.3a can be noticed even at this close proximity to the wavemaker. The reason for this distortion is clearly seen from comparison of the corresponding amplitude spectra in Figs. 8.2b and 8.3b. In contrast to Fig. 8.2b with a nearly bimodal spectrum, at high amplitude in Fig. 8.3b the spectrum is characterized by prominent peaks related to the second harmonic

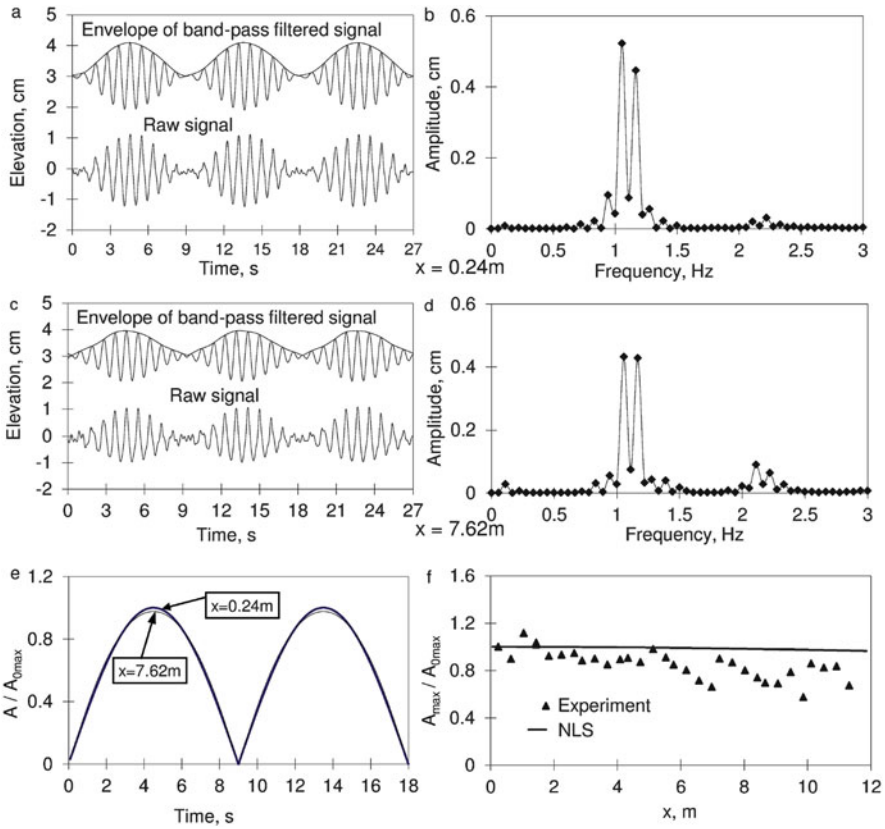

Fig. 8.2 Bichromatic wave group: driving signal is given by Eq. (8.2), $T_0 = 0.9\,\mathrm{s}$; $k_0 = 7.18\,\mathrm{m}^{-1}$; $h = 0.0118\,\mathrm{m}$; $\epsilon = 0.07$: (**a**) and (**c**) recorded surface elevation and its the module of the envelope computed using the Hilbert transform; (**b**) and (**d**) amplitude spectra of the measured surface elevation; (**e**) envelope shape at two locations along the tank computed using Eq. (8.8); (**f**) variation of the maximum wave height along the tank

of the carrier wave. Far from the wavemaker, the generation of free waves at the second harmonics of the carrier may be identified, in particular between the wave groups, in the unfiltered signals of Fig. 8.2c ($x = 7.62\,\mathrm{m}, x/\lambda_0 = 8.71$) and Fig. 8.3c ($x = 9.47\,\mathrm{m}$, $x/\lambda_0 = 9.63$). The low frequency peaks are also clearly visible in these spectra. The generation of free second order harmonics that is more prominent for wavemaker-excited wave fields in shallower water was discussed in detail by Kit et al. [28]. Only relatively minor changes occur in the spectrum around the dominant frequency at the remote location in Fig. 8.2d as compared to the initial spectrum at this relatively weak forcing amplitude. At stronger forcing, widening of the spectrum with the distance becomes essential, and the spectrum becomes more complicated with numerous harmonics both in the vicinity of the carrier wave frequency and its second harmonic, see Fig. 8.3b, d. The shape of the envelope in

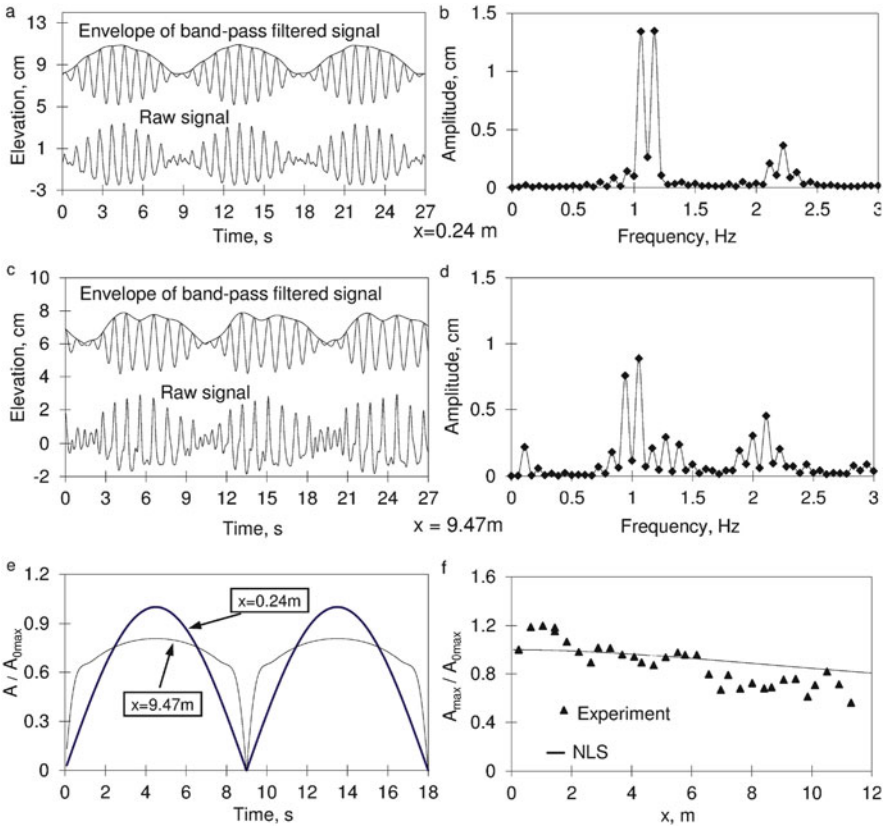

Fig. 8.3 Bichromatic wave group: driving signal is given by Eq. (8.2), $T_0 = 0.9\,\mathrm{s}$; $k_0 = 7.18\,\mathrm{m}^{-1}$; $h = 0.0118\,\mathrm{m}$; $\epsilon = 0.21$: (**a**) and (**c**) recorded surface elevation and its the module of the envelope computed using the Hilbert transform; (**b**) and (**d**) amplitude spectra of the measured surface elevation; (**e**) envelope shape at two locations along the tank computed using Eq. (8.8); (**f**) variation of the maximum wave height along the tank

Fig. 8.2c is only slightly distorted, while at the high amplitude, Fig. 8.3c, this shape changes drastically and becomes notably asymmetric.

The model computations presented in Figs. 8.2e and 8.3e are only in a qualitative agreement with the experimental observations. At low forcing amplitudes, the calculated shape of the group in Fig. 8.2e remains virtually unchanged, while at high amplitude, Fig. 8.3e, notable distortion of the group shape accompanied by decrease in the maximum amplitude is obtained. In the simulations, however, the envelope retains symmetric shape in the process of evolution along the tank, contrary to the experimental results. For both forcing amplitudes, the decay of the maximum wave amplitude along the tank is observed experimentally, although the slope in Fig. 8.2f is more moderate than that in Fig. 8.3f. The model computations indicate the same

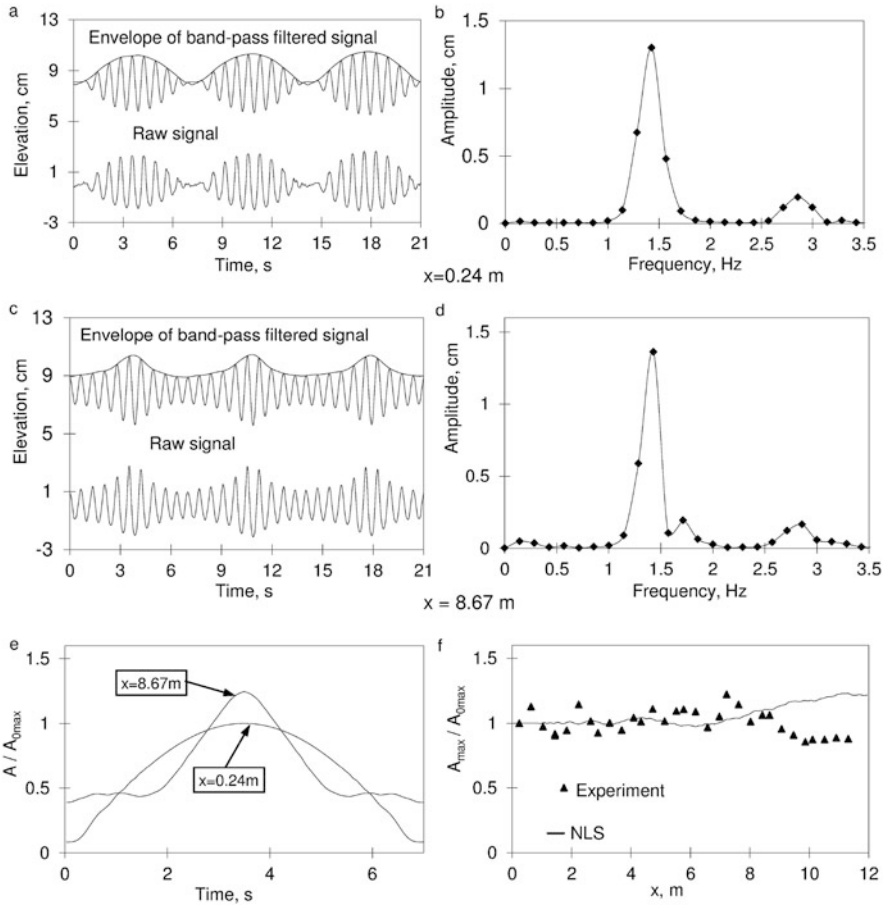

Fig. 8.4 Bichromatic wave group: driving signal is given by Eq. (8.3), $T_0 = 0.9\,\mathrm{s}$; $k_0 = 7.18\,\mathrm{m}^{-1}$; $h = 0.17\,\mathrm{m}$; $\epsilon = 0.21$: (**a**) and (**c**) recorded surface elevation and its the module of the envelope computed using the Hilbert transform; (**b**) and (**d**) amplitude spectra of the measured surface elevation; (**e**) envelope shape at two locations along the tank computed using Eq. (8.8); (**f**) variation of the maximum wave height along the tank

trend, with the decrease in the maximum amplitude much more pronounced for the high amplitude case.

The wave group excited by the driving signal given by Eq. (8.3) for the intermediate depth $h = 0.17\,\mathrm{m}$ that corresponds to very small nonlinearity coefficient $\beta = 0.19$ is presented in Fig. 8.4 for high forcing amplitude $\epsilon = 0.21$. In the vicinity of the wavemaker, $x = 0.24\,\mathrm{m}$, $x/\lambda_0 = 0.39$, the shape of the wave group in Fig. 8.4a resembles that of the driving signal and does not look very different from that in Fig. 8.3a. The spectrum in Fig. 8.4b, however, is very different from that in Fig. 8.3b; it exhibits a dominant peak at the carrier frequency and is not bimodal. The higher

harmonics are quite visible, similarly to the cases presented above. At the remote location, $x = 8.67$ m, $x/\lambda_0 = 13.73$, Fig. 8.4c, the waves are distributed somewhat more uniformly along the group. Since in this case the wave field is essentially linear when analyzed in the framework of the NLS equation, the frequency spectrum od the surface elevation is supposed to remain practically unchanged along the tank. The spectrum plotted in Fig. 8.4d is however, somewhat different from that at the wavemaker. The theoretically computed wave group shapes in Fig. 8.4e resemble closely those obtained in the experiments. In contrast to the results obtained for the shallower water case, the measured maximum wave amplitude in Fig. 8.4e does not change notably along the tank. This experimental result is confirmed by the numerical solution of the model equation for a considerable part of the tank, up to x of about 8 m.

Comparison of Figs. 8.3 and 8.4 reveals that wave groups having identical initial envelope shapes but different spectral contents may undergo completely different evolution processes. Specifically, in Fig. 8.3 groups having a bimodal spectrum retain their clear identity in the process of propagation, and their envelope periodically attains zero. For wave groups with the same shape and more complicated spectra, Fig. 8.4, the wave energy tends to become more uniformly distributed along the group, so that the clear distinction between the groups vanishes.

The behavior of wave groups generated using the Gaussian driving signal given by Eq. (8.4) is presented in Fig. 8.5 for nearly deep water with $h = 0.60$ m, $T_0 = 0.7$ s, $k_0 h = 4.93$, $\beta = 0.78$ and high amplitude of forcing, $\epsilon = 0.21$. The frequency spectrum of the driving signal in this case also has a Gaussian shape. As in previous figures for strongly nonlinear cases, the higher harmonics are clearly visible already in the spectrum of the signal measured close to the wavemaker (Fig. 8.5b, $x = 0.24$ m, $x/\lambda = 0.32$). The unfiltered signal therefore exhibits a clear asymmetry with respect to the mean value. As the wave group propagates along the tank, the shape of the wave group envelope changes notably, it becomes quite complicated and strongly asymmetric with respect to its maximum Fig. 8.5c. Correspondingly, the surface elevation frequency spectrum at the remote location Fig. 8.5d now deviates strongly from its initial nearly Gaussian shape and exhibits considerable spreading over a wide frequency range. The substantial distortion of the initial group shape along the tank in this case is also obtained in the numerical simulations, Fig. 8.5e, but the calculated shape is symmetric and has only a weak resemblance to that measured in the tank, Fig. 8.5c. Probably the most striking difference between this case and the previously considered sets of parameters is in the variation of the maximum wave amplitude in the group along the tank, Fig. 8.5f. In contrast to the results of Figs. 8.2f–8.4f, the maximum amplitude in Fig. 8.5f increases notably with the distance from the wavemaker. This result obtained in the numerical solutions of the NLS equation is confirmed by experiments. Similar results were observed for this water depth when the driving signals given by Eq. (8.2) or Eq. (8.3) were applied.

The following discussion is based on Figs. 8.2, 8.3, 8.4, and 8.5, as well as on additional results of measurements and simulations presented in [21, 64]. For all wave group shapes and for all effective water depths, variation of the wave

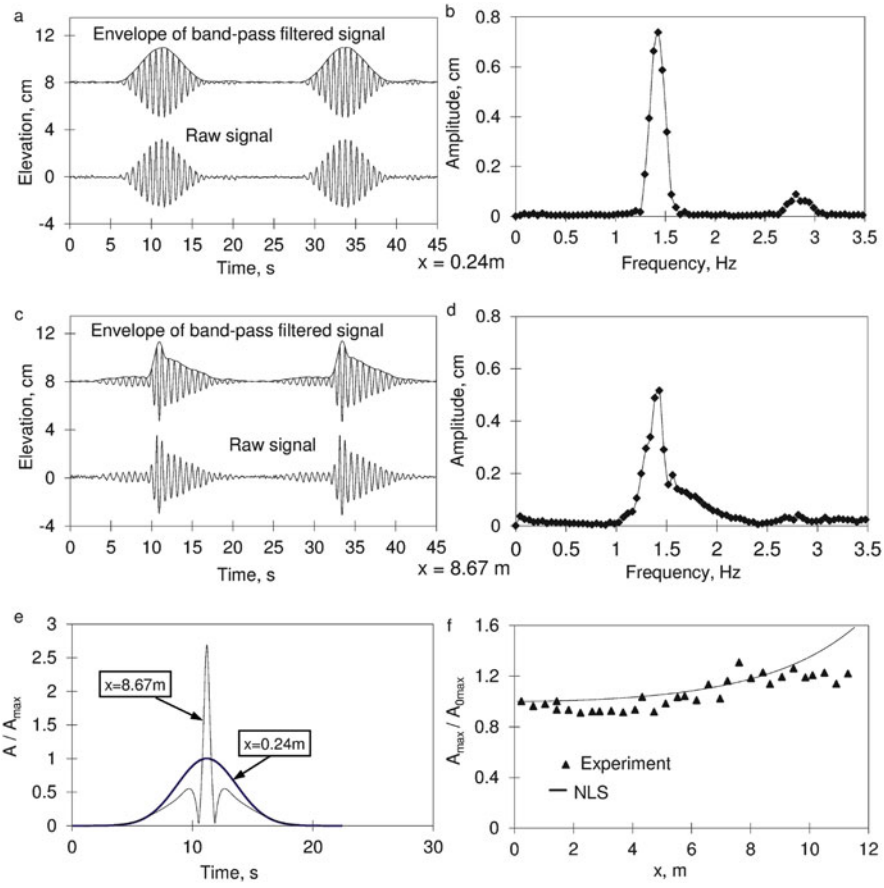

Fig. 8.5 Bichromatic wave group: driving signal is given by Eq. (8.4), $T_0 = 0.9\,\mathrm{s}$; $k_0 = 7.18\,\mathrm{m}^{-1}$; $h = 0.60\,\mathrm{m}$; $\epsilon = 0.21$: (**a**) and (**c**) recorded surface elevation and its the module of the envelope computed using the Hilbert transform; (**b**) and (**d**) amplitude spectra of the measured surface elevation; (**e**) envelope shape at two locations along the tank computed using Eq. (8.8); (**f**) variation of the maximum wave height along the tank

group envelopes and of the frequency spectra along the tank became much more pronounced as the forcing amplitude increased. The evolution of all wave groups studied thus exhibited an essentially nonlinear behavior. The important details of wave field variation with the distance, however, depend strongly on the values of the coefficient of the nonlinear term β in the NLS equation (8.8). For the deep water case ($k_0 h = 4.93$), this coefficient is positive, see Fig. 8.1, resulting in focusing of the wave energy of the selected group envelope shapes that becomes more evident for high values of the wave steepness ϵ. For low values ϵ, the focusing effect is barely noticeable for the dimensional time and length scales considered in this study. Note that all shapes of the driving signal employed in this study are different from

that of an equilibrium envelope soliton (cf. [39]), thus resulting in wave energy focusing for $\beta > 0$. For the experimental conditions of point Fig. 8.4, which are close to the critical water depth $q = 1.36$, both the experiments and the numerical simulations indicate that the maximum amplitude does not change notably along the tank.

At the conditions of Figs. 8.2 and 8.3, the coefficient of the nonlinear term is negative, resulting in defocusing and a more uniform wave energy distribution along the group. Thus both the experimental and the numerical results seem to support the conjecture that strongly nonlinear wave groups undergo a demodulation process while propagating over shallow water. Barnes and Peregrine [5] computed numerically evolution of a deterministic wave group envelope over a sloping bottom using a full irrotational flow solver. They, too, report on a somewhat surprising result that the maximum wave height in the group becomes decreases relative to its initial value. Kit et al. [27] studied a similar problem of wave group shape modification in shallow water when approaching a beach using the Korteweg-deVries (KdV) equation. They have also observed certain demodulation effects in their numerical solutions. The tendency of the ratio of the maximum possible wave height and the significant wave height to decrease with approaching the coastal zone was also observed in field measurements, see [44, 54]. This process can be seen as nonlinear wave amplitude demodulation in the group with decrease in water depth. Comparison of the experimental results on wave group propagation in shallow water with model predictions based on the KdV equation was performed in [28].

While the theoretical model employed here is non-dissipative, dissipation is apparently present in all experiments. The net effect of dissipation is the gradual decrease of wave height along the tank. The experimentally observed increase of the maximum wave amplitude in deep water at high initial wave steepness indicates that the nonlinear effects in this case dominate over those due to dissipation as well as dispersion. On the other hand, in more shallow water, the relative contribution of dissipation is more pronounced, and the measured wave amplitude decay along the tank may exceed significantly the prediction based on a non-dissipative theoretical model. Detailed analysis of the relative importance of various dissipation mechanisms in a laboratory wave tank was carried out by Kit and Shemer [25].

The free waves frequency spectrum in the initially symmetric wave groups is initially symmetric around the carrier frequency. The NLS equation conserves the symmetry of the initial conditions. The wave envelopes and the spectra in intermediate and in particular in deep water conditions, however, develop significant asymmetry, in clear contradiction to the experimental findings. The reason for this discrepancy between the model and the experiment is related to the finite width of the wave amplitude spectrum in the vicinity of the carrier, which is supposed to be vanishing in the derivation of the NLS equation.

8.4 The Modified Nonlinear Schrödinger (Dysthe) Equation

8.4.1 Formulation of Temporal and Spatial Evolution Problems

The results of Sect. 8.3 demonstrate that the NLS equation is adequate for qualitative description of the global properties of the envelope evolution of unidirectional nonlinear wave groups, such as focusing of water waves in sufficiently deep water. This model, however, is incapable of capturing more subtle features, for example the emerging front-tail asymmetry observed in experiments due to the asymmetric spectral widening. Such widening of the initially narrow spectrum can occur due to nonlinear interactions, violating the spectrum width assumptions of the NLS equation. More advanced models that account for non-negligible width of spectra evolving from an initially narrow spectrum are therefore required for accurate description of nonlinear wave group evolution. The mNLS equation derived by Dysthe [11] is a higher (fourth) order extension of the NLS equation, where the higher order terms account for finite spectrum width, see [73]. Further modification of the NLS equation appropriate for wider wave spectra was presented by Trulsen and Dysthe [80] and Trulsen et al. [82]. Kit and Shemer [26] have demonstrated that this modification can be easily derived by expanding the dispersion term in the Zakharov equation into the Taylor series.

The theoretical model derived by Dysthe [11] describes the evolution of the wave field in time. Complete information on the wave field along the tank at a prescribed instant constitutes the initial condition required for the solution of the problem. In laboratory experiments, however, waves are generated by a wavemaker usually placed at one end of the experimental facility. The experimental data are commonly accumulated using sensors placed at fixed locations within the tank. Hence, to perform quantitative comparison of model predictions with results gained in those experiments, the governing equations have to be modified to a spatial form, to describe the evolution of the temporally varying wave field along the experimental facility. Such a modification of the Dysthe model was carried out by Lo and Mei [32] who obtained a version of the equation that describes the spatial evolution of the group envelope. Gramstad and Trulsen [14] modified the version of the Dysthe equation for finite depth originally derived by Brinch-Nielsen and Jonsson [6], starting from the version of the Hamiltonian-conserving version of the Zakharov [86] equation offered by Krasitskii [29].

Numerical computations based on the Dysthe model for unidirectional wave groups propagating in a long wave tank indeed provided good agreement with experiments and exhibit front-tail asymmetry, see Shemer et al. [66]. The spatial version of the Dysthe equation was also derived by Kit and Shemer [26] from the spatial form of the Zakharov equation [65, 67] that is free of any restrictions on the spectrum width.

For a narrow-banded unidirectional deep-water wave group with the dominant frequency $\omega_0$and wave number k_0 that are related by the deep-water dispersion

relation for gravity waves $\omega_0^2 = k_0 g$. In the Dysthe equation, in addition to variation in time and space of the surface elevation $\zeta(x,t)$, the velocity potential ϕ at the free surface, $\psi(x,t) = \phi(x, z = \zeta, t)$ is also considered. For a narrow-banded wave group it is convenient to express the variation of ζ and ψ at the leading order in terms of their complex envelope amplitudes:

$$\zeta(x,t) = Re\left[a_\zeta(x,t)e^{i(k_0 x - \omega_0 t)}\right], \tag{8.12}$$

$$\psi(x,t) = Re\left[a_\psi(x,t)e^{i(k_0 x - \omega_0 t)}\right]. \tag{8.13}$$

The mNLS coupled system of equations, which describes the evolution of the complex envelope $a(x,t)$ and of the potential of the induced mean current $\phi(x,z,t)$ was in fact derived by Dysthe for the surface velocity potential amplitude, a_ψ. It was demonstrated by Hogan [19], see also [26], that while at the third order the governing equation for both amplitudes, that of the surface elevation, a_ζ, and of the free surface velocity potential, a_ψ, are identical, and thus there is no difference in the NLS equation for either of those amplitudes, at the fourth order the governing equations differ somewhat. For quantitative comparison of the model predictions with the experiment that directly provides data on the surface elevation variation, the equation describing the variation of a_ζ is applied in sequel, with the index ζ omitted. In fixed coordinates, the governing system of equations has the following form:

$$\frac{\partial a}{\partial t} + \frac{\omega_0}{2k_0}\frac{\partial a}{\partial x} + i\frac{\omega_0}{8k_0^2}\frac{\partial^2 a}{\partial x^2} + \frac{i}{2}\omega_0 k_0^2 |a|^2 a - \frac{1}{16}\frac{\omega_0}{k_0^3}\frac{\partial^3 a}{\partial x^3} + \frac{\omega_0 k_0}{4}a^2\frac{\partial a^*}{\partial x} + \frac{3}{2}\omega_0 k_0 |a|^2\frac{\partial a}{\partial x} + ik_0 a\left(\frac{\partial \phi}{\partial x}\right)_{z=0} = 0 \tag{8.14}$$

$$\frac{\partial^2 \phi}{\partial x^2} + \frac{\partial^2 \phi}{\partial z^2} = 0 \qquad z \le 0. \tag{8.15}$$

These equations are subject to the boundary conditions at the free surface

$$\frac{\partial \phi}{\partial z} = \frac{\omega_0}{2}\frac{\partial |a|^2}{\partial x} = 0; \qquad (z = 0) \tag{8.16}$$

and at the bottom

$$\frac{\partial \phi}{\partial z} = 0; \quad (z \to -\infty) \tag{8.17}$$

The first four terms in Eq. (8.14) constitute the cubic Schrödinger equation for deep water in the fixed frame of reference. The Dysthe model is of the third order in the wave steepness ϵ and can be derived from the third order Zakharov integral equation by adding the narrow-band assumption with spectral width $O(\epsilon)$ [73].

Incorporation of the narrow-band assumption results in the overall fourth order of the Dysthe equation.

The sign of the term $\frac{\omega_0 k_0}{4} a^2 \frac{\partial a^*}{\partial x}$ in Eq. (8.14) is positive, while in the velocity potential version used in Dysthe [11] and Lo and Mei [32] it is negative. The opposite signs of this term constitute the only difference between the two versions of the fourth order envelope evolution equation.

Two different formulations of the problem of wave field evolution in a tank were considered in Shemer and Dorfman [59]. In the so-called temporal formulation, the spatial distribution of the complex envelope $a(x)$ is presumed to be known at a prescribed instant t_0, and its variation in time is obtained by numerical solution of the model equation. Alternatively, the variation of the complex envelope in time, $a(t)$, can be specified at a prescribed location $x = x_0$, and the variation of $a(t)$ along the tank is then studied in the spatial formulation using the appropriately modified model equations. It should be stressed that the spatial formulation is routinely applied in the experiment-related studies [32, 66], since the wave gauges provide information on the temporal variation of the surface elevation at fixed locations. The experimental approach in [59] made it possible to measure the variation with time of the instantaneous complex group envelope along the tank, as well as the variation of the surface elevation with time at any location within the tank. Both temporal and spatial formulations of the Dysthe equation were therefore employed.

Consider first the temporal model. In analogy to Lo and Mei [32], in a coordinate system moving at the group velocity $c_g = \omega_0/2k_0$, the following dimensionless scaled variables are introduced:

$$\tau = \epsilon^2 \omega_0 t; \quad \xi = \epsilon k_0 (x - c_g t); \quad A = a/a_0; \quad \Phi = \omega_0 a_0^2 \phi; \quad Z = \epsilon k_0 z. \tag{8.18}$$

In these variables, the equations for A and Φ are:

$$\frac{\partial A}{\partial \tau} + \frac{i}{8}\frac{\partial^2 A}{\partial \xi^2} + \frac{i}{2}|A|^2 A - \epsilon \frac{1}{16}\frac{\partial^3 A}{\partial \xi^3} + \epsilon \frac{1}{4} A^2 \frac{\partial A^*}{\partial \xi} + \epsilon \frac{3}{2}|A|^2 \frac{\partial A}{\partial \xi} + \epsilon i A \left(\frac{\partial \Phi}{\partial \xi}\right)_{Z=0} = 0 \tag{8.19}$$

$$\frac{\partial^2 \Phi}{\partial \xi^2} + \frac{\partial^2 \Phi}{\partial Z^2} = 0 \quad (Z < 0), \tag{8.20}$$

with Φ satisfying the following boundary conditions:

$$\frac{\partial \Phi}{\partial Z} = \frac{1}{2}\frac{\partial |A|^2}{\partial \xi}, \quad Z = 0, \qquad \frac{\partial \Phi}{\partial Z} = 0, \quad Z \to -\infty. \tag{8.21}$$

Equations (8.18)–(8.21) and the appropriate initial conditions constitute the temporal version of the Dysthe model.

The corresponding spatial version can be obtained either from Eq. (8.14) as in Lo and Mei [32], or from the spatial version of the Zakharov equation [66]. Instead of Eq. (8.18), the scaled dimensionless space and time variables now are identical to those in the spatial NLS equation given by Eq. (8.7). The governing equations assume the following form

$$\frac{\partial A}{\partial X} + i\frac{\partial^2 A}{\partial \tau^2} + i|A|^2 A + 8\epsilon|A|^2\frac{\partial A}{\partial \tau} + 2\epsilon A^2\frac{\partial A^*}{\partial \tau} + 4i\epsilon A\left(\frac{\partial \Phi}{\partial \tau}\right)_{Z=0} = 0. \tag{8.22}$$

$$\frac{4\partial^2 \Phi}{\partial \tau^2} + \frac{\partial^2 \Phi}{\partial Z^2} = 0 \quad (Z < 0), \tag{8.23}$$

$$\frac{\partial \Phi}{\partial Z} = \frac{\partial |A|^2}{\partial \tau}, \quad Z = 0, \qquad \frac{\partial \Phi}{\partial Z} = 0, \quad Z \to -\infty. \tag{8.24}$$

The formulation of the spatial model given by Eq. (8.18) and Eqs. (8.22)–(8.25) is completed by specifying the temporal variation of the envelope at the prescribed location $A(X_0, \tau)$. In both temporal and spatial formulations, the normalized envelope shape $A(X, \tau)$ determines the surface elevation at the leading order. With $A(X, \tau)$ known, application of Eq. (8.12) yields free waves only. The second order bound, or locked, waves can be determined using:

$$B(A) = \frac{1}{2}\epsilon A^2 - \frac{ik_0}{\omega_0} A\frac{\partial A}{\partial \tau}, \tag{8.25}$$

see [68]. The surface elevation that contains the second order bound waves with frequencies and wave numbers that are respectively twice higher than those of the free waves are thus obtained for both temporal and spatial formulation as

$$\zeta(x,t)/a_0 = Re\left[Ae^{i(k_0 x - \omega_0 t)} + B(A)e^{2i(k_0 x - \omega_0 t)}\right]. \tag{8.26}$$

The effect of each one of the fourth order terms in the Dysthe model was studied in Shemer et al. [66]. The spatial version of the Dysthe model is given by Eqs. (8.22)–(8.24); they were solved using pseudo-spectral method and split-step Fourier method as described in [32]. The numerical results obtained for the strongly nonlinear case with $\epsilon = 0.24$ and the initial condition given by Eq. (8.4) with $m = 4$, are presented in Fig. 8.6. The numerical solution of the deep-water NLS equation [the first 3 terms in Eq. (8.22)] is plotted in Fig. 8.6a. At this high forcing amplitude, the model yields considerable energy focusing along the tank, while retaining the symmetric shape of the envelope. At the next stage, the effect of the induced current only is considered in Fig. 8.6b by adding to the NLS equation the last term in (8.22). In this case, the simultaneous solution of the coupled Eqs. (8.22)–(8.24) is required. This modification retains the symmetry of the NLS solution, but leads to an essential modification of the envelope shape as compared to the NLS solution in Fig. 8.6a. Further, in Fig. 8.6c all fourth order terms expect for the last one in Eq. (8.22)

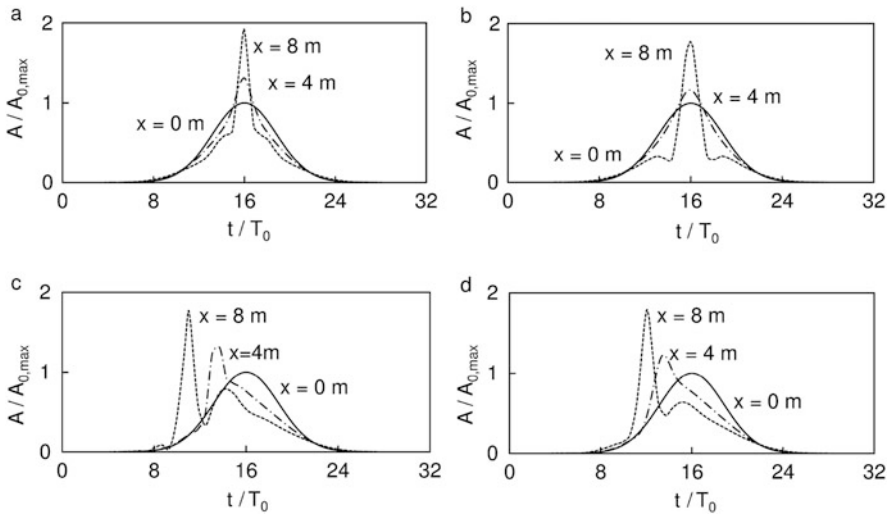

Fig. 8.6 Effect of various terms in the Dysthe model for $T_0 = 0.7$ s, $\epsilon = 0.24$ and the Gaussian initial shape given by Eq. (8.4) with $m = 4$: (**a**) NLS equation; (**b**) NLS + the last fourth order term in Eq. (8.22); (**c**) Dysthe equation without the last term; (**d**) the full Eq. (8.4)

are considered, while the term which represents effect of the current potential is disregarded. As expected, addition of terms that contain first derivatives of the envelope cause the dramatic change in the initially symmetric envelope shape as observed in the experiments. Comparison of Fig. 8.6c with the solution of the full Dysthe model presented in Fig. 8.6d reveals that contribution of the induced current-related term is non-negligible. It thus appears that all fourth order terms in Eq. (8.22) are of comparable importance to the accuracy of the solution and neither of them can be neglected.

8.4.2 Experiments on Spatial and Temporal Evolution of Wave Groups Based on Digital Video Image Processing

Shemer and Dorfman [59] studied the evolution along the tank of narrow-spectra unidirectional nonlinear wave groups excited by a wavemaker using digital processing of video-recorded sequences of images of the contact line movement at the tank side wall. The technique allows accurate measurements of the spatial variation of the instantaneous surface elevation along the whole tank, as well as of the temporal variation of the surface elevation at any prescribed location within the tank. More details of the experimental approach are given [10]. The experimentally obtained data thus can be compared with the solutions of the model equations presented in either temporal or spatial form.

The wave gauges in this study were applied mainly for validation of the accuracy of surface elevation measurements by digital processing of video clips that record the contact line movement at the tank's wall. The instantaneous contact line shapes were recorded by a single monochrome CCD video camera at a rate of 30 fps. The field of view of the camera spanned 50 cm along the tank. The spatial resolution was about 0.8 mm/pixel. Advantage was taken of extremely high repeatability of the wave field emanating from the prescribed wavemaker driving signal. The camera was placed on the instrument carriage to enable imaging of different regions of the tank. Each camera recording session was synchronized with the wavemaker driving signal using a common reference signal. A single wave group was generated for each recording session. For consecutive recording session, the carriage was shifted along the tank, so that slightly overlapping images of the contact line movement along the whole experimental facility were obtained. Every frame of the recorded video clip at each camera location was processed separately.

Experiments were performed for a wave group with Gaussian envelope given by Eq. (8.4) generated by the wavemaker. The selected dominant wave period $T_0 = 0.7$ s corresponds to the wave length $\lambda_0 = 0.76$ m. The value of $m = 3.5$ in Eq. (8.4) corresponds to the spectral width that is sufficient to satisfy the narrow spectrum constraint for the applicability of the Dysthe equation. On the other hand, the spatial extent of the group is short enough to enable studying of the temporal evolution of the group within the tank. To determine the instantaneous spatial envelope shape of the wave group and to study its nonlinear temporal evolution, the entire group has to be present in the tank. Hence, on one hand, the group generation by the wavemaker has to be completed before initiation of the study of the temporal variation of the envelope shape, and on the other hand, measurements of spatial wave group structure remain meaningful as long as the front of the group does not reach the beach. The group propagates along the tank with the group velocity $c_g = 0.54$ m/s. The length of the group for the adopted parameters does not exceed 6–7 m. When the generation of the group by the wavemaker is completed, the group front is about 5 m from the beach, leaving the duration that does not exceed 10 s to study the wave group evolution before its front reaches the far end of the tank. According to Eq. (8.7), the time scale of the nonlinear effects is $O(\epsilon^2)$. Hence, for the duration of the process prescribed by the group shape, the dominant frequency and the length of the tank, higher wave steepness increases the effective evolution time at the slow scale τ. To eliminate breaking not accounted for by the Dysthe model, the wave steepness must not exceed the value that can lead to wave breaking. The maximum adopted initial wave steepness of $\epsilon = 0.18$ ($a_0 = 22$ mm) was selected on the basis of visual observations of wave group propagation along the tank with different values of a_0. For this value of ϵ, $\tau = 1$ corresponds to dimensional duration $t = 3.44$ s, or 4.9 dominant wave periods. This is well below the experiment duration limit of about 7 s imposed by the effective length of the tank.

In the spatial evolution formulation the initial condition emerges naturally from the water surface elevation variation in time excited by a wavemaker located at $x = 0$. In the temporal evolution case the initial conditions defining the wave field in the whole tank are to be prescribed at a certain instant. One possibility to define the

initial conditions for the temporal formulation of the problem is to use the actually measured instantaneous wave field when the whole group emerges in the tank. For a relatively short wave tank used in the present study this option, however, severely restricts the duration of the wave group evolution and thus the role of nonlinearity that is in the center of the study. An alternative approach was therefore employed. Since nonlinear effects become prominent at slow scales, it can be assumed that the initial evolution of the wave group is mainly governed by linear dispersion effects, while nonlinearity can be neglected. This assumption enables linearization of Eq. (8.12), yielding

$$\frac{\partial A}{\partial X} + i\frac{\partial^2 A}{\partial \tau^2} = 0. \tag{8.27}$$

Following [49], the solution of Eq. (8.27) for a Gaussian envelope at the wavemaker given by Eq. (8.4) can be written in the physical variables (x, t) as

$$A(x,t) = |A(x,t)|exp(i\theta); \tag{8.28}$$

where the amplitude $|A(x,t)|$ and the phase θ of the envelope are given by

$$|A(x,t)| = \frac{m\pi}{\sqrt[4]{m^4\pi^4 + 4k_0^2x^2}}exp - \left[\frac{m^2\pi^2}{4(m^4\pi^4 + 4k_0^2x^2)}(\omega_0 t - 2k_0x)^2\right] \tag{8.29}$$

$$\theta = \frac{k_0x(\omega_0 t - 2k_0x)^2}{2(m^4\pi^4 + 4k_0^2x^2)} - \frac{1}{2}tan^{-1}(\frac{2k_0x}{m^2\pi^2}). \tag{8.30}$$

While Eqs. (8.28)–(8.30) represent the solution of the spatial evolution problem; they describe the complex group envelope variation in time and space, and thus can be used to define the initial conditions for the solution of the temporal evolution problem. The calculated according to Eq. (8.29) envelope shape is presented in Fig. 8.7 at two instants. The broken line corresponds to the instant when the maximum of the envelope is at the wavemaker located at $x = 0$. The solid line represents the spatial distribution of the group envelope immediately before the entrance of the group to the tank and corresponds to the instant when the wave group excitation by the wavemaker is initiated in the experiments. This wave envelope is somewhat wider than the first one, with the maximum value below unity. This complex envelope shape prior to the group's entrance to the tank served as the initial condition. Time in the present study is thus measured relative to that instant of initiation of the wavemaker movement. The wavenumber spectrum of the surface elevation presented in Fig. 8.7b apparently does not vary in time for the linearized problem and therefore can be seen as the initial spectrum for the nonlinear evolution problem.

The computed according to Eqs. (8.22)–(8.24) temporal variation of the surface elevation at a number of locations along the tank is compared in Fig. 8.8 with the

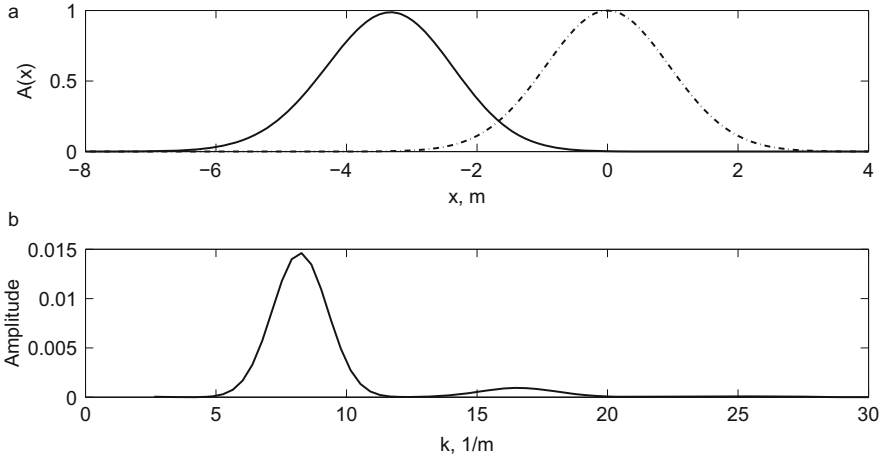

Fig. 8.7 Initial conditions for the temporal evolution computations. (**a**) Envelope shape centered at the wavemaker ($x = 0$ m) and at the instant corresponding to initiation of the wavemaker operation ($t = 0$ s); (**b**) initial wavenumber amplitude spectrum

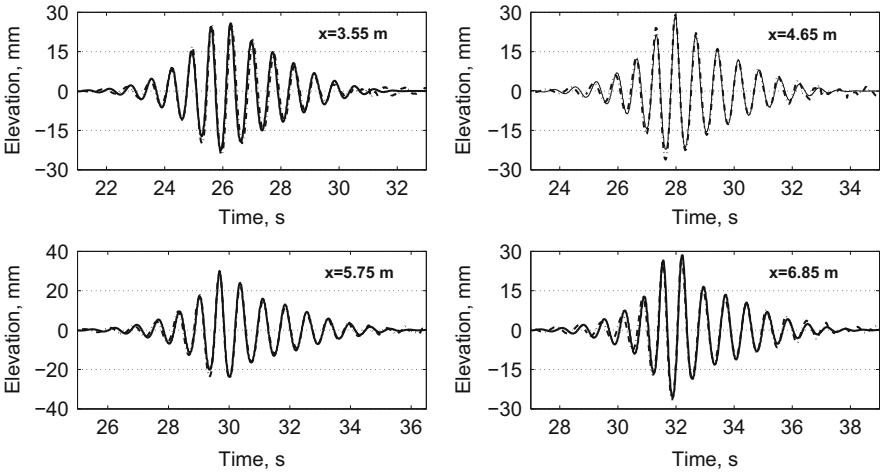

Fig. 8.8 Variation of the surface elevation within the group with time at different distances x from the wavemaker: *solid line*—simulations; *broken line*—experiments

results of video image processing. The shift in the horizontal scale in the consecutive frames of Fig. 8.8 reflects the time elapsed while the group traveled between the measuring stations. Excellent agreement is obtained between the experimental results and the computations based on the spatial Dysthe model. The sequence of frames in Fig. 8.8 clearly demonstrates that the duration of the group extends with x and that the initially symmetric Gaussian envelope shape, Fig. 8.7a, gradually exhibits stronger left-right asymmetry, with increasingly steep front and elongated

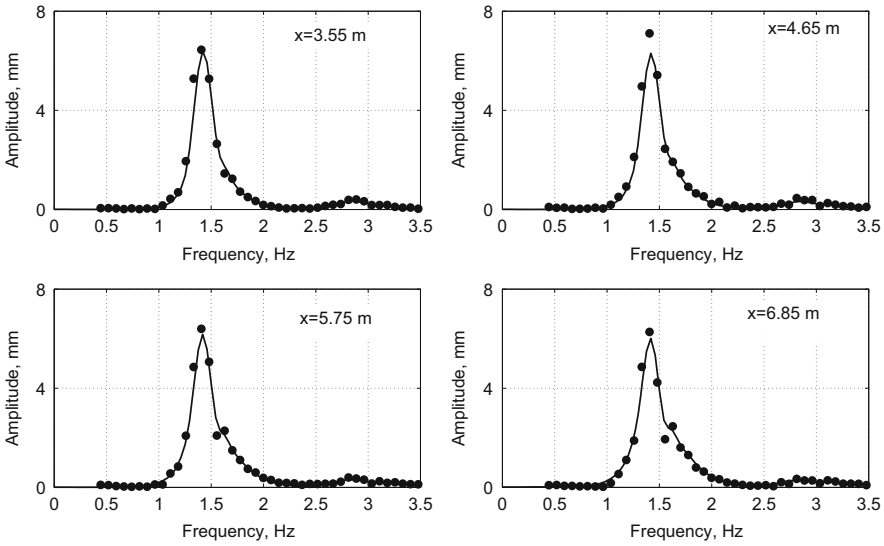

Fig. 8.9 Variation of the frequency spectra along the tank: *symbols*—experiments, *line*—simulations

tail. This behavior is consistent with that plotted in Fig. 8.5. The maximum surface elevation within the group may exceed significantly the nominal value of a_0. This increase of the maximum amplitude is associated in part with the focusing properties of the NLS equation as discussed in Sect. 8.3. An apparent additional reason for higher maximum values of the surface elevation in Fig. 8.8, as well as for the crest-trough asymmetry, is the contribution of the second order bound (locked) waves.

The variation of the group shape along the tank in Fig. 8.8 is due to both linear dispersion and nonlinear effects. To separate linear and nonlinear contributions, frequency spectra of surface elevation variation in time that vary only due to nonlinear effects, are presented in Fig. 8.9. The frequency spectra of Fig. 8.9 are plotted for the same locations along the tank as in Fig. 8.8. The spectra are computed for those parts of the surface elevation records that contain the whole group with duration of about 13 s (about $20T_0$). The spectra are thus discrete with the frequency increment of about 0.077 Hz. For demonstration purposes only, the amplitude spectra obtained for the computed temporal variation of the surface elevation that naturally are smoother than the results derived from the experimental data, are drawn as a solid line.

The agreement between experiments and computations in Fig. 8.9 is quite good. While the initial amplitude spectrum corresponding to the envelope given by Eq. (8.4) is also symmetric and Gaussian, the spectra of Fig. 8.9 are asymmetric and deviate from the Gaussian shape. Note the existence of a kink in the spectral shape at the frequency slightly exceeding the dominant one, $f_0 = 1/T_0 = 1.43$ Hz, that is visible at $x = 5.75$ m and becomes stronger at $x = 6.85$ m. The kink is observable

both in the measured and in the computed spectra. Even for a relatively short extent of the spatial evolution, widening of the spectrum is visible in Fig. 8.9. This spectral widening and non-Gaussian spectral shape indicate that nonlinearity is essential in the wave group evolution along the tank.

The contribution of the second order bound waves to the amplitude spectrum is quite significant at all locations. The measured using the digital processing of the video images spectrum of bound waves around the second harmonic of the dominant frequency f_0 is in excellent agreement with the model predictions. The bound waves' spectrum also becomes wider with the distance from the wavemaker, in agreement with the variation of the free wave spectrum around the dominant frequency f_0.

As stressed above, the main motivation for developing the data acquisition method based on the processing of sequences of video images is in its capability to measure instantaneous spatial distribution of the surface elevation. Application of this method enables following the temporal evolution of the whole wave group as well. This information can be compared with the numerical solution of the system of Eqs. (8.18)–(8.21) that constitute the Dysthe model in its temporal formulation. The initial conditions for the temporal evolution case $A(x, 0)$ are obtained using Eqs.(8.28)–(8.30), as presented in Fig. 8.7.

It should be stressed that direct juxtaposing of the theoretical and the experimental results on the temporal evolution of a wave field is quite challenging since it is limited to the time interval when the whole group is physically present within the wave tank boundaries. The numerical solution of Eqs. (8.18)–(8.21) indicates that at the dimensional time $t = 12\,\mathrm{s}$ (relative to the instant depicted in Fig. 8.7) the advancement of the group along the tank is sufficient for the tail of the computed instantaneous spatial envelope distribution to emerge within the tank, thus enabling comparison with the experiment. Similarity of the numerical and the experimental results is examined also at three additional instants: $t = 14\,\mathrm{s}$; $16\,\mathrm{s}$ and $18\,\mathrm{s}$. Equations (8.25), (8.26) are used again to account for the contribution of the second order bound waves.

The spatial variation of the surface elevation as a result of the temporal evolution of the complex wave envelope is presented at the selected instances in Fig. 8.10. As in the spatial evolution case, good agreement is obtained between the numerical simulations and the experimental observations. At the earliest instant presented in Fig. 8.10, $t = 12\,\mathrm{s}$, the formation of the group has just been completed and the group in its entirety emerges in the tank, while at the last instant, $t = 18\,\mathrm{s}$, the front of the group approaches the far end of the wave tank.

Deviation of the group shape in Fig. 8.10 from the initial envelope presented in Fig. 8.7a is obvious. Both left-right and trough-crest asymmetries observed in the temporal records presented in Fig. 8.8, as well as significant variations in the extreme values of the surface elevation within the group, are visible in Fig. 8.10 as well. Note, however, that the left-right asymmetry in Fig. 8.10 is opposite to that of Fig. 8.8, where the steeper part of the group appears at earlier sampling times. The experimental results are in agreement with the numerical solutions of the temporal Dysthe model.

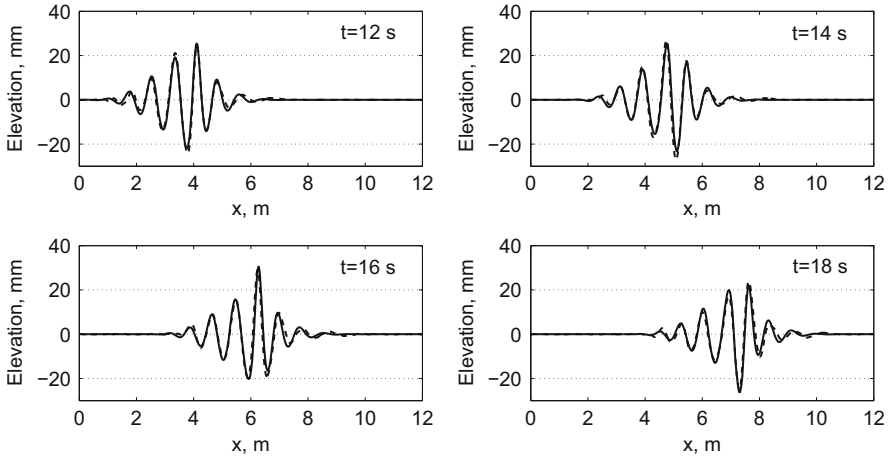

Fig. 8.10 The instantaneous surface elevation at various instants: *solid line*—simulations; *broken line*—experiments

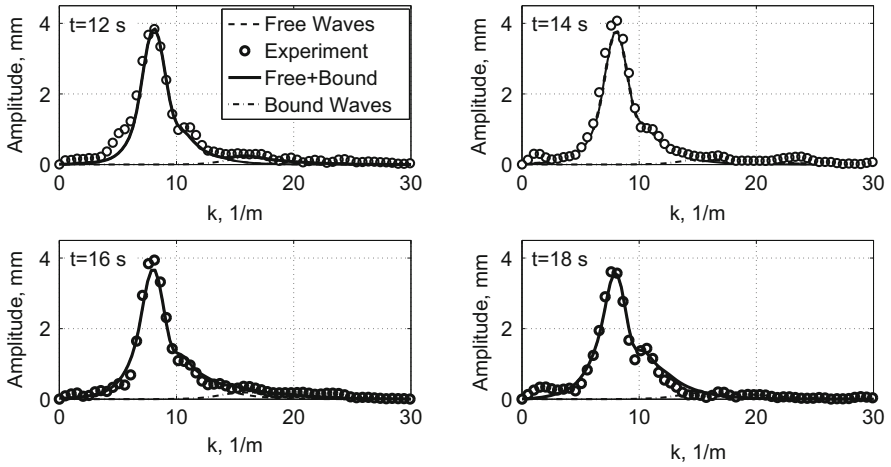

Fig. 8.11 Wavenumber spectra of the surface elevation at various instants: *symbols*—experiments; *lines*—simulation

Comparison of Figs. 8.8 and 8.10 also illustrates the well known fact that since the group velocity of deep water waves is a half of their phase velocity, the number of waves within the group in the temporal surface elevation variation records of Fig. 8.8 is twice larger than in the instantaneous spatial snapshots of the same group plotted in Fig. 8.10.

The wave-number amplitude spectra corresponding to Fig. 8.10 are presented in Fig. 8.11. The spectra based both on the experimental data and on the numerical simulations were computed for instantaneous surface elevation distributions along

12 m of the tank and contain the whole group. This longitudinal extent of the synthesized from the numerous images 'snapshot' determines the wave number resolution of the resulting discrete spectra. As in Fig. 8.9, the spectra derived from the numerical solutions of the Dysthe model are plotted as solid lines. All spectra in Fig. 8.11 exhibit essential differences from the initial wavenumber spectrum presented in Fig. 8.7b. The agreement between the simulated and the experimental results in Fig. 8.11 is quite good at all instances presented; the differences can be attributed in part to inaccuracy associated with choosing the initial condition. There are similarities but also essential differences between the frequency spectra given in Fig. 8.9, and the wave number spectra of Fig. 8.11. In both figures the spectra become wider in the course of the wave group evolution. The wave number spectra in all frames of Fig. 8.11 are however much wider than the frequency spectra in Fig. 8.9.

The larger width of the wave number spectra relative to the frequency spectra follows from the dispersion relation for deep water $\omega^2 = kg$ that is appropriate for the present experiments. In the narrow spectrum approximation the relative widths of those spectra are related by

$$\frac{\Delta k}{k_0} = 2\frac{\Delta \omega}{\omega_0} \tag{8.31}$$

As a result, in all frequency spectra of the temporal variation of the surface elevation for a narrow-band wave group moving along the tank, Fig. 8.9, the free waves and the bound waves are totally separated. For the initial condition presented in Fig. 8.7b, the separation of free and bound waves spectral domains still exists. The spectral widening in course of group propagation along the tank, however, leads to overlapping domains of the free and of the second harmonic bound waves in the wave number spectra of Fig. 8.11. Each measured spectrum apparently contains free as well as bound waves. In numerical simulations, complex group envelope that corresponds to free waves only is computed first. Bound waves are then obtained from the free wave field. The computed wave number spectra of free and bound waves are also plotted in Fig. 8.11. The overlapping of free and bound waves domains in the wave number spectra precludes straightforward filtering out of the free wave spectrum from the experimental results. This difficulty complicates significantly the determination of the spatial group envelope's shape that contains the free-wave part only, from the experimental data. The initial conditions for solving the temporal evolution problem could not therefore be determined from experiment. This difficulty forced to apply the linearized approach presented by Eqs. (8.28)–(8.30) in order to translate the temporal variation of the surface elevation at the wavemaker into the spatial form. Accounting for the second harmonic bound waves is essential to get a better agreement with the measured spectra at high wave numbers. The disagreements between computations and measurements in the low wave number region of the spectrum in Fig. 8.11 may partially stem from the fact that the depth of the experimental facility of 0.6 m is not large enough for those longer wave components to be

considered deep. The low wave number bound waves may become significant and can constitute a important contribution to the spectral shape. The validity of Dysthe equation that served as the theoretical model in the present study, however, is restricted to deep waves. The long bound waves were therefore not considered.

Theoretical studies of nonlinear water-waves are often performed by solving temporal evolution models, while in laboratory as well as in field experiments surface elevation variation with time at fixed locations is usually recorded; sometimes these data also contain information on the wave propagation directions. Attempts are sometimes made to translate the measured by point sensors frequency spectrum into the corresponding wave number (or wave vector in the two-dimensional case) spectrum. However, direct quantitative comparison of the frequency and the wave number spectra can not be carried out in a consistent way. Instantaneous snapshot of the whole wave field taken to get the wave number spectrum, on one hand, and measurements of the temporal variation of the surface elevation variation with time at a fixed location to get the wave frequency spectrum, on the other hand, constitute essentially different ways of studying an evolving in space and in time water-wave field.

Moreover, as demonstrated in this section, direct computation of the wave number spectrum from the measured frequency spectrum can not be carried out even assuming that the evolution is slow as compared to the relevant temporal scale (represented by the duration of continuous sampling that determines the frequency resolution of the spectrum) and the spatial scale (the extent of the imaged wave field that determines the wave number spatial resolution) of the data acquisition process. The linear dispersion relation between wave frequencies and wave numbers only holds for the free wave components. Therefore, it is possible in principle to relate quantitatively frequency and wave number spectra for the free wave domain only. Comparison of the frequencies and wave numbers that correspond to the spectrum peaks and clearly represent free waves in Figs. 8.9 and 8.11, respectively, indeed reveals that they are related by the deep water dispersion relation. The present results, however, demonstrate that in general separation of the wave number spectra into free and bound waves is not always possible. For a relatively narrow initial free-wave spectrum, the high frequency/wave number part of the spectrum consists almost exclusively of bound components. The calculation of spectral bound components from the free wave spectrum is often not straightforward and requires information on the phases of each free wave component. Such information is usually not readily available in reported data on the experimentally measured frequency spectra. It thus appears virtually impossible to evaluate quantitatively the shape of the high end of the wave number spectrum from the measured surface elevation variation in time at a fixed location and the corresponding frequency spectrum the shape of the high end of the wave number spectrum.

8.4.3 Experimental Studies of Evolution of Peregrine Breather

Shemer and Alperovich [57] applied both NLS and Dysthe models to the problem of extremely steep freak (or rogue) waves. A possibility to generate deterministic steep waves is of special interest. The NLS equation attracts considerable interest in this respect since it admits breather type soliton solutions. The so-called Kuznetsov-Ma breathing solitons present spatially localized patterns that oscillate in time [30, 36]. Akhmediev breather [1] is a related type of solitons that is periodic in space. When the periodicity in time and space tends to infinity, both these types of solution tend to a simple Peregrine soliton [50] that is localized in time and space and breathes only once. In scaled variables, Eq. (8.7), the complex envelope of Peregrine breather (PB) is written as

$$A(X,\tau) = -\sqrt{2}\left[1 - \frac{4(1-4iX)}{1+4\tau^2+16X^2}\right]e^{-2iX}. \tag{8.32}$$

At the origin of the scaled coordinate system $A(0,0) = 3\sqrt{2}$, and $A(X \to \pm\infty, \tau \to \pm\infty) = \sqrt{2}$, so the maximum wave amplitude at the origin exceeds the background amplitude by a factor of 3.

Experimental observations of PB for water waves were recently presented in several publications, see, e.g. [8]. These observations show that an initially small "hump" in a nearly monochromatic wave train may indeed evolve along the tank in a qualitative agreement with Eq. (8.32). Nevertheless, some marked quantitative differences between experiments and calculations could not be attributed solely to experimental inaccuracy. The Peregrine breather was suggested as a major route to deterministic freak waves' generation [70]. The importance of PB for freak water waves prompted a closer experimental investigation of its qualitative and quantitative characteristics.

Measurements of wave group evolution along the TAU tank were performed at 72 locations along the tank, up to the distance of 13.3 m from the wavemaker. At every carriage location, three realizations of the prescribed wave field were recorded, with the sufficient time delay between the consecutive events to ensure decay of any disturbances left in the tank from the previous run. Each measurement session, including probe calibration, wave generation, data recording and carriage movement was performed automatically utilizing a LabView program.

Selection of wave parameters in any given experimental facility is largely prescribed by the scaling relations given by Eq. (8.7). To enable investigation of the wave form evolution up to the maximum amplification and beyond, as well as in order to mitigate the effect of contamination by reflected waves that cannot be fully eliminated, the maximum amplification location x_0 should be sufficiently far from the end of the tank. For the TAU facility, this means that X_0 should not exceed about 10 m. The values of $A(X,\tau)$ defined by Eq. (8.32) differ notably from the background envelope only for $X < 1$. Noticeable variation of the breather maximum between the wavemaker at $x = 0$ and X_0 can be expected if $X(x_0) = \epsilon^2 k_0 x_0 = O(1)$,

thus the background wave steepness ϵ should be as large as possible. Waves with $\zeta_0 k_0 > 0.3$ may break, rendering both the NLS and the Dysthe equations inapplicable. The expected PB amplification factor of 3 thus limits the maximum steepness $\zeta_0 k_0$ to about 0.1. These considerations limit the carrier wave lengths λ_0 to values below 0.65 m. Experiments performed for a few sets of parameters within those restrictions provided consistent results. Thus the results for parameters identical to those in [8] only are discussed here: carrier wave amplitude $\zeta_0 = 0.01$ m, period $T_0 = 0.587$ s, corresponding to $k_0 = 11.67\,\mathrm{m}^{-1}$; $\lambda_0 = 0.538$ m, and $\epsilon = 0.0825 (\zeta_0 k_0 = 0.117)$. This relatively high wave steepness indeed results in waves on verge of breaking, however, no actual breaking or significant decay of wave energy along the tank was observed. The wavemaker driving signal was calculated using Eqs. (8.5), (8.7) and (8.32), the maximum amplitude of PB was set at $x_0 = 9$ m ($X(x_0) = 0.715$). The total duration of the group was selected to be $70T_0$, with tapering windows over 2 end periods. The data processing was based on segments with the duration of $64T_0$ or $32T_0$ around the instant of the peak; the sampling rate corresponded to 128 data points recorded during each period for every sensor, thus facilitating Fourier analysis.

The recorded variation of the surface elevation $\zeta(t)$ is presented in Fig. 8.12 at four locations along the tank in the frame of reference moving with the wave packet. No results in close vicinity of the wavemaker are shown as they are affected by evanescent modes [9]. The records of $\zeta(t)$ are in general agreement with [8] and demonstrate notable amplification of the peak elevation, from 14.2 mm at $x = 2.25$ m to 25.2 mm at the prescribed maximum location $x_0 = 9$ m. Several important features of Fig. 8.12, however, suggest a need for a closer look at the results. First, the maximum crest height at $x = 11.6$ m, well beyond x_0, is 31.7 mm, significantly exceeding that at x_0 and very different from the maximum crest height

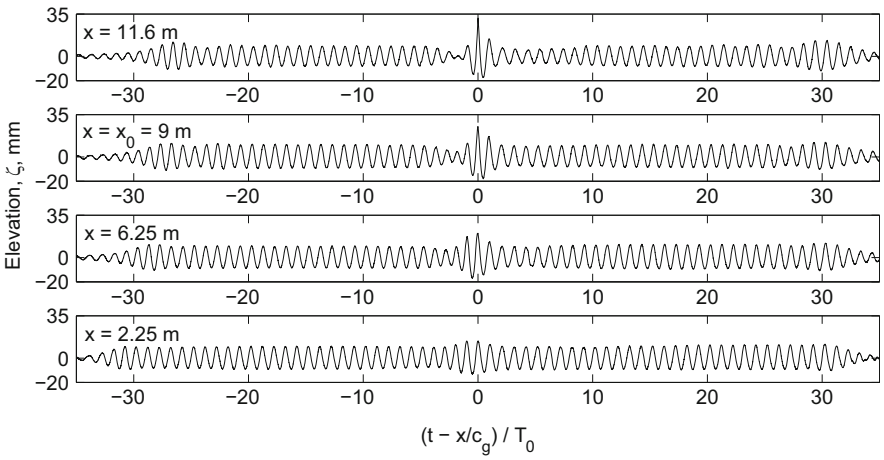

Fig. 8.12 Evolution of the wave train along the tank in the frame of references moving with the group velocity c_g ($T_0 = 0.587$ s; $\zeta_0 = 0.01$ m; $x_0 = 9$ m)

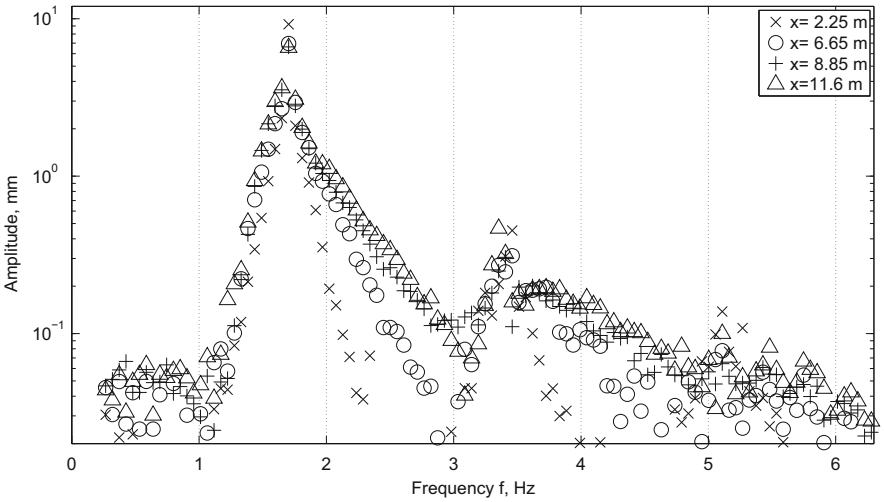

Fig. 8.13 The wave amplitude spectra at various locations along the tank

of 20.1 mm at $x = 6.25$ m, while the solution of Eq. (8.32) is symmetric about x_0. The recorded wave forms also exhibit vertical asymmetry, with crests heights consistently larger than troughs.

The nonlinear wave train evolution is characterized by variations of the amplitude spectra along the tank, see Fig. 8.13. These spectra present an average of three realizations recorded at each location. Close to the wavemaker, at $x = 2.25$ m, the amplitude spectrum still retains the characteristic BP shape, with a sharp peak at the carrier frequency and an isosceles triangle-shaped pedestal. The pedestal widens along the tank and retains its triangular shape around the carrier frequency $f_0 = 1/T_0$, however, while the spectral shape for $f < f_0$ does not vary notably, the contribution of higher frequencies increases with x, so that the spectra become strongly asymmetric. The second and even the third harmonics can be identified and become increasingly essential in the process of spatial evolution.

The Peregrine Breather is a solution of the NLS equation that provides at best qualitative agreement with the experiment for wave groups with wider spectra, as demonstrated in Sect. 8.3. This suggests application of the spatial Dysthe model Eqs. (8.22)–(8.25) to examine the evolution of the initially narrow-banded PB wave train that undergoes significant spectral widening. Since the dramatic increase in the maximum amplitude constitutes the major feature of PB, the dimensional maximum envelope moduli provided by the Dysthe and the NLS equations are compared in Fig. 8.14 with the experimental results. As in Figs. 8.2, 8.3, 8.4, and 8.5, in order to eliminate contribution of higher order low- and high-frequency bound waves, the recorded signals were band-pass filtered in the range $1\,\text{Hz} < f < 3\,\text{Hz}$, see Fig. 8.13. The envelopes of the band-passed filtered records were then computed using the Hilbert transform. The variation along the tank of the resulting envelopes

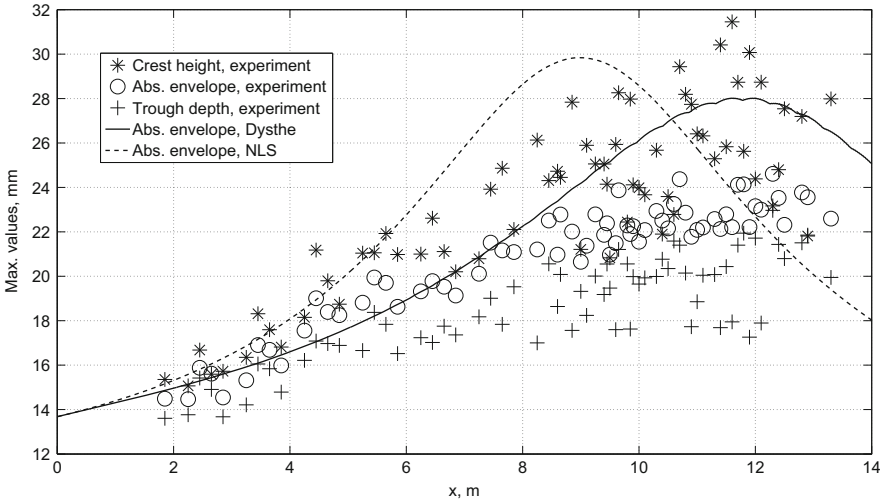

Fig. 8.14 Calculated (NLS and Dysthe equations) and measured maxima of the absolute values of the wave train envelope. The measured extreme values of crests and troughs are also presented

moduli maxima averaged over the three realizations is presented in Fig. 8.14. For comparison, the averaged highest crests and the deepest troughs recorded in every wave train at each location are also plotted.

The salient feature of Fig. 8.14 is the difference in the maximum envelope growth rate between the PB soliton given by Eq. (8.32) and the solution of the Dysthe equation. For identical initial conditions, the equation yields significantly more moderate increase rate of the envelope maxima than that predicted by Eq. (8.32); the maximum amplification by a factor of 2.8 only (instead of 3.0 for PB) is attained at $x = 11.6$ m, far away from $x_0 = 9$ m, and maximum region is flatter than that for PB. The experimental results are in a very good agreement with the MNLS solution up to the distance of about 8 m from the wavemaker. At larger distances, the maximum envelope amplification in the experiments is slightly below that predicted by the Dysthe model; the largest amplification factor of 2.5 in the experiment is attained at distances comparable with the theoretical prediction. Decay in the experimentally determined maximum following $x \approx 11.5$ m may be identified, in agreement with the numerical solution. During the initial stages of evolution, up to about $x = 5$ m, the differences between the extreme crests, troughs and envelopes are relatively minor. At larger distances characterized by stronger amplification and wider spectra (cf. Fig. 8.13), the contribution of higher order components cannot be neglected. The exact ratio between the maximum crest height, the deepest trough and the maximum envelope module apparently depends also on the local phases of the complex envelope and of the carrier wave, see Eq. (8.5). These varying along the tank phase relations contribute to the observed scatter in the extreme crest and trough values. The absolute measured crest height maximum is close to 32 mm, exceeding the PB amplification.

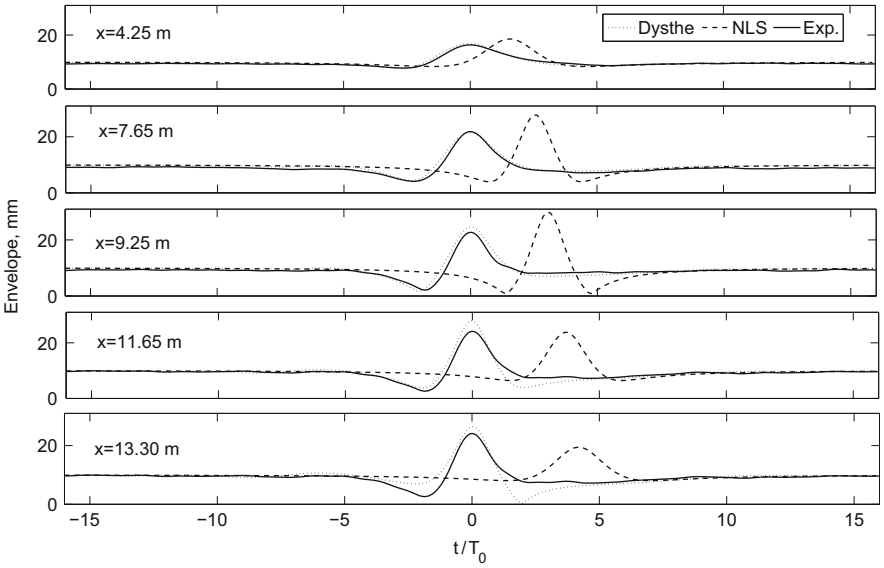

Fig. 8.15 Comparison of the computed and evaluated from the experiments shapes of the modules of complex wave train envelope

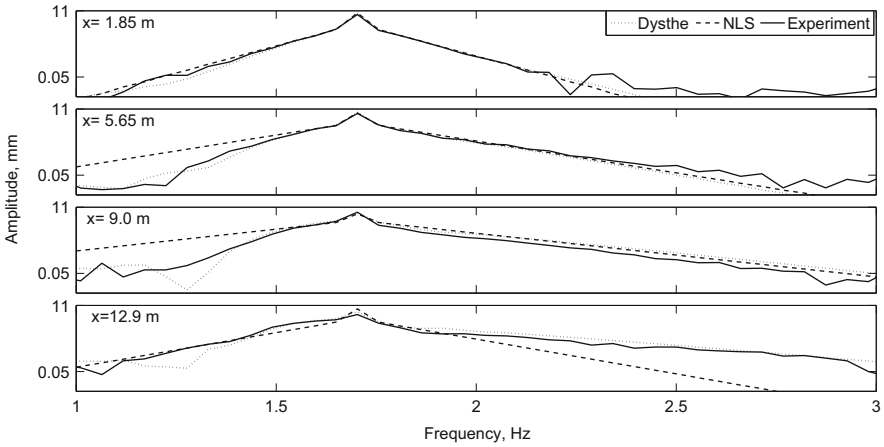

Fig. 8.16 Evolution of the dominant part of the amplitude spectrum: comparison of measurements and simulations using NLS and Dysthe models

A more detailed comparison of simulations with measurements is carried out in Figs. 8.15 and 8.16. The temporal variations of the absolute values of the complex envelope are presented in Fig. 8.15 at five locations. The PB envelopes computed using Eq. (8.32) retain symmetry around the peak along the test section and for $x < 13$ m over predict the maximum values; the peaks are attained

somewhat later as compared to the Dysthe model. Good quantitative agreement exists between experiments and computations based on Eqs. (8.22)–(8.25) up to $x = 9.25\,\mathrm{m}$. The mNLS model correctly describes the wave group asymmetry around the peak value, with the front being much steeper than the back. The discrepancies between the experimental and numerical results then increase with x.

The evolution of the computed and the measured spectra with the distance from the wavemaker is demonstrated in Fig. 8.16. Only the leading order part of the spectrum around the carrier wave frequency directly computed from the numerical simulations is plotted. The results of simulations are in excellent agreement with experiments at all locations. The higher frequency part of the PB NLS spectrum agrees with experiment and with the Dysthe computations up to the prescribed maximum at $x_0 = 9\,\mathrm{m}$. Beyond this point, the higher frequency part of the NLS-derived spectrum starts to shrink, no such decrease is observed in Fig. 8.16 in the measured spectral amplitudes and in MNLS results. Up to x_0, the lower frequency part of the spectrum is significantly below the NLS-derived prediction. After the maximum wave train height is attained, the bottom plate indicates that the spectral widening becomes more prominent at lower frequencies.

These results thus demonstrate significant quantitative and qualitative differences between the spatial evolution of the NLS Peregrine soliton and the experiments. The measurements confirm that due to the focusing properties of the NLS equation, a small hump in a nearly monochromatic wave train can indeed be amplified as suggested by the PB solution. The amplification, however, is slower and weaker than predicted, so that the maximum gain of less than 3 is attained farther away than the PB maximum. The growth in the wave height is accompanied by a significant spectral widening, initially at frequencies exceeding f_0 and then at lower frequencies. As was the case with other initially narrow-banded wave group shapes considered in Sect. 8.3, this widening violates the basic assumptions in the derivation of the NLS equation for water gravity waves. As the wave spectrum widens and becomes increasingly asymmetric with the distance, the deviation of the PB NLS-derived wave and spectral shapes from those observed in the experiments and in the solutions of Dysthe equation enhances.

The relatively simple Dysthe model thus captures accurately fine details of the observed wave field evolution even for peak steepness approaching breaking conditions. The remarkable feature of the NLS Peregrine soliton is its reversibility. The results presented above suggest, however, that the wave height growth is not reversible. Both the available experimental data and Dysthe simulations show that the decrease in the maximum wave height following the maximum is only partial. The soliton observed in the experiments and described fairly well by the Dysthe model in fact does not ‘breathe’.

8.5 The Spatial Zakharov Equation

8.5.1 The Model Equations

As mentioned above, both the NLS and the mNLS (in Dysthe form) equations can be derived from the Zakharov equation by applying appropriate limits on the spectral width [73, 86]. For this reason one can expect that the numerical calculations based on the Zakharov equation, which is free of any constraints on the spectral width, can be advantageous for predictions of the evolution of nonlinear wave fields. This conjecture was suggested by several authors (Yuen and Lake [85], Lo and Mei [32], and Trulsen and Dysthe, [81]). The Zakharov equation is indeed the most general nonlinear wave model, which describes temporal evolution of deep nonlinear waves in Fourier space and has no restrictions on spectral bandwidth. The modulation of each wave component is due to nonlinear near resonant interaction of four waves (the so-called Class I interactions). Stiassnie and Shemer [74] extended the derivation to intermediate depth and to the next order, to account for the so-called Class II (five waves) near-resonant interactions. Although the approach applied in [86] is based on the Hamiltonian formalism, the Hamiltonian is not fully conserved in those formulations. Krasitskii [29] modified the original derivation of Zakharov conserving the Hamiltonian structure of the water-wave problem. The accuracy in predicting the domains of the Benjamin-Feir instability of nonlinear Stokes waves was demonstrated in [74] where the results based on the Zakharov equation were compared with the exact potential flow computations by Longuet-Higgins [35] and McLean et al. [37, 38]. Quantitative agreement between these two computations was obtained up to Stokes wave steepness exceeding 0.3. Results on the instability domains of gravity-capillary waves obtained using an appropriate modification of the Zakharov equation were supported by experiments in a laboratory wave tank experiments by Shemer and Chamesse [58].

As discussed in Sect. 8.4.1, in order to perform quantitative comparison of the predictions based on the Zakharov equation with the measurements of wave train evolution in a wave tank, a modification of the governing equation is required to describe the spatial (as opposed to temporal) evolution of the wave field. Shemer et al. [65] suggested a spatial version of the Zakharov equation. A somewhat modified version of the equation was presented in [67]. The unidirectional discretized spatial Zakharov equation has the following form:

$$i\frac{dB_j(x)}{dx} = \sum_{\omega_j+\omega_l=\omega_m+\omega_n} \alpha_{j,l,m,n} B_l^* B_m B_n e^{-i(k_j+k_l-k_m-k_n)x}; \tag{8.33}$$

where * denotes complex conjugate and the spatial interaction coefficient $\alpha_{j,l,m,n}$ in its general form is given by

$$\alpha_{j,l,m,n} = V(\kappa, k(\omega_l), k(\omega_m), k(\omega_n)\frac{k(\omega_l)-\kappa}{\chi-\omega(\kappa)}. \tag{8.34}$$

Here $\kappa = k(\omega_m) + k(\omega_n) - k(\omega_l)$ and $\chi = \omega_m + \omega_n - \omega_l$. In Eq. (8.34), the values of V represent the quartet interaction coefficient in the temporal Zakharov equation as given by Krasitskii [29]. Equations (8.33), (8.34) accurately describe the slow evolution along the tank of each free spectral component $B_j = B(\omega_j)$ of the surface elevation spectrum in inviscid fluid of constant (infinite or finite) depth. The dependent variables $B(\omega_j, x)$ are related to the generalized complex "amplitudes" $a(\omega_j, x)$ composed of the Fourier transforms of the surface elevation $\hat{\zeta}(\omega_j, x)$ and of the velocity potential at the free surface $\hat{\psi}(\omega_j, x)$:

$$a(\omega, x) = (\frac{g}{2\omega})^{1/2}\hat{\zeta}(\omega, x) + i(\frac{\omega}{2g})^{1/2}\hat{\psi}(\omega, x) \tag{8.35}$$

The amplitudes $a(\omega_j)$ can be seen as consisting of a sum of free and the bound waves. The appropriate modification of Eq. (8.26) is

$$a(\omega_j, x) = \left[\epsilon B(\omega_j, x) + \epsilon^2 B'(\omega_j, x) + \epsilon^3 B''(\omega_j, x)\right] e^{ikx} \tag{8.36}$$

The higher order bound components B' and B'' can be computed at each location once the free wave solution $B_j(x)$ is known. Only bound waves of the second order resulting from interactions of all possible wave pairs i and j; $i, j = 1, \ldots N$, are considered here. Those waves have frequencies $\omega_i + \omega_j$ and $\omega_i - \omega_j$. The phase velocity of these components depends on the parent free waves and can not be determined using Eq. (8.6). The corresponding formulae, as well as the kernels necessary for their computations are given in [29, 74]. Expressions given in the Appendix of [74] are used for computation of the second order bound waves. Inversion of Eq. (8.35) allows computing the Fourier components of the surface elevation. Inverse Fourier transform then yields the temporal variation for the surface elevation ζ.

The spatial Zakharov equation given by Eqs. (8.33)–(8.35) was verified experimentally by Shemer et al. [65]. As in Sect. 8.3, the simplest possible initial wave trains were considered given by Eqs. (8.2)–(8.4). The experiments were performed in the TAU wave tank described in Sect. 8.2. Similarly to [64], two carrier wave periods, $T_0 = 0.7$ s and $T_0 = 0.9$ s were employed in the experiments.

The wave train excited by a bi-chromatic driving signal given by Eq. (8.2) with carrier wave period $T_0 = 0.9$ applied at the water depth $h = 0.6$ m for the high amplitude case, $\epsilon = 0.21$, is studied in Fig. 8.17. Note that the dimensionless depth $k_0 h = 3.0$ in this case corresponds to intermediate water depth (cf. Sect. 8.3), thus the deep-water Dysthe equation is inapplicable. Due to imperfections, the spectral contents of surface elevation variation in the vicinity of the wavemaker is somewhat different from that of the driving signal and varies slightly from one experimental run to another. An example of the surface elevation spectrum measured in the tank in a close vicinity of the wavemaker ($x = 0.24$ m) is plotted in Fig. 8.17a. The corresponding spectrum measured at a remote location ($x = 9.47$ m) is presented in Fig. 8.17c. The spectrum presented in Fig. 8.17a is characterized by two dominant peaks of slightly unequal amplitudes of about

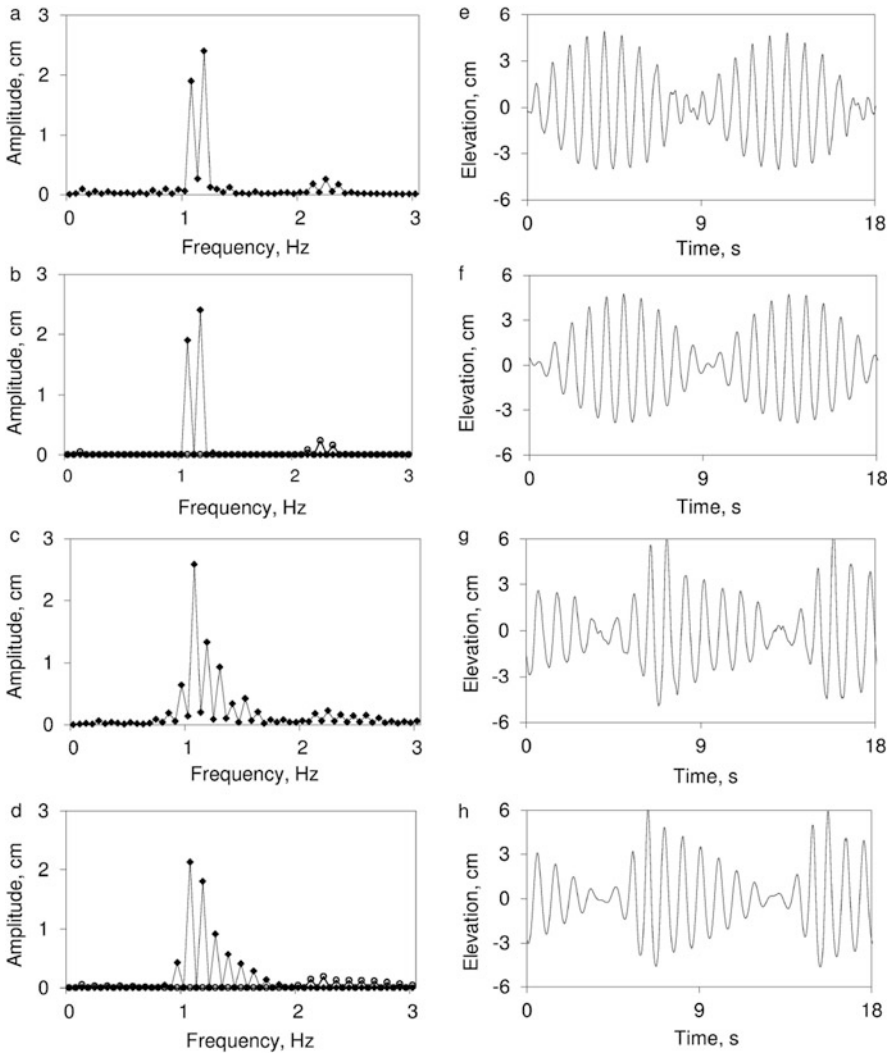

Fig. 8.17 *Left column*: frequency spectra of the surface elevation, *right column*: surface elevation for bi-chromatic driving signal (8.2), $T_0 = 0.9\,\mathrm{s}$, $\epsilon = 0.21$. Panels (**a**, **b**, **e**, **f**): $x = 0.24\,\mathrm{m}$; panels (**c**, **d**, **g**, **h**): $x = 9.47\,\mathrm{m}$. Panels (**a**, **c**, **e**, **g**)—measurements; panels (**b**, **d**, **f**, **h**)—simulations based on 12 free modes. The *open circles* in panels (**b**) and (**d**) denote bound waves

2 cm each at frequencies $f_1 = (\omega_0 - \Omega)/2\pi$ and $f_1 = (\omega_0 + \Omega)/2\pi$ and several lesser peaks with amplitudes smaller than 0.25 cm. The frequency resolution of the experimentally obtained spectra is $\Delta f = (f_2 - f_1)/2$, in agreement with the period of the driving signal (8.2). Minor peaks are observed in Fig. 8.17a, c at the carrier wave frequency $f_0 = \omega_0/2\pi$, as well as at frequencies separated from f_0 by integer multiples of $2\Delta f$. Comparison of panels (a) and (c) on Fig. 8.17 indicates

that those peaks remain of minor importance along the tank. Introduction of these harmonics into the initial condition in a number of numerical simulations resulted in a similar behavior, and those peaks remained small throughout the whole process of the spatial evolution. These experimental and numerical results therefore provide justification for reducing the spectral resolution of computations with the driving signal given the Eq. (8.2) by disregarding those harmonics. The initial spectral shape corresponding to the dominant peaks measured in the tank is selected in computations, see Fig. 8.17c. The bound components are also plotted in Fig. 8.17b, d. It should be noted that in contrast to the model simulations, the free and bound components could not be separated in experimental observations. The simulated bound components are plotted as open symbols, while the free waves in those panels are plotted as filled symbols. The comparison of the simulated and measured spectra at a remote location, Fig. 8.17c, d shows very good agreement.

The temporal variation of the surface elevation demonstrates that the simulations reflect properly the evolution of the group shape as well. The envelope shape develops both left-right and trough-crest asymmetries, as can be clearly seen in the experimental results as well as in the simulations, Fig. 8.17g, h. Similar left-right asymmetry, which is manifested in the forward leaning of the wave group front, was reported in [32] and in [64] for an initial bimodal spectrum.

The results for the same conditions and at the same locations as in Fig. 8.17 but for the driving signal given by Eq. (8.3) are presented in Fig. 8.18. Both the simulated results and the experimental observations demonstrate similar energy spreading in the course of the propagation of waves away from the wavemaker. This spreading can be observed both in the amplitude spectra and in the surface elevation.

These and additional results presented in [21, 65] demonstrate that simulations based on the set of the discrete Eqs. (8.33)–(8.35) that constitutes the spatial unidirectional version of the Zakharov equation compared favorably with the experimental results in deep and intermediate depth water. However, in order to attain these results, in some occasions the wave frequency spectrum considered included quite a large number of free modes N. The number of equations in the set is equal to N, while the number of nonlinear terms in the resulting set of ODEs is growing roughly proportionally to N^3 [21].

8.5.2 The Spatial Zakharov Equation vs. the Dysthe Model

The considerable numerical effort required to solve the set of ordinary differential equations resulting from the spatial Zakharov model prompted Shemer et al. [66] to examine the limits of applicability of the Dysthe equation that requires essentially lesser computer resources, by direct comparison of the simulations results obtained for wave groups with spectra of varying width using both models with measurements carried out in the TAU wave tank. Note that in the derivation of the Dysthe equation it is assumed that $\Delta\omega/\omega_0 = O(\epsilon)$.

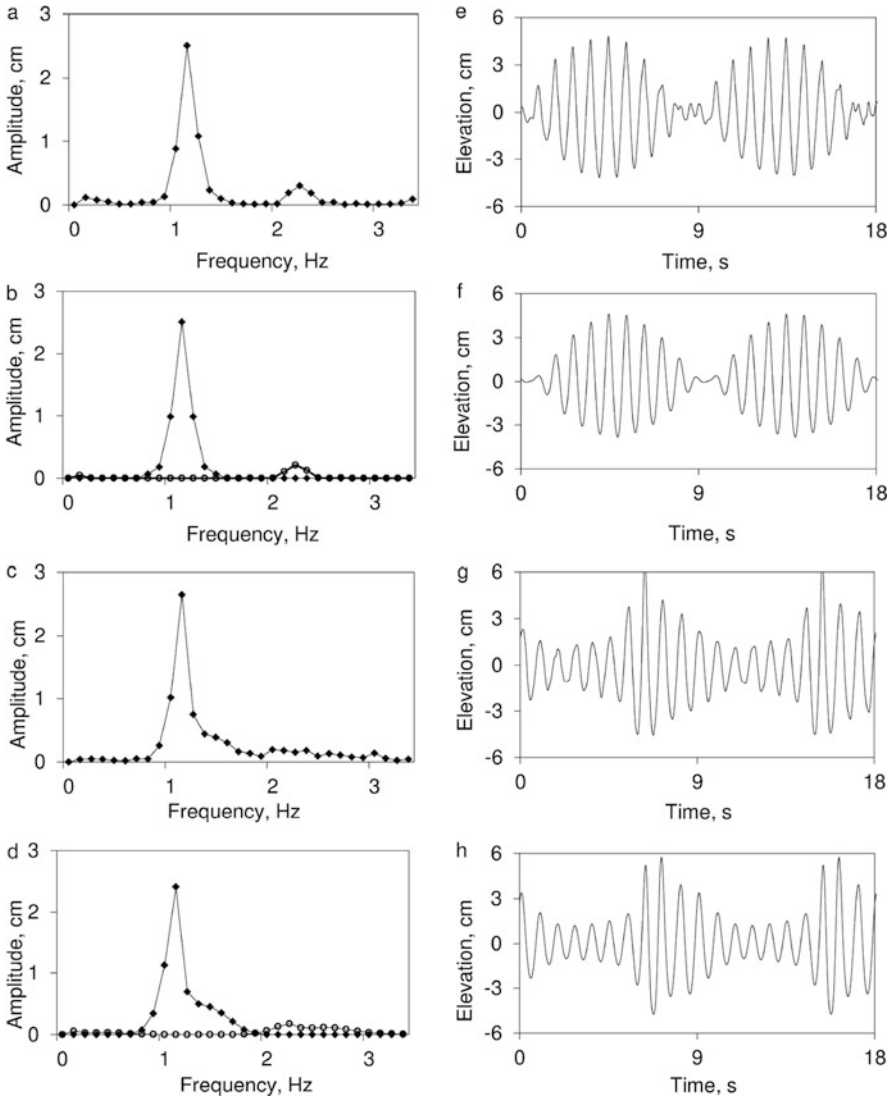

Fig. 8.18 *Left column*: frequency spectra of the surface elevation, *right column*: surface elevation for bi-chromatic driving signal (8.3), $T_0 = 0.9$ s, $\epsilon = 0.21$. Panels (**a, b, e, f**): $x = 0.24$ m; panels (**c, d, g, h**): $x = 9.47$ m. Panels (**a, c, e, g**) - measurements; panels (**b, d, f, h**) - simulations based on 12 free modes. The *open circles* in panels (**b**) and (**d**) denote bound waves

The Gaussian-shaped driving signal given by Eq. (8.4) is particularly suited for that purpose. Its energy spectrum also has a Gaussian shape with the relative width at the energy level of 1/2 of the spectrum maximum given by

$$\frac{\Delta\omega}{\omega_0} = \frac{1}{m\pi}\sqrt{\frac{1}{2}ln2}. \tag{8.37}$$

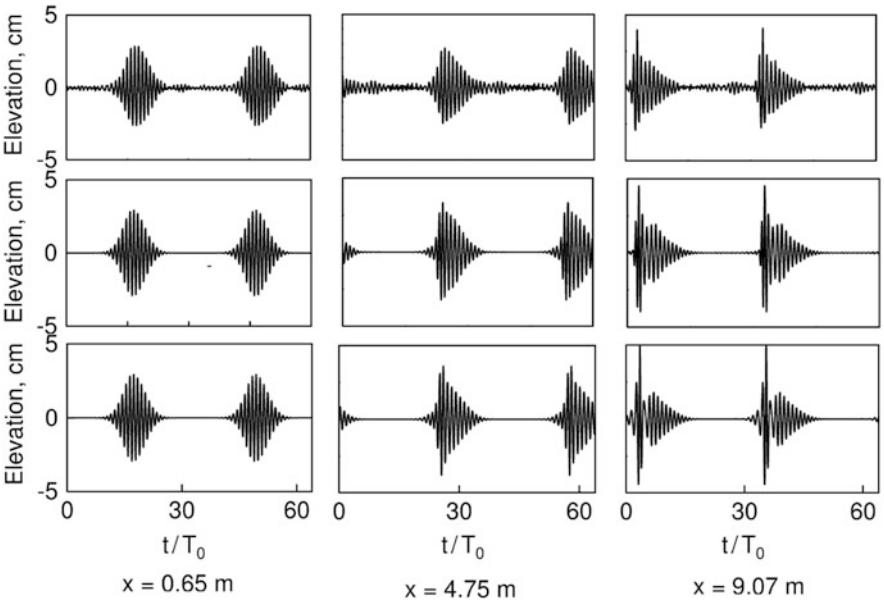

Fig. 8.19 Measured and computed variation of the instantaneous surface elevation at three locations along the tank for $T_0 = 0.7$ s; $\epsilon = 0.24$ and the Gaussian forcing signal with $m = 4.0$. *Upper row*—experiment, *middle row*—Zakharov equation, *bottom row*—Dysthe model

The value of the parameter m thus determines the spectral width.

Carrier wave period $T_0 = 0.7$ s was selected, corresponding to the wave number $k_0 = 8.22$ 1/m, so that $k_0 h \approx 5$, and the deep-water dispersion relation is satisfied. The forcing amplitude a_0 was chosen so that the maximum wave amplitude in the group $a_0 = 2.92$ cm, corresponding to the maximum wave steepness $k_0 a_0 = \epsilon = 0.24$. For the value of $m = 4.0$ selected in the experiments, the relative spectrum width $\Delta\omega/\omega_0 = 0.047 < \epsilon$, thus satisfying the narrow spectrum assumption of the Dysthe model.

Comparison of the numerical simulations of the temporal and spatial variation of the surface elevation performed according to both models with the experiments is carried out in Fig. 8.19. The spatial Zakharov equation is solved by using the modified Runge-Kutta method following the procedure described in [65]. The results are shown at three locations: close to the wavemaker, in the middle of the tank and far away from the wavemaker. The experimental results are band-pass filtered to eliminate the contribution of bound waves. The total number of free modes considered in the solution of the Zakharov equation (8.33), $N = 60$, although much less modes are actually required to obtain satisfactory results. Close to the wavemaker, the group envelope still retains its Gaussian shape, but farther away strong distortion of the initially symmetric shape appears, and the characteristic triangular shape of the envelope emerges. Both theoretical models

faithfully describe the experimental oscillations, including the fine features of the observed wave shapes.

The agreement between the numerical results of the Dysthe and the Zakharov models is observed in Fig. 8.19. These results, together with extensive comparison of the numerical simulations based on the Zakharov equation with wave tank experiments carried out in [65] that were presented in part in Sect. 8.5.1 demonstrated that the spatial Zakharov equation represents an adequate model to describe evolution of a nonlinear wave field along the tank. In the narrow spectrum case, results of Fig. 8.19 clearly demonstrate that the Dysthe model is sufficient to emulate appropriately the details of the wave field evolution.

Generation of narrow initial wave group envelopes (with correspondingly wide initial spectrum) represents not an easy task in a relatively short experimental wave tank, in part due to the presence of long waves in the spectrum. On the other hand, the validity of the spatial Zakharov model for wave groups with narrow initial spectra was confirmed by extensive experiments. Since this model is free of any restrictions on the spectral width, the numerical solutions based on the Zakharov equation can serve as a basis to determine the domain of applicability of the Dysthe model. Computations based on both those models were carried out for the initial conditions that violate the formal limitations on the spectral width inherent to the Dysthe model. Simulations were carried out for the carrier wave period and steepness as in Fig. 8.19 and three values of the coefficient m in Eq. (8.4), $m = 1.0, 0.6$ and 0.4. For $m = 1.0$, the effective relative spectral width given by Eq. (8.37) is 0.19, just below the value of ϵ. For $m = 0.6$, $\Delta\omega/\omega_0 = 0.31$, somewhat higher that the maximum wave steepness. Finally, for $m = 0.4$, the relative initial spectrum width attains an extremely high value of 0.47, exceeding the maximum possible steepness of propagating deep gravity waves. Variation of the surface elevation with time and the amplitude spectra are presented at three distances from the location of wave generation, at $x = 5$ m, $x = 10$ m and $x = 20$ m.

Results for the surface elevation variation with the distance for $m = 1.0$ are presented in Fig. 8.20. Strong dispersion leads to dramatic variation of the group shape, which is obvious in both computations. The resemblance between the results of both models seems to indicate that the Dysthe model remains adequate for these parameters even at relatively large distances [$x = 20$ m corresponds to more than 26 carrier wave lengths and to the dimensionless distance $X = 9.47$, see Eq. (8.7)]. Additional insight into the nonlinear physics of the wave group transformation along the tank is obtained by analyzing the amplitude spectra of the surface elevation. The spectra at the three selected locations are compared with the initial spectral Gaussian shape in Fig. 8.21. The similarity between the two simulations is impressive, excluding the low frequency range. The Dysthe model correctly represents the gradual narrowing of the high-frequency part of the spectrum with the distance, with the corresponding growth of the peak value.

For $m = 0.6$, the Dysthe-based simulated temporal variation of the surface elevation at different locations along the tank plotted in Fig. 8.22 still compare favorably with the Zakharov computations, although in this case the agreement becomes less impressive at a larger distance of 20 m. The groups retain their identity

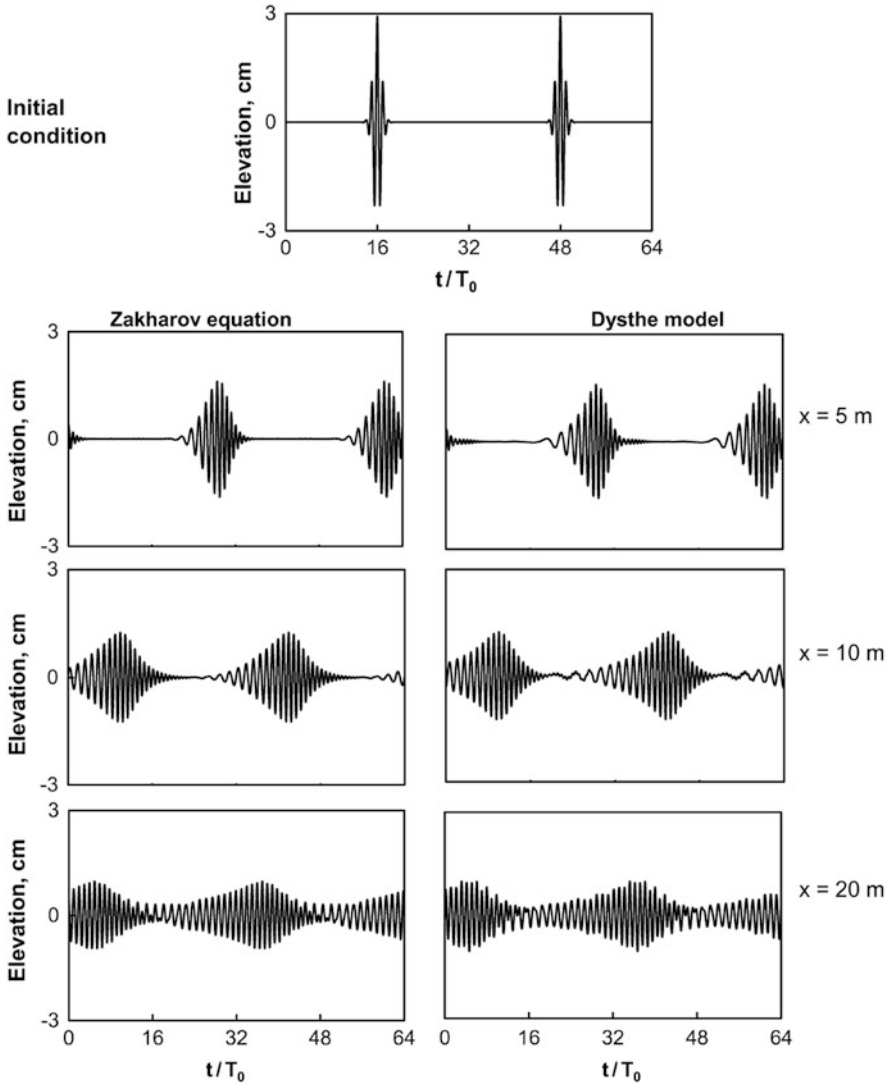

Fig. 8.20 Wave field evolution along the tank for carrier wave parameters as in Fig. 8.19 and $m = 1.0$

up to the distance of about $x = 10$ m; farther away the faster moving longer waves penetrate the slower moving shorter waves of the previous group.

The corresponding Dysthe-derived amplitude spectra, Fig. 8.23, retain definite similarity to those obtained using the Zakharov equation, especially at higher frequencies. As in Fig. 8.21, in both simulations the spectrum becomes narrower with the distance, although for $m = 0.6$ this effect is less pronounced than for $m = 1.0$. The rate of variation of the spectrum in Fig. 8.23 is quite fast at the first stages

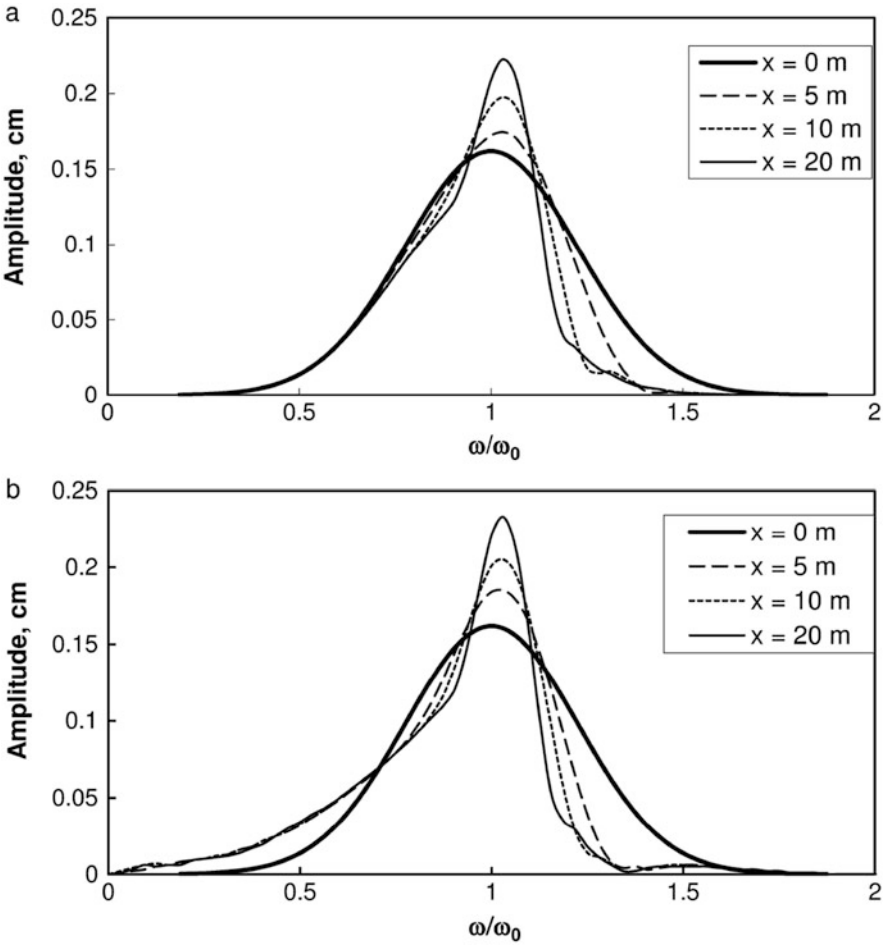

Fig. 8.21 Amplitude spectra of the surface elevation for carrier wave parameters as in Fig. 8.20; (**a**)—computed according to the Zakharov equation; (**b**) according to the Dysthe model

of evolution, but at larger distances the spectral shape remains nearly constant. This can be attributed to the spreading of the wave energy over the computational domain visible in Fig. 8.22, which results in gradual effective linearization of the problem with distance. At the lower end of the spectrum, however, the Dysthe model exhibits notable noise, in contrast to the smooth behavior of the spectrum obtained from the Zakharov equation at those frequencies.

When an even wider spectrum is considered, $m = 0.4$, the wave energy spreads quite fast, so that already at $x = 10$ m the consecutive groups become indistinguishable, Fig. 8.24. In this case, 70 free modes were considered in the solution of the Zakharov equation. Although the initial spectrum can by no means be considered as narrow, the temporal variation of the simulated using the Dysthe model surface

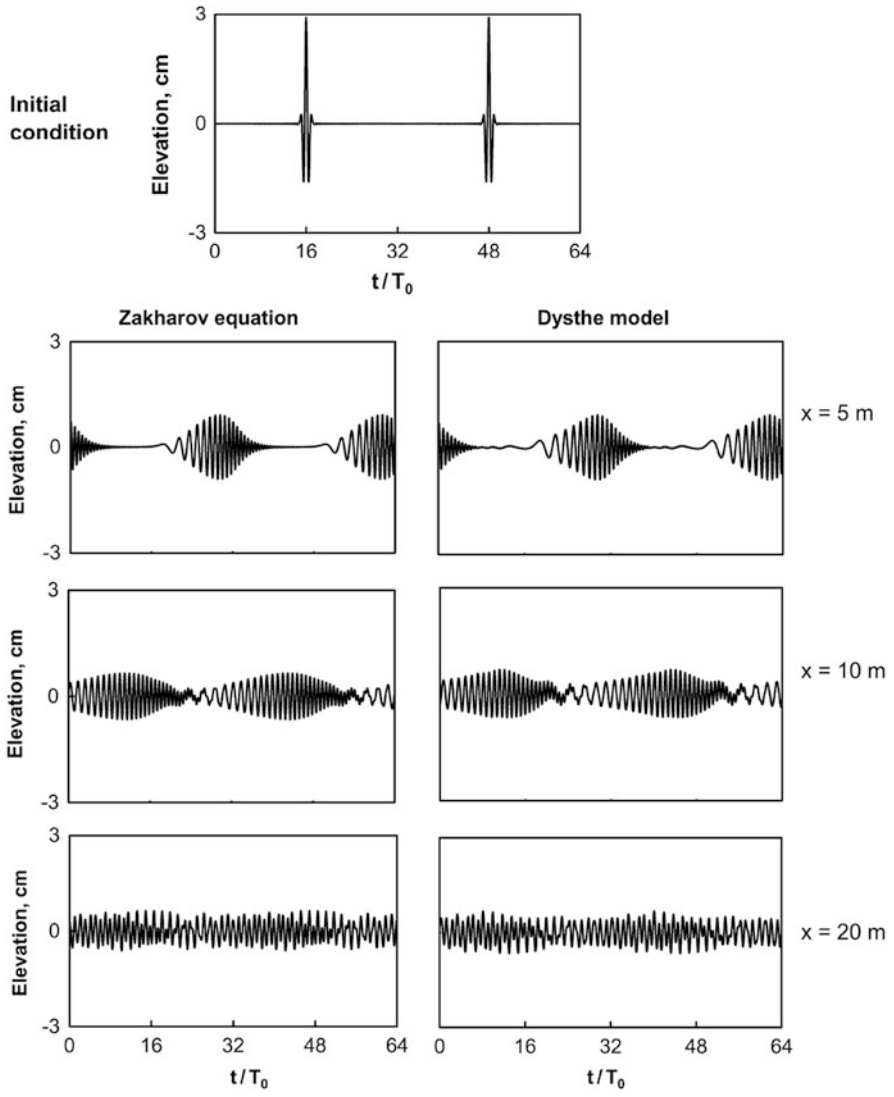

Fig. 8.22 As in Fig. 8.20 for $m = 0.6$

elevation up to the distance of about 10 m is similar to the results of the Zakharov equation. At larger distance, $x = 20$ m, quite a chaotic temporal variation of $\zeta(t)$ is obtained by the Dysthe model, qualitatively (but not quantitatively) similar to the solution at this location of the Zakharov equation.

Comparison of the corresponding amplitude spectra in Fig. 8.25 sheds additional light on the nonlinear wave transformation process. The solution of the Zakharov equation indicates that the energy spreading along the group is in this case even

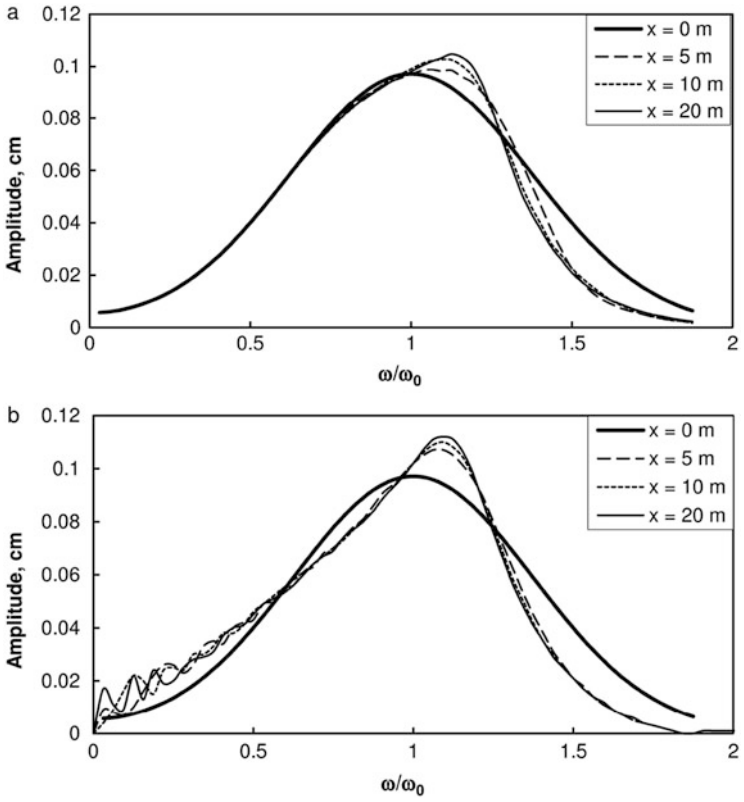

Fig. 8.23 As in Fig. 8.21 for $m = 0.6$

faster than that for $m = 0.6$, so that already at $x = 5\,\mathrm{m}$ the wave spectrum attain its finite shape and no energy transfer occurs anymore among various wave components. This final spectrum shape, however, for $\omega/\omega_0 > 0.8$ is notably different from the initial Gaussian spectrum; it is narrower and exhibits a wider peak. The performance of the Dysthe model cannot be considered as adequate. It still reflects relatively well the behavior of the higher-frequency part of the spectrum, but the shape of the spectrum at energy-containing frequencies is notably different from that obtained from the Zakharov equation. Moreover, the oscillations in the spectral amplitudes at the low-frequency end of the spectrum, which were already clearly visible in Fig. 8.23, become now much stronger, indicating that the Dysthe model fails for this wider initial spectrum.

Figures 8.19, 8.20, 8.21, 8.22, 8.23, 8.24, and 8.25 demonstrate that a better understanding of the complex problem of the nonlinear wave evolution can be achieved by analyzing both surface elevation history and amplitude spectra at various locations. The surface elevation plots make apparent the effects of dispersion, while the spectra clearly show the contribution of nonlinearity. For wider

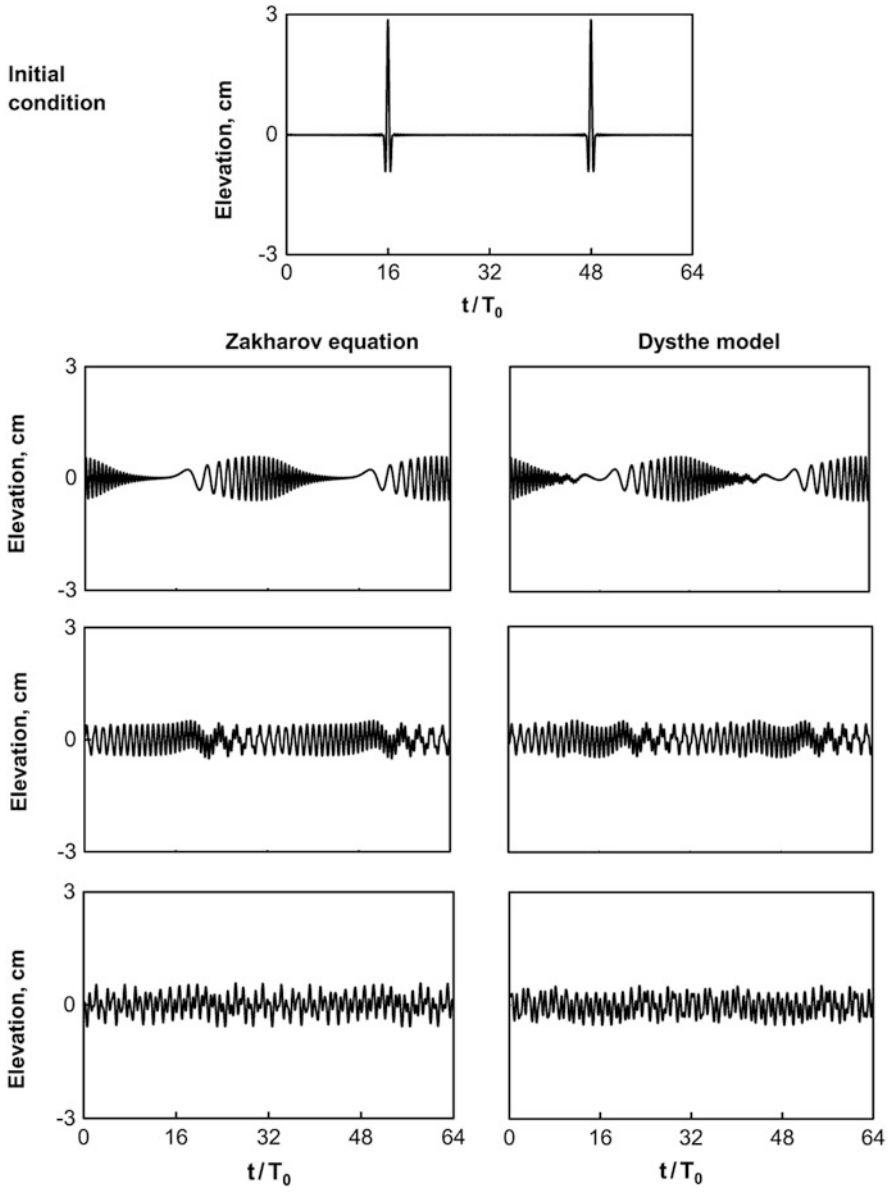

Fig. 8.24 As in Fig. 8.22 for $m = 0.4$

initial spectra the presented results demonstrate that in the course of the evolution process, the wave energy from the high-frequency part of the spectrum is shifted towards lower frequencies, changing substantially the spectral shape. The frequency of the peak in an initially wide spectrum, though, shows a trend towards higher

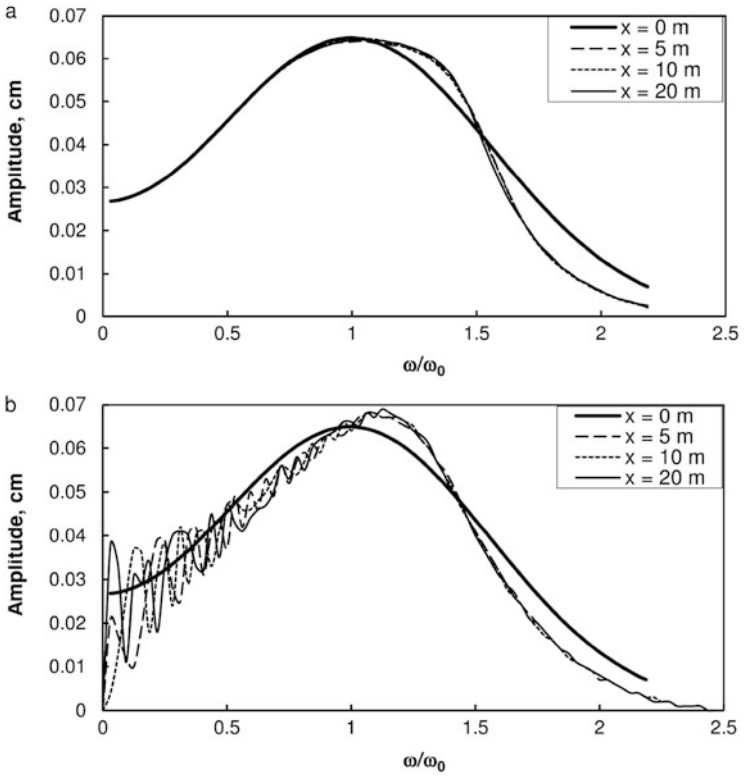

Fig. 8.25 As in Fig. 8.21 for $m = 0.4$

frequencies. No significant energy exchange is observed in the low-frequency range of the spectrum.

8.5.3 Nonlinear Focusing Based on the Spatial Zakharov Equation

Beyond the general interest in rogue waves, excitation of very steep waves in wave tanks enables experimental study of the wave damage potential and is thus of great importance. Generation of a single steep wave at a prescribed location in a laboratory wave tank of constant depth is also often required for model testing in coastal and ocean engineering. It is well known that such waves can be generated by focusing a large number of waves at a given location and instant. Dispersive properties of deep or intermediate-depth surface gravity waves can be utilized for this purpose. Since longer gravity waves propagate faster, a wave group generated at the wave maker in which wave length increases from front to tail may be designed

to focus the wave energy at a desired location. Such wave sequence can be seen as a group that is modulated both in amplitude and in frequency. In the frequency space, a single steep wave constitutes a superposition of a number of harmonics, each having a moderate steepness that can easily be generated by a wavemaker; these harmonics reach the prescribed location with identical phases, so that the amplitude of the resulting wave is a sum of amplitudes of all frequency components. Focusing is therefore more effective when the number of free wave harmonics initially generated at the wavemaker is large. Excitation of a single wave with extreme amplitude thus requires wide spectrum of the initial wave group generated at the wavemaker. Very steep (freak) wave therefore can be seen as a wave group with a very narrow envelope and correspondingly wide spectrum. Results of Sect. 8.5.2 demonstrate that the narrow-banded Dysthe model is not suitable for wider spectra. It is thus natural to apply the spatial Zakharov equation given by Eqs. (8.33)–(8.35) for this problem.

The goal of the study carried out by Shemer et al. [67] was to generate a single steep wave at a prescribed focusing location x_f in the tank. The wave is presented by a wave group given by (8.4) with the width parameter $m = 0.6$, see the upper panel in Fig. 8.22. In order to compute the wavemaker driving signal required to obtain the desired wave group shape at the distance x_f from the wavemaker, the spectrum corresponding to Eq. (8.4) plotted in Fig. 8.23 is integrated from x_f backwards up to the wavemaker at $x = 0$. Due to an essentially nonlinear character of the steep waves studied, see also [7], the resulting spectrum at the wavemaker is notably different from the Gaussian shape at the focusing location x_f. Experiments on nonlinear focusing were carried out in both facilities described in Sect. 8.2: in the large wave tank in Hanover, GWK, and in TAU. These experimental facilities differ in size by an order of magnitude.

The experiments in GWK were carried out for two carrier wave periods, $T_0 = 2.8\,\mathrm{s}$ (carrier wave length $\lambda_0 = 12.1\,\mathrm{m}$) and $T_0 = 4.34\,\mathrm{s}$ (carrier wave length $\lambda_0 = 25.0\,\mathrm{m}$), corresponding to dimensionless depths of $k_0h = 2.59$ and $k_0h = 1.26$, respectively. For the shorter carrier wave length, the deep-water dispersion relation is satisfied approximately, whereas for the longer carrier wave, water at wave number corresponding to $\lambda_0 = 25\,\mathrm{m}$ cannot be considered deep. Even for $\lambda_0 = 12.1\,\mathrm{m}$, since wide-spectrum wave groups were considered, intermediate-depth waves were present. Therefore, in all expressions finite-depth version of the interaction coefficients were used. The focusing location, x_f, in the GWK experiments was located at the dimensionless distance x_f/λ_0 of about 10 carrier wave lengths from the wavemaker for $\lambda_0 = 12.1\,\mathrm{m}$, and at half that distance in terms of the wave lengths for $\lambda_0 = 25.0\,\mathrm{m}$.

The designed temporal variation of the surface elevation at the wavemaker $\zeta_{des} = \zeta(x,t)$ was computed by backward integration of (8.33) from the focusing location to $x = 0$. For each carrier wave period T_0 and focusing location x_f, the solution of the system of N ODEs, N being the total number of wave harmonics considered, was obtained for distances ranging from the wavemaker location at $x = 0$ up to x_f and beyond. The number of free wave harmonics N considered in those computations was in the range from 56 to 76. The wavemaker driving signal was

then calculated from ζ_{des} employing the wavemaker transfer function. This function relates the amplitudes and phases of the harmonic wavemaker displacement at a given frequency to the corresponding parameters of the propagating monochromatic wave. For a given wavemaker shape, i.e. piston or paddle, this function can be found using the linear wavemaker theory (see, e.g. [9]). It is well known, however, that for finite amplitude waves significant nonlinear effects may become important (see, e.g. [12]). The complex wavemaker transfer function for a given experimental facility is therefore found empirically by performing a series of experiments on excitation of monochromatic waves. Generation of water gravity waves by a wavemaker is, however, an essentially nonlinear process [53]. To account for the nonlinearity of wave generation, an experimental procedure was applied, in which the wavemaker driving signal was adjusted iteratively to obtain the desired wave train shape at a prescribed location away from the wavemaker, thus eliminating effect of evanescent modes. The details of this iterative procedure were presented in [67]. In GWK, adjustment was carried out at $x = 52.2$ m.

Evolution of the wave group shape along the tank is illustrated in Fig. 8.26. The solid line shows the variation of the surface elevation computed by backward integration of Eq. (8.33) starting from the prescribed Gaussian shape given by Eq. (8.4) at the focusing location, with the carrier wave period $T_0 = 2.8$ s (frequency $f_0 = 0.357$ Hz) and steepness $\zeta_0 k_0 = 0.3$. Computations are carried out for $N = 76$ harmonics, corresponding to frequencies in the range $0.039\,\text{Hz} \le f \le 0.76\,\text{Hz}$. The system of 76 ODEs was solved using the Runge-Kutta procedure with integration step of 5 cm. Test of the integration procedure with the halved integration step of 2.5 cm demonstrated that the solution remains insensitive to step size variation. Surface elevation variation is shown at this figure also for the wavemaker location (actually, the wave gauge is attached at the distance of 5 cm from the piston surface), and for the location of the wavemaker driving signal adjustment $x = 52.2$ m. The results of measurements by the corresponding wave gauges are plotted as well. Note that as the time reference from here on in this subsection is the instant of the initiation of the wavemaker motion.

The agreement between the water elevation measurements and the corresponding computations in Fig. 8.26a is quite good even though only free wave components are accounted for in the computations. The selected value of $m = 0.6$ in (8.4) yields indeed a narrow wave group with a single steep wave at the focusing location. The period of waves within the group at the wavemaker gradually increases, resulting in a quite complicated envelope shape, in contrast to the symmetric Gaussian shape at the focusing. This group envelope shape is also reproduced well in the numerical simulations. This agreement is particularly good at the adjustment location $x = 52.2$ m. The maximum wave crest height above the mean water level that is about 0.2 m at the wavemaker increases to more than 0.6 m at the focusing location. The agreement of experiments and computations is less impressive at the wavemaker, most probably due to effect of the evanescent modes. The measured crest height at the focusing location is notably higher than the computed value. Disagreement between experiments and computations also manifests itself in some asymmetry of

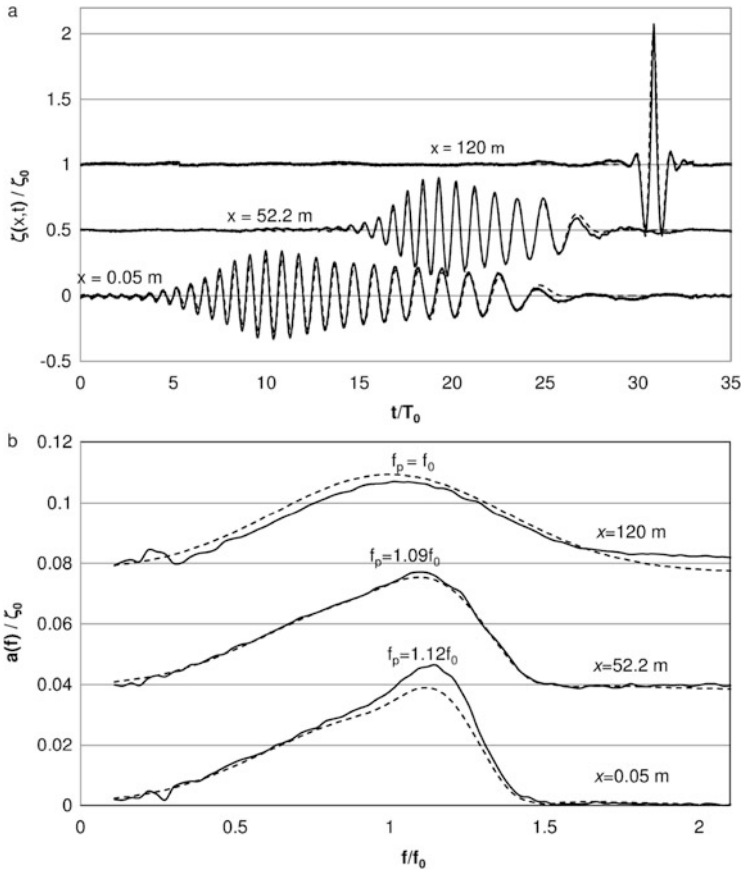

Fig. 8.26 Evolution of the wave group along the GWK for $T_0 = 2.8$ s and $\epsilon = 0.3$: (**a**) temporal variation of the surface elevation at various locations along the tank; (**b**) the corresponding amplitude spectra and the peak frequencies. *Solid lines*—experiment; *broken lines*—computations. Records have been shifted vertically for better visibility

troughs at $x = 120$ m, as well as in the presence of long waves that are clearly seen in the wave gauge output.

Focusing is sometimes attempted by constructive interference of linear propagating dispersive waves. To asses the accuracy of this approach in view of the effects of nonlinearity, comparison of the computed and the measured amplitude spectra of the surface elevation at the same locations is carried out in Fig. 8.26b. As in previous sections, the discrete spectra are plotted by continuous lines for convenience due to the large number of frequency harmonics f_i considered. The frequency resolution is determined by the decrement $\Delta f = 1/\tau$, where τ is the measurement duration of experiments or computations. The dimensional discrete amplitudes $a_i = a(f_i)$ are normalized by the maximum designed amplitude at the focusing location, ζ_0. The

essential nonlinearity of the evolution process manifests itself in significant change of shape along the tank of both measured and computed spectra. The peak frequency is shifted to a lower value, and the whole spectrum widens as the group moves along the tank. Note that the modification of the spectrum between $x = 0.05$ m and $x = 52.2$ m is relatively minor, indicating that as long as the maximum wave height within the group remains small, the nonlinear interactions are weak and the variation of the group shape results mainly from the linear dispersion. Nonlinearity becomes dominant as the maximum wave height increases with approach to the focusing location, and the spectrum at $x = 120$ m is very different from those measured for a wider group closer to the wavemaker.

As in Fig. 8.26a, the agreement between the computed and the measured spectra is the best, although not perfect, for the adjustment location of $x = 52.2$ m. The measured amplitudes at the wavemaker are considerably higher than the computed ones, especially in the vicinity of the peak frequency. This disagreement can be attributed to the appearance of evanescent modes, as well as to local nonlinear effects related to finite wavemaker stroke. Most interesting, however, is the difference between experiments and computations at the focusing location that is visible practically at all frequencies. The ratio between the measured spectral amplitudes and the numerically obtained ones is particularly large at frequencies exceeding about 0.6 Hz. To account for this discrepancy, the contribution of the second order bound waves as defined by Eq. (8.36) was computed. The detailed analysis of the bound wave contribution carried out in [67] demonstrates that their relative contribution increases as the focusing location is approached and that accounting for their contribution significantly decreases the deviation of the computational results from the measurements.

The difference between computations and measurements gradually grows as the wave group propagates along the tank. Moreover, this difference appears to increase with frequency. These results suggest that dissipation, albeit weak, cannot be totally neglected in the numerical simulations. Since the dissipation in the boundary layers at the tank walls and bottom is relatively weak, it is sufficient to account for the wave energy loss along the tank by adding an additional linear term to the governing equation, as suggested for gravity-capillary waves in [58]. The spatial Zakharov equation (8.33) that accounts for dissipation along the tank can thus be written as

$$i\frac{dB_j(x)}{dx} = \sum_{\omega_j+\omega_l=\omega_m+\omega_n} \alpha_{j,l,m,n} B_l^* B_m B_n e^{-i(k_j+k_l-k_m-k_n)x} - i\gamma B_j(x). \tag{8.38}$$

The complex spatial dissipation rate coefficient γ for a wave of an arbitrary frequency ω in a channel of width w and depth h that accounts for the Stokes layer at the side walls and the bottom of the tank was given in [25]:

$$\gamma = \frac{k}{\omega\sqrt{\omega/\nu}} \frac{2(sinh2kh + kw)}{sinh2kh + 2kh} exp(-i\frac{\pi}{4}). \tag{8.39}$$

Application of Eq. (8.39) yields for the present experimental conditions the following values of the viscous dissipation coefficient: $\gamma = 1.34 \cdot 10^{-4} e^{-i\pi/4}$ 1/m for the carrier wave period $T_0 = 2.8$ s, and $1.50 \cdot 10^{-5} e^{-i\pi/4}$ 1/m for $T_0 = 4.34$ s. The expected decay of amplitude at the carrier wave period T_0 for the distance of 120 m is about 1.6 % for the shorter wave and about 0.9 % for the longer wave. Viscous dissipation becomes thus noticeable only for the high frequency part of the spectrum.

The results presented in Fig. 8.26, as well as additional extensive results obtained in the GWK experiments and reported in [67] demonstrate that computations of the wave field evolution with wide spectrum based on the adopted version of the spatial Zakharov equation provide good agreement with the measurement results, although some quantitative differences between experiments and computations exist. These differences were attributed mainly to the limited ability to reproduce by a wavemaker the required wave train shape in a large facility. Based on the extensive experience gained in running experiments in the GWK and processing the results, additional series of measurements was carried out in a much smaller TAU wave tank, where many drawbacks of the GWK experiments could be eliminated.

The designed wave group shape at the focusing location in TAU facility was identical to that in the Hanover experiments. The maximum wave steepness in the experiments ranged from 0.1 to 0.4, most runs were performed for $\zeta_0 k_0 = 0.3$. A number of carrier wave periods T_0 was employed. Some experiments were performed for identical dimensionless water depth $k_0 h$ in both facilities. The values of $k_0 h$ of 2.6 and 1.26 used in Hanover yield for the TAU tank depth of 0.6 m carrier wave lengths of 1.45 m and 2.99 m, respectively. The shortest carrier wave period employed in these experiments was $T_0 = 0.6$ s ($\lambda_0 = 0.56$ m, $k_o h = 6.71$), so that the deep water conditions were approximately satisfied even for the low frequency part of the spectrum. Experiments with shorter waves in a tank of a given length allow longer dimensionless (in carrier wave lengths λ_0) evolution distances, resulting in a considerable modification of the wave group shape and of the spectrum. These conditions, though, make it difficult to reproduce by the wavemaker motion the computed complex waveform that is supposed to serve as the initial condition due to small wave heights at the wavemaker.

Viscous dissipation along the tank was accounted for in computations of the required surface elevation at the TAU tank wavemaker, see Eq. (8.38). The iterative driving signal adjustment was performed by comparing the computed and the measured signal at the distance of 1 m from the wavemaker.

Representative experimental results are given in Figs. 8.27 and 8.28 and compared with those obtained numerically. The computational results presented in those figures include also the contribution of the second order bound waves. In each figure, the variations of the surface elevation and of the amplitude spectra along the wave tank are plotted at four locations. The selected locations include the adjustment point at the distance of $x = 1$ m from the wavemaker, the focusing location, as well as two additional positions, one before and one after the focusing. Results are given for two extreme values of the carrier wave period used in TAU experiments: in Fig. 8.27 $T_0 = 0.6$ s (carrier wave length 0.562 m, corresponding to dimensionless depth

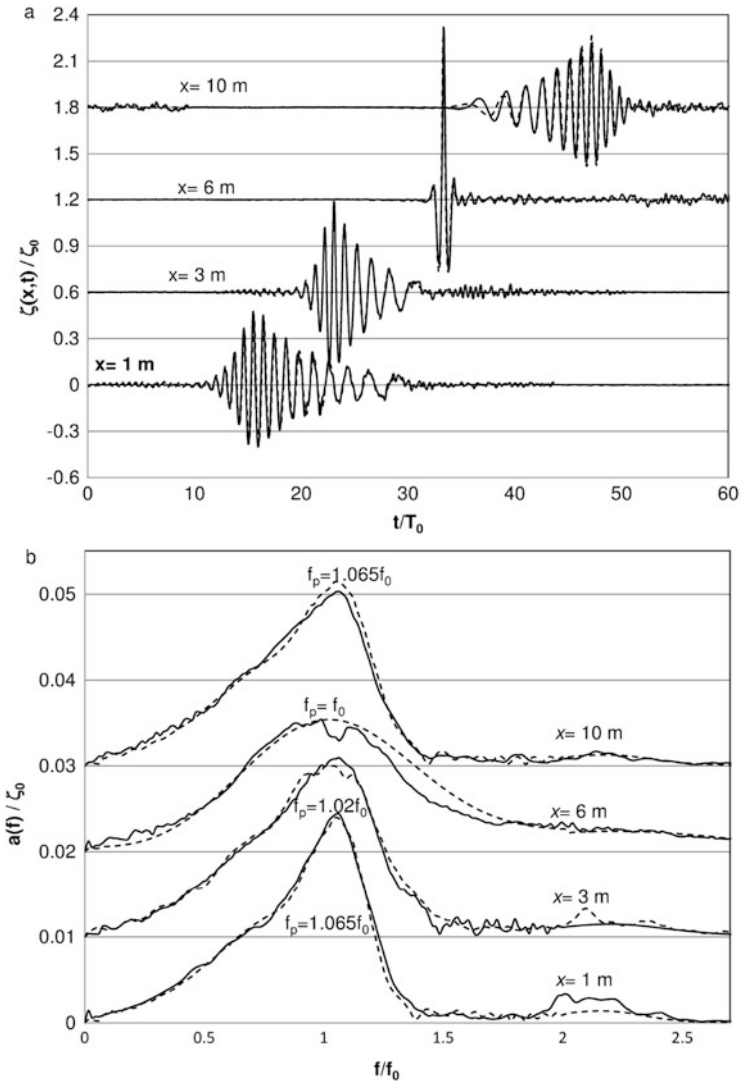

Fig. 8.27 Evolution of the wave group along the GWK for $T_0 = 0.6\,\mathrm{s}$ and $\epsilon = 0.35$. (**a**) temporal variation of the surface elevation at various locations along the tank; (**b**) the corresponding amplitude spectra and the peak frequencies. *Solid lines* - experiment; *broken lines* - computations. Records have been shifted vertically for better visibility. Computations account for the second order bound waves

$k_0h = 6.71$), and in Fig. 8.28 $T_0 = 0.97\,\mathrm{s}$ (carrier wave length 1.45 m, $k_0h = 2.60$, identical to that in the GWK experiments for $T_0 = 2.8\,\mathrm{s}$). In both figures the driving amplitudes considered are selected so that at the focusing location, the resulting wave is quite steep, with the maximum wave amplitudes ζ_0 corresponding to the steepness $\epsilon = k_0\zeta_0 = 0.35$ in Fig. 8.27 and to $\epsilon = k_0\zeta_0 = 0.3$ in Fig. 8.28.

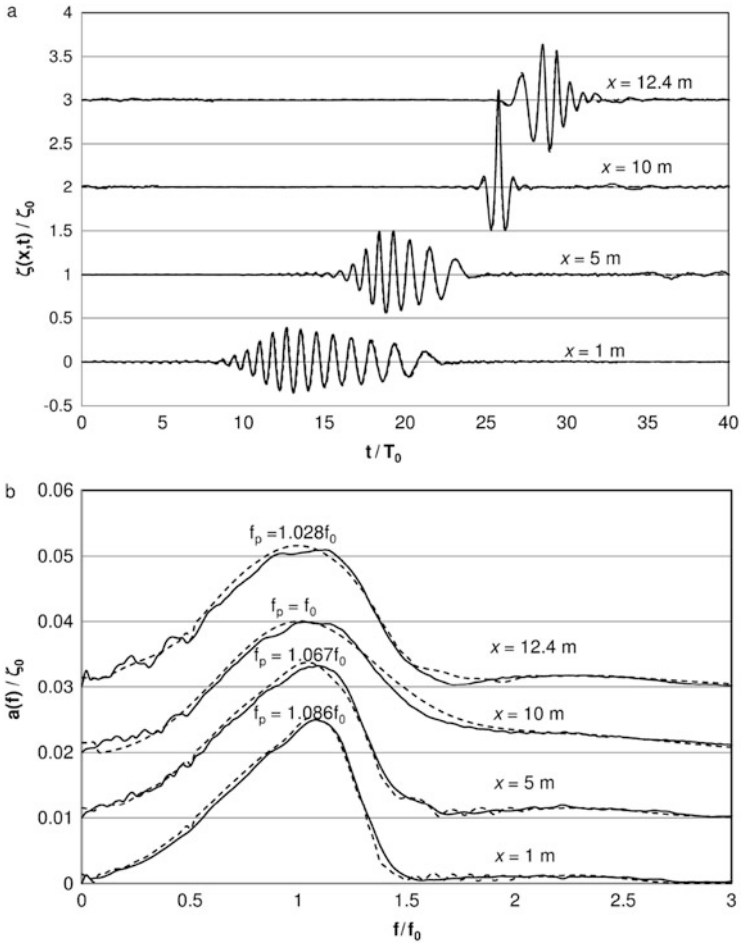

Fig. 8.28 Evolution of the wave group along the GWK for $T_0 = 0.97$s and $\epsilon = 0$. (**a**) temporal variation of the surface elevation at various locations along the tank; (**b**) the corresponding amplitude spectra and the peak frequencies. *Solid lines* - experiment; *broken lines* - computations. Records have been shifted vertically for better visibility. Computations account for the second order bound waves

Focusing location as far as possible from the wavemaker ensures longer evolution domain but requires lower wave heights at the wavemaker. In view of difficulties in faithful reproduction of group shapes with very low wave heights, the focusing distance of 6 m was selected in Fig. 8.27, relatively short compared to the tank length, and constitutes about 10.7 carrier wave lengths λ_0. To improve the accuracy of results, the maximum wave steepness in this case is also chosen to be somewhat higher than that for longer carrier waves. In computations, 131 frequency harmonics were considered, covering free wave frequency range of $0.125\,\text{Hz} \leq f \leq 3.375\,\text{Hz}$.

For a longer wave in Fig. 8.28 with $T_0 = 0.97$ s (106 free harmonics, 0.1 Hz $\leq f \leq$ 2.2 Hz), focusing is designed to occur at a larger distance from the wavemaker, $x = 10$ m. Note, however, that in terms of the carrier wave lengths those focusing distances of $6.9\lambda_0$ is shorter than in Fig. 8.27.

A very good agreement between the computed superposition of the free and the second order bound waves and the measurements is obtained for the variation of the wave group shape along the tank. Similarly good agreement is observed in all amplitude spectra in Figs. 8.27b and 8.28b for each one of the spectral harmonic. Modulation of the amplitude and of the frequency within the group is clearly seen in Figs. 8.27a and 8.28a at $x = 1$ m; the maximum wave amplitude within the group then increases towards the focusing location. At the focusing, a single steep wave with height very close to the designed value is obtained in all cases. Close to the wavemaker, the envelope of the wave group with the shortest carrier wave in Fig. 8.27a is more asymmetric than in the other case. The amplitude spectra allow estimation of variation of contribution of each harmonic in the course of the evolution. The spectral shape variation in both Figs. 8.27b and 8.28b is quite similar, indicating that the variation of dimensionless depth does not affect the evolution pattern strongly. The spectrum has the maximum width at the focusing location, while close to the wavemaker it is somewhat narrower. The peak frequency drifts in the course of the evolution process. The minimum value of the peak frequency, corresponding to that of the carrier wave, is obtained at the focusing location. The upward shift of the peak frequency from the carrier wave value increases with the distance from the focusing location. The full symmetry of the spectral shapes at equal distances from the focusing is violated by the viscous dissipation; this effect is more visible for free harmonics at higher frequencies.

Results on evolution of wave groups with wide spectra presented above were obtained in two wave tanks that differ in size considerably. In spite of that, the evolution patterns observed in the experiments and obtained in the numerical simulations are quite similar in both facilities. Those patterns are determined by combination of linear and nonlinear contributions. The effects of nonlinearity are governed by the maximum wave steepness at the focusing location, $\epsilon = \zeta_0 k_0$. The values of ϵ in experiments and computations in both facilities were very close, and the results presented above are mostly for high values of the maximum steepness of about $\epsilon = 0.3$. Nonlinear effects are readily identified in the variation of the spectral shapes that would remain constant if nonlinearity were negligible. Results of Figs. 8.26b–8.28b demonstrate that the variations of the spectral shape with the distance from the wavemaker obtained in both facilities were essential.

Evolution of the wave group shape along the tank, while being dependent on nonlinearity, is strongly affected by linear effects. The dominant linear effect in the evolution process is the dispersion that for gravity waves depends on the dimensionless water depth, $k_0 h$. The dimensionless water depth was in the range of $2.6 \leq k_h \leq 6.7$ for the TAU tank, and had the values of $k_0 h = 2.6$ and $k_0 h = 1.26$ in the GWK experiments. For the majority of cases carrier waves can be seen thus as propagating over deep water. It should be reiterated, however, that since wave groups with wide spectra were considered, the free wave spectrum always contained

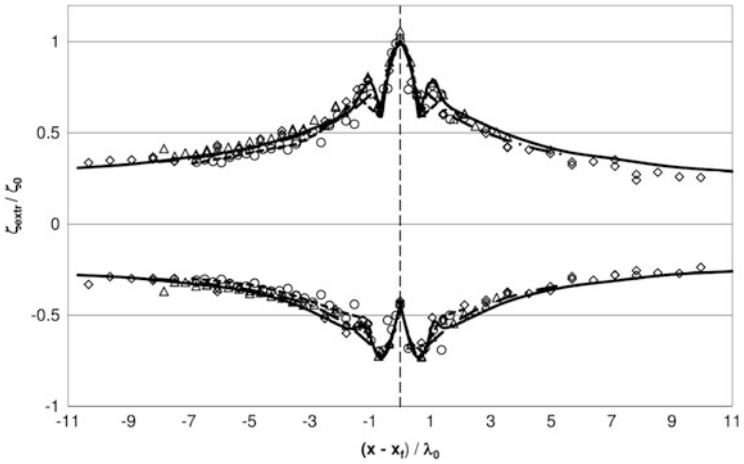

Fig. 8.29 Extreme values of crest and trough deviations from the undisturbed water level in the TAU tank: experiments vs. computations for $\epsilon = 0.3$. *Diamonds*—$T_0 = 0.6$ s; *triangles*—$T_0 = 0.85$ s; *circles*—$T_0 = 0.97$ s

also harmonics corresponding to quite long and thus weakly dispersive waves. Good agreement between experiments and computations in all cases demonstrated in the previous sections indicates that the spatial evolution model based on the Zakharov equation performs adequately for intermediate-depth wave as well.

The focusing process along the tank can be followed in greater detail if the highest wave crest attained at a given location during the passage of the group is plotted against the distance from the wavemaker. The resulting curve can be seen as the boundary of the wetted surface left by the propagating wave group at the tank side wall. Similarly, the variation along the tank of the deepest trough can also be plotted. In order to compare quantitatively the focusing processes for different experimental conditions and in the two facilities, appropriate normalization is required. The propagation distance in each experiment is thus measured relative to the designed focusing location and normalized by the corresponding carrier wave length λ_0. The maximum wave crest height above the undisturbed level at the focusing location serves as the normalizing factor for both crest and trough elevations. The computed values that include the contribution of the second order bound waves are used for normalization.

The normalized extreme values of wave crest and trough obtained experimentally in the TAU tank at the maximum designed wave steepness of $\epsilon = 0.3$ for three values of the carrier wave period, $T_0 = 0.6$ s, $T_0 = 0.85$ s and $T_0 = 0.97$ s, are presented in Fig. 8.29. The corresponding computed quantities are also shown. Good agreement between computations and experiments is obtained for all frequencies. For all cases, the maximum elevation at the focusing is increased by a factor of about 3 relative to that at the wavemaker, whereas the increase in the through depth is smaller. The rate of decrease of the maximum elevation declines with the distance

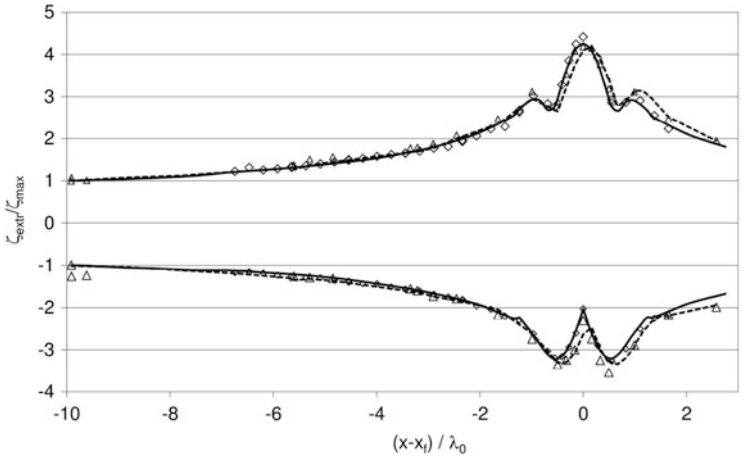

Fig. 8.30 Comparison of evolution of normalized extreme elevations along both tanks for $k_0h = 2.6$ and $\epsilon = 0.2$. *Solid line* and *diamonds*—free and bound waves computations for $T_0 = 0.6$ in TAU tank; *broken line* and *triangles*—the same for $T_0 = 2.8$ s in GWK

from the focusing location. For identical nonlinear parameters and the scaled by f_0 free wave spectra at the focusing location, the shapes of all curves relative to focusing should also be identical, provided effects related to water depth are negligible. At distances exceeding about $5\lambda_0$ from the focusing, the rate of decrease of the maximum surface elevation becomes quite slow. All curves in Fig. 8.29 have common salient feature: the variation of the extreme surface elevation with x in the vicinity of the focusing location is quite complicated, as a result of interplay of the phases of various harmonics as they approach the same value at the focusing. Note also that at focusing, the maximum trough depth has a local minimum. Hence, the maximum wave height, defined as the difference between the extreme values of the surface elevation at crest and trough, does not attain its maximum value at the focusing location, but rather is shifted and exhibits two maxima at both sides of the focusing. The slight dissimilarity in shapes of curves may be attributed to depth effects.

Closer investigation of the similarity between the shapes is carried out in Fig. 8.30, where comparison is carried out between evolution of normalized extreme elevation along both tanks at identical values of dimensionless depth $k_0h = 2.6$. Computations corresponding to the GWK experiments are performed using the measured complex wave spectrum at the wavemaker adjustment location as the initial condition. To demonstrate that the wave group evolution pattern does not vary notably with forcing amplitude, the results in this figure are presented for a somewhat weaker forcing with $\epsilon = 0.2$. To enable comparison, the numerical solution corresponding to TAU conditions was extended beyond the actual wavemaker location to the dimensional distance of $(x - x_f)/\lambda_0 = -9.91$, as in the GWK experiments. The dependencies of both maximum and minimum elevation for both

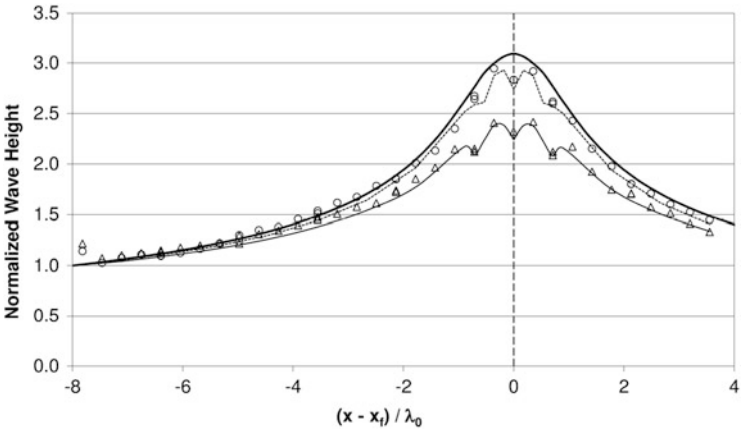

Fig. 8.31 The effect of nonlinearity on the variation along the tank of the maximum wave height normalized by its value at the wavemaker in TAU for $T_0 = 0.85$ s. *Thick solid line*—linear solution of Eqs. (8.28)–(8.30); *circles* (experiments) and *broken line* (computation)—$\epsilon = 0.2$; *thin solid line* and *triangles*—$\epsilon = 0.3$

facilities in Fig. 8.30 collapse on the same curves. The minor differences can be attributed to several factors. First, the effect of dissipation is more pronounced in the TAU tank, as discussed in greater detail in [67]. Dissipation affects not just the amplitudes but also the phases of each harmonic. In addition, the adjustment of the wavemaker driving signal in the GWK experiments was less accurate as specified in above. Figure 8.30 also confirms the conclusion from Fig. 8.29 that the effect of focusing is mainly restricted to the last five carrier wave lengths before the focusing point. At larger distances, the extreme values of the surface elevation do not change significantly.

The effect of nonlinearity on the focusing process in both facilities is studied in Fig. 8.31 for two values of the nonlinearity parameter, $\epsilon = 0.2$ and $\epsilon = 0.3$. As a reference condition for the assessment of the role of finite wave height on the focusing process, the solution of the linearized NLS equation for the evolution of wave group with the shape given by (8.4) can be invoked, see Eqs. (8.28)–(8.30). The variation of the maximum wave heights within the group normalized by the maximum computed wave height at the wavemaker, with the normalized by λ_0 distance from the focusing location, is shown in Fig. 8.31 for the carrier wave period $T_0 = 0.85$ s in the TAU tank. The effectiveness of focusing apparently decreases with increase in wave steepness. For the dimensionless focusing distance of about eight carrier wave lengths, the relative increase in the maximum wave height is still close to the linear value of 3 for $\epsilon = 0.2$, and remains below 2.5 for $\epsilon = 0.3$. These values were obtained when contribution of the second order bound waves were accounted for in the finite amplitude cases. In spite of the significant contribution of the bound waves to the maximum crest height for finite wave amplitudes, the relative effectiveness of focusing is higher in the linear case. Note also that the spatial

variation of the maximum wave height obtained from the linear solution is smooth also around the focusing location, in contrast to the behavior of the computed and experimental results for finite amplitudes.

8.6 Statistics of Nonlinear Unidirectional Water Waves

Sections 8.3–8.5 describe evolution of unidirectional deterministic waves along wave tanks. As stressed in the Introduction, nonlinear ocean waves, however, are stochastic in nature. Theoretical investigations aimed at describing the statistical properties of nonlinear wave fields were originated by Longuet-Higgins [33] who showed that for a narrow-banded wave field with random phases, wave heights satisfy the Rayleigh distribution. An improved model that takes into account nonlinear effects has been suggested later [34]. More recently, numerous models appropriate to unidirectional wave fields were proposed, see [43, 77–79] and additional references therein. The probability of appearance of very high rogue waves attracts particular attention. The relatively high occurrence of those waves that may exceed the predictions based on the Rayleigh distribution suggests that the occurrence of freak waves is related to nonlinearity of the wave field. Determination of freak waves' probability for a given sea state is important practically and requires in depth study using the most advanced theoretical approaches and laboratory experiments.

The effect of directional spreading on the statistics of random waves was also considered in a number of numerical and experimental studies [48, 72, 83]. Measurements of the evolution of unidirectional random wave fields have been performed in very large experimental installations [45, 46, 48, 72]. The present section summarizes the results of experimental and numerical investigations of the evolution of a random wave field in a large wave tank presented in [62, 68, 69]. In these studies variation along the tank of various statistical properties of the wave field is investigated for a range of parameters in view of their relevance to appearance of freak waves. The effects of nonlinearity and of spectral shape were investigated. The experiments were carried out in the Large Wave Channel (GWK) in Hanover. Spatial evolution of numerous realizations of a wave field that have identical initial frequency power spectra for the free wave components and random phases in each realization was studied.

The dimensionless spectral width ν is of a random wave field is defined as

$$\nu = \sqrt{(m_0 m_2/m_1^2) - 1}, \tag{8.40}$$

where the jth spectral moment of the power spectrum $S(\omega)$ is

$$m_j = \int_{\omega_{min}}^{\omega_{max}} \omega^j S(\omega) d\omega. \tag{8.41}$$

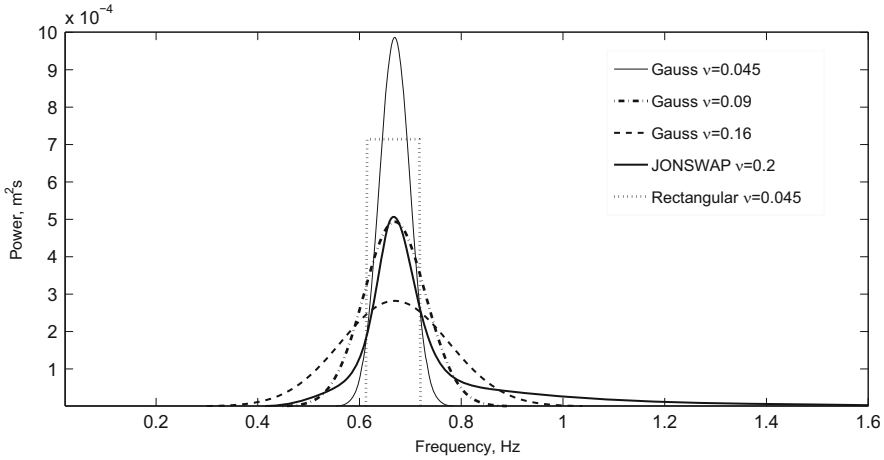

Fig. 8.32 Initial spectral shapes of the surface elevation

In (8.41), the integration is carried out over the free waves' frequency domain only. The following initial free wave spectral shapes were considered: (a) a narrow Gaussian spectrum corresponding to (8.4) as in Sects. 8.3–8.5, with $m = 3.5$ resulting in $\nu = 0.045$; (b) rectangular spectrum with $f_{max,min} = f_0 \pm 0.047$ Hz; $\nu = 0.045$; (c) an intermediate width Gaussian spectrum with $\nu = 0.09$; (d) a wide Gaussian spectrum with $\nu = 0.16$; (e) JONSWAP spectrum, see e.g. Goda [13]:

$$S(f) = Af^{-5} exp\left[-1.25(T_0 f)^{-4}\right] \gamma^{exp\left[-(T_0 f-1)^2/2\mu^2\right]}. \tag{8.42}$$

In (8.42), A is an adjustable amplitude parameter, the peak enhancement parameter $\gamma = 7$; $\mu = 0.07$ for $f \leq f_0$; $\mu = 0.09$ for $f > f_0$. These parameters yield the dimensionless width $\nu = 0.20$. The initial spectral shapes are plotted in Fig. 8.32.

To follow variation of the wave field over distances containing as many dominant wave lengths λ_0 as possible, the shortest possible carrier wave period $T_0 = 1.5$ s was selected based on the frequency response of the hydraulically-driven GWK wavemaker. The corresponding wave length $\lambda_0 = 3.51$ m and the dimensionless water depth $k_0 h = 8.95 \gg 1$. For each initial shape of the spectrum, the selected duration of the basic unit of the wavemaker driving signal was 81.92 s, corresponding to 4096 data points at the wavemaker driver frequency of 50 Hz and the spectral resolution of the driving signal of 1/81.92 Hz. In every realization of a given spectrum this basic unit was repeated twice. The measured in the vicinity of the wavemaker spectral amplitudes of each harmonic do not remain fully deterministic due to nonlinear response of the water-wave field to the non-monochromatic wavemaker motion; each of them varies in different realizations of the spectrum around the prescribed value. For random waves, the nonlinearity

parameter ϵ can be defined as $\epsilon = k_0\sigma$, where the $\sigma = m_0^{1/2}$ is the r.m.s. value of the surface elevation. It is customary to characterize waves by the significant wave heights $H_{1/3}$ representing the average trough-to-crest height of 1/3 highest waves in each record [13]. For linear narrow-band waves with Rayleigh-distributed amplitudes, the values of $H_{1/3}$ and σ are related by $H_{1/3} = 4/004\sigma$.

Higher values of ϵ result in more prominent manifestation of the nonlinear effects along the tank. In visual observation of the wave field during initial runs performed with $\epsilon = 0.065$ [62] for the narrow Gaussian spectral shape, $\nu = 0.045$, occasional wave breaking within the tank was observed. Since wave breaking is not accounted for in the deterministic models of wave field evolution, it was decided to run most experiments for $\epsilon = 0.054$. The effect of nonlinearity on the wave field evolution for the narrow spectrum was studied in [62] by carrying out some experimental runs for $\epsilon = 0.043$ and $\epsilon = 0.065$. Additional details of the experimental procedure can be found in [62, 69].

The spatial evolution of the initially narrow Gaussian spectrum with $\epsilon = 0.054$ is shown in Fig. 8.33. In the initial stages of evolution shown in the top panel, the spectral density widens around the carrier wave frequency $f_0 = 0.67$ Hz up to the distance x of about 100 m, or $30\lambda_0$. This spectrum widening is more pronounced at the high-frequency side. At the subsequent stages of the spatial evolution, presented in the bottom panel, the spectrum tends to its initial shape at a distance of about 200 m or $60\lambda_0$ from the wavemaker. The patterns of spatial evolution of the spectra at both lower, $\epsilon = 0.043$ and higher, $\epsilon = 0.065$, initial forcing amplitudes are similar, and also exhibit the effect of quasi-recurrence.

The measured evolution along the tank of the wave spectra with different initial spectral shapes is studied in Fig. 8.34. For all initial spectra considered, the results are shown at four locations along the tank, up to $x = 240$ m where the most distant wave gauge was located. For all cases presented, the peak frequency does not change notably along the tank. Considerable variation of the spectral shape with the distance x from the wavemaker is obtained mainly for the initially rectangular narrow spectrum in Fig. 8.34a. This spectrum does not retain its rectangular shape; similarly to the pattern observed in Fig. 8.33, the spectrum becomes substantially wider at $x = 80$ m; it then becomes narrower again. Note that at $x = 80$ m only the part of the spectrum at frequencies exceeding the peak value differs notably from that at more distant locations, whereas the low frequency part of the spectrum does not change significantly after few tens of dominant wave lengths λ_0. The effect of widening of the higher frequency part of the spectrum at $x = 80$ m can be distinguished also in Fig. 8.34b. For even wider initial spectral shapes in panels (c) and (d), no such widening is obtained. The results of Fig. 8.34a–d demonstrate that equilibrium spectral shapes are attained in those cases at distances exceeding about $40\lambda_0$. Those equilibrium shapes, however, are not universal and are strongly dependent on the initial spectrum. For the initial JONSWAP spectral shape, panel (d), the high frequency part of the spectrum seems to decay monotonically, and the total power decreases along the tank. Certain wave energy decay in Fig. 8.34d may be attributed to sporadic wave breaking that was observed only for the JONSWAP

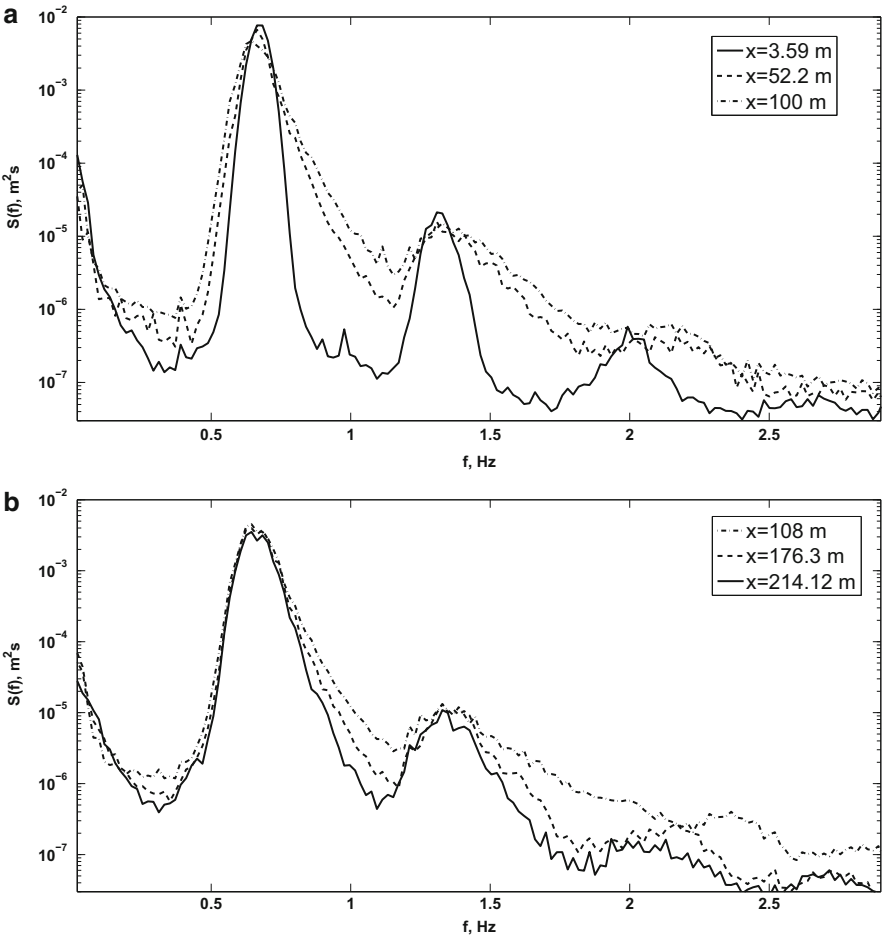

Fig. 8.33 Evolution of the frequency spectrum for the initially Gaussian spectrum with $\nu = 0.045$ and $\epsilon = 0.054$: (**a**) spectrum broadening during the initial stages of the evolution; (**b**) partial relaxation to a narrower spectrum farther away from the wavemaker

spectrum. The characteristic wave frequency ω_m remains nearly constant along the tank with the average value of about 4.22 rad/s for all forcing amplitudes.

The variation of $H_{1/3}$ with the fetch presented in the top panel of Fig. 8.35 indicates that for each forcing amplitude, the significant wave height remains approximately constant. The frequency limits in the Eq. (8.41) are defined by the first minima of $S(f)$ in Fig. 8.33 on both sides of the characteristic frequency $f_0 = \omega_0/2\pi$. As shown in the bottom panel of Fig. 8.35, the spectral width ν varies notably along the tank and does not recover its initial value fully. The widening of the free-wave spectrum around 100 m from the wavemaker causes even

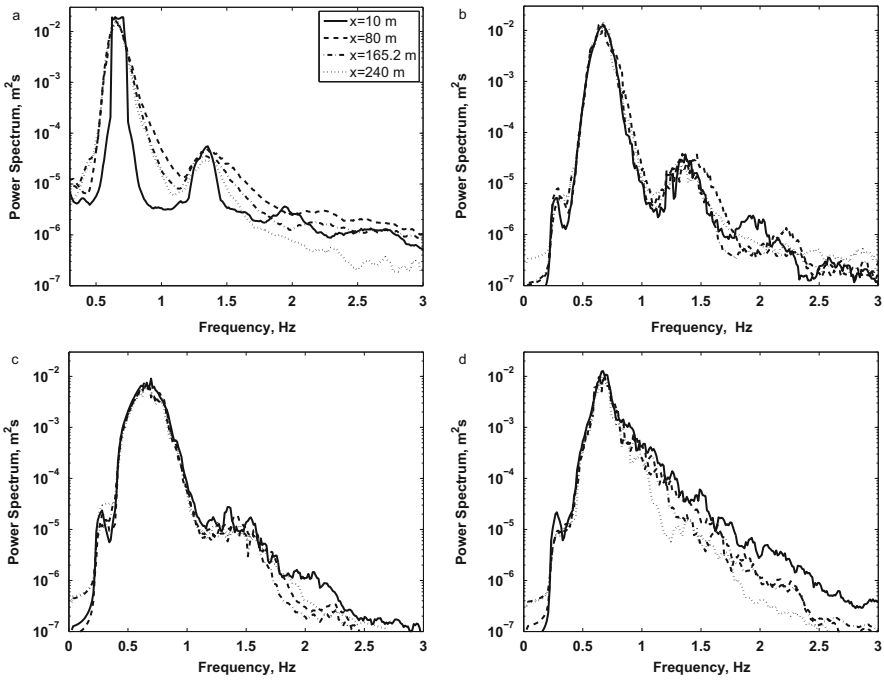

Fig. 8.34 Evolution of the ensemble-averaged wave spectra along the tank, $\epsilon = 0.054$: (**a**) initial rectangular spectrum $\nu = 0.045$; (**b**) initial Gaussian spectrum, $\nu = 0.09$; (**c**) initial Gaussian spectrum, $\nu = 0.16$; (**d**) initial JONSWAP spectrum, $\nu = 0.20$

stronger widening of the bound-wave spectrum complicating the determination of the boundary between the two domains.

It can be clearly seen in Figs. 8.34a–d that the separation of domains of free and second order bound waves changes significantly with the initial spectral width. For narrow spectra the frequency domains corresponding to free and bound waves are clearly separated (Figs. 8.33 and 8.34a) thus making the distinction between those waves relatively simple. The domains around the dominant frequency and its second bound harmonic are still somewhat separated in the case of a wider spectrum in Fig. 8.34b. For even wider spectra, however, the free and the bound waves may have overlapping frequency domains, and the separation between them requires more attention. To extract free wave field from the wave records that apparently contain bound as well as free waves, iterative procedure that was originally implemented for deterministic wave fields with a wide spectrum in Shemer et al. [67] was applied (see also Sect. 8.5.3). For each realization of the prescribed initial spectrum and for each wave gauge, the wave-containing part of the record was divided into 20 s long segments (with 50 % overlap between the consecutive segments), and the separation of free and bound waves was performed for each such segment. Following [67], the measured temporal variation of the surface elevation is taken as the initial guess

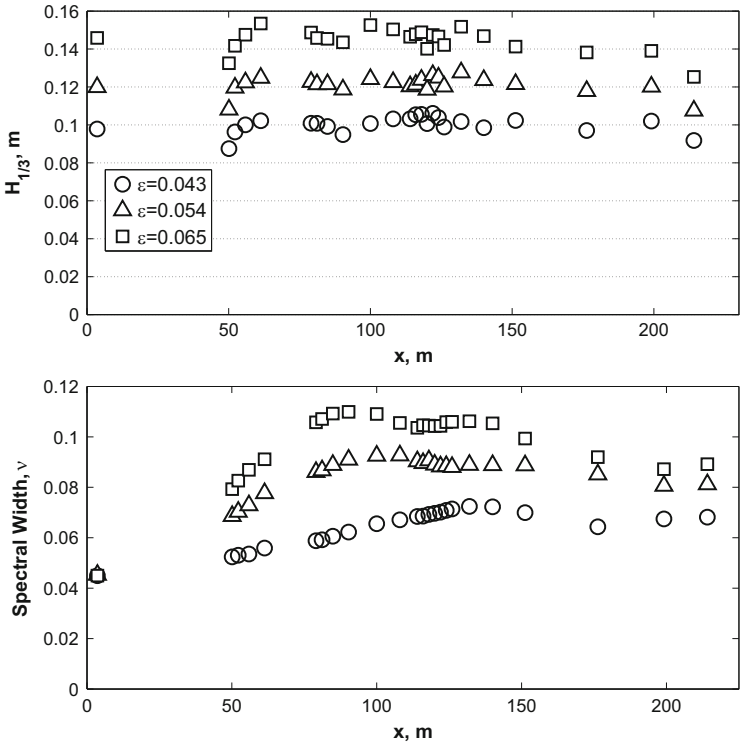

Fig. 8.35 Variation along the tank of the measured significant wave height $H_{1/3}$ (*top panel*) and of the spectral width ν (*bottom panel*). Wave conditions as in Fig. 8.33

of the free wave field. The computed second order bound waves corresponding to this free wave field are then subtracted from the full record, and the result serves as the next approximation of the free waves field. The process converges after few iterations. The wave spectra corresponding to the free and the second order bound waves were calculated for each segment, and then averaged over all segments of all realizations for each gauge separately.

To examine the efficiency of separation of free and bound-wave parts, the third order moment of the surface elevation, the skewness coefficient defined as

$$\lambda_3 = \langle \eta^3 \rangle / \sigma^3 \tag{8.43}$$

was calculated. The values of λ_3 are plotted in Fig. 8.36 for two cases with the initially Gaussian spectral shape and different widths, $\nu = 0.09$ and $\nu = 0.16$. In both cases, the skewness for the free wave field remains very small along the whole tank, as expected. The vanishingly small values of λ_3 corresponding to the computed free wave field serve as an indication that the separation between free and bound waves is performed properly. Contrary to the free wave field, the full wave

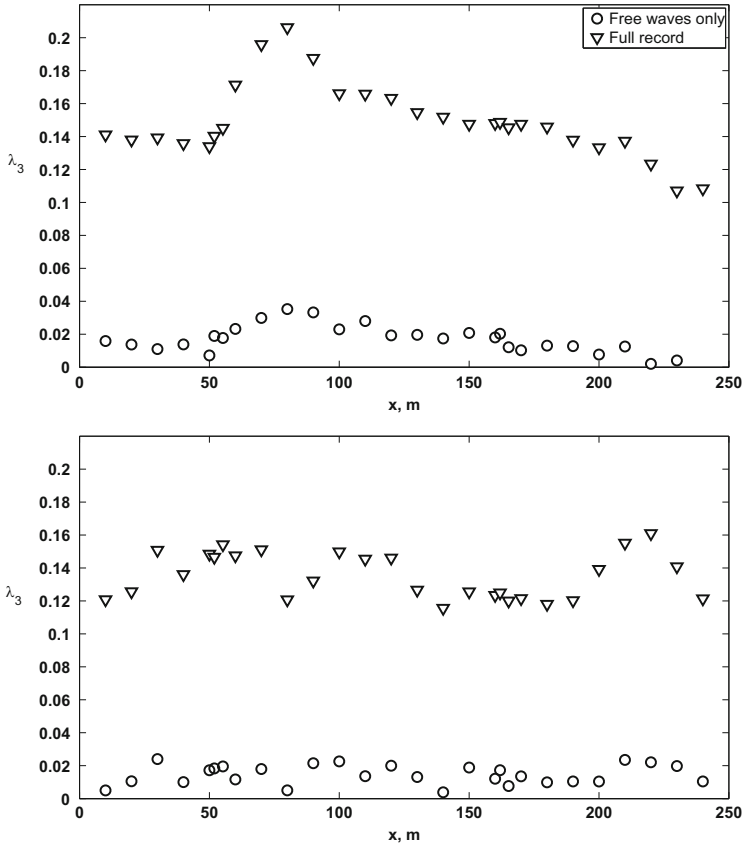

Fig. 8.36 The variation along the tank of the skewness λ_3 for the initial spectra with the Gaussian shape: $\nu = 0.09$—*top panel*; $\nu = 0.16$—*bottom panel*

field exhibits significant positive values of λ_3 that are quite similar for both initial spectral widths along the whole tank, being mostly somewhat below $\lambda_3 = 0.2$. These positive values of λ_3 result from the crest-trough asymmetry of nonlinear waves that apparently is sensitive primarily to the nonlinearity, which is very similar in both panels of Fig. 8.36. The only significant differences between the two panels occurs for an initially narrower spectrum where at about $x = 70$ m the values of λ_3 grow notably to attain maximum that exceeds 0.2. This variation of the skewness coefficient with the distance in the top panel is qualitatively similar to that reported in Shemer and Sergeeva [62] for initially narrower Gaussian spectrum.

The variation along the tank of the spectral width ν computed according to Eqs. (8.40), (8.41), with integration in Eq. (8.41) carried out for the free wave field only, is presented in Fig. 8.37. The variation of ν with the distance x from the wavemaker is virtually identical for both Gaussian and rectangular spectra with identical initial value of $\nu = 0.045$. For this initially very narrow spectrum,

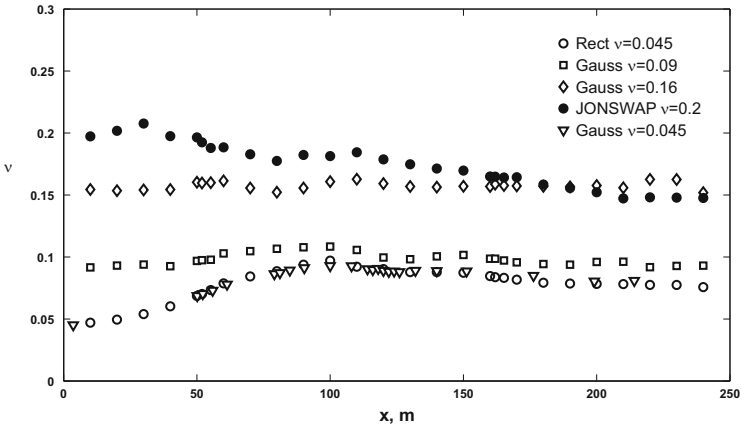

Fig. 8.37 The spectral width ν as a function of the distance from the wavemaker for different initial spectral shapes

the number of discrete free harmonics in the wavemaker driving signal is less than 10 in both cases. The actual difference the initial spectra is thus not very significant, and in fact after about 50 m, the ensemble averaged spectra become essentially identical. The results of Fig. 8.37 are presented for all wave gauges employed and corroborate the qualitative conclusion obtained from observing the spectra in Fig. 8.34 that the evolution of the spectral width along the tank is strongly dependent on the initial values of ν. For all Gaussian shapes considered, as well as for the initially rectangular free wave spectrum, the spectral width seems to attain a quasi-equilibrium value at distances exceeding about 170 m (about $50\lambda_0$) from the wavemaker. Those quasi-equilibrium spectral widths are different for all spectral shapes considered. For initially very narrow spectra with $\nu = 0.045$, the quasi-equilibrium width corresponds to $\nu \approx 0.08$, while for the initially widest Gaussian spectral shape employed in the present experiments, as well as for the JONSWAP spectrum, the far-field value of ν is nearly twice larger, attaining $\nu \approx 0.15$. The evolution of the spectral width of random wave field with the initial spectral shape given by (8.42) (JONSWAP spectrum) is somewhat different from that observed for other initial conditions. The initial width of this spectrum exceeds that of other spectral shapes considered. The values of ν in Fig. 8.37 tend to decrease along the tank, so that at $x > 200$ m the spectral width in this series of experiments falls below values of ν that correspond to the initially narrower Gaussian spectrum. The decrease in the spectral width with the distance seems to be closely related to decay to the level of nonlinearity along the tank as discussed with relation to Fig. 8.34d.

The deviation of the wave field statistics from Gaussianity can be characterized by the fourth momentum, the kurtosis λ_4:

$$\lambda_4 = \langle \eta^4 \rangle / \sigma^4. \tag{8.44}$$

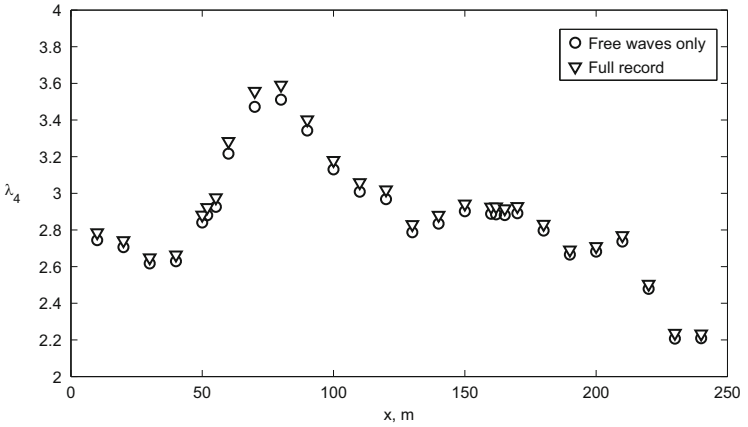

Fig. 8.38 Variation of full and dynamic (for free waves only) kurtosis λ_4 along the tank for the initial Gaussian spectrum, $\nu = 0.16$

For a Gaussian wave field, $\lambda_4 = 3$. The variation of λ_4 with the distance x is plotted in Fig. 8.38 for a Gaussian-shaped initial spectrum. The kurtosis values calculated for the random wave field that contains free waves only do not differ significantly from $\lambda_4(x)$ based on the full wave records. The contribution of second order bound waves to λ_4, although apparently always positive, appears to be insignificant. These observations differ somewhat from the numerical results of Annenkov and Shrira [4] who carried out Monte Carlo simulations of temporal evolution of initially unidirectional wave field using the Zakharov [86] equation. The simulations in [4] were performed for the spectral width similar to that of Fig. 8.38, but for higher nonlinearity of the wave field. Their numerical results indicate that while the part of kurtosis due to free waves only (dubbed in this study the "dynamic" kurtosis following Janssen [20]) is indeed dominant in the determination of the total value of λ_4, the contribution of bound waves nevertheless remains important. The variation of kurtosis along the tank presented in Fig. 8.38 exhibits both similarities and differences with the results of previous studies. In agreement with both [4, 62], during the initial stages of evolution, up to about 70 m (or $20\lambda_0$) the values of kurtosis increase sharply, and decrease farther away from the wavemaker, exhibiting some oscillations. It should be stressed, however, that the deviations of λ_4 from the value of 3 that corresponds to the Gaussian distribution are relatively modest and in most cases do not exceed 0.5. This is in contrast with the results of [4, 62], where the excursions of λ_4 from the value that corresponds to the Gaussian distribution were much more significant. It is also worth noting that starting from about $x = 120$ m, the kurtosis assumes values that are mostly below $\lambda_4 = 3$, thus indicating that deviations from Gaussianity for wider spectra are qualitatively different from those observed for the narrow initial spectrum.

The experimentally determined wave height distributions $F(H)$, normalized by the r.m.s. values of the surface elevation σ, are presented in Fig. 8.39 for the

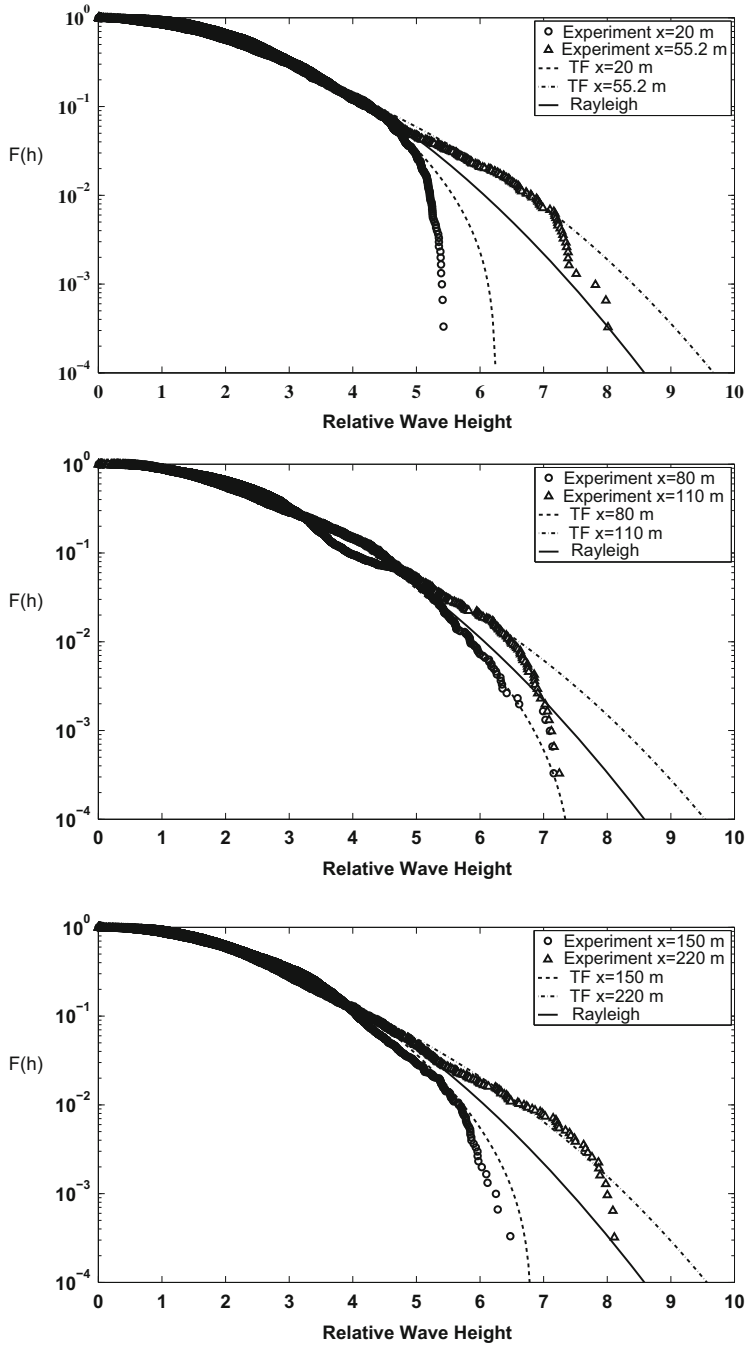

Fig. 8.39 Comparison of the normalized by σ experimentally determined wave height probability distributions with the Rayleigh and the third order Tayfun-Fedele distributions at various locations along the tank for the initially Gaussian spectrum with $\nu = 0.16$

initially Gaussian spectrum with $\nu = 0.16$ at 6 distances from the wavemaker. The experimental results are compared with the Rayleigh distribution, as well as with the distribution developed by Tayfun and Fedele [79] that accounts for the nonlinearities of the third order. The experimental curves do not differ significantly from the Rayleigh distribution, as long as the wave heights do not exceed about 4σ, although some deviations are observed, most prominently at $x = 80$, 150 and 220 m. For higher values of H/σ, deviations of the wave height probability distributions from the Rayleigh shape in both directions seem to be closely related to the local value of λ_4. The measured probability distributions exceed the Rayleigh values when the local kurtosis is above 3, and fall below the corresponding Rayleigh values for $\lambda_3 < 3$. The oscillations of the distribution tails are predicted reasonably well by the Tayfun and Fedele distribution. It should be stressed, however, that the theoretical distribution in most cases seems to over predict the probability of appearance of the steepest waves in the ensemble. A prominent feature of the distributions plotted in Fig. 8.39 is the virtual absence in the accumulated ensemble of waves with heights exceeding 8σ that can be considered as "freak"İ waves. This result is quite different from the distributions presented in Shemer and Sergeeva [62] for a narrow Gaussian-shaped initial spectrum ($\nu = 0.045$), where the probability of extremely high waves was significantly larger than that corresponding to the Rayleigh distribution. Moreover, in the measured distributions plotted in Fig. 8.39 the tail of the distribution that corresponds to the steepest waves in the ensemble turns sharply down. This part of the distribution is in most cases not presented adequately by the Tayfun-Fedele curves. The corresponding distributions for wave crests and troughs are presented in Shemer et al. [69]. Due to the wave asymmetry the crest heights attain higher values that the troughs.

In [68] the advantage was taken of the accumulated in [62, 69] experimental results to examine the accuracy of simulating the spatial evolution of a random unidirectional wave field by nonlinear envelope models. Monte Carlo-type simulations were performed over large scales unique to the GWK. The experimentally determined temporal variation of the surface elevation in the vicinity of the wavemaker in each random-phased realization of the given spectrum was used to derive the corresponding initial condition for numerical simulations. The emphasis is put on the narrow-banded initial Gaussian spectrum with the spectral width of $\nu = 0.045$ and steepness $\epsilon = 0.054$ in order not to deviate too far from the domain of validity of the envelope models.

The accuracy of the envelope model equations for prediction of the spatial evolution of individual wave groups is examined first. As demonstrated in Sects. 8.3 and 8.4, the NLS equation is inadequate to describe evolution of narrow-banded nonlinear deterministic wave groups with symmetric envelopes even for relatively short propagation distances, while the application of the modified NLS, or Dysthe, equation yields considerably better agreement with experiments. In Fig. 8.40 the accuracy of simulations based on these two models is examined on an example of a single realization in the GWK experiments. The contribution of bound waves is accounted for in the numerical simulations. Due to random phases of free harmonics, the group envelope in each realization has an irregular shape. For the

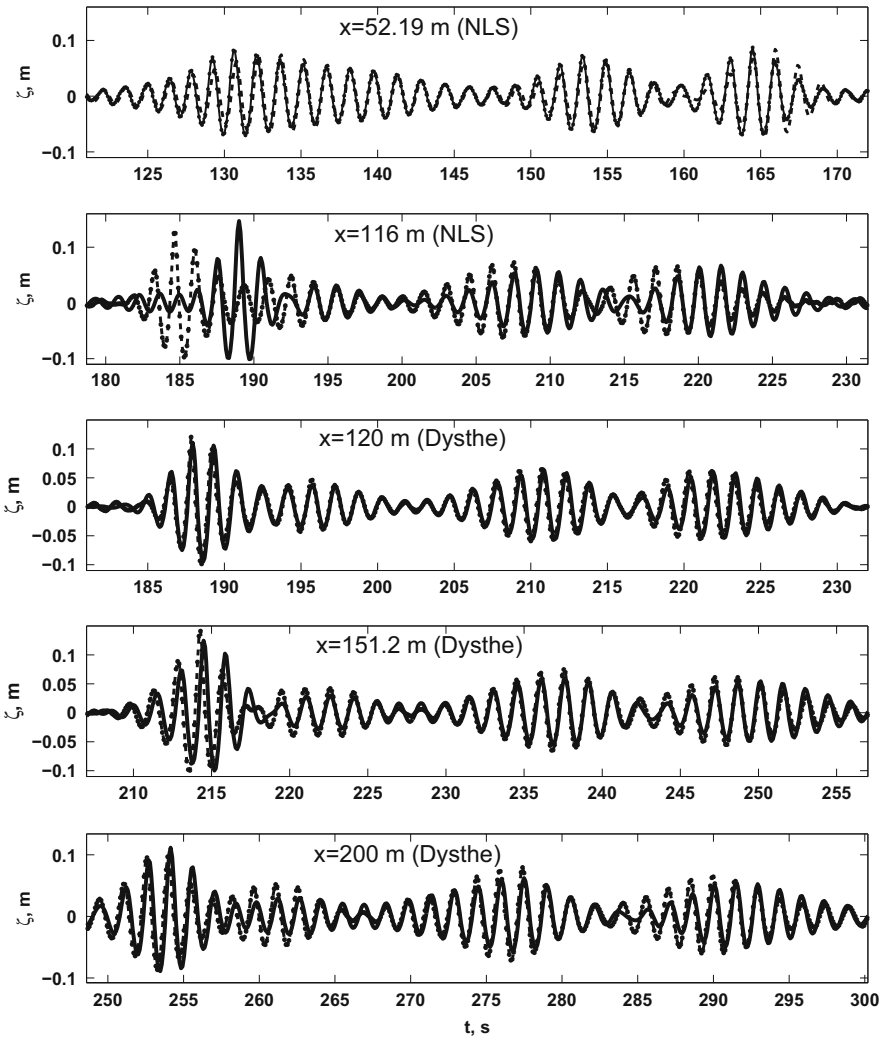

Fig. 8.40 Comparison of the NLS and Dysthe simulations of spatial evolution of a single realization with experiments at various distances from the wavemaker: *broken lines*—experiments; *solid lines*—simulation

NLS simulations, the measured and the computed surface elevations are presented at two distances x from the wavemaker. The results at $x = 52.2$ m show that already at a relatively short distance corresponding to about $15\lambda_0$, notable differences appear between computations and measurements. At a larger distance corresponding to about $33\lambda_0$, any quantitative agreement between the simulated and the measured wave fields practically ceases to exist. Nevertheless, some qualitative features of the group shapes, such as focusing of wave energy visible in the first group at

$x = 116\,\mathrm{m}$, as well the distribution of waves within individual groups, are retained to some extent in the NLS simulations. At even larger distances, any resemblance between the computations and the measurements fades away. The three bottom panels of Fig. 8.40 convincingly demonstrates that the performance of the Dysthe model is far superior to that of the NLS equation. The measured and the computed temporal variation of the surface elevation is presented at 3 distances from the wavemaker, all exceeding the values of x in the two top panels of Fig. 8.40. Excellent qualitative agreement between the simulations and the experiments is obtained for the whole extent of the measurements domain. The results at $x = 120\,\mathrm{m}$ ($\approx 35\lambda_0$) exhibit good quantitative agreement between computations and measurements, although some deviations are visible. The quantitative agreement seems to deteriorate somewhat with the distance.

The statistical quantitative analysis of the deviation of the Dysthe simulations from the experiment carried out in Shemer et al. [68] suggests that the modified NLS model provides a quantitatively accurate description of the deterministic nonlinear wave field up to distances of the order of $O(10^2\lambda_0)$. The results of Fig. 8.40 thus indicate that evolution of an individual realization of a random wave field can be described adequately over large distances by the Dysthe model, whereas the NLS equation is at best appropriate for revealing some qualitative properties of the evolution process.

The relevance of those nonlinear envelope evolution equations to prediction of the statistical properties of the unidirectional random wave field is now considered. The experimental results on variation along the tank of the power spectrum of the surface elevation, which is one of the most important statistical parameters describing random wave field, are compared in Fig. 8.41 with simulations based on both models. The initial spectrum, as measured at $x = 3.59\,\mathrm{m}$, is also plotted as a reference. The free wave part of this spectrum, which is based on the initial group shape given by Eq. (8.4), is also symmetric relative to the carrier wave frequency and has a shape close to Gaussian, as expected. Since the initial spectrum is quite narrow for the value of $m = 3.5$ in Eq. (8.4), the frequency domains of the second and the third order bound waves are clearly separated. The initial spectral shape undergoes fast variations and already at $x = 52.2\,\mathrm{m}$ ($x \approx 15\lambda_0$) the free wave spectrum changes notably. The spectrum becomes wider and develops visible asymmetry. The Dysthe model faithfully describes both these effects, and the agreement between the computed and the measured surface elevation spectrum in the free wave frequency domain remains good at all distances from the wavemaker. In simulations based on the NLS equation the widening of the free waves spectrum is obtained as well. However, the NLS model is incapable to reflect the asymmetry of the developing spectral shape. As noticed in Sect. 8.3, the initially symmetric shape of the group envelope is retained by the NLS equation in the process of evolution. In the experiments described in this section, the symmetry of the envelope of the generating group as given by Eq. (8.4) is lost once random phases are prescribed to the various harmonics. The power spectrum of Eq. (8.4), however, remains symmetric relative to the carrier wave frequency. Since the experiments clearly show that the frequency spectrum loses its symmetry quite fast, the agreement of

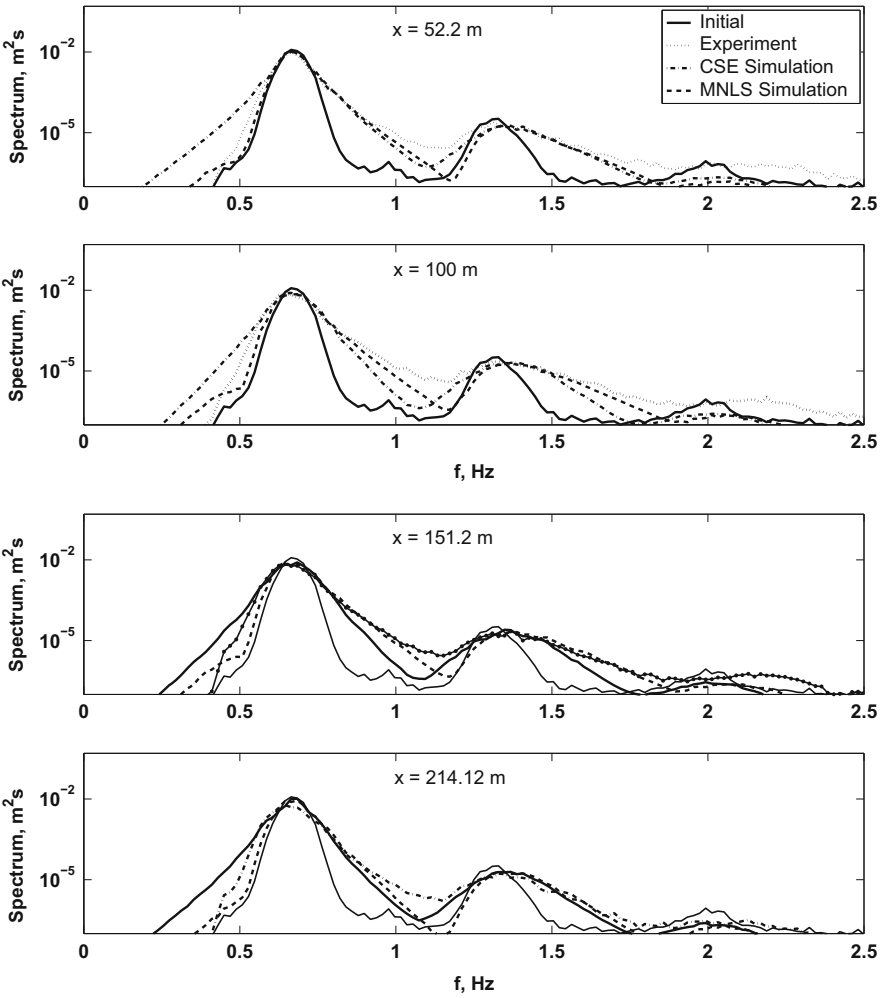

Fig. 8.41 Ensemble averaged spectra: measurements vs. computations using the cubic NLS equation and the Dysthe model

the spectra computed using the NLS equation with the experiments is imperfect, and the NLS-based free wave frequency spectra are significantly wider than either those derived from the Dysthe simulations or the measured ones. The width of the free waves' spectrum seems to attain maximum at distances about 100 m, and then decreases somewhat.

The agreement between the second order bound waves as measured in the experiment and as computed using the Dysthe model is reasonable at all distances from the wavemaker. Those waves have amplitudes that are comparable with the sensitivity of the wave gauges. The simulations based on both models agree quite

well with the measurements around the peak of the second order bound waves (close to 1.3 Hz); away from the peak the Dysthe simulations yield a much better agreement with the experiments than the NLS equation. The dip in the spectrum between the domains of free and second order bound waves is much deeper in simulations than in experiments. This can be attributed to the limited accuracy of the wave gauges.

The results of Figs. 8.40 and 8.41 clearly demonstrate good quantitative and qualitative agreement of the Dysthe model simulations with the experiments for all distances from the wavemaker covered in the GWK experiments, with deviations that can be plausibly attributed to experimental inaccuracies. Such an agreement seems to justify the extension of simulations to distances beyond the domain of experiments in order to gain some insight on the wave field evolution pattern at longer scales. In sequel, the results of simulations are presented for distances exceeding the actual length of the GWK by a factor of 2, whereas the experimental results apparently are only shown where available.

The computed and the derived from the experiments variations with x of the spectral width of the free wave part of the spectrum, ν, as well as of the skewness λ_3 and of kurtosis λ_4 are plotted in Fig. 8.42. The computed values of ν, Fig. 8.42a for both model equations are in a reasonable agreement with the experimental results. Both models correctly predict the experimentally observed spectral widening, with ν increasing nearly twice from its initial value $\nu \approx 0.45$ during the first 100 m of the evolution. The spectral width then decreases somewhat. The simulations farther away from the wavemaker exhibit irregular, relatively weak oscillations of the spectral width (around the mean value of $\nu \approx 0.65$ for the Dysthe model and of $\nu \approx 0.75$ for the NLS model); the characteristic length scale of these oscillations exceeds 100 m, or about $30\lambda_0$.

The variation of the skewness λ_3 along the tank, as measured in the experiment, is compared in Fig. 8.42b with the results of simulations based on both models. The models yield values of λ_3 that are quite close to the measurements. The dependence of λ_3 on the distance x in Fig. 8.42b bears some similarity to the behavior of $\nu(x)$ in the panel (a) of this figure. The skewness coefficient increases quite sharply initially, up to about $x = 100$ m, and then decreases somewhat, exhibiting relatively weak variability at length scales similar to those of Fig. 8.42a. The values of λ_3 were also calculated for the surface elevation records that were band-pass filtered for the free waves' domain, $f_{min} \le f \le f_{max}$. The variation of the skewness coefficient λ_3 that represent free waves only is also plotted in Fig. 8.42b. The values of λ_3 due to free waves are virtually zero at all locations, both in the experiments and in the simulations based on the Dysthe model (similar results obtained within NLS model are not presented). The results of Fig. 8.42b thus demonstrate that skewness, which is determined nearly solely by the contribution of the bound waves, is adequately described by both envelope equations.

Variation of the kurtosis coefficient λ_4 along the tank is presented in Fig. 8.42c. Again, the Dysthe model yields good agreement with the experiments, while the NLS equation significantly overestimates the maximum values of the kurtosis in the transitional domain at about 50 m $< x <$ 120 m. At larger distances the predictions

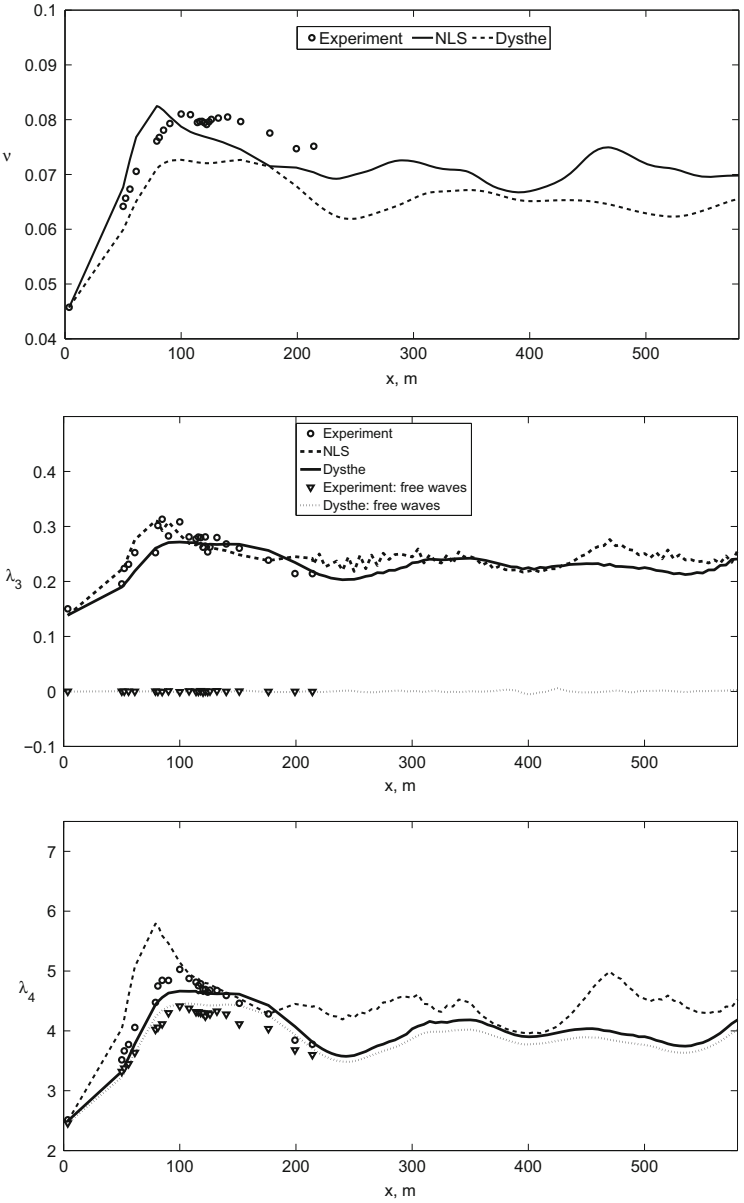

Fig. 8.42 Computed and measured variations along the tank of the spectral width ν (**a**), skewness λ_3 (**b**) and kurtosis λ_4 (**c**)

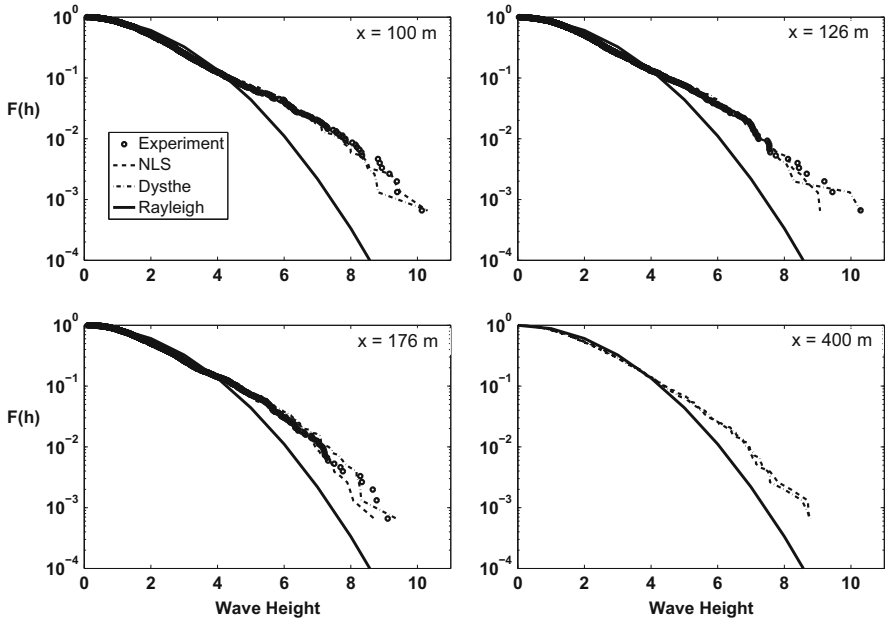

Fig. 8.43 Computed and measured wave height distributions at several distances from the wavemaker for the Gaussian driving signal given by Eq. (8.4) with $m = 3.5$ and $\epsilon = 0.054$

based on both those models seem to be closer, and the computed values of λ_4 vary somewhat (at the characteristic length scale of about 30 carrier wave lengths, similar to other statistical parameters), but remains in the vicinity of $\lambda_4 \approx 4$, indicating that the wave field departs significantly from the Gaussian distribution. As in Fig. 8.38, an attempt is made to separate the "dynamic" kurtosis λ_{4d} based on free waves only. The results at large distances from the wavemaker differ somewhat from those of [4] and do show any substantial difference between λ_{4d} and the full kurtosis λ_4. This discrepancy may be attributed in part to the total lack of 2D effects in the simulations based on the Dysthe model.

Measured and computed from Dysthe and NLS simulations wave height exceedance distributions for different locations along the tank are plotted in Fig. 8.43. The exceedance distributions are normalized by the standard deviation σ of the surface elevation variation. The Rayleigh distribution for the scaled wave height is plotted as well. The wave height exceedance distributions derived from both models agree well with the measured probabilities. In simulations as well as in experiments, the Rayleigh distribution overestimates the exceedance probability for $H < 4\sigma$ and underestimates it for higher values of wave heights. Moreover, the models are capable of providing adequate prediction of probability of appearance of waves with heights below 8σ. Both simulation and the experiment clearly indicate that the probability of those extremely high waves exceeds that corresponding to the Rayleigh distribution by an order of magnitude. Still, since the probability of

such high waves is quite low, spread of data in Fig. 8.43 for $H > 8\sigma$ is evident both for the distributions based on the laboratory data and those obtained from the numerical simulations. This spread seems to be a result of insufficient size of the ensemble. The behavior of the distribution tail in Fig. 8.43 is qualitatively different from the wider spectrum case plotted in Fig. 8.39 where no extremely high waves with $H > 8\sigma$ that may be considered 'rogue' waves were detected. As demonstrated in [69], rogue wave were not recorded ion experiments with even wider JONSWAP spectrum. The correlation between the probability appearance of extremely high waves and kurtosis was demonstrated in that study as well.

8.7 Discussion and Conclusions

The total body of presented experimental and numerical results allows drawing some conclusions regarding mechanisms leading to appearance of extremely steep (rogue) waves. As mentioned in the Introduction, in recent years, the problem of appearance of those waves in the ocean is often related in the literature to specific properties of the NLS equation that admits breather type soliton solutions. As stressed in Sect. 8.3, the NLS equation is the simplest theoretical model describing evolution of unidirectional gravity waves that is valid only for narrow-banded wave groups. The breathing solitons represent spatially, temporally, or both, localized patterns in which an initially small "hump" in a nearly monochromatic wave train is amplified attaining wave heights that exceed significantly the initial level. The wave evolution patterns that are characteristic for the NLS breathers in deep water bear resemblance to appearance of freak waves in the ocean and for that reason attract considerable attention. It was asserted in some studies that different types of breathers were indeed observed in laboratory experiments. On the other hand, Shemer and Alperovich [57] demonstrated that for a Peregrine Breather (PB), the agreement between the experiments and measurements is only obtained at the initial stages of the wave train evolution, (see Sect. 8.4.3). Similar conclusions were obtained in fully nonlinear simulations by Slunyaev and Shrira [71] and by Shemer and Ee [60]. The velocity of propagation of the 'hump' in the PB envelope differs from the linear group velocity c_g as assumed in the NLS equation. Similarly, envelope maxima of other narrow-banded wave groups of different shapes studied in Sects. 8.3–8.5 also propagate with velocity exceeding c_g. The faster movement of the highest crest in the group is correctly described by the modified NLS (Dysthe) equation. The failure of the NLS model to describe adequately the propagation of breathers beyond the initial stages was attributed in Sect. 8.4 to considerable spectral widening associated with amplification of the steepest wave that violates the basic assumptions adopted in the derivation of the NLS equation. The NLS equation results in symmetric shapes, whereas in experiments as well as in the Dysthe simulations essentially asymmetric wave shapes were observed. It should be noted that the fully nonlinear simulations [71] did not show the left-right asymmetry. As demonstrated by Shemer and Dorfman [59], the symmetry of the

spatial distribution may differ from that in the temporal presentation, cf. Figs. 8.8 and 8.10. The numerical simulations carried out in [60] indeed demonstrated that the asymmetry in the spatial 'snapshot' of PB is barely noticeable, whereas in the temporal variation $\zeta(t)$ is becomes more prominent.

The limited validity of the NLS equation thus leads to significant deviation of the PB shape from the NLS solution given by Eq. (8.32) in measurements as well as in more advanced computations based on either Dysthe equation or on the fully nonlinear approach. The question therefore arises whether different solitons indeed represent a special class of wave shapes that differ essentially from non-soliton wave envelopes and constitute prototype of rogue waves as often suggested, see e.g. [70]. In fact, notable amplification of both the maximum wave crests and maximum envelope values occurs in the course of evolution in deep water of initially narrow-banded deterministic wave groups with different initial shapes, see Fig. 8.5 and additional results presented in [21, 64–66]. All characteristic features that often are specifically attributed to the evolution of NLS breathers were in fact observed for a variety of arbitrarily selected initial wave group shapes. The increase of maximum crest height may be seen as manifestation of the focusing properties of the NLS equation. Indeed, no such focusing was observed for experiments conducted in shallower water, when the coefficient of the nonlinear term in the NLS equation nearly vanishes or becomes negative, see Sect. 8.3. Moreover, as demonstrated in [62, 69], initially narrow-banded random-phased wave groups with no characteristic envelope shape also exhibit strong wave height amplification accompanied by significant spectral widening in the process of their evolution along the tank, see Sect. 8.6.

It thus appears that NLS breathers do not possess any special qualities distinct from those of any initially narrow banded wave groups. They seem to be essentially irrelevant to rogue wave formation even in unidirectional and controlled setting of laboratory wave tank experiments. As stressed in [56], all types of breathers, as well as rogue waves that were actually recorded in the ocean, exhibit fast variation of the wave train envelope (on scales comparable with the dominant wave period) and are essentially wide-banded. The emergence of a single high wave can be seen as resulting from a positive interference of numerous harmonics. In this sense, both breathers and rogues waves in the ocean (such as the well-known New Year wave, see e.g [23]) are not different from those observed by focusing of an initially wide-banded unidirectional wave train [67] as presented in Sect. 8.5.3. The relation between the height of the steepest wave in the train of finite duration and the shape of its discrete spectrum can be examined on the basis of simple considerations. For a given complex amplitude spectrum of the surface elevation $a_i = a(\omega_i)$, the crest height cannot exceed the value attained when the phases of all harmonics coincide: $\zeta_{max} = \sum |a_i|$ (perfect coherence). For an initially nearly monochromatic wave with a narrow spectrum, like PB away from the focusing location, the energy is concentrated at the carrier wave frequency, so that the 'hump' does not exceed significantly the background carrier wave and $\eta_{max} \approx |a_{carrier}|$. In the initially narrow spectrum, nonlinear interactions among neighboring harmonics are strong leading to fast widening of the spectrum [55]. The energy conservation at the leading

order requires that at any instant $\sum a_i^2(t) \approx |a_{carrier}(t=0)|^2$. The maximum possible wave corresponding to the sum of the amplitudes of all harmonics in the spectrum thus can be obtained when the wave energy is distributed uniformly among numerous harmonics. In this respect it can be noted that the Dirac δ-functions that can be seen as an ultimate model of a rogue wave, has uniform white spectrum. Therefore in order to obtain a single extremely steep wave in the evolution process, significant spectral widening needs to occur. The rogue wave in deterministic as well as in a random wave field then can be seen a result of an essentially linear constructive interference of numerous harmonics [62, 67, 69]. Note that the relative to the background amplification of the maximum wave crest due to nonlinear focusing as a result of constructive interference may exceed the threefold gain of the Peregrine breather, see Fig. 8.30. The role of nonlinearity in this process is limited to modification of the initial spectrum to the prescribed shape at the focusing locations identical phases of all harmonics.

An even stronger amplification of the steepest wave was recorded in experiments on initially narrow-banded random wave groups by Shemer and Sergeeva [62].The mechanism leading to appearance of rogue waves in that case seems to be similar to that suggested for focusing of deterministic waves. For narrow initial spectrum, a relatively small number of harmonics with close frequencies interact strongly generating new sideband harmonics [55]. The complex amplitudes in the initial spectrum have random phases, however, in each realization the newly generated sideband harmonics have phases related to those of their 'parents'. Once those harmonics grow to be sufficiently strong, the probability of appearance of extreme waves increases due to their intrinsic coherence. Increase in the number of harmonics in the initial spectrum, either by widening or by directional spreading, effectively eliminates this mechanism, resulting in virtual absence of freak waves in those cases, in agreement with experimental observations. Note also that contrary to the instantaneous surface shape that can vary fast due to the change of phases of the harmonics at fast time and space scales, the spectral modifications are essentially nonlinear and thus occur on slow scales. It thus appears that rogue waves constitute an inherently wide-banded phenomenon where separation of slow/fast scales is not applicable. This renders the intrinsically narrow-banded NLS equation inadequate for quantitatively accurate modeling.

In summary, a thorough examination of performance of different unidirectional nonlinear wave models, based on a detailed quantitative comparison of model predictions with extensive experimental results is presented. Deterministic wave groups as well as random wave fields in deep and intermediate-depth water were investigated. Experiments were carried out in two facilities that differ significantly in size and for a wide range of characteristic wave parameters, i.e nonlinearity, spectral width and envelope or spectral shape. The consistent approach was adopted in the experiments in both facilities to make it possible to identify the effect of scaling. Advantages and disadvantages of larger size of the experimental facility are discussed. The dimensionless parameters that determine the effective size of the facility are introduced; under certain conditions, a smaller tank that has

greater flexibility in running experiments can be advantageous for studies of spatial evolution problems due to higher accuracy of results and possibility to carry out large number of experimental runs at a reasonable price. On the other hand, for many applications the absolute (dimensional) wave height is important. In those cases, bigger facilities offer substantial benefits.

An effective method developed for identification of the instantaneous contact line shapes in a sequence of recorded video images allows studying temporal evolution of the instantaneous wave field in the whole tank and thus determination of the wavenumber spectra and of their variation in time. This ability is important for carrying out quantitative comparison of prediction of nonlinear evolution models with the experimental results. The suggested in [59] experimental approach enables studying both the spatial and the temporal evolution of narrow-banded unidirectional wave groups. The essential differences between the temporal and the spatial formulation of the evolution problem are specified in Sect. 8.4.2. The temporal evolution is routinely considered in theoretical studies of water waves based on the Zakharov equation and on fully nonlinear simulations. In laboratory tanks waves evolve in space rather than in time. The shapes of the spectra are apparently quite different in the spatial and temporal formulations; the wave number spectra are twice wider than the corresponding frequency spectra. As specified in [59, 60], direct quantitative comparison of theoretical results based on the temporal evolution approach with experiments is far from being straightforward. For a narrow-bounded spectrum, the group velocity c_g enables simple transition between the spatial and the spatial formulations, as demonstrated by Lo and Mei [32] for the NLS and Dysthe equations. The benefit offered by the NLS equation, however, is limited, as this model is incapable of describing the finer features of the propagating wave group, and may provide quantitative results with reasonable accuracy only as long as the spectrum remains very narrow, Sect. 8.3, or for some statistical parameters, Sect. 8.6. Nevertheless, the applicability of the analytic solution of NLS equation for the Peregrine breather given by Eq. (8.32) to the early stages of wave group evolution was recently utilized by Shemer and Liberzon [61] to study experimentally the inception of a spilling breaker. The modified Dysthe equation that is formally valid as long as the spectral width does not exceed nonlinearity, proved to be a an accurate model for description of the spatial evolution of both deterministic and random deep-water wave groups with moderate spectrum width. However, for an even wider spectrum, the Dysthe equation ceases to be valid.

The Zakharov equation that is free of any restriction on the spectral width is thus the most appropriate third order model for wide-banded wave groups. The modification of the standard temporal version of the Zakharov equation to the form that describes evolution in space is required for quantitative comparison of the theoretical and experimental results. For a wide spectrum, the group velocity is not defined, thus the straightforward transformation used for transition from temporal to spatial evolution formulation for the NLS and Dysthe equations is not applicable. Generalization of the notion of the group velocity for a wide spectrum was suggested in [67] resulting the spatial version of the Zakharov equation given by Eqs. (8.33) and (8.34). The validity of this equation for description of evolution

along an experimental wave tank of nonlinear wave fields with wide spectrum is verified in Sect. 8.5. Experiments were carried out in two very different experimental facilities for deep and intermediate depth water-waves. In particular, the ability to excite focused steep waves at any desired location along the tank was demonstrated. It is shown that the focusing process is accompanied by a notable change of the spectral shape and is thus essentially nonlinear. The modified unidirectional spatial discrete version of the Zakharov equation given by Eq. (8.38) takes into account all quartet interactions among numerous spectral harmonics of the wave field and accounts for viscous dissipation at the tank walls. This equations was proved to be an accurate and effective computational model for description of essentially nonlinear wave fields with no limits on their spectral width in the course propagation along experimental wave tanks.

Acknowledgements The support of this study by Grant # 2010219 from US-Israel Binational Science Foundation is gratefully acknowledged.

References

1. Akhmediev, N.N., Eleonskii, V.M., Kulagin, N.E.: Exact first-order solutions of the nonlinear Schrödinger equation. Theor. Math. Phys. **72**, 809–818 (1987)
2. Annenkov, S.Y., Shrira, V.I.: Direct numerical simulation of downshift and inverse cascade for water wave turbulence. Phys. Rev. Lett. **96**(20), 204501 (2006)
3. Annenkov, S.Y., Shrira V.I.: Role of non-resonant interactions in the evolution of nonlinear random water wave fields. Fluid Mech. **561**, 181–207 (2006)
4. Annenkov, S.Y., Shrira, V.I.: Evolution of kurtosis for wind waves. Geophys. Res. Lett. **36**(13), L13603 (2009)
5. Barnes, T., Peregrine, D.H.: Wave groups approaching a beach: full irrotational flow computations. In: International Conference on Coastal Research in Terms of Large Scale Experiments, Abstracts, Poland, pp. 7–8 (1995)
6. Brinch-Nielsen, U., Jonsson, I.G.: Fourth order evolution equation and stability analysis for Stokes waves on arbitrary water depth. Wave Motion **8**, 455–472 (1986)
7. Brown, M.G., Jensen A.: Experiments on focusing unidirectional water waves. J. Geophys. Res. **106**(C8) 917–16, 928 (2001)
8. Chabchoub, A., Hoffmann N.P., Akhmediev, N.: Rogue wave observation in a water wave tank. Phys. Rev. Lett. **106**, 204502 (2011)
9. Dean, R.G., Dalrymple, R.A.: Water Wave Mechanics for Engineers and Scientists. World Scientific, Singapore (1991)
10. Dorfman, B., Shemer, L.: Video image-based technique for measuring wave field evolution in a laboratory wave tank. In: Guedes Soares, C., Kolev, P. (eds.) Maritime Industry, Ocean Engineering and Coastal Resources, vol. 2, pp. 711–720. Taylor & Francis, London (2007)
11. Dysthe, K.B.: Note on the modification of the nonlinear Schrödinger equation for application to deep water waves. Proc. R. Soc. Lond. **A369**, 105–114 (1979)
12. Flick, R.E., Guza, R.T.: Paddle generated waves in laboratory channels. J. Waterway Port Coast. Ocean Eng. **106**, 79–96 (1980)
13. Goda, Y.: Random Seas and Design of Marine Structures. World Scientific, Singapore (2000)
14. Gramstad, O., Trulsen, K.: Hamiltonian form of the modified nonlinear Schrödinger equation for gravity waves on arbitrary depth. J. Fluid. Mech. **670**, 404–426 (2011)
15. Hahn, S.L.: Hilbert Transforms in Signal Processing. Artech House, Boston (1996)

16. Hasimoto, H., Ono, J.: Nonlinear modulation of gravity waves. J. Phys. Soc. Jpn. **33**, 805–811 (1972)
17. Hasselmann, K.: On the nonlinear energy transfer in a gravity wave spectrum. Part 1. General theory. J. Fluid Mech. **12**, 481–500 (1962)
18. Hasselmann, K., Barnett, T.P, Bouws, E., Carlson, H., Cartwright, D.E., Enke, K., Ewing, J.A., Gienapp, H., Hasselmann, D.E., Krusemann, P., Meerburg, A., Müller, P., Olbers, D.J., Richter, K., Sell, W., Walden, H.: Measurements of wind-wave growth and swell decay during the Joint North Sea. Deutsche Hydrographische Zeitschrift **8**(Suppl A), 1–95 (1973)
19. Hogan, S.J.: The potential form of the fourth-order evolution equation for deep-water gravity-capillary waves. Phys. Fluids **29**, 3479–3480 (1986)
20. Janssen, P.A.E.M.: Nonlinear four-wave interactions and freak waves. J. Phys. Ocean. **33**, 863–884 (2003)
21. Jiao, H.-Y.: Experimental measurements and numerical simulations of nonlinear water-wave groups. Ph.D. Thesis, Tel-Aviv University (1999)
22. Johannessen, T.B., Swan, C.: On the nonlinear dynamics of wave groups produced by the focusing of surface-water waves Proc. R. Soc. **A459**, 1021–1052 (2003)
23. Kharif, C., Pelinovsky, E., Slunyaev, A.: Rogue Waves in the Ocean. Springer, Berlin (2009)
24. Kharif, C., Kraenkel, R., Manna, M., Thomas, R.: The modulational instability in deep water under action of wind and dissipation. J. Fluid Mech. **664**, 138–149 (2010)
25. Kit, E., Shemer, L.: On dissipation coefficients in a wave tank. Acta Mech. **77**, 171–180 (1989)
26. Kit, E., Shemer, L.: Spatial versions of the Zakharov and Dysthe evolution equations for deep water gravity waves. J. Fluid Mech. **450**, 201–205 (2002)
27. Kit, E., Pelinovsky, E., Talipova, T.: Transformation of probability distribution of wind waves in coastal zone. In: Proceedings of the COPEDEC IV, Brazil, pp. 2344–2353 (1995)
28. Kit, E., Shemer, L., Pelinovsky, E., Talipova, T., Eitan, O., Jiao, H.-Y.: Nonlinear wave group evolution in shallow water. J. Waterway Port Coast. Ocean Eng. **126**, 221–228 (2000)
29. Krasitskii, V.P.: On reduced equations in the Hamiltonian theory of weakly nonlinear surface waves. J. Fluid Mech. **272**, 1–20 (1994)
30. Kuznetsov, E.A.: Solitons in a parametrically unstable plasma. Sov. Phys. Dokl. (English Transl.) **22**, 575–577 (1977)
31. Lake, B.M., Yuen, H.C., Rungaldier, H., Ferguson, W.E.: Nonlinear deep-water waves: theory and experiment. Part 2. Evolution of a continuous wave train. J. Fluid Mech. **83**, 49–74 (1977)
32. Lo, E., Mei, C.C.: A numerical study of water-wave modulation based on a higher-order nonlinear Schrödinger equation. J. Fluid Mech. **150**, 395–416 (1985)
33. Longuet-Higgins, M.: On the statistical distribution of the heights of sea waves. J. Mar. Res. **11**, 245–266 (1952)
34. Longuet-Higgins, M.: The effect of nonlinearities on statistical distributions in the theory of sea waves. Fluid Mech. **17**, 459–480 (1963)
35. Longuet-Higgins, M.: The instabilities of gravity waves of finite amplitude in deep water. II. Subharmonics. Proc. R. Soc. Lond. Ser. A **360**, 489–505 (1978)
36. Ma, Y.C.: The perturbed plane wave solutions of the cubic nonlinear Schrödinger equation. Stud. Appl. Math. **60**, 43 (1979)
37. McLean, J.W.: Instabilities of finite amplitude water waves. Fluid Mech. **114**, 331–341 (1982)
38. McLean, J.W., Ma, Y.C., Martin, D.U., Saffman, P.G., Yuen, H.C.: A new type of three-dimensional instability of finite amplitude gravity waves. Phys. Rev. Lett. **46**, 817–820 (1981)
39. Mei, C.C.: The Applied Dynamics of Ocean Surface Waves. World Scientific, Singapore (1989)
40. Melville, W.K.: Wave modulation and breakdown. Fluid Mech. **128**, 489–506 (1983)
41. Mori, N., Onorato, M., Janssen, P.A.E.M., Osborne, A.R., Serio, M.: On the extreme statistics of long-crested deep water waves: theory and experiments. J. Geophys. Res. **112**, C09011 (2007)
42. Nazarenko, S.V.: Wave Turbulence. Springer, Berlin (2011)
43. Naess, A.: On the distribution of crest-to-trough wave heights. Ocean Eng. **12**, 221–234 (1985)

44. Ochi, M.K.: Stochastic analysis and probabilistic prediction of random seas. Adv. Hydrosci. **13**, 217–375 (1982)
45. Onorato, M, Osborne, A.R, Serio, M, Cavaleri, L.: Modulational instability and non-Gaussian statistics in experimental random water-wave trains. Phys. Fluid. **17**, 078101 (2005)
46. Onorato, M, Osborne, A.R, Serio, M, Cavaleri, L., Brandini, C., Stansberg, C.T.: Extreme waves, modulational instability and second order theory: wave flume experiments on irregular waves. Eur. J. Mech. B Fluids **25**, 586–601 (2006)
47. Onorato M., Osborne A.R., Serio M.: On the relation between two numerical methods for the computation of random gravity waves. Eur. J. Mech. B Fluids **26**, 43–48 (2007)
48. Onorato, M., Onorato, M., Cavalieri, L., Fouques, S., Gramstad, O., Jansses, P.A.E.M., Monbaliu, J., Osborne, A.R., Pakozdi, C., Serio, M., Stansberg, C.T., Toffoli, A., Trulsen, K.: Statistical properties of mechanically generated surface gravity waves: a laboratory experiment in a three-dimensional wave basin. J. Fluid Mech. **627**, 235–257 (2009)
49. Pelinovsky, E., Kharif, C.: Simplified model of the freak wave formation from the random wave field. In: Miloh, T., Zilman, G. (eds.) Proceedings of 15th International Workshop on Water Waves and Floating Bodies, Caesaria, pp. 142–145 (2000)
50. Peregrine, D.H.: Water waves, nonlinear Schrödinger equations and their solutions. J. Aust. Math. Soc. Ser. B **25**, 16–43 (1983)
51. Phillips, O.M.: On the dynamics of unsteady gravity waves of finite amplitude. Part 1. The elementary interactions. J. Fluid Mech. **9**, 193–217 (1960)
52. Phillips, O.M.: Wave interactions: the evolution of an idea. Fluid Mech. **106**, 215–227 (1981)
53. Schäffer, H.A.: Second order wavemaker theory for irregular waves. Ocean Eng. **23**, 47–88 (1996)
54. Shahul Hameed, T.S., Baba, M.: Wave height distribution in shallow water. Ocean Eng. **12**, 309–319 (1985)
55. Shemer, L: On Benjamin-Feir instability and evolution of a nonlinear wave with finite-amplitude sidebands. Nat. Hazards Earth Syst. Sci. **10**, 2421–2427 (2010)
56. Shemer, L.: The advantages and limitations of the nonlinear Schrödinger equation in description of evolution of nonlinear water-wave groups. Proc. Est. Acad. Sci. **64**(3), 17 (2015)
57. Shemer, L., Alperovich, L.: Peregrine breather revisited. Phys. Fluids **25**(1) 051701 (2013)
58. Shemer, L., Chamesse, M.: Experiments on nonlinear gravity-capillary waves. Fluid Mech. **380**, 205–232 (1999)
59. Shemer, L., Dorfman, B.: Experimental and numerical study of spatial and temporal evolution of nonlinear wave groups. Nonlinear Process. Geophys. **15**, 931–942 (2008)
60. Shemer, L., Ee, B.K.: Steep unidirectional wave groups - fully nonlinear simulations vs. experiments. Proc. 34th Int. Conf. on Offshore Mechanics and Arctic Engineering, St. John's, Newfoundland, Canada (ASME Paper OMAE2015-41057)
61. Shemer, L., Liberzon, D.: Lagrangian kinematics of steep waves up to the inception of a spilling breaker. Phys. Fluids **26**(1), 016601 (2014)
62. Shemer, L., Sergeeva, A.: An experimental study of spatial evolution of statistical parameters in a unidirectional narrow-banded random wavefield. J. Geophys. Res. **114**, C01015 (2009)
63. Shemer, L., Kit, E., Miloh, T.: Measurements of two- and three-dimensional waves in a channel including the vicinity of cut-off frequencies. Exp. Fluids **5**, 66–72 (1987)
64. Shemer, L., Kit, E., Jiao, H.-Y, Eitan, O.: Experiments on nonlinear wave groups in intermediate water depth. J. Waterway Port Coast. Ocean Eng. **124**, 320–327 (1998)
65. Shemer, L., Jiao, H.-Y., Kit, E., Agnon, Y.: Evolution of a nonlinear wave field along a tank: experiments and numerical simulations based on the spatial Zakharov equation. Fluid Mech. **427**, 107–129 (2001)
66. Shemer, L., Kit, E., Jiao, H.-Y.: An experimental and numerical study of the spatial evolution of unidirectional nonlinear water-wave groups. Phys. Fluids **14**, 3380–3390 (2002)
67. Shemer, L., Goulitski, K., Kit, E.: Evolution of wide-spectrum wave groups in a tank: an experimental and numerical study. Eur. J. Mech. B Fluids **26**, 193 (2007)

68. Shemer, L., Sergeeva, A., Slunyaev, A.: Applicability of envelope model equations for simulation of narrow-spectrum unidirectional random field evolution: experimental validation. Phys. Fluids **22**, 011601 (2010)
69. Shemer, L., Sergeeva, A., Liberzon, D.: Effect of the initial spectrum on the spatial evolution of statistics of unidirectional nonlinear random waves. J. Geophys. Res. **115**, C12039 (2010)
70. Shrira, V.I., Geogjaev, V.V.: What makes the Peregrine soliton so special as a prototype of freak waves? J. Eng. Math. **67**, 11–22 (2010)
71. Slunyaev, V.V., Shrira, V.I.: On the highest non-breaking wave in a group: fully nonlinear water wave breathers versus weakly nonlinear theory. Fluid Mech. **735**, 203–248 (2013)
72. Socquet-Juglard, H., Dysthe, K, Trulsen, K., Krogstad, H.E., Liu, J.: Distribution of surface gravity waves during spectral changes. Fluid Mech. **542**, 195–216 (2005)
73. Stiassnie, M.: Note on the modified nonlinear Schrödinger equation for deep water waves. Wave Motion **6**, 431–433 (1984)
74. Stiassnie, M., Shemer, L.: On modifications of the Zakharov equation for surface gravity waves. Fluid Mech. **143**, 47–67 (1984)
75. Stiassnie, M., Shemer, L.: On the interaction of four water-waves. Wave Motion **41**, 307–328 (2005)
76. Su, M.Y.: Evolution of groups of gravity waves with moderate to high steepness. Phys. Fluids **25**, 2167–2174 (1982)
77. Tayfun, M.A.: Narrow-band nonlinear sea waves. J. Geophys. Res. **85**(C3), 1548–1552 (1980)
78. Tayfun, M.A.: Statistics of nonlinear wave crests and groups. Ocean Eng. **33**, 1589–1622 (2006)
79. Tayfun, M.A., Fedele, F.: Wave height distributions and nonlinear effects. Ocean Eng. **34**, 1631–1649 (2007)
80. Trulsen, K., Dysthe, K.B.: A modified nonlinear Schrödinger equation for broader bandwidth gravity waves on deep water. Wave Motion **24**, 281–289 (1996)
81. Trulsen, K., Dysthe, K.B.: Frequency downshift in three-dimensional wave trains in a deep basin. Fluid Mech. **352**, 359–373 (1997)
82. Trulsen, K., Kliakhandler, I., Dysthe, K.B., Velarde, M.G.: On weakly nonlinear modulation of waves on deep water. Phys. Fluids **12**, 2432–2437 (2000)
83. Waseda, T., Kinishita, T., Tamura, H.: Evolution of a random directional wave and freak wave occurrence. J. Phys. Ocean **39**, 621–639 (2009)
84. Yuen, H.C., Lake, B.M.: Nonlinear deep water waves: theory and experiment. Phys. Fluids **18**, 956–960 (1975)
85. Yuen, H.C., Lake, B.M.: Nonlinear dynamics of deep water gravity waves. Adv. Appl. Mech. **22**, 67–229 (1982)
86. Zakharov, V.E.: Stability of periodic waves of finite amplitude on a surface of deep fluid. J. Appl. Mech. Tech. Phys. (English Transl.) **2**, 190–194 (1968)
87. Zakharov, V.: Statistical theory of gravity and capillary waves on the surface of a finite-depth fluid. Eur. J. Mech. B Fluids **18**, 327–344 (1999)
88. Zakharov, V.E., Shabat, A.B.: Exact theory of two-dimensional self-focusing and one-dimensional self-modulation of waves in nonlinear media. Sov. Phys. JETP **34**, 62–69 (1972)

Index

A
Akhmediev breather, 239

B
Benjamin–Feir instability, v, 13, 118, 128, 149, 245
Benjamin–Oro equation, 15, 84, 117, 119–122, 124, 129
Bolzman kinetic equation, 7
Boussinesq equation, 136, 140, 146, 198, 205
Breather, 2, 15, 136–142, 144–146, 148, 149, 239–244, 286–289

C
Canonical variable(s), 5, 15, 16, 168, 170, 174, 175, 184–186, 192
Capillary waves, 2, 6
Carrier wave, 13, 14, 92, 93, 95, 96, 181, 214, 216–220, 240, 242, 244, 246, 247, 250–253, 258, 259, 262–266, 268, 270, 271, 281, 285, 287
Charney–Hasegawa–Mima (CHM) equation, 11, 22, 28–32, 38, 40
Chen–Lee–Liu equation (CLL), 148
CHM equation. *See* Charney–Hasegawa–Mima (CHM) equation
CLL. *See* Chen–Lee–Liu equation (CLL)
Conservation law, 109, 163, 184
Cross-phase modulation (XPM), 147

D
Davey–Stewartson system, 148
Demodulation, 225
Detuned resonance, 8–11, 72–73. *See also* Near-resonant interactions
Dispersion, 59, 83, 84, 107, 109, 116–118, 121, 122, 128, 130, 146, 147, 182, 190, 212, 213, 217, 225, 226, 251, 257, 265
Dispersion function
  linear, 11, 92
  nonlinear, 11, 94–98
Dispersion relation, 4, 23, 28, 86, 92–95, 97, 107–109, 117, 118, 122, 142, 143, 148, 154, 174, 176, 179, 206, 216–218, 237
  linear, 11, 12, 140, 141, 143, 238
  nonlinear, 7, 10, 11, 92, 95
Dissipation, 7, 10, 11, 14, 15, 23, 26–28, 36–40, 109, 130, 155, 161, 186, 211–213, 225, 261, 262, 265, 268, 290
Dysthe equation, 149, 198, 213, 226–246, 248, 279, 280, 286, 287, 289

E
Effective equation, 11, 22–26, 29, 32, 38–40
  method, 21–40
Energy conservation, 6, 7, 11, 190, 212, 287–288
Energy exchange, 9, 13, 22, 73, 257
Energy spectrum, 5, 7, 11, 40, 249
  Kolmogorov–Zakharov, 7
  power law of, 7–8, 32–38
Energy transport, 26, 27, 44, 190–191, 255
Envelope approximation, 155
Envelope equation, 155, 156, 173, 178, 180–184, 193, 283

E. Tobisch (ed.), *New Approaches to Nonlinear Waves*, Lecture Notes in Physics 908, DOI 10.1007/978-3-319-20690-5

Envelope "fast," 156
Envelope "slow," 155, 160, 193
Equation of motion, 169, 191
Euler–Lagrange equations, 198, 201, 204, 206

F
Floquet–Bloch theory, 100, 118
Fourier analysis, 125, 240
Fourier coefficients, 27, 179
Fourier harmonic(s), 3
Fourier multiplier, 117
Fourier space, 3, 7, 11, 14, 245
Fourier spectrum, 11
Fourier transform, 1, 158, 246
Four-wave system, 2, 6–8
Freak waves, 14, 197, 211, 239, 258, 269, 286, 288

G
Gardner equation, 15, 85
Gardner–Zakharov–Faddeev (GZF) bracket, 169, 173–176, 183
Group envelope, 217, 219, 223–226, 228, 232, 237, 250, 251, 259, 279, 281
Group velocity dispersion (GVD), 181
GZF bracket. *See* Gardner–Zakharov–Faddeev (GZF) bracket

H
HAM. *See* Homotopy analysis method (HAM)
Hamiltonian, 16, 22, 39, 91, 155, 161, 163–166, 169, 171, 173, 174, 176, 183, 186, 187, 189–192, 198, 201, 245
  equation, 16, 38, 164–167, 169, 171–174, 183, 191, 193
  formalism, 16, 245
  framework, 14, 16, 153–193
  functional, 16
  variable, 15, 184
Hilbert transform, 117, 158, 219–222, 224, 241
Hirota equation, 146, 147
Hirota method, 141, 144
Hirota–Satsuma model, 15, 142–145
Homotopy analysis method (HAM), 12, 13, 45–52, 68, 69, 79, 80

I
Inertial interval, 3, 7–8, 37
Instability, 13, 14, 84, 99, 245
Integrable equation, 2, 15, 84, 117, 130, 136, 137, 146, 182
Integral of motion, 163, 164, 169, 186, 190
Inverse scattering transform (IST), 1, 2, 136

J
Jacobi elliptic function(s), 5, 87
JONSWAP spectrum, 205, 215, 270–273, 276, 286

K
Kadomtsev–Petviashvili equation, 1
Kaup–Newell equation (KN), 148
KdV modified, 14, 15, 84, 85, 87–89, 113–115, 117, 121, 129, 138, 143, 146, 154–155
  defocusing, 87–89, 113–115, 136
  focusing, 87–89, 113–115
KdV-type equation(s), 2, 15, 84, 130
Korteweg-de Vries equation (KdV), 1, 14, 15, 84–91, 101–109, 112–115, 117, 118, 120, 122, 129, 130, 136–140, 142, 143, 145, 146, 155, 171, 198, 225
  extended, 15, 116, 130, 136–140, 145
  fractional, 84, 117, 122, 128–129
  integrable, 15, 113, 117, 137

L
Lagrange–Cauchy equation, 200
Lagrange multipliers, 202
Lagrangian, 15–16, 202, 206
  density, 201, 202, 204, 205
  framework, 16
  of Luke, 198, 201, 206
Laplace equation, 52, 74, 200
Large Wave Channel in Hanover, Germany (GWK), 214, 258, 269
Long-wave model, 15, 146

M
Manakov model, 146, 147
Maxwell equation, 154, 155, 176, 180, 189
Mode
  Fourier, 7, 21, 22, 28
  frozen, 6
  non-resonant, 6, 7
  resonant, 7, 13
Modulation, 2, 83, 135, 158, 205, 216

Modulation/modulational instability (MI), v, 2, 13–15, 83–130, 135–149
Monte–Carlo simulations, 213, 277

N
Near-resonant interactions, 213, 245
NLS. *See* Nonlinear Schrödinger equation (NLS)
Nonlinearity, vi, 1, 4, 9, 10, 12, 14, 16, 21–26, 29, 33, 38, 40, 45, 46, 74, 76–79, 85, 86, 89, 91, 97, 110, 111, 115, 117, 118, 122–123, 129, 146–148, 158, 160, 174, 180, 188, 190, 212, 213, 222, 232, 235, 259–261, 265, 268–271, 275–277, 279, 288, 289
Nonlinear Schrödinger equation (NLS), vi, 1, 2, 11, 14–16, 27–30, 32–38, 40, 135–137, 141, 143, 146, 148, 149, 173, 179, 182, 213, 215, 217–219, 223–227, 229, 230, 234, 239–245, 268, 279–283, 285–289
  cubic, 27, 282
  focusing, 14, 15
  higher-dimensional, 28, 29
  modified (mNLS), 213, 226, 227, 242, 244, 245
  non-focusing, 14
Nonlinear Schrödinger equation generalized (gNLS), 16, 173, 179, 180, 182, 184, 189–193
Nonlocal dispersion, 84, 116–129
Non-resonant interaction, 8, 9, 212
Non-resonant (nonresonant) term, 25, 168, 189

O
ODE. *See* Ordinary differential equation (ODE)
Ordinary differential equation (ODE), 2, 85, 88, 99, 120, 248
Ornstein–Uhlenbeck equation, 39

P
Partial differential equation (PDE), v, 1, 2, 4–6, 10, 11, 13, 21, 22, 26, 40, 54, 97, 109
  Hamiltonian, 22
  stochastically averaged, 11
  weakly nonlinear, 4, 21, 40
PB. *See* Peregrine breather (PB)
PDE. *See* Partial differential equation (PDE)
Peregrine breather (PB), 136, 146, 149, 239–244, 286–289
Perturbation, 4, 12, 21, 47, 49, 50, 69, 73–74, 79, 97–99, 101, 103, 105, 121, 125, 146, 147, 161, 197–208
  long wavelength, 101
  nonlocalized, 109
  technique, 44, 45, 50, 198
  theory, 44, 74, 79, 101, 104, 105, 168, 208
Poisson bracket, 161–176

Q
Quasi-resonance, 8–10

R
Random phase approximation, 212
Rayleigh distribution, 269, 271, 279, 285
Regime, 10, 24, 107, 115, 117, 118, 146–148, 218
  discrete, vi, 3, 5, 10–12
  kinetic, vi, 3, 5, 10–12
  weakly nonlinear, 23
Relaxed variational principle (RVP), 16, 208
Resonance, 2, 22, 44, 141, 160, 212
  cluster, 6–7, 10, 11, 38–40
  condition(s), 4–6, 8, 13, 25, 27, 30, 59, 189
  exact, 9–11, 46, 79, 201, 213
  Phillips criterion, 79
Resonant quartet(s), 13, 59–67
  coupled, 45, 63, 65–66, 80
Resonant set, 25, 26, 28, 29, 69
Resonant term, 22, 24, 25
Resonant triad, 6, 9, 31
Rogue wave, 135–149, 154, 211, 214, 239, 257, 286–288. *See also* Freak waves
RVP. *See* Relaxed variational principle (RVP)

S
Sasa–Satsuma equation, 146, 147
Self-phase modulation (SPM), 147
Serre equation, 203–205, 207
Shallow water, 14, 15, 17, 122–123, 135–149, 198, 203–205, 207, 216, 217, 219, 225
Shamel equation, 15
Sideband, 84, 149, 215, 288
Sine–Gordon equation, 155
Slowly varying envelope approximation (SVEA), 155, 156, 159
Small parameter, 1, 2, 4, 7, 11, 12, 22, 37, 51, 198, 207, 208

Soliton, 1, 2, 87, 138, 139, 154–156, 215, 224–225, 239, 242, 244, 286, 287
Spatial formulation, 228, 229, 289
SPM. *See* Self-phase modulation (SPM)
Stability, 2, 45, 84, 136
Steady state, 43–80
Steady-state class-I Bragg resonant waves, 71–79
Steady-state resonance, 45, 59, 70, 71
Steady-state resonant quartet, 12
Steady-state resonant waves, multiple, 45, 46, 58, 59, 67, 69, 71
Steady-state wave spectra, 46, 79
Stokes wave, 14, 84, 245
  instability, 13, 118
  nonlinear, 13, 245
Supercontinuum, 160, 190
Surface water waves, 2, 12–14, 117, 122, 149, 197, 200
SVEA. *See* Slowly varying envelope approximation (SVEA)

T
Tel-Aviv University (TAU) wave tank, 214, 239, 246, 248, 258, 262, 265–268
Temporal formulation, 228, 231–232, 235, 289
Three-wave system, 2, 5–8
Time scale, 4, 6–8, 10, 11, 23–25, 93, 101, 155, 231
  separation, 11
Traveling wave, 84–92, 94–96, 110, 112–115, 118–124, 127–129, 206
  instability, 15, 84, 110, 111, 130
  stability, 86, 97, 98, 110, 111, 130

V
Variables
  action-angle, 91
  canonic, 5
  slow, 93–96
Variational method, 208

W
Water waves, v, vi, 2, 12–16, 43–80, 84, 85, 117, 118, 122–123, 135, 140, 146, 149, 197–208, 211–213, 219, 226, 238, 239, 245, 270, 289
Wave group, 149, 205, 213, 215–226, 230–232, 235, 237, 239, 241, 244, 248, 251, 257–268, 279, 286–289
3-Wave interaction, 2
4-Wave interaction, 2
Wave kinetic (WK) equation, 2, 3, 5, 7, 32, 33, 36
Wave resonance, 2, 6
Waves
  in deep water, 2, 14, 44–46, 52, 56, 58–69, 78–80, 84, 117, 146, 205, 212, 215, 217, 223, 225, 226, 237, 250, 258, 262, 265, 286, 287, 289
  in finite water depth, 70
Wave spectrum
  narrow-band, 206, 207
  wide, 235, 244, 265–266
Wave steepness, 212, 224, 225, 227, 231, 239–240, 245, 250, 251, 262, 264–266, 268
3-Wave system, 2, 5–8
4-Wave system, 2, 6–8
Wave turbulence (WT)
  discrete, 3–7, 11
  frozen, 3
  kinetic, 3, 5, 7, 11
Weakly nonlinear system, 2, 3, 6, 7, 10, 11
Weak/wave turbulence theory (WTT), 2–7, 11, 14, 36
Whitham equation, 15, 84, 117, 118, 122–129
Whitham's modulation theory, 84, 86, 92–98, 108–110, 130
WK equation. *See* Wave kinetic (WK) equation
WT. *See* Wave turbulence (WT)

X
XPM. *See* Cross-phase modulation (XPM)

Z
Zakharov equation, 2, 45, 71, 213, 226, 227, 229, 245, 246, 248, 250–255, 266, 277, 289, 290
  spatial, 245–269
Zakharov transformation, 37